35

Antarctic Sea-Ice Extent, Southern Hemisphere Circulation and South African Rainfall

Debra Alison Hudson

Thesis Presented for the Degree of

DOCTOR OF PHILOSOPHY

in the Department of Environmental and Geographical Science

UNIVERSITY OF CAPE TOWN

October 1998

ABSTRACT

Antarctic Sea-Ice Extent, Southern Hemisphere Circulation and South African Rainfall

The study examines the response of an atmospheric general circulation model (GCM) to a reduction in Antarctic sea-ice extent during summer and winter, with emphasis on non-polar and southern African climates.

Following an evaluation of the GCM, the control and perturbation simulations are analysed. The controls are forced by prescribed, observed sea surface temperatures (SSTs) and sea-ice extents, while in the perturbation simulations sea-ice is reduced and replaced with SSTs. The introduced anomalies are derived from an algorithm based on observed ice variability. The simulations are restarts of an AMIP (Atmospheric Model Intercomparison Project) configured simulation, and two summers (1979/80 and 1984/85) and two winters (1980 and 1985) have been selected for the study. Three replicates have been performed for each time period for both the control and perturbation conditions.

The results show that the atmospheric response is sensitive to the positioning and magnitude of the introduced anomalies. In summer the response is more zonally uniform, and consistent between 1980 and 1985 than in winter. The sea-ice reduction produces an increase in surface air temperature, and sensible and latent heat fluxes over the anomalies in both seasons. There is also a general decrease in sea level pressure at high latitudes, and an increase in midlatitude cyclone densities around 60°S. In summer there is increased subsidence between 30°S and 50°S, and in winter there is a southward shift of the Hadley Cell over the western Pacific, but a northward shift of pressure systems over the Atlantic. In both seasons, there is a general increase in 500 hPa wind speeds in middle to high latitudes (~50°S - 65°S) and a reduction in wind speeds to the north of this (~30°S - 40°S), although this change is less uniform in winter. The perturbation produces a reduction in the amplitude of Rossby wave number 1 in both seasons, related to reduced asymmetry of the SST distribution around the pole in the perturbations. In winter, the amplitude of wave number 3 increases and undergoes a phase shift, triggered by the large sea-ice perturbation in the Atlantic sector. The results show that the atmosphere is quite sensitive to relatively small ice changes.

Regional-scale precipitation over South Africa is derived from the GCM using empirical downscaling. In summer the sea-ice perturbation causes a decrease in rainfall over the north-east coast, and an increase in rainfall over the interior of the country. In winter there is an increase in precipitation over the west and south coasts. In both seasons the precipitation response is small, but the physically plausible and similar nature of the changes in 1980 and 1985 lends credence to the results and suggests that an Antarctic sea-ice anomaly has the potential to alter circulation patterns and precipitation over the South African region.

Debra Alison Hudson **University of Cape Town**
October 1998

for

my parents and Paul

PREFACE

There is little doubt that Antarctic sea-ice is of considerable importance in determining the climate at high latitudes. The large seasonal variation of sea-ice is such that it virtually doubles the size of the Antarctic continent during winter (Carleton, 1992), thus having a profound effect on climate dynamics and energy balances. Little is known, however, of the impact that Antarctic sea-ice anomalies have on the climates of lower latitudes. Even at polar latitudes, the non-linear and complex nature of sea-ice atmosphere interactions, together with a lack of observational data, has to some extent hampered investigations of the interplay between these two components of the climate system. Hanna (1996, p373) notes that "sea-ice climatic feedbacks are crucial and more complex than hitherto believed". The present research is a modelling study which examines the effect that a reduced Antarctic sea-ice extent has on the climate of the Southern Hemisphere, especially non-polar climates. A particular focus is to investigate the regional response of circulation dynamics over southern Africa to a reduction in sea-ice extent, and to assess whether sea-ice anomalies have the potential to influence precipitation over South Africa.

The research is approached from a climatological, rather than meteorological, perspective. Although there is a large degree of overlap between meteorology and climatology, there are some fundamental differences. Meteorology deals primarily with the study of the physics of weather processes. Climatology, on the other hand, is concerned with longer time scales than meteorology, for example time periods extending from months to centuries, and is the study of the aggregate effect of weather phenomena, thus investigating average and extreme conditions, as well as variability within the system.

The study is presented in 4 sections, encompassing 10 chapters. **Section I** is an introductory section containing three chapters. Within this section, **Chapter 1** provides background information concerning the current state of knowledge of sea-ice atmosphere interactions. In addition, the use of General Circulation Models is discussed, and previous modelling studies which have examined the influence of anomalies of Antarctic sea-ice on the atmosphere are described. The chapter also introduces the concept behind the technique of downscaling, which is used to facilitate a regional analysis of precipitation over South Africa. Finally, the major objectives of the research are outlined. **Chapter 2** describes the observed and model

data sets used in the study, as well as details of the GENESIS General Circulation Model. An account of the analysis and statistical tools that are used is provided in **Chapter 3**.

Section II encompasses a single chapter, **Chapter 4**, which is concerned with the evaluation of the present-day, control simulation of the GENESIS General Circulation Model against observed data. This simulation is used as the control in the sea-ice perturbation section of the study. Thus, the reliability of the results from the experiment simulations will be partially related to the model's ability to simulate present-day conditions.

Section III is the largest section, comprising 5 chapters, and is concerned with the sea-ice extent reduction experiments. **Chapter 5** provides a description of an algorithm, which has been developed in the present study to obtain the anomalous sea-ice fields for the perturbation experiments. The experimental design and nature of the model simulations are also discussed. An analysis of the results of the summer season sea-ice perturbations on the Southern Hemisphere climate is presented in **Chapter 6**, while **Chapter 7** focuses on the regional response of the climate over southern Africa, including an assessment of the implication of a sea-ice extent reduction on South African rainfall. Similarly, **Chapter 8** and **Chapter 9** consider the results of the sea-ice perturbations for the winter season over the Southern Hemisphere and southern Africa respectively.

Lastly, **Section IV** consists of the final chapter, **Chapter 10**, which includes a summary of the primary conclusions, provides an appraisal of the constraints and caveats of the study, and presents some recommendations for future research. For the convenience of the reader, a list of acronyms that have been used in the text is provided in Appendix A.

I have benefited from the help of many people over this period of research. Firstly, I would like to thank the **Earth Systems Science Center** at the Pennsylvania State University for allowing me to use the GENESIS GCM on their CRAY supercomputer. I am particularly grateful to **Bill Peterson**, the systems administrator, for customising the GCM for my sea-ice experiments, for patiently answering all my questions concerning the implementation and running of the model, and for allowing me the freedom to perform my own model simulations.

I am most appreciative of the continual support and encouragement that I have received from my colleagues in the Environmental and Geographical Science Department. In particular, I

would like to thank **Susan Sayers** for producing the map of Antarctica, **Kevin Winter** for assistance with computer problems and **Peter Holmes** for all his "thesis tips", after the experience of recently having completed his own Ph.D. I am especially indebted to **Debbie Shannon, Jeremy Main** and **Chris Jack**, my peers in the Climate Systems Analysis Group, as well as my sister, **Susie Tyson**, for their camaraderie, valuable discussions and assistance in many facets of my thesis.

I am very grateful for the financial support which the **Foundation for Research Development** has provided me with for the period of this research.

I would like to acknowledge and thank my parents, **Ray** and **Alison Tyson**, for instilling in me the love of acquiring knowledge and a passion for the natural environment, and for always providing me with their love and support in all matters. I would like to thank my uncle, **Peter Tyson**, for inspiring me with his own climatological research and for all his valuable advice. I am grateful for the support and motivation provided by all my family and friends. In particular, I would like to thank my husband, **Paul**, for all his patience, unwavering love and encouragement over this period.

Finally, I am fortunate to have had a supervisor, **Bruce Hewitson**, who has taken such an interest in both my research and future career, and who has provided me with so many opportunities during my Ph.D. I would like to thank Bruce for his supervision, for his advice, guidance and encouragement, and for all the stimulating discussions.

CONTENTS

SECTION I

Introduction

CHAPTER 1

Background

1.1 Sea-Ice and Atmosphere Interactions

The seasonal formation and retreat of sea-ice in the polar regions is an extremely important process which affects the global climate. Sea-ice cover influences heat, moisture and momentum exchanges between the ocean and atmosphere, and is of central importance to climate dynamics and energy balances (Wadhams, 1994). The seasonal cycle of Antarctic sea-ice displays large changes in ice extent (Figure 1.1), in addition to considerable interannual variability. Gloersen *et al.*, (1993) analysed satellite data of Antarctic sea-ice extent for the years 1978 through to 1987 and found that average seasonal extents varied between a summer minimum of 3.5 million km^2 in February and a winter maximum of 19 million km^2 in September, with an interannual variability of ±5% in the winter ice cover. The presence or absence of sea-ice can have a large impact on the surface energy balance, often controlling both the sign and magnitude of fluxes. During summer, regions covered with sea-ice have much higher albedos compared to sea surface albedos, and therefore absorb and store less energy than the surrounding ocean. In contrast, during winter when there is negligible insolation, the presence of sea-ice acts to decrease heat losses from the ocean.

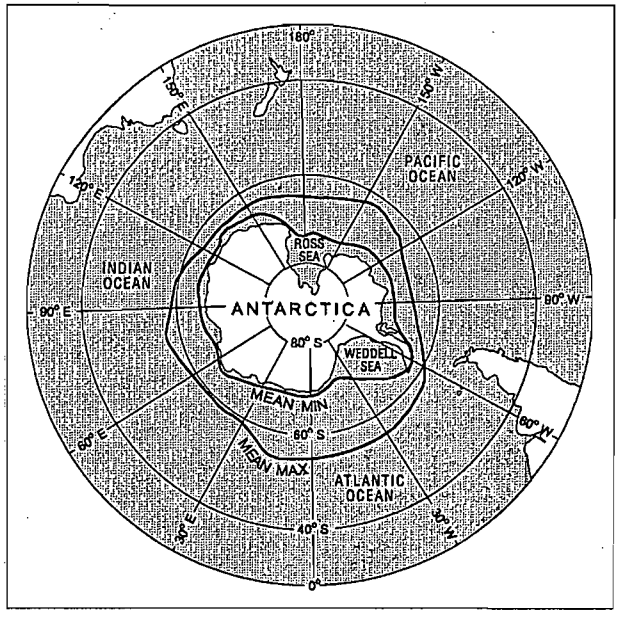

Figure 1.1 Map showing the mean maximum and mean minimum sea-ice extents for 1973 to 1982 (after Carleton, 1989).

A topic that has been of great scientific and public concern over the past decade is that of anthropogenically induced global warming. Carbon dioxide (CO_2) concentrations have been

increasing steadily over the last few decades, and the Intergovernmental Panel on Climate Change (IPCC) has calculated that if emissions are maintained at 1994 levels, then concentrations will reach double pre-industrial levels (280 ppmv) by the end of the 21st century (IPCC, 1996). CO_2 absorbs long-wave radiation emitted from the earth's surface and as such, with increasing concentrations, we would expect substantially warmer future climates. Current suggestions are that global warming will impact substantially on the polar regions and that changes in the areal coverage of sea-ice may be one of the first signs of climate change. The latitudinal extent of Antarctic sea-ice cover is strongly related to atmospheric temperature and oceanic heat flux, as well as to winds, ocean currents and the wave field (e.g. Weatherly *et al.* 1991; Squire, 1994; Wadhams, 1994). It is unclear how these factors will be affected with the advent of climate change, but it is thought that with higher sea-surface and atmospheric temperatures under a warming climate, sea-ice reductions are likely to occur.

Independent analyses of satellite-derived sea-ice extents for 1978-1987 (Gloersen and Campbell, 1991) and 1978-1994 (Johannessen *et al.*, 1995) respectively, have, however, shown no significant trends in Antarctic sea-ice cover. De la Mare (1997) managed to extend the sea-ice data to periods prior to the advent of satellite technology by using whaling records as proxy data for sea-ice extent, based on the fact that the southern-most limit of whaling was constrained by the sea-ice boundary and that whaling fleets were often found to spread along the sea-ice edge, since it is a region of high biological productivity. De la Mare's (1997) results suggest that there was a large and rapid decrease in Antarctic summertime sea-ice extent between the 1950's and 1970's, with sea-ice extent remaining fairly stable after the 1970's. It is thus still uncertain whether Antarctic sea-ice extent has been responding to purported anthropogenically induced global warming.

Nearly all equilibrium General Circulation Model simulations under doubled CO_2 conditions show considerable polar warming and an associated reduction in sea-ice extent (e.g. Schlesinger and Mitchell, 1987; Wilson and Mitchell 1987; Meehl and Washington, 1990; Boer *et al.*, 1992; Pollard and Thompson, 1994; Hunt *et al.*, 1995, Hudson, 1997). However, the results from atmospheric General Circulation Models coupled to full ocean models suggest that vertical mixing in the Southern Ocean is likely to retard and diminish warming in the polar regions (e.g. Stouffer *et al.*, 1989), compared to the results obtained from atmospheric General Circulation Models coupled to mixed layer ocean models. Despite the possible reduction in sea-ice limits with global warming, there is also the considerable

interannual variation in Antarctic sea-ice extent to consider (Gloersen *et al.*, 1993). The controls of this interannual variability are not well known (Hanna, 1996) and we still do not have a good understanding of the influence which these present-day Antarctic sea-ice variations exert on the climate, especially non-polar climates. The question of how an anomalously reduced sea-ice extent (reduced either in the future in response to global warming, or in response to interannual variability) would feed back and impact on global and synoptic circulation patterns remains largely unanswered.

Studies of sea-ice atmosphere interactions in the Southern Hemisphere have been restricted by limited observed data, both spatially and temporally. However, the availability of data over the last two decades has improved, largely due to increased satellite coverage of the Southern Ocean and the advent of weather prediction models, which can be used to assimilate observed data and create operational analyses. Research has also been limited by the complexity of the non-linear processes and feedbacks involved in sea-ice atmosphere interactions. These two factors have combined to produce some confusing and quite frequently conflicting results in the literature, especially concerning the relationship between sea-ice and non-polar climates. Nonetheless, a wide range of studies using observed data of varying quality have examined a host of relationships between Antarctic sea-ice and the atmosphere. These studies have ranged in scale, both spatially and temporally, from those examining local and/or short-term case studies (e.g. Cavalieri and Parkinson, 1981; Mayes, 1985; Jacobs and Comiso, 1993; King, 1994), to those studies which have investigated the possible links between Antarctic sea-ice and large-scale indices of the circulation, such as the El Niño Southern Oscillation (ENSO) (e.g. Chiu, 1983; Carleton, 1988, 1989, 1992; Xie *et al.*, 1994; Simmonds and Jacka, 1995).

There is substantial evidence that sea-ice can force changes in atmospheric circulation in the region of the sea-ice margin (e.g. Ackley and Keliher, 1976; Ackley, 1981; Carleton, 1981; Streten, 1983; Mayes, 1985; Watkins and Simmonds, 1995), but of more interest is the suggestion that sea-ice variations around Antarctica can cause an atmospheric response in the midlatitudes and subtropics, as well as in polar and sub-polar latitudes. In contrast to the Arctic, Antarctic sea-ice has an outer boundary which is unconstrained by land, and therefore interacts both dynamically and thermodynamically with the atmospheric and oceanic circulation of middle and lower latitudes of the Southern Hemisphere (Carleton, 1992). Research has indicated that Antarctic sea-ice variations may influence cyclogenesis and the behaviour of midlatitude cyclones. In a modelling study, Simmonds and Wu (1993) recorded

significant increases in midlatitude cyclone densities near 60°S, and enhanced cyclogenesis in the western Weddell Sea in response to reduced Antarctic sea-ice concentrations in winter. In addition, results from the Fine Resolution Antarctic Model appear to show that the seasonal extent of sea-ice may control the passage of cold fronts towards South Africa during winter (Lucas and Lindesay, 1991). Some studies suggest that Antarctic sea-ice atmosphere interactions are regionally specific, for example, Godfred-Spenning and Simmonds (1996) found that the sea-ice–cyclone relationship for the period 1973-1991 was only evident in certain regions of the sea-ice zone and during particular seasons, for instance there was a relationship between sea-ice and cyclone density in the Amundsen Sea during summer. Howarth (1983) similarly found little correlation between sea-ice and cyclone tracks on a hemispheric scale, but relationships were evident in specific regions or over short time periods. Further research with observed data seems to indicate that temperature gradients in the region of the sea-ice margin may induce baroclinic instability, and this, combined with air-sea interactions, may enhance mesoscale cyclogenesis near the ice-ocean interface (Carleton and Carpenter, 1990; Carleton, 1995). These mesocyclones (polar lows), in contrast to the larger 'synoptic' or 'frontal' cyclones, constitute up to 50% of all cyclones recorded during winter over the Southern Hemisphere oceans (Carleton, 1995). Through the impact of sea-ice variations on midlatitude cyclones, the effect of sea-ice extent anomalies may be transmitted to lower latitudes.

Some modelling studies have shown changes in tropical pressures and a reduction in the strength of the midlatitude westerlies in response to a reduction in Antarctic sea-ice extent (Simmonds, 1981; Mitchell and Hills, 1986; Simmonds and Dix, 1987). Carleton (1989) has also suggested, based on statistical analyses with observed data, that changes in sea-ice extent may preceed changes in midlatitude sea level pressure wave number one. He found that greater ice extents during late winter for the period 1973-1982 were related to a displacement of wave number one towards Australia. In addition, these changes preceded changes in the tropical Southern Oscillation Index (SOI) by approximately 5 months. In terms of the planetary long waves in the Southern Hemisphere, it is thought that they may be forced, in part, by thermal effects associated with the asymmetric sea surface temperature (SST) and ice distribution around Antarctica (Anderssen, 1965; Grose and Hoskins, 1979; Trenberth, 1980; Karoly, 1985; James, 1988; Simmonds *et al.*, 1989). Therefore, a modification of this asymmetry, for example through a change in sea-ice extent, has the potential to alter the characteristics of the planetary long waves. Lastly, Meehl *et al.* (1997) have suggested that an alteration of the seasonal cycle of surface temperatures at 50°S and 65°S could alter the

manifestation of the semiannual oscillation (SAO). The SAO describes the biannual contraction and intensification of the circumpolar trough surrounding Antarctica. Sea-ice cover influences temperatures at 65°S and it is therefore possible that anomalous sea-ice extents may influence the SAO.

The key objective in the present study is to further explore and clarify the role of Antarctic sea-ice extent as a non-local climate forcing factor. The effect that a reduced Antarctic sea-ice extent has on the general climate of the Southern Hemisphere and, more specifically, southern Africa will be investigated. The analysis of observed data is of limited use when attempting to investigate such a question, since the relationships found between the observed seasonal behaviour of sea-ice extent and some atmospheric variable may not necessarily be the same as a response of that variable to sea-ice anomalies within a given season. In addition, with statistical studies using observed data, it is often difficult to establish cause and effect. An ice anomaly itself is the response to atmospheric forcing, and therefore determining the ice's subsequent influence on the atmosphere is problematic. It is also possible that the atmospheric response to sea-ice is non-linear, and therefore one should be cautious in interpreting the results from studies with observed data that use linear statistical methods, such as correlations. Thus, the approach adopted in the current study is to use a General Circulation Model in order to isolate the effect of prescribed anomalies of sea-ice extent. A General Circulation Model represents a controlled environment, within which the impact of various anomalies on the climate system can be studied. By comparing an anomaly simulation to a control simulation, the climatic impact of a sea-ice perturbation can be elucidated.

1.2 General Circulation Models

General Circulation Models (GCMs) are numerical models of the earth-atmosphere system which are capable of reasonably simulating many of the large-scale features of the observed climate. They model global weather by attempting to solve the basic physical equations which govern the processes operating within and between the atmosphere, ocean, cryosphere and land surface. Figure 1.2 shows a simplified view of the climate system and the important interactions which occur between the various components.

Some physical processes take place at scales smaller than a GCM's grid resolution, for example those related to clouds, and cannot be modelled explicitly. Instead, their effects are taken into account by relating them to larger-scale phenomena that are resolved by the model, through a

process known as parameterisation. Contemporary GCMs used for climate modelling have horizontal grid resolutions ranging between 2° and 4° of latitude or longitude and typically have 18 or more atmospheric levels in the vertical. Many GCMs are spectral models, i.e. the equations are solved using spherical harmonic techniques, and the horizontal resolution is given as the wave number of truncation, with higher wave numbers representing finer resolutions. Current GCMs used for climate modelling studies (as opposed to weather forecasting) usually have wave numbers of truncation between 21 and 42. GCM simulations are most reliable at hemispheric or continental scales, and less accurate at regional scales. There are still many sources of uncertainty associated with GCM simulations, most of which are related to resolution, processes which are parameterised and interactions with the boundary (Trenberth, 1996). As has been mentioned previously, parameterisations are required to deal with sub-grid scale processes, and this may contribute to significant errors in GCM simulations at regional scales. The IPCC (1996) has stated that the largest areas of uncertainty in climate models are clouds, the hydrological cycle and the treatment of the land surface, and that these appear to cause the largest discrepancies between the present-day control simulations of different GCMs.

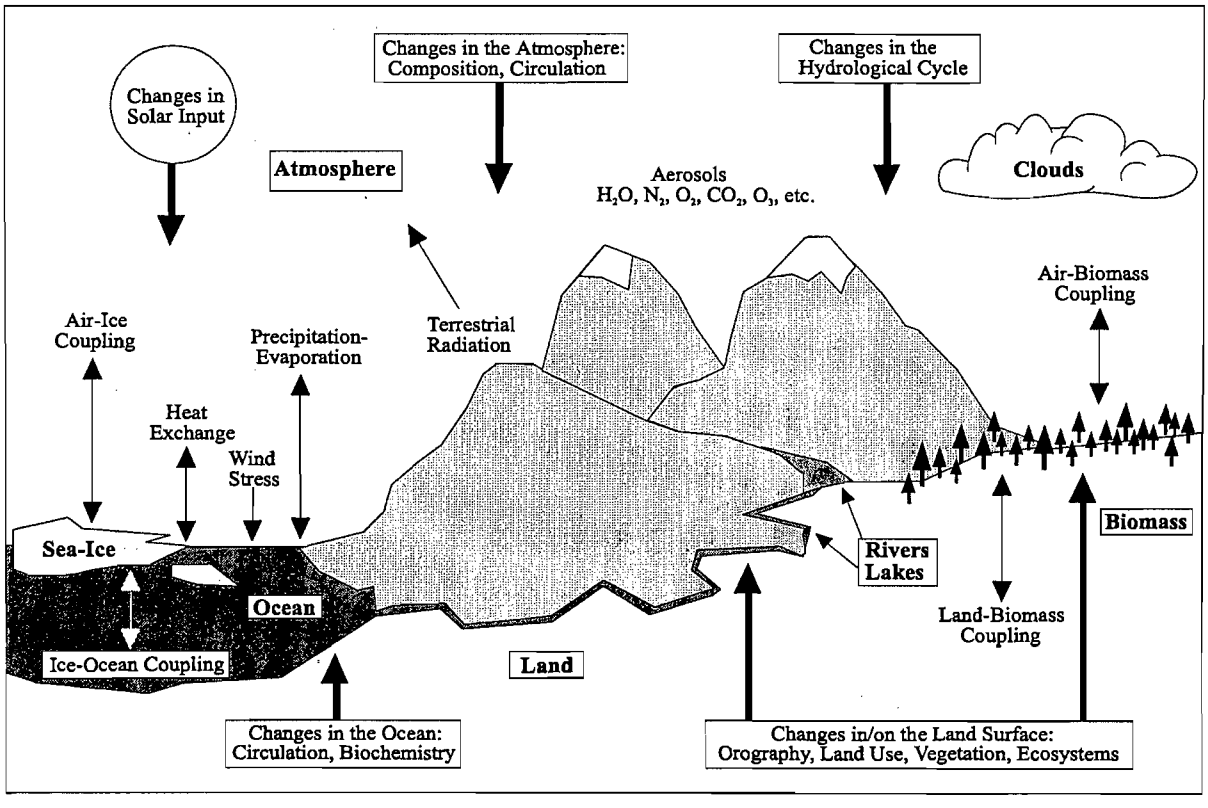

Figure 1.2 Schematic view of the components (bold) of the climate system and interactions between the components (thin arrows). The bold arrows designate aspects of the climate system which have the potential to change (modified from IPCC, 1996).

A GCM consists of a number of components or sub-models of varying complexity, encompassing the atmosphere, ocean, cryosphere and land surface. The atmospheric

component is the most sophisticated, primarily due to development for the purposes of daily weather prediction, whereas development of the other components has lagged somewhat. The oceanic component of a GCM can be represented in a variety of ways. Firstly, instead of using an ocean model, prescribed present-day sea-surface temperatures (SSTs) and sea-ice extents can be specified as a boundary condition for the atmospheric general circulation model (ACGM). Secondly, the ACGM may be coupled to a simple slab or mixed-layer ocean model, usually with prescribed heat transport, and lastly, the AGCM may be coupled to a full ocean model. In the latter two cases, models of sea-ice are also incorporated. Sea-ice models range from those which consist of a motionless ice layer whose thickness is governed by thermodynamics, to more complex and less frequently used models which incorporate sea-ice dynamics, fractional coverage, multilayer ice and the effects of salinity and snow on ice (IPCC, 1996).

It is important to have a range of model complexities, because they suit different needs. It is not always desirable to utilise the most complex of the models i.e. the fully coupled ocean-atmosphere models. Apart from the fact that these models are both computationally and financially expensive to run, they may not provide the best solutions to the problem being investigated. For example, Joubert and Tyson (1996) have suggested that owing to evidence showing errors in the simulation of the Southern Ocean by fully-coupled ocean-atmosphere models, the mixed-layer models may, at this stage, be more reliable for GCM studies over the southern African region. In addition, when dealing with processes that are not fully understood, it may be better to keep associated values constant, or as observed, rather than trying to model them incorrectly. The lower order models are also often better at highlighting dominant mechanisms in the earth-atmosphere system and may be especially useful for providing insight into the role played by key processes. Nonetheless, whenever a model is used in a study, it is important that it is applied with suitable appreciation of its limitations.

The present study utilises a GCM which is forced with prescribed SSTs and sea-ice extents, where the fields in the control are as observed and anomalies are introduced in the experiment. By using prescribed fields, one is able to isolate the forcing from the sea-ice perturbation, whereas results from a GCM using a sea-ice model would be complicated by feedbacks between the atmosphere and sea-ice, and the effect of the sea-ice on the atmosphere would be more difficult to determine. By nature of the model used, the sea-ice reduction experiments cannot take into account the subsequent feedback of the atmosphere to the ocean or cryosphere.

1.3 Modelling the Impact of Sea-Ice Reductions

Once a specific GCM has been validated, and the simulations deemed realistic, it can be a useful tool for investigating scientific questions, such as how reduced sea-ice limits may impact on the atmosphere. A number of modelling experiments investigating the atmospheric response to a reduction in sea-ice, have been performed for the Arctic (Fletcher *et al.*, 1973; Newson, 1973; Warshaw and Rapp, 1973; Herman and Johnson, 1978; Serafini and LeTreut, 1988; Dümenil and Schröder, 1989; Raymo *et al.*, 1990; Royer *et al.*, 1990; Crowley *et al.*, 1994; Murray and Simmonds, 1995). However, results obtained from studies with the Arctic are not necessarily transferable to the Antarctic, primarily due to the different distribution of land masses in the hemispheres. In addition, the seasonal variation of sea-ice cover is about 6 times greater around Antarctica than in the Arctic (Simmonds, 1981).

The Southern Hemisphere experiments that have been performed, can be grouped into those examining the impact of reduced sea-ice concentration, on the one hand, and reduced sea-ice extent on the other. In terms of sea-ice concentration, Ledley (1988) used an energy balance climate model coupled to a three layer thermodynamic sea-ice model to investigate the feedback between atmospheric temperature and small areas of open ocean (leads) within the winter sea-ice zone. She found that due to changes in the sensible heat flux, leads have a large impact on the atmospheric temperature of polar regions. Similarly, Simmonds and Budd (1990, 1991) examined the response of the atmosphere to changes in the open water fraction of Antarctic sea-ice in perpetual July simulations with an R21 spectral resolution GCM using prescribed SSTs and sea-ice extents. They also found substantial atmospheric warming in those areas where leads were included, and the experiments appeared to indicate westerly wind anomalies south of 60°S and anomalous easterlies between 40° and 60°S in response to reduced sea-ice concentrations. In addition, they found that some variables, such as sea-level pressure and precipitation, did not respond monotonically to reductions in sea-ice concentration. For example, pressure reductions were recorded over the Weddell Sea in response to the reduction in sea-ice concentration, but a larger pressure decrease was recorded in this area for the case when the open water fraction was set to 0.8 than was recorded when the open water fraction was set to 1.0. Simmonds and Wu (1993) extended the previous research by examining the effect of reduced sea-ice concentrations on midlatitude cyclones. They found a general tendency for an increase in the number of cyclones surrounding the Antarctic continent and a decrease further north, as well as enhanced cyclogenesis south of about 65°S, especially over the western Weddell Sea. In contrast to the above studies, Watkins and Simmonds (1995) performed a number of short simulations (5 days) using an

R31 spectral resolution GCM with prescribed SSTs and sea-ice extents in order to determine the atmospheric response to Antarctic sea-ice concentrations on synoptic time scales. The results suggested that real-time Antarctic sea-ice data may be particularly useful for numerical weather prediction.

In contrast to varying Antarctic sea-ice concentration, there have been a number of studies which, as is the focus in the present study, have modified sea-ice extent. Simmonds (1981) replaced September sea-ice extent with that for March in a perpetual September simulation using a hemispheric GCM with an R15 horizontal resolution and 9 levels in the vertical. Where sea-ice was removed, it was replaced by water with a temperature of -1°C. In another study, Mitchell and Hills (1986) examined the effect of removing all Antarctic sea-ice equatorward of 66°S and replacing it with water at 0°C. To do this they performed three 4-month (June, July, August, September) replicate experiment simulations using a GCM with a horizontal grid length of about 330 km and 5 layers in the vertical. In response to the latter paper, Simmonds and Dix (1987) expanded upon the 1981 research (Simmonds, 1981), using a global version of the same GCM as before, although with some improvements. In a perpetual July simulation, they removed all sea-ice in the experiment and replaced it with open water at 0°C. Lastly, Mitchell and Senior (1989) repeated the experiments of Mitchell and Hills (1986) using an 11-layer GCM in order to produce an improved control simulation. Three 4-month experiment simulations were performed as before, although ice equatorward of 67.5°S was removed, in contrast to 66°S in the Mitchell and Hills (1986) experiment, and the ice was replaced with water at -1.8°C, in contrast to 0°C in the Mitchell and Hills (1986) experiment.

In response to the various imposed sea-ice extent reductions, all the above studies (Simmonds, 1981; Mitchell and Hills, 1986; Simmonds and Dix, 1987; Mitchell and Senior, 1989) found a decrease in the zonally averaged westerly component of the wind between about 45°S and 65°S in the middle to upper troposphere. In addition, they all noted zonally averaged warming of the lower troposphere south of about 55°S as a result of the sea-ice reduction. There are, however, a number of inconsistencies between the results of the different experiments. For example, Mitchell and Hills (1986) and Mitchell and Senior (1989) found a reduction in surface pressure in the regions from which sea-ice was removed, whereas Simmonds (1981) and Simmonds and Dix (1987) found both increases and decreases in surface pressure in the regions from which sea-ice was removed, although the spatial

distribution of these increases and decreases did not coincide. It has been suggested that differences in the results of these modelling studies may be due to the different sea-ice anomalies used (Mitchell and Hills, 1986; Mitchell and Hills, 1987; Mitchell and Senior, 1989), the high variability of the model circulation over midlatitude, sub-polar and polar latitudes (Mitchell and Senior, 1989) and to differences between the respective models (Mitchell and Hills, 1986; Mitchell and Hills, 1987; Simmonds and Dix, 1987; Mitchell and Senior, 1989).

The above mentioned experiments were conducted with large and sometimes unrealistic sea-ice extent anomalies. The removal of ice north of a designated latitude (Mitchell and Hills, 1986; Mitchell and Senior, 1989) does not take into account asymmetrical melting around the Antarctic continent, such as the substantial seasonal ice changes that occur in the region of the Ross and Weddell Seas (Ackley, 1981). It is also unrealistic for the sea-ice distribution in the experiment simulation to remain constant from June through to September, as was the case in the studies by Mitchell and Hills (1986) and Mitchell and Senior (1989). Furthermore these experiments, together with those of Simmonds (1981) and Simmonds and Dix (1987), imposed extreme changes in sea-ice extent, and one should be cautious in applying the results to smaller perturbations in ice extent that are actually observed. In these types of studies there is, however, the problem of what anomalous sea-ice data set to introduce into the model.

The current study will present an algorithm which has been devised to generate sea-ice data sets for experiment simulations similar to those mentioned above. For any given month of the GCM control sea-ice data set, the algorithm will produce a corresponding month with reduced sea-ice coverage, which can be used in the experiment simulation. Where sea-ice is removed, it is replaced by an interpolated gradient of SSTs extending to the new ice boundary, thus including the effect of the warming of ice-free surface waters, whereas the previous studies did not. Observed sea-ice coverage is analysed as the basis for reducing sea-ice extents, and depending on the stage in the seasonal cycle, the algorithm either exacerbates the observed pattern of melting, or diminishes the observed pattern of freezing. The algorithm allows for the formulation of fairly realistic sea-ice input data, in that the sea-ice reductions are not applied uniformly around the Antarctic continent, reductions are consistent with observed patterns of sea-ice decay, and data sets of multiple months can be obtained where a realistic seasonal cycle is clearly evident. As well as examining the effect of reduced freezing during winter, this also facilitates the investigation of the atmospheric impact of enhanced sea-ice melt during the summer months. The effect of reduced sea-ice limits on the

atmosphere during the summer season of the Southern Hemisphere has previously not been considered. There are also options available in the algorithm for producing ice reductions ranging from perturbations of the same order of magnitude as those seen in interannual variability, to those which are more extreme perturbations. In this study, the algorithm has been applied to the Antarctic, but could be used equally well for the Arctic.

1.4 GCM Skill Level and the Regional-Scale Response

One of the aims of the present study is to examine the potential influence that Antarctic sea-ice extent has on the climate of southern Africa, and in particular, precipitation. Although GCMs are the most appropriate tools for addressing such a topic, the typical grid resolution is such that the complex regional precipitation patterns over the sub-continent are often not captured. In addition, the skill level (von Storch *et al.*, 1993) of GCMs is usually poor at the scale of the grid cell, but increases as results are averaged over a larger grid, such that simulations are reasonably accurate at synoptic scales and larger (Hewitson and Crane, 1996). This problem of poor regional-scale accuracy is especially true for precipitation, and has been attributed, in part, to the variable's dependence on grid resolution and cumulus parameterisation (IPCC, 1990; IPCC, 1992). Owing to the semi-arid nature of much of southern Africa, and the high variability of rainfall, precipitation is one of the key variables of interest.

The variability of South African rainfall has been extensively investigated and a number of empirical controls have been proposed in the literature. The ENSO phenomenon has been found to exert a controlling influence on summer rainfall over South Africa (Harrison, 1986; Lindesay, 1988*a*, 1988*b*; van Heerden *et al.*, 1988; Mason and Lindesay, 1993), although the effect of ENSO appears to be modulated by the phase of the stratospheric Quasi-Biennial Oscillation (QBO) (Mason and Lindesay, 1993). The QBO refers to the periodic reversal of the equatorial stratospheric winds. During the high (low) phase of ENSO and when the QBO is in its westerly phase, significantly wet (dry) conditions occur over the summer rainfall region of South Africa between January and March (Mason and Lindesay, 1993). However, when the QBO is in its easterly phase, the association between ENSO and summer rainfall between January and March is statistically insignificant (Mason and Lindesay, 1993). It has also been recognised that SST anomalies in the oceans surrounding southern Africa are important in controlling the variability of rainfall over South Africa (Gillooly and Walker, 1984; Brundrit and Shannon, 1989; Walker and Lindesay, 1989; Mey *et al.*, 1990; Walker, 1990; Mason, 1990; Mason, 1992), and Mason (1992) has shown that on a year to year basis,

these SST changes exert a greater influence on South African rainfall than does ENSO. In addition, variations in the tropical easterly waves are important in accounting for wet and dry years over the interior of the country (Tyson, 1984; Jury and Pathack, 1991; Jury *et al.*, 1991), and deviations in the westerlies, for example in the frequency and amplitude of the westerly waves, influence precipitation over the southern portion of the country.

In order to examine the potential influence that Antarctic sea-ice extent has on precipitation over South Africa, the technique of downscaling has been applied. Downscaling has been utilised so as to obtain precipitation results of a finer resolution than the GCM grid and to overcome the inadequacies of GCM derived precipitation. There are two major downscaling approaches. The first is a process-based approach, for example the technique of nested modelling, and the second is an empirical approach that uses identified relationships derived from observed data. Nested modelling is computationally demanding and there are still problems concerning the handling of the interface between the GCM and the nested model that need to be considered (Hewitson and Crane, 1996). As such, the approach of empirical downscaling has been selected for the current study. This technique initially derives a relationship or transfer function between observed synoptic-scale circulation and a regional climate variable of interest, e.g. precipitation, over a certain spatial domain. The regional-scale variable is therefore expressed as a function of the larger-scale circulation. Then, once the synoptic-scale circulation of the GCM has been validated against observed data, the transfer function can be applied to the model circulation in order to obtain the specific regional variable. In this study, the relationship will be derived using an artificial neural network, following the procedure developed by Hewitson (1998). The advantage of using neural networks for downscaling over other, usually statistically-based techniques like regression, is that they are not restricted to linear relationships or prescribed non-linearities and they are fairly robust in the presence of noise.

1.5 Objectives of the Study

The primary aim of this study is to examine the role of Antarctic sea-ice extent as a non-local climate forcing factor. As such, the effect that a reduced Antarctic sea-ice extent has on the climate of the Southern Hemisphere, particularly the lower latitudes, will be investigated. This research will increase our knowledge of the atmospheric processes involved in the translation of a remote event, in this case changes in Antarctic sea-ice extent, into regional climatic variations and impacts. In order to do this, a number of four month, summer and

winter GCM simulations have been performed so as to isolate the impact of prescribed anomalies of sea-ice extent.

This work is an extension over earlier, similar modelling studies for a number of reasons. Firstly, an algorithm, mentioned previously, has been developed in order to introduce smaller and more realistic sea-ice anomalies into the GCM than have been used before. The sea-ice perturbations used in the present study resemble the observed magnitude of interannual differences in sea-ice extents. Although the sea-ice perturbation is smaller than those previously used, the present study also considers the effect of warming the ice-free surface waters whereas previous studies replaced the ice with water at a constant temperature, less than or equal to 0°C, depending on the study (Simmonds, 1981; Mitchell and Hills, 1986; Simmonds and Dix, 1987; Mitchell and Senior, 1989). Secondly, this research is more comprehensive than the former studies, in terms of both the number of simulations performed and the number of variables considered. The number of simulations is significant, due to the inherent climatic variability of middle and high latitudes. A true sea-ice–atmosphere signal should become more apparent above the noise as more simulations are conducted. In terms of the variables analysed, previous studies only focused on a few variables, usually sensible and latent heat fluxes, surface temperature, sea level pressure and winds, and most of these (all except for sea level pressure) were exclusively examined from a zonally averaged perspective (cf. Simmonds, 1981; Mitchell and Hills, 1986; Simmonds and Dix, 1987; Mitchell and Senior, 1989). Thirdly, the study focuses more on the response outside the polar region than previous modelling studies did, and examines the sensitivity of the atmosphere to changes in Antarctic sea-ice extent during the winter and summer seasons, while past modelling studies only addressed the winter months. It should also be mentioned that other Antarctic sea-ice sensitivity studies emphasised changes in the mean state of the atmosphere, yet changes in variability may result in more significant impacts and are thus considered in the present study. Fourthly, all the Antarctic modelling studies that considered sea-ice extent were done prior to 1990 (*viz.* Simmonds, 1981; Mitchell and Hills, 1986; Simmonds and Dix, 1987; Mitchell and Senior, 1989), and considering the subsequent improvement of GCMs, both in terms of resolution and physical parameterisation, it would seem appropriate to repeat such experiments using a current generation model. The reliability of the atmospheric response to the sea-ice forcing is obviously related to the model's ability to simulate present-day conditions. The present study uses the latest version of the GENESIS[1] GCM (version 2.0.a) which was released for use in 1996.

[1] Global Environmental and Ecological Simulation of Interactive Systems

An important focus of this research, which has not been addressed previously, is to examine the effect which Antarctic sea-ice extent may have on the climate, and especially precipitation, of southern Africa. This arid sub-continent is characterised by highly variable rainfall and water is a limiting resource, therefore any studies which aim to increase our understanding of the controls on regional precipitation are of the utmost importance. The technique of empirical downscaling will be used to obtain sub-grid scale fields of precipitation over South Africa from the synoptic-scale circulation of the GENESIS model, so as to facilitate a regional analysis and overcome the inadequacies of GCM derived grid-cell precipitation.

Finally, comparatively little effort has been devoted to evaluating the GENESIS GCM's simulation of the present-day climate, particularly of the Southern Hemisphere. The present study therefore aims to provide a more comprehensive validation of the Southern Hemisphere climate of GENESIS than has been done previously. It has already been mentioned that the reliability of results from sensitivity studies is related to the model's ability to simulate present-day conditions. In addition, validation studies play an important role in facilitating the improvement of GCMs and provide a perspective on the limitations of the model, which need to be taken into account when performing experiment or sensitivity simulations.

The broad objectives of the present study can therefore be summarised as follows:

- To evaluate the GENESIS GCM's control simulation of the present-day climate of the Southern Hemisphere. This is necessary in order to determine whether the model is capable of reproducing the major features of the climate, such that it can be deemed valid for use for the sensitivity simulations.

- To develop a sea-ice algorithm which generates SST and sea-ice data sets for GCM sensitivity simulations.

- To perform GCM sea-ice sensitivity simulations, in both summer and winter, in order to evaluate the influence of a reduced Antarctic sea-ice extent on the climate of the Southern Hemisphere.

- To establish whether Antarctic sea-ice anomalies have the potential to affect non-polar regions, and if so, in what manner.

- To contrast the sea-ice sensitivity simulation results obtained for the summer season with those obtained for the winter season.

- To compare the results obtained from the sea-ice sensitivity simulations with those of previous, similar modelling studies, as well as studies which have made use of observed data.

- To determine whether sea-ice perturbations have the potential to affect circulation dynamics in the southern African region in particular.

- To obtain sub-grid scale fields of precipitation over South Africa, using the technique of downscaling, in order to assess the possibility that Antarctic sea-ice extent may have an influence on South African precipitation.

The present study should be viewed in the context of improving our understanding of present-day climate variations, of perhaps aiding long-term forecasting and helping to predict the climatic outcome of possible future global warming. The study may also highlight the significance, or lack thereof, of errors in coupled ocean-atmosphere GCMs with respect to their simulation of sea-ice, and may provide some indication of the likely effect of these errors in the models.

CHAPTER 2

Data and Model Description

2.1 Introduction

An important component of climate modelling studies is the evaluation of model performance. To do this, model output must be compared to observed data. In the present study, the NCEP[1]/NCAR[2] assimilation reanalyses are used to represent the observed data. This chapter will describe this database, together with the nature of the variables, spatial extent and time period extracted for the validation study. In addition, a description of the GENESIS[3] (version 2.0.a) GCM will be provided, as well as an explanation of the model output data used. The data that have been used for the sea-ice and SST experiments will be addressed at a later stage, in Chapter 5.

2.2 Observed Data

The NCEP/NCAR reanalysis data, provided by the NOAA[4] Climate Diagnostics Center (CDC), have been used as the observational database for comparison with the GCM data. The quality of the reanalysis data and the methods used to obtain the data have been documented by Kalnay *et al.* (1996) and can also be found at the NOAA website[5], along with various updates relating to the data. The data extends from 1957 to 1996 and encompasses an assimilation of observed data measurements from land stations, ships, rawinsondes, pibal, aircraft and satellites. The NCEP Medium Range Forecasting Global Model (T62 horizontal resolution and 28 vertical levels), together with a global data assimilation system were used to create the reanalyses such that the method of quality controlling and assimilation of the data remained the same throughout the reanalysis period (Kalnay *et al.*, 1996).

Higgins *et al.* (1996) compared the NCEP/NCAR reanalyses to the NASA[6]/Data Assimilation Office reanalyses for the common period of 1985 to 1993. They found that the NCEP/NCAR reanalyses capture the mean climate and the seasonal evolution of basic prognostic fields very well. The largest differences between the two data sets are generally over the high latitudes

[1] National Centers for Environmental Prediction (USA)
[2] National Center for Atmospheric Research (USA)
[3] Global Environmental and Ecological Simulation of Interactive Systems
[4] National Oceanic and Atmospheric Administration (USA)
[5] http://www.cdc.noaa.gov
[6] National Aeronautics and Space Administration (USA)

of the Southern Hemisphere, where observations are sparse and model bias is introduced into the data. Furthermore, some variables, such as those linked with the hydrological cycle, are strongly influenced by the model and less so by the observed data, and therefore model biases can affect results. Problems that have been identified in the NCEP/NCAR reanalyses are discussed by Higgins *et al.* (1996) and can also be found at the NCEP/NCAR reanalysis website[7]. The problem that is most relevant to the present study is the error introduced through the use of Southern Hemisphere surface pressure bogus data (i.e. PAOBS). The PAOBS data set was created by the Australians for the data-poor regions of the Southern Ocean and is different from conventional data in that the data are estimated by human analysts based on, for example, satellite data[8]. In the process of producing the NCEP/NCAR reanalysis data, the PAOBS data set was erroneously shifted by 180° longitude, affecting the years extending from 1979 to 1992 of the reanalyses. The impact of this error on the reanalyses has been investigated by the Environmental Modeling Center (EMC) and the Climate Prediction Center (CDC) and the results are documented at the NCEP/NCAR reanalysis website[9]. They found that the Southern Hemisphere south of about 50°S is the most affected, since this region is very sensitive to any changes. The winter months are influenced more than the summer months and the impact of the error decreases as time scales increase from daily to monthly. The impact is insignificant on the global scale, but may be important on the synoptic scale. In a letter[10] dated 14 May 1996 from E. Kalnay (EMC) to A. Oort (head of reanalysis project), Kalnay provides three reasons for why the impact of mislocating the PAOBS data is fairly small. Firstly, "geostrophic adjustment indicates that surface pressure is a type of data 'hard to swallow' by the model"[11]. Secondly, the quality control system rejected about 50% of the PAOBS data, and lastly, the PAOBS data were weighted less than the ship and buoy data. Owing to these reasons, and in the context of the usage of the reanalysis data in the present study as a basis of comparison with the GENESIS GCM data, it is unlikely that the error with the PAOBS data will have a significant impact on the results of the validation study. The purpose of using the NCEP/NCAR data is to evaluate whether the GCM performs within the bounds of observations and as such, the data are being used to identify fairly large scale biases in the GCM output. The validation study is also primarily performed over the entire hemisphere, i.e. with a somewhat broad perspective,

[7] http://wesley.wwb.noaa.gov/paobs/paobs.html
[8] Refer to http://wesley.wwb.noaa.gov/paobs/paobs.html
[9] http://wesley.wwb.noaa.gov/paobs/paobs.html
[10] This letter can be found at the following website: http://wesley.wwb.noaa.gov/paobs/ek.letter.html
[11] Refer to http://wesley.wwb.noaa.gov/paobs/ek.letter.html

therefore small, local errors in surface pressure resulting from the mislocation of the PAOBS data will probably not be apparent.

For the present study, twice-daily data for the period 1979 to 1988 have been extracted from the 40-year data set. This 10-year interval was chosen because it corresponds to the model time period used in the investigation (refer to section 2.4). Analyses of the data have been performed over the entire Southern Hemisphere, as well as over a window (20°S to 50°S; 2°E to 47°E) encompassing South Africa. The variables that have been used are shown on Table 2.1. The pressure level reanalysis data are archived on a 2.5° latitude-longitude grid, while the surface data are saved on a T62 Gaussian grid (Table 2.1). The study is restricted to mid-winter (JJA - June, July and August) and mid-summer (DJF - December, January and February) and as such, the extracted reanalysis data have been averaged to obtain the respective seasonal averages. However, the twice-daily data have been used for Fourier analysis, a cyclone and storm track analysis and the classification of spatial sea level pressure data using a Self-Organising Map.

Variable	Grid	Levels
Air Temperature	2.5° × 2.5°	500 hPa
Air Temperature at 2 m	T62 (1.88° × 1.88°)	2m above the surface
Geopotential Height	2.5° × 2.5°	500 hPa
Sea Level Pressure	2.5° × 2.5°	sea level
Specific Humidity	2.5° × 2.5°	500 hPa
Specific Humidity at 2 m	T62 (1.88° × 1.88°)	2m above the surface
U-Wind	2.5° × 2.5°	700 hPa and 500 hPa
V-Wind	2.5° × 2.5°	700 hPa and 500 hPa
Precipitation Rate	T62 (1.88° × 1.88°)	surface

Table 2.1 Variables extracted from the NCEP/NCAR reanalysis data, together with their grid dimensions and the levels used.

In order to validate the GENESIS GCM, the model data must be compared to the NCEP/NCAR reanalysis data on a grid-point by grid-point basis. However, the data sets are not presented on the same horizontal grids. To overcome this problem, the reanalysis data are

regridded to the GENESIS GCM T31 (3.75° × 3.75°) grid using a spherical interpolation routine (Willmott *et al.*, 1985a) described in the following chapter. The interpolation is therefore done from the higher-resolution reanalysis grid to the lower-resolution GENESIS grid, since the reanalysis data are either on a 2.5° × 2.5° grid or a T62 (1.88° × 1.88°) grid, depending on the variable concerned (Table 2.1). This method is preferred over interpolating the GCM data to the higher resolution reanalysis grids, since the latter would introduce unnecessary errors into the model data. The interpolated NCEP/NCAR reanalysis data will hereafter be referred to as the observed data or the NCEP data.

2.3 The GENESIS GCM

The GENESIS model originated out of an effort to develop a first-generation earth system model which especially emphasises terrestrial physical, biophysical and cryospheric processes (Thompson and Pollard, 1995, 1997). Version 1.02 of this GCM has been widely used by climatologists and has found a particular niche in paleoclimate modelling (Barron *et al.*, 1993; Crowley *et al.*, 1993; Otto-Bliesner, 1993; Crowley and Baum, 1994; Foley, 1994; Barron *et al.*, 1995; Jenkins, 1995; Crowley *et al.*, 1996). Since the model has been used extensively for paleoclimatic experiments, it is one of the few GCMs that has been found to be satisfactory under a climate regime other than the present day. Studies with GENESIS version 2.0.a have included an examination of Greenland and Antarctic mass balances for the present-day and doubled CO_2 situations (Thompson and Pollard, 1997), an analysis of the density, distribution and characteristics of midlatitude cyclones in the oceans south of Africa (Hudson and Hewitson, 1997) and an investigation into the climatic response over southern Africa and the adjacent oceans to a doubling of CO_2 in the model (Hudson, 1997). GENESIS version 2.0.a is currently being used by South African climatologists, as well as researchers from other disciplines, (e.g. hydrology), in order to assess regional climate change impacts and generate climate change scenarios for the country. Hereafter, "GENESIS GCM" will refer to version 2.0.a, unless otherwise mentioned.

GENESIS is a current generation global model which consists of an atmospheric general circulation model coupled to multi-layer models of vegetation, soil, land ice, snow, sea-ice and a 50 m slab mixed-layer ocean. The atmospheric general circulation model (AGCM) has a T31 spectral resolution with 18 atmospheric levels, and is coupled to the 2° by 2° land surface models by means of a Land-Surface-Transfer (LSX) scheme. The model fields are transferred between the AGCM and the surface by bilinear interpolation or area-averaging at

each time step (Pollard and Thompson, 1995a). The primary features of the model are summarized below, but for a more detailed description of GENESIS version 2.0.a the reader is referred to the paper by Thompson and Pollard (1997). The previous version (1.02) of the model has also been described by Pollard and Thompson (1994, 1995b) and Thompson and Pollard (1995).

The AGCM dynamics make use of the spectral transform method in the horizontal for calculations dealing with mass, heat and momentum. Clouds in the model are predicted using prognostic cloud liquid water amounts in each grid cell (e.g. Smith, 1990; Senior and Mitchell, 1993), and are defined as either stratus, convective or anvil cirrus. They are mixed vertically by convection plumes and diffusion, and advected by semi-Lagrangian transport. Also included in the model is cloud conversion to precipitation, evaporation, aggregation by falling precipitation, re-evaporation of falling precipitation, and turbulent deposition of lowest-layer cloud particles onto the surface (Thompson and Pollard, 1997). Convection is modelled using a convective plume model and the planetary-boundary-layer plumes that are triggered by surface fluxes can condense and precipitate. Other features of the AGCM include a diurnal cycle with solar radiation calculations every 1.5 hours, gravity wave drag (the McFarlane (1987) scheme), the radiative effects of prescribed tropospheric dust aerosols and the ability to prescribe uniform mixing ratios of individual greenhouse gases (CO_2, CH_4, N_2O, CFC_{11} and CFC_{12}) (Thompson and Pollard, 1997).

The LSX model calculates the fluxes between the AGCM and open surface water, as well as determining the radiative and turbulent fluxes through the vegetation layers to the soil or snow surface. Characteristics of vegetation, such as leaf area index, leaf albedo and fractional cover, are prescribed from the results of a predictive vegetation model (Bergengren and Thompson, 1998) which is run off-line using observed present-day climatology. The soil and ice-sheet model has six layers and extends to a depth of 4.25 m. Details of this model, as well as the snow model are provided by Thompson and Pollard (1997).

The ocean of GENESIS can either be represented by a 50 m mixed-layer ocean model and a dynamical sea-ice model, or by prescribing present-day monthly climatological SSTs and sea-ice extents. The latter is used in the present study, but information on the mixed-layer ocean model and the sea-ice model can be viewed in the paper by Thompson and Pollard (1997).

2.4 GCM Data

The AMIP (Atmospheric Model Intercomparison Project) configured simulation from the GENESIS GCM is used for the current study. The AMIP project is an international effort to compare different GCM simulations, performed with a set of standard experimental conditions, in the hope of finding systematic errors that may lead to model improvement (Gates, 1992). In an AMIP simulation, like the one used with GENESIS, the climate for the decade of 1979 to 1988 is simulated by prescribing observed monthly distributions of SSTs and sea-ice extent. Atmospheric CO_2 concentration is set to 345 ppm and the solar constant is specified as 1365 W m^{-2}. In the present study, the perturbation and control simulations, used to determine the impact of reduced sea-ice limits, are embedded in the AMIP simulation i.e. they are model restarts of portions of the 10-year period. The nature of these short simulations, as well as the experimental design, are discussed in Chapter 5, along with the details of the sea-ice algorithm used to create input fields for the perturbations. The remaining portion of the current chapter will refer to the baseline AMIP simulation (i.e. no restarts for experimental purposes), which is used for comparison with the observed data in order to evaluate the performance of the model.

Twice-daily Southern Hemisphere data for the summer (DJF) and winter (JJA) months have been extracted from the 10-year AMIP simulation. The same variables that were used from the NCEP/NCAR reanalyses, shown in Table 2.1, have been selected from the AMIP simulation. The data are averaged to produce seasonal means for comparison with the regridded observed data. As mentioned previously, Fourier analysis, a cyclone and storm track analysis and the classification of spatial sea level pressure data using a Self-Organising Map have been performed on the twice-daily data.

2.5 Summary

Twice-daily data for the summers and winters of the 1979 to 1988 period have been extracted from the NCEP/NCAR reanalyses and the GENESIS GCM AMIP simulation for selected variables. The model output will be compared to the reanalysis data in a subsequent chapter in order to validate the model. The following chapter will describe the analysis techniques which have been applied to the extracted data considered here, as well as to the data from the sea-ice experimental simulations, which will be discussed in Chapter 5.

CHAPTER 3

Analysis Techniques

3.1 Spatial Interpolation

Spatial interpolation is used to regrid the observed data to the GCM grid, as mentioned in the previous chapter. The algorithm is based on simple inverse-square interpolation and is described by Willmott *et al.* (1985a). The equations used for the interpolation procedure are provided in Appendix B. In this algorithm, surrounding data points influence the interpolated value of a grid point by varying degrees, depending on the distance from the grid point to the data point, as well as the directional relationship which exists between the points. An important feature of this routine is that distances between points are calculated as spherical distances, rather than as Cartesian distances. This is advantageous, since significant errors may occur if linear interpolation is applied to spherical spatial data (Willmott *et al.*, 1985a).

For each interpolated value that must be calculated at a point, the procedure searches for surrounding data points within a preselected radius of that point. The radius used in the present study is 10 degrees. The radius is, however, adjusted such that at least 4 data points and not more than 10 data points fall within the radius, as suggested by Willmott *et al.* (1985a). The data points are then weighted according to their spherical distance from the grid point to be interpolated to, as well as the "directional isolation" of each data point relative to all nearby data points within the search radius. The latter procedure has the effect of removing any directional bias in terms of the angular separation between data points. Finally, the weights are applied to the data values within the search radius and the values are linearly summed in order to obtain the interpolated value.

3.2 Fourier Analysis

The circumpolar westerlies consist of a number of ridges and troughs, which can be seen as the product of a series of superimposed sinusoidal waves of differing wavelength. By studying the characteristics of these wave trains, one stands to learn a great deal about the dynamical processes involved in the general circulation of the atmosphere. Fourier or spectral analysis enables the decomposition of a function into sinusoids of different frequencies (which sum to the original waveform), thus allowing an objective description of

these wave trains. Each resolved wave train is characterised by a wave number, which is the number of waves along the latitude circle; an amplitude, which gives its intensity; and the phase angle, which determines its longitudinal location. Wave trains vary from large-wavelength planetary-scale waves (e.g. wave numbers 1, 2, 3 and 4) to smaller, synoptic-scale and short waves with wavelengths of the order of a few hundred kilometers. There have been numerous studies done on zonal waves in the Southern Hemisphere (for example, Anderssen, 1965; Kao *et al.*, 1970; Kao *et al.*, 1971; van Loon and Jenne, 1972; Hartmann, 1977; Trenberth, 1980; Karoly, 1985; Randel, 1988; Young and Houben, 1989; Jones and Simmonds, 1993; Quintanar and Mechoso, 1995a, 1995b).

A function describing the variation of pressure along a latitude circle is transformed by a Fourier transform from a function defined in space (longitude) to a series of functions defined in the wave number domain. In the current application, the phase angle of a particular wave number represents the longitudinal position (in degrees) of the first ridge. One-dimensional Fourier analysis of the 500 hPa heights along latitude circles is used in the present study to examine the zonal waves of the Southern Hemisphere. Analyses have been conducted on both twice-daily and seasonally averaged data.

3.3 Statistics

3.3.1 Mean Absolute Error

Mean absolute error (MAE) is used in the present study as an index of model performance. Willmott *et al.* (1996) suggest that it is preferable to use MAE over the more common root-mean square error (RMSE), since RMSE almost always overestimates the average error and can be deceptive. RMSE is calculated by squaring the differences between model-predicted values and observed values prior to summation, and in this way the influence of large errors becomes unrealistically inflated. In addition, dimensionless or scaled measures of mean-squared error have also been shown to be biased (Willmott *et al.*, 1996). The use of the word "error", in the current study, may be misleading, since reanalysis data, which are used as a baseline of comparison of model performance, are not always a perfect representation of what is observed. Therefore, MAE in the present study is referred to more as a quantification of the difference between the model and NCEP reanalysis data, in order to highlight potential biases in the model output.

MAE is obtained by summing the absolute difference between corresponding variates from the model (m_j) and the observed (o_j) data, as is shown by

$$\mathrm{MAE} = \frac{\sum_{j=1}^{N} \omega_j |m_j - o_j|}{\sum_{j=1}^{N} \omega_j}, \tag{3.1}$$

where N is the sample size and ω_j is a weight which corrects for $|m_j - o_j|$ when j is spatially under- or over-represented (i.e. $\omega_j \neq \overline{\omega}$) (Willmott *et al.*, 1985b). Grid-points on the T31 grid of the GENESIS GCM are irregularly spaced, with the area of the grid cells decreasing as distance from the equator increases. Therefore, each ω_j represents the relative size of the grid cell (j), such that MAE will be unbiased.

3.3.2 Student's t Test

The Student's t test is a parametric test used to compare the means of two samples in order to establish whether they are significantly different from each other and therefore represent two separate "populations". This test is used in the present study to determine if there are statistically significant differences between control and perturbation model simulations. Using the twice-daily data, a t test is performed at each grid point of the data concerned and the confidence levels are calculated. The null hypothesis for each grid point is that there is no significant difference between the corresponding grid point means of the control and perturbation data sets of the variable concerned. The decision of whether or not to reject the null hypothesis depends on the chosen significance level (α), which is the probability that a true null hypothesis may be incorrectly rejected. A significance level of 5% (95% confidence level) has been chosen for the present study.

A potential problem with the t test as it stands in the above paragraph is that atmospheric data often do not satisfy the key assumption that observations are mutually independent. The data to be tested are observations over time and are likely to exhibit serial autocorrelation. This lack of independence due to time dependence leads to an underestimate of the variance of the sampling distribution of the test statistic, which in turn leads to an inflated value of the test statistic (Wilks, 1995). One approach to dealing with the problem is to estimate an effective sample size, n', such that $n' < n$ and consists of independent values for which the sampling distribution of the average has the same variance as the sampling distribution of the average over the n autocorrelated values in the data set (Wilks, 1995). In this approach, n' is

substituted for n in the t test equations and the test is then carried out as before. n' is estimated using the following approximation:

$$n' \cong n\frac{1-\rho_1}{1+\rho_1}, \tag{3.2}$$

where ρ_1 is the lag-1 autocorrelation coefficient. The ratio $(1-\rho_1)(1+\rho_1)$ serves as a variance inflation factor, which adjusts the variance of the sampling distribution in order to reflect the influence of serial autocorrelation (Wilks, 1995).

When the t test was applied to the control and perturbation data without correcting for serial autocorrelation, then there were statistically significant results for a number of grid points for the different variables tested. In contrast, when the correction was applied, it was found that very few of the changes between the control and perturbation grid point results were significantly different. This is to be expected since the correction procedure substantially reduces the size of n and makes it more difficult to reject the null hypothesis.

In the present study, the shading on the maps in the results sections represent areas of statistically significant differences based on the application of the t test *without* correction for autocorrelation. Statistically, it would be more valid to show the results from the t test procedure that takes time dependence into account, but this has not been done for a number of reasons. For most of the variables considered, very few, if any, of the grid point value changes are statistically significant when the corrected t test procedure is adopted. This is obviously valid from a statistical viewpoint and the result is not surprising since it will be shown that very small forcing anomalies are applied to the perturbation simulations compared to the control simulations. Thus, the changes invoked by the anomalous forcing are unlikely to result in large enough differences between the perturbation and control grid point values with respect to the new sample size, n', to cause rejection of the null hypothesis. However, a statistically insignificant result does not imply a climatically insignificant result. Although t tests are applied, the focus in the present study is the cohesiveness of the changes in spatial patterns between the years to which the anomalous forcing is applied. However, the t test examines the point-wise response to the perturbation. It therefore does not take into account the spatial response to the perturbation. In addition, as was mentioned in chapter one, the skill level of GCMs is usually poor at the scale of the grid cell, but increases as results are averaged over a larger area. Thus, the t test is focused on the scale of the GCM which is least proficient. The less conservative approach (using the t test without the correction factor for serial autocorrelation) is advantageous because it serves as an aid to highlight the important

spatial patterns of change. The statistical significance shading should therefore be viewed *only* as a relative guide to highlight possible key regions of importance.

3.4 Cyclone and Storm Track Analysis

Studies of Northern Hemisphere cyclones date back to the 1800s (e.g. Van Bebber, 1882). Unfortunately, Southern Hemisphere studies have been restricted by poor data coverage of the southern oceans (Murray and Simmonds, 1991). Taljaard (1967) made the first major contribution by producing hemispheric charts and analysing midlatitude cyclone distributions for the years 1957 and 1958. Subsequently, a number of studies making use of both daily weather charts (e.g. Van Loon, 1965) and satellite imagery (e.g. Streten and Troup, 1973; Carleton, 1979) have been undertaken. The majority of Southern Hemisphere studies have been based on manual techniques with observed data. These schemes may have suffered from subjectivity and have the problem of being time consuming. It is only in relatively recent times that the development of automated analyses have facilitated the rapid and objective identification of cyclones from observed digital data as well as allowing the examination of midlatitude cyclones in model generated data. These numerical analyses have been based on a number of different algorithms (for example Le Marshall and Kelly, 1981; Lambert, 1988; Le Treut and Kalnay, 1990; Murray and Simmonds, 1991; König *et al.*, 1993; Serreze *et al.*, 1993; Sinclair, 1994, 1995; Changnon *et al.*, 1995). In this study, an automated cyclone identification program has been written, where midlatitude cyclones are defined by the existence of pronounced cyclonic vorticity maxima in the pressure field.

The cyclone identification program is based on the algorithm presented in the paper by Murray and Simmonds (1991). The cyclone tracking section of their algorithm has not been implemented. In the program, a bicubic spline function is applied to a gridded pressure field, on a 47 × 47 polar stereographic grid, so that the best estimate of the location of the low can be obtained. Identification of lows is performed on this nominally equidistant grid, which is centred on the South Pole and has an effective resolution of approximately 508 km at 60°S. It is necessary to interpolate the observed and model data from their respective latitude-longitude (non-conformal) grids to the polar stereographic grid and this has been done by means of the spherical interpolation routine (Willmott *et al.*, 1985a) mentioned earlier in the chapter. At the first stage of the program, the gridded pressure data are scanned in order to identify grid-points at which the Laplacian of the pressure,

$$\nabla^2 p(x_i, y_j) = p_{xx} + p_{yy}, \tag{3.3}$$

is greater than any of the 8 surrounding grid-points and greater than a prescribed positive value. The prescribed value used in this study is 4 hPa. These identified grid-points serve as starting points for an iterative differential routine, based on ellipsoidal minimisation techniques, which is used to search for a local pressure (p) minimum. In this iterative process, the first and second space derivatives of the pressure at a point define an ellipsoid, whose centre then becomes the next point in the iteration. The orientation (θ) of the axes of the ellipsoid can be obtained from

$$\tan 2\theta = \frac{2p_{xy}}{p_{xx} - p_{yy}}, \tag{3.4}$$

and the second derivatives in the axial directions are calculated using

$$p_{uu} = \frac{p_{xx} + p_{yy}}{2} - \sqrt{\left(\frac{p_{xx} - p_{yy}}{2}\right)^2 + p_{xy}{}^2} \tag{3.5}$$

and

$$p_{vv} = \frac{p_{xx} + p_{yy}}{2} + \sqrt{\left(\frac{p_{xx} - p_{yy}}{2}\right)^2 + p_{xy}{}^2}\,. \tag{3.6}$$

The letters u and v denote the coordinates of the centre of the ellipsoid taken along the major and minor axes respectively. Equations 3.4, 3.5 and 3.6 are used iteratively to determine the coordinates of the local pressure minimum ($u;v$) by means of a two-dimensional version of the Newton-Raphson algorithm, where u is given by

$$u_{(n+1)} = u_{(n)} - \frac{p_u(u_{(n)})}{p_{uu}(u_{(n)})}, \tag{3.7}$$

and v by

$$v_{(n+1)} = v_{(n)} - \frac{p_v(v_{(n)})}{p_{vv}(v_{(n)})}\,. \tag{3.8}$$

If a pressure minimum is not found within 100 iterations (convergence usually occurs in far fewer iterations if a local minimum exists), then the process will begin again from the next identified grid-point. An identified pressure minimum corresponds to the position of a closed low (a system possessing a closed isobar at a certain interval). The algorithm of Murray and Simmonds (1991) also allows for the inclusion of open lows (an inflexion in the pressure field i.e. not possessing a closed isobar), however, this has not been included in the current study, since it was found, upon validation of the scheme, that closed low identification was sufficient for identifying the major systems. In addition, the inclusion of open lows often meant that zones of curved isobars, not usually regarded as cyclones, tended to be included. Sinclair (1994), who used a cyclone identification scheme based on the algorithm of Murray and Simmonds (1991), also noted that the inclusion of open lows in his study sometimes resulted in

the identification of certain zones of curvature and regions of elongated geostrophic shear, which would not be identified as cyclones in manual analyses. As in the present study, Taljaard (1967) also restricted cyclones to those systems possessing a closed isobar.

In order to exclude heat lows and other small-scale and shallow features, a minimum average value of $\nabla^2 p$ over a specified radius of the cyclone centre is stipulated. In the present study, this has been obtained by calculating $\nabla^2 p$ at the 8 compass points at a 0.5 grid unit radius from the cyclone centre and also at a 1 grid unit radius from the cyclone centre. The average of these 17 points (including the cyclone centre) is then calculated (let the value = *AVE*) and evaluated according to the following statement:

$$\text{If} \quad AVE \geq 2\sin\alpha + 4.5, \quad \text{then the low is accepted,} \tag{3.9}$$

where α is the absolute value of the degrees latitude. This equation was obtained through a tuning process with the observed data, such that the major systems are located and the more insignificant ones discarded. The cyclone finding program was sometimes found to converge on the same low pressure from different starting points. In order to eliminate the problem of finding two output positions very close together on the same day, a minimum cyclone separation distance of 8° is imposed. In this study, cyclone densities refer to the average number of midlatitude cyclones per (degree latitude)^2 at any one time. As such, densities are normalised for area and the total number of investigated time steps.

For the storm track analysis, the variance in the pressure field associated with midlatitude cyclones has been examined. Trenberth (1981) analysed the variance of the pressure fields in the Southern Hemisphere midlatitudes and found that fluctuations on 2- to 8-day time scales are largely associated with the passage of cyclones and anticyclones. As such, in a study of storm tracks in the Southern Hemisphere, Trenberth (1991) used a 2- to 8-day bandpass filter. This filter is broader than the common 2.5- to 6-day filter of Blackmon (1976), which has been used for studies of Northern Hemisphere storm tracks, but it is in keeping with observed variability over the midlatitudes of the Southern Hemisphere (Trenberth, 1981). In the present study, the standard deviation of the bandpass filtered sea-level pressure data has been calculated and displayed in an attempt to identify major storm tracks. The bandpass filter of 1.5- 8.5 days has been used and was calculated by means of moving averages.

3.5 Neural Networks and Downscaling

3.5.1 Introduction

The technique of downscaling is used to obtain regional-scale fields from larger, synoptic-scale circulation. GCMs are known to be relatively poor at simulating regional scale climates, largely by virtue of their coarse resolution. In addition, certain variables, especially precipitation, are inadequately represented at the scale of the GCM grid cell. In other words, the skill level (von Storch *et al.*, 1993) of GCMs is usually poor at the scale of the grid cell, but increases as results are averaged over a larger grid. One of the aims of the present study is to examine the effect that the sea-ice and SST perturbations have on precipitation over southern Africa. Thus, in order to obtain results of a finer resolution than the GCM grid and to overcome the inadequacies of the GCM derived precipitation, the technique of downscaling has been applied. The use of downscaling to derive sub-grid-scale information from GCMs has become a recognised research methodology. There are two major downscaling approaches: nested modelling and empirical downscaling. Empirical downscaling has been selected for the present study because it is computationally efficient and can be easily applied to multiple GCM simulations. In contrast, nested modelling is computationally very demanding. The assumptions and caveats associated with empirical downscaling have been discussed by Hewitson (1997), and will be partially addressed in this chapter.

Empirical downscaling identifies relationships derived from observed data, which can then be applied to the GCM data. The procedure aims to derive a function which relates the observed synoptic-scale atmospheric dynamics over a region with the observed (smaller-scale) local climate variable of interest, in this case, precipitation. Once this function has been derived, it is then applied to the GCM synoptic-scale circulation over the region in order to obtain the local-scale precipitation. This technique assumes that the GCM is capable of adequately simulating the synoptic-scale dynamics over the specific region. To this end, it has been shown that the GENESIS GCM captures the atmospheric dynamics over South Africa fairly well (Hudson, 1997; Hudson and Hewitson, 1997). In addition, empirical downscaling assumes that local climates are primarily a function of the larger scale atmospheric forcing. This has been shown to be largely true, although synoptic circulation controls cannot completely describe the local climate, and the roles of atmospheric humidity and local forcing, in particular, need to be addressed (Hewitson, 1998).

The downscaling methodology that is used in the present study has been devised by Hewitson (1997, 1998), Hewitson and Crane (1996) and Crane and Hewitson (1998). In this approach, an artificial neural network (ANN) is used to derive the relationship between the synoptic-scale circulation and local-scale precipitation. The advantage of using ANNs for downscaling over other, usually statistically-based techniques like multiple regression, is that they are not restricted to linear relationships or prescribed non-linearities and they are fairly robust in the presence of noise. The subsequent section will present the basic attributes of an ANN, followed by a description of the downscaling procedure. A more detailed description and discussion of ANNs and a complete account of the downscaling methodology used in the present study can be found in Hewitson and Crane (1994) and Hewitson (1998) respectively.

3.5.2 Artificial Neural Networks

In the context of downscaling, an artificial neural network (ANN) is used to derive a function which relates two data sets, such as those representing synoptic-scale circulation and local-scale precipitation. An ANN is composed of a number of nodes or processors which are connected by weighted links. The nodes are arranged in layers to form a network, such that there is usually an input layer which is connected to one or more "hidden" layers, which are in turn connected to an output layer. Figure 3.1 shows an example of a typical ANN structure. It is apparent from this figure that a node in a particular layer will receive information from every node in the previous layer, and likewise it will transmit information to every node in the following layer. The information which a particular node receives is the weighted sum of the inputs. This sum is then transformed by a function, such as a step or linear function, or more usually a bounded non-linear function like a sigmoid, to produce the output for the particular node. In the present study, the ANN is configured such that there is an input layer of nodes, one "hidden" layer and a single output node which provides the downscaled precipitation value for the specific target location.

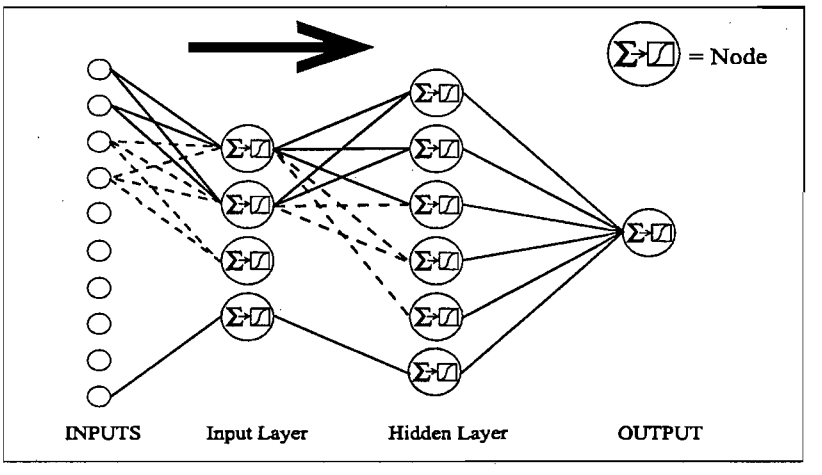

Figure 3.1 Construction of a simple artificial neural network (after Hewitson and Crane, 1994).

The function which relates the two data sets is obtained by the ANN through a training procedure. Initially the ANN represents a random function and the weights associated with each node are set to random numbers. The ANN is then trained with a sample of observed data, whereby the network is presented with a set of inputs for which known target output values are available. These inputs are sequentially applied to the ANN until the error between the ANN output and the target output is minimised. This is referred to as supervised learning or training, since the network has information about what the output should be for a particular input. In the present study the training is achieved using a back-propagation algorithm, which is described in detail by Hewitson and Crane (1994). Essentially, each input is propagated forwards though the network to determine an output value. This ANN output is compared to the target output and the error between the two is propagated back through the network, from the output node to the input nodes. In this backward propagation of the error, the weights associated with each node are adjusted in a direction that minimises the error. When training an ANN, a random portion of the observed data is usually set aside for testing purposes. The performance of the ANN is repeatedly assessed against this data, and training continues until there is no further improvement in the results with respect to the test data. The process of continually appraising the training procedure using independent test data, prevents the ANN from becoming overtrained (Hewitson, 1998). The danger with an overtrained ANN is that it may have started to relate the noise between the input and output data sets (Hewitson, 1998).

At the end of training, the ANN will represent the relationship between the desired input and output data sets. The trained ANN can then be presented with independent input data, such as that from a GCM, in order to derive the necessary output data.

3.5.3 The Downscaling Procedure

The details of the downscaling procedure have been described in full by Hewitson (1998), but are summarised here. In order to determine the local-scale precipitation, three major sources of variance are accounted for, namely, atmospheric circulation dynamics, atmospheric water vapour content and local sources of variance. Atmospheric circulation dynamics represent the primary controls on precipitation and encompass attributes of air mass movement such as vorticity, convergence, and vertical and horizontal velocities. The indicators of circulation dynamics that have been used in the present study are the 500 hPa and 700 hPa temperatures and geopotential height fields. In addition, Hewitson (1998) discusses the importance of including some indication of the amount of precipitable water in the atmosphere as a predictor in the downscaling, and as such the surface (2 m height) specific humidity and

700 hPa and 500 hPa specific humidities are also used as inputs to the ANN. There is, however, always going to be a portion of the regional-scale precipitation which is not accounted for by the afore-mentioned atmospheric variables, largely due to the influence of local factors, such as the particular trajectory that a convective cell may follow, or the amount of antecedent soil moisture that is present. Thus, it is desirable to include the influence of local sources of variance in producing the downscaled precipitation, and this will be discussed at a later stage.

The geopotential heights, temperatures and specific humidities, for the atmospheric levels mentioned above, are used as inputs for the ANN. A lag and lead of these variables are also included as inputs in order to take into account antecedent and forthcoming conditions. However, research has shown that it is also beneficial to provide the ANN with some indication of the coarse state of the atmosphere (Hewitson, 1998). The easiest way to do this is to perform some kind of synoptic indexing and then provide the ANN with this information in addition to the inputs mentioned above. In the present study this is done by means of a Kohonen Self-Organising Map (SOM) (Kohonen, 1989, 1990; Kohonen *et al.*, 1996). SOMs will be described in detail in the following section, therefore only the major concepts will be provided here. A SOM is a special form of neural network that can be used to classify data. In the present application, it is used to identify preferential modes of state of the atmosphere, similar to traditional synoptic typing techniques. However, Hewitson (1998) notes that the use of a SOM over more traditional methods is advantageous, since unlike the SOM, traditional means of synoptic typing are linear in nature and assume that the variables are orthogonal and that the data represents groups rather than a continuum.

In contrast to the ANN described in the sub-section above, a SOM is trained without a target data set and is said to be able to find structure within the data (Kohonen, 1990). A SOM possesses a single layer of nodes, arranged in a two-dimensional array, and each node is described by a set of weights. The data which are used as inputs for the ANN (see the above paragraph) are also used as inputs for the SOM and are mapped, by a process of unsupervised competitive learning, to the two-dimensional array of nodes. As with an ANN, the weights associated with each node are updated in the process of training the SOM. Once the SOM has been trained, each node will represent a particular "cluster", analogous to a cluster group in regular cluster analysis. The trained SOM is then presented with independent input data and for each input, the nodes will compete to try to best match the structure in the input data, with the position of the "winning" node or "cluster" being recorded. Neighbouring nodes in

the array represent related "clusters", therefore similar data samples will map to adjacent nodes. In the present downscaling application, a SOM of 15 output nodes has been used (3 nodes in the x-direction and 5 nodes in the y-direction), and each node can be referenced with respect to its x;y coordinates in the array. Thus, there are 15 different "clusters" to which the input data can be mapped. For each day of the observed data that is applied to the trained SOM, the x;y coordinates of the node which is mapped to is recorded. These x;y indices are then used as additional inputs for the ANN.

Figure 3.2 is a flow diagram outlining the procedure which has been used for downscaling over South Africa (refer to Chapters 7 and 9). The observed data used in the training and validation procedures are the twice-daily NCEP assimilation reanalyses extending from 1980 to 1988, and extracted for the summer (DJF) and winter (JJA) seasons respectively. As previously mentioned, the variables used are:

- 700 hPa level geopotential heights, temperatures and specific humidities
- 500 hPa level geopotential heights, temperatures and specific humidities
- surface specific humidity.

The data are presented on the grids described in Chapter 2, but are interpolated to the T31 grid of the GENESIS GCM using the spatial interpolation routine described earlier in the chapter. This is done because the data which are used to train the ANN, and the data which are applied to the ANN must be on the same grid. These interpolated variables will hereafter be referred to as the observational atmospheric variables. The observed daily precipitation data, used as the target output when training the ANN, are area averaged station data on a 0.5° grid which have been obtained from the South African Computer Center for Water Research (CCWR[1]). In the creation of the area averaged data set, grid cell averages that were derived from less than 3 stations were not used.

Figure 3.2 shows how the observational atmospheric variables are used to obtain a function f which relates synoptic-scale characteristics to the observed local-scale precipitation. Once validated, this function is applied to GCM synoptic-scale circulation and humidity in order to derive precipitation on a 0.5° grid. The downscaling is performed separately for summer and winter, and the procedure shown on Figure 3.2 is executed for each target local grid cell, i.e. a different downscaling function may be derived for each cell. For each target precipitation grid cell (0.5° CCWR data), the observational atmospheric variables from the co-located T31

[1] http://www.aqua.ccwr.ac.za/

grid cell, as well as the circulation data from the 8 surrounding cells, are selected. In other words, the downscaling predictors for a certain location include the humidity and temperature of the column above the location, and the circulation (geopotential heights) of the column and surrounding area. A lag of 36 hours and a lead of 12 hours are then calculated for these data and included as additional inputs for the ANN and SOM. Prior to training the SOM and the ANN, the data are randomly subset into two groups, such that 75% of the data in the time series are used for training, and 25% are used for testing the training process in order to determine when to stop training the ANN.

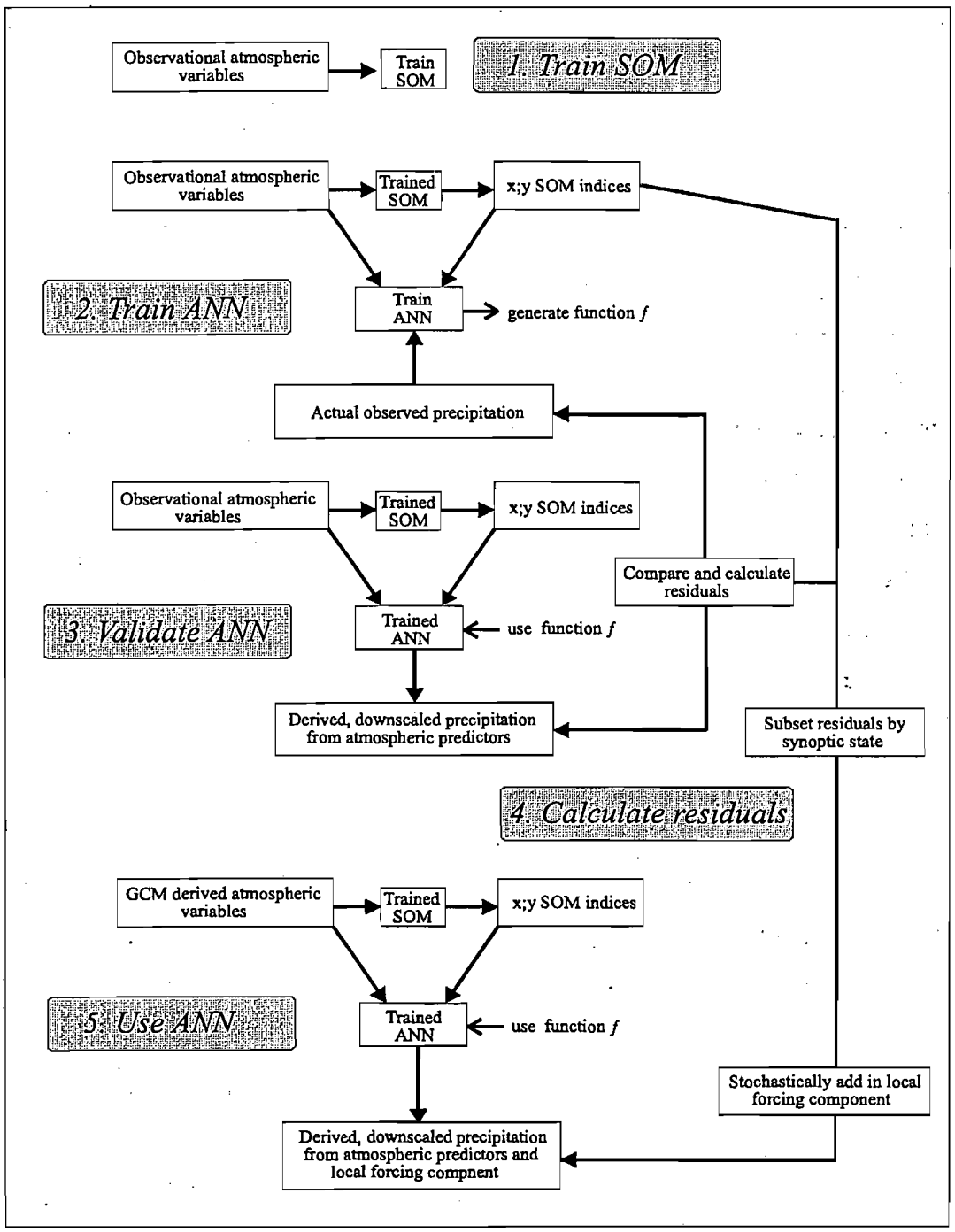

Figure 3.2 A flow chart showing the procedural steps in downscaling (adapted from Hewitson, 1998).

The process depicted on Figure 3.2 can be summarised as follows. Initially, the observational atmospheric variables, mentioned above, are used to train the SOM. Once the SOM has been trained, the data are reapplied to the SOM in order to obtain the x;y indices of the nodes which are mapped to, for each respective time step. These indices, together with the observational atmospheric variables, are used to train the ANN. Before the trained ANN can be used for application purposes, the functions which have been derived for each target grid cell should be validated. This is done by applying independent test data to the ANN and comparing the ANN derived downscaled precipitation to actual observed precipitation at the 0.5° resolution. If the derived downscaled precipitation is suitably similar to the actual precipitation, then the ANN can be used to generate precipitation data from other data sets (using the same atmospheric predictor variables), such as those from a GCM.

However, earlier in this section it was mentioned that it is important to take into account local sources of variance. In this application, local sources of variance are referred to as those forcing factors which contribute to the variance in the precipitation field that is unaccounted for by the atmospheric predictors. Hewitson (1998) has found that if one does not in some way include this residual variance, then the downscaling procedure will generally produce too many trace precipitation days and will under-predict peak precipitation events compared to what is actually observed. This is because the ANN generalises a precipitation response for a given atmospheric state. This is problematic for extreme precipitation events, because, for example, the difference between receiving no precipitation and trace precipitation may not be distinguishable by the synoptic atmospheric controls and may be due more to local forcing factors. Hewitson (1998) discusses how the locally forced variance can be considered as a stochastic factor which has a particular distribution depending on the state of the synoptic circulation. The state of the synoptic-scale circulation is important when considering the locally forced variance, because some circulation patterns may dominate the local climate response such that the variance from local forcing factors is small (e.g. with frontal activity), whereas other circulation patterns may be weak, such that the variance from local forcing factors is likely to be large (e.g. thermally induced thunderstorm activity).

The locally forced variance is obtained from a set of residuals. These residuals are determined by calculating the difference between the ANN derived downscaled precipitation and the actual observed precipitation (Figure 3.2) i.e. it is the variance not accounted for by the downscaling using the atmospheric predictors. By randomly selecting a residual and adding it to the ANN downscaled precipitation value, the locally forced variance can be taken

into account. Prior to this, however, the residuals must be determined as a function of the state of the synoptic-scale circulation. Thus, the residuals are subset according to the SOM "cluster" to which a particular time step mapped. Once this has been performed, there will be a distribution of residuals for each of the 15 SOM "clusters".

At this stage, the ANN has been trained and validated with observed data, and the distribution of residuals associated with each SOM "cluster" (representing the locally forced variance) has been determined. Downscaled precipitation can now be derived from independent data (e.g. from a GCM). Firstly, the atmospheric predictors are applied to the SOM in order to obtain the SOM "cluster" identification indices. Then, these indices and the atmospheric predictors are applied to the ANN and the downscaled precipitation is derived. Lastly, in order to take into account the locally forced variance, the distribution of residuals are utilised. For any time step for which downscaling has been performed, the state of the synoptic-scale circulation has been determined through the SOM procedure, thus a residual from the distribution associated with the specific SOM "cluster" is randomly selected and added to the ANN derived downscaled precipitation value.

3.6 Self-Organising Maps

Apart from using SOMs in the downscaling procedure, they are also used in the present study for validation purposes and for assessing possible changes in circulation in response to the sea-ice and SST perturbations. This section will describe the use of SOMs in the context of the latter two applications. In these cases, a SOM is used to organize circulation data (sea-level pressure and 500 hPa heights) into discrete types. Each of the output nodes in the trained SOM will represent a particular atmospheric circulation state, for example, a certain node may represent circulation associated with anticyclonic ridging over South Africa. The SOM is used to identify differences between the model and observed data, or control and experiment simulations, with respect to the frequency and distribution of synoptic circulation types.

Input data of n dimensions (for example, twice-daily data presented on a particular grid) are mapped, by a process of unsupervised competitive learning, to a two-dimensional array of nodes where neighbouring nodes represent related types. This map of nodes depicts categories in a continuum which have been projected onto a two-dimensional plane. Each node has a set of m weights, where m is the number of grid-points on the input circulation maps. These weights are updated in the process of training the SOM, and at the end of

training, the weights represent a particular circulation map at each node. Ultimately, a trained SOM is presented with a circulation map and each node will compete to try to best match the input circulation pattern, with the position of the "winning" node being recorded (Figure 3.3).

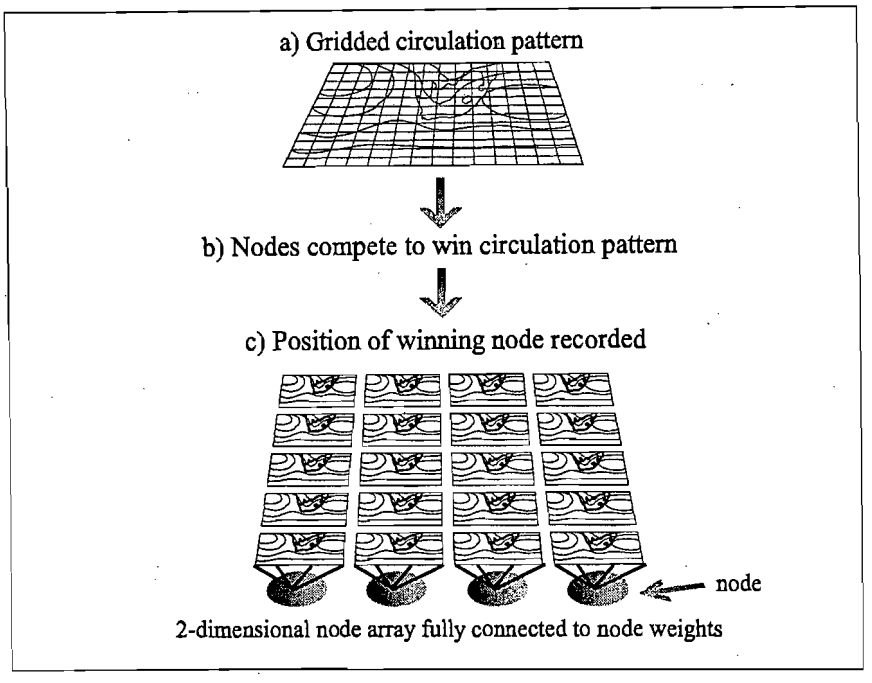

Figure 3.3 A schematic indicating the process of events in the presentation of a circulation pattern to a SOM (adapted from Main, 1997).

Once this has been performed on a time series of data, it is possible to observe the frequency of mappings associated with each node, and then decompose the weights of the nodes to examine the circulation type that was being mapped to. In the present study, the SOM Program Package of Kohonen *et al.* (1996) has been used to perform the analyses.

There are a number of decisions that must be made concerning the training and structure of the SOM. Firstly, the size and topology of the SOM must be considered. The size of the nodal array will determine the number of categories or types into which the input data will be divided. For example, a 3 by 5 array of nodes defines a maximum of 15 classification types. Dimensions are therefore selected that will be suitable for a particular application. In the SOM Program Package (Kohonen *et al.*, 1996) the array of nodes can be arranged in either a hexagonal or rectangular lattice (Figure 3.4). The hexagonal lattice provides better coverage of the two-dimensional space, but it does not seem to matter too much which lattice is selected (Openshaw, 1994). In the present study, a rectangular topology has been used for the purposes of ease of analysis and visual display.

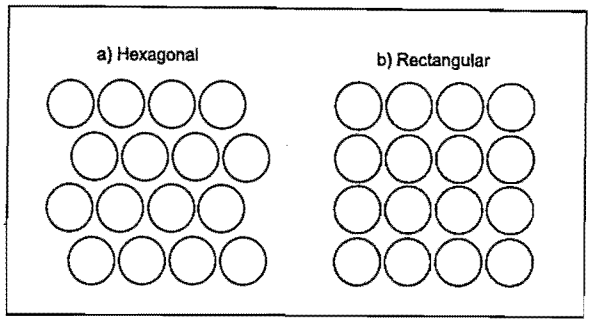

Figure 3.4 The topology of the SOM can be either *a*) hexagonal or *b*) rectangular.

The next step is to initialise the weights associated with each node. The SOM Program Package (Kohonen *et al.*, 1996) provides two means of initialisation: random initialisation, where the weights are ascribed random numbers, and linear initialisation, where the weights are initialised in an ordered manner. In the process of linear initialisation, the weights of the two nodes in diagonally opposite corners of the node-space are set to the two principal eigenvectors of the input data. The remaining intermediate nodes are then set to various combinations of the two eigenvectors relative to their distance from each corner. Linear initialisation has been used in the present study.

A data set, which in the present study would comprise a time series of gridded circulation "maps" (i.e. consecutive vectors of data), is then presented to the array in order to train the SOM. For each circulation map, the winning node is the node whose vector of weights is most similar to the input vector of data. The weights of the nodes in the "neighbourhood" of the winning node are then updated, based on

$$m_i(t+1) = m_i(t) + h_{ci}(t)[x(t) - m_i(t)], \tag{3.10}$$

where $x(t)$ is the input vector of data at time t, m_i is the vector of weights associated with node i and $h_{ci}(t)$ is the neighbourhood kernel (Kohonen *et al.*, 1996). The neighbourhood kernel is a function which determines which of the surrounding nodes will be updated. A Gaussian function is used in the present study and is described by

$$h_{ci} = \alpha(t).\exp\left(-\frac{d^2}{2\sigma^2(t)}\right), \tag{3.11}$$

where d is the distance from the winning node, $\sigma(t)$ is the radius of the neighbourhood at time t, and $\alpha(t)$ is the learning rate at time t (Kohonen *et al.*, 1996). In essence, the function describes a bell-shaped curve, such that within a certain radius, the update rate of nodes decreases outwards from the winning node. The learning rate $(0 < \alpha(t) < 1)$ determines how

easily the weights can be altered and decreases linearly to zero by the end of training. Therefore, towards the end of training, extreme input data configurations will have less of an effect on the nodes. The size of the neighbourhood radius also decreases linearly to a value of one through the training process. The number of training iterations (t) should ideally be selected such that convergence is achieved by the end of training. It has been suggested that, as a rule of thumb, the number of iterations should be equal to about 500 times the dimensions of the nodal array (Kohonen, 1990). Iterations may vary from around 10 000 steps for fast learning, to up to about 100 000 steps (Kohonen, 1990). If the sample of input data is smaller than the number of iterations, then the data is used reiteratively in the training. As previously mentioned, after training, the vectors of weights can be mapped to display the circulation features associated with each node. In addition, input data are presented to the trained SOM and the frequency of mappings to each node (circulation type) is recorded.

3.7 Summary

This chapter has described the procedures and principles behind the primary analysis techniques used in the present study. The techniques or tools included are: spatial interpolation, Fourier analysis, mean absolute error, Student's t statistic, cyclone and storm track algorithms, artificial neural networks, downscaling and self-organising maps.

SECTION II

Simulation of the Present-Day Climate

	T_{sfc} K	T_{500} K	*SLP* hPa	HGT_{500} m	u_{700} m s^{-1}	u_{500} m s^{-1}	q_{sfc} g kg^{-1}	q_{500} g kg^{-1}	*Precip.* mm day^{-1}	*Cyclone density* $\times 10^{-3}$.(°lat.)$^{-2}$	*Storm track* std. dev.
SHEM mean bias											
DJF	-1.5	-1.9	4.2	3.1	-0.2	0.2	-1.3	-0.14	0.4	0.073	0.1
JJA	2	-1.7	0.1	11.3	-0.3	0.1	-1.1	-0.19	0.2	0.079	0.1
SHEM zonal mean MAE											
DJF	0.9	1.8	2.2	27.1	2.2	2.9	1.6	0.16	0.6	0.212	0.3
JJA	1.7	1.7	1.7	39.6	2.7	3.8	1.5	0.27	0.8	0.154	0.3
SHEM field MAE											
DJF	1.2	1.8	2.8	30.2	2.8	3.2	1.6	0.28	1.4	0.261	0.4
JJA	2.2	1.7	2.8	42.6	3	4	1.6	0.29	1.2	0.223	0.4
South African field MAE											
DJF	1.5	2.2	1.4	41.5	1.6	2.6	1.7	0.26	1.1	0.171	0.4
JJA	2.2	3.2	1.2	57.0	2.1	3.4	1.6	0.21	1	0.096	0.3

Table 4.1 Southern Hemisphere (SHEM) mean biases and SHEM mean absolute errors (MAE) for the zonal mean fields and full fields, and the MAE for the full South African field are shown for summer (DJF) and winter (JJA). The South African window extends from 20°S to 50°S and from 2°E to 47°E. The variables examined are air temperature (*T*), sea level pressure (*SLP*), geopotential heights (*HGT*), the u-component of the wind (*u*), specific humidity (*q*), precipitation, midlatitude cyclone density and storm tracks. The subscripts *sfc*, *700* and *500* denote the surface, the 700 hPa level and the 500 hPa level respectively.

4.2 Temperature

4.2.1 Surface Air Temperature

On average over the Southern Hemisphere, the model exhibits a surface air temperature cold bias of 1.5° during summer, but is warmer than observed during winter (Table 4.1). This is reflected in the zonal plots (Figure 4.1) and full fields (Figure 4.2) of surface temperature which show that the Antarctic region contributes the most to these biases, with the air over the continent being too cold in summer and too warm in winter. The positive winter anomalies over Antarctica were also found with the previous version of the model and Thompson and Pollard (1995) suggested that there is probably too much horizontal heat transport from lower latitudes. The biases may also be linked to errors in the predicted cloud amounts, i.e. if cloudiness were overestimated in the polar regions, then warm anomalies would result during winter and cold anomalies during summer.

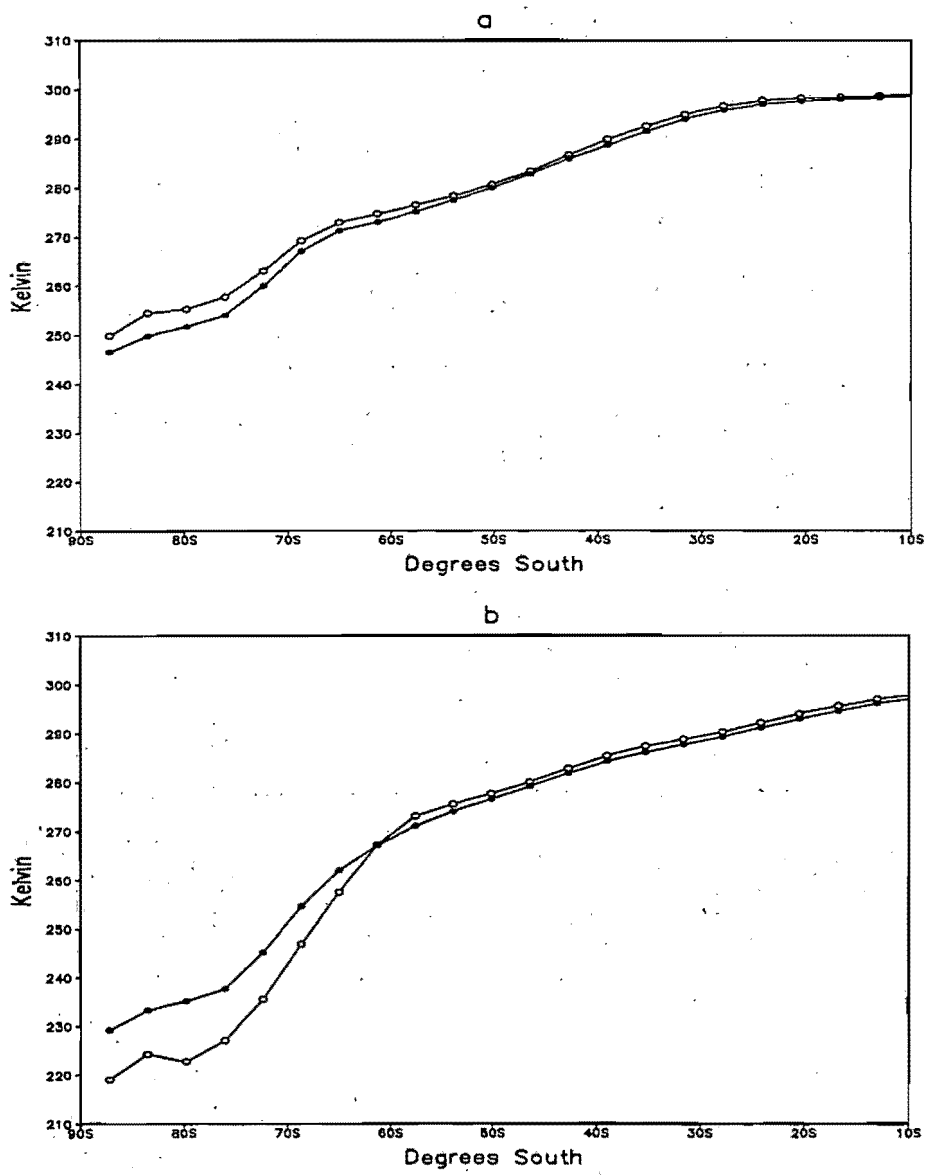

Figure 4.1 Zonally averaged surface temperature (K) for the observed (open circles) and GCM (closed circles) data in *a*) summer and *b*) winter.

to pressures in the model south of about 55°S being higher than observed (Figures 4.7 and 4.8). Heights north of this latitude are, however, lower than observed (Figures 4.7 and 4.8). This is similar to the result found for sea level pressure and may be partially related to the course resolution of the AGCM, such that it is unable to simulate the steep meridional pressure gradients. This difference between the model and observed geopotential heights amounts to a MAE in the zonal averages of about 30 m (27.1 m in summer and 39.6 m in winter) (Table 4.1).

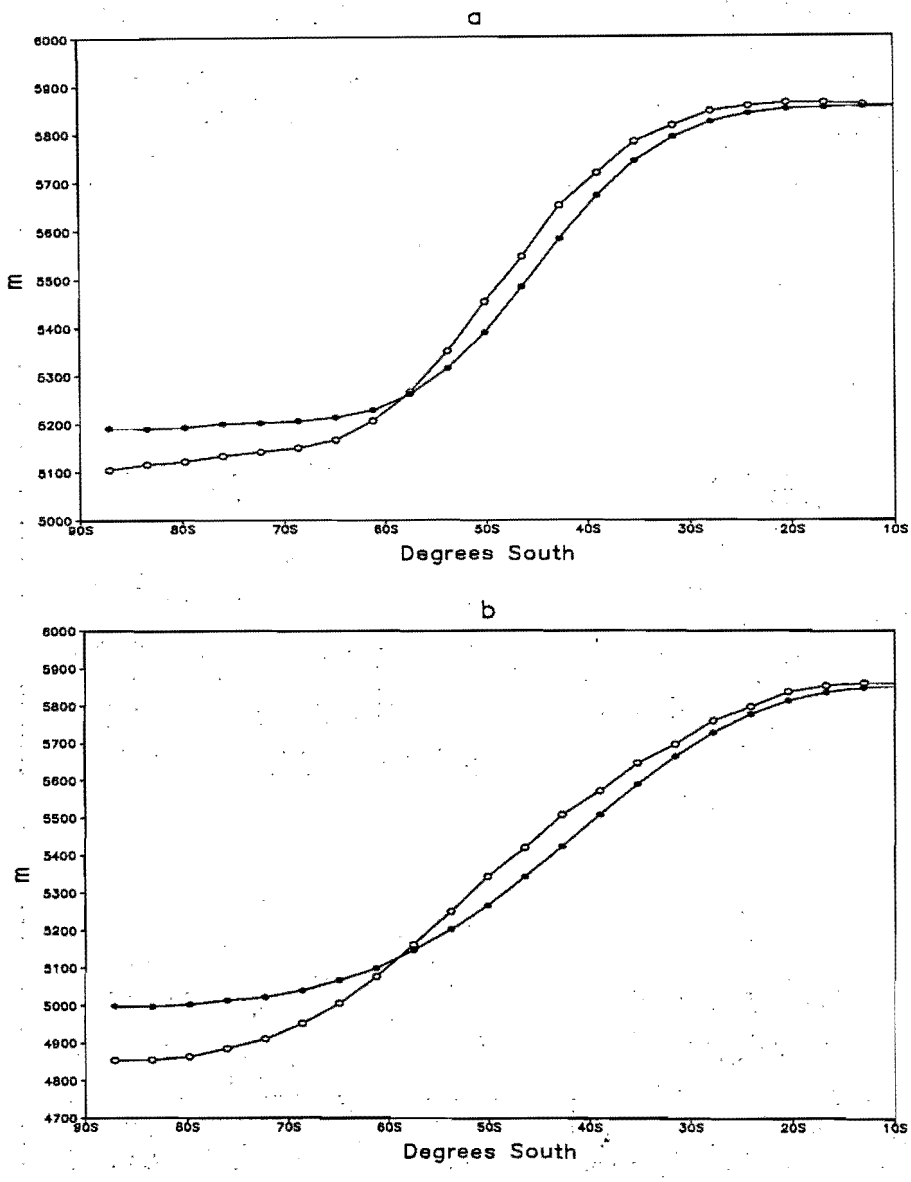

Figure 4.7 Zonally averaged 500 hPa heights (m) for the observed (open circles) and GCM (closed circles) data in *a*) summer and *b*) winter.

The seasonal expansion of lower pressures further northwards, and the deepening of the circumpolar trough in winter compared to summer, appears to be captured by the model (Figure 4.8). In a subsequent section of this chapter, Fourier analysis will facilitate a comparison between the model and observed data in terms of the long waves which contribute to asymmetries in the 500 hPa height field. This will enable a more complete

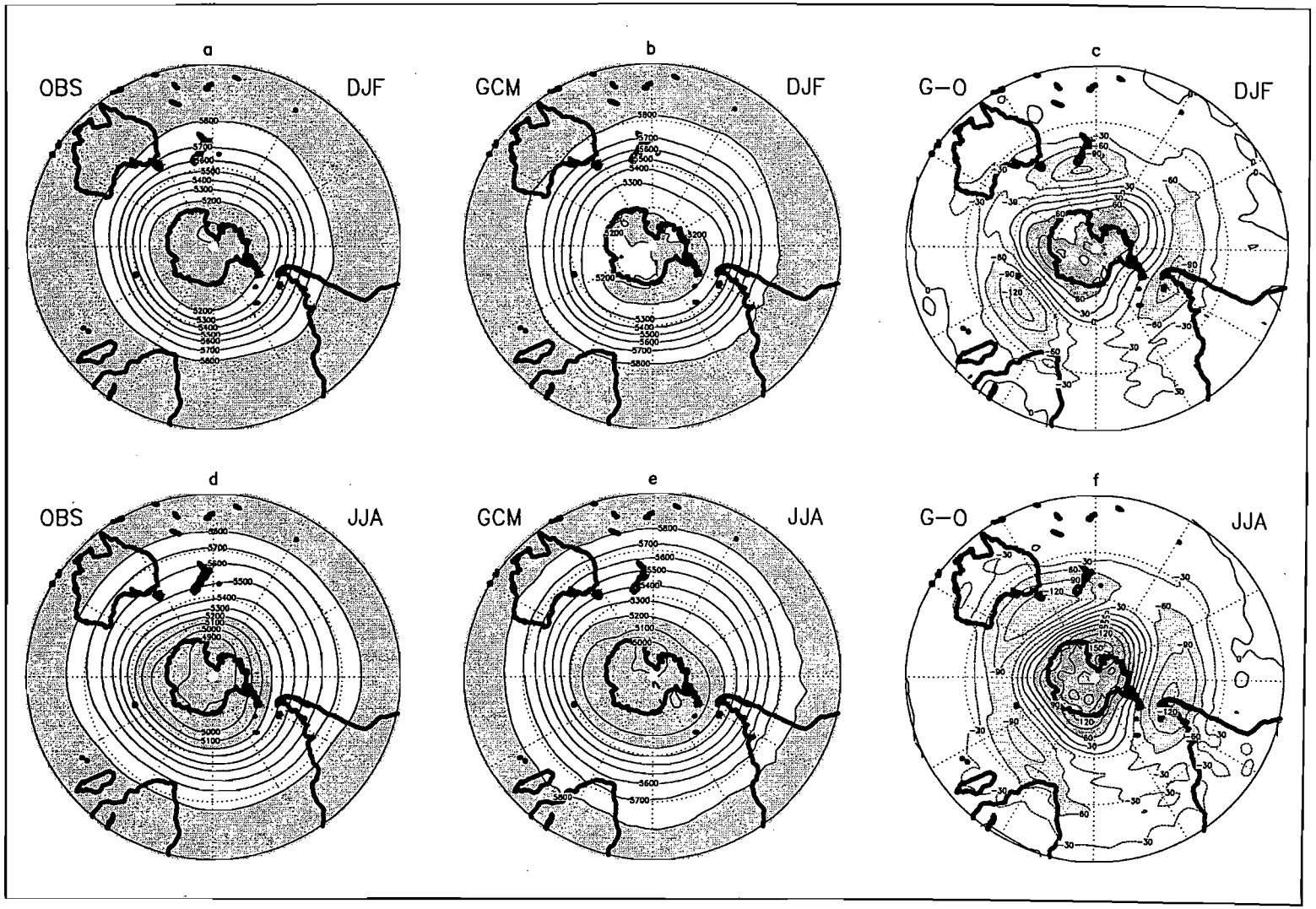

Figure 4.8 Mean 500 hPa heights (m) for the observed data (*a* and *d*) and the GCM control simulation (*b* and *e*) for summer (DJF) and winter (JJA). Regions with heights above and below 5800 m and 5200 m respectively have been shaded. Also shown are the corresponding anomaly maps, i.e. GCM minus observed (*c* and *f*), where the shaded regions indicate positive (dark shading) and negative (light shading) differences greater than 60 m.

description of the differences between the patterns of the 500 hPa field in the two data sets than is possible from a visual examination of the maps in Figure 4.8.

The 500 hPa heights over southern Africa are too low in both seasons, with a MAE of about 50 m (41.5 m in summer and 57.0 m in winter) (Table 4.1). In this region, the largest differences between the model and the NCEP reanalyses are found over the southern-most portion of the subcontinent (south of about 30°S) and decrease as one moves further north (Figure 4.8).

4.4 Wind

4.4.1 700 hPa Wind

In both summer and winter the wind speed maximum occurs too far north, particularly in winter where the observed peak is situated at 50°S and the model peak at 40°S (Figure 4.9). This is related to the previously discussed northward offset of subpolar and midlatitude pressure systems in the model. The 2-dimensional field maps (Figure 4.10) reflect this difference, showing weaker (~6 m s^{-1}) than normal winds between about 50°S and 70°S, and stronger (~4 m s^{-1}) than normal winds between about 30°S and 50°S in both seasons. The zonal plots (Figure 4.9) show that in general during summer, apart from the northward offset of the model data, the size and shape of the observed and model curves are in good agreement. However, during winter the region of high wind speeds are spread over fewer latitudes than in the observed data i.e. the model curve is too peaked (Figure 4.9).

Wind directions are generally well simulated by the model, with most of the discrepancies found for the weakest winds in the easterlies (Figure 4.10). It is evident, however, that the winds south-east of New Zealand are too zonal in the model during winter (Figure 4.10).

Over the South African region, the easterlies are too weak in both seasons (Figure 4.10) and in winter, the westerlies are too strong. The MAE over this region is 1.6 m s^{-1} in summer and 2.1 m s^{-1} in winter (Table 4.1).

4.4.2 500 hPa Wind

Many of the same problems that were evident with the 700 hPa winds are apparent in the 500 hPa wind field. Once again there appears to be a northward shift of the modelled winds,

such that winds in the midlatitudes are too weak (up to 10 m s^{-1} in JJA) and winds in the subtropics are too strong (up to 8 m s^{-1} in JJA) (Figures 4.11 and 4.12). Liang *et al.* (1995),

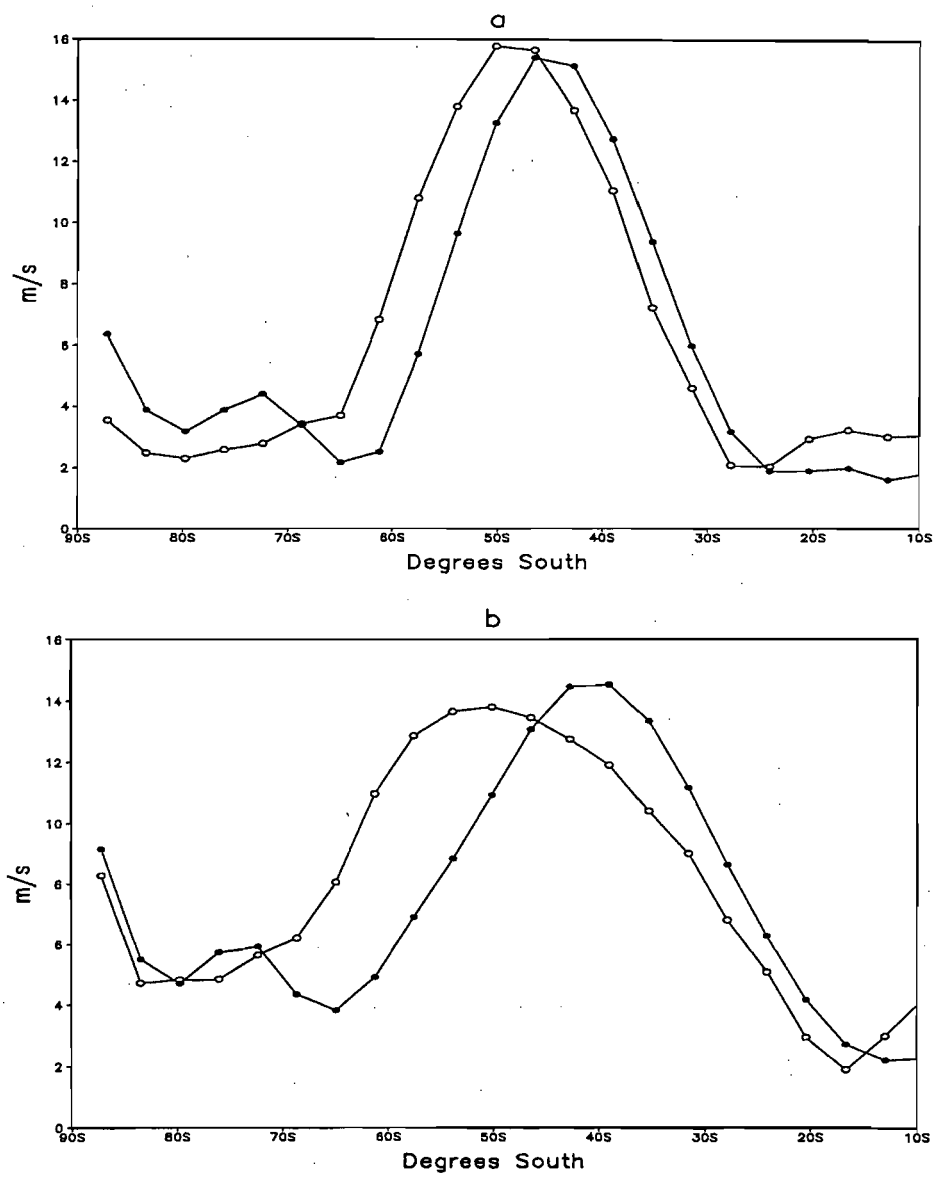

Figure 4.9 Zonally averaged 700 hPa wind (m s^{-1}) for the observed (open circles) and GCM (closed circles) data in *a)* summer and *b)* winter.

Kiehl and Williamson (1991) and Watterson *et al.* (1995) also found a northward offset of the jet streams upon examination of the 200 hPa winds of their respective GCMs and found that this improves as horizontal resolution increases (Liang *et al.*, 1995, Kiehl and Williamson, 1991). Furthermore, in a tuning process with version 1.02 of GENESIS, Thompson and Pollard (1995) found that by improving the vertical profiles of atmospheric radiative heating, the position of the jet streams moved closer to what is observed.

In winter, the zonal averages show that the higher wind speeds in the model should be spread over a greater range of latitudes (Figure 4.11). Linked to this is the inability of the model to

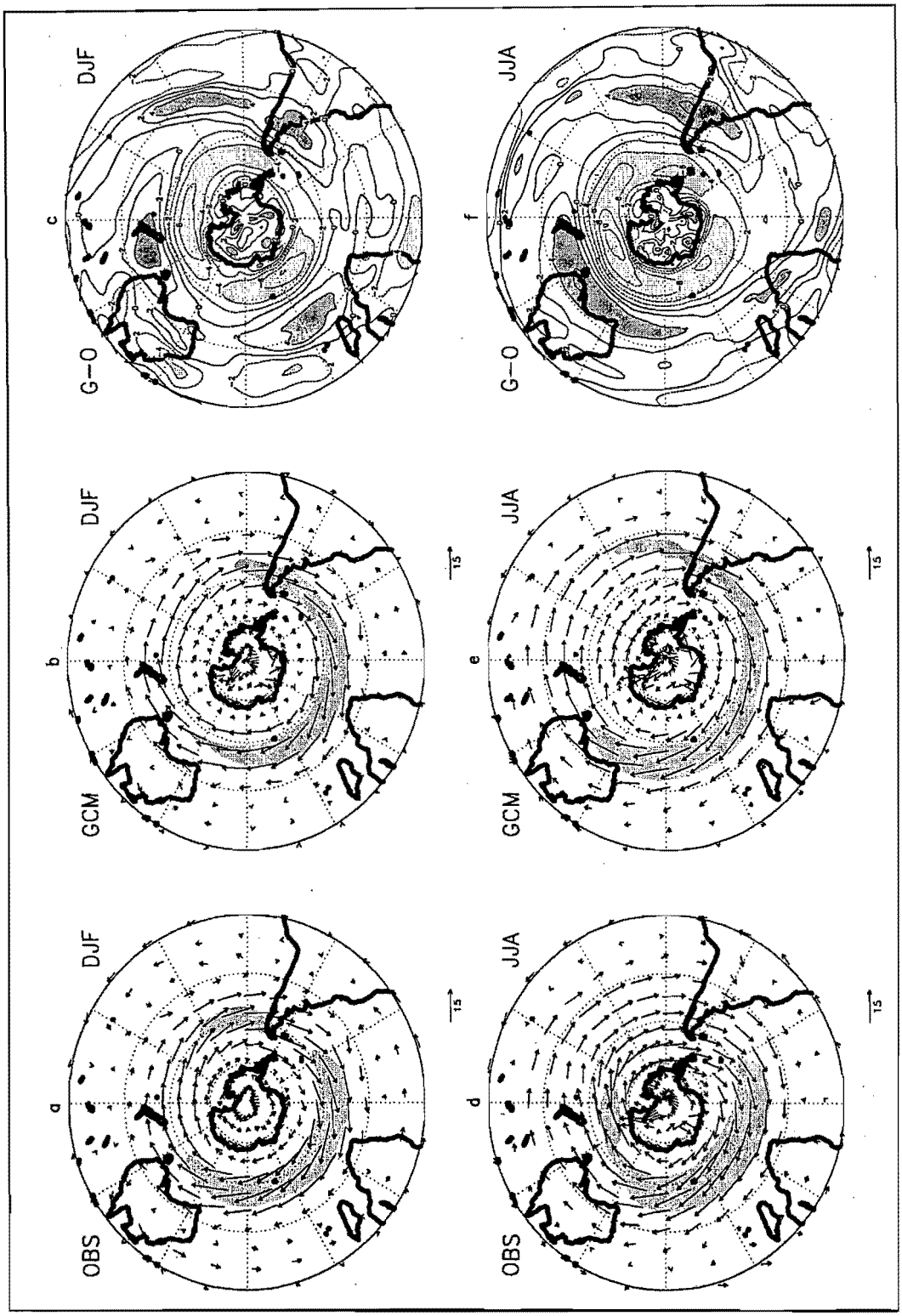

Figure 4.10 Mean 700 hPa wind vectors (m s^{-1}) for the observed data (*a* and *d*) and the GCM control simulation (*b* and *e*) for summer (DJF) and winter (JJA). The shaded regions depict wind speeds greater than 15 m s^{-1}. Also shown are the corresponding wind speed anomaly maps, i.e. GCM minus observed (*c* and *f*), where the shaded regions indicate positive (dark shading) and negative (light shading) differences greater than 4 m s^{-1}.

clearly simulate the double jet in the region of New Zealand, with the need for a stronger high latitude component (Figure 4.12). The westerlies are also generally too zonal between 50°S and 60°S, especially south-east of New Zealand. In winter in the observed data, weak easterlies are evident near 10°S (Figure 4.12) and they strengthen slightly north of this (not shown), whereas in the model the easterlies are only apparent north of 10°S and they are not as prominent as in the observed data (not shown). Over southern Africa in winter the westerlies are up to 6 m s^{-1} too strong. The 500 hPa wind field in summer is more realistic than the winter field, especially over southern Africa.

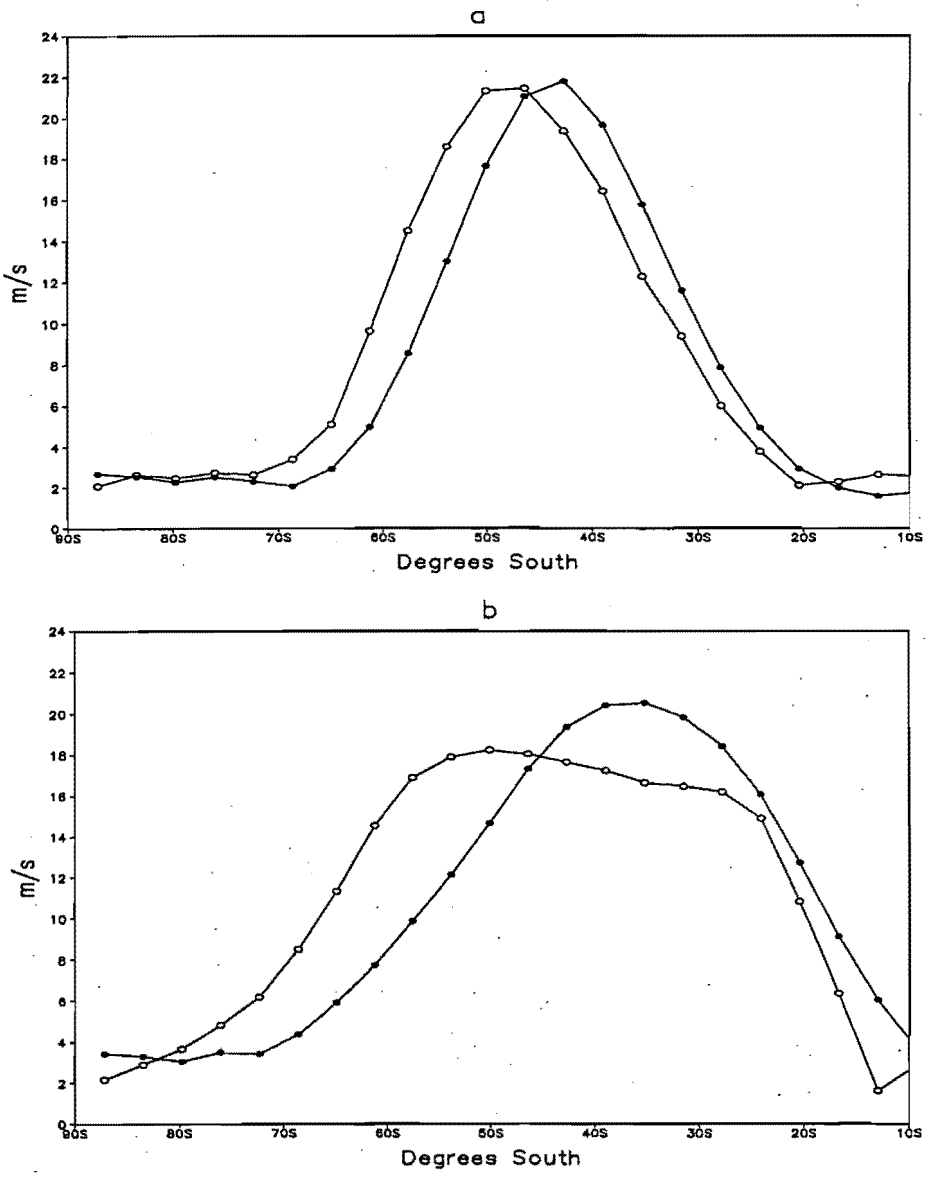

Figure 4.11 Zonally averaged 500 hPa wind (m s^{-1}) for the observed (open circles) and GCM (closed circles) data in *a*) summer and *b*) winter.

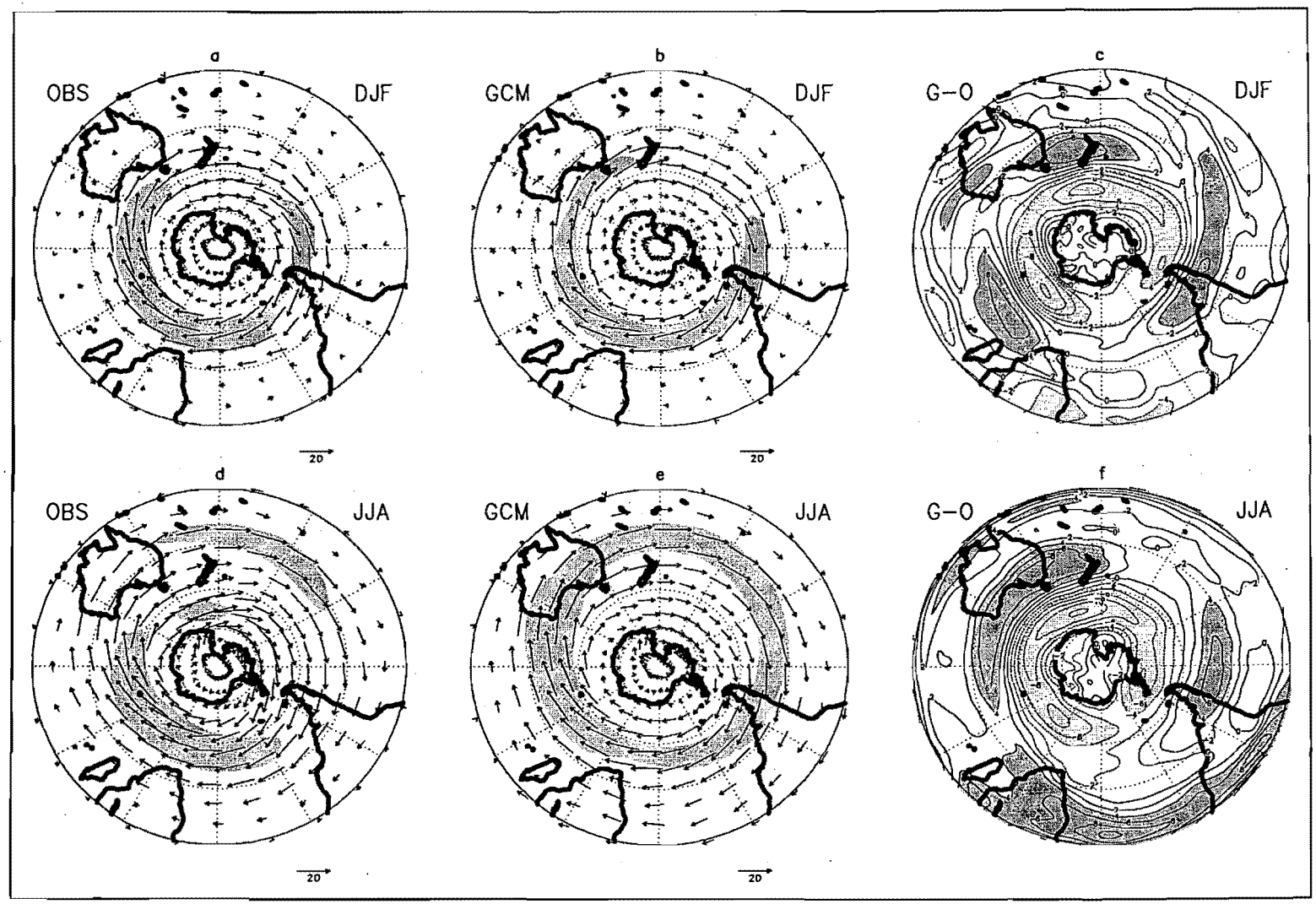

Figure 4.12 Mean 500 hPa wind vectors (m s^{-1}) for the observed data (*a* and *d*) and the GCM control simulation (*b* and *e*) for summer (DJF) and winter (JJA). The shaded regions depict wind speeds greater than 20 m s^{-1}. Also shown are the corresponding wind speed anomaly maps, i.e. GCM minus observed (*c* and *f*), where the shaded regions indicate positive (dark shading) and negative (light shading) differences greater than 4 m s^{-1}.

4.5 Humidity

4.5.1 Surface Specific Humidity

There is a negative specific humidity bias over the Southern Hemisphere of 1.3 g kg^{-1} and 1.1 g kg^{-1} in summer and winter respectively (Table 4.1). This is largely from too little atmospheric water in the tropics and subtropics (Figures 4.13 and 4.14). The pattern of modelled specific humidities over the Southern Hemisphere compares well to the observed data, although gradients are sometimes not as sharp (Figure 4.14).

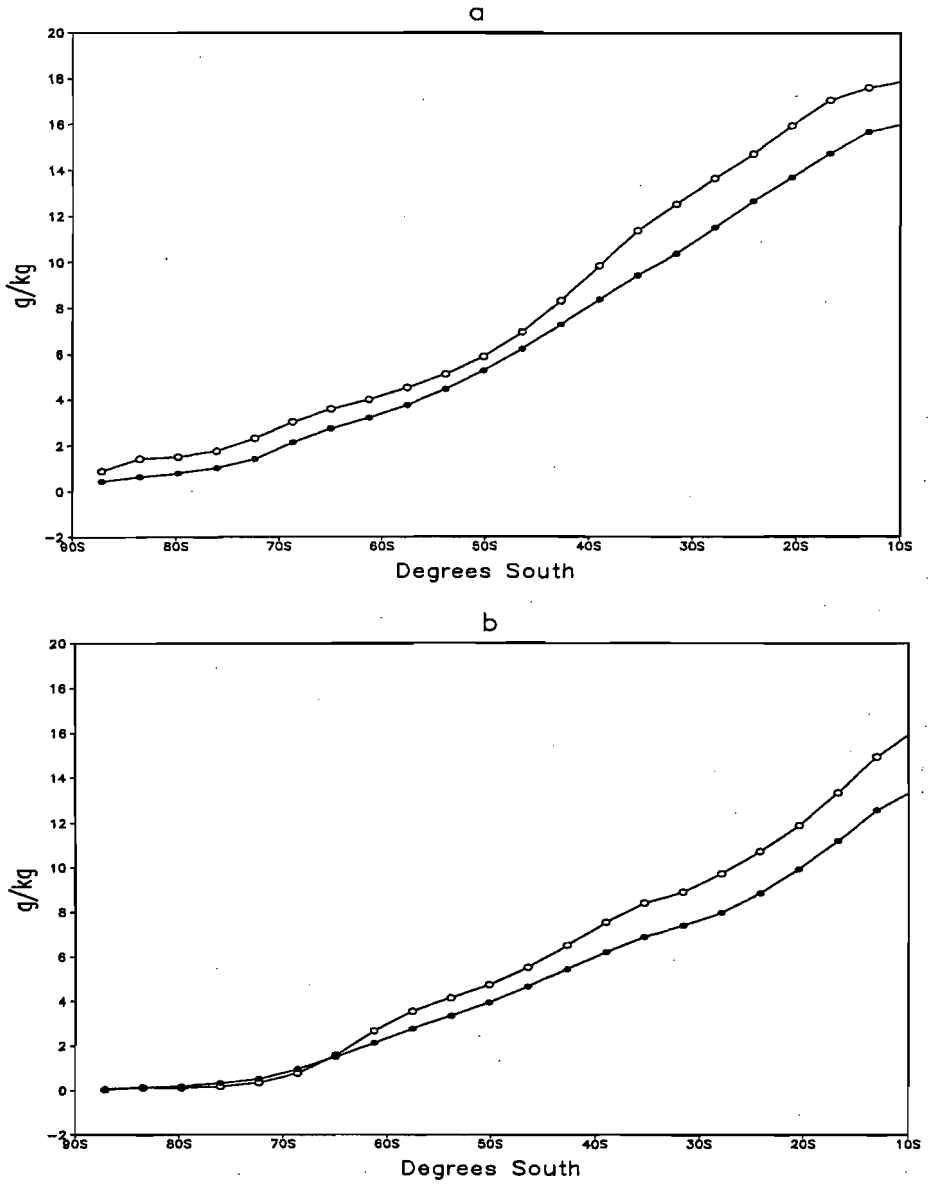

Figure 4.13 Zonally averaged surface specific humidity (g kg^{-1}) for the observed (open circles) and GCM (closed circles) data in *a*) summer and *b*) winter.

4.5.2 500 hPa Specific Humidity

As with the surface specific humidity, the 500 hPa surface also displays an overall negative bias (Table 4.1 and Figure 4.15), although it is evident from the 2-dimensional field maps that there are regions of positive bias associated with the continents during summer (Figure 4.16).

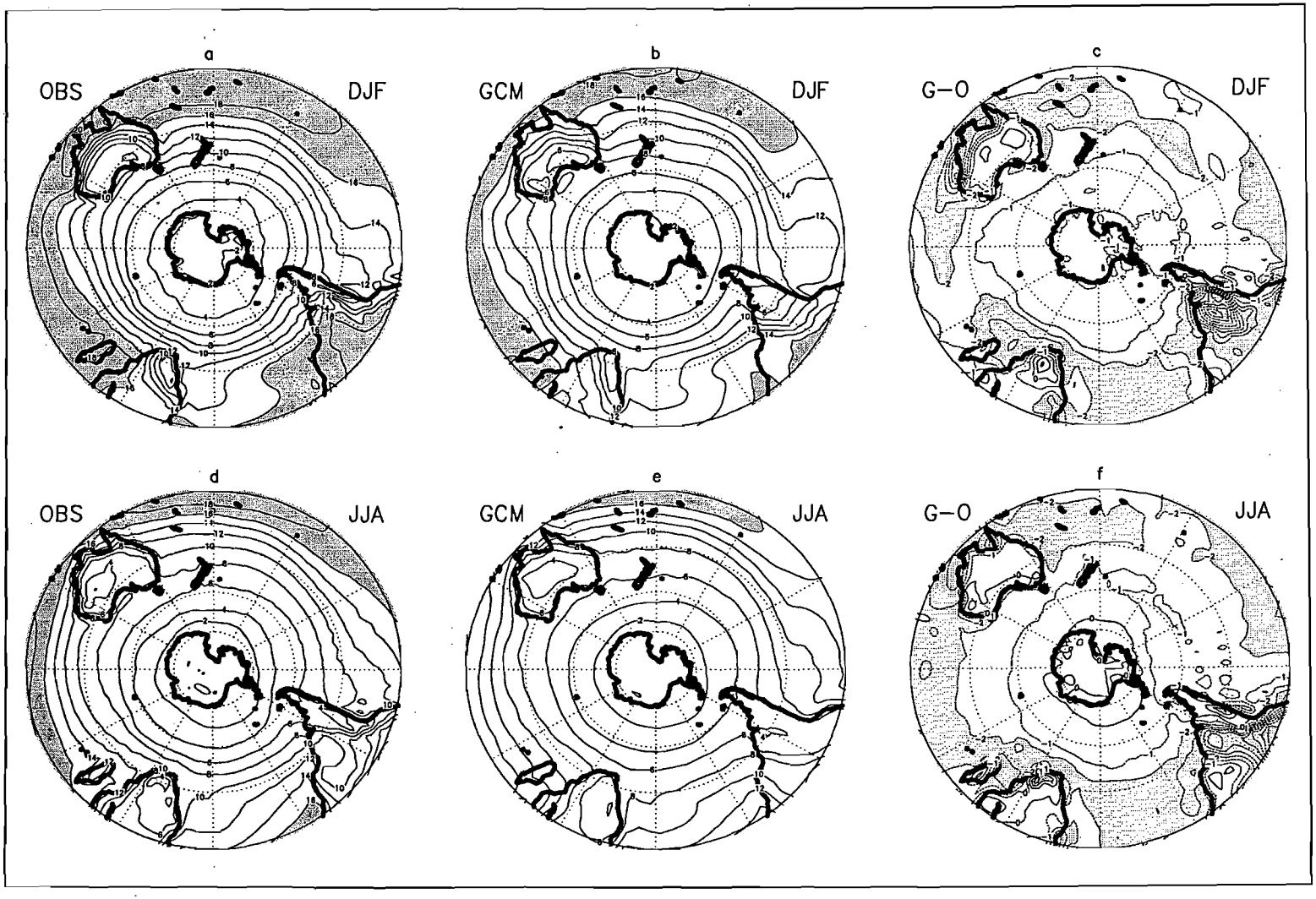

Figure 4.14 Mean surface specific humidity (g kg^{-1}) for the observed data (*a* and *d*) and the GCM control simulation (*b* and *e*) for summer (DJF) and winter (JJA). Regions with humidities above 16 g kg^{-1} have been shaded. Also shown are the corresponding anomaly maps, i.e. GCM minus observed (*c* and *f*), where the shaded regions indicate positive (dark shading) and negative (light shading) differences greater than 2 g kg^{-1}.

The difference in specific humidity between summer and winter, due to the movement of the Intertropical Convergence Zone (ITCZ), is captured by the model.

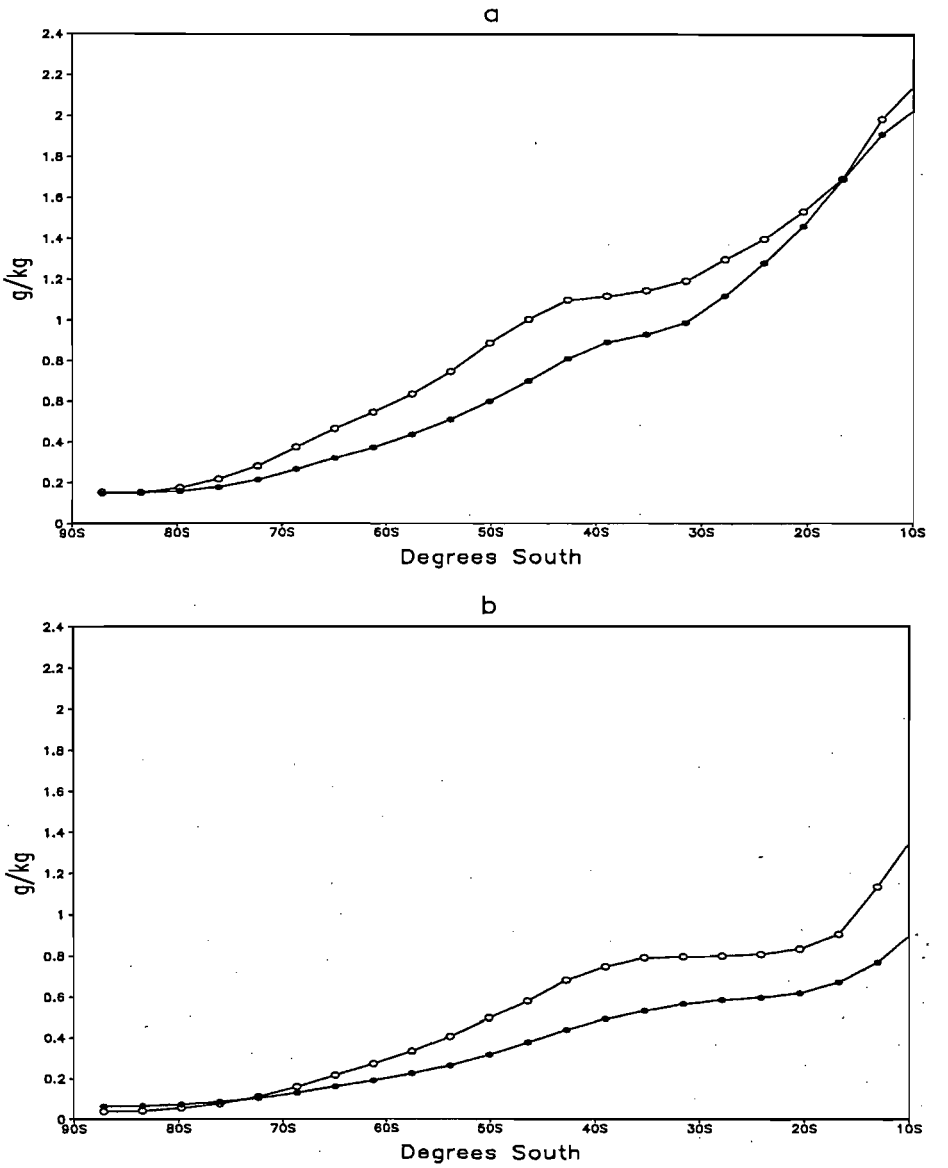

Figure 4.15 Zonally averaged 500 hPa specific humidity (g kg^{-1}) for the observed (open circles) and GCM (closed circles) data in *a*) summer and *b*) winter.

4.6 Precipitation

The model predicted precipitation values over the Southern Hemisphere are in general too high, with a positive bias of 0.4 mm day^{-1} in summer and 0.2 mm day^{-1} in winter (Table 4.1). The overestimation of precipitation may be due to an overactive convective plume scheme in the model. The greatest deviations from observed occur around the latitudinal positions of the local maxima and minima in the zonal averages for both seasons (Figure 4.17). However, although the magnitudes differ, the seasonal latitudinal *positions* of the precipitation maxima and minima in the model correspond well with the NCEP data, showing a minimum at 35°S

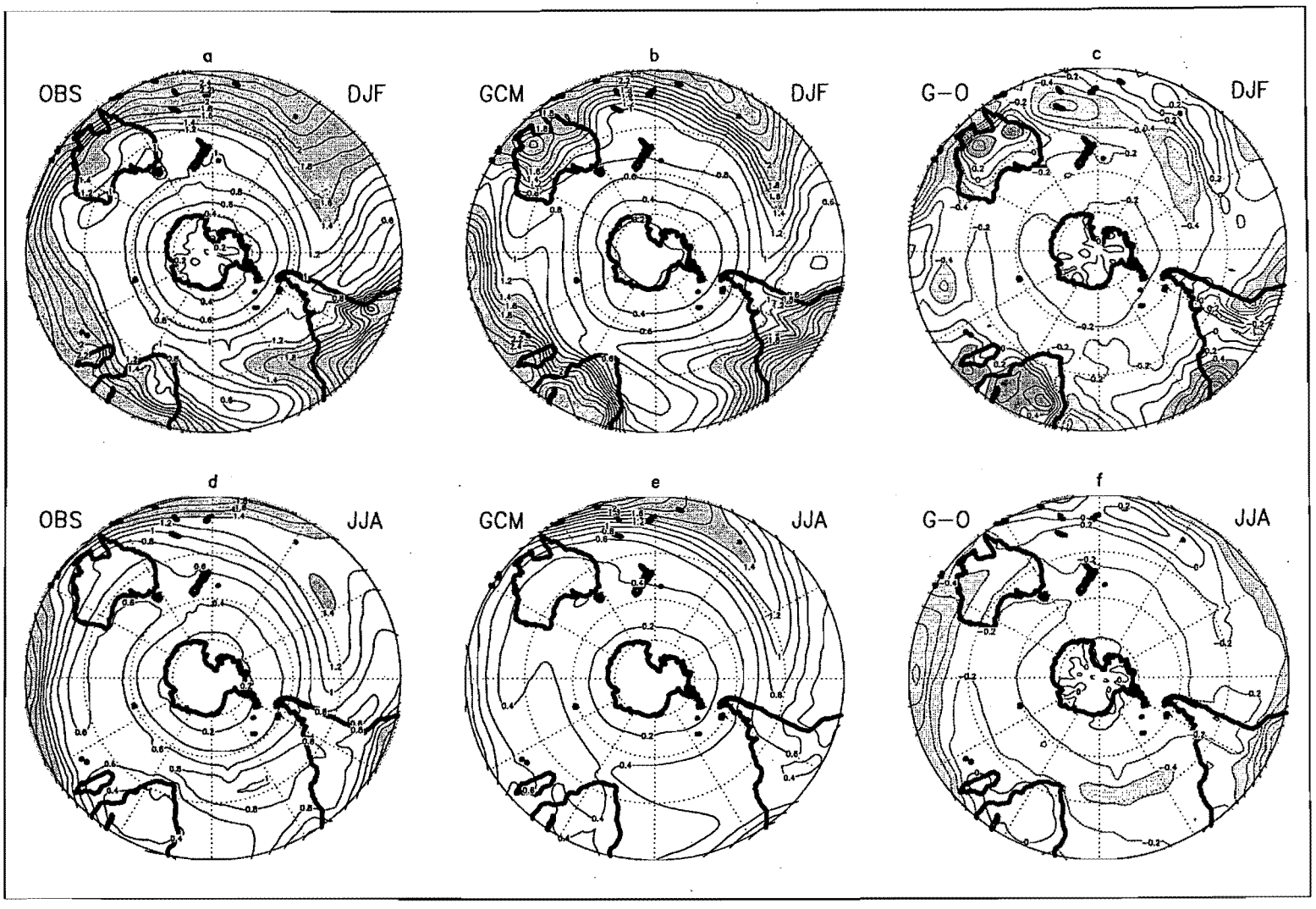

Figure 4.16 Mean 500 hPa specific humidity (g kg^{-1}) for the observed data (*a* and *d*) and the GCM control simulation (*b* and *e*) for summer (DJF) and winter (JJA). Regions with humidities above 1.4 g kg^{-1} have been shaded. Also shown are the corresponding anomaly maps, i.e. GCM minus observed (*c* and *f*), where the shaded regions indicate positive (dark shading) and negative (light shading) differences greater than 0.4 g kg^{-1}.

and maxima at 10°S and 50°S during summer, and a minimum at 20°S and a maximum at 40°S during winter (Figure 4.17).

In both seasons the equatorial/tropical central Indian Ocean and South America receive too little rainfall, and the subtropics in general (extending into the midlatitudes to about 50°S) and central tropical Pacific receive too much rainfall (Figure 4.18). The spatial pattern of precipitation receipt is fairly good, despite the difference in magnitudes in some regions. In both the modelled and NCEP fields, high precipitation values are evident in summer in the South Pacific Convergence Zone, western tropical Atlantic and Indian Oceans, and over Southern Africa and South America (Figure 4.18). During winter, the rainfall in these regions decreases with the northward movement of the ITCZ (Figure 4.18). The MAE over the South African window is about 1 mm day^{-1} in both seasons (Table 4.1).

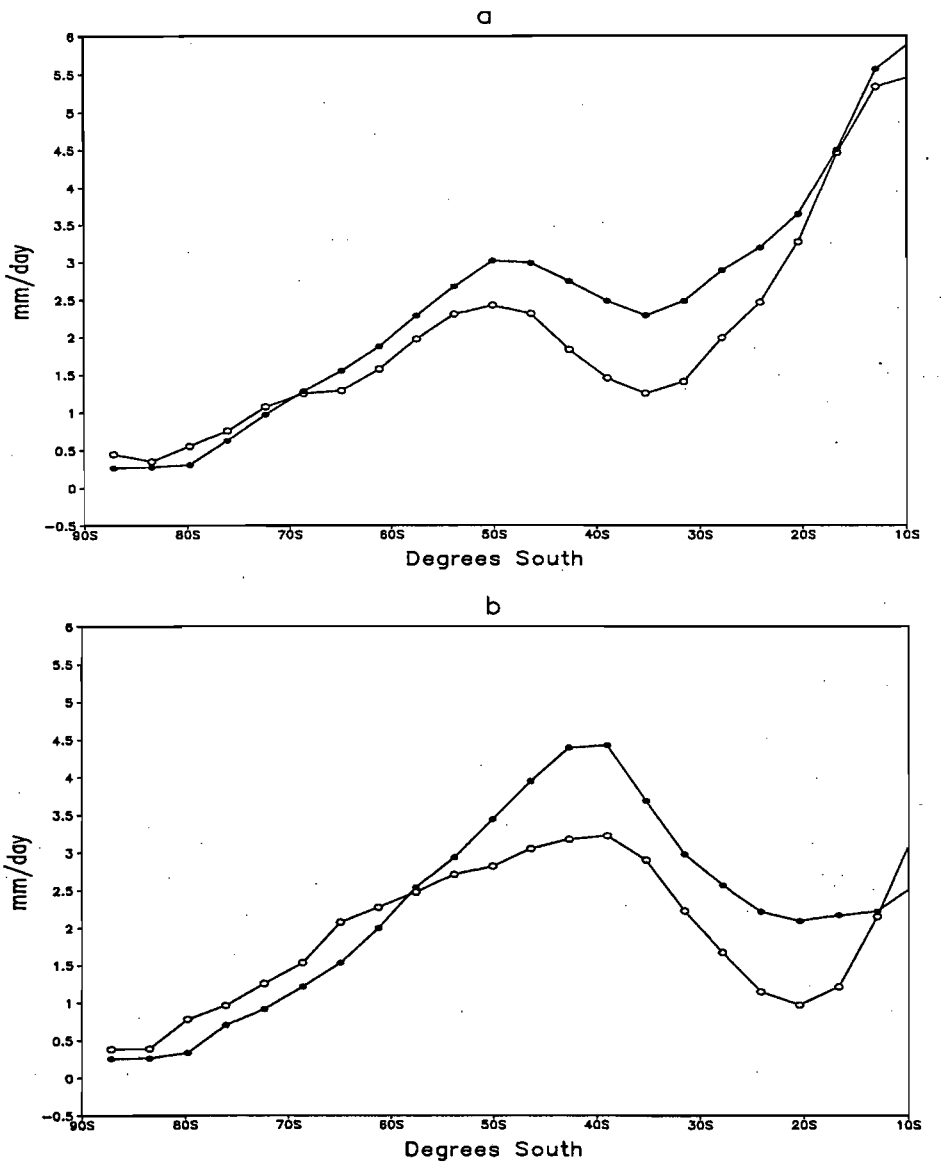

Figure 4.17 Zonally averaged precipitation (mm day^{-1}) for the observed (open circles) and GCM (closed circles) data in *a*) summer and *b*) winter.

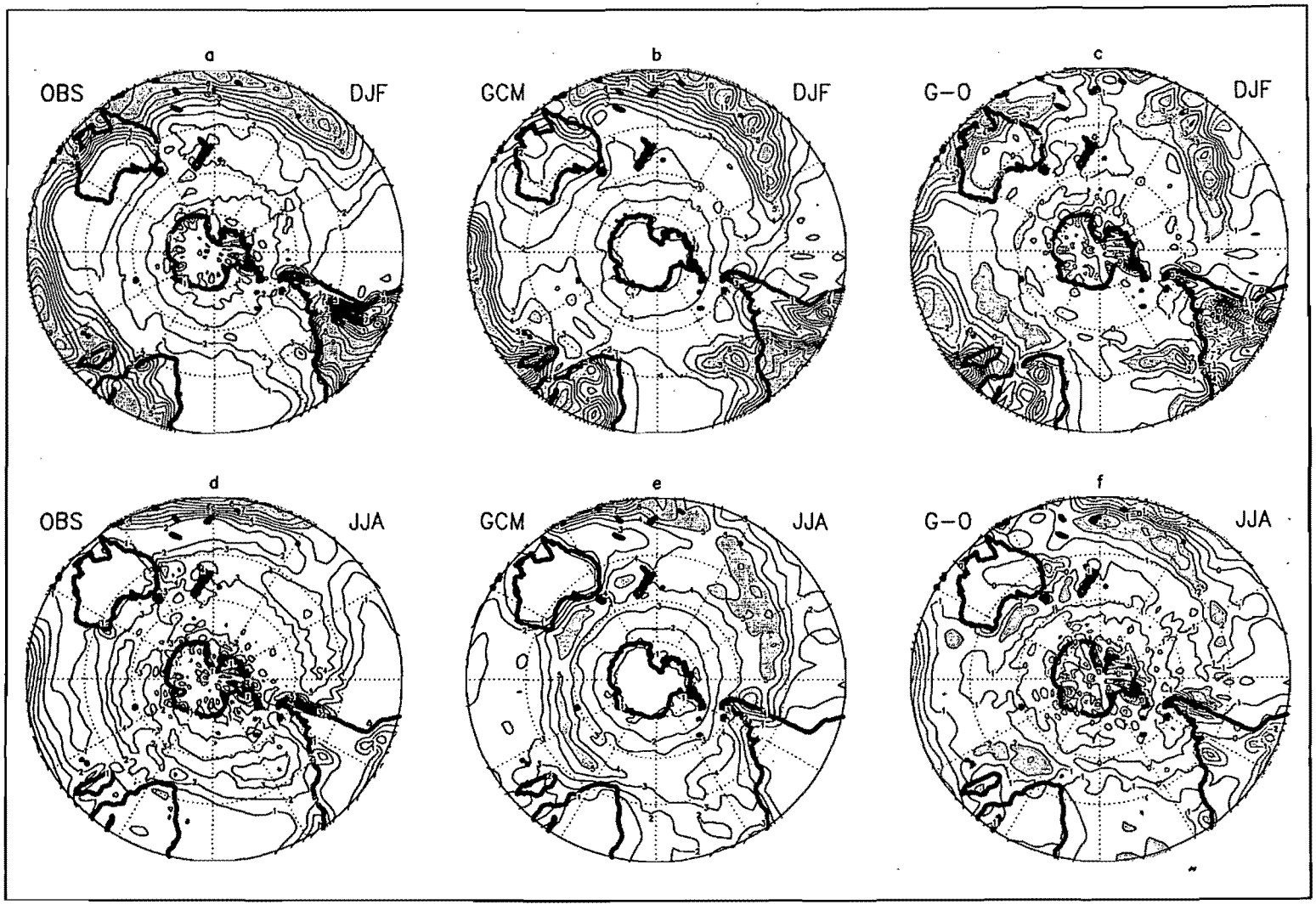

Figure 4.18 Mean precipitation (mm day^{-1}) for the observed data (*a* and *d*) and the GCM control simulation (*b* and *e*) for summer (DJF) and winter (JJA). Regions with precipitation above 5 mm day^{-1} have been shaded. Also shown are the corresponding anomaly maps, i.e. GCM minus observed (*c* and *f*), where the shaded regions indicate positive (dark shading) and negative (light shading) differences greater than 2 mm day^{-1}.

It is important to note that there may be biases in the precipitation field of the NCEP reanalyses. In the reanalyses, precipitation data are not assimilated, but are derived from the 6-hour model forecasts and are therefore strongly influenced by the climatology of the forecast model (Kalnay *et al.*, 1996). Thus, if the model is biased in any way, then there will be regional biases in the precipitation field. Higgins *et al.* (1996) compared the reanalysis precipitation for the period 1985-1993 to the monthly, 2.5°×2.5°, merged precipitation analyses of, firstly, Xie and Arkin (1996), which are based on gauge observations, satellite estimates and model predictions, and secondly, to the precipitation estimates derived by Xie and Arkin (1998) based on outgoing longwave radiation. They found that in general the tight gradients associated with the ITCZ and the South Pacific Convergence Zone are not well captured in the NCEP reanalyses, and there is a tendency for the ITCZ to be slightly north of its observed position during all seasons (Higgins *et al.*, 1996). In addition, during summer (DJF) there is too much rainfall over South America compared to observed and too little rainfall in the band extending south-eastwards from the continent (Higgins *et al.*, 1996). In general, the variability of precipitation in the NCEP reanalyses is too small in all seasons compared to observed (Higgins *et al.*, 1996). Lastly, it is important to realise that the reliability of any observed climatology of precipitation over the mid- to high-latitude oceans of the Southern Hemisphere may be suspect, owing to the data-sparce nature of the region.

In the light of the above discussion, it appears that not all the differences between the GENESIS GCM and NCEP reanalysis precipitation fields are necessarily due to errors in the GENESIS model. Precipitation from both data sources, although exhibiting the general patterns that are observed, are biased in certain ways and this highlights the fact that precipitation output from GCMs is often problematic. This has been attributed, in part, to the variable's dependence on grid resolution and cumulus parameterisation (IPCC, 1990; IPCC, 1992). In addition, there is a demand for precipitation information at far finer spatial resolutions than a GCM grid cell, yet the skill level (von Storch *et al.*, 1993) of GCMs for precipitation is usually poor at the scale of the grid cell (Hewitson and Crane, 1996). The technique of downscaling is used in the present study to obtain higher resolution, and arguably more realistic precipitation data over South Africa compared to the data output by the model. The downscaled regional precipitation fields obtained over South Africa from the model and observed data, will be presented in Chapters 7 and 9, where the atmospheric response of the sea-ice and SST perturbation during summer and winter respectively, is determined.

4.7 Midlatitude Cyclones and Storm Tracks

4.7.1 Midlatitude Cyclone Density

The pattern and magnitude of cyclone densities found in the present study (Figures 4.19 and 4.20) are comparable to those obtained by Jones and Simmonds (1993), who used the Australian Bureau of Meteorology numerical analyses as their observed data set, although values in the present study are marginally lower. This is most likely due to the inclusion of open lows in their study and not in the present study. One discrepancy, however, is that there appear to be too few heat lows over the continents during summer in the observed data compared with Jones and Simmonds's (1993) climatology. Assuming that Jones and Simmonds's (1993) cyclone climatology is correct, the GENESIS GCM results look more realistic in this respect than the NCEP results (Figure 4.20) and this may be related to deficiencies in the NCEP reanalysis sea level pressure data.

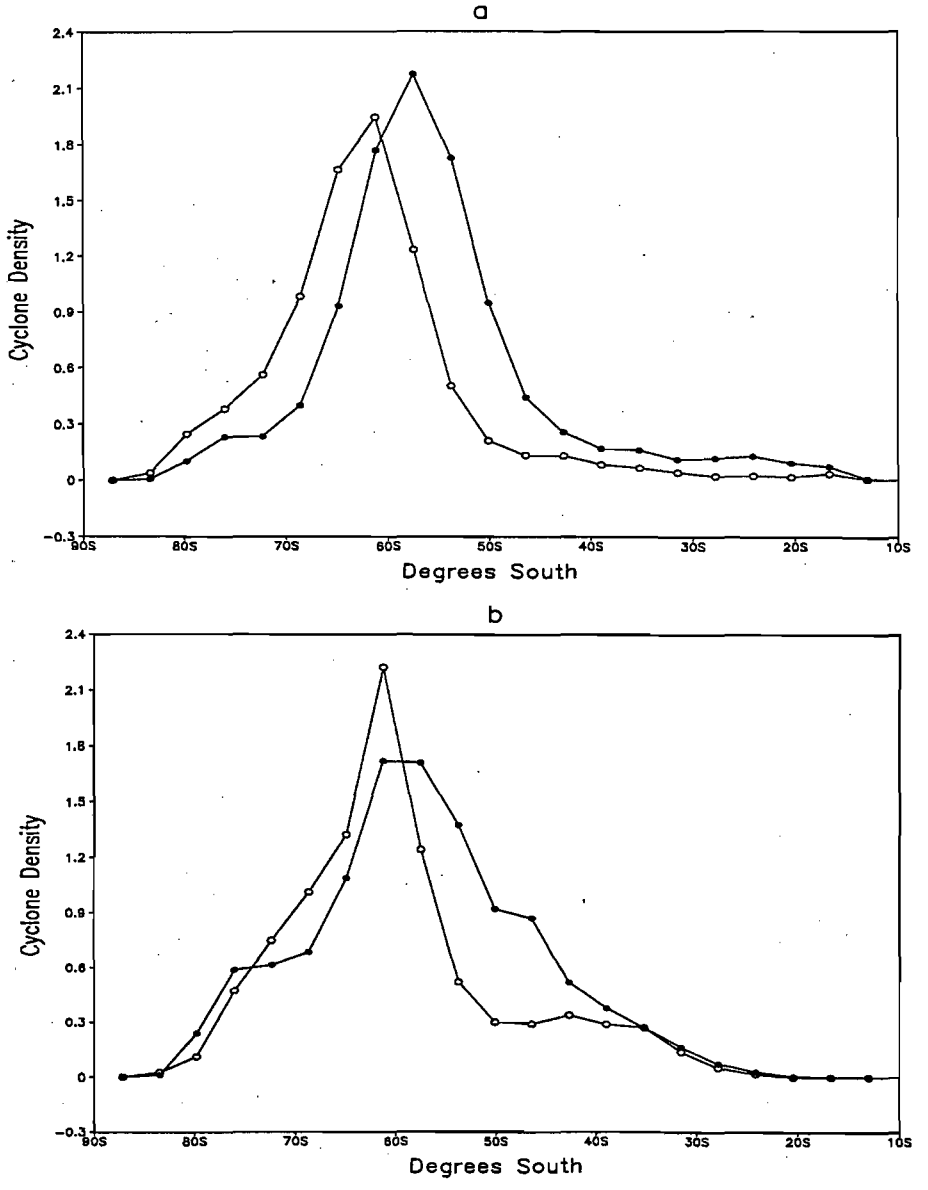

Figure 4.19 Zonally averaged cyclone densities ($\times 10^{-3}$ cyclones (degrees latitude)$^{-2}$) for the observed (open circles) and GCM (closed circles) data in *a*) summer and *b*) winter.

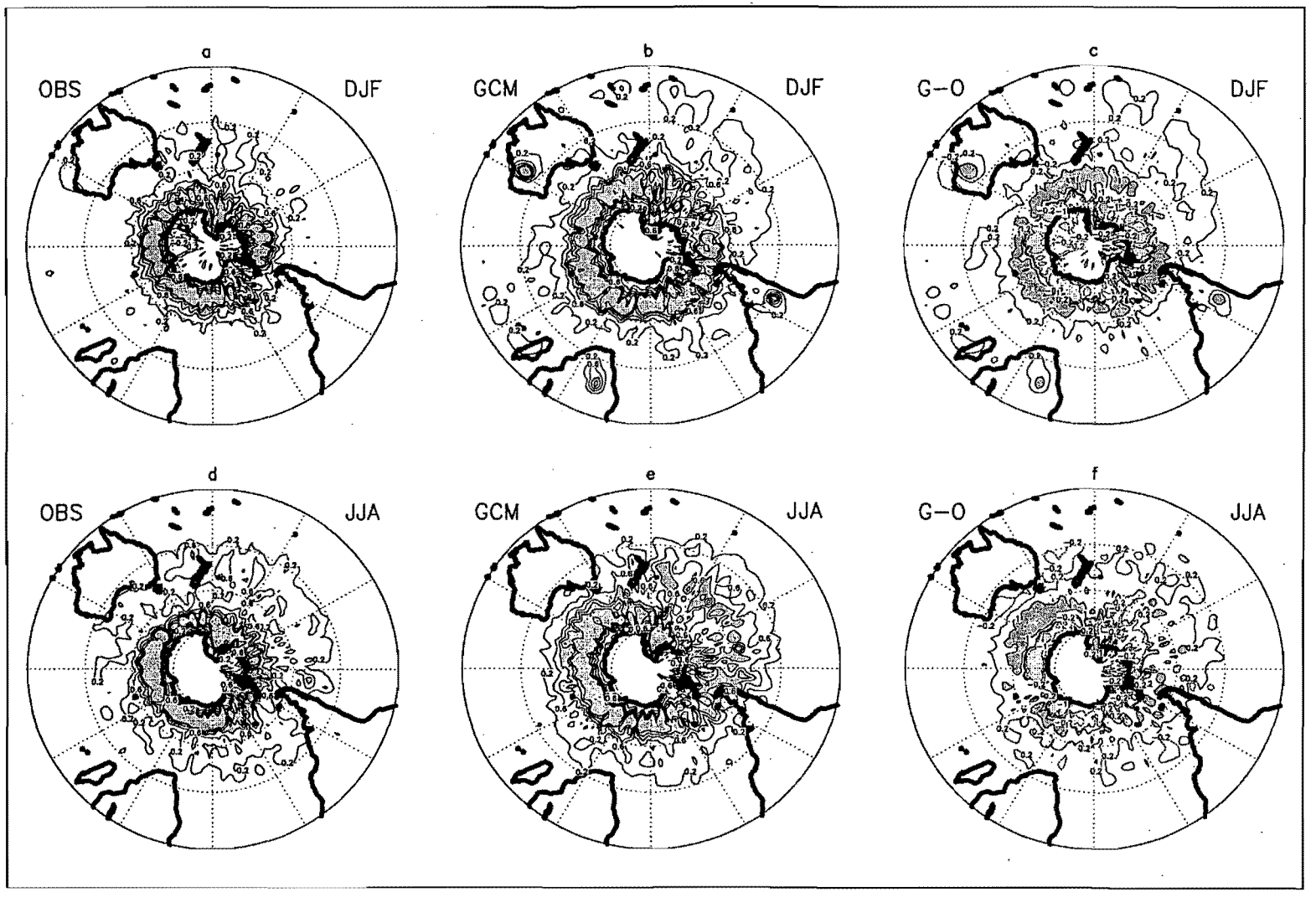

Figure 4.20 Mean cyclone densities ($\times 10^{-3}$ cyclones deg.lat.$^{-2}$) for the observed data (*a* and *d*) and the GCM control simulation (*b* and *e*) for summer (DJF) and winter (JJA). Regions with densities above 1×10^{-3} cyclones deg.lat.$^{-2}$ have been shaded. Also shown are the corresponding anomaly maps, i.e. GCM minus observed (*c* and *f*), where the shaded regions indicate positive (dark shading) and negative (light shading) differences greater than 1×10^{-3} cyclones deg.lat.$^{-2}$.

The high density core of cyclones around Antarctica in the observed and model data (Figure 4.20) is consistent with other manual and automated analyses (for example Taljaard, 1967; Le Marshall and Kelly, 1981; Jones and Simmonds, 1993), and is associated with the circumpolar trough. Taljaard (1967) found that cyclone centers are most numerous 2°-6° equatorward of the hemispheric mean position of the circumpolar trough. From the zonally averaged sea level pressure (Figure 4.5) and cyclone densities (Figure 4.19) it is evident that the same phenomenon is found in the present study for both the observed and model data, even though the model positions are shifted northwards compared to observed. During both seasons in the observed data, the circumpolar trough is centred around 65°S and the cyclone density peak occurs at about 62°S, and in the model data the trough is centred around 60°S and the cyclone peak is found near 58°S.

For both seasons in the model there are too many cyclones north of 60°S and too few south of this latitude (Figures 4.19 and 4.20). This is partly due to the northward offset of the circumpolar trough in the model, that has been shown in the sea level pressure data (Figure 4.5) and is evident in the zonal plots of cyclone densities (Figure 4.19). The model zonal averages (Figure 4.19) and 2-dimensional fields (Figure 4.20) also seem to show that the high density region of cyclones around Antarctica extends over a broad band of latitudes, especially during winter, instead of occupying a narrow region in association with the circumpolar trough. This discrepancy is probably related to the modelled sea level pressure field in winter, which shows that the low pressures representing the circumpolar trough occupy a broader latitudinal band than does the trough in the observed data (Figure 4.5).

In addition, there appears to be a band of cyclone densities extending eastwards from New Zealand across the Pacific which are too high in the model during winter (Figure 4.20). However, the magnitude of the model predicted values agree well with the observed cyclone climatology obtained by Jones and Simmonds (1993) and again may point towards errors in the twice-daily sea level pressure NCEP reanalyses. As was mentioned in Chapter 2, an error was introduced into the reanalyses through the mislocation of the Southern Hemisphere PAOBS sea level pressure data. Although the previously discussed seasonally averaged NCEP/NCAR sea level pressure data (Figure 4.6) agrees well with other reanalysis data, for example the seasonal averages obtained by Jones and Simmonds (1993) with the Australian Bureau of Meteorology numerical analyses, the cyclone analysis relies on twice-daily data,

and the EMC and CDC have found that the impact of the mislocation error increases as time scales decrease[1].

4.7.2 Storm Tracks

As was mentioned in the previous chapter, in the Southern Hemisphere midlatitudes atmospheric variability on 2- to 8-day time scales can largely be attributed to the passage of cyclones and anticyclones (Trenberth, 1981, 1991). Variability in the sea level pressure field on this time scale has therefore been used to identify the major storm tracks in the present study. It is evident from Figures 4.21 and 4.22 that the largest variability in the sea level pressure field, in terms of the standard deviation of the bandpass (1.5 - 8.5 days) filtered data,

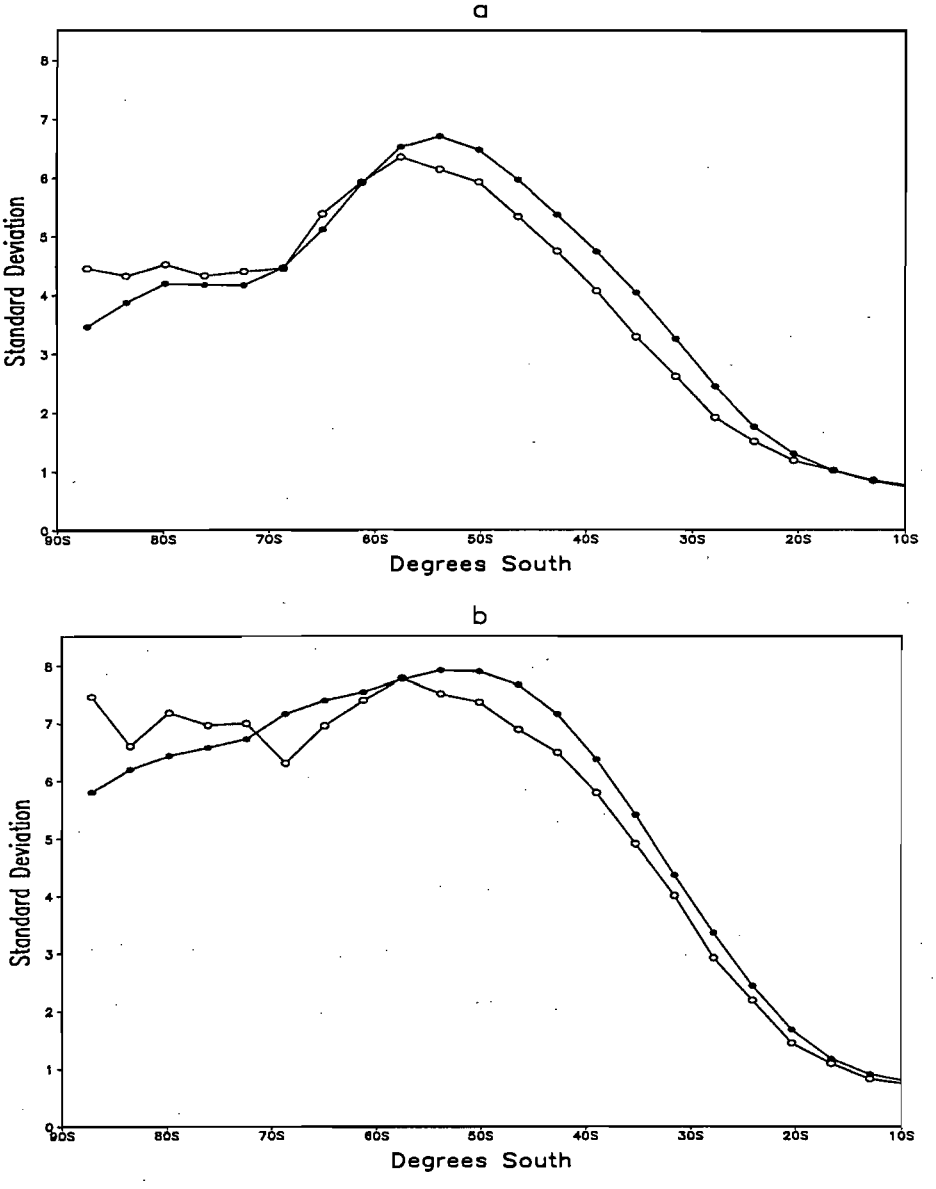

Figure 4.21 Zonally averaged standard deviations of the bandpass (1.5-8.5 days) filtered sea level pressure data (hPa) for the observed (open circles) and GCM (closed circles) data in *a*) summer and *b*) winter.

[1] Refer to http://wesley.wwb.noaa.gov/paobs/paobs.html

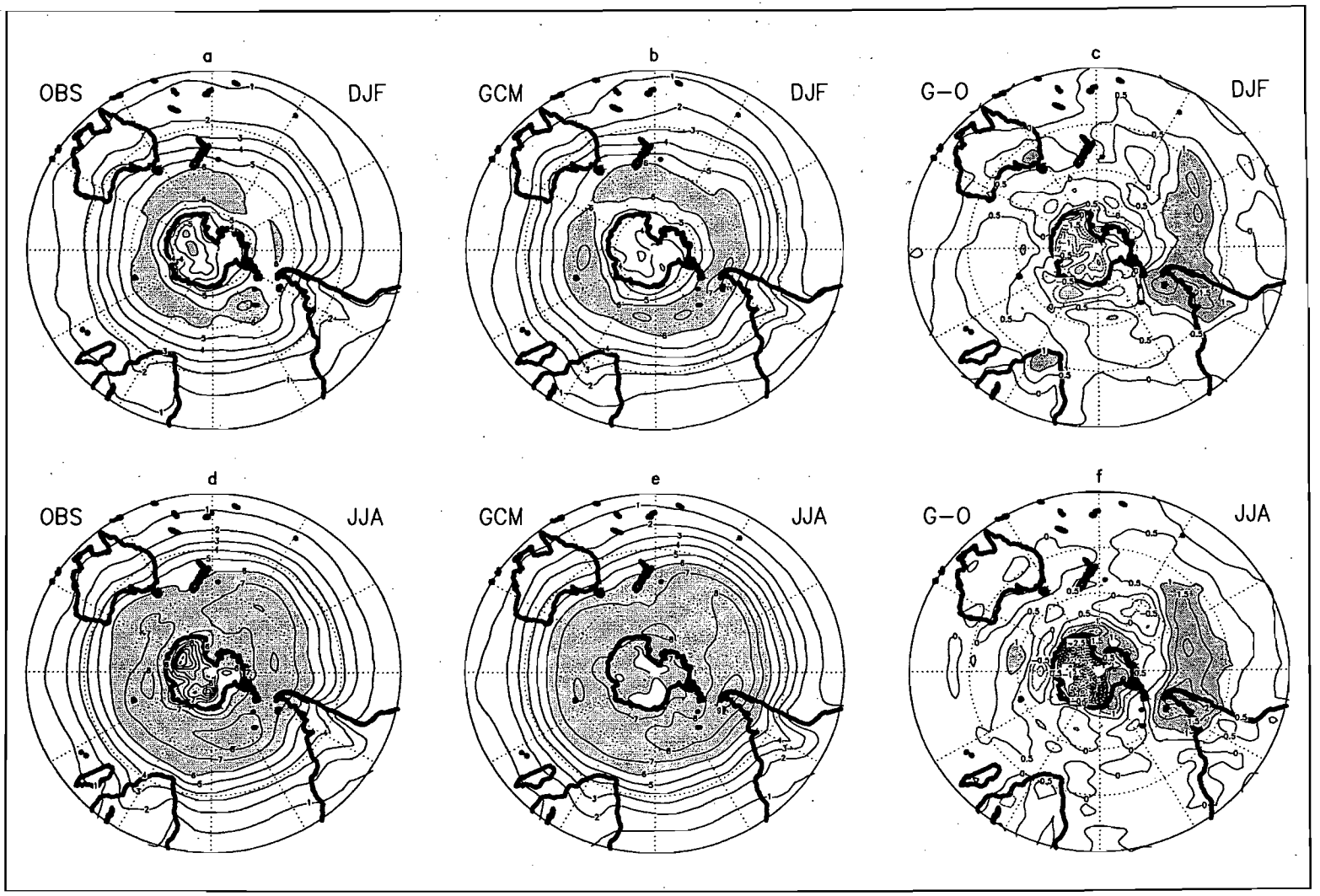

Figure 4.22 Mean standard deviation of bandpass (1.5-8.5 days) filtered sea level pressure data for the observed data (*a* and *d*) and the GCM control simulation (*b* and *e*) for summer (DJF) and winter (JJA). Regions above 6 hPa have been shaded. Also shown are the corresponding anomaly maps, i.e. GCM minus observed (*c* and *f*), where the shaded regions indicate positive (dark shading) and negative (light shading) differences greater than 1 hPa.

lies in a zone near 55°S in both seasons, although the latitudinal extent of high variabilities is greater during winter compared to summer and occurs over a broader band in the midlatitudes. The model simulates this observed seasonal difference fairly well, although, as seen with other variables, the subpolar and midlatitude model patterns appear to be shifted slightly north compared to the observed data (Figures 4.21 and 4.22). In both the observed and model data, this band of maximum bandpass variances lies further equatorward than the zone of maximum cyclone densities, as has been found in other studies (Wallace *et al.*, 1988; König *et al.*, 1993; Sinclair, 1994). The cyclones found near the circumpolar trough tend to be slow moving and as such, Trenberth (1991) noted that this region of high cyclone density is almost uncorrelated with those areas of maximum atmospheric variability originating from the passage of cyclones and anticyclones. Sinclair (1994) found that the region of greatest cyclone mobility lay near 50°S and Le Marshall and Kelly (1981) calculated average daily sea level pressure standard deviations about their monthly means and found that the area of maximum variability lay in a band near 55°S. Le Marshall and Kelly (1981) attributed this band of variability to the region of maximum overlap of average cyclone and anticyclone densities. It is also evident from the observed data that there are local maxima in the band of high variabilities, which are generally situated south-east of the continents (Figure 4.22). Le Marshall and Kelly (1981) found local maxima in similar positions to the present study and attributed them to regions of preferred blocking.

In general, the model exhibits too much variability in the sea level pressure field in both seasons, especially over the eastern Pacific Ocean where differences of up to two standard deviations are recorded for winter (Figures 4.21 and 4.22). This is in part due to the unusually high density of cyclones simulated north of 55°S (Figures 4.19 and 4.20).

4.8 500 hPa Planetary Waves

The 500 hPa geopotential height field is composed of a number of quasi-stationary and transient waves of differing wavelengths. As was mentioned in Chapter 3, these wave trains vary from large-wavelength planetary-scale waves (e.g. wave numbers 1, 2, 3 and 4) to smaller, synoptic-scale and short waves with wavelengths of the order of a few hundred kilometers. The present study is primarily concerned with the planetary-scale waves. Wave number 1 contributes the most to the quasi-stationary wave variance, since the other waves are primarily eastward moving and more transient than wave 1 (Quintanar and Mechoso, 1995). Wave numbers 1, 2, 3 and 4 in summer, and wave numbers 1, 2 and 3 in winter have

all been found to make important contributions to the zonal asymmetries in Southern Hemisphere climatological fields (Karoly, 1985).

All year round at 55°S there is a ridge in the mean flow near 175°E, while at 30°S there is a trough at the same longitude (Trenberth, 1980). The effect of these features is to produce a split in the flow across New Zealand and a minimum in the strength of the zonal westerlies in this region (Trenberth, 1980; Trenberth and Mo, 1985). This background flow produces a favourable environment for blocking to occur and as such, the region near the dateline experiences the highest frequency of blocking (Trenberth and Mo, 1985). Most of this mean flow can be explained by wave number 1, but Trenberth (1980) notes that the wavelength is less than that of wave number 1 and in order to adequately describe the asymmetrical shape of the 500 hPa field, wave numbers 1, 2 and 3 are all required. Nonetheless, wave number 1 is the principal wave and has been found to account for between 70 and 90% of the variance in the long term mean field in middle to high latitudes, whereas wave numbers 2 and 3 together account for about 26% of the variance in the mean (van Loon and Jenne, 1972; Trenberth, 1980). Wave number 3, however, contributes more to the interannual variability at 55°S than waves 1 and 2 (Trenberth, 1980), and appears to play an important role in determining the location of blocking in the Southern Hemisphere (Trenberth and Mo, 1985; Preston-Whyte and Tyson, 1988; Sinclair *et al.*, 1997). In this section, the 500 hPa phases of wave numbers 1, 2 and 3 and amplitudes of wave numbers 1, 2, 3 and 4 are obtained from the GENESIS GCM and the NCEP data in order to evaluate these large-scale waves in the model. The phase of wave number 4 is not presented because it is a transient wave and its phase is therefore essentially random. In contrast, the phase of wave number 1, and to a lesser extent waves 2 and 3, occur consistently at certain longitudes in the zones where the waves are strongest. The subsequent text, unless otherwise stated, deals with waves decomposed from the seasonal mean field.

Wave number 1 exhibits two peaks of strength in both seasons, one being in the subtropics near 30°S and the other in subpolar latitudes near 55°S (Figure 4.23*a* and *e*). The model captures the latitudinal position of both the subpolar and subtropical amplitude peaks, but the magnitude of the subpolar peak in the model is about 30% smaller than the size of the peak in the observed data in both seasons (Figure 4.23*a* and *e*). The amplitude of the subpolar expression of the wave in the observed data appears to be reasonable in terms of what has been recorded in previous studies (van Loon and Jenne, 1972; Trenberth, 1980). Similarly, the size of the subtropical peak in the model and observed data corresponds to what has

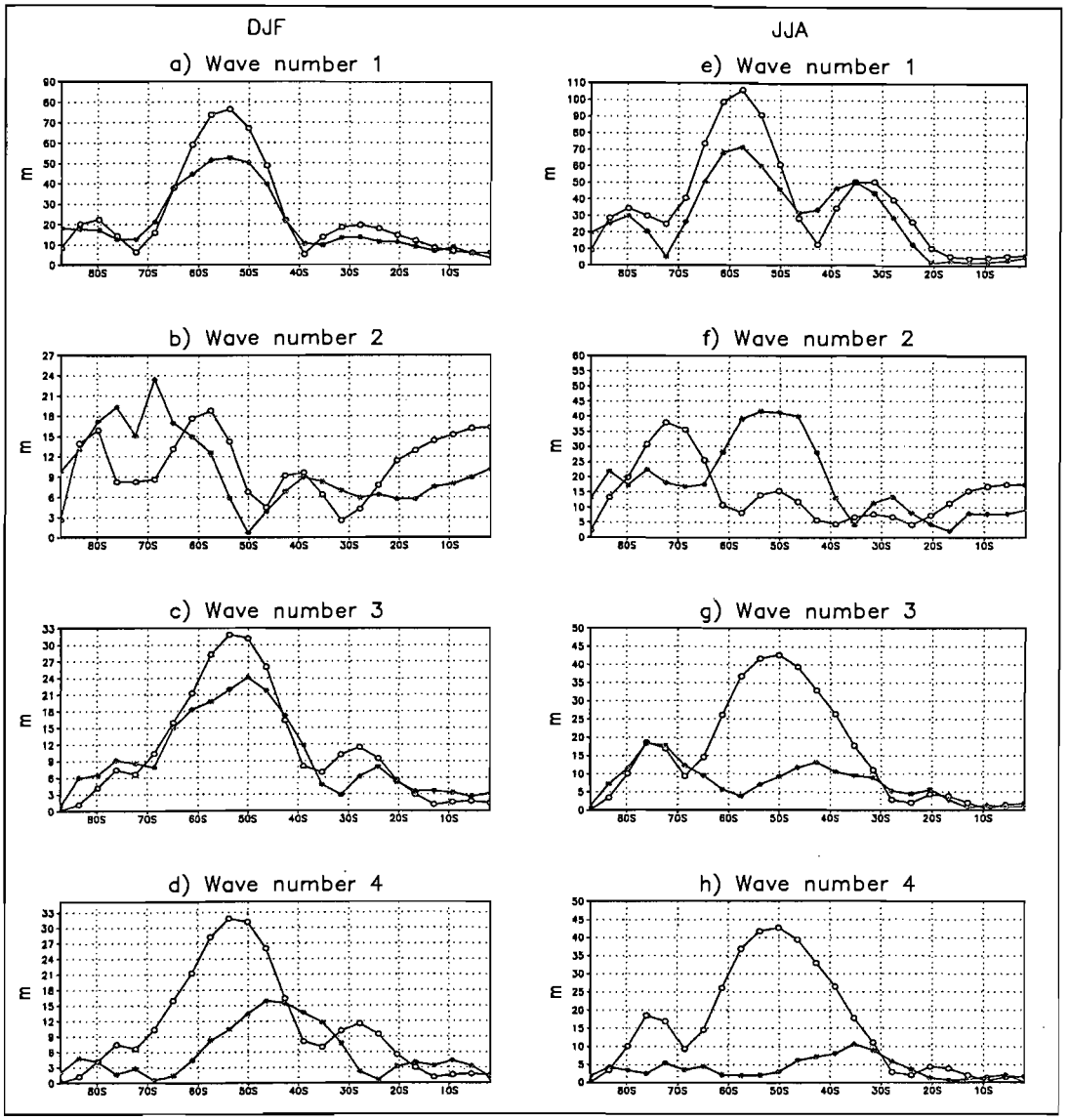

Figure 4.23 The amplitude (m) of seasonal wave numbers 1 to 4 for summer (*a-d*) and winter (*e-h*) for the observed (open circles) and GCM (closed circles) data.

previously been noted, i.e. between about 10 and 20 m in summer and 40 and 50 m in winter (van Loon and Jenne, 1972; Trenberth, 1980). The model simulates the slight poleward movement of the subpolar and subtropical peaks from summer to winter, as well as the increase in amplitude of the peaks (Figure 4.23*a* and *e*). Near 40°S, between the subpolar and subtropical expressions of the wave, the amplitude of wave number 1 is small (Figure 4.23*a* and *e*). In this region, the phase is essentially random since there is a change in phase between the subpolar and subtropical waves. The ridge of wave number 1 at 55°S (where the wave is strongest) is situated near 210°E in both the model and observed data for summer and winter (Figure 4.24*a* and *d*). This corresponds to the results from other studies which have shown that the ridge of the subpolar expression of the wave is positioned in the Pacific between about 210°E and 240°E (Anderssen, 1965; van Loon and Jenne, 1972; Trenberth, 1980; Karoly, 1985). The subtropical ridge of the wave (near 30°S) is found near the

Greenwich Meridian in both seasons in the model and observed data (Figure 4.24*a* and *d*), which again agrees with previous studies (Anderssen, 1965; van Loon and Jenne, 1972; Trenberth, 1980; Karoly, 1985). In summary, the model adequately simulates the phase of wave number 1 and the latitudinal position of the amplitude peaks, but the wave is too weak.

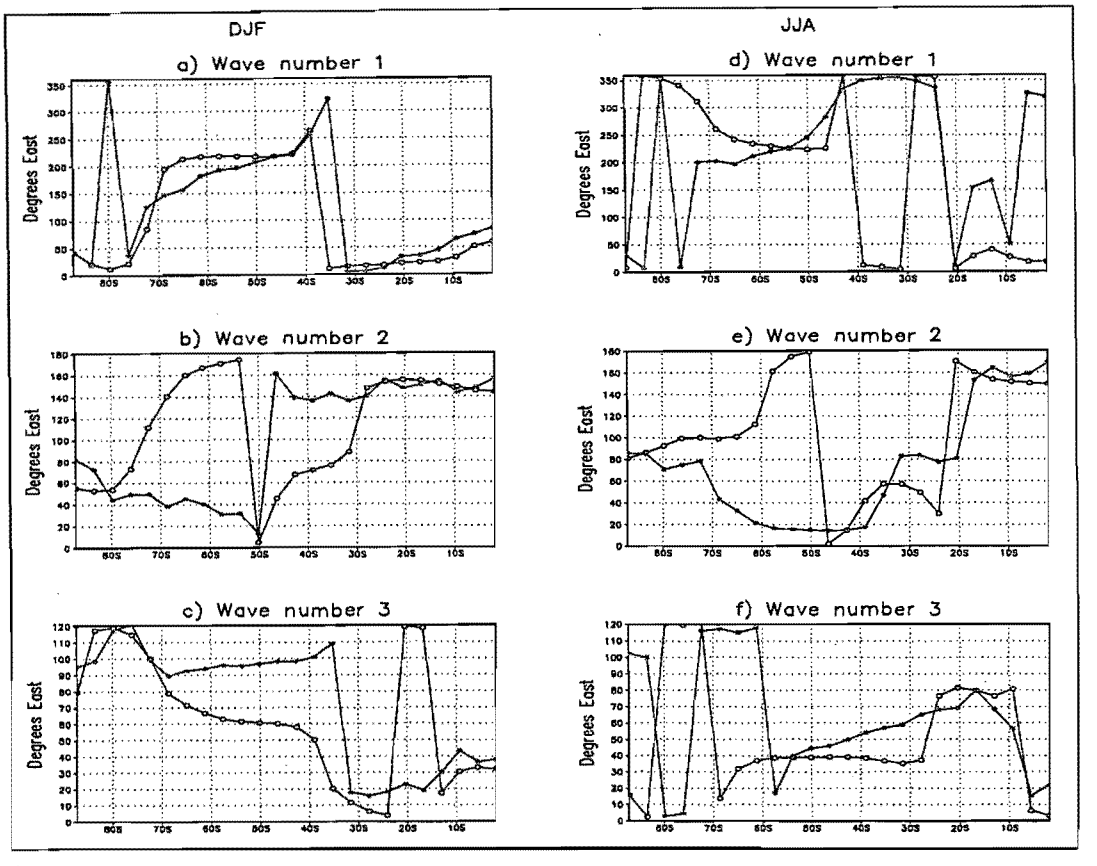

Figure 4.24 The phase (position of the first ridge) of seasonal wave numbers 1 to 3 for summer (*a-c*) and winter (*d-f*) for the observed (open circles) and GCM (closed circles) data.

Results from the literature suggest that the nature of wave number 2 is less clearly known compared to wave numbers 1 and 3. Van Loon and Jenne (1972) reported that climatological mean (annual) wave number 2 only had an amplitude of 4 m at 50°S and was insignificant, except over Antarctica. In contrast, using different data sets to the above study, Trenberth (1980) and Karoly (1985) both recorded much larger amplitudes for wave number 2. The amplitude of the wave obtained from the NCEP reanalyses in the present study (Figure 4.23) resemble those obtained by Trenberth (1980) (his Figure 3) and Karoly (1985) (his Figures 9 and 10), showing two amplitude peaks, one near 75°S and one between 50°S and 60°S. It is the peak between 50°S and 60°S that is missing from van Loon and Jenne's (1972) results. For summer, Trenberth (1980) and Karoly (1985) both recorded a high latitude (near 75°S) amplitude peak of between 10 and 20 m and a middle latitude (50°S - 60°S) peak in the low 20's, thus being very similar to the results obtained from the NCEP data in the present study (Figure 4.23*b*). The high latitude peak is perhaps slightly further south in the NCEP data

compared to the results obtained by Trenberth (1980) and Karoly (1985). The GENESIS model does not seem to differentiate well between these two peaks in summer, instead simulating one peak over the region, such that the amplitude is too large between 65°S and 75°S and too small between 50°S and 60°S (Figure 4.23*b*).

For winter, Trenberth (1980) and Karoly (1985) both recorded high latitude (near 75°S) and middle latitude (50°S - 60°S) amplitude peaks for wave number 2 of between about 30 and 40 m, although Trenberth's (1980) results suggest that the midlatitude peak may exceed 40 m. In comparison to their results, the NCEP data has a similar magnitude high latitude peak, but a much weaker midlatitude peak (Figure 4.23*f*). The GENESIS model in winter does better in terms of differentiating between the high and middle latitude expressions of the wave compared to summer (Figure 4.23*f*). The amplitude of the high latitude wave is perhaps too small in the model, and the midlatitude amplitude is of a similar magnitude to that obtained by Trenberth (1980) and Karoly (1985), but is much larger than the amplitude obtained from the NCEP data (Figure 4.23*f*). It is not possible at this stage to say which of the amplitudes for the midlatitude expression of the wave is more correct.

Van Loon and Jenne (1972) and Trenberth (1980) found that the high latitude expression of wave number 2 (near 75°S) had a phase of 90°E. In contrast, Karoly (1985) found a phase of 60°E in summer and 120°E in winter from his results (see his Figures 9 and 10). To be conservative, one might therefore suggest that the high latitude phase is positioned preferentially between 60°E and 120°E. The results in the present study generally fall within these bounds for both the observed and model data, except perhaps in summer where the model phase may be slightly too far west (Figure 4.24*b* and *e*). For the phase of the midlatitude peak of the wave (between 50°S and 60°S), Anderssen (1965) found a tendency for the wave to be located between 10°E and 70°E, Trenberth (1980) reported a phase of 0° and Karoly (1985) found that the wave was positioned near 0° in summer and between 30°W and 0° in winter. In the present study, there is a ridge between 10°W and 0° for the midlatitude phase in the observed data, and between 10°E and 40°E for the model data (Figure 4.24*b* and *e*). Both of these results fall within the range of what has previously been reported. The variability in the phases of wave number 2 that are found within the data sets used in the present study, as well as those from previous studies, show that the wave is less stationary compared to wave number 1.

Wave number 3 experiences a peak amplitude in the midlatitudes, near 50°S, according to the NCEP data (Figure 4.23*c* and *g*), as well as the results from previous studies (van Loon and Jenne, 1972; Trenberth, 1980; Karoly, 1985). Van Loon and Jenne (1972) found that the amplitude of the climatological mean (annual) wave at 50°S was 21 m, and Trenberth (1980) and Karoly (1985) recorded amplitudes of between about 20 and 40 m for summer and 30 and 40 m for winter. The amplitude of the wave at this latitude in the observed data in the present study generally falls within this range for summer and winter (Figure 4.23*c* and *g*). For summer, the GENESIS model captures the position of the midlatitude peak, yet the peak is smaller than the observed data (Figure 4.23*c*), but within the range of what has been previously recorded. In contrast, for winter the model peak is offset northwards and is much too small (Figure 4.23*g*). This may mean that in general the flow in the model is too zonal, or that the wave in the model is more transient than in the observed data such that it cancels itself out when added to form the seasonal mean. This issue will be further addressed later in this section.

Wave number 3 moves eastwards with a phase velocity greater than that of wave numbers 1 and 2 (Anderssen, 1965), but it does slow down and persist at particular locations. In a study of blocking in the Southern Hemisphere, Trenberth and Mo (1985) found that between 46°S and 62°S there are two preferred locations of the wave. In summer this occurs with the first ridge positioned near 10°E or 75°E, and in winter with the first ridge positioned near 55°E or, secondarily, near 85°E (Trenberth and Mo, 1985). This highlights the transitory nature of the wave, even though it may favour particular locations. Most previous work seems to suggest that at 50°S the wave has a phase of between 30°E and 60°E in both summer and winter (van Loon and Jenne, 1972; Trenberth, 1980; Karoly, 1985). The phase of the wave at 50°S in the observed data in the present study agrees with the above results and seems to be adequately represented by the GENESIS model in winter, but not in summer, where there is a 40° difference in phase between the model and observed data (Figure 4.24).

The amplitude of wave number 4 is shown in Figure 4.23, and it is clear that the peak in the model occurs too far north and is much smaller compared to the observed data. However, van Loon and Jenne (1972) found that the amplitude of the climatological mean (annual) 500 hPa wave at 50°S was only 5 m and Karoly (1985) found that the amplitude of the wave in the mean seasonal field was generally less than 10 m in both summer and winter at most latitudes and less than 20 m at all latitudes. These results cast doubt on the NCEP amplitudes and suggest that the GENESIS model results may not be as "incorrect" as they may first seem

(Figure 4.23). It is, however, important to note that small changes in the seasonal mean field can lead to large changes in the individual wave number phases and amplitudes (Trenberth, 1980), perhaps serving to exaggerate observed differences when viewed from the perspective of the individual waves. In summary, the results of the validation of seasonal wave number 4 in the model are inconclusive.

The average amplitudes of wave numbers 1 to 4 at the 500 hPa level, as calculated from twice-daily data and averaged without regard to phase, are presented in Figure 4.25. It is clear from this figure that waves 2, 3 and 4 are much more important on a twice-daily time scale than they are in the seasonal mean field. In general, the model simulates the position of

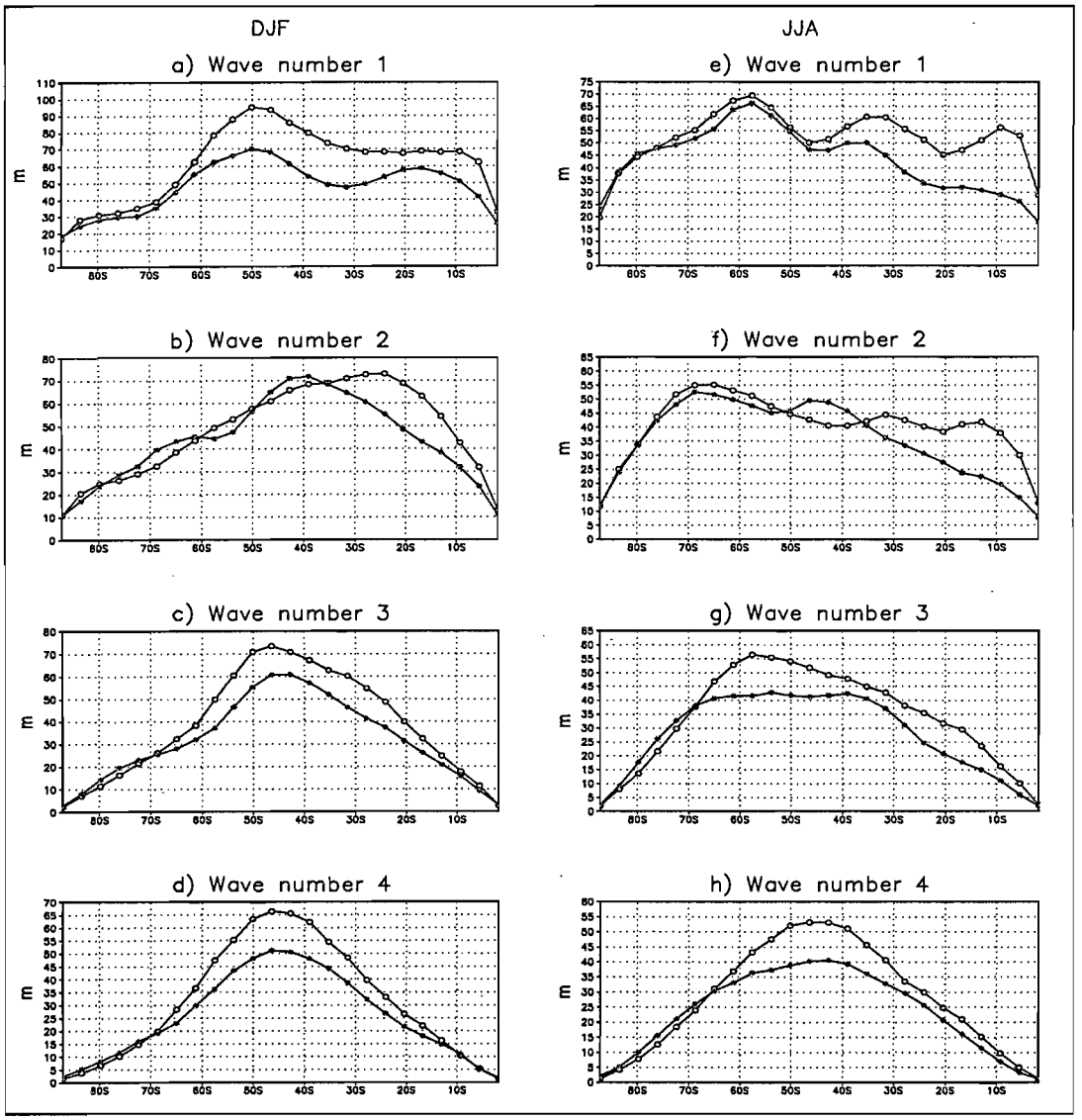

Figure 4.25 The amplitude (m) of twice-daily wave numbers 1 to 4 for summer (*a-d*) and winter (*e-h*) for the observed (open circles) and GCM (closed circles) data.

the observed peaks in amplitude, except perhaps for wave number 2, but the peaks are lower in the model compared to observed (Figure 4.25). The model fields are therefore slightly more zonal than observed. This is not entirely unexpected, since the model only operates on

a T31 resolution and therefore cannot capture all the high frequency forcings that may contribute to the energy of the large scale waves.

If one examines wave number 3 in winter (Figure 4.25) then it is apparent that there is less of a difference in amplitude between the model and observed data than was shown for the seasonal mean wave (Figure 4.23), and the same can be said for wave number 4. This suggests that these waves are more transient in the model compared to the observed data, such that their daily phases are more random and the waves largely cancel themselves out when added to form the seasonal mean. This may be partly a result of the baroclinic zones and topographical forcing not being as strong in the model compared to observed, thus offering weaker constraints on the wave positions.

4.9 Classification of Circulation over Southern Africa

A Self-Organising Map (SOM), described in Chapter 3, is used to classify the twice-daily sea level pressure data over the South African window into related categories, in order to examine whether the model is capturing the observed distribution of circulation types over the region. Too often in the past the validation of GCMs has been restricted to looking at monthly and long term means of variables and it is important that the synoptic climatologies and variability in the models begin to receive closer attention. This SOM technique, as well as the cyclone and storm track analysis discussed previously, address this aspect of validation.

Before the model and observed data are presented to the SOM they are standardised. Standardisation is an effective tool to use when there is a bias in the means of the two data sets that are being compared. From the results shown in this chapter thus far, it is evident that the model data are biased in some respects (Table 4.1) and therefore it was decided that standardisation should be employed. This is also justified in terms of the focus of this section, which is to examine the resulting circulation *patterns*, rather than the absolute values. The data at each grid point of the time series have been standardised in terms of the long-term areal mean for the observed and model data sets respectively. The means and standard deviations of the two data sets prior to standardisation are shown in Table 4.2. It is clear that the observed and model data agree well over the region, with the exception of the model exhibiting slightly more variability in the sea level pressure field than the observed data during summer (Table 4.2).

	DJF		JJA	
	μ	σ	μ	σ
Observed	1011.29	7.76	1016.98	10.09
Model	1011.13	8.73	1016.82	10.64

Table 4.2 The mean (μ) and standard deviation (σ) of the sea level pressure data over southern Africa (20°S to 50°S; 2°E to 47°E) prior to standardisation for summer (DJF) and winter (JJA).

Two SOMs were trained using twice-daily standardised sea level pressure data from the 10-year (1979-1988) period of the observed data. The one SOM was used for the data corresponding to the summer (DJF) months (t = 1806) and the other for the twice-daily data corresponding to the winter (JJA) months (t = 1840). Both SOMs comprise 15 nodes (3 in the x-direction and 5 in the y-direction) and the weights of the nodes in each SOM were initialised using linear initialisation. The reader is referred back to Chapter 3 for a discussion of the different options available in the SOM Program Package (Kohonen *et al.*, 1996). A rectangular topology was used for the array of nodes, and the initial learning rate was set to 0.05, with an initial training radius of three. Training was run for a total of 30 000 iterations. The rule of thumb, mentioned in Chapter 3, is that the number of iterations should be about 500 times the dimensions of the nodal array, which makes the value in the present study 7 500 (3×5×500). It was decided that this value was too close to the fast training limit of 10 000, thus 30 000 iterations were subjectively selected.

After the respective SOMs have been trained with the observed data, the nodes can be displayed graphically in what has been called a meta-map (Main, 1997). This is shown on Figure 4.26 for the summer SOM, and Figure 4.27 for the winter SOM. Each map on the meta-map represents a node of the SOM and the contoured data on each map are the weights associated with each node. The meta-maps (Figures 4.26 and 4.27) are each configured in the form of the nodal array, i.e. 3 nodes/maps in the x-direction and 5 nodes/maps in the y-direction, and neighbouring maps represent related circulation types. The trained summer and winter SOMs are then individually presented with twice-daily standardised sea level pressure from the observed data (the same data that were used to train the SOM) and the model control simulation data. Each respective time step is mapped to the node whose weights it most closely resembles. The number of days which map to each node are recorded and the percentage difference between the observed and model data are shown in Figure 4.28. This figure displays two grids which corresponds to the meta-maps on Figures 4.26 and 4.27 for

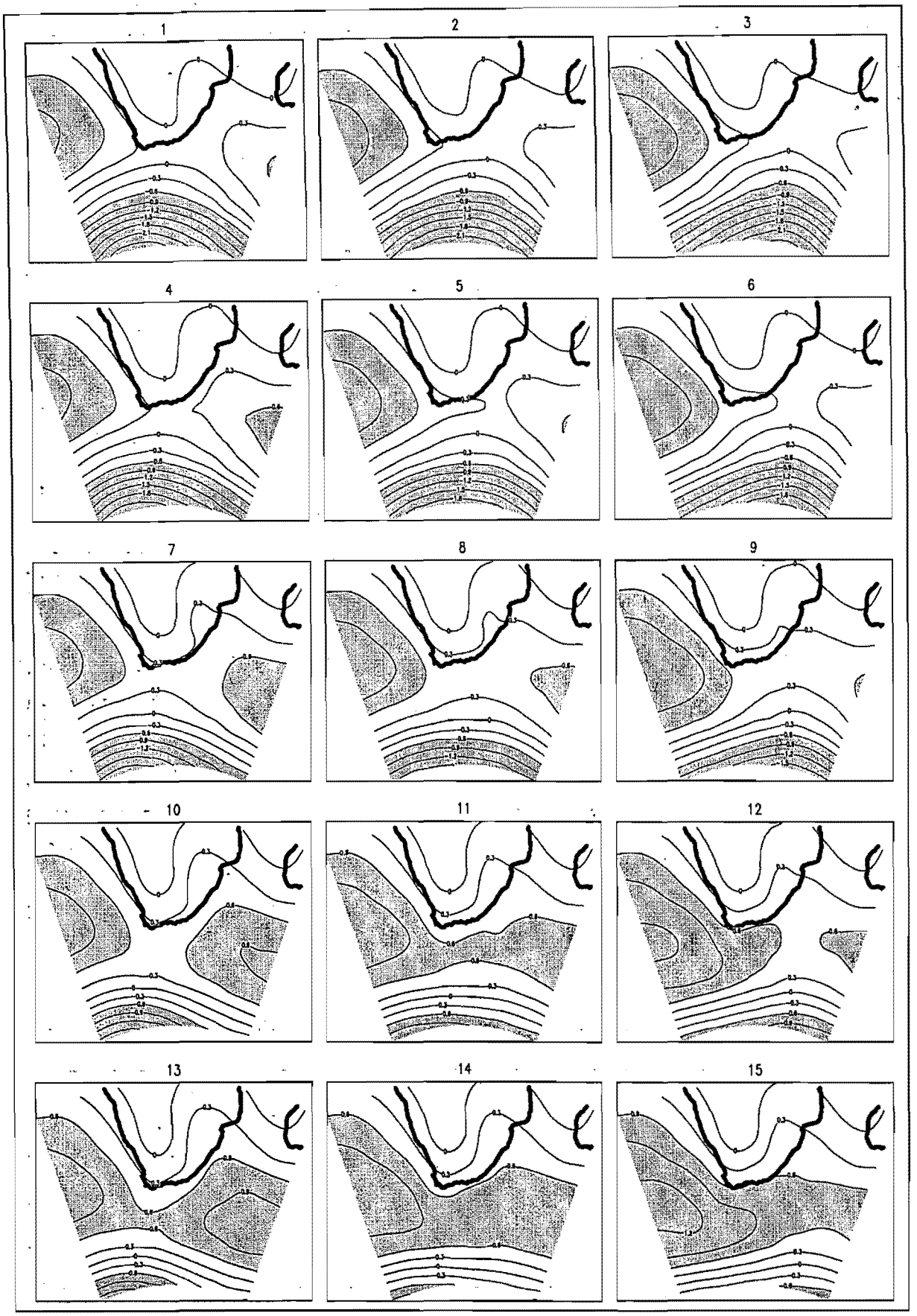

Figure 4.26 The meta-map for the summer (DJF) SOM over the South African region, showing the 15 nodes (3×5) with their contoured weights. The weights represent standardised sea level pressure, and values greater than 0.6 and less than -0.6 have been shaded.

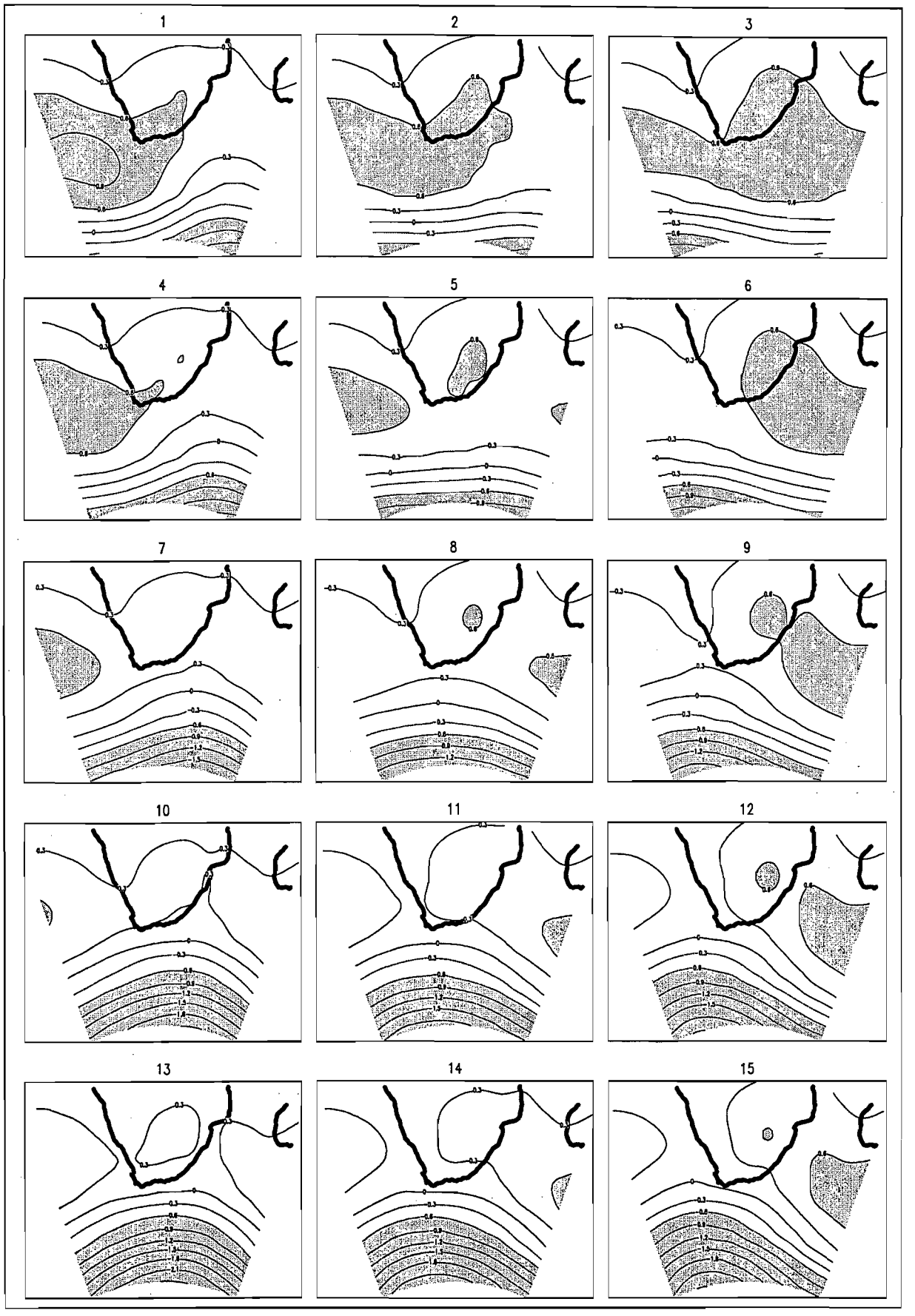

Figure 4.27 The meta-map for the winter (JJA) SOM over the South African region, showing the 15 nodes (3×5) with their contoured weights. The weights represent standardised sea level pressure, and values greater than 0.6 and less than -0.6 have been shaded.

summer and winter respectively, i.e. the top left-hand grid block on Figure 4.28*a* corresponds to the top left-hand map on Figure 4.26, and likewise for Figures 4.28*b* and 4.27.

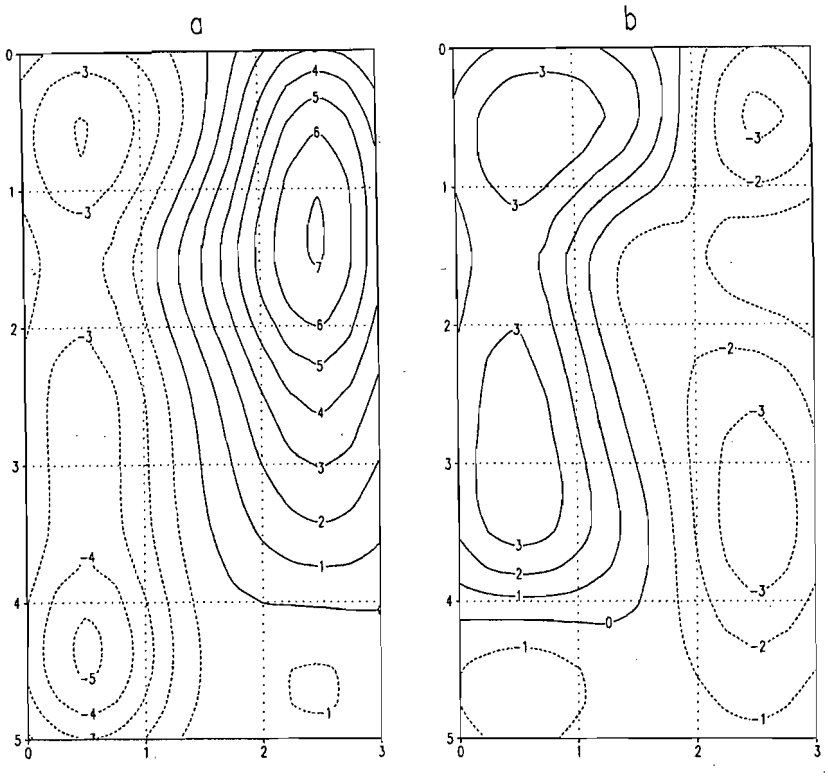

Figure 4.28 The percentage difference between the observed and GCM data (GCM minus observed) in the frequency of days mapping to each node (each grid block) of the meta-map in *a*) summer and *b*) winter. The corresponding summer and winter meta-maps are shown on Figures 4.26 and 4.27 respectively.

The summer meta-map (Figure 4.26) displays the different circulation types found during the season, with varying influence of the major sea level pressure features, i.e. the westerly wave south of the country, the South Atlantic Subtropical High Pressure (SAHP), the South Indian Subtropical High Pressure (SIHP) and the easterly trough over the land. It is evident that as one moves from left to right across the meta-map, the circulation types change from those showing a strong SIHP and a westerly wave with a westward tilt, to those types/maps showing a dominant SAHP and a westerly wave with an associated eastward tilt (Figure 4.26). Moving from the top to the bottom of the meta-map shows a strengthening of the subtropical high pressures and an associated weakening of the westerly wave (Figure 4.26). The model has too many days which fall on the right-hand side of the meta-map and too few days which fall on the left-hand side compared to the observed data (Figure 4.28*a*). This implies that the model is favouring circulation types which show a strong SAHP compared to the SIHP. The model is deficient in those days which, firstly, show a deep westerly wave with a westward tilting axis (top left of the meta-map), and which, secondly, show dominant, similar strength, Atlantic and Indian high pressure cells situated south of the country (bottom left of the meta-map) (Figure 4.28*a*). The latter circulation type, and the maps at the bottom

of the meta-map in general, display the subtropical high pressures lying quite far south, and may be under-represented due to the pressure systems being shifted northwards in the model compared to the observed data.

To summarise, during summer the model over-represents days that have a strong and dominant SAHP and under-represents days with a strong SIHP. This affects the tilt of the westerly wave, such that days with westward-tilting waves are less common in the model compared to observed. The model also does not significantly capture those days where the strong subtropical high pressures lie quite far south of the country and dominate the circulation over the analysis window. This may be due to the previously discussed northward offset of the model pressure belts compared to observed.

Moving from left to right on the winter meta-map shows an increase in strength of the SIHP, a decrease in strength of the SAHP and a change in the tilt of the westerly wave axis from eastward sloping to westward sloping (Figure 4.27). Moving from the maps at the top to those at the bottom demonstrates an increase in intensity of the westerly wave and a decrease in the strength of the subtropical high pressures (Figure 4.27). As for summer, the model favours those days with a strong SAHP and under-represents those days with a strong SIHP (Figure 4.28*b*). In addition, the model has too few days which have deep westerly waves over the analysis window. This will have an impact on precipitation over the south western portion of the country.

4.10 Should the Model be Trusted?

From the results presented above, as well as from previous validation studies with version 2.0.a of GENESIS (Thompson and Pollard, 1997; Hudson, 1997; Hudson and Hewitson, 1997), it appears that the model is performing reasonably well. It is also clear that there are a number of discrepancies between the model and observed data. The key question is, do these differences constitute a problem and do they jeopardise the validity of performing and interpreting sensitivity simulations? Before discussing the pitfalls of the model, it is important to remember that not all the variables in the *observed* data are equally reliable (refer to Chapter 2). The NCEP/NCAR reanalyses are based on observed data, but in data sparse regions the model component of the data assimilation system will affect the results more than it would in data rich regions. Hence, in some cases, biases of the forecast model can influence the data. This may be particularly relevant to variables such as humidity and precipitation, and regions such as the Southern Hemisphere high latitudes where observations

are sparse. With this in mind, one must decide whether or not the GENESIS model adequately simulates reality.

Some variables from the GENESIS model are more robust than others. For example, sea level pressure is a derived variable in the model, i.e. surface pressure must be interpolated to sea level, using assumptions of lapse rates to obtain the values. This is obviously not too problematic over oceanic and low-lying regions, but it can be a source of error over mountainous and high-lying areas. This could account for differences between the model and the observed data over the continents. Also, those variables in the model, for example precipitation and specific humidity, that rely heavily on grid cell parameterisations are often not very reliable. This does not, however, necessarily mean that the dynamics of the model are incorrect. If one looks at the pattern of sea level pressures over the oceans, and the 500 hPa heights, it is clear that the model is correctly simulating the large scale features of the observed climate. Most of the discrepancies in the 500 hPa height surface of the model, which is a fairly robust variable, and the sea level pressure field over the oceans are probably due more to grid resolution than erroneous model physics. Hudson and Hewitson (1997) found a marked improvement in the definition of sea level pressure features in the current version (2.0.a) of GENESIS, which operates on a T31 resolution, compared with the previous version (1.02), which operated on an R15 resolution. The region of the subtropical high pressure cells was indistinct in version 1.02 (R15 resolution) and the circumpolar trough was about 15 hPa too weak. In other words, the coarse resolution grid of version 1.02 resulted in pressure values being smoothed in the model. Circulation dynamics in the atmosphere are the fundamental processes which affect variables such as temperature, humidity and precipitation. From this and other validation studies (Thompson and Pollard, 1997; Hudson, 1997; Hudson and Hewitson, 1997) it appears that GENESIS (version 2.0.a) is capturing the circulation dynamics of the present-day climate. In addition, the GENESIS model has been compared to the NCAR Climate System Model[2] and the Hadley Centre Unified Model[3] (HadCM2) and has been found to demonstrate comparable performance in terms of circulation (Hewitson, pers. comm.).

Since the changes that will occur as a result of varying sea-ice extent in the model will be a function of the dynamics, one is therefore justified in examining the impact of sea-ice perturbations. The sensitivity experiment anomalies of dependent variables such as upper air

[2] http://www.cgd.ucar.edu/csm/
[3] http://www.meto.govt.uk/sec5/NWP/NWP_sys.html

temperature, even though demonstrating a mean bias in the control simulation with respect to observed data, may still be evaluated as representing a response to a sea-ice anomaly, since they respond to changes in the circulation dynamics which the model appears to adequately capture. In the present study, it is not so much the magnitude of change in response to a sea-ice perturbation that is important, but rather the nature or pattern of this change. With this confidence in the model's simulation of present-day conditions and bearing in mind the limitations of some of the variables, the effect of varying sea-ice extent can now be considered.

4.11 Summary

In order to gauge model performance, the GENESIS (version 2.0.a) GCM's simulation of the present-day climate has been examined for the summer (DJF) and winter (JJA) seasons over the Southern Hemisphere, as well as over a window encompassing southern Africa. Model output from the 10-year (1979-1988) AMIP simulation has been compared to the corresponding period of the NCEP/NCAR reanalysis data. The major findings are summarised below:

- The model captures the primary features of the observed circulation, including the seasonal position and strength of the subtropical high pressures and the decrease in pressures moving south, reaching a minimum in the circumpolar trough.

- The pattern of seasonal changes is generally well represented for most variables.

- The Antarctic region contributes the most to biases in surface temperature and sea level pressure.

- There is a cold bias in the 500 hPa temperature field over much of the Southern Hemisphere in both seasons.

- The circumpolar trough is not as deep as observed and appears to be shifted about 5° north in the model. This affects the wind and midlatitude cyclone data, such that their respective zonally averaged distributions are similarly offset.

- At the 500 hPa level, the model adequately simulates the phase of seasonal wave number 1 and the latitudinal position of the amplitude peaks, but the wave is too weak. The amplitude peak for seasonal wave number 3 in winter is also too weak compared to observed. The results from twice daily waves 1 to 4 show that the peak amplitudes of the respective waves from the model are smaller than observed, but in general the latitudinal positioning of the peaks is captured by the model.

- Surface specific humidities are generally too low over the Southern Hemisphere in both seasons.

- The seasonal positions of precipitation maxima and minima correspond well with the observed data in summer and winter. However, precipitation is generally overestimated in the model, especially in the region of the South Pacific Convergence Zone, where average differences of up to 5 mm day^{-1} are recorded between the observed and model data. The MAE over the South African region is about 1 mm day^{-1} for both seasons.

- The model generally exhibits too much variability in the sea level pressure field in both seasons.

- The classification of twice-daily circulation over the South African region shows that the model over-represents days with a strong South Atlantic High Pressure and under-represents days with a strong South Indian High Pressure in both seasons. In addition, for summer the model does not seem to adequately capture those days with strong, dominant subtropical high pressures lying south of the country, and in winter, the model has too few days with a notably deep westerly wave.

It is important to consider that some of the differences between the observed and model data may be due to inadequacies in the NCEP/NCAR observed data set. The model has been deemed adequate for use in the present study and the following section will thus deal with the sensitivity simulations.

SECTION III

Sea-Ice and SST Sensitivity Simulations

CHAPTER 5

Sea-Ice Algorithm and Experimental Design

5.1 Introduction

The present study uses a GCM run with prescribed SSTs and sea-ice extent in order to investigate the impact that reduced Antarctic sea-ice limits have on the general climate of the Southern Hemisphere. The SST and sea-ice input fields are as observed in the control simulations, whereas in the perturbation simulations the sea-ice extent is reduced. As has been mentioned in the introductory chapter, a modelling study using prescribed fields has the advantage of allowing one to isolate the sea-ice forcing and the effect that the sea-ice and SST changes have on the atmosphere. In order to perform GCM sea-ice sensitivity simulations, it is necessary to decide what the perturbed sea-ice limits will be. Previous modelling studies appear to have used large and sometimes unphysical sea-ice extent anomalies, for example using a data set with no sea-ice (Simmonds and Dix, 1987), using a data set with no sea-ice north of a designated latitude (Mitchell and Hills, 1986; Mitchell and Senior, 1989) or using a data set where the September sea-ice field has been replaced with a March sea-ice field (Simmonds, 1981). The impact of these extreme sea-ice perturbations may not be applicable to the smaller variations in ice extent that are actually observed. In addition, the removal of ice north of a designated latitude, as was done by Mitchell and Hills (1986) and Mitchell and Senior (1989), does not take into account the asymmetrical melting that occurs around Antarctica.

A sea-ice algorithm has been developed for the present study in order to facilitate the generation of sea-ice perturbation data sets that are fairly realistic, in that the sea-ice reductions are not applied uniformly around the Antarctic continent, and data sets of multiple months can be obtained where a realistic seasonal cycle is clearly evident. The latter permits simulations where the sea-ice distribution changes from month to month, in keeping with the seasonal cycle, rather than having a fixed sea-ice distribution over the multi-month simulation period or using a perpetual simulation, as has been done in the past. The severity of the perturbation can also be varied, depending on the purpose of the study. Where sea-ice was removed in previous modelling studies (Simmonds, 1981; Mitchell and Hills, 1986; Simmonds and Dix, 1987; Mitchell and Senior, 1989), it was replaced with a constant temperature, less than or equal to 0°C, depending on the study. However, in the present study

in those regions where sea-ice is removed, it is replaced by a gradient of SSTs extending to the new sea-ice boundary, thus including the effect of the warming of ice-free surface waters, whereas previous studies did not.

The SST and sea-ice perturbation data sets that are created in the present study by the sea-ice algorithm are used in a number of four month summer and winter replicate simulations from the GENESIS GCM. As has been mentioned previously, the control simulations make use of observed distributions of SSTs and sea-ice, while the experiment simulations utilise corresponding months with reduced sea-ice limits. This chapter explains the sea-ice algorithm used to generate the sea-ice and SST fields for the perturbation simulations, and then moves on to describe the experimental design.

5.2 Sea-Ice Algorithm

5.2.1 Conceptual Overview

The sea-ice algorithm is conceptually fairly simple, but the details make it appear complicated. Therefore, this first section will provide a brief overview of the algorithm, which is then followed in subsequent sections by a more detailed explanation.

The algorithm is designed for perturbation studies using GCMs run with prescribed SSTs and sea-ice extent. It relies on the analysis of observed sea-ice coverage in order to obtain the anomalous SST and sea-ice data set. The observed data set in the present study is that which is used for the AMIP control simulation with the GENESIS model, and is the COLA[1]/CAC[2] AMIP SST and sea-ice data set (Reynolds and Roberts, 1987; Reynolds, 1988). Pixel specific melt/freeze indicators are determined for each month of the observed data and are then used as a basis for exacerbating the melt or diminishing the freeze. For any given month of the observed data, the algorithm will produce a corresponding month with reduced sea-ice coverage which can be input into the model. The perturbation simulation is then compared to the control simulation and the climatic impact of the sea-ice perturbation can be elucidated.

The flow chart on Figure 5.1 shows the general procedure used in the creation of the perturbation sea-ice data set, including the decision criterion used to determine whether a particular pixel in a certain month should remain as ice or be changed to water. The procedure is carried out for every sea-ice pixel in each month of the observed data (AMIP

[1] Center for Ocean, Land and Atmosphere (USA)
[2] Climate Analysis Center (USA)

SST and sea-ice data) for which a corresponding month with reduced sea-ice limits is required. The decision criterion of whether or not to alter a pixel from ice to water differs depending on whether the month falls in a general melting or freezing trend (Figure 5.1). In both cases, the 8 surrounding pixels of the pixel under consideration are examined in order to determine the degree to which it is surrounded by water. However, should the month fall in a melting trend, then the degree to which the pixel is surrounded by water is examined in both the month under examination (t) and the following month (t+1). It is desirable to "melt" those pixels in the current month (t) that have a greater chance of melting in the following month. Therefore, those pixels that are largely surrounded by water in months t and (t+1) are changed from ice to water.

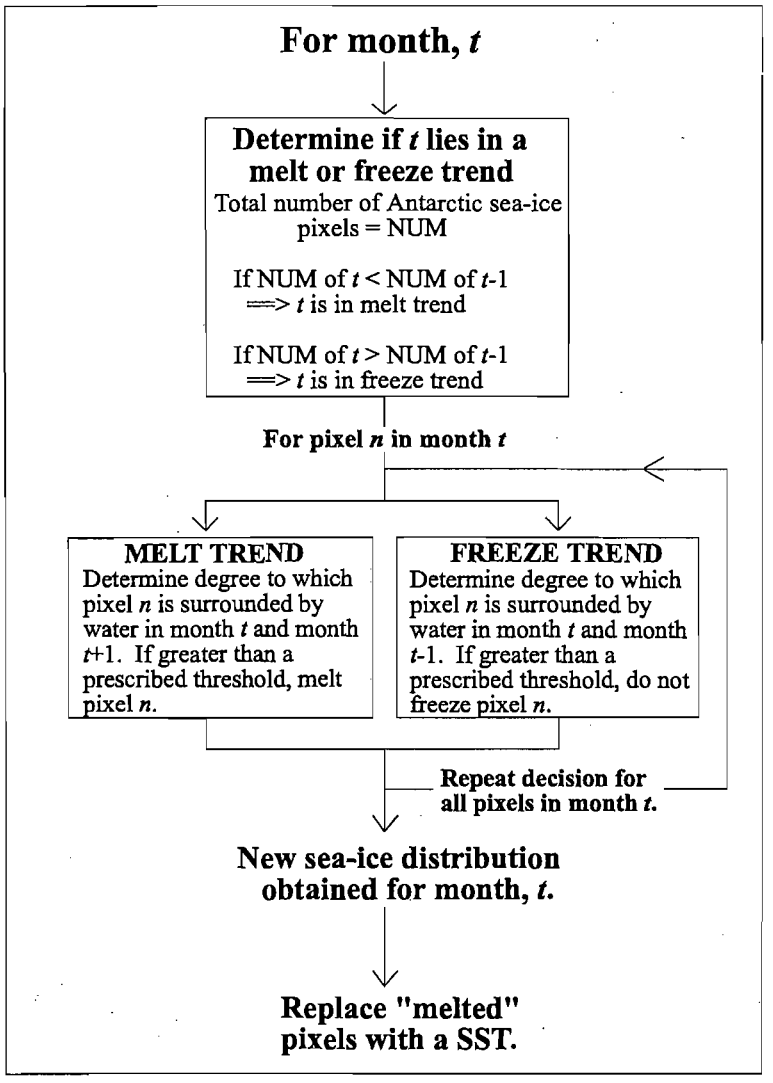

Figure 5.1 A flow chart showing the procedures involved in the creation of a perturbation sea-ice data set, where the sea-ice limits are smaller than the corresponding control sea-ice data. The algorithm is applied to each pixel of each month of the control sea-ice data in order to create the new sea-ice distribution. The control sea-ice and the new sea-ice data (with a reduced sea-ice extent) can then be used in GCM sensitivity simulations.

On the other hand, if the month falls in a freezing trend, then the degree to which the pixel is surrounded by water is examined in both the month under examination (t) and the previous

month (t-1). It is desirable to melt those pixels which, although they froze in the observed data in month t, had a fairly low chance of freezing, as is shown by the degree of influence of water in month (t-1). Therefore, those pixels that are largely surrounded by water in months t and (t-1) are changed from ice to water.

The examination of the previous and following months (for freezing and melting trends respectively), as well as the month under consideration, allows one to take into account the observed asymmetrical melting around Antarctica. The thresholds which are used to determine whether the degree of "influence" of water is sufficient to allow modification of a pixel from ice to water are explained later in the chapter, suffice to say that they can be altered to the satisfaction of the user in order to create perturbations of differing magnitude. The decision procedure of whether or not to change the value of a pixel is repeated for every sea-ice pixel of the observed data such that a new sea-ice distribution is obtained for the particular month. Those pixels which are changed from ice to water in the process of creating the new sea-ice data set, are assigned a SST, thus producing a new SST distribution for the corresponding month.

The algorithm will now be described in detail under the following three headings:

- Analysis of Observed Data
- Perturbing the Ice Extent
- Manipulating the SSTs.

5.2.2 Analysis of Observed Data

In this section the observed data are examined and the melt/freeze indicators, necessary for the ice perturbation, are determined. Execution of this part of the algorithm need only be done once. When completed, it provides the basis for performing many different ice perturbations. The perturbed ice-field is obtained from examining the sea-ice behaviour in the COLA/CAC AMIP SST and sea-ice data set. This data set is used in the AMIP control simulation of the GENESIS model. It is a 10-year observational data set, based on a 2° latitude-longitude grid, and contains two data arrays for each month of the period from January 1979 to December 1988. The first array is a sea-ice mask, where a pixel is either 1 or 0, denoting ice or ocean respectively, and the second array is the SSTs.

The first stage is to loop through the observational data set and for each month determine previous, current and future states for each pixel. "Previous" refers to the month prior to the

month under consideration and "future" refers to the month following the month under consideration. In this context, the "state" of a pixel is the number of the 8 surrounding pixels that are water. These previous, current and future state values are thus an indication of the degree to which the center pixel in question is surrounded by water or ice. A value greater (smaller) than 4 implies that water (ice) is the dominant phase.

The next step is to examine each month of the control sea-ice data and determine whether the month under consideration lies in a melting or freezing trend. This is calculated based on the total number of pixels that are designated as sea-ice in each month. If there are more (fewer) pixels that are ice in the previous month, compared to the month under examination, then the month is classified as lying in a melting (freezing) trend. Now that the previous, current and future states of each pixel have been determined, as well as the melting/freezing trends for each month in the 10-year data set, the sea-ice perturbation data sets can be obtained.

5.2.3 Perturbing the Ice Extent

In order to obtain the perturbation data set, months are treated differently depending on whether they fall in a melting or freezing trend. If a particular month falls in a melting trend, then the decision of whether or not to alter a pixel's value from 1 (ice) to 0 (water) is based on what happens in the following month, i.e. examine the future state value of the specific pixel, together with the condition of the month under examination, i.e. examine the current state value of the pixel. Those pixels that are largely surrounded by water in their current or future states have their values changed to zero. The current state value is not used in isolation, because then melt propensities of certain pixels would not be taken into account and the pattern of melt around the Antarctic continent would not be captured. In other words, in a certain region the future state value may be more inclined towards water than the current state value, due to melting taking place from the current month to the following month. However, this may not be the case in a different region which could be more resistant to melting at that time of year. It is desirable to "melt" those pixels in the current month that have a greater chance of melting into the following month. The thresholds that are used to determine whether the degree of "influence" of water is sufficient to allow alteration of the value of a pixel are the values of three constants, PST, CST and FST. PST, CST and FST are constants that are set for comparison with the previous state value, the current state value and the future state value of a pixel respectively. The constants are set at a default value of three. In a particular month, for each pixel that is ice the melt rule is as follows: if the current state value is greater than the value of CST or if the future state value is greater than FST, then the

pixel is "melted". This implies that if in the following or current month (future state value and current state value) there are more than three (the default) surrounding pixels that are water (i.e. fewer than 5 pixels are ice), then the central pixel of the current month is changed from ice to water. If the condition does not hold true, then the pixel is left as ice. The constants are set at a default value of three, so that "melting" will only occur if at least half of the surrounding pixels are water.

If a month falls in a freezing trend, then the decision of whether or not to "melt" a pixel is based on the degree to which the pixel is surrounded by water in the month under examination and the previous month. The rationale behind this is that those pixels which are largely surrounded by water in the previous month are less likely to freeze in the following month compared to those that are surrounded by relatively more ice. It is desirable to melt those pixels which, although they froze, had a fairly low chance of freezing. Therefore, the algorithm is such that a pixel's value is altered if its previous state value is greater than PST or if its current state value is greater than CST.

Figure 5.2 shows the result of perturbing the 10-year sea-ice data set according to the method described thus far. As an aside, it is interesting to note the difference in sea-ice extent in the observed data in the period of 1982 to 1987, compared to the years 1979, 1980, 1981 and 1988 (Figure 5.2). In the former period (1982-1987) there is consistently less sea-ice than the latter mentioned years.

It is evident that there is a problem with the months which display a minimum sea-ice extent (February). These months are not altered sufficiently, since based on the observed data there should be a greater difference between the two adjacent months and the minimum month than is shown in the perturbation data set (Figure 5.2). This is because according to the algorithm, the ice minimum month lies in a melting trend and therefore the decision of whether or not to "melt" pixels is based on the current state value and the future state value. Since the following month has a greater ice extent than the current month, very few pixels will be changed from ice to water based on their future state values, and therefore the algorithm has less of an impact on the ice minimum month. In order to circumvent this problem, these months are manipulated after the other months have been perturbed. The ice minimum months are identified in the unperturbed sea-ice data set, and at each longitude the difference between the position of the sea-ice boundary for the ice minimum month and the previous month is determined. For each longitude, if there is one pixel difference between the two

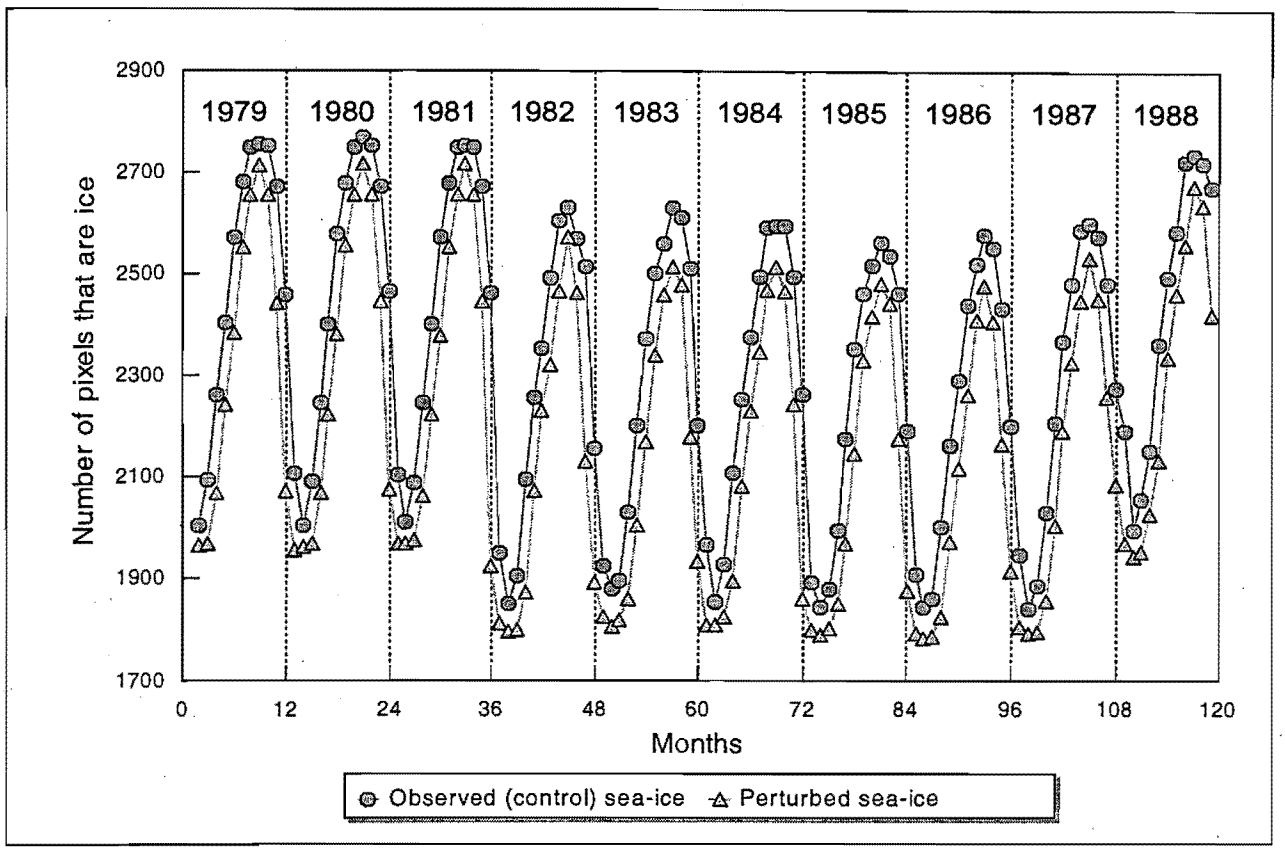

Figure 5.2 The total number of pixels in the Southern Hemisphere that are designated as sea-ice for both the observed (control) and perturbed sea-ice data sets. The plotted data extends from February 1979 (month 2) to November 1988 (month 119).

months in the unperturbed sea-ice data, then one pixel is "melted" at the sea-ice ocean boundary in the perturbed ice minimum month. Similarly for two or three pixel differences between the two months. The modified perturbed total sea-ice which accounts for the ice minimum months is shown on Figure 5.3*b*, and the mean monthly spatial distribution of sea-ice from the perturbation and control data sets (averaged over the 10-year period) is displayed on Figure 5.4, together with an example of three individual summer and winter months in Figure 5.5.

The algorithm also incorporates three possible ways of obtaining perturbations of differing strengths. Firstly, the algorithm can be executed in an iterative procedure, such that the greater the number of iterations the larger the perturbation. In subsequent iterations, the calculations are based on the perturbed ice extent obtained at the end of the previous iteration. The impact of increasing the number of iterations from one to two is shown on Figure 5.3*c* and an example of three individual summer and winter months is shown on Figure 5.6.

Secondly, the values of the constants can be altered. If the value of the constants is decreased, then the conditions for changing á pixel's value are less stringent. For example, if

the values of CST and FST are decreased from three to two, then in the case of a melting trend, if more than two surrounding pixels are water (i.e. fewer than 6 pixels are ice) in the following or current month, the central pixel of the current month is changed from ice to water. The effect of decreasing the value of the constants from three to two (using one iteration) produces a very similar result to increasing the iterations from one to two. Figure 5.3*d* displays the effect on total ice extent by changing a combination of the settings. It is important to note that, for ease of computation, the counts of sea-ice pixels shown on Figures 5.2 and 5.3 include pixels covering the Antarctic continent. Therefore, in mid-summer on some of the curves, especially curve *d* on Figure 5.3, there may actually be very little sea-ice.

Lastly, perturbations intermediate between the control and a specified perturbation, e.g. that produced with default settings, can be obtained by selecting a fractional position (*f*) between the two data sets. For example, if *f* is set to 0.5, then for each longitude of every month the new ice edge is positioned halfway between the control and the specified perturbation.

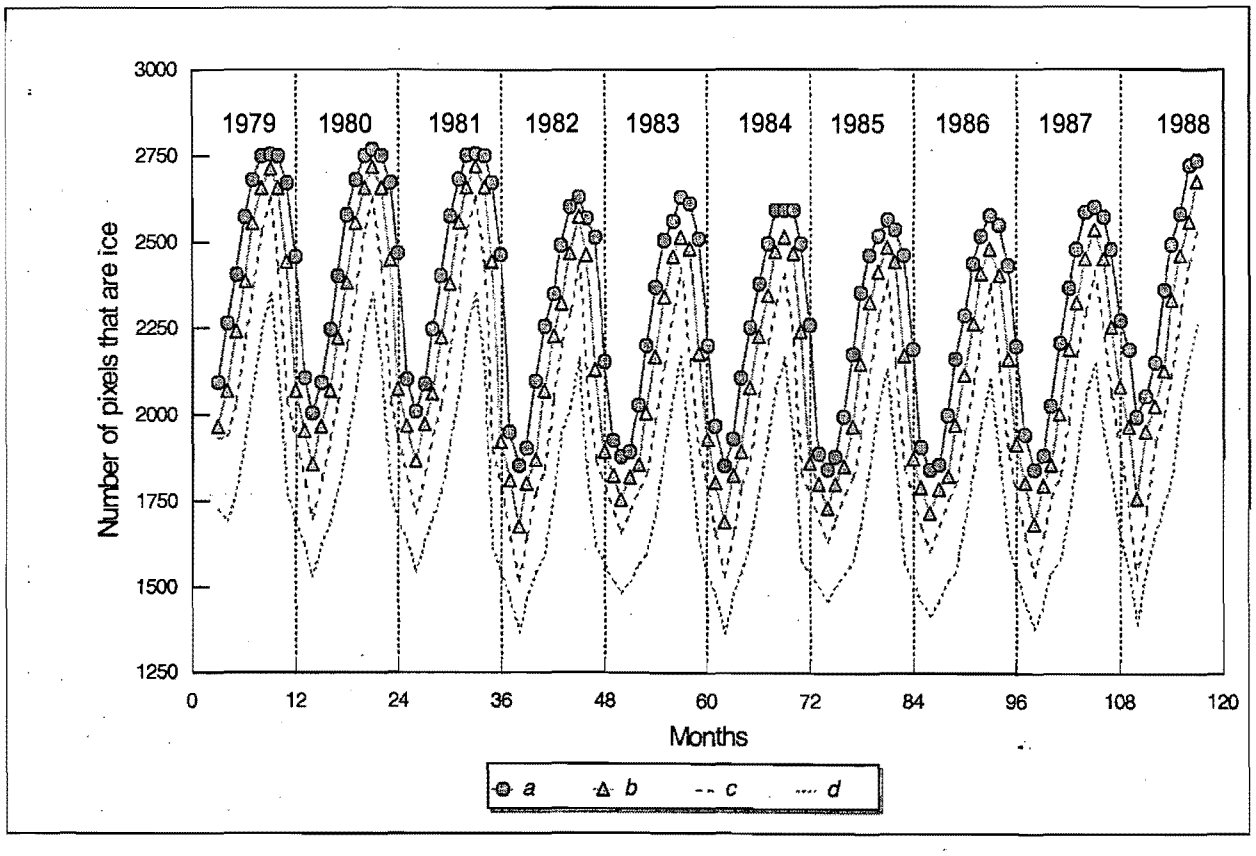

Figure 5.3 The total number of pixels in the Southern Hemisphere that are designated as sea-ice for the observed (*a*) and perturbed sea-ice data sets (*b, c, d*), with the ice minimum month accounted for in the perturbations (unlike in Figure 5.2). Data set *b* shows sea-ice with default settings (i.e. PST=CST=FST=3; iterations=1). The settings for data set *c* are PST=CST=FST=3 with two iterations, and for data set *d*, PST=FST=2, CST=3 with two iterations. The plotted data extends from March 1979 (month 3) to September 1988 (month 117).

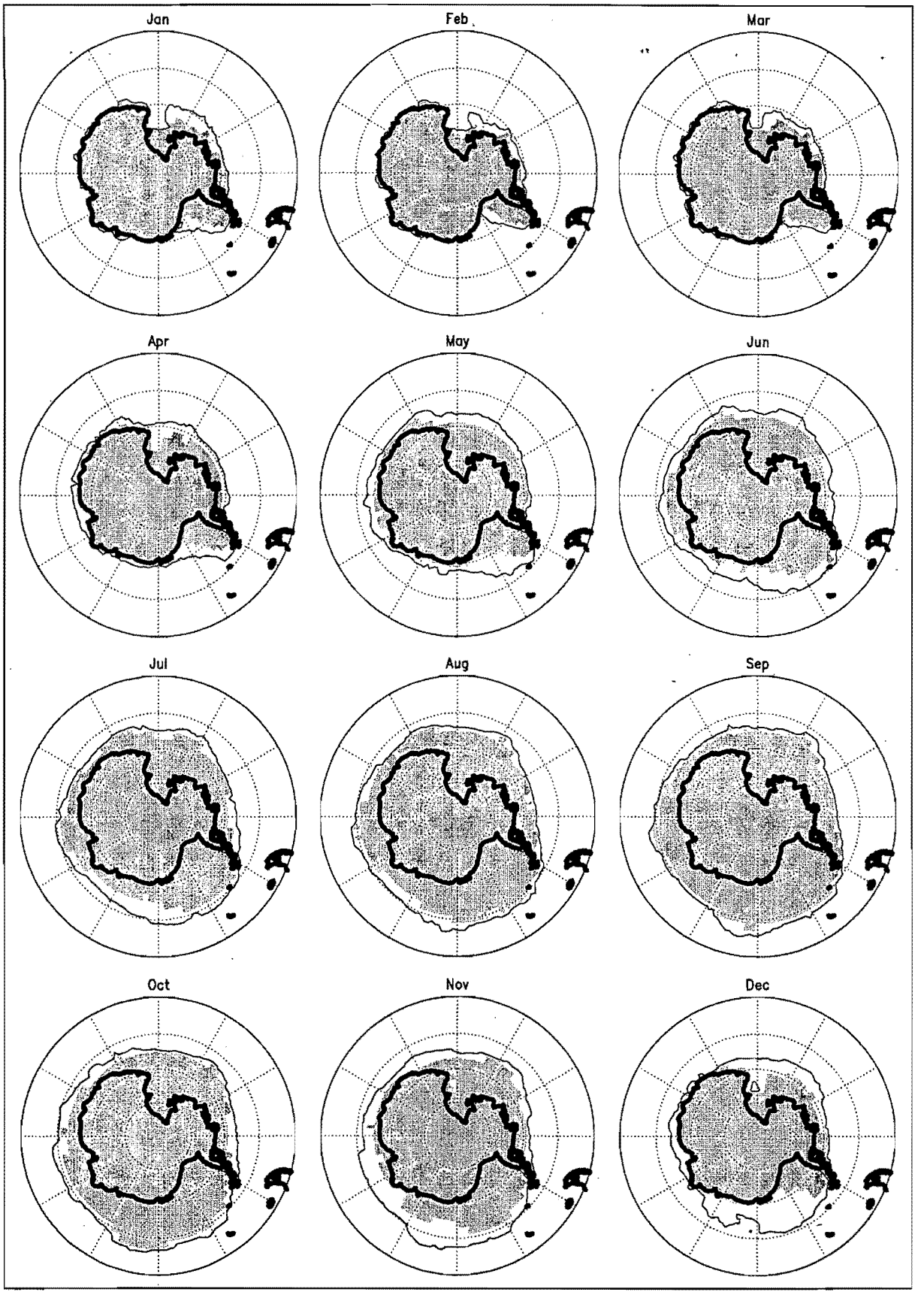

Figure 5.4 The mean monthly position of the sea-ice margin, averaged over the 10-years (1979-1988) of data. The contour line represents the average ice extent for the observed data, and the shading represents the average perturbed sea-ice extent. The algorithm was used with default settings (i.e. PST=CST=FST=3 with one iteration).

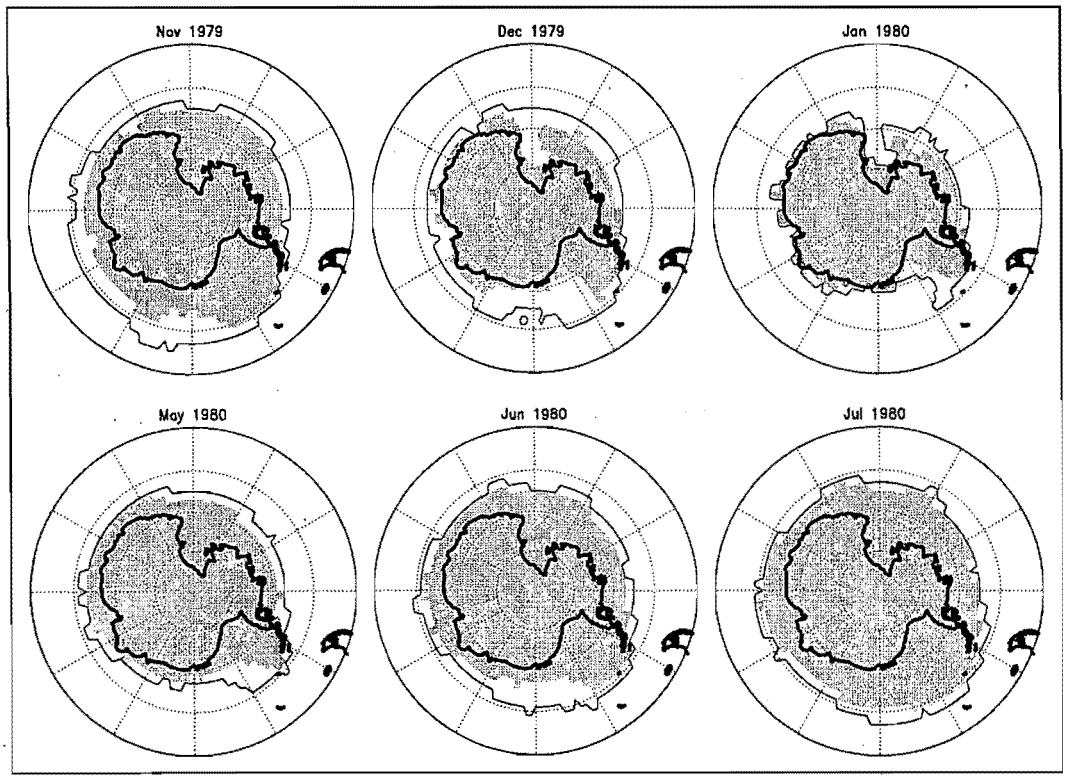

Figure 5.5 The position of the sea-ice margin during three summer and winter months for the observed (contour) and perturbed (shaded) sea-ice data. The algorithm was used with default settings (i.e. PST=CST=FST=3 with one iteration).

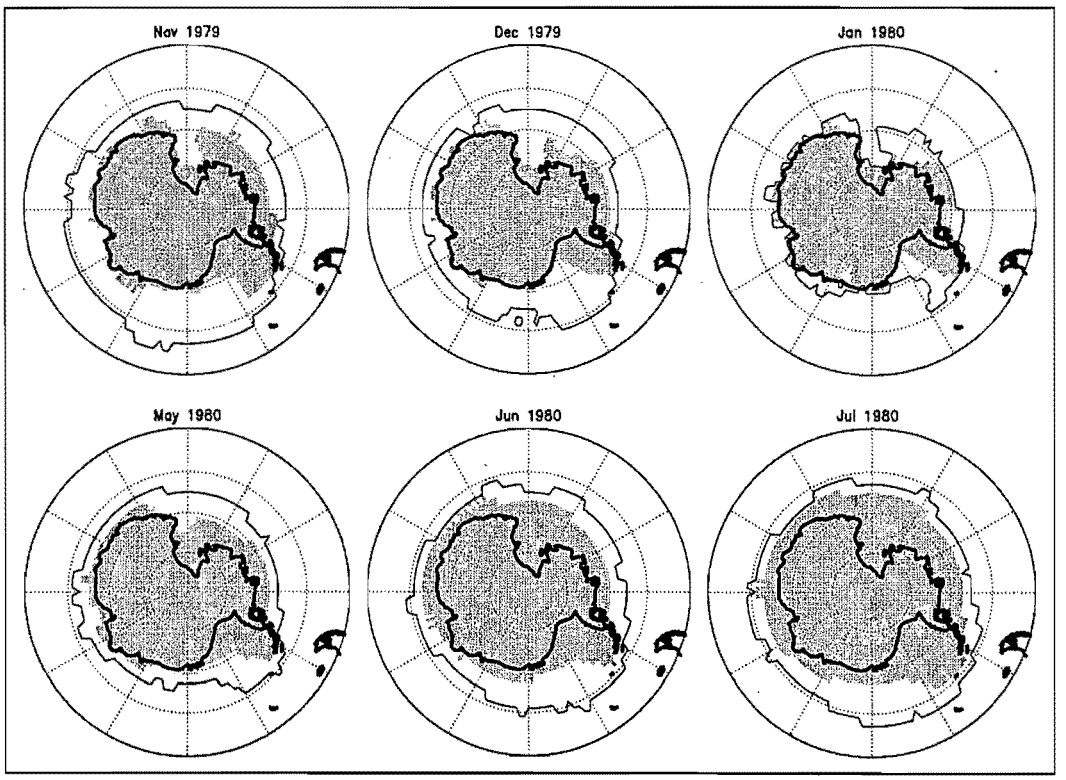

Figure 5.6 The position of the sea-ice margin during three summer and winter months for the observed (contour) and perturbed (shaded) sea-ice data. The algorithm was used with two iterations and PST=CST=FST=3.

5.2.4 Manipulating the SSTs

Before the perturbed ice-field can be introduced into a GCM, the SSTs need to be adjusted. SSTs are assigned to those new ice-free ocean areas and the temperature field is therefore extended to the new ice boundary.

The position of the new (perturbed) ice boundary is smoothed across longitudes along the ice margin using a 9 point running mean. The smoothing is applied only as an intermediate step for the purpose of obtaining the SSTs and the unsmoothed margin is still ultimately used. This is done in order to obtain a fairly smooth SST field extending to the new ice boundary. Without the smoothing, unacceptable cross latitudinal spikes become evident in the SST field. The processes that follow are carried out at each longitude of pixels and are schematically represented in Figure 5.7.

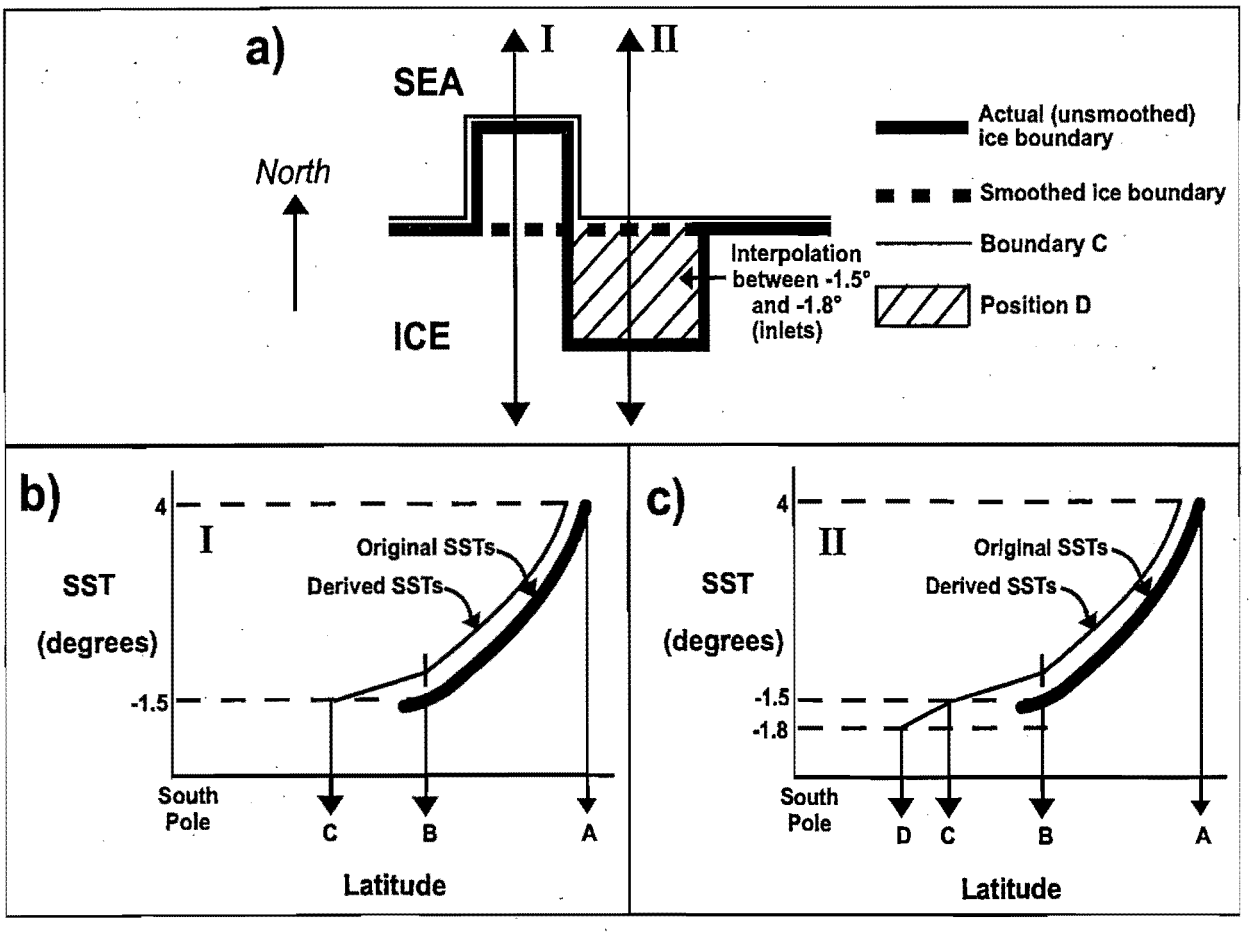

Figure 5.7 *a*) A plan view of the perturbed sea-ice boundary showing both smoothed and unsmoothed components. Two cross-sections, I and II, are taken through the diagram, represented in *b*) and *c*) respectively, to help show the procedure of obtaining new SSTs. In *a*), *b*), and *c*), A denotes the latitudinal position of the observed 4°C isotherm; B the position of the observed -1.5°C isotherm; C the position of the most equatorward margin between the smoothed and unsmoothed ice boundaries and D denotes the position of the unsmoothed ice boundary where it is poleward of the smoothed ice boundary.

The first stage is to select the most equatorward sections of the smoothed and unsmoothed ice boundaries considered together. This most equatorward margin is represented on Figure 5.7 as boundary C. Secondly, those positions where the unsmoothed boundary is poleward of the smoothed boundary must be determined. This is referred to as position D on Figure 5.7 and essentially represents the inlets. In the algorithm, SSTs poleward of the 4°C isotherm are manipulated. This temperature was chosen subjectively, owing to minimal seasonal movements of the isotherm apparent from the observed data. In order to obtain the new SSTs, there are three distinct steps involved:

i) New SSTs ($SST_{new}(n)$) are obtained for each successive longitude south of the observed 4°C isotherm (position A in Figure 5.7) down to and including the position of the -1.5°C isotherm (position B in Figure 5.7) using the following equation:

$$SST_{new}(n) = SST_{obs}(n+1) - \left(\frac{SST_{obs}(n+1) - SST_{obs}(n)}{k} \right), \qquad (5.1)$$

where n refers to the latitudinal position at the specified longitude, $SST_{obs}(n)$ is the observed SST and k is the average difference between the perturbed and observed sea-ice margins. To calculate k, the difference between the number of pixels that are ice in the observed and perturbed (unsmoothed) sea-ice data is calculated at each longitude and then averaged around the hemisphere, excluding those longitudes where there is no difference between the two data sets.

ii) As mentioned previously, boundary C (Figure 5.7) is the most equatorward extension of the smoothed and unsmoothed sea-ice boundaries. The new water at this boundary is set to -1.5°C and temperatures are obtained by linear interpolation from the position where the observed -1.5°C isotherm was (position B in Figure 5.7), down to boundary C (Figure 5.7).

iii) The final interpolation to obtain new SSTs occurs between boundary C (Figure 5.7) and those regions where the unsmoothed sea-ice boundary is poleward of the smoothed ice boundary, which corresponds to position D in Figure 5.7. SSTs at position D are set to -1.8°C. Linear interpolation is used to obtain the new temperatures between C and D.

The values of -1.5°C and -1.8°C have been used in parts ii) and iii) as the temperatures adjacent to the new, perturbed sea-ice boundary, since they are associated with the ice boundary in the COLA/CAC AMIP SST and sea-ice data set. In this data set for the period January 1979 to December 1981, for which there is no satellite data, the data comprises a combination of three analyses: an *in situ* SST analysis, the COADS[3]/ICE SST climatology and the "realistic" sea-ice analysis from the Navy-NOAA-Joint Ice Center. The SST for those grid points where sea-ice was present at least 50% of the time in the realistic sea-ice data (a 10-year data set) was set to -1.8 °C and where the COADS/ICE climatology indicated sea-ice at some points where the realistic sea-ice data did not, then the SST at these points was set to -1.57 °C (Reynolds and Roberts, 1987; Reynolds, 1988). Thus, based on their usage of these two temperatures, it was decided that -1.5°C should be used at the parts of the ice boundary equatorward of the smoothed ice boundary and -1.8 °C where the boundary was poleward of the smoothed ice boundary (i.e. for the inlets).

Lastly, in order to create an even field, the new SSTs created by sections i) and ii) are smoothed using a moving block average (5 pixels in the x direction and 3 pixels in the y direction). This method of manipulating the SSTs is preferable to replacing the removed ice with a single ocean temperature, as has been done in some other similar simulations (e.g., Mitchell and Hills 1986; Mitchell and Senior 1989; Crowley *et al.* 1994), since a SST gradient is retained. Figure 5.8 shows an example of a perturbed ice extent and its associated new SST field.

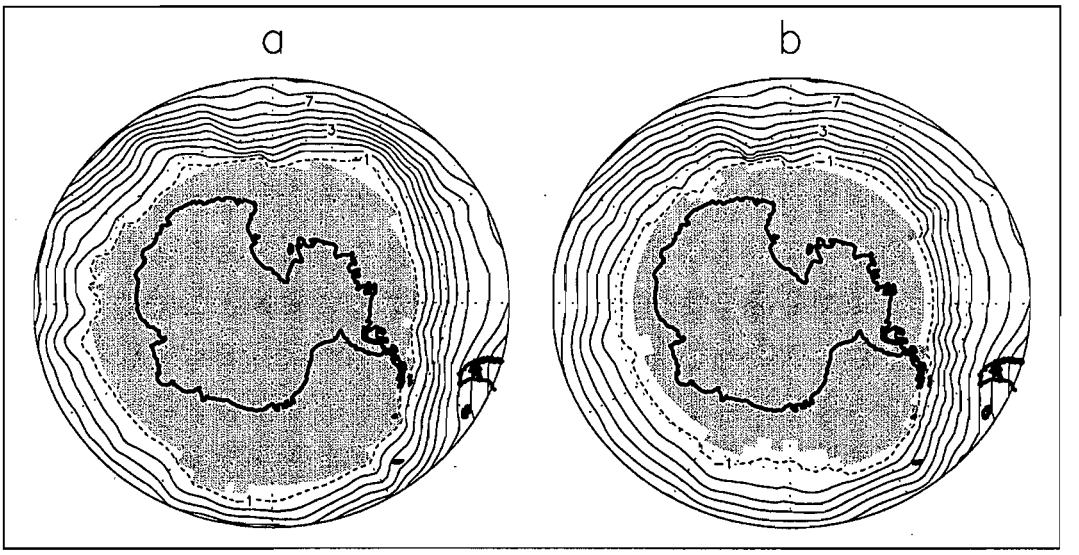

Figure 5.8 November 1979 with *a*) control sea-ice and SSTs and *b*) perturbed sea-ice and SSTs. The sea-ice perturbation was performed using default settings in the algorithm.

[3] Comprehensive Ocean Atmosphere Data Set

5.3 Experimental Design

As mentioned in Chapter 2, the perturbation and control simulations used to determine the impact of reduced sea-ice limits are embedded in the AMIP simulation of the model. That is, they are model restarts of certain portions of the 10-year period. Like the perturbation simulations, the control simulations in the experiment are also restarts of the AMIP simulation. The reason for doing a restart, instead of using the control data from the continuous 10-year run, is because a simulation that is restarted from a file differs slightly from a continuous simulation. A restart file contains values of initial conditions that have been truncated compared to the values that exist when there is no interruption in the calculations, as in a continuous simulation (Dave Pollard, pers. comm.). Thus, in order to be consistent, all the simulations that are examined in the sensitivity study are generated from appropriate restart files.

The summers of 1979/80 (hereafter referred to as 1980) and 1984/85 (hereafter referred to as 1985) and the winters of 1980 and 1985 have been selected for the study. These periods have been selected from the available 10 years because they do not exhibit strong El Niño signals (Figure 5.9) and they appear to have extremes in sea-ice distribution, such that 1980 is characterised by more extensive sea-ice than 1985 (Figures 5.3*a* and 5.10). With regards to the latter, the intention is to determine whether the amount of sea-ice present affects the results.

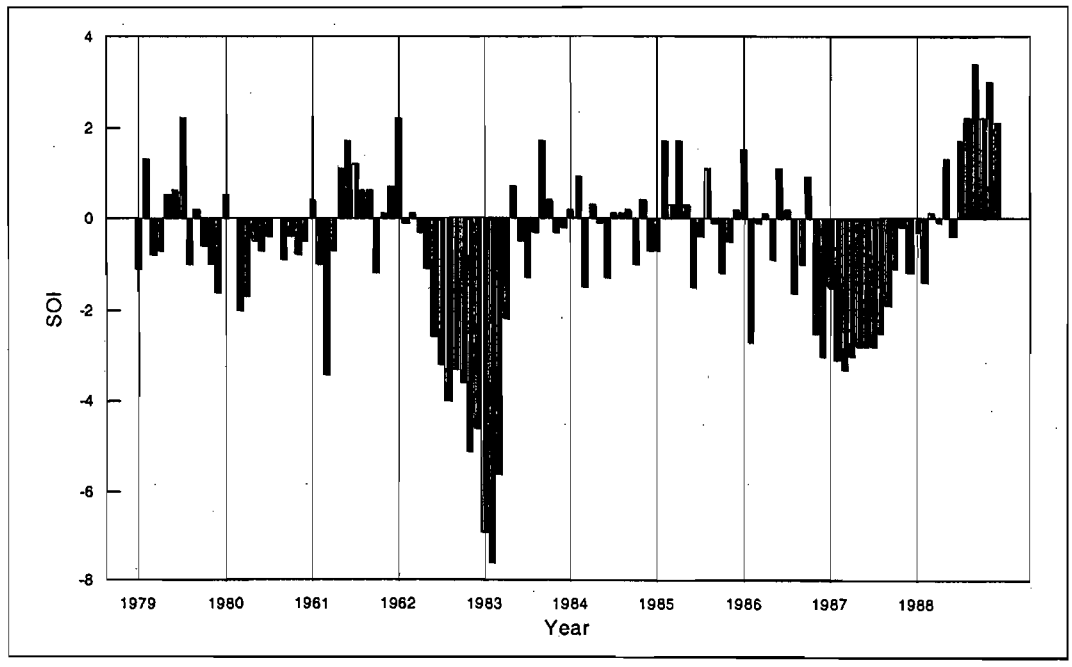

Figure 5.9 Monthly values of the Southern Oscillation Index (SOI) obtained from NOAA for the period January 1979 to December 1988. The SOI is calculated as the sea level pressure difference between Taihiti and Darwin. Negative (positive) values indicate a tendency towards El Niño (La Niña) conditions.

Non-El Niño time periods were selected such that the periods would be relatively consistent in terms of the phase of the Southern Oscillation, and so that the influence of a strong El Niño signal could be eliminated as having a possible confounding effect on the results. However, in the future it would be advantageous to perform similar experiments, but in El Niño years.

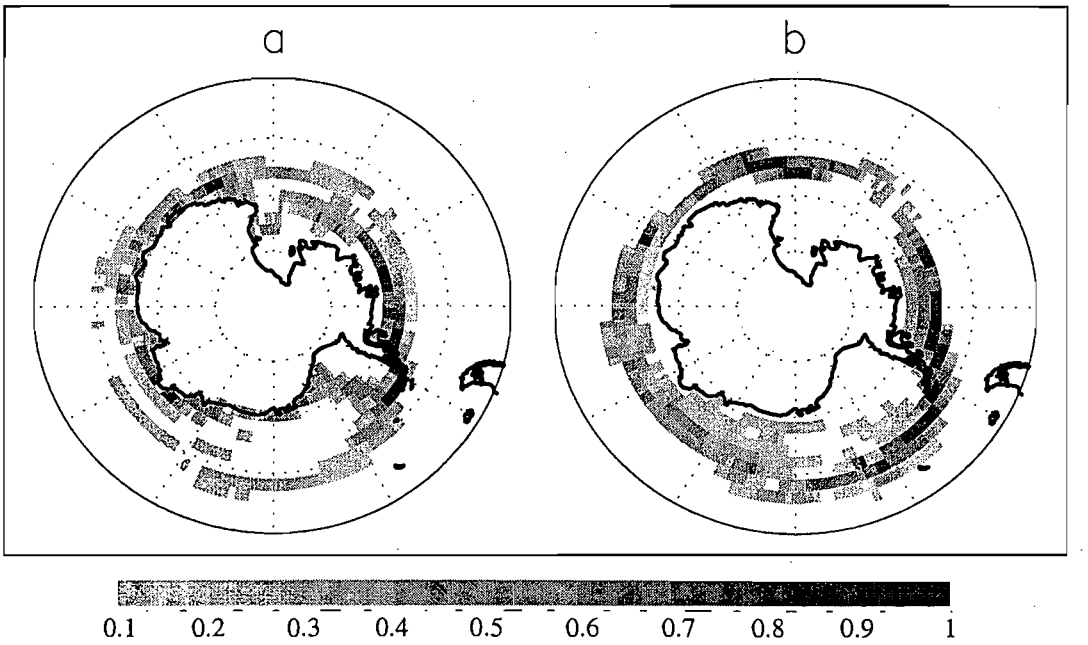

Figure 5.10 The 1980 sea-ice fraction minus the 1985 sea-ice fraction for *a*) summer i.e. averaged over November, December, January, February and March and for *b*) winter i.e. averaged over May, June, July, August and September. The shading is comparable between the maps.

A summary of the details of the experimental design is shown in Table 5.1. Three replicates have been performed for each of the four periods for both the control and perturbation conditions, producing a total of 24 simulations. The replicates do not, however, start from exactly the same date, since simulations started from identical restart files, with the same boundary conditions, will produce results that are bit-by-bit identical. There is a stochastic precipitation parameter in the model, but its random seed is always set to the same value on the first time step and thus will produce the identical random sequence (Dave Pollard, pers. comm.). For this reason, the replicates are started successive months earlier, as shown on Table 5.1. They have to be started months earlier rather than a day or two earlier, because the version of the model used requires a restart to commence at the beginning of a month, since restart files for the vegetation component of the model are only available for the start of each month.

For the control simulations, the boundary conditions and restart files saved from the continuous 10-year simulation are not altered. In contrast, for the perturbations the SST and sea-ice input file is modified, with November, December, January, February and March being perturbed for the summer simulations and May, June, July, August and September being

	Months with perturbed sea-ice in the perturbation simulations	Length of model run (controls and perturbations)			Months analysed
		1	2	3	
1979/80 SUMMER	Nov ('79) Dec ('79) Jan ('80) Feb ('80) Mar ('80)	Nov ('79) Dec ('79) Jan ('80) Feb ('80)	Oct ('79) Nov ('79) Dec ('79) Jan ('80) Feb ('80)	Sep ('79) Oct ('79) Nov ('79) Dec ('79) Jan ('80) Feb ('80)	Dec ('79) Jan ('80) Feb ('80)
1984/85 SUMMER	Nov ('84) Dec ('84) Jan ('85) Feb ('85) Mar ('85)	Nov ('84) Dec ('84) Jan ('85) Feb ('85)	Oct ('84) Nov ('84) Dec ('84) Jan ('85) Feb ('85)	Sep ('84) Oct ('84) Nov ('84) Dec ('84) Jan ('85) Feb ('85)	Dec ('84) Jan ('85) Feb ('85)
1980 WINTER	May June July Aug Sep	May June July Aug	Apr May June July Aug	Mar Apr May June July Aug	June July Aug
1985 WINTER	May June July Aug Sep	May June July Aug	Apr May June July Aug	Mar Apr May June July Aug	June July Aug

Table 5.1 Details of the experimental design, in terms of the months for which sea-ice has been perturbed, the months that have been included in the simulations and the months that have been analysed.

perturbed for the winter simulations (Table 5.1). In the model, daily values of SSTs and sea-ice extent are obtained from the monthly input fields by linear interpolation in time from the two surrounding mid-month values (Pollard and Thompson, 1995a). This implies that, for example, the first half of November's SST and sea-ice field in the perturbation simulations is obtained from interpolation between the unperturbed October field and the perturbed November field. Furthermore, March and September's SST and sea-ice fields, for summer and winter respectively, have been perturbed even though the simulations do not extend to these months (Table 5.1), so that the latter half of February and August respectively can use perturbed fields for the interpolation. With the perturbation simulations it is important to note that although the replicates commence from different months, the SST and sea-ice input fields are identical, i.e. for summer the perturbation is always introduced in November and for winter the perturbation is always introduced in May.

Only the last three months of the simulations have been analysed i.e. December, January, February (DJF) and June, July, August (JJA) (Table 5.1), in order to diminish the problem of the initial jump from observed to perturbed settings and thus allow the model to adapt to the new boundary conditions in the perturbations. Mitchell and Hills (1986), Mitchell and Senior (1989) and Royer *et al.* (1990) also analysed the data one month after their respective sea-ice perturbations had been introduced. Similarly, the results from other sea-ice sensitivity studies using simulations run in perpetual mode, were also based on data subsequent to a period of supposed stabilisation (Simmonds and Dix, 1987; Simmonds and Budd, 1991; Murray and Simmonds, 1995).

The sea-ice perturbation fields that have been used are shown on Figures 5.11 and 5.12 for summer, and on Figures 5.13 and 5.14 for winter. Default settings were used in the algorithm for the winter perturbations i.e. PST=CST=FST=3, iterations=1 and f was disabled. The summer perturbations made use of the same settings, except that f was prescribed as 0.45 in order to produce a less severe perturbation. Using the same settings in the algorithm produces a far greater impact on the summer months than on the winter months. This is because the observed decay rate of sea-ice in summer is more than the growth rate in winter by nearly a factor of two (Gordon, 1981). It was decided that a smaller summer perturbation, than that produced with default settings in the algorithm, would be favoured for the present study. A comparison between the average reduction in sea-ice in the perturbations (Figures 5.12 and 5.14) and the observed difference in sea-ice extent between 1980 and 1985 (i.e. an indication of natural variation) (Figure 5.10) shows that the anomalies introduced into the

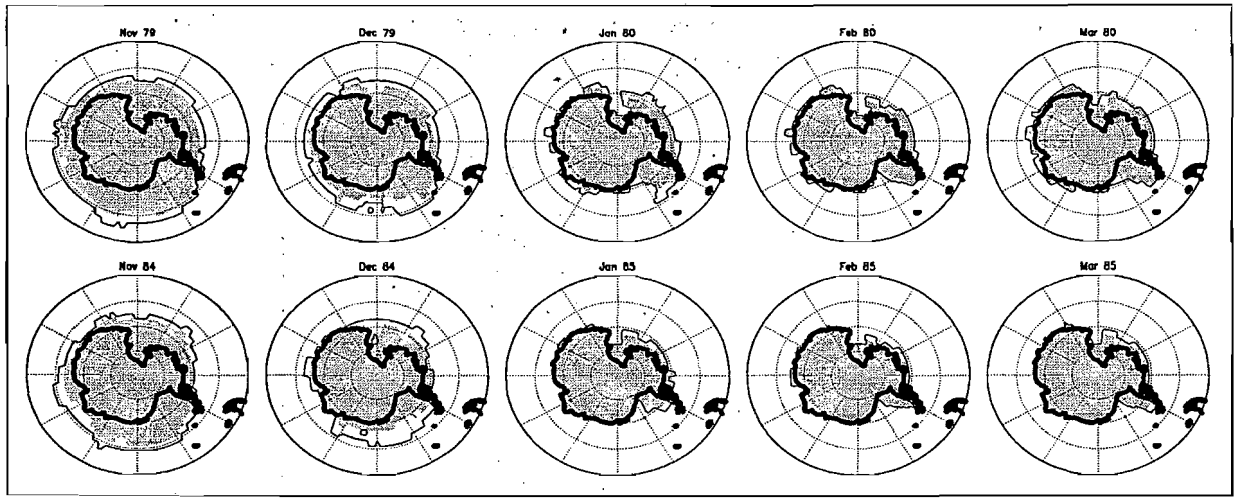

Figure 5.11 The position of the sea-ice margin for the observed (contour) and perturbed (shaded) sea-ice data for the 1979/80 and 1984/85 summer months. These are the input boundary conditions for the GENESIS GCM sensitivity simulations. The sea-ice algorithm was used with default settings (i.e. PST=CST=FST=3 with one iteration), although *f* was utilised and set to 0.45.

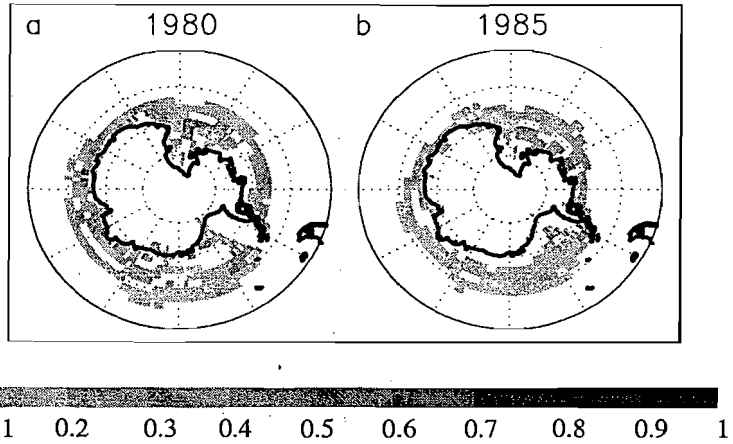

Figure 5.12 The control sea-ice fraction minus the perturbed sea-ice fraction for the *a*) 1980 summer i.e. averaged over November (1979), December (1979), January, February and March and the *b*) 1985 summer i.e. averaged over November (1984), December (1984), January, February and March. The shading is comparable between the maps.

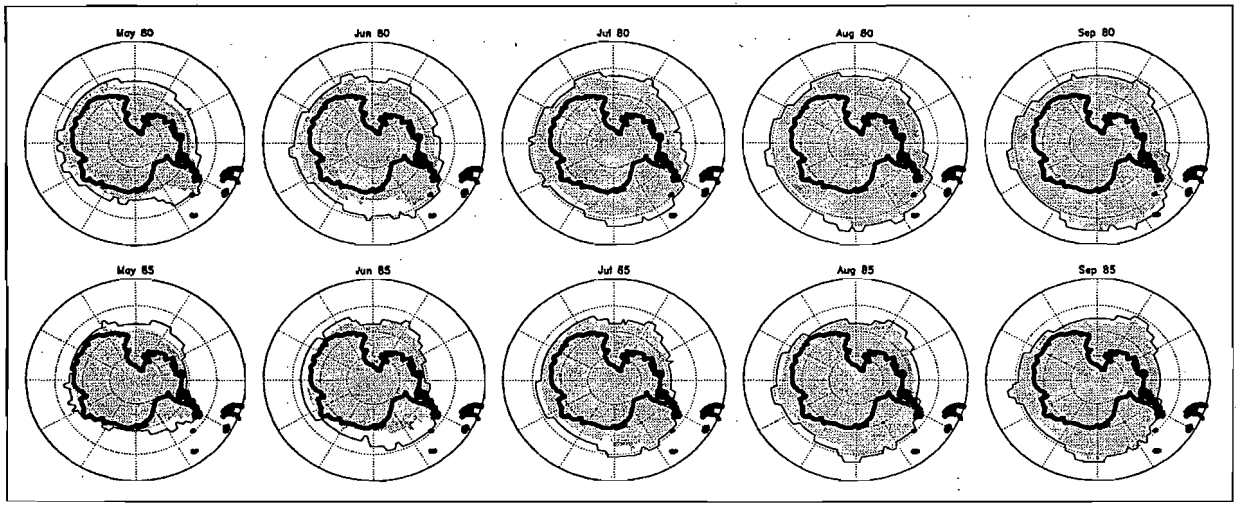

Figure 5.13 The position of the sea-ice margin for the observed (contour) and perturbed (shaded) sea-ice data for the 1980 and 1985 winter months. These are the input boundary conditions for the GENESIS GCM sensitivity simulations. The sea-ice algorithm was used with default settings (i.e. PST=CST=FST=3 with one iteration).

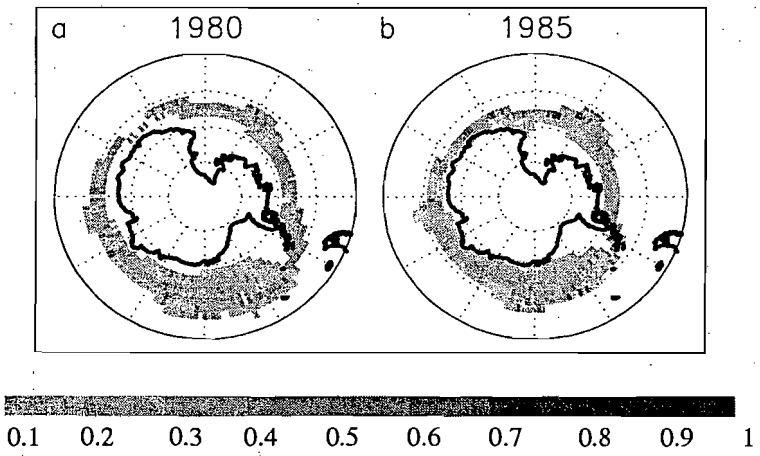

Figure 5.14 The control sea-ice fraction minus the perturbed sea-ice fraction for the *a*) 1980 winter i.e. averaged over May, June, July, August and September and the *b*) 1985 winter i.e. averaged over averaged over May, June, July, August and September. The shading is comparable between the maps.

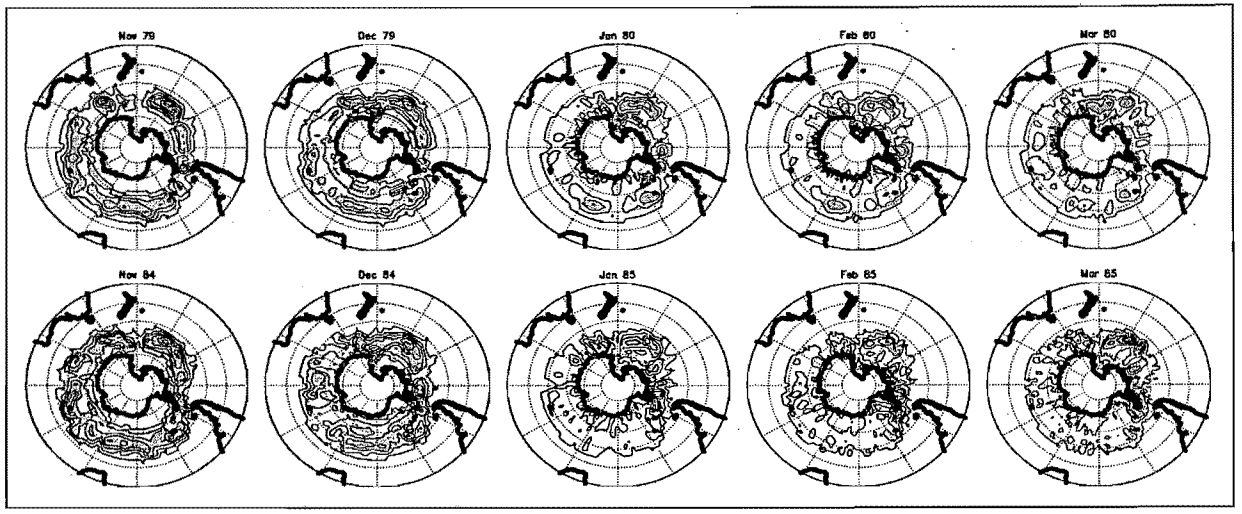

Figure 5.15 The perturbation SSTs minus the control SSTs for the 1979/1980 and 1984/1985 summer months. The SST fields are those used in the sensitivity simulations. Differences greater than 1°C have been shaded and the contour interval is 0.5°C.

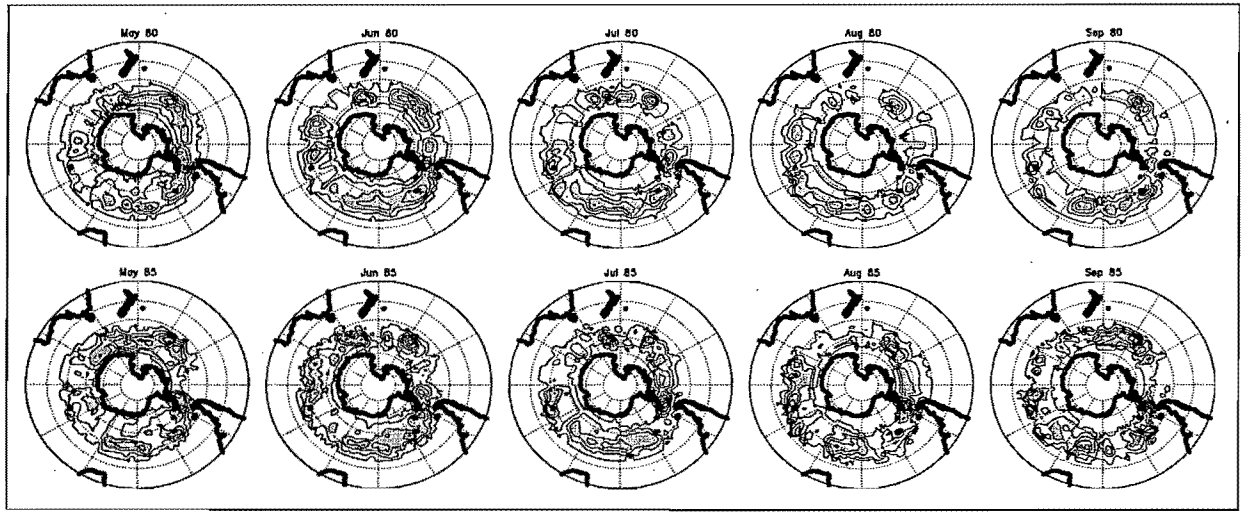

Figure 5.16 The perturbation SSTs minus the control SSTs for the 1980 and 1985 winter months. The SST fields are those used in the sensitivity simulations. Differences greater than 1°C have been shaded and the contour interval is 0.5°C.

model are not unreasonable in terms of spatial pattern and strength. Figures 5.15 and 5.16 show the difference between the observed and perturbed SSTs for each month of the summer and winter perturbations respectively. SSTs are higher in the perturbations, since in the algorithm when sea-ice is removed, the SST gradient is extended to the new sea-ice boundary, thus warming the ice-free waters.

5.4 Summary

The procedures employed to generate the sensitivity simulations for the present study have been discussed. A description of the sea-ice algorithm, used to create the perturbed SST/sea-ice boundary files for the GCM, has been provided, together with details of the input data sets that were ultimately used for the experiment simulations. A total of 24 simulations have been conducted, encompassing the controls and perturbations for the summer and winter of 1980 and 1985 respectively. Three replicates have been performed for each time period. The results of these simulations and the implications of the sea-ice perturbations are presented in the following chapters.

CHAPTER 6

The Summer Response over the Southern Hemisphere

6.1 Introduction

This chapter considers the Southern Hemisphere response to the sea-ice perturbation during the summer months. The sea-ice and SST input fields for the control and perturbation simulations have been described in Chapter 5. Previous modelling studies done on the effects of a reduced Antarctic sea-ice extent have been restricted to the winter season, therefore direct comparisons are limited to studies done with observed data. It is important to note, however, that one should be cautious using observations to corroborate or reject model results, since unlike reality the atmosphere cannot affect the surface conditions in the model.

In modelling studies examining the impact of reduced Arctic sea-ice limits, Crowley *et al.* (1994) and Raymo *et al.* (1990) considered both the summer and winter seasons. In these studies, September sea-ice was removed and March sea-ice extent was set to the observed September boundary, with sea-ice coverage for the other months varying between these two extremes. Where ice was removed they replaced it with very cold (-1°C) SSTs, so as to focus the sensitivity test on the removal of ice, rather than the effect of warming ice-free surface waters (Crowley *et al.*, 1994; Raymo *et al.*, 1990). Both studies recorded increases in surface temperature in the regions where ice was removed, although there was a smaller response for summer compared to winter. Raymo *et al.* (1990) found no significant changes in sea level pressure and zonal wind speeds, while Crowley *et al.* (1994) found a curious pattern of sea level pressure change, which was apparent as a wavelike feature over the Atlantic sector extending from pole to pole. However, Crowley *et al.* (1994) noted that this pattern may have originated from a numerical artifact associated with the removal of the Greenland Ice Sheet.

This chapter will assess the response of the Southern Hemisphere to the perturbation in terms of the zonally averaged results, the geographical distribution of the anomalies, the 500 hPa planetary waves and the twice-daily circulation. The results shown for each time period and/or experimental condition (i.e. control or perturbation) in this and subsequent chapters represents an average of the 3 respective replicate simulations. Statistical significance tests[1]

[1] The t tests have been used *without* the correction for serial autocorrelation (refer to chapter 3). The significance shading is primarily meant as an aid to highlight the important spatial patterns of change.

of the atmospheric response to the perturbation have been applied to the two-dimensional fields of surface temperature, 500 hPa level temperature, sea level pressure and 500 hPa geopotential heights. Not a lot of emphasis has been placed on statistical significance in the present study, rather, it is the patterns and direction of change which are important, such that the processes that might play a key role in the atmospheric response to reduced sea-ice cover can be identified. In addition, it is important to remember that a statistically significant result does not necessarily imply a climatologically significant result, and *vice versa*. The variables chosen for the statistical significance tests have been selected because they are the most robust of the variables from GCMs and are also the most closely examined variables in model validation and diagnostic studies. Furthermore, pressure and temperature fields represent an integration of a number of different forcings in the atmospheric system, thereby encompassing an integrated response, whereas other variables, such as humidity, largely represent individual processes. In terms of GCM derived precipitation, it is questionable whether it is valid to perform inferential statistics on the data. Precipitation data from GCMs are spatially and temporally interrupted and furthermore rely heavily on model parameterisations. The results of the inferential statistical tests which have been performed are meant as a guide in order to identify which anomalies are more important than others. Perhaps more meaningful than statistical significance is the agreement between the results in 1980 and 1985. Where there are consistent anomalies between the two years, one can have greater confidence that there is a real response to the sea-ice and SST perturbation.

This chapter will demonstrate that, in general, the sea-ice and SST perturbation in the summer season causes increased uplift and a decrease in pressures around Antarctica, together with an increase in the intensity of the subtropical high pressure belt and a slight southward extension of the descending limb of the Hadley Cell. These changes will be shown to result in an increase in 500 hPa wind speeds in middle to high latitudes and a decrease in the subtropics, as well as a general reduction in the amplitude of the 500 hPa planetary long waves. In addition, the perturbation appears to cause an increase in midlatitude cyclone densities at high latitudes (60°S - 70°S), with a decrease further north. It will also be shown that the atmospheric response is to some degree sensitive to the magnitude and positioning of the SST and sea-ice perturbation and that the examination of zonal averages can be misleading, since the introduced disturbances are not zonally orientated and the averages obscure anomalies which are longitude specific. In this chapter the results of the atmospheric cross sections and zonal averages will be presented, followed by the two-dimensional field results, and the changes to the 500 hPa planetary waves and twice-daily circulation.

6.2 Cross Sections

6.2.1 Temperature

In response to the sea-ice and SST anomalies there is an increase in surface temperatures, although very small, between about 40°S and 65°S in both years (Figure 6.1*c* and *f*). The increase between 60°S and 65°S is probably a direct response to reduced sea-ice limits, whereas the surface increases further north are due to the manipulation of SSTs. Since summer is the season of high insolation in the polar region, the mechanism producing the higher latitude surface temperature increase is likely to be the lower albedo in the perturbations due to less expansive sea-ice. For example, sea-ice covered with a thick layer

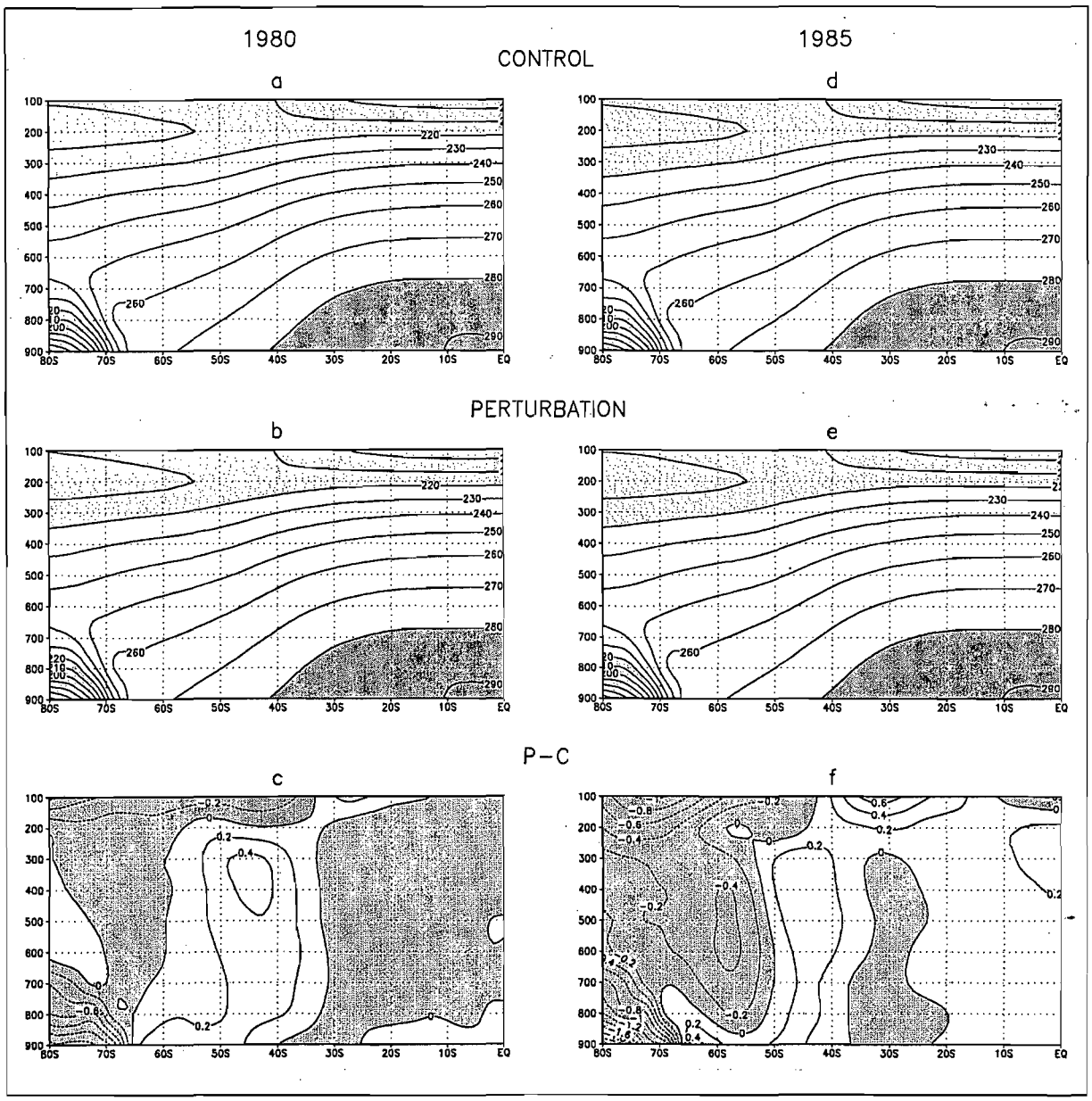

Figure 6.1 Vertical cross sections (y-axis denotes the pressure level in hPa) of the zonally averaged temperature (K) for the *a*) control and *b*) perturbation of 1980, and the *d*) control and *e*) perturbation of 1985. Temperatures in *a*, *b*, *d* and *e* which are greater than 280 K and less than 220 K have been shaded. Maps *c*) and *f*) show the plots of the perturbation field minus the control field for 1980 and 1985 respectively. Decreases in temperature have been shaded.

of snow has an albedo of about 80%, whereas the open ocean has an albedo of about 10% (Budd, 1991). The polar temperature increase for 1985 appears to be stronger than that of 1980, and is positioned slightly southward (Figure 6.1*c* and *f*). This can be related to differences in the perturbations and extent of sea-ice cover in the two years. Referral back to Chapter 5 (Figures 5.11, 5.12 and 5.15) shows firstly that the control sea-ice of 1985 is located further poleward (less expansive) than 1980 and hence the sea-ice and SST perturbations are located further poleward, and secondly, Figure 5.11 shows that the largest sea-ice perturbation imposed was for December 1984 (part of the "1985" summer) and perhaps this explains the slightly stronger temperature response in 1985. The high latitude surface warming in both years does not extend over the Antarctic continent, and in fact the response is that of surface cooling over the land (Figure 6.1*c* and *f*). Katabatic winds blowing off the plateau may have prevented the penetration of the warmer air over the Antarctic continent. It is important to note for all the cross sections presented in this section, that the 700 hPa surface actually intersects with much of the Antarctic plateau and therefore the results displayed in this region below 700 hPa level are likely to be fictitious.

It is clear from the results presented here that the temperature response to the sea-ice perturbation is small and may not be climatically significant. The atmosphere at high latitudes during summer is far less stable than during winter and this may account for a smaller temperature perturbation than expected from an examination of similar studies performed for the winter season. It is also important to remember, however, that zonal averages may be misleading and may underestimate the change, especially since the imposed perturbations in sea-ice and SSTs are azonal.

6.2.2 Vertical Velocity

As expected, during the summers of 1980 and 1985 the ascending limbs of the northern and southern Hadley cells are visible in the Southern Hemisphere, with maximum uplift for the southern cell positioned at about 12°S (Figure 6.2*a* and *d*). The region of maximum subsidence between the southern portion of the Hadley cell and the northern portion of the Ferrel cell is situated near 35°S, and the core of the ascending limb of the Ferrel cell occurs at about 55°S (Figure 6.2*a* and *d*). The patterns and magnitudes of vertical velocities are very similar for the two periods, although 1985 exhibits slightly stronger corresponding regions of ascent and subsidence than 1980, and these regions are situated slightly poleward in 1985 compared to 1980 (Figure 6.2*a* and *d*).

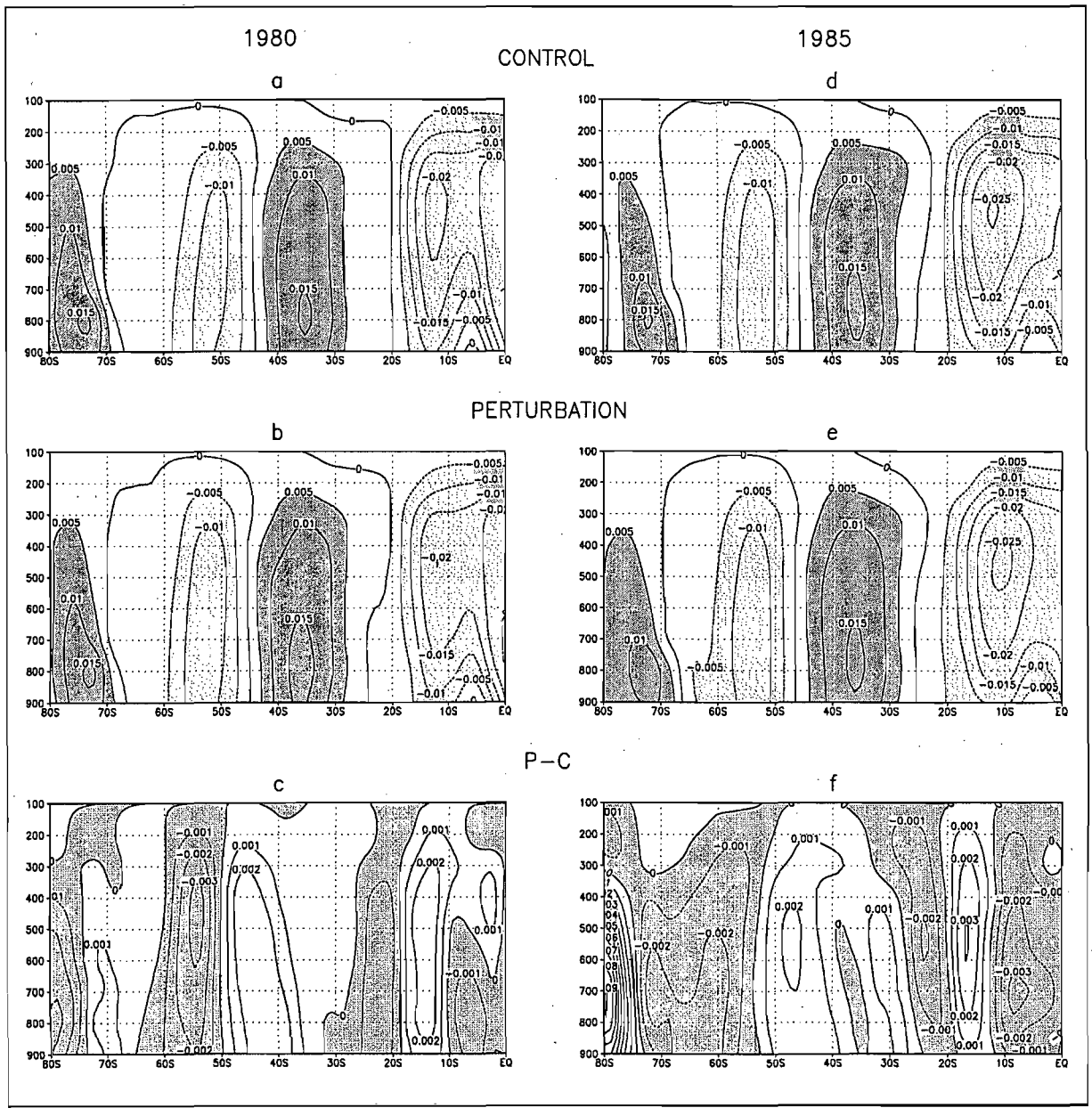

Figure 6.2 Vertical cross sections (y-axis denotes the pressure level in hPa) of the zonally averaged vertical velocities (Pa s^{-1}) for the *a*) control and *b*) perturbation of 1980, and the *d*) control and *e*) perturbation of 1985. Vertical velocities in *a*, *b*, *d* and *e* which are greater than 0.005 Pa s^{-1} and less than -0.005 Pa s^{-1} have been shaded. Maps *c*) and *f*) show the plots of the perturbation field minus the control field for 1980 and 1985 respectively. Decreases in vertical velocity have been shaded.

In response to the sea-ice perturbation, there appears to be an intensification and southward shift of the regions of ascent and subsidence between 30°S and 70°S for both 1980 and 1985 (Figure 6.2). As in the controls, the response during 1985 appears to be slightly south of that in 1980 (Figure 6.2*c* and *f*). In general for both years, there is increased ascent in the upward limb of the Hadley cell between 0° and 10°S (below the 500 hPa level) and a slight southward extension of the ascending limb of the southern Hadley cell, accounting for the region of increased uplift between 20°S and 25°S. There is increased subsidence between 40°S and 50°S which, judging from the control and perturbation plots (Figure 6.2), appears to be

related to a strengthening and southward extension of the descending limb of the Hadley cell. The ascending limb of the Ferrel cell strengthened in response to sea-ice perturbation for both years, although this strengthening extends further south during 1985 compared to 1980, which arguably produces the contrasting results south of 65°S in the two years.

These results can be related to the temperature response shown in the previous section. The near-surface temperature change induced by the sea-ice perturbation is greatest at about 57°S in 1980 and at 63°S in 1985, and is larger for 1985 (Figure 6.1). Similarly, the increased uplift in the Ferrel cell is centred at about 55°S in 1980 and at 65°S in 1985, and is more expansive in 1985. It is suggested that with the exposure of warmer surfaces, due to the sea-ice reduction and SST manipulation south of about 50°S (refer to Figures 5.11 and 5.15 showing the sea-ice and SST perturbations), there is a modification of surface fluxes or change in baroclinicity such that increased uplift is favoured. It is likely that it is this increased ascent that is driving the other anomalies of vertical velocity shown on Figure 6.2, producing alternating bands of ascent and descent. When this rising air in the region of 60°S reaches the tropospause, it diverges and some moves southward and some northward. The air that is moving northwards would eventually become impeded by air moving poleward in the upward branch of the Hadley cell and would thus subside, producing the increased subsidence that is seen between 40°S and 50°S and contributing to a southward extension of the general region of subsidence (Figure 6.2). On the other hand, the air that moves southwards in the upper atmosphere from the region of increased ascent, probably causes increased subsidence in the adjacent latitudes (around 70°S in 1980 and 80°S in 1985) due to the air being radiationally cooled and becoming denser as it moves towards the pole.

Lastly, the changes in vertical velocities can aid further explanation of the resulting pattern of temperature anomalies seen previously. The increase in temperature which extends into the upper atmosphere in the region of about 45°S in both years (Figure 6.1*b* and *d*) corresponds to the zone of increased subsidence (Figure 6.2*c* and *f*). Thus, the temperature change appears to be a response to an increase in adiabatic warming. Similarly, the high latitude temperature increase (Figure 6.1*b* and *d*), obtained in response to the sea-ice removal, does not extend into the upper atmosphere, especially in 1985 where temperatures above the 800 hPa level are actually seen to decrease (55°S - 65°S). This may be a result of increased uplift (Figure 6.2*c* and *f*) causing increased adiabatic cooling.

6.2.3 Zonal Wind

As expected for summer, the zonal westerlies are strongest near the 200 hPa level at about 45°S in both 1980 and 1985 (Figure 6.3*a* and *d*). As with observed data, this subtropical jet is located above the descending limb of the Hadley cell in both years (Figures 6.2 and 6.3). The tropical and polar easterlies are also clearly evident below the 500 hPa level in the control simulations (Figure 6.3*a* and *d*). The 1985 wind field north of 60°S is situated slightly poleward of the 1980 field, as was shown with the vertical velocity field.

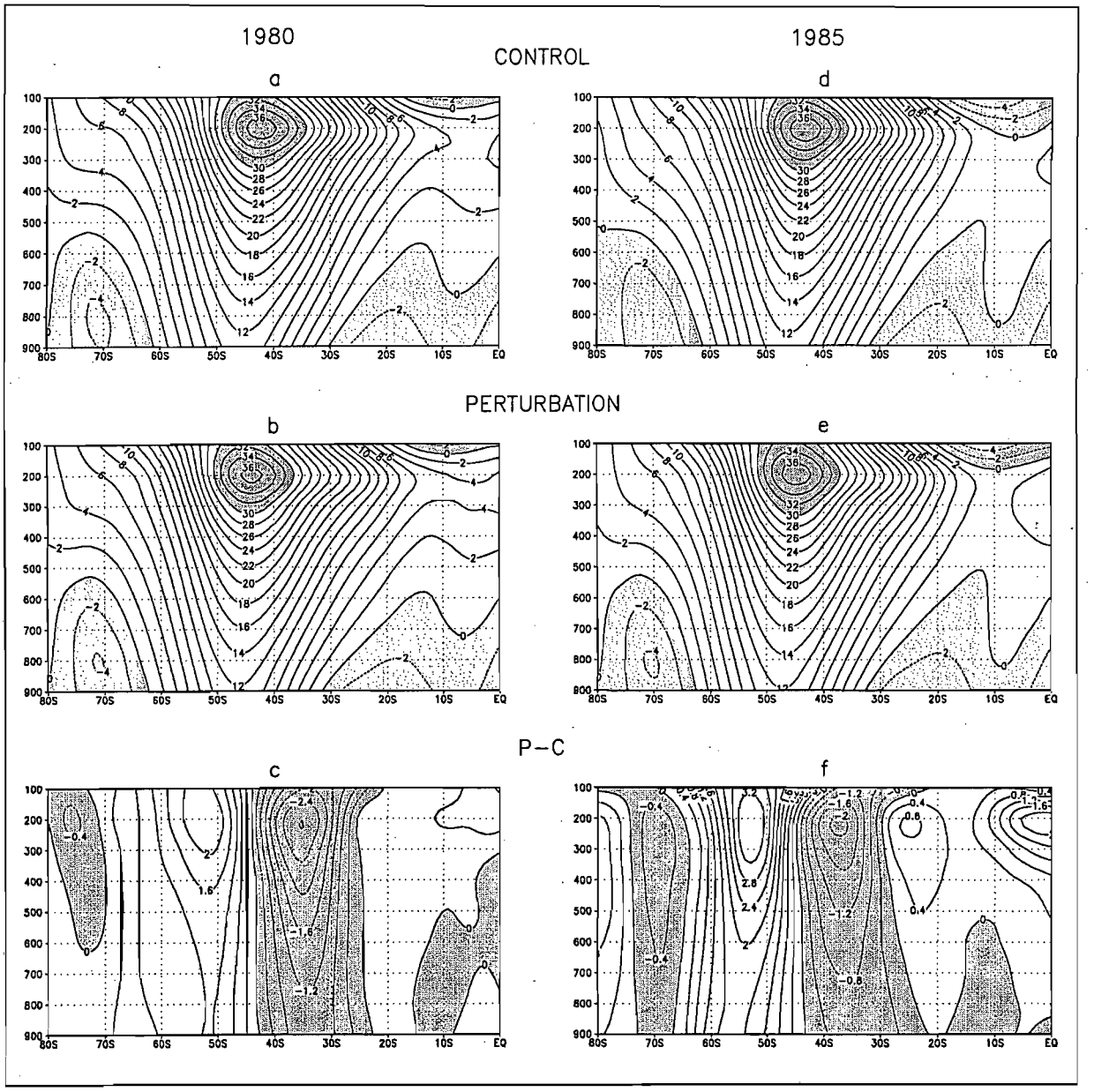

Figure 6.3 Vertical cross sections (y-axis denotes the pressure level in hPa) of the zonally averaged u-component of the wind speed (m s^{-1}) for the *a*) control and *b*) perturbation of 1980, and the *d*) control and *e*) perturbation of 1985. Wind speeds in *a*, *b*, *d* and *e* which are greater than 30 m s^{-1} and less than 0 m s^{-1} (i.e. easterlies) have been shaded. Maps *c*) and *f*) show the plots of the perturbation field minus the control field for 1980 and 1985 respectively. Decreases in wind speed have been shaded.

In response to the SST and sea-ice perturbation in both years, there is an increase in wind speeds in the midlatitudes (45°S - 65°S) and a decrease in the westerly flow in the subtropics (30°S - 40°S) throughout the troposphere (Figure 6.3*c* and *f*). The greatest changes are found at the 200 hPa level and the transition between the increase and decrease in wind speeds occurs at about 45°S, where the subtropical jet is located in the control data. This suggests that there has been a southward shift of the subtropical jet and westerly wind belt and can be seen by careful examination of the control and perturbation plots (Figure 6.3). For example, in 1980 the 10 m s^{-1} contour line intersects the 900 hPa level slightly north of 50°S, whereas in the perturbation it is situated just south of 50°S. This southward shift of the jet stream is in agreement with the southward extension of the descending limb of the Hadley cell that was observed for the vertical velocity fields in both years. A slight southward extension of tropical easterlies near the surface is also evident from the control and perturbation plots in both years (Figure 6.3).

6.2.4 Specific Humidity

The magnitude of the specific humidity anomalies produced in response to the sea-ice perturbation are very small (Figure 6.4), but nonetheless the pattern of change is interesting. The response for 1980 (Figure 6.4*c*) reveals a pattern which is almost an exact inverse of the pattern of change recorded for the vertical velocities (Figure 6.2*c*). This suggests that on a large-scale, where there is increased subsidence there is a drying of the atmospheric column, and where there is increased uplift the atmospheric humidity increases. This inverse pattern is not as clear for 1985, but the general relationship can still be observed. Both years exhibit a clear increase in low level specific humidity at high latitudes (~50°-60°S for 1980 and ~60°-70°S for 1985) (Figure 6.4*c* and *f*). This may be due to the exposure of the ocean surface which was covered by ice in the control simulations and therefore the addition of a potential moisture source. Most of the changes in specific humidity are found below the 500 hPa level.

Viewing the atmosphere from a zonally averaged perspective can be useful for highlighting the broad prominent patterns of change, but it may also hide changes that occur on a longitudinal basis. The following section also focuses on zonal averages of certain variables, but the averaging has been performed over longitudinal sectors in order to aid interpretation and emphasize longitudinally specific responses.

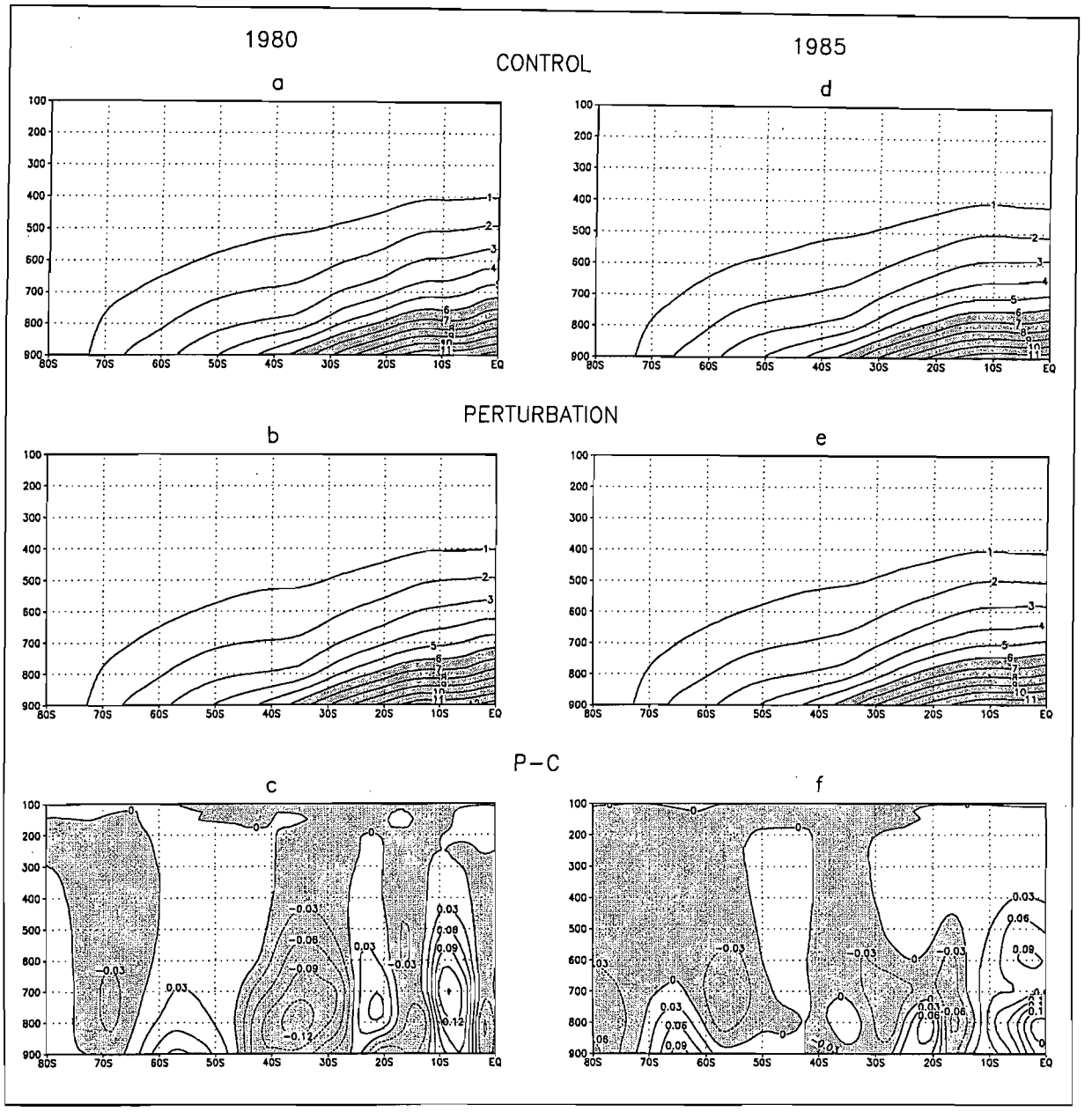

Figure 6.4 Vertical cross sections (y-axis denotes the pressure level in hPa) of the zonally averaged specific humidity (g kg^{-1}) for the *a*) control and *b*) perturbation of 1980, and the *d*) control and *e*) perturbation of 1985. Humidities in *a*, *b*, *d* and *e* which are greater than 6 g kg^{-1} have been shaded. Maps *c*) and *f*) show the plots of the perturbation field minus the control field for 1980 and 1985 respectively. Decreases in specific humidity have been shaded.

6.3 Zonal Averages

The zonal averaging has been performed over 6 regions: the entire hemisphere (i.e. across all longitudes), the Weddell Sea (60°W to 0°), the western Indian (0° to 90°E), the eastern Indian (90°E to 160°E), the Ross Sea (160°E to 130°W) and the eastern Pacific (Amundsen and Bellingshausen Seas) (130°W to 60°W). The 5 longitudinal sectors, shown in Figure 6.5, correspond to those used by Carleton (1989) in a study of Antarctic sea-ice extent relationships with low frequency atmospheric variations, and are very similar (apart from a

slightly larger Weddell Sea sector and smaller western Indian sector) to those defined by Zwally *et al.* (1983) in a study of satellite observations of Antarctic sea-ice.

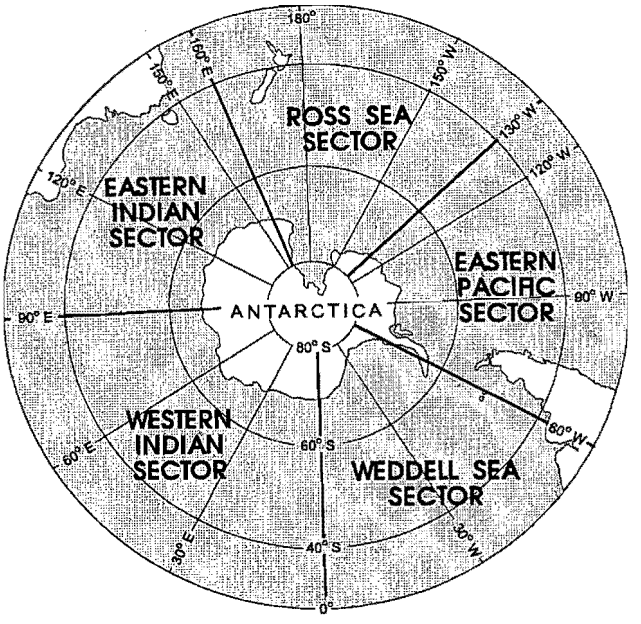

Figure 6.5 A map showing the 5 longitudinal sectors over which the zonal averages have been calculated.

As mentioned in Chapter 5, for each of the summer periods there are three replicate control simulations and three replicate perturbation simulations. On the zonal plots presented in this section, the average seasonal anomaly (perturbation minus control) and the standard deviation are presented. This is determined by calculating the anomaly for each possible perturbation and control pair, i.e. n=9.

6.3.1 Surface Air Temperature

The three control simulations for 1980, and also for 1985, yield virtually identical profiles of seasonally averaged surface temperatures (Figures 6.6*a* and 6.7*a*). The lack of variability between replicates is obviously because for each year identical SSTs are prescribed, i.e. the boundary conditions are the same for each replicate, and this has a direct effect on the surface air temperature.

In response to the sea-ice perturbation there is an increase in surface temperature between 45°S and 70°S in all the sectors for both years (Figures 6.6 and 6.7). The average for all longitudes (Figures 6.6*g* and 6.7*g*) shows a maximum warming of about 0.5 K, near 58°S in 1980, and near 61°S in 1985. In both years, the peak response in the western Indian and Weddell Sea sectors is situated further north, positioned at about 56°S, compared to the other three sectors whose maxima are situated near 62°S (Figures 6.6 and 6.7). This is to be

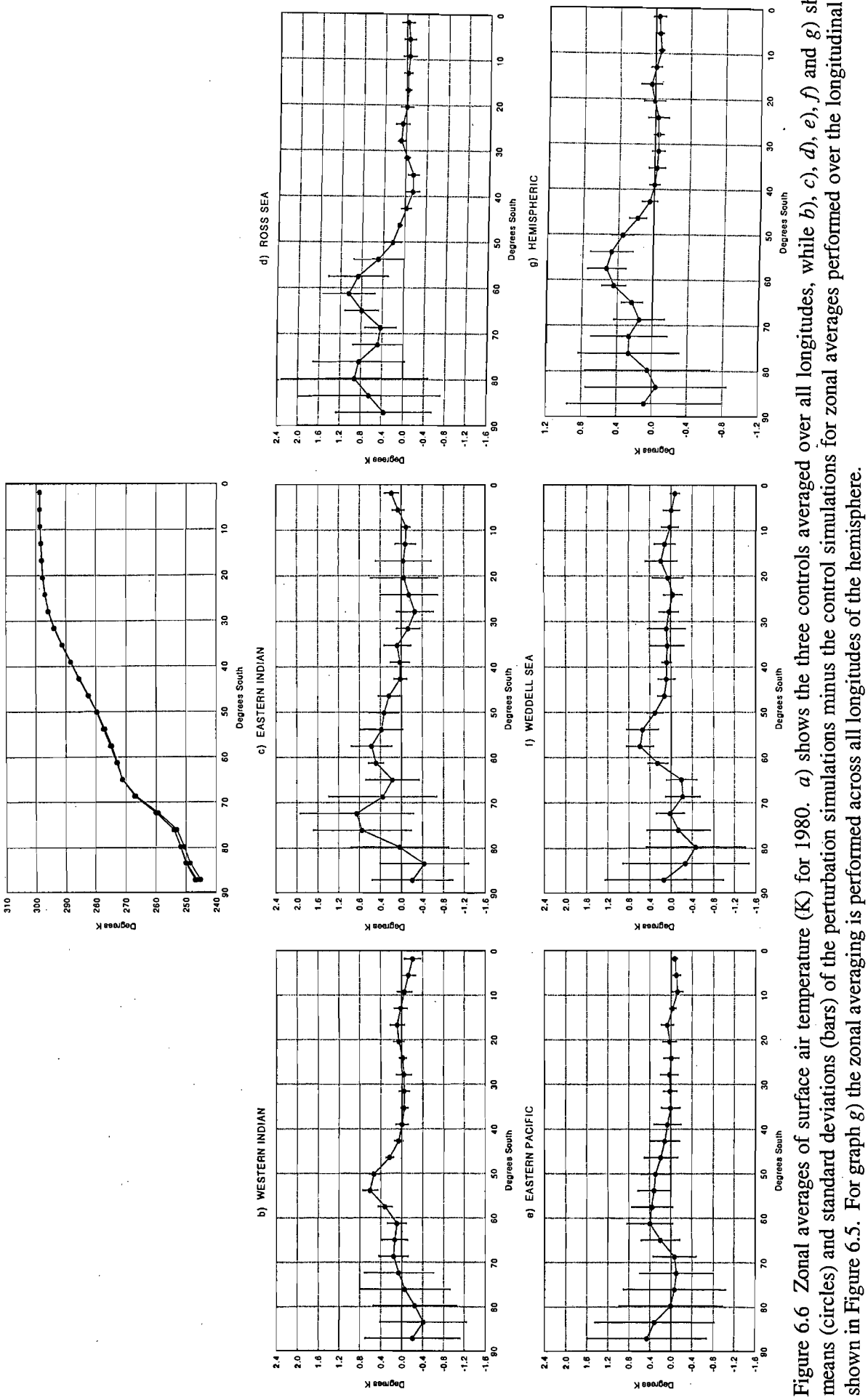

Figure 6.6 Zonal averages of surface air temperature (K) for 1980. *a)* shows the three controls averaged over all longitudes, while *b), c), d), e), f)* and *g)* show the means (circles) and standard deviations (bars) of the perturbation simulations minus the control simulations for zonal averages performed over the longitudinal sectors shown in Figure 6.5. For graph *g)* the zonal averaging is performed across all longitudes of the hemisphere.

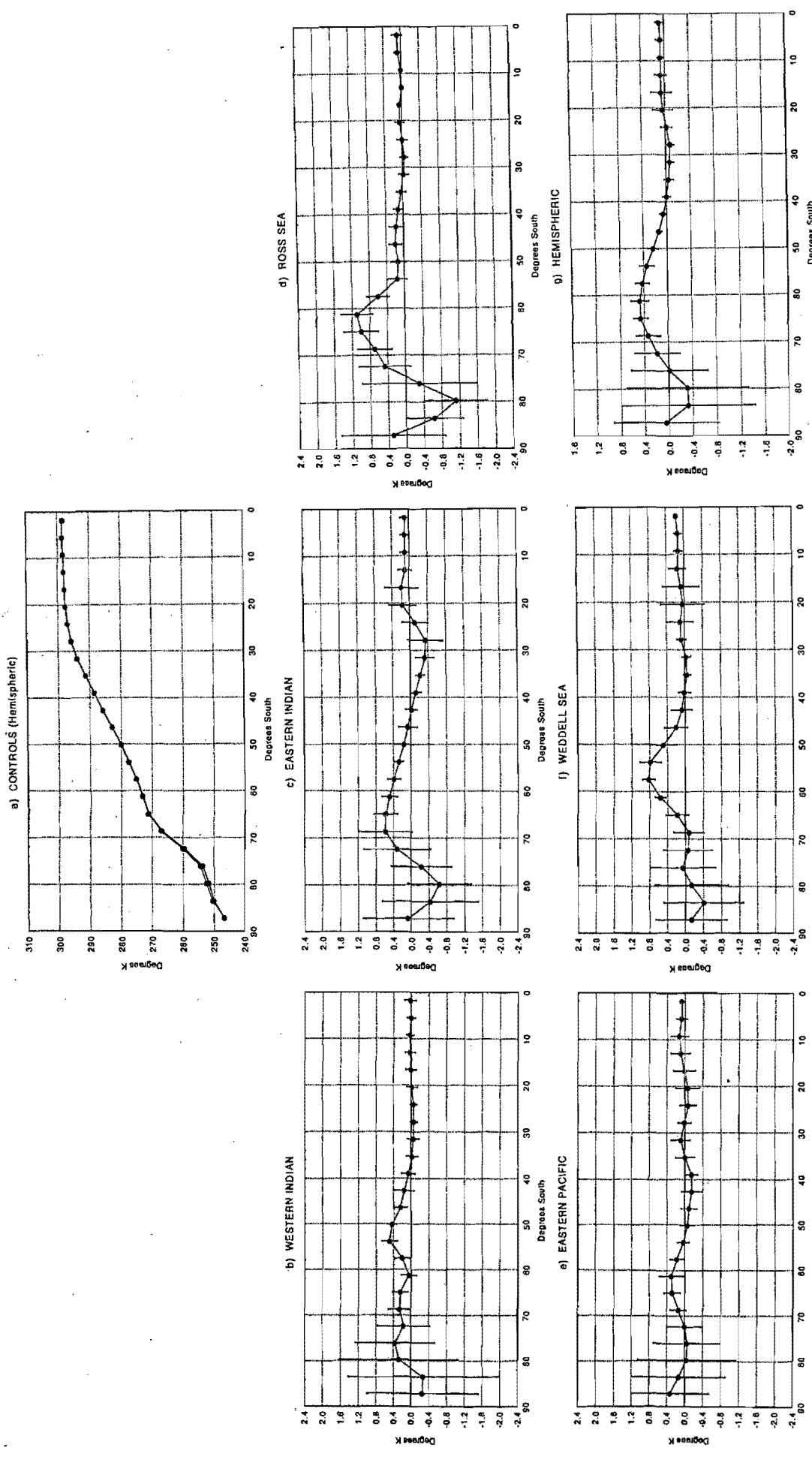

Figure 6.7 Zonal averages of surface air temperature (K) for 1985. *a)* shows the three controls averaged over all longitudes, while *b), c), d), e), f)* and *g)* show the means (circles) and standard deviations (bars) of the perturbation simulations minus the control simulations for zonal averages performed over the longitudinal sectors shown in Figure 6.5. For graph *g)* the zonal averaging is performed across all longitudes of the hemisphere.

expected, since sea-ice extends further north in the western Indian and Weddell Sea sectors compared to the other sectors and thus the perturbations also occur further equatorward than in the other sectors (refer to Figures 5.11, 5.12 and 5.15). The smallest changes are recorded in the eastern Pacific sector, since the perturbations in this region are minor (Figures 5.11 and 5.15).

6.3.2 Sensible Heat Flux

The plots of the three controls in 1980 (Figure 6.8*a*) and 1985 (Figure 6.9*a*) show that the seasonally averaged sensible heat flux is directed upwards for all Southern Hemisphere latitudes, except over the Antarctic continent where a temperature inversion exists and the flux is directed downwards. It is hypothesised, based on observations and modelling studies investigating reductions in *winter* sea-ice extent, that the increase in surface temperature produced by the experiments should produce an increase in turbulent fluxes of sensible heat.

Although an increase in the surface sensible heat flux can be seen in some of the sectors in the region of the ice perturbation, it is clear that in both years the change produced by the experiments is very small (Figures 6.8 and 6.9). Furthermore, in most cases the standard deviations are large, and the sign of the anomaly in the different sectors is not always consistent between the two years. Many of the plotted changes are therefore likely to be representing natural variability rather than a direct response to the sea-ice perturbation. This is not a particularly surprising result, as summer is the season of high insolation in the polar regions and the small perturbation introduced is unlikely to produce as significant results as one might expect for the winter season. In addition, compared to winter, summer is characterised by greater instability of the atmosphere at high latitudes, therefore in winter where anomalous surface heating may be trapped by the strong polar inversion, in summer it is more likely to be dispersed and the surface temperature change diminished. Changes in stability, wind speed and advection due to the perturbation would also complicate the results and perhaps obscure the initial response.

6.3.3 Latent Heat Flux

The latent heat flux increases from a minimum in the polar region to a maximum of about 130 W m^{-2} near 15°S, where strong surface heating and convection promote evaporation (Figures 6.10*a* and 6.11*a*). As for the sensible heat flux, the change in the surface latent heat flux in response to the sea-ice and SST perturbation is generally small and not always consistent between the two years for corresponding sectors (Figures 6.10 and 6.11).

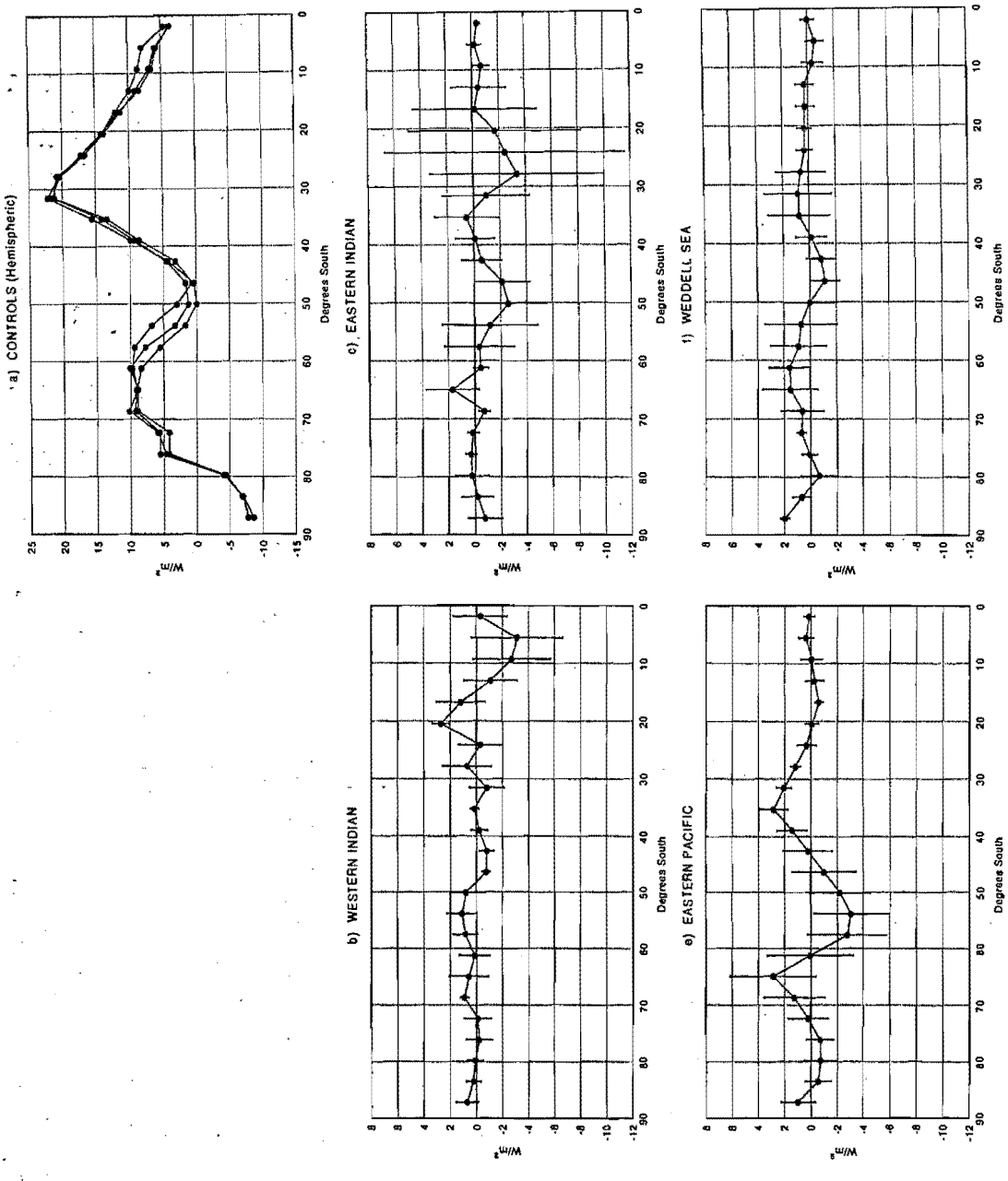

Figure 6.8 Zonal averages of the surface sensible heat flux (W/m^2) for 1980. *a)* shows the three controls averaged over all longitudes, while *b), c), d), e), f)* and *g)* show the means (circles) and standard deviations (bars) of the perturbation simulations minus the control simulations for zonal averages performed over the longitudinal sectors shown in Figure 6.5. For graph *g)* the zonal averaging is performed across all longitudes of the hemisphere.

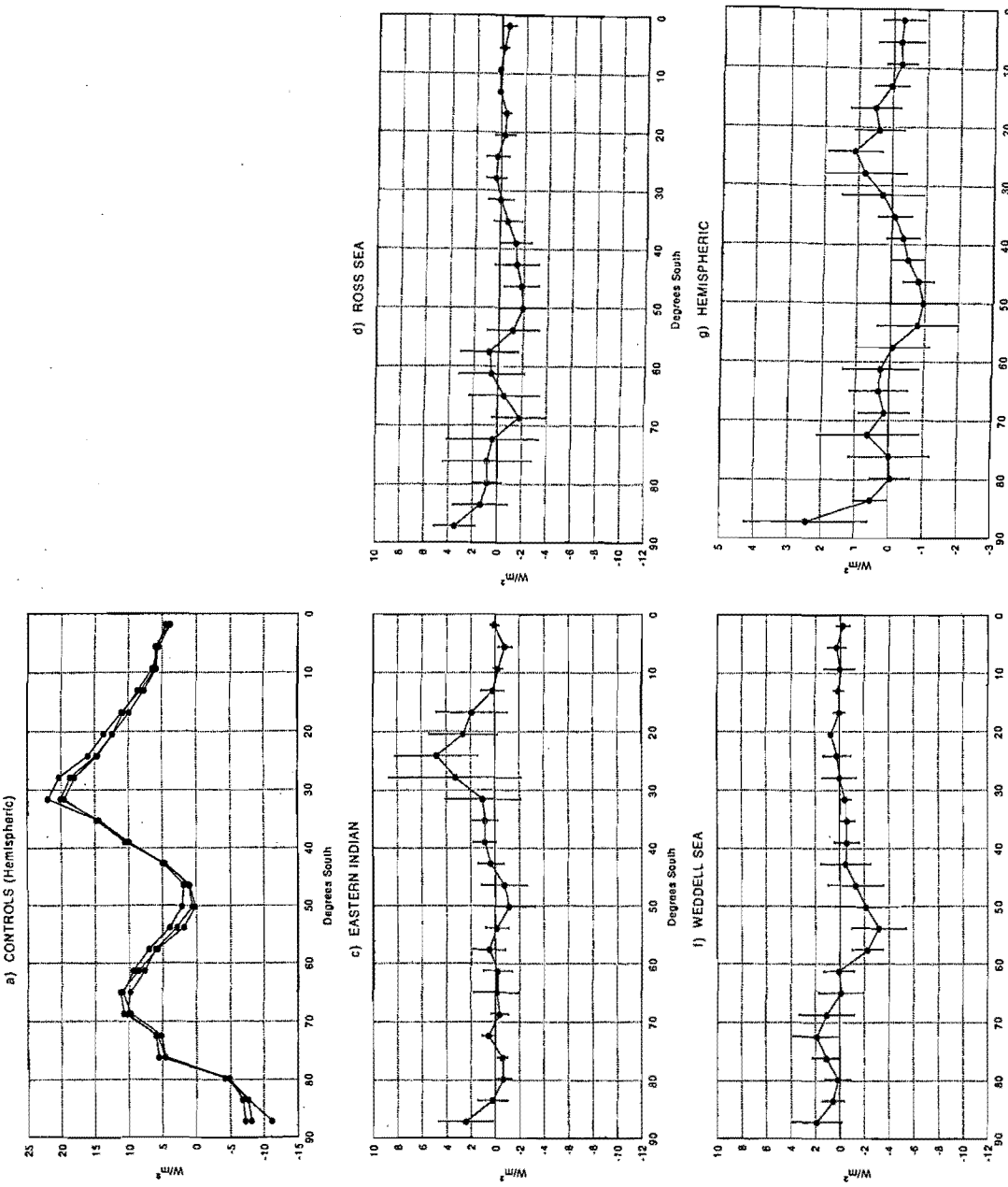

Figure 6.9 Zonal averages of the surface sensible heat flux (W/m^2) for 1985. *a)* shows the three controls averaged over all longitudes, while *b), c), d), e), f)* and *g)* show the means (circles) and standard deviations (bars) of the perturbation simulations minus the control simulations for zonal averages performed over the longitudinal sectors shown in Figure 6.5. For graph *g)* the zonal averaging is performed across all longitudes of the hemisphere.

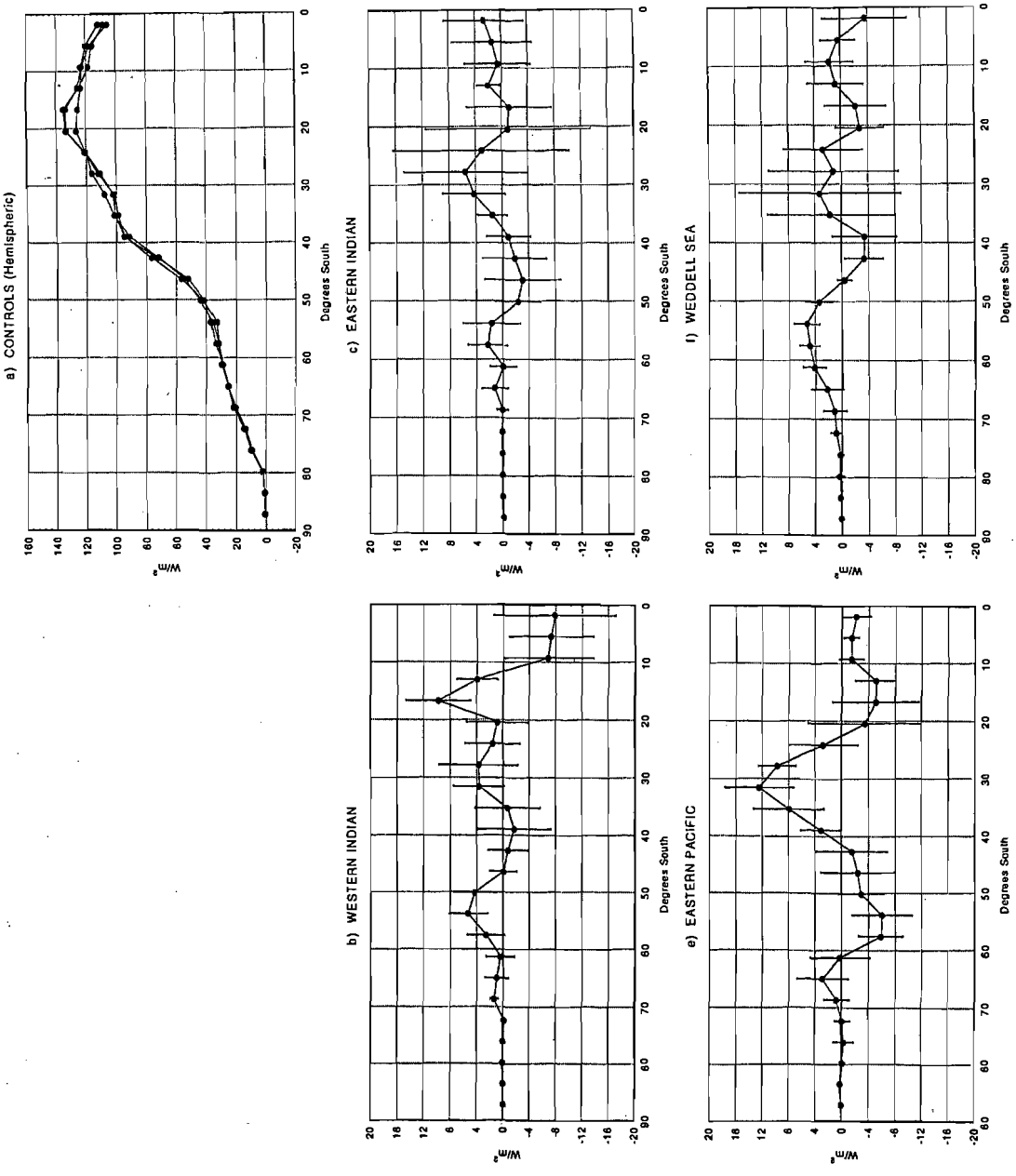

Figure 6.10 Zonal averages of the surface latent heat flux (W/m^2) for 1980. *a)* shows the three controls averaged over all longitudes, while *b), c), d), e), f)* and *g)* show the means (circles) and standard deviations (bars) of the perturbation simulations minus the control simulations for zonal averages performed over the longitudinal sectors shown in Figure 6.5. For graph *g)* the zonal averaging is performed across all longitudes of the hemisphere.

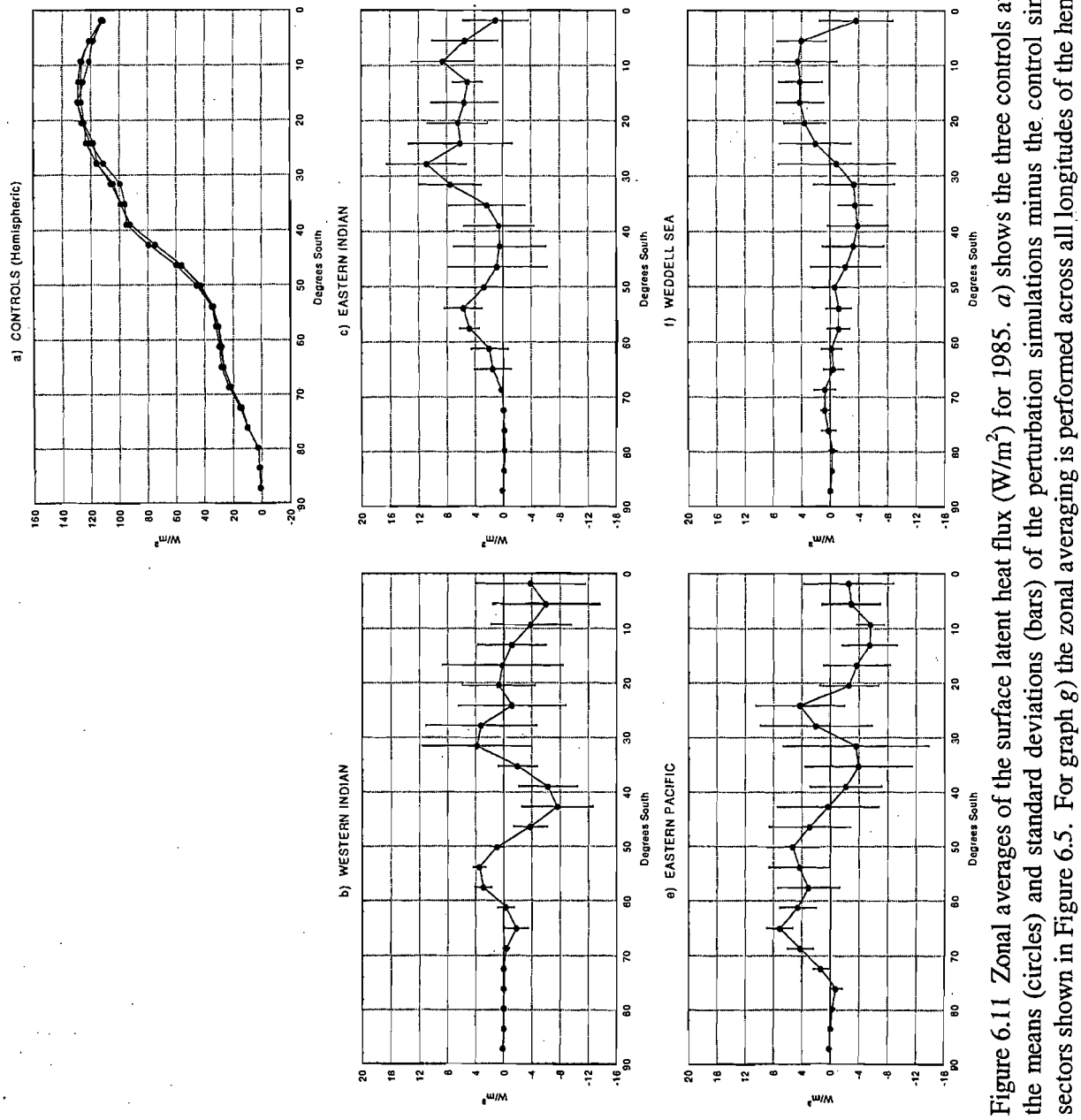

Figure 6.11 Zonal averages of the surface latent heat flux (W/m^2) for 1985. *a)* shows the three controls averaged over all longitudes, while *b), c), d), e), f)* and *g)* show the means (circles) and standard deviations (bars) of the perturbation simulations minus the control simulations for zonal averages performed over the longitudinal sectors shown in Figure 6.5. For graph *g)* the zonal averaging is performed across all longitudes of the hemisphere.

However, the hemispherically averaged latitudinal profile shows a very similar pattern of change for both years (Figures 6.10*g* and 6.11*g*). Perhaps the most significant of these changes is the increase in latent heat flux between 50°S and 75°S. Sea-ice cover inhibits the transfer of moisture to the atmosphere, thus with a reduction in sea-ice extent one would expect an increase in the latent heat flux. The changes in sea-ice cover and the manipulation of SSTs produce an increase in surface temperatures which raises the saturated vapour pressure at the surface and causes an increase in evaporation. With a larger sea-ice perturbation, one might expect to see a larger surface temperature change and thus a greater modification of the surface heat fluxes.

6.3.4 Sea Level Pressure

As is seen from the controls for each year, there is a large degree of variability in sea level pressure between the replicates south of 60°S (Figures 6.12*a* and 6.13*a*) and thus there are large standard deviations in the anomalies for all the sectors in this region. Although the standard deviations are large, there is a common response in virtually all the sectors and in both years and this suggests that there is a real sea level pressure response to the sea-ice and SST perturbation. Slight differences between replicates in the positioning of sea level pressure features can cause large increases in the standard deviations of the response, especially since there are only 9 observations. The profiles suggest that there is a reduction in sea level pressure south of 55°S and an increase in pressure between 30°S and 50°S (Figures 6.12 and 6.13). This agrees well with the changes in vertical velocities that were shown in Figure 6.2, where there was increased uplift in the ascending limb of the Ferrel cell (near 60°S) and increased subsidence between 35°S and 50°S.

6.3.5 500 hPa Wind

As for sea level pressure, there is a fair degree of variability between the replicate controls for the 500 hPa wind speed in both years (Figures 6.14*a* and 6.15*a*). Wind speeds peak near 45°S in both years, with a maximum of about 23 m s^{-1}.

Overall, the standard deviations of the wind speed anomalies are large, but a clear pattern of change emerges in most sectors and for both years, where the dominant response is an increase in wind speeds in the midlatitudes (45°S - 60°S) and a decrease in wind speeds in the subtropics (30°S - 45°S) (Figures 6.14*g* and 6.15*g*). This corresponds to the earlier suggestion of a southward shift of the subtropical jet stream. This change is, however, shifted

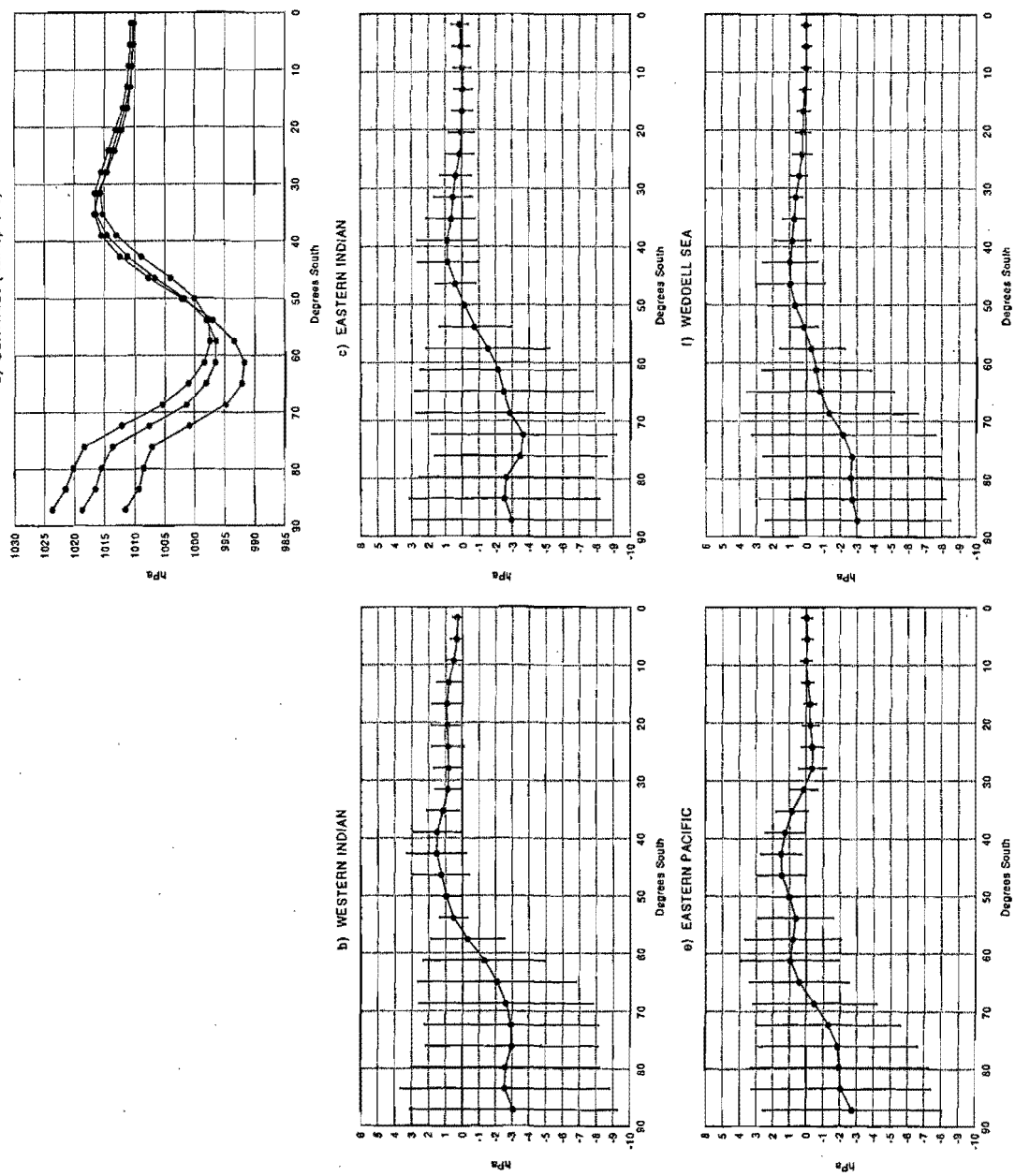

Figure 6.12 Zonal averages of sea level pressure (hPa) for 1980. *a*) shows the three controls averaged over all longitudes, while *b*), *c*), *d*), *e*), *f*) and *g*) show the means (circles) and standard deviations (bars) of the perturbation simulations minus the control simulations for zonal averages performed over the longitudinal sectors shown in Figure 6.5. For graph *g*) the zonal averaging is performed across all longitudes of the hemisphere.

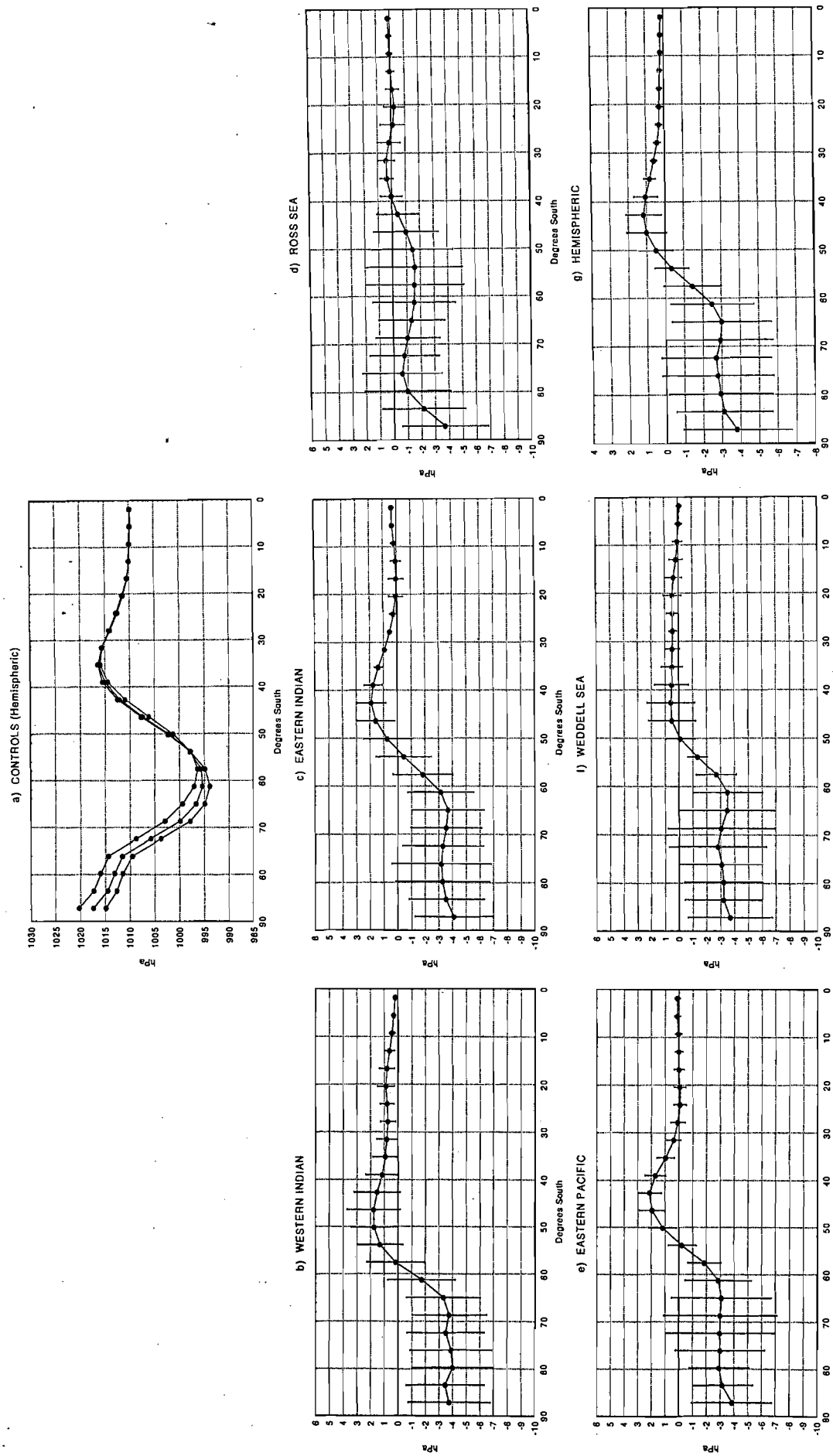

Figure 6.13 Zonal averages of sea level pressure (hPa) for 1985. *a)* shows the three controls averaged over all longitudes, while *b), c), d), e), f)* and *g)* show the means (circles) and standard deviations (bars) of the perturbation simulations minus the control simulations for zonal averages performed over the longitudinal sectors shown in Figure 6.5. For graph *g)* the zonal averaging is performed across all longitudes of the hemisphere.

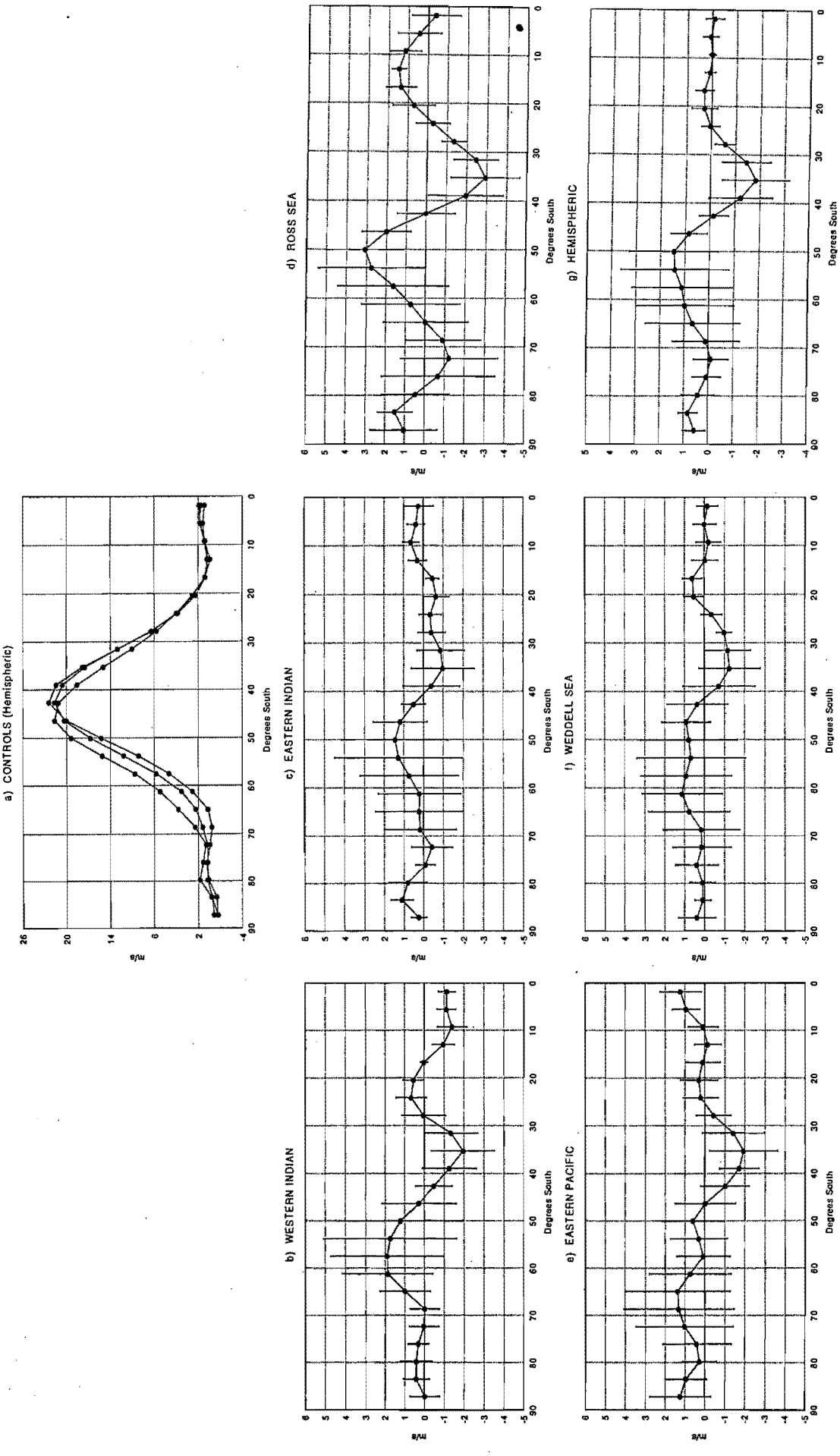

Figure 6.14 Zonal averages of the u-component of the 500 hPa wind speed (m/s) for 1980. *a)* shows the three controls averaged over all longitudes, while *b), c), d), e), f)* and *g)* show the means (circles) and standard deviations (bars) of the perturbation simulations minus the control simulations for zonal averages performed over the longitudinal sectors shown in Figure 6.5. For graph *g)* the zonal averaging is performed across all longitudes of the hemisphere.

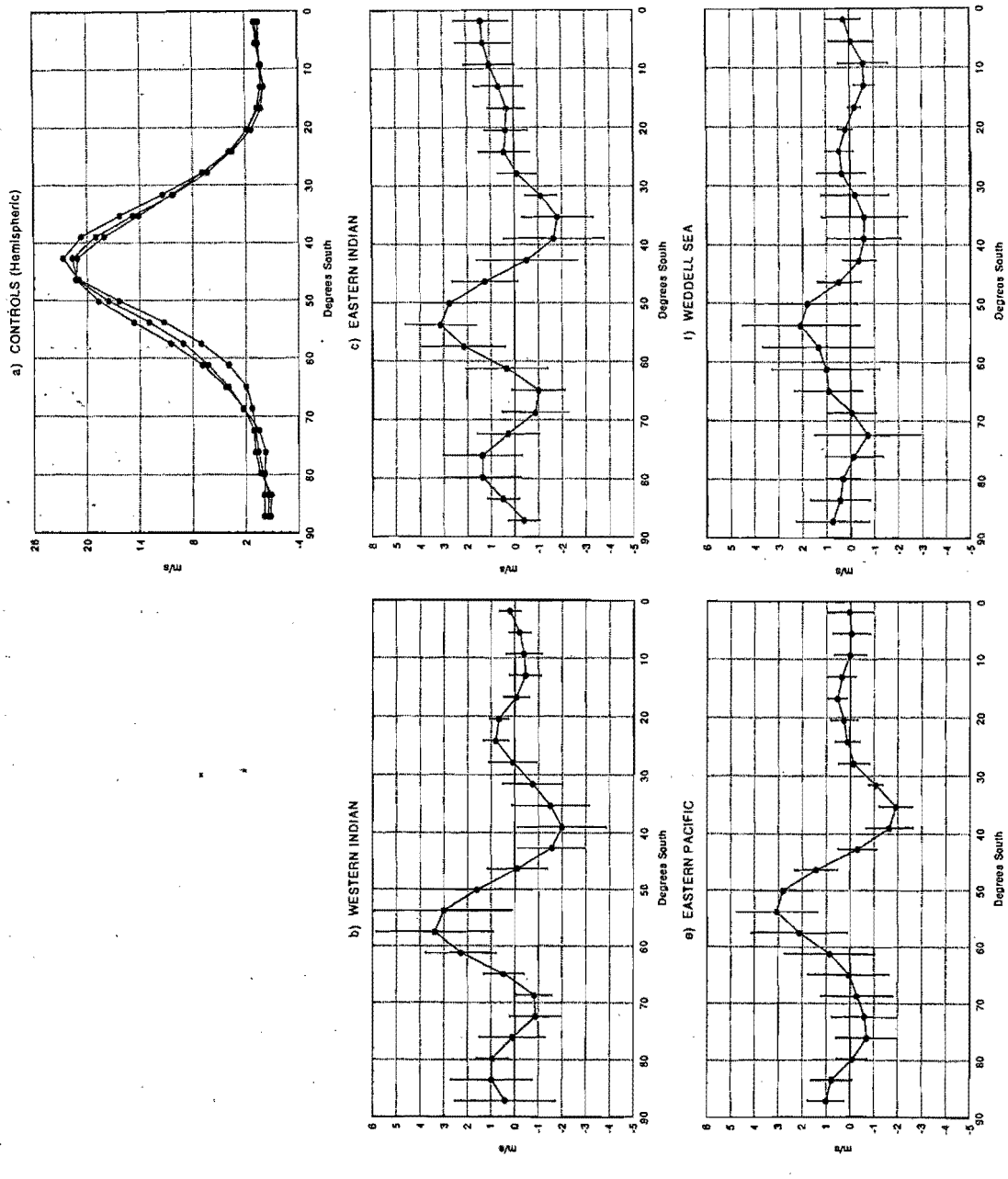

Figure 6.15 Zonal averages of the u-component of the 500 hPa wind speed (m/s) for 1985. *a*) shows the three controls averaged over all longitudes, while *b*), *c*), *d*), *e*), *f*) and *g*) show the means (circles) and standard deviations (bars) of the perturbation simulations minus the control simulations for zonal averages performed over the longitudinal sectors shown in Figure 6.5. For graph *g*) the zonal averaging is performed across all longitudes of the hemisphere.

latitudinally by varying degrees depending on the sector concerned. For example, in 1985 the midlatitude increase in wind speed peaks at about 55°S in the eastern Indian sector (Figure 6.15*c*), whereas in the Ross Sea sector it peaks closer to 45°S (Figure 6.15*d*). This highlights the azonal nature of the response and may contribute to some of the large error bars *within* each sector and to differences that are observed between 1980 and 1985. The wind speed changes are more distinct for 1985 compared to 1980.

6.4 Two-Dimensional Field Response

The cross sections and zonal averages shown above have painted a broad picture of the possible changes that occurred in response to the sea-ice and SST perturbations. However, as mentioned previously, these averages obscure changes of a regional nature and in certain cases may be misleading since the introduced disturbances are not zonally orientated. It is thus expedient to investigate the two-dimensional Southern Hemisphere field response to the perturbation. This will be presented under four headings dealing with the changes to temperature and pressure fields, the 500 hPa wind field, midlatitude cyclones and storm tracks, and atmospheric moisture.

6.4.1 Temperature and Pressure

As expected, the surface air temperature response south of 50°S (Figure 6.16*b* and *d*) largely mirrors the imposed change in SSTs (Figure 5.15), with greatest increases recorded north of the Ross Sea (up to about 1.5 K) and north and north-east of the Weddell Sea (about 0.9 K) in both years (Figure 6.16*b* and *d*). As with the SST perturbations, the surface temperature increase in these two regions is situated slightly more poleward in 1985 compared to 1980. Furthermore, the temperature increase for the Ross and Weddell Sea regions in 1985 is shifted slightly west compared to 1980. These small differences between the two years are related to differences in the magnitude and positioning of the imposed sea-ice and SST anomalies (Figure 5.11, 5.12 and 5.15). For example, if one focuses on the Weddell Sea sector, it is clear from Figure 5.15 that the SST perturbation in this sector is closer to the pole for 1985 and is also larger directly north of the Sea than it is for 1980.

These regions of temperature increase (Figure 6.16*b* and *d*) are associated with regions of significant sea level pressure decrease around Antarctica in both years (Figure 6.17*b* and *d*), such that the largest falls in pressure generally coincide with the greatest increases in diabatic heating. The decreases in pressure are largest over the Weddell Sea, south Indian and Ross

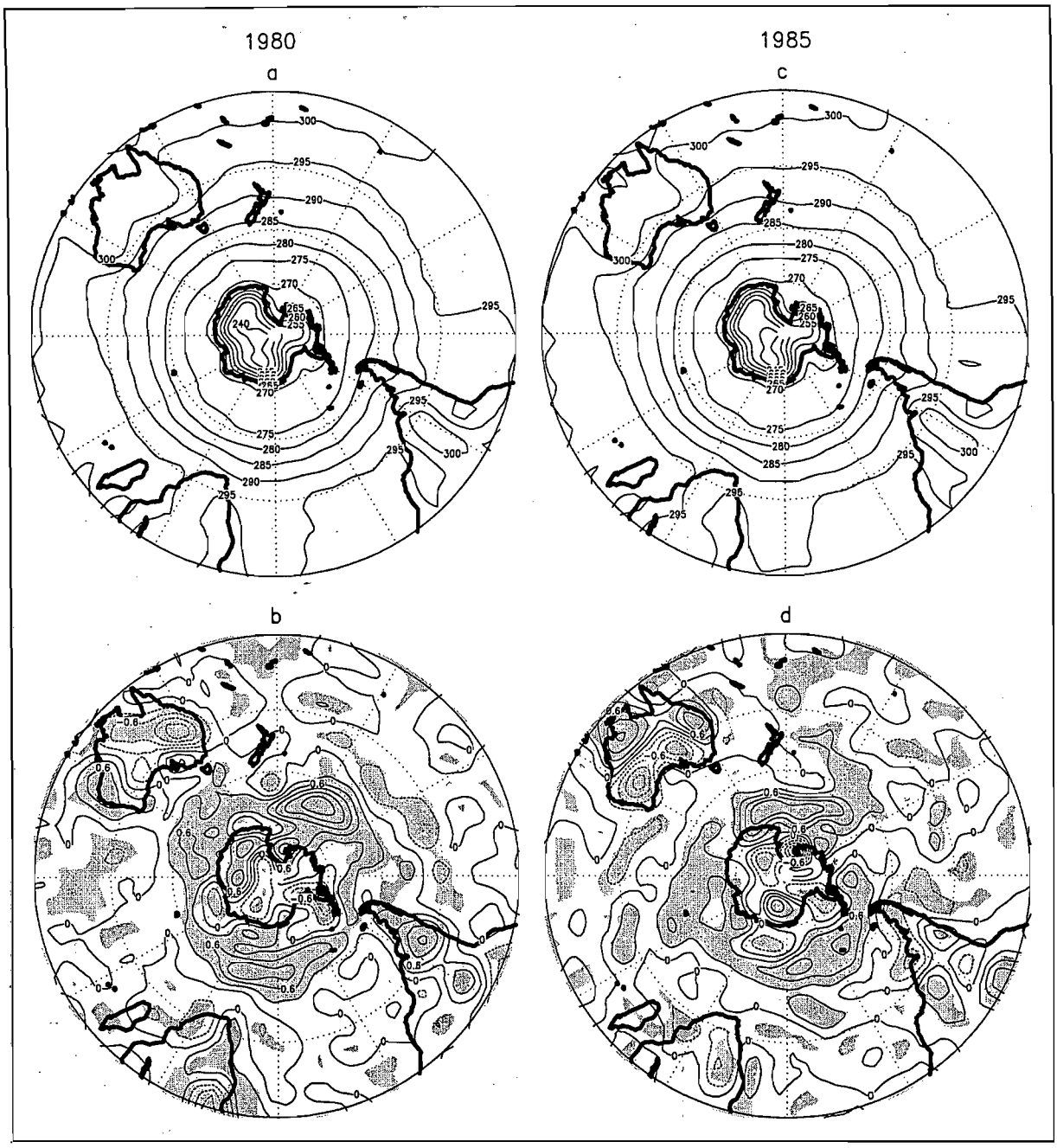

Figure 6.16 Surface temperature (K) for the controls of *a*) 1980 and *c*) 1985, and the perturbations minus the controls for *b*) 1980 and *d*) 1985. Statistically significant differences at the 95% confidence level have been shaded. Negative anomalies in *b*) and *d*) are depicted as dotted contours.

Sea sectors (Figure 6.17), where the introduced anomalies in sea-ice extent and SSTs are largest, and gives rise to a 3-wave pattern of change, especially for 1980. As mentioned previously, the temperature increase for the Ross and Weddell Sea regions in 1985 is shifted slightly west compared to 1980. A similar difference between the two years is evident in the sea level pressure anomalies. For example, in 1985 there appears to be a larger increase in surface temperature in the region between South America and the Antarctic Peninsula, and slightly west and east of this area compared to 1980 (Figure 6.16). Similarly, the zone of sea level pressure decrease in the Weddell Sea sector extends westwards past the Antarctic Peninsula in 1985, whereas it does not extend past the peninsula in 1980 (Figure 6.17). It

thus appears that some of the observed differences in the positioning of the sea level pressure anomalies may be related to differences in the positioning and size of the imposed perturbations in the two years.

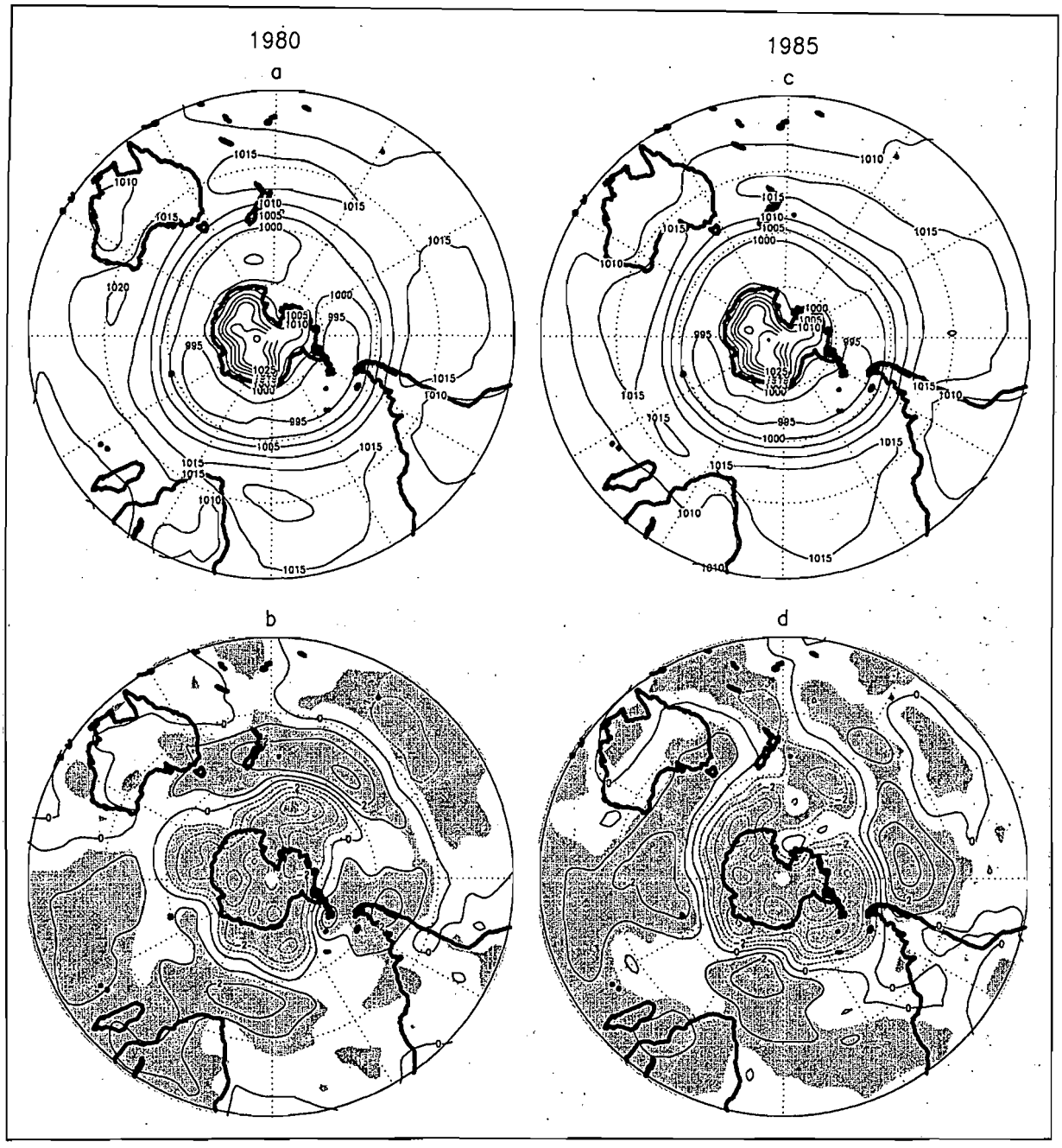

Figure 6.17 Sea level pressure (hPa) for the controls of *a*) 1980 and *c*) 1985, and the perturbations minus the controls for *b*) 1980 and *d*) 1985. Statistically significant differences at the 95% confidence level have been shaded. Negative anomalies in *b*) and *d*) are depicted as dotted contours.

The general surface temperature increase south of 50°S does not extend to the 500 hPa level, and in fact in both years there are areas of significant reductions in upper air temperature around Antarctica (Figure 6.18*b* and *d*). There are three primary regions of temperature decrease over the Southern Ocean in both years, which are situated south-east of the continents for 1980 and south of the continents for 1985. Therefore, as for surface temperature, the 500 hPa temperature response for 1985 appears to be situated slightly west

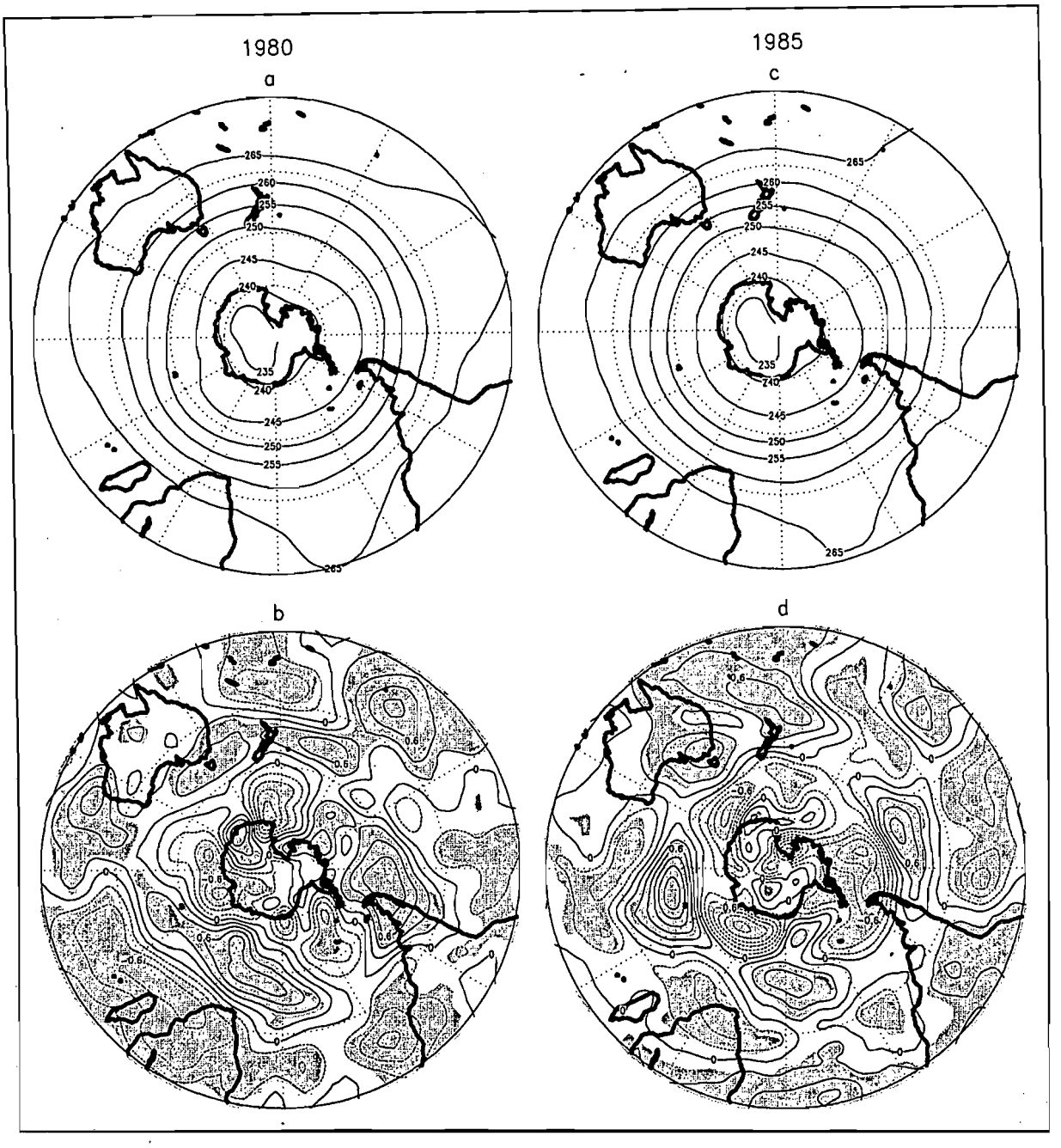

Figure 6.18 500 hPa level temperature (K) for the controls of *a*) 1980 and *c*) 1985, and the perturbations minus the controls for *b*) 1980 and *d*) 1985. Statistically significant differences at the 95% confidence level have been shaded. Negative anomalies in *b*) and *d*) are depicted as dotted contours.

of the response in 1980. If the pattern of sea level pressure decrease (Figure 6.17) is compared to the 500 hPa temperature decrease around Antarctica (Figure 6.18), then it is clear that in each year the 500 hPa temperature decreases are located near the anomalous sea level pressure troughs. The temperature decreases also correspond with decreases in the 500 hPa heights (Figure 6.19). This suggests that the temperature decrease in the upper atmosphere is a response to adiabatic cooling due to increased uplift induced by increased lower level convergence. This increase in lower level convergence may have been triggered by the increase in surface temperatures, which largely correspond to the regions of sea level

pressure decrease in both years (Figures 6.16 and 6.17), or by changes in baroclinicity induced by the sea-ice and SST perturbation. As expected, the regions of pressure decrease around Antarctica at the 500 hPa level (Figure 6.19) are positioned slightly west of the regions of sea level pressure decrease (Figure 6.17).

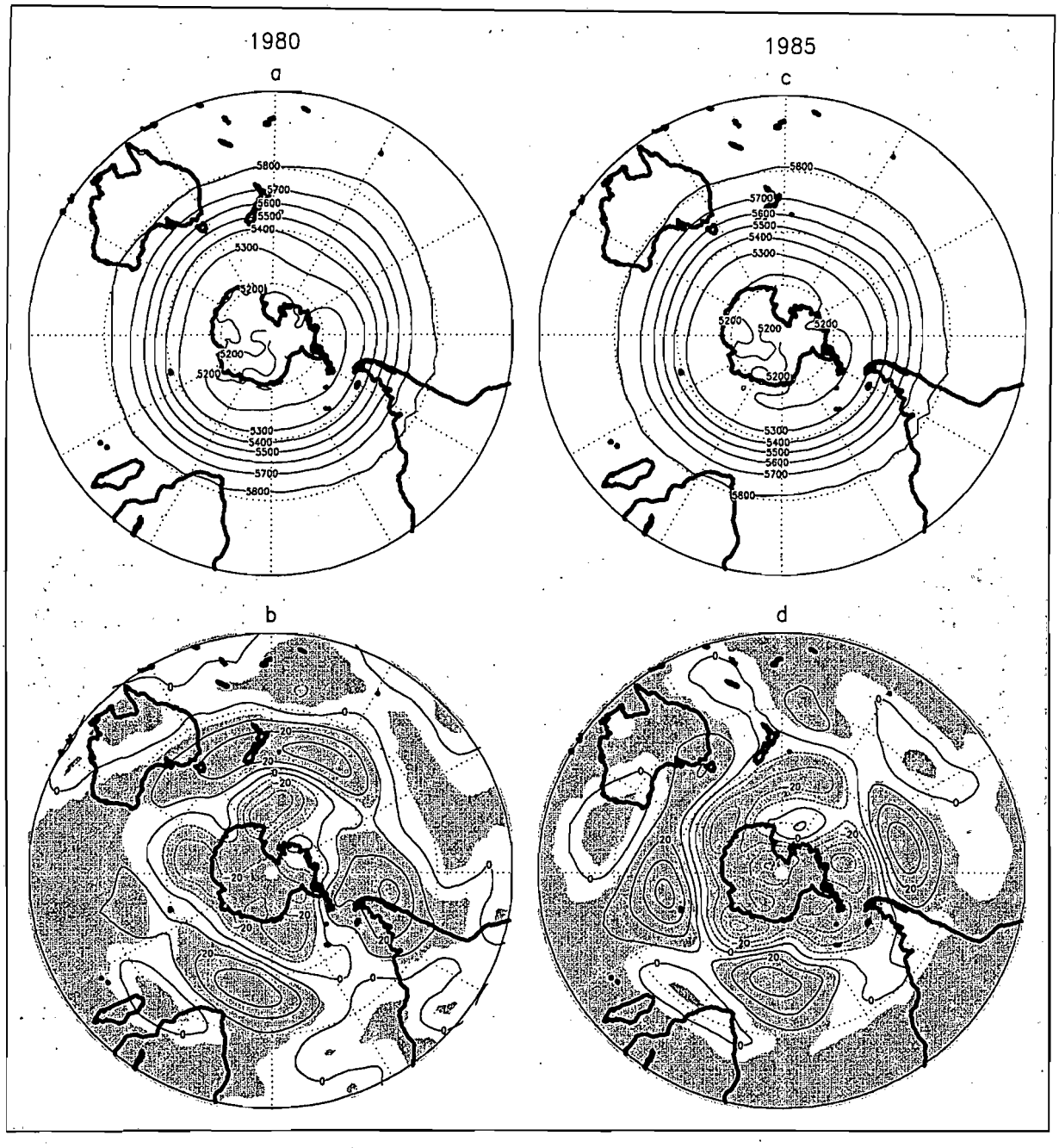

Figure 6.19 500 hPa geopotential heights (m) for the controls of *a*) 1980 and *c*) 1985, and the perturbations minus the controls for *b*) 1980 and *d*) 1985. Statistically significant differences at the 95% confidence level have been shaded. Negative anomalies in *b*) and *d*) are depicted as dotted contours.

There are also significant increases in 500 hPa temperature in certain regions of the midlatitudes and extending into the subtropics (generally between 30°S and 50°S) (Figure 6.18). For 1980 there are significant increases over and slightly west of the tip of South America, south of Africa extending eastwards over the southern Indian Ocean, over Hobart

and east of New Zealand (Figure 6.18*b*). For 1985 there are similar significant increases in upper air temperature which are located west of the tip of South America, south-west of Africa, over the central southern Indian Ocean and over Hobart (Figure 6.18*d*). These increases in upper air temperature are associated with increases in sea level pressure (Figure 6.17) and 500 hPa heights (Figure 6.19) in both years. It thus appears that the temperature change is a consequence of adiabatic warming due to increased subsidence. In 1980 and 1985 there are also corresponding significant decreases in subtropical and tropical 500 hPa temperatures over Africa, the western Indian Ocean, the eastern Pacific Ocean and the Atlantic.

The aforementioned changes in sea level pressure and 500 hPa heights agree well with the changes in zonally averaged vertical velocities, which showed increased uplift in the region of 60°S and increased subsidence between 30°S and 50°S (Figure 6.2). The results from the zonally averaged vertical velocities seemed to suggest that the increased subsidence between 40°S and 50°S was caused by a strengthening and southward extension of the descending limb of the Hadley cell (Figure 6.2). This result is supported by the sea level pressure changes, where a comparison of the control and perturbation maps in the two years (not shown) indicates that the positive sea level pressure anomalies (Figure 6.17) are the result of both a strengthening and southward extension of the subtropical high pressure belt.

An examination of the change in north-south 500 hPa height gradients shows that the sea-ice and SST perturbation causes a general increase in gradients in middle to high latitudes in both years, with slightly weaker gradients between about 30°S and 40°S (Figure 6.20*b* and *d*). The zone of zero change between these two opposing anomalies appears to generally coincide with the region of maximum gradients in the controls, especially over the Atlantic and western Indian Oceans (Figure 6.20*a* and *c*). The increase in gradients in middle to high latitudes relates to the general increase in intensity of the subtropical high pressure belt and circumpolar low pressure belt, as well as to the southward extension of the subtropical high pressure belt. The reduction in 500 hPa height gradients north of this region, between 30°S and 40°S, may be due to the southward extension of the subtropical high pressure belt, causing greater influence of weaker high pressure gradients over stronger westerly wave pressure gradients.

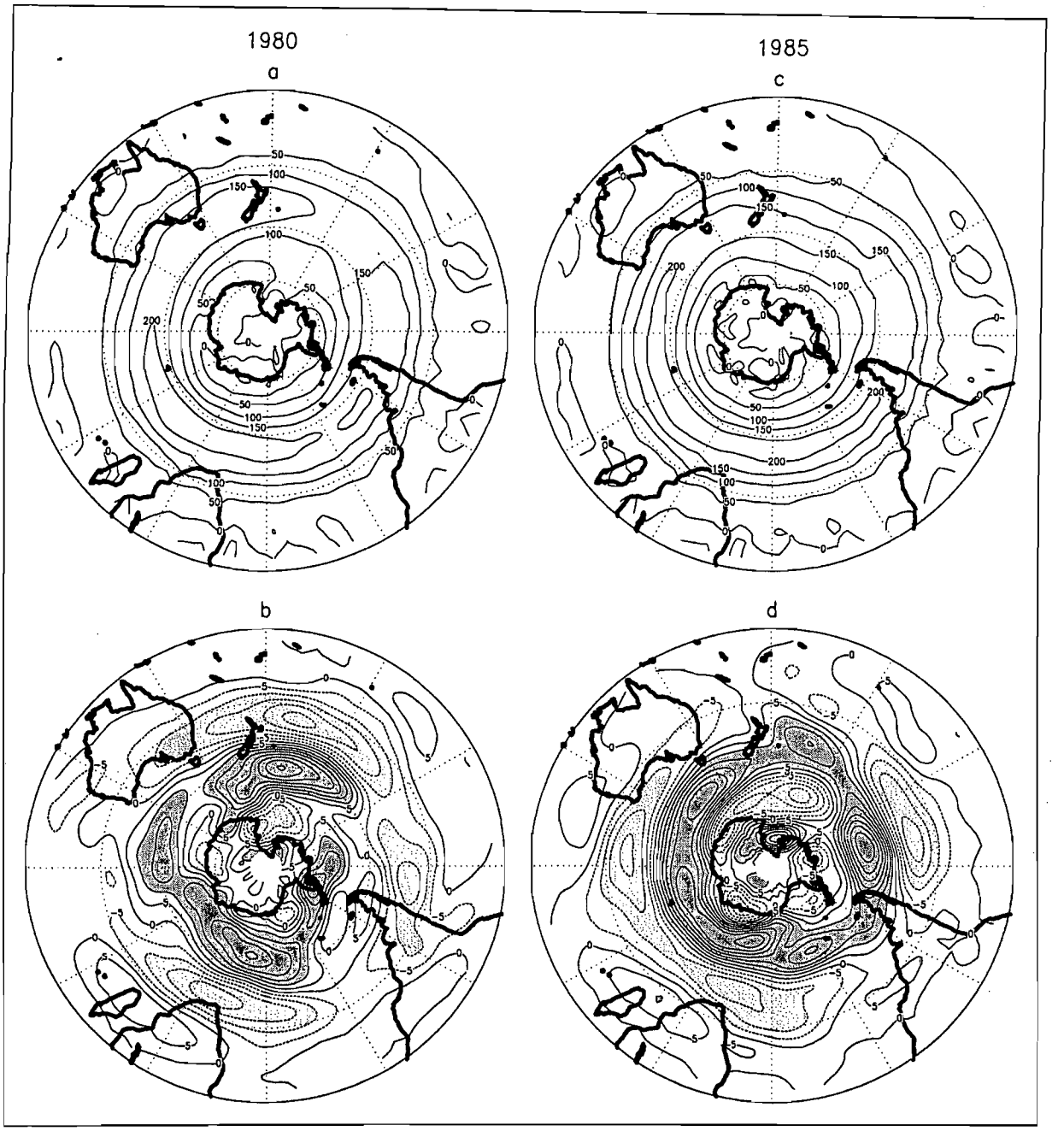

Figure 6.20 The 500 hPa geopotential height gradients (m per 3.7° latitude) (calculated for the north-south direction) for the controls of *a*) 1980 and *c*) 1985, and the perturbations minus the controls for *b*) 1980 and *d*) 1985. Anomalies greater than 10 m per 3.7° latitude and less than -10 m per 3.7° latitude have been shaded in *b*) and *d*).

6.4.2 500 hPa Wind

The 500 hPa wind speed changes (Figure 6.21) can be related to this alteration of the north-south 500 hPa height gradient (Figure 6.20). There is a virtually exact match between the pattern of increased (decreased) gradients and increased (decreased) wind speeds in each year. As was shown with the zonally averaged results, there appears to be a general increase in 500 hPa wind speeds in middle to high latitudes (45°S - 65°S) and a decrease in wind speeds in the subtropics (30°S - 40°S) in response to the perturbation in both years (Figure 6.21*c* and *f*). In other words, the induced pressure changes appear to have caused a slight southward

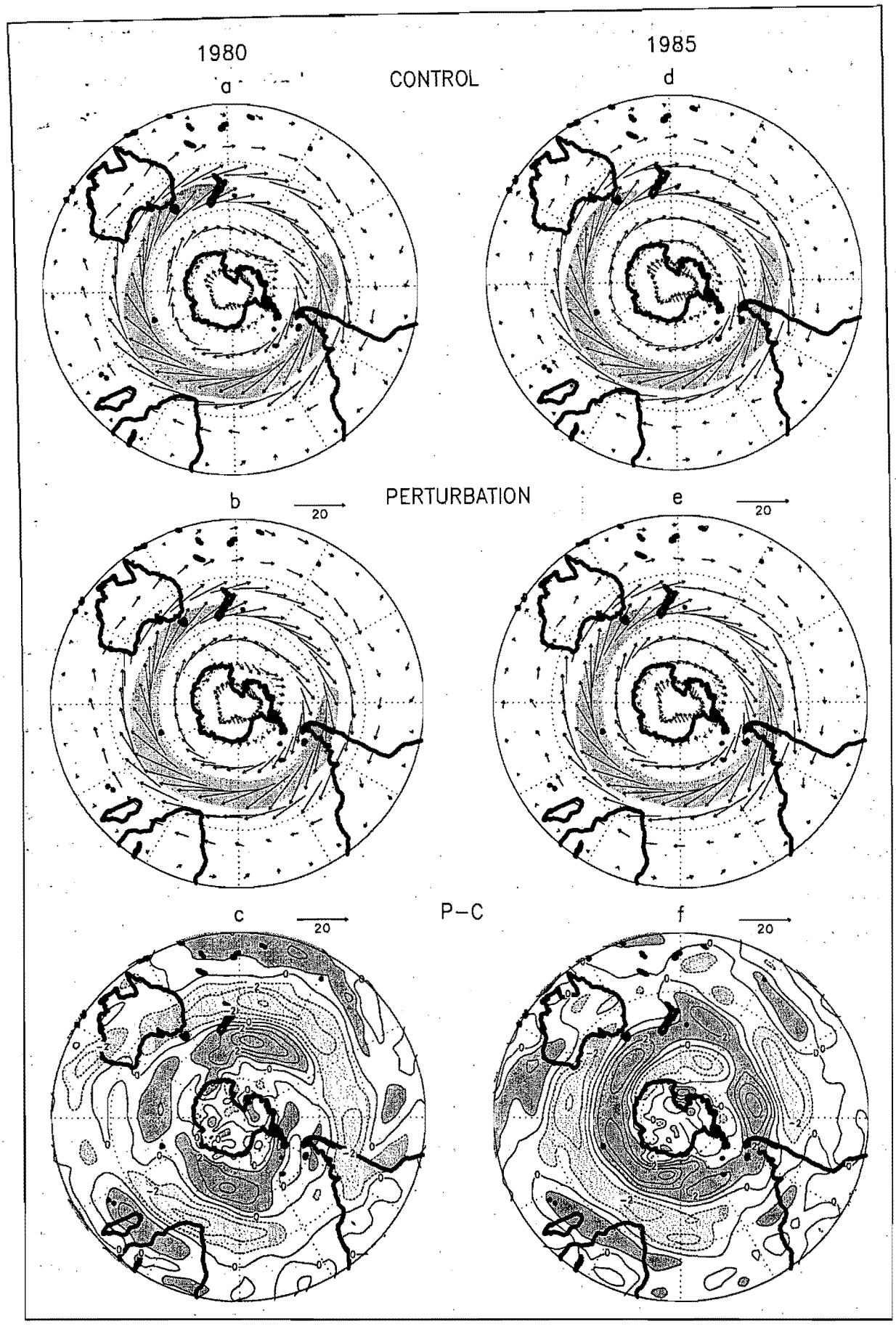

Figure 6.21 500 hPa wind direction and speed (m s^{-1}) for the controls of *a*) 1980 and *d*) 1985, and the perturbations of *b*) 1980 and *e*) 1985. Wind speeds greater than 20 m s^{-1} have been shaded. Maps *c*) and *f*) show the change in wind speed between the perturbations and the controls in 1980 and 1985 respectively. Anomalies greater than 1 m s^{-1} and less than -1 m s^{-1} have been shaded in *c*) and *f*).

shift of the jet stream[2], an intensification of westerly flow south of 45°S and a weakening of winds between about 30°S and 40°S. Streten (1983) analysed the below average ice extent that occurred in the Ross Sea sector in early 1979 (with maximum anomalies during February and March) and showed that the negative ice anomalies were associated with a strong westerly midlatitude circulation and ridging from lower latitudes over the eastern portion of the Ross Sea sector. This observation appears to be compatible with the results mentioned above.

There is also a general increase in wind speeds north of 30°S in both years (Figure 6.21*c* and *f*), which again matches the changes in 500 hPa height gradient (Figure 6.20). Portions of these regions of increased wind speed correspond with regions of statistically significant 500 hPa height decreases between 10°S and 30°S (Figure 6.19*b* and *d*), suggesting that the pressure reduction may be caused by increased upper air divergence due to an increase in wind speeds.

It has become clear that the perturbation in both years has resulted in a pattern of alternating bands of positive and negative change extending outwards from the pole, which is evident in both the pressure (sea level pressure and 500 hPa heights) and wind field. The pattern of pressure change obtained in the present study resembles the "high-latitude" mode, which refers to the pattern of the first sea level pressure and 500 hPa height eigenvectors explaining summer circulation (e.g. Rogers and van Loon, 1982; Sinclair *et al.*, 1997). The "high-latitude" mode is associated with departures around Antarctica which are opposite in sign to those of latitudes equatorward of ~50°S. In the 500 hPa pattern, the eigenvector loadings at lower latitudes over the Pacific and Atlantic Oceans (generally north of 20°S) have the same sign as those around Antarctica, giving a characteristic "see-saw" pattern between middle and low/high latitudes (Rogers and van Loon, 1982), as is seen in the present study. It has been hypothesised that this pattern suggests that the westerlies tend to strengthen south of 40°S, while they weaken north of 40°S, concurrent with a strengthening of the tropical easterlies, and *vice versa* (Trenberth, 1979). In an examination of pressure anomalies for 40 summer months between 1972 and 1980, Mo and White (1985) also found a pattern of zonally symmetric pressure anomalies, where anomalies in the midlatitudes were negatively correlated with anomalies at low and high latitudes. They suggested that this pattern may reflect latitudinal shifts in the jet stream. As mentioned previously, the jet stream did shift

[2] The 500 hPa level only provides an approximation of the intensity of the jet stream. A fuller representation of jet streams would come from an analysis of winds in the region of the 200 hPa level.

slightly southwards in the present study, and the 500 hPa wind speed changes match those suggested to be associated with the obtained pattern of pressure change (Trenberth, 1979).

The pattern of change could also be explained in terms of what was previously hypothesised concerning the change in vertical velocities, i.e. that the alternating bands of increased ascent and descent may be driven by the increased ascent near 60°S. This rising air would cause increased flow both north- and southwards near the top of the atmosphere. It was suggested that the air moving northwards would eventually become impeded by air moving poleward in the upward branch of the Hadley cell and would thus subside, producing the increased subsidence that is seen between 30°S and 50°S and contributing to a southward extension of the general region of subsidence. These assertions have been examined more closely by looking at the v-component (north-south) of the 500 hPa wind (Figure 6.22).

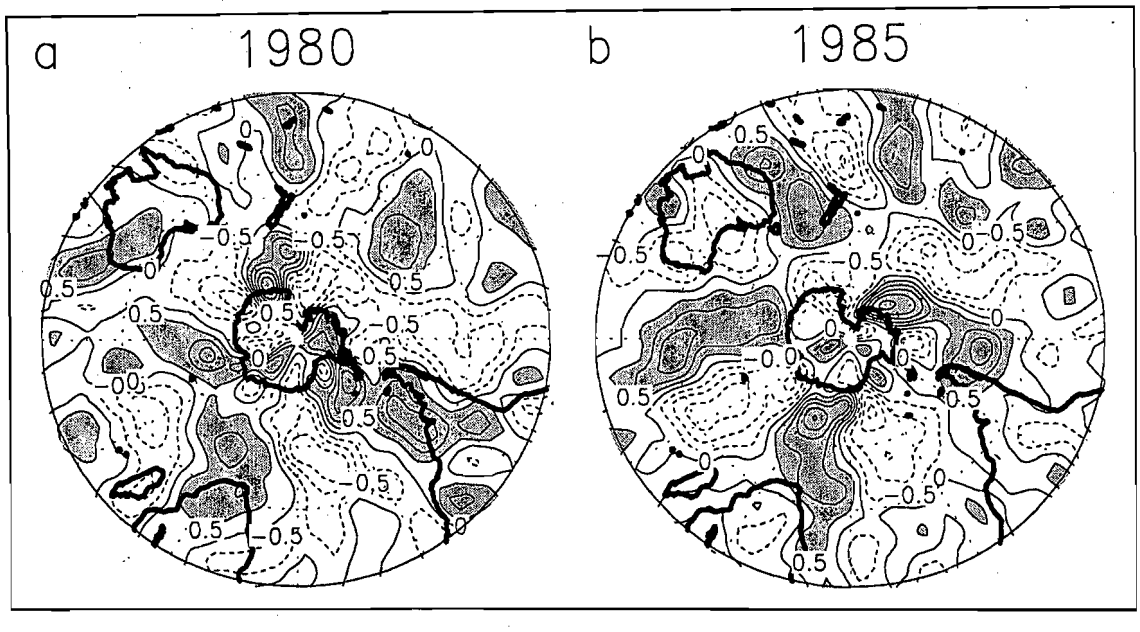

Figure 6.22 The v-component of the 500 hPa level wind (m s^{-1}) for the perturbations minus the controls in *a*) 1980 and *b*) 1985. Anomalies greater than 0.5 m s^{-1} have been shaded.

Those regions of positive v-wind anomalies in Figure 6.22 are regions of increased upper level equatorward flow. In both years there are longitudinal bands of increased equatorward flow south of 30°S and these bands coincide with the longitudes of increased pressures between 30°S and 50°S (Figures 6.17 and 6.19). For example, in 1985 there is an increase in the 500 hPa equatorward flow south of South Africa, over the eastern Indian Ocean and west of South America (Figure 6.22) and there are clear coincident increases in sea level pressure in these three specific longitudinal sectors between 30°S and 50°S (Figure 6.17). This appears to substantiate the hypothesis mentioned above, in that the anomalous rising air near 60°S, shown by the change in vertical velocities and pressure, is transported northwards in the upper atmosphere at certain longitudes, resulting in increased subsidence in these sectors

between 30°S and 50°S. This response is further supported by the results for midlatitude cyclones, where there seems to be a general pattern of density increase at high latitudes, with decreases further north (Figure 6.23).

6.4.3 Midlatitude Cyclones and Storm Tracks

Midlatitude cyclones are vital for meridional energy transport in the Southern Hemisphere and arise through baroclinic instability of the mean flow (Trenberth, 1991). Frontal cyclogenesis takes place in the midlatitudes, especially where there are strong gradients of

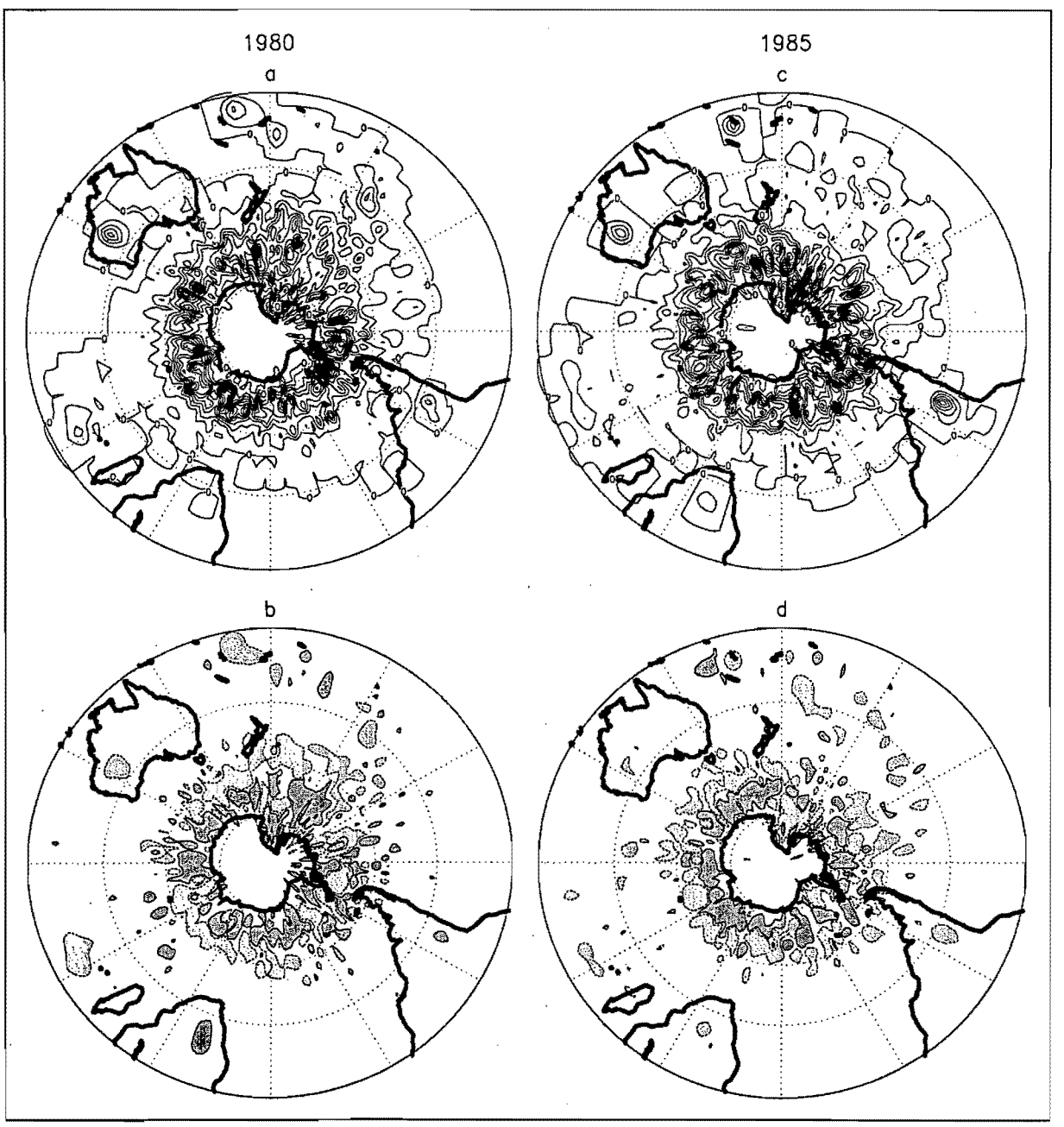

Figure 6.23 Midlatitude cyclone densities ($\times 10^{-3}$ cyclones (degrees latitude)$^{-2}$) for the controls of *a*) 1980 and *c*) 1985, where the contour interval is 0.5×10^{-3} cyclones (degrees latitude)$^{-2}$. Densities for the perturbations minus the controls are shown in *b*) and *d*) for 1980 and 1985 respectively. For clarity in *b*) and *d*), only anomalies greater than 0.4×10^{-3} cyclones (degrees latitude)$^{-2}$ (dark shading) and less than -0.4×10^{-3} cyclones (degrees latitude)$^{-2}$ (light shading) are presented, and only the aforementioned contour lines are plotted.

SST, and the local meridional temperature gradient appears to be a good indicator of the position of a storm track (Trenberth, 1991). In the present study, the SST manipulations caused a decrease in the meridional SST gradient near 50°S in the perturbations compared to the controls (Figure 6.24), which could result in reduced baroclinic activity and may account for many of the cyclone density decreases in this zone (Figure 6.23). This perhaps best explains the cyclone density change between 30°W and 120°E in both years (Figure 6.23). In this sector, the zone of maximum SST increase in the perturbation occurred at 50°S in both years (Figure 5.15), thus weakening the meridional temperature gradients near this latitude. Corresponding to this region of relaxed gradients, there is a reduction in cyclone densities in both years (Figure 6.23). This region of reduced cyclone densities largely coincides with an increase in sea level pressure (Figure 6.17), which extends northwards from about 50°S. The regions of reduced sea level pressure in this sector are largely confined to latitudes south of 50°S (Figure 6.17) and thus coincide with the increase in cyclone densities between 60°S and 70°S (Figure 6.23). This zone corresponds to the sea-ice zone and the latitude band where SST gradients are increased in the perturbations compared to the controls (Figure 6.24), which suggests that cyclone densities may have increased due to baroclinic changes and a modification of the surface fluxes caused by the sea-ice reductions.

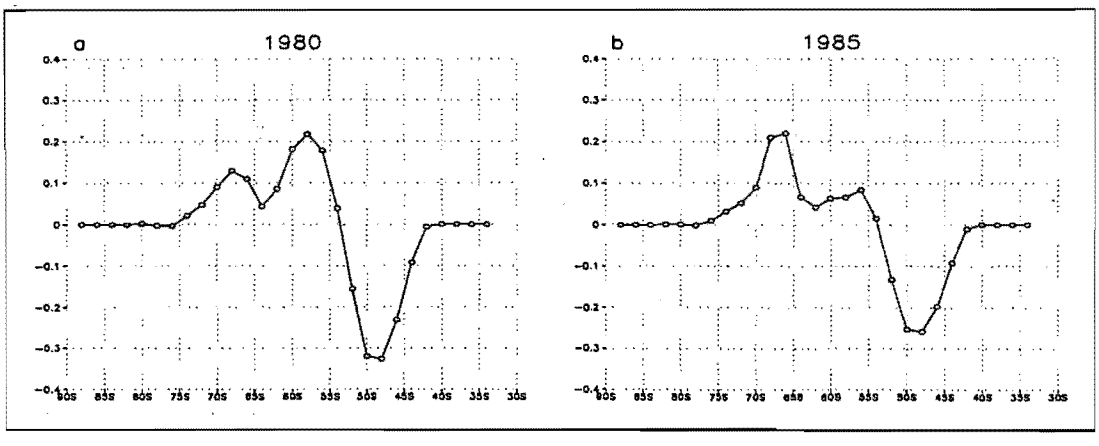

Figure 6.24 Change in the SST gradient (K per 3.7° latitude) (calculated for the north-south direction), in terms of the perturbation minus the control for *a*) 1980 and *b*) 1985.

The relationship between reduced SST gradients and reduced cyclone densities does not, however, seem as clear for the sector north of the Ross Sea. In both years in this region there is an increase in SSTs near 60°S (Figure 5.15), suggesting that this is where SST gradients are primarily reduced, and there is also a general increase in cyclone densities at this latitude (Figure 6.23). This implies that other processes are playing a larger role. South of 55°S, mesocyclones (also referred to as polar lows) are more common than the larger 'synoptic' or frontal cyclones (Carleton and Carpenter, 1990). Mesocyclones are vortices that develop in

cold air streams and may be a relatively common form of cyclogenesis over the higher latitude oceans (Carleton and Carpenter, 1990). They have average diameters of about 3.4° (Carleton, 1995), therefore some of the larger mesocyclones may be resolved by the model. It appears that low level thermal forcing may be an important factor contributing to the development of mesocyclones (Carleton and Carpenter, 1990). Therefore, the cyclone density increase north of the Ross Sea may indicate an increase in mesocyclogenesis in response to the increase in surface temperatures. This could also be used as an explanation for the increases in cyclone density apparent at other longitudes in the sea-ice zone (60°S - 70°S). Jacobs and Comiso (1993) studied a record decrease in sea-ice extent in the Bellingshausen Sea (62°W - 100°W) from mid-1988 through to early 1991. They showed that this decrease coincided with a rise in surface air temperatures on the west side of the Antarctic Peninsula and an increase in cyclonic activity, as was seen in the present study. In addition, a study done by Carleton (1995) highlighted that a relatively large proportion (approximately 25 - 45%) of mesocyclones develop close to the sea-ice margin, probably in response to baroclinic instability aloft, sea-air interactions and lower level instability. Carleton (1992) noted that the baroclinicity that is associated with the strong horizontal surface temperature gradients at the sea-ice boundary may enhance mesocyclogenesis even during summer. Thus, with less expansive sea-ice cover in the perturbations, we may expect to see fewer cyclones in the vicinity of the ice margin in the control simulations, and an increase in densities in the region where the margin is located in the perturbation simulations. This may account for some of the cyclone density anomalies around Antarctica.

From studies done with observed data, it appears that the potential relationship between Antarctic sea-ice extent and the formation and movement of midlatitude cyclones is largely inconclusive. Godfred-Spenning and Simmonds (1996) examined correlations between the position of the Antarctic sea-ice boundary and midlatitude cyclone density for the period 1973 to 1991. They found that the link between sea-ice and cyclone density was not very strong and tended to be confined to certain regions around the Antarctic coastline. Averaged over the hemisphere, sea-ice extent showed a positive correlation with cyclone density during summer in the region of the sea-ice margin and a negative correlation 5° to 20° north of the sea-ice margin, although the correlations were very small (less than 0.2) (Godfred-Spenning and Simmonds, 1996). These results do not seem to be supported by the present study. However, one should be cautious in comparing the results of the correlation study to the present study, since the association between two variables in a correlation study does not necessarily imply cause and effect, and correlation analysis considers only linear

relationships. Furthermore, the authors conclude that the forcing of sea-ice extent by the atmosphere is a more dominant factor than sea-ice affecting cyclone density (Godfred-Spenning and Simmonds, 1996), and the former is not considered in the present study.

Howarth (1983) also found little correlation between sea-ice and cyclone tracks on a hemispheric scale in a study of the period 1973 to 1975. He suggested that the shape of Antarctica, and thus maybe the continental-ice/sea-ice boundary, is more important in determining the longitudinal position of cyclone tracks. However, Howarth (1983) does not eliminate the possibility that the sea-ice margin may influence cyclone movements, but proposes that this may be restricted to short time periods and specific locations. It has been repeatedly stated that it is unclear how Antarctic sea-ice extent, which undergoes an annual cycle of contraction and expansion, can directly affect the position of midlatitude cyclones, which experience a semi-annual oscillation in latitudinal position (e.g. van Loon, 1967; Howarth, 1983; Carleton, 1992). However, it has been shown that the semi-annual oscillation is not that apparent when considering patterns of cyclogenesis (Budd, 1982), since the latitude of maximum cyclogenesis is located furthest north in September and furthest south in March (Carleton, 1992). Therefore, the formation of new midlatitude cyclones may be related to sea-ice advance and retreat (Carleton, 1992).

Sinclair *et al.* (1997) examined the relationship between the leading modes of sea level pressure variability and cyclone activity. They found that the first sea level pressure EOF (empirical orthogonal function), which is the previously mentioned "high-latitude mode", modulates cyclone activity between high and middle latitudes. When there are increased (decreased) westerlies in the region of 55°-65°S, then there are more (fewer) cyclones in the circumpolar regions and fewer (more) in middle and lower latitudes (Sinclair *et al.*, 1997). This result agrees with the present study, where a general increase in westerly flow between 45°S and 65°S is associated with a general increase in cyclone densities between 60°S and 70°S and a decrease further north (40°S - 60°S).

In the present study, storm tracks have been defined as the standard deviation of the bandpass filtered (1.5 - 8.5 days) sea level pressure data and thus provide some indication of atmospheric variability due to the passage of cyclones and anticyclones. Any changes to the tracks in response to the perturbation (Figure 6.25) may be related to changes in cyclone densities, changes in cyclone mobility or changes in the regions of maximum overlap between

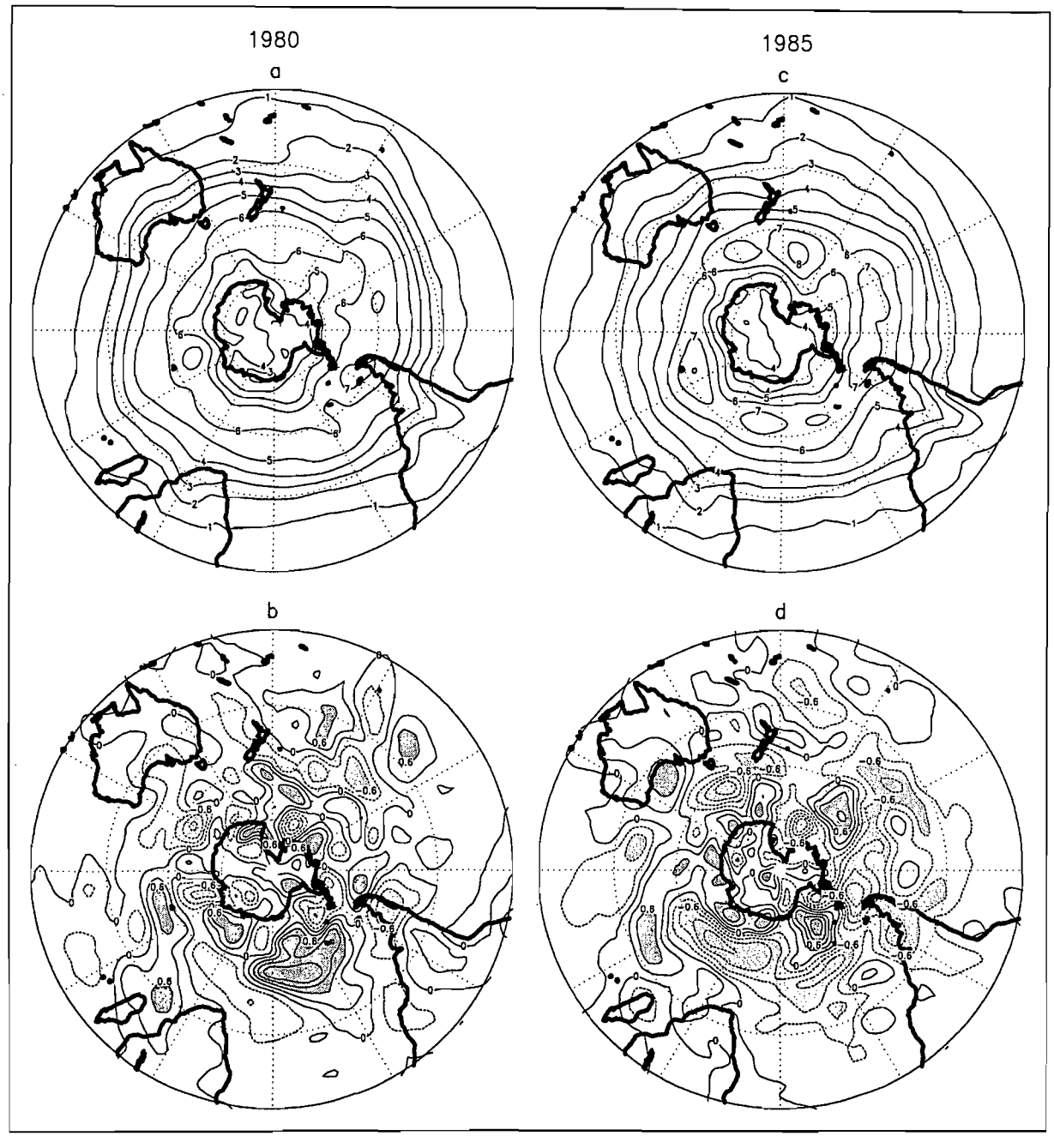

Figure 6.25 The standard deviation (hPa) of the bandpass (1.5-8.5 day) filtered sea level pressure data for the controls of *a*) 1980 and *c*) 1985, and the perturbations minus the controls for *b*) 1980 and *d*) 1985. Anomalies greater than 0.6 hPa and less than -0.6 hPa have been shaded in *b*) and *d*).

cyclone and anticyclone densities. As expected, in many regions there is a good match between the storm track anomalies, the seasonal mean sea level pressure changes and the cyclone density changes, with a decrease (increase) in storm track standard deviation being associated with an increase (decrease) in the seasonal mean sea level pressure and a decrease (increase) in cyclone density (Figures 6.17, 6.23 and 6.25). For example, in both years there are decreases in the midlatitude (35°S - 55°S) storm track south of South Africa, south and south-west of Australia and over the southern-most portion of South America and regions of the Pacific (central Pacific for 1980 and eastern Pacific for 1985) (Figure 6.25). These

regions are also all associated with positive sea level pressure anomalies and a reduction in cyclone densities (Figures 6.17 and 6.23). This suggests that the increased subsidence between 30°S and 50°S has lead to a predominance of high pressure systems and reduced variability in the sea level pressure field due to the passage of midlatitude cyclones, which are perhaps being steered southwards in these regions. In this zone (35°S - 55°S) there are also small regions where the storm track has intensified. These are situated near 30°W (especially in 1980) and 70°E in both years (Figure 6.25). This positions the regions in the "gaps" between the major positive sea level pressure anomalies (Figure 6.17) and means that to some degree they are influenced by the higher latitude sea level pressure decrease, i.e. they are located near the trough axis of sea level pressure decrease (Figure 6.17). Therefore, the increased sea level pressure variability in these regions has probably resulted from a combination of increased cyclone densities, as well as an increase in the degree of overlap of average cyclone and anticyclone densities.

6.4.4 Atmospheric Moisture

In both years the surface specific humidity response to the perturbation is generally less than 1 g kg^{-1} and largely evident in the tropics and subtropics (Figures 6.26). Many of the regions of decreased (increased) specific humidity coincide with regions of increased (decreased) sea level pressure (Figures 6.17 and 6.26), suggesting that enhanced subsidence (uplift) caused a drying (moistening) of the atmospheric column. This is, however, a simplification which does not always hold true, and does not apply at mid-tropospheric (500 hPa) levels (Figure 6.27). For example, between 40°S and 50°S over the eastern Atlantic and central Indian Oceans there are increases in 500 hPa specific humidity (Figure 6.27) where there are increases in the 500 hPa heights (Figure 6.19). The same can be seen for 1980 between 50°S and 55°S over the Pacific (Figures 6.19 and 6.27). Apart from lying near the southern flank of the anomalous high pressures, these regions are also positioned near the eastern side of the anomalous low pressure troughs at higher latitudes. It therefore appears that the anomalous circulation is such as to advect more moist air from lower latitudes into these regions than previously occurred.

There is a general decrease in 500 hPa specific humidity in the South Pacific convergence zone (Figure 6.27). This decrease extends from the region of highest specific humidities, as shown in the controls near 10°S (~165°W for 1980 and ~155°W for 1985), southwards across the central Pacific to between about 30°S and 50°S (Figure 6.27). This decrease is associated

with corresponding precipitation (Figure 6.28) and midlatitude cyclone density decreases (Figure 6.23). On the flanks of the tongue of high humidities over the central Pacific there are, however, humidity (Figure 6.27) and precipitation (Figure 6.28) increases, i.e. between about 70°W and 150°W in the region north of 30°S, and also near 50°S.

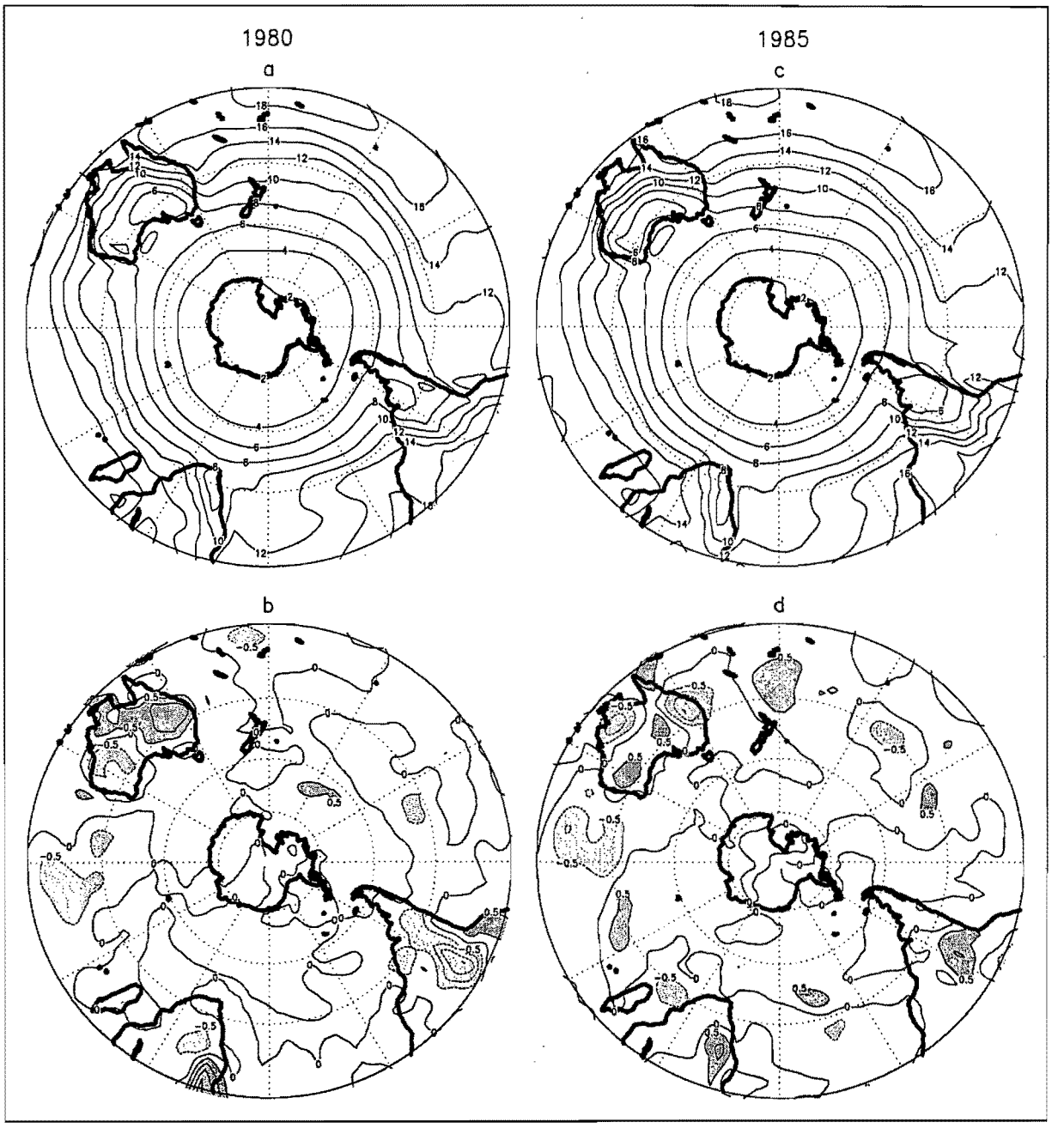

Figure 6.26 Surface specific humidity (g kg^{-1}) for the controls of *a*) 1980 and *c*) 1985, and the perturbations minus the controls for *b*) 1980 and *d*) 1985. Anomalies greater than 0.5 g kg^{-1} and less than -0.5 g kg^{-1} have been shaded in *b*) and *d*).

Precipitation anomalies, in general, are small in both years, with changes greater than 1 mm day^{-1} being largely confined to the tropics (Figure 6.28). Apart from the aforementioned changes, in both years there are increases in tropical precipitation near 10°S in the Australian sector (90°E to 180°E), between 10°S and 30°S over the western portion of South Africa and between 20°S and 30°S to the east of Madagascar (Figure 6.28). These

areas correspond to those regions experiencing an increase in 500 hPa specific humidities (Figure 6.27). In both years there are also decreases in tropical precipitation between 10°S and 20°S over the western Indian Ocean, between 10°S and 30°S in the region north-east of New Zealand and between 10°S and 30°S over the western Atlantic Ocean (Figure 6.28). Again, these regions largely coincide with the regions of reduced 500 hPa specific humidities (Figure 6.27).

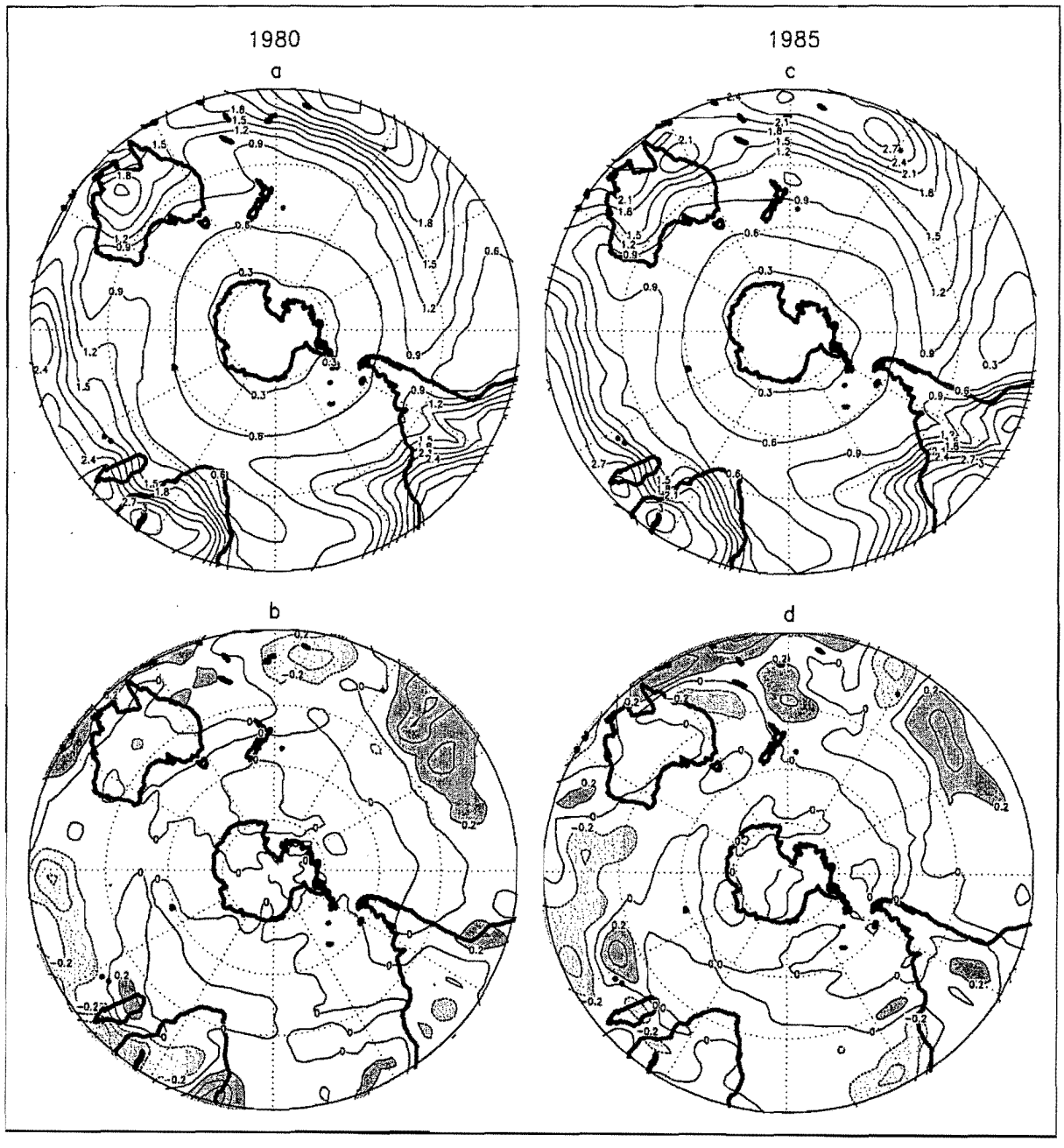

Figure 6.27 500 hPa level specific humidity (g kg^{-1}) for the controls of *a*) 1980 and *c*) 1985, and the perturbations minus the controls for *b*) 1980 and *d*) 1985. Anomalies greater than 0.2 g kg^{-1} and less than -0.2 g kg^{-1} have been shaded in *b*) and *d*).

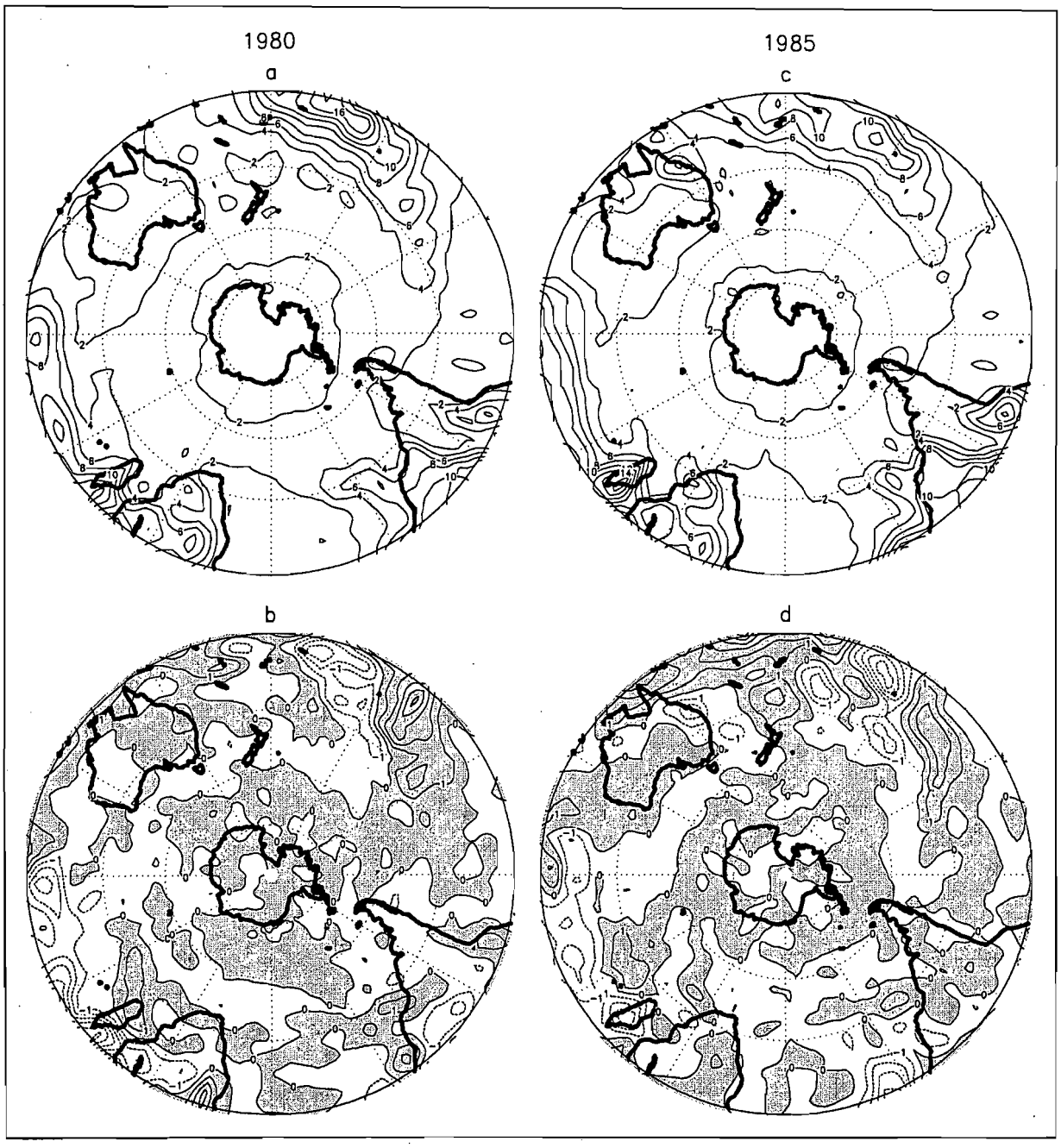

Figure 6.28 Precipitation (mm day^{-1}) for the controls of *a*) 1980 and *c*) 1985, and the perturbations minus the controls for *b*) 1980 and *d*) 1985. Positive anomalies have been shaded in *b*) and *d*).

6.5 500 hPa Planetary Waves

6.5.1 Phase Changes

The phase and amplitude of the planetary waves are strongly influenced by forcing at the surface (Anderssen, 1965; Peixoto and Oort, 1992; Quintanar and Mechoso, 1995a), therefore one might expect to see changes in response to the sea-ice and SST perturbation in the present study. The ridges and troughs of wave numbers 1, 2 and 3 occur consistently at certain longitudes in the zones where the waves are strongest, since they are largely semi-stationary. The phases of the shorter wavelength waves are not shown, because they are travelling waves and their phases are therefore essentially random. With increasing wave number there is an

increase in the eastward movement of the waves, otherwise referred to as the phase velocity (Anderssen, 1965; van Loon and Jenne, 1972; Quintanar and Mechoso, 1995a).

Figure 6.29 displays the phase of the controls and perturbations for seasonally averaged wave numbers 1, 2 and 3 in 1980 and 1985. In general, the phase changes in response to the perturbation are small. Perhaps the most physically justifiable is the phase change for wave number 1 that is seen for both years between 65°S and 70°S (Figure 6.29). Wave number 1 moves eastwards at these high latitudes such that the ridge is positioned near 170°E in 1980 and 150°E in 1985 (Figure 6.29). This implies that the phase of the wave has adjusted to the perturbation so that the trough (10°W in 1980 and 30°W in 1985) is aligned with the anomalous low pressure in the Weddell Sea sector (Figures 6.21 and 6.29). The changes are such that the 1985 response is closer to the pole and located westward of the 1980 response (Figure 6.29). This difference in positioning between the two years is also visible in the 500 hPa height anomalies (Figure 6.21).

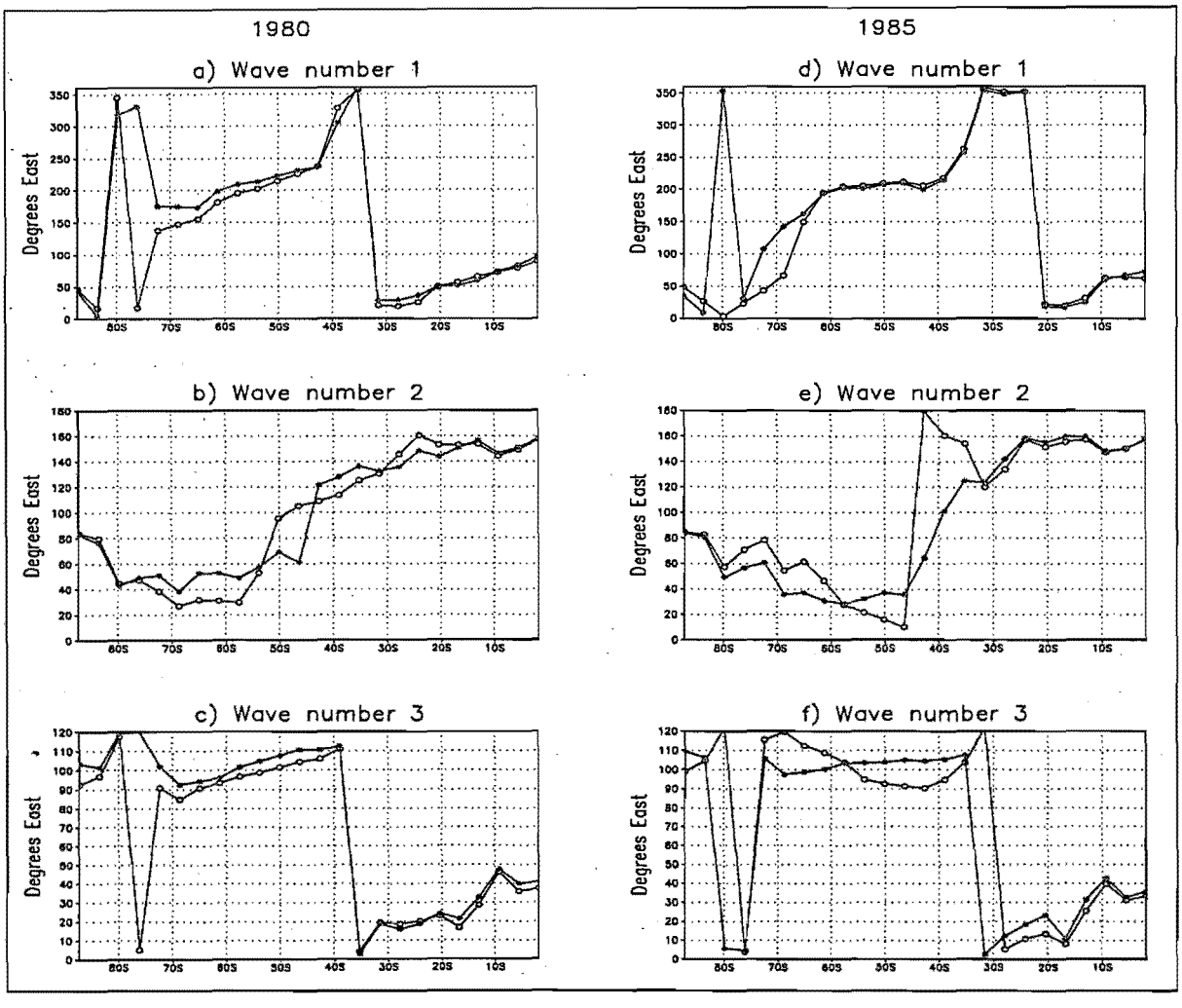

Figure 6.29 The phase (position of the first ridge) of seasonal wave numbers 1 to 3 for 1980 (*a-c*) and 1985 (*d-f*) for the control (open circles) and perturbation (closed circles) data.

The direction of the phase anomalies for wave numbers 2 and 3 are generally not consistent between the two years and therefore, based on the small sample size, the induced changes are largely inconclusive. However, it is apparent that for both waves the phases of the controls for 1980 and 1985 are quite different, especially between 30°S and 50°S for wave number 2 and between 30°S and 70°S for wave number 3 (Figure 6.29). In fact, for each wave in these regions, the phase of the perturbations in the two years resemble each other more closely than do the controls (Figure 6.29). This suggests that the similar nature of the perturbation in the two years has forced a phase response, such that the positioning of wave numbers 2 and 3 are now more similar between the two years.

Between 55°S and 65°S for wave number 2, the first ridge in the perturbation is located near 55°E in 1980 and near 35°E in 1985 (Figure 6.29). This places the axis of the troughs through the Weddell Sea and Australian sectors, thus coincident with the anomalous low pressures seen in the 500 hPa height field at these latitudes (Figure 6.21). At 40°S in the perturbations, the position of the first ridge is near 125°E in 1980 and near 100°E in 1985. This positions the ridge axis at 40°S through the Australian (125°E) and South American (55°W) sectors in 1980 and through the Indian (100°E) and Atlantic (80°W) sectors in 1985 (Figure 6.29). These regions correspond with 500 hPa height increases (Figure 6.21).

Between 30°S and 70°S for wave number 3, the experiment seems to cause the subpolar expression of the wave to be situated slightly westwards of the midlatitude expression of the wave, rather than the other way around as is seen with the control in 1985 (Figure 6.29).

6.5.2 Amplitude Changes

It has been suggested that the long waves in the Southern Hemisphere are primarily forced by orographic and thermal forcing associated with the zonal asymmetries of Antarctica (Anderssen, 1965; Grose and Hoskins, 1979; Trenberth, 1980; Karoly, 1985; James, 1988; Simmonds *et al.*, 1989). Wave number 1 has been identified as being the most dominant component of the climatological mean geopotential height field in the Southern Hemisphere (van Loon and Jenne, 1972; Quintanar and Mechoso, 1995a). Wave numbers 2 and 3, as well as the shorter waves, contribute less to the quasi-stationary field, because they have larger phase velocities and thus their position around the hemisphere is more variable (van Loon and Jenne, 1972; Quintanar and Mechoso, 1995a). However, Karoly (1985) notes that wave numbers 2, 3 and 4 all make significant contributions to the mean 500 hPa height field. The

amplitude changes for seasonal wave numbers 1 to 4 are shown on Figure 6.30 for both years. The amplitudes have been calculated without regard to phase.

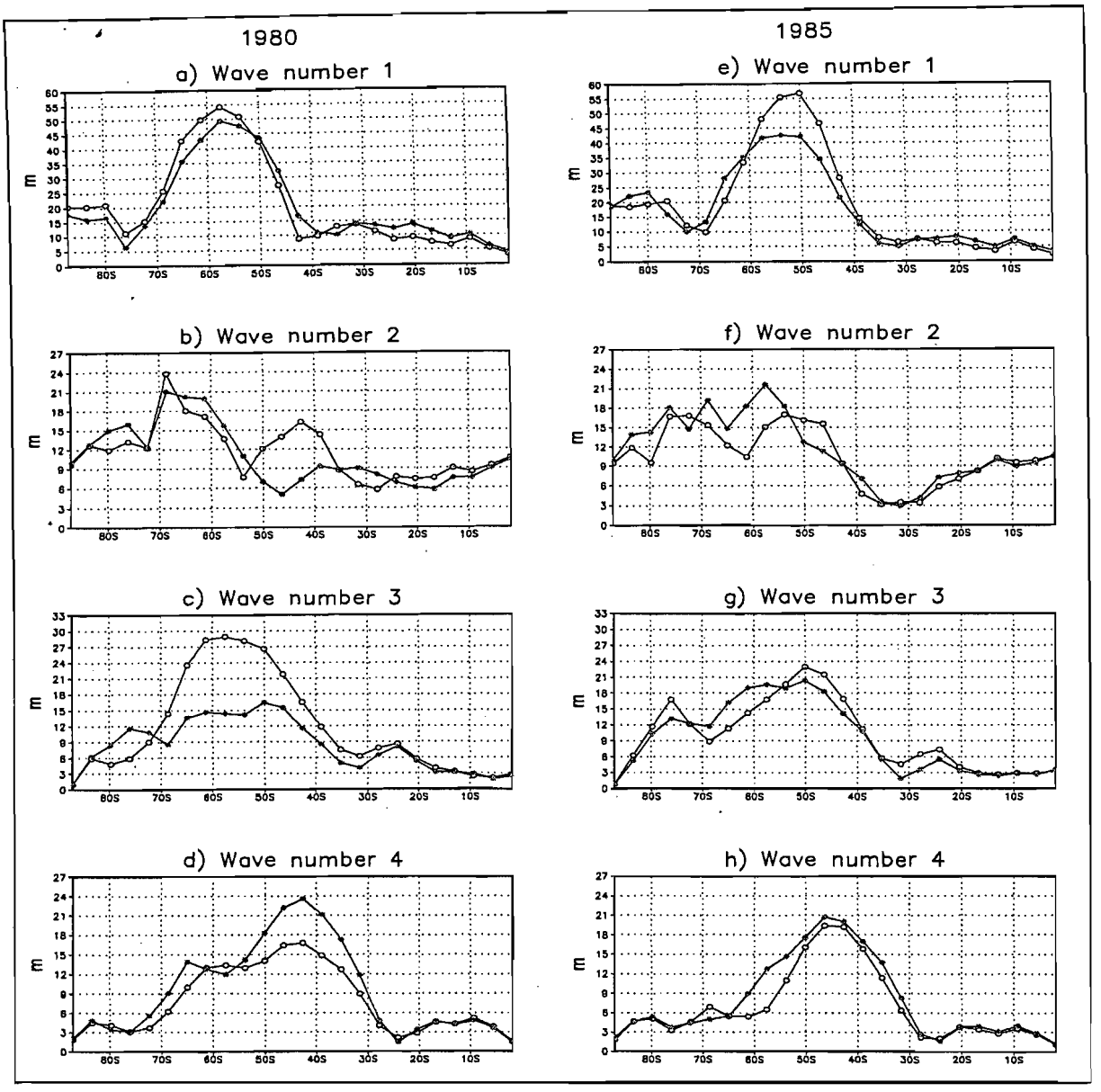

Figure 6.30 The amplitude (m) of seasonal wave numbers 1 to 4 for 1980 (*a-d*) and 1985 (*e-h*) for the control (open circles) and perturbation (closed circles) data.

Wave number 1 is largest at high to middle latitudes and peaks near 57°S in 1980 and near 50°S in 1985 (Figure 6.30). In the perturbations, there is a reduction in the amplitude of the peaks in both years, especially in 1985 (Figure 6.30). Anderssen (1965) has suggested that the existence of wave number 1 may be due to thermal effects associated with the asymmetric SST distribution around Antarctica. In order to investigate the possible influence of the SST distribution on wave number 1, the control and perturbation SSTs at 54°S (midway between the peaks of the two years) have been examined for both years and are shown in Figure 6.31. As has been found by other researchers, the position of the trough of wave number 1 at this latitude occurs near 20°E in both years (Figure 6.29), which coincides with the region of

coldest SSTs (Figure 6.31). In other words, wave number 1 has the same asymmetric distribution about the pole as the SST distribution, in that the trough (ridge) is located over the African (Pacific) sector where the SST distribution as manifested by the Antarctic Convergence is located furthest north (south). The manipulation of SSTs in the experiment resulted in a reduction of the asymmetry of the SSTs at 54°S (Figure 6.31), and this may therefore partially account for the reduced amplitude of wave number 1 (Figure 6.30). In addition, Trenberth (1980) found that the relationship between wave number 1 and the zonal westerlies is such that if the westerlies are stronger in the midlatitudes and weaker to the north and south, then the amplitude of wave number 1 tends to be smaller than usual. This corresponds with the results from the present study.

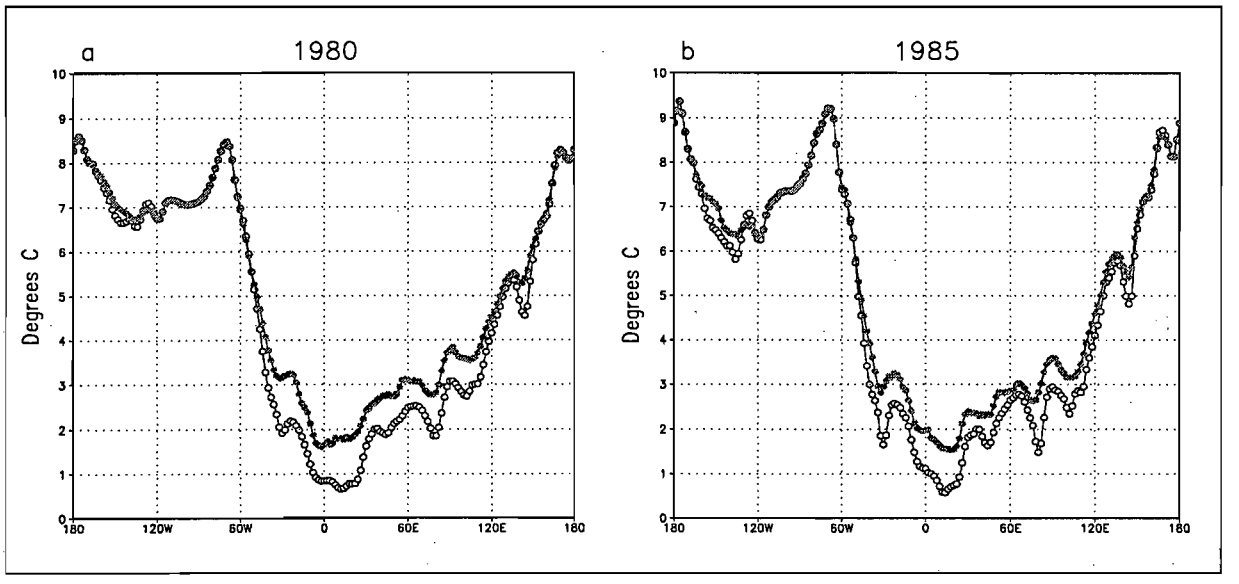

Figure 6.31 The SST (°C) distribution for the control (open circles) and perturbation (closed circles) data at 54°S in *a*) 1980 and *b*) 1985.

For wave number 2, there is a reduction in amplitude between 40°S and 52°S and an increase in amplitude between 52°S and 68°S in response to the perturbation in both years (Figure 6.30). Wave number 3 also exhibits a decrease in amplitude in the middle latitudes (40°S - 55°S), whereas wave number 4 displays an increase in amplitude over this region (Figure 6.30). The increase in amplitude of wave number 4 near 40°S (Figure 6.31) may be due to the pattern of positive 500 hPa height anomalies at this latitude, which do, to some extent, exhibit a 4-wave pattern (Figure 6.21).

On a daily or twice-daily time frame compared to a seasonal average, the shorter waves have larger amplitudes and contribute to a larger proportion of the variability of the 500 hPa height field (van Loon and Jenne, 1972). It is therefore desirable to examine the change in amplitude of the twice-daily waves. In this analysis, waves 1 and 2 have been grouped

together as representing the long, semi-stationary waves, and waves 5, 6, and 7 have been grouped to represent the medium wavelength waves. Wave numbers 5, 6 and 7 were selected, since Kao *et al.* (1971) found that most of the poleward flux of sensible heat is achieved by eastward moving waves of medium wavelengths. Figure 6.32 shows the average amplitude for the long and medium waves for the controls and perturbations. There is a reduction in amplitude of the long waves between 45°S and 60°S in both years (Figure 6.32*a* and *c*). The reduction in amplitude of the longer waves over the midlatitudes in the perturbation may be due to a combination of reduced SST and sea-ice asymmetries about the pole, and increased subsidence between 40°S and 50°S related to a strengthening and southward extension of the subtropical high pressure belt.

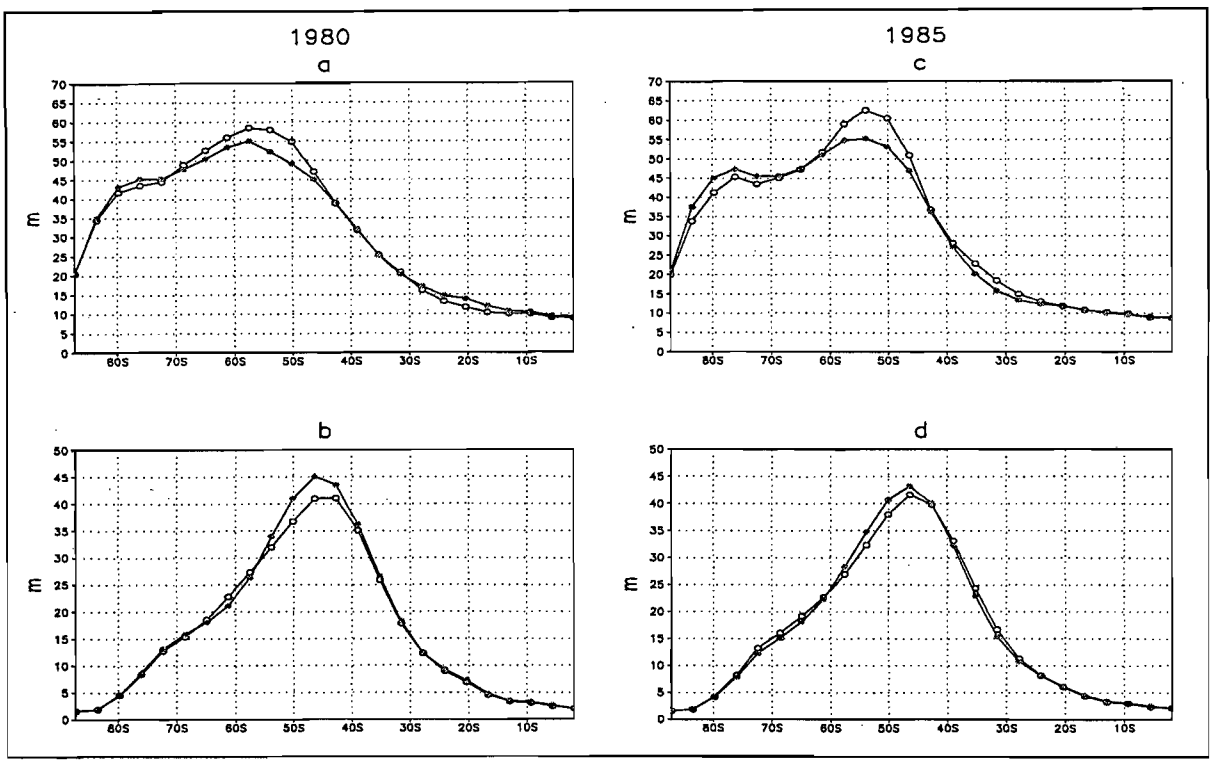

Figure 6.32 The amplitude (m) of the twice-daily long waves grouped together (wave numbers 1 and 2) for the controls (open circles) and perturbations (closed circles) of *a*) 1980 and *c*) 1985; and the twice-daily medium length waves grouped together (wave numbers 5, 6 and 7) for the controls (open circles) and perturbations (closed circles) of *b*) 1980 and *d*) 1985.

Since the perturbation causes an increase in temperatures around Antarctica, one might expect a decrease in the meridional transport of sensible heat and thus a reduction in the amplitudes of the waves that are primarily responsible for the heat transport. This is, nonetheless, not the case in the present study, where there is actually a small increase in the amplitude of the medium length waves in the perturbations (Figure 6.32*b* and *d*). The increase may, however, not be significant and the simulations are perhaps not long enough to elicit a response above the level of noise in the data. In addition, the temperature increase induced by the

perturbation is small and does not extend to the 500 hPa level, thus perhaps not being strong enough to cause a significant change in the meridional transport of sensible heat.

6.6 Change in Twice-Daily Circulation at Sea Level and the 500 hPa Level

In this section, a Self-Organising Map, described in Chapter 3, is used to classify the twice-daily sea level pressure and 500 hPa height data over the Southern Hemisphere (30°S to 60°S) into related categories, in order to examine whether the perturbation has caused a change in the frequency of circulation types simulated over the season. Unlike the SOM procedure used in the validation section of the study (Chapter 4), the data are not standardised prior to presentation to the SOM. This is because it is desirable that the SOM results represent any biases which the perturbation may have caused. The following paragraph outlines the procedure that was employed for both the sea level pressure and the 500 hPa height data respectively.

A SOM was trained with twice-daily data corresponding to the 6 summer controls of 1980 and 1985 (total t=1080). Owing to the large region under examination, it was advantageous to have as many nodes (circulation types) as possible without making the analysis too difficult. As such, a network of 48 nodes (6 in the x-direction and 8 in the y-direction) was selected for the SOM and the weights of the nodes were initialised using linear initialisation. A rectangular topology was used for the array of nodes, and the initial learning rate was set to 0.05, with an initial training radius of 4. Training was run for a total of 30 000 iterations. After the SOM had been trained with the control data from both years, the weights of each node could be decomposed and the array of nodes displayed on a meta-map. Each node/map on the meta-map represents a circulation type and neighbouring nodes depict related circulation types. The trained SOM was then separately presented with twice-daily data associated with the controls of 1980, the controls of 1985, the perturbations of 1980 and the perturbations of 1985. In each case, every time step is mapped to the node whose circulation it most closely resembles.

6.6.1 Sea Level Pressure

The meta-map for sea level pressure is shown in Figure 6.33, and the percentage of time steps which map to each node are shown in Figure 6.34 for the controls and the perturbations of 1980 and 1985 respectively. The grids displayed in Figure 6.34 each correspond to the meta-map (Figure 6.33), such that the top left-hand grid block matches the top left-hand node/map on the meta-map. In the text, the nodes will be referred to by their numbers as shown on the

meta-map (Figure 6.33). The distributions of the percentage of time steps which map to each node are more similar between the perturbations of 1980 and 1985 than between the controls (Figure 6.34*a, b, d* and *e*). In both years in the perturbations the importance of the right-hand side of the meta-map can be seen (Figure 6.34*b* and *e*). This is reflected in the change in frequency of time steps mapping to each node, where there are increases in the representation of circulation types on the right-hand side of the meta-map in both years (top right for 1980 and middle right for 1985) (Figure 6.34*c* and *f*). When one considers the average response for 1980 and 1985 (Figure 6.34*g*), it seems that there is a general decrease in the representation of circulation types which lie down the left-hand side of the meta-map, in the middle of the meta-map and at the bottom of the meta-map and an increase in types which lie down the middle right-hand side of the meta-map.

It thus appears that the perturbation is *favouring* sea level pressure circulation types between 30°S and 60°S (Figure 6.33) which are characterised by:

- a distinct and deep (<992 hPa) 3-wave pattern south of 50°S, where the troughs are positioned south-east of the continents.
- the area of lower pressures (<1000 hPa) being generally constrained to south of 50°S.
- a steep midlatitude pressure gradient at most longitudes.
- strong subtropical high pressures, especially off the west coasts of the continents.
- fairly symmetrical, zonal flow in the midlatitudes (~45°S).
- weak, as opposed to pronounced, blocking in the central Pacific.

These features can be seen in the nodes near and down from node number 18 on the meta-map (Figure 6.33), where there is a common increase in types between the two years (Figure 6.34*g*). These changes in twice daily sea level pressure circulation are generally consistent with the changes in the seasonal mean (Figures 6.19 and 6.20), which showed a general reduction in sea level pressure around Antarctica (in a 3-wave pattern), an increase in pressure between 30°S and 50°S and steeper pressure gradients in the midlatitudes. The circulation types that experience reduced representation in response to the perturbation, generally violate one or more of the features in the bulleted list. For example, the largest common decreases in the representation of certain circulation types (Figure 6.34*g*) lie near nodes 1, 13 and 48 on the meta-map (Figure 6.33). Node 1 shows a fair degree of meridional circulation, strong blocking in the central Pacific and relatively weak pressure gradients over the central Indian Ocean (Figure 6.33). Node 13 has a shallow and not very clear 3-wave

pattern south of 50°S and has weak pressure gradients over the Indian and Pacific Oceans (Figure 6.33). Node 48 also does not clearly show the distinct surface 3-wave pattern south of 50°S, pressures are generally above 992 hPa near 60°S and the meridional pressure gradient is fairly weak (Figure 6.33).

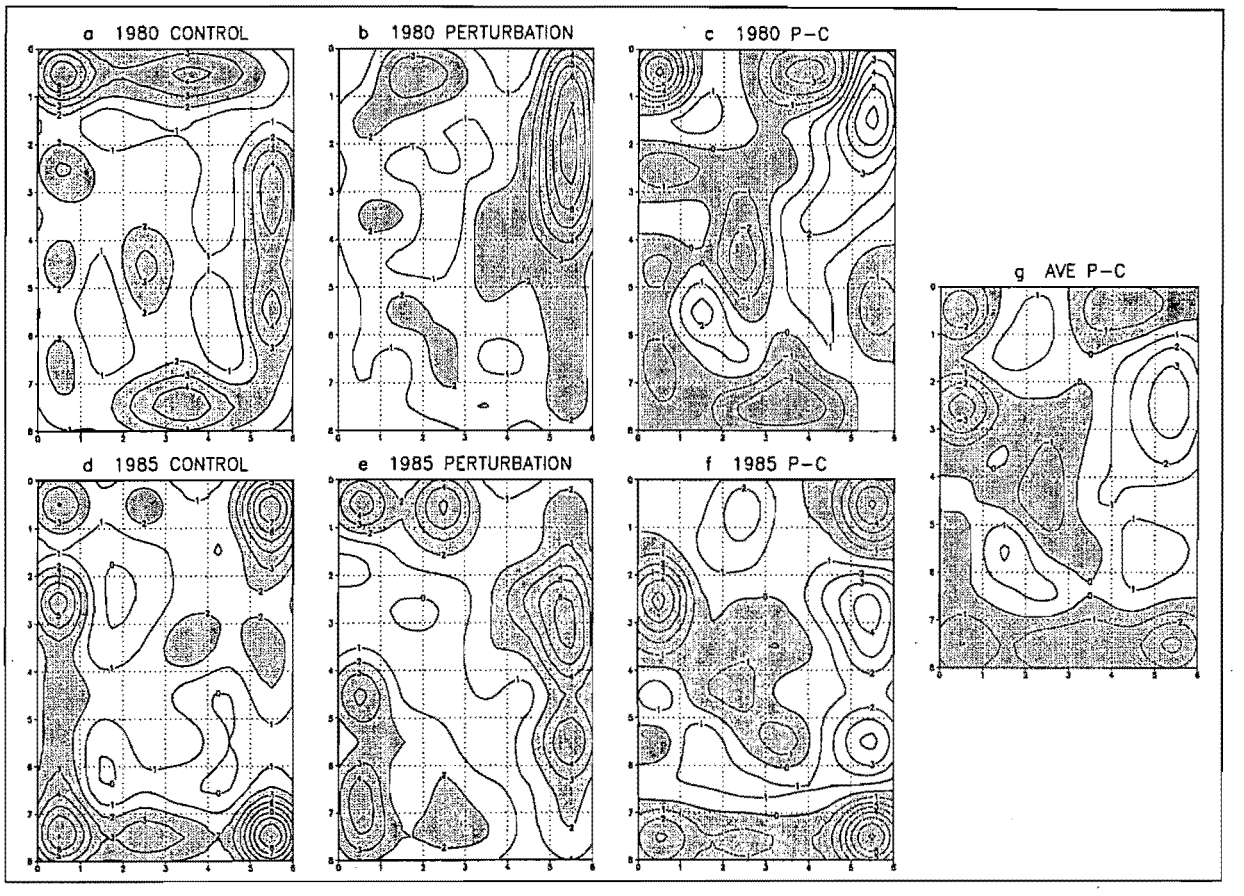

Figure 6.34 The percentage of days mapping to each node of the meta-map (Figure 6.33) for the controls of *a*) 1980 and *d*) 1985 and the perturbations of *b*) 1980 and *e*) 1985. Plots *c*) and *f*) show the difference between the controls and perturbations (perturbation minus control) in terms of the percentage of days mapping to each node in 1980 and 1985 respectively. Plot *g*) represents the average between the plots on *c*) and *f*), i.e. showing the average response between 1980 and 1985.

There are, however, differences in the nodes which are favoured in response to the perturbation in the two years. The increase in the representation of circulation types is focused on node number 12 in 1980 (the upper half of the right-hand column of maps) (Figures 6.33 and 6.34*c*) and on nodes 18 and 36 in 1985 (the middle portion of the right-hand column of maps) (Figures 6.33 and 6.34*f*). These differences are related, in part, to the positioning of the three troughs south of 50°S. As one moves down the extreme right-hand column of the meta-map, the 3-wave pattern shifts slightly westwards. This implies that the position of the three troughs in 1985 are preferentially positioned slightly west of those in 1980. The same result was found in the seasonal mean sea level pressure response (Figure 6.19) and was related to differences in the positioning of the sea-ice and SST perturbations in the two years. 1980 also favours circulation types that have higher pressures over the eastern

Pacific Ocean, between 50°S and 60°S, compared to 1985 (Figure 6.33). Again, this difference is mirrored in the seasonal sea level pressure response, where the high pressure anomaly over the eastern Pacific extends further south in 1980 compared to 1985.

6.6.2 500 hPa Heights

The meta-map for the 500 hPa heights is shown in Figure 6.35, and the percentage of time steps which map to each node are shown in Figure 6.36 for the controls and the perturbations of 1980 and 1985 respectively. It is clear that the distribution of circulation types simulated has changed in response to the perturbation such that the NW-SE diagonal of the meta-map is favoured in both years (Figure 6.36). Circulation types that have experienced a reduction in representation are generally located near the top and left-hand side of the meta-map for 1980 and near the bottom and right-hand side for 1985 (Figure 6.36*c* and *f*).

Characteristics of the circulation types in the central NW-SE diagonal of the meta-map, which are favoured in both years, appear to include:

- fairly zonal and symmetrical flow.
- a 3-wave pattern, but it is not as meridional as some of the types which experience a decrease in representation.
- heights between 50°S and 60°S are generally higher than 5200 m, whereas some of the types which experience a decrease in representation have heights less than 5200 m in this region.

The results from this SOM are in agreement with the conclusions drawn from the Fourier analysis, i.e. there appears to be a reduction in amplitude of the long waves.

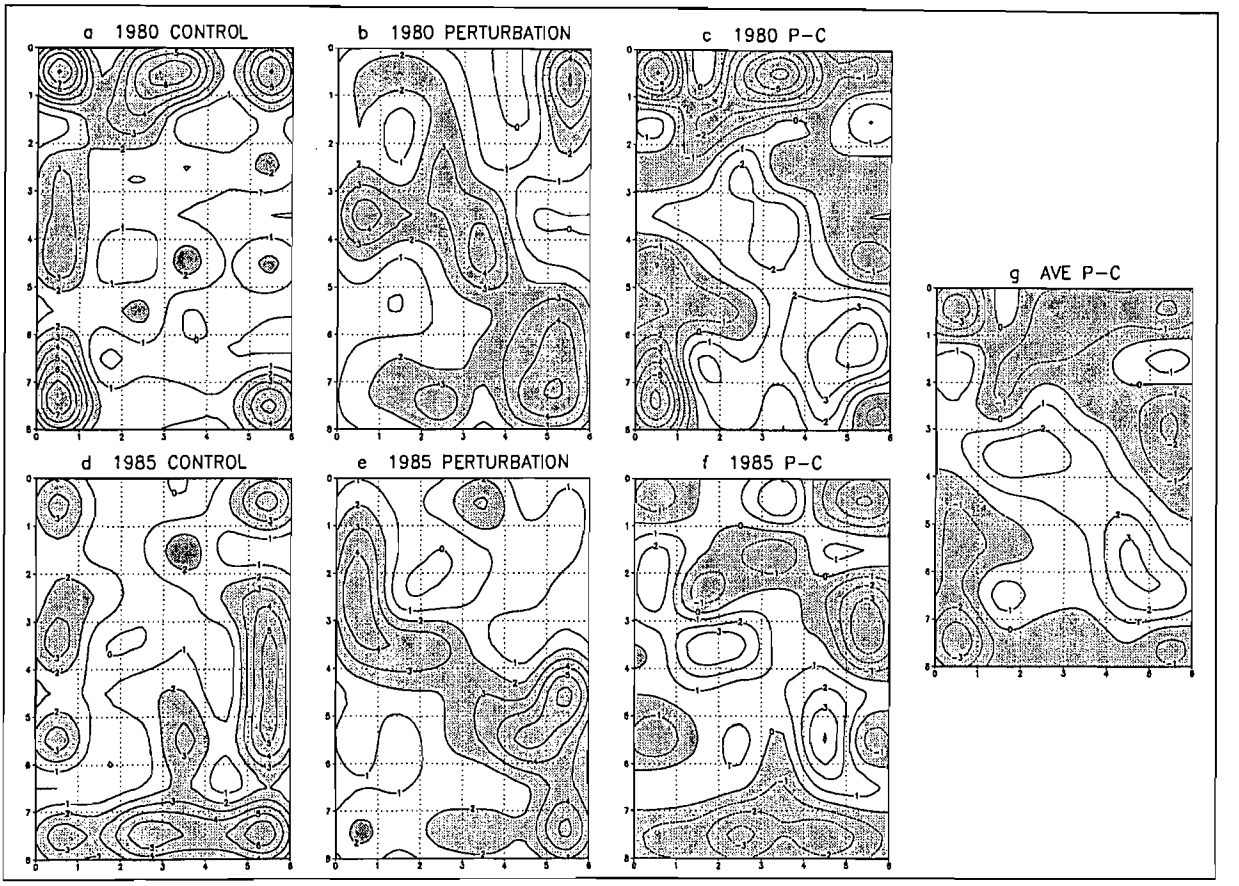

Figure 6.36 The percentage of days mapping to each node of the meta-map (Figure 6.35) for the controls of *a*) 1980 and *d*) 1985 and the perturbations of *b*) 1980 and *e*) 1985. Plots *c*) and *f*) show the difference between the controls and perturbations (perturbation minus control) in terms of the percentage of days mapping to each node in 1980 and 1985 respectively. Plot *g*) represents the average between the plots on *c*) and *f*), i.e. showing the average response between 1980 and 1985.

6.7 Summary

This chapter has described the Southern Hemisphere results of the sea-ice and SST perturbations applied to the summers of 1980 and 1985. Even though the perturbations are relatively small, they have elicited a fairly consistent response between the two years. Differences between 1980 and 1985 can probably be ascribed to the slightly different sea-ice and SST anomalies used, differences in their control sea-ice extent and the high variability of circulation at middle and high latitudes. The major findings of the response to the perturbation are summarised below:

- The longitudinal distribution of the atmospheric response is sensitive to the positioning and magnitude of the sea-ice and SST perturbation. For example, the perturbation for 1985 is located poleward and slightly westward of the 1980 perturbation. Thus, the 1985 response (in terms of temperature and pressure changes) in the region of the perturbation is shifted accordingly in comparison to the 1980 response.

- There are increases in surface air temperature around Antarctica which largely correspond to the regions of SST increase in the perturbation simulation. Consequently, largest increases are found in the Weddell and Ross Sea sectors.

- The zonally averaged vertical velocities show increased uplift in the region of 60°S and increased subsidence between 30°S and 50°S. The results suggest that the increased subsidence between 40°S and 50°S is caused by a strengthening and slight southward extension of the descending limb of the Hadley cell.

- There are corresponding regions of significant sea level pressure and 500 hPa height decrease around Antarctica (50°S - 60°S). The pattern of decrease is clearly related to the pattern of surface temperature increase around Antarctica.

- There are regions of significant sea level pressure and 500 hPa height increase between 30°S and 50°S.

- The surface temperature increase south of 50°S does not extend to the 500 hPa level, where there are in fact temperature decreases. These 500 hPa temperature decreases are located in the region of the anomalous sea level pressure and 500 hPa height troughs, which suggests that the temperature response is caused by adiabatic cooling due to increased uplift.

- There are increases in 500 hPa temperature in certain regions between 30°S and 50°S. These regions coincide with the sea level pressure and 500 hPa height increases, which suggests that the temperature increase is caused by adiabatic warming due to increased subsidence.

- 500 hPa height gradients become steeper in middle to high latitudes, and slightly weaker between 30°S and 40°S. This is a response to the general increase in intensity of the subtropical high pressure belt and circumpolar low pressure belt, as well as to the slight southward extension of the subtropical high pressure belt.

- There are increases in 500 hPa wind speeds in middle to high latitudes (45°S - 65°S), and decreases in the subtropics (30°S - 40°S). The pressure changes appear to have induced a

slight southward shift of the jet stream. The wind speed changes coincide with the change in pressure gradients.

- Where there are longitudinal sectors of increased equatorward 500 hPa wind flow (v-wind) south of 30°S, there are corresponding longitudes exhibiting an increase in pressure between 30°S and 50°S. This suggests that the anomalous rising air near 60°S, shown by the change in vertical velocities and pressure, is transported northwards in the upper atmosphere at certain longitudes, resulting in increased subsidence in these sectors between 30°S and 50°S.

- There is a general decrease in cyclone densities between 40°S and 60°S and an increase in densities between 60°S and 70°S.

- The phase of hemispheric wave number 1 appears to have shifted eastwards at high latitudes (65°S - 70°S) so that the trough is aligned with the anomalous low pressure in the Weddell Sea sector.

- There is a general reduction in amplitude of wave numbers 1, 2 and 3 in middle to high latitudes. The reduction in amplitude of the longer waves may be due to a combination of reduced SST and sea-ice asymmetries about the pole, and increased subsidence between 40°S and 50°S.

CHAPTER 7

Implications of the Summer Sea-Ice Perturbation for Southern Africa

7.1 Introduction

This chapter examines the southern African atmospheric response to the summer season sea-ice and SST perturbation. Many of the variables that are examined here have been discussed and displayed in the previous chapter, but the focus now shifts to a regional scale and the variables are re-examined in a southern African context. Analyses of the data are performed over a window (20°S to 50°S; 2°E to 47°E) encompassing South Africa and the results are interpreted in the framework of the large-scale Southern Hemisphere response that was presented in the previous chapter.

The purpose of this chapter is to establish whether sea-ice changes have the potential to affect the climate of southern Africa. This is examined in the context of the sea-ice reduction experiments that have been performed in the present study, in order to investigate whether the imposed perturbations have elicited a consistent response over the region. The variable of primary concern for southern Africa is precipitation. As has been mentioned in Chapter 1, southern Africa is a semi-arid region which is characterised by highly variable rainfall, exhibiting periods of both severe drought and floods. The majority of research on the controls on rainfall have focused on the summer season, since apart from the south-western tip of South Africa, which receives rainfall during winter, and the south coast of South Africa, which receives rainfall all year round, the region receives most of its rainfall during summer. Over Africa south of 20°S in the summer season, the tropical controls on the near-surface circulation are prominent, and take the form of easterly waves and lows. Over the adjacent oceans, the subtropical South Atlantic Anticyclone and South Indian Anticyclone dominate the circulation patterns, and cold fronts, associated with travelling westerly waves and lows in the midlatitudes, generally pass south of the sub-continent during summer.

The first section of the chapter considers the mean seasonal response of the climate and incorporates a wide range of variables. An exclusive investigation of average changes can be limiting and in order to address changes on a twice-daily time frame, the circulation types simulated at sea level are determined using a Self-Organising Map. The chapter culminates

in an examination of the influence of the perturbation on precipitation over southern Africa. A separate section is devoted to this issue, since the downscaling procedures and results require additional explanations and it is desirable to focus on precipitation due to its significance for the sub-continent.

7.2 Mean Seasonal Response

In the controls of 1980 and 1985, the South Atlantic Anticyclone is evident, as is the high pressure over the Indian Ocean adjacent to South Africa (Figure 7.1*a* and *d*). The South Indian Anticyclone is not as prominent over the analysis window as the South Atlantic Anticyclone, since the centre of the former high pressure cell is situated further east over the Indian Ocean. The trough associated with the easterly wave is positioned over the western part of the subcontinent, and the sharp pressure gradients associated with the midlatitude flow are located in the southern portion of the analysis window, generally south of 40°S (Figure 7.1*a* and *d*). The South Atlantic and South Indian Anticyclones are stronger in 1980 compared to 1985, but the easterly wave trough is weaker (Figure 7.1*a* and *d*). The results of the previous chapter suggested that the sea-ice and SST perturbation causes a strengthening and southward extension of the subtropical high pressure belt. This result is confirmed over the southern African region. In both years, there is a clear southward extension and intensification of the South Atlantic and South Indian Anticyclones, although the changes are not as prominent over the Indian Ocean (Figure 7.1). The increase in pressures south-west of the subcontinent occur further north in 1980 compared to 1985 (Figure 7.1*c* and *f*), which may be related to the equatorward positioning of the sea-ice and SST anomalies in 1980 compared to 1985. In addition, the pressure increases in 1985 are positioned slightly west of those in 1980 (Figure 7.1*c* and *f*). This may be related to the positioning of the sea-ice anomalies, since in the previous chapter it was noted that the SST and sea-ice anomalies, as well as the resulting temperature increases and sea level pressure decreases around Antarctica were situated further west in 1985 compared to 1980 over the Atlantic Ocean sector.

The changes to the South Atlantic Anticyclone seem to suggest increased eastward ridging over the southern portion of South Africa and south of the continent in the perturbations. There is also an increase in pressures over the south-eastern portion of South Africa, which may be related to a combination of increased ridging of the South Atlantic Anticyclone and an intensification of the South Indian Anticyclone (Figure 7.1). In both years there is a significant increase in sea level pressure over the south-western Indian Ocean and eastern half of the subcontinent, being largest in the vicinity of the Mozambique Channel (Figure 7.1).

This increase is manifest by a strengthening of the ridge of the easterly wave in this region, producing greater meridionality of the tropical wave east of about 25°E. There is not a corresponding strengthening of the easterly wave trough over the north-western portion of the subcontinent, and in fact the trough is weaker and narrower (it narrows from the east) in the perturbations compared to the controls (Figure 7.1).

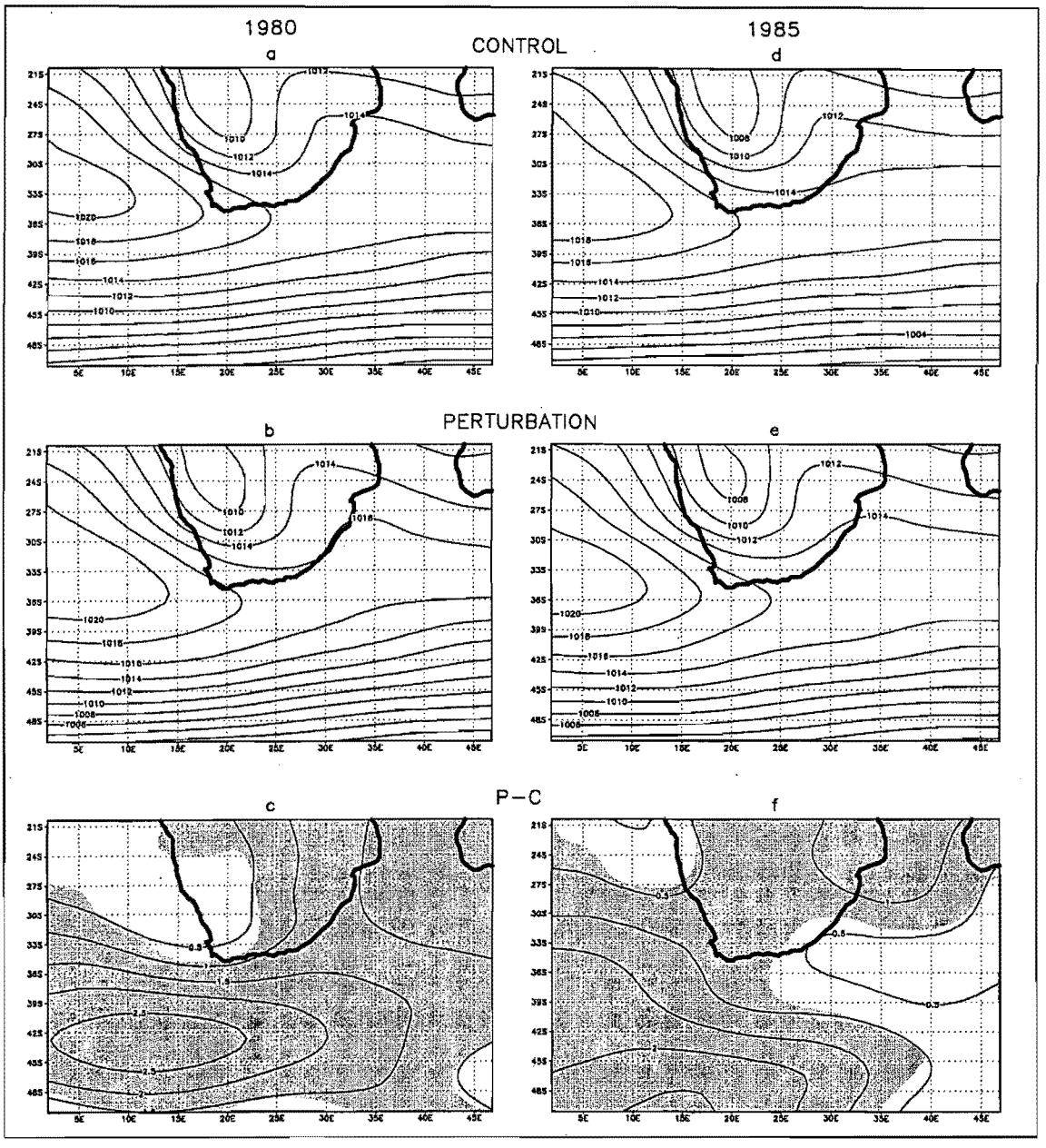

Figure 7.1 Sea level pressure (hPa) for the controls of *a*) 1980 and *d*) 1985, and the perturbations of *b*) 1980 and *e*) 1985. Maps *c*) and *f*) show the perturbations minus the controls for 1980 and 1985 respectively. Statistically significant differences at the 95% confidence level have been shaded.

The change in near-surface wind speeds at the 900 hPa level are related to these sea level pressure changes and are shown on Figure 7.2. As a result of the southward extension of the South Atlantic Anticyclone (Figure 7.1), there are decreases in the wind speed south of South Africa in both years (Figure 7.2). The increase in wind speeds north of 33°S over the south-eastern Atlantic in both years is probably the result of a combination of the intensification of

the anticyclone, causing a steepening of pressure gradients between about 27°S and 33°S, as well as a southward shift of the centre of the anticyclone, which is situated near 33°S and is associated with the weakest winds (Figure 7.2). The changes in wind speed over the south-western Indian Ocean are small and generally conflicting between the two years.

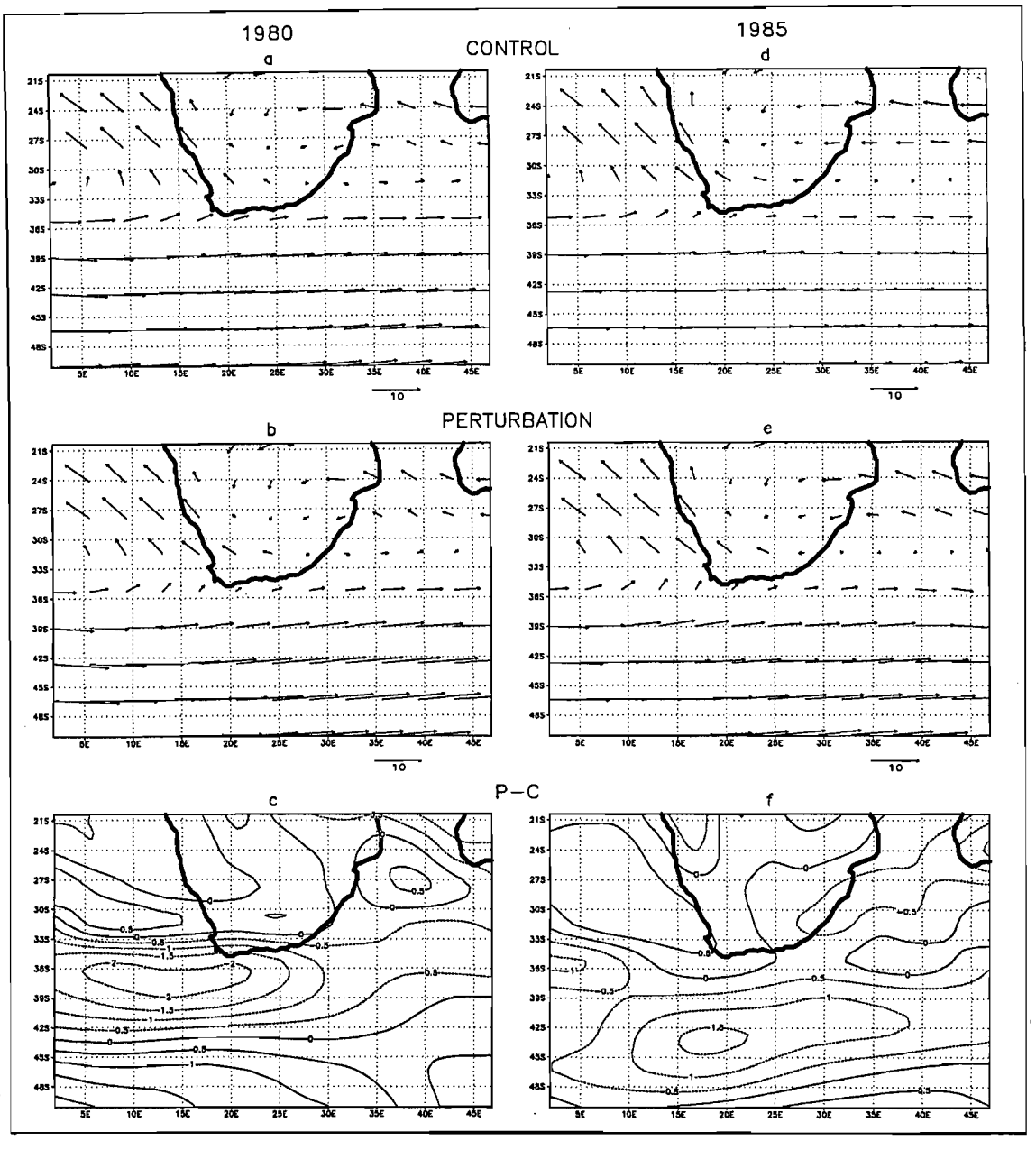

Figure 7.2 900 hPa wind direction and speed (m s^{-1}) for the controls of *a*) 1980 and *d*) 1985, and the perturbations of *b*) 1980 and *e*) 1985. Maps *c*) and *f*) show the change in wind speed between the perturbations and the controls in 1980 and 1985 respectively.

It is difficult to identify changes in the north-south component of the wind from the uv-wind vectors displayed on Figure 7.2., therefore Figure 7.3 shows the meridional component of the wind at 900 hPa in the controls, as well as the change in this component due to the sea-ice and SST perturbation. The meridional component is small in comparison to the zonal component of the wind, but is very important in terms of the transportation of heat, moisture and momentum across latitudes. The equatorward flow associated with the South Atlantic

Anticyclone is evident over the west coast of South Africa and the south-eastern Atlantic Ocean in the controls (Figure 7.3). In both years, there is an increase in the equatorward flow south, south-west and west of Cape Town, which is related to the southward expansion and intensification of the South Atlantic Anticyclone (Figure 7.3). The southward expansion of the South Atlantic Anticyclone also affects the near-surface midlatitude flow, causing increased meridionality in the perturbations, primarily in the form of increased northward flow between about 15°E and 40°E in the region south of 40°S (Figure 7.3). This result is also evident in the sea level pressure fields, in the form of a slight increase in the slope of the westerly wave south of the subcontinent in the perturbations compared to the controls (Figure 7.1 *a,b,d* and *e*). The general increase in equatorward flow over the southern half of the analysis window (Figure 7.3) suggests a strengthening of the surface manifestation of the Hadley Cell over that region.

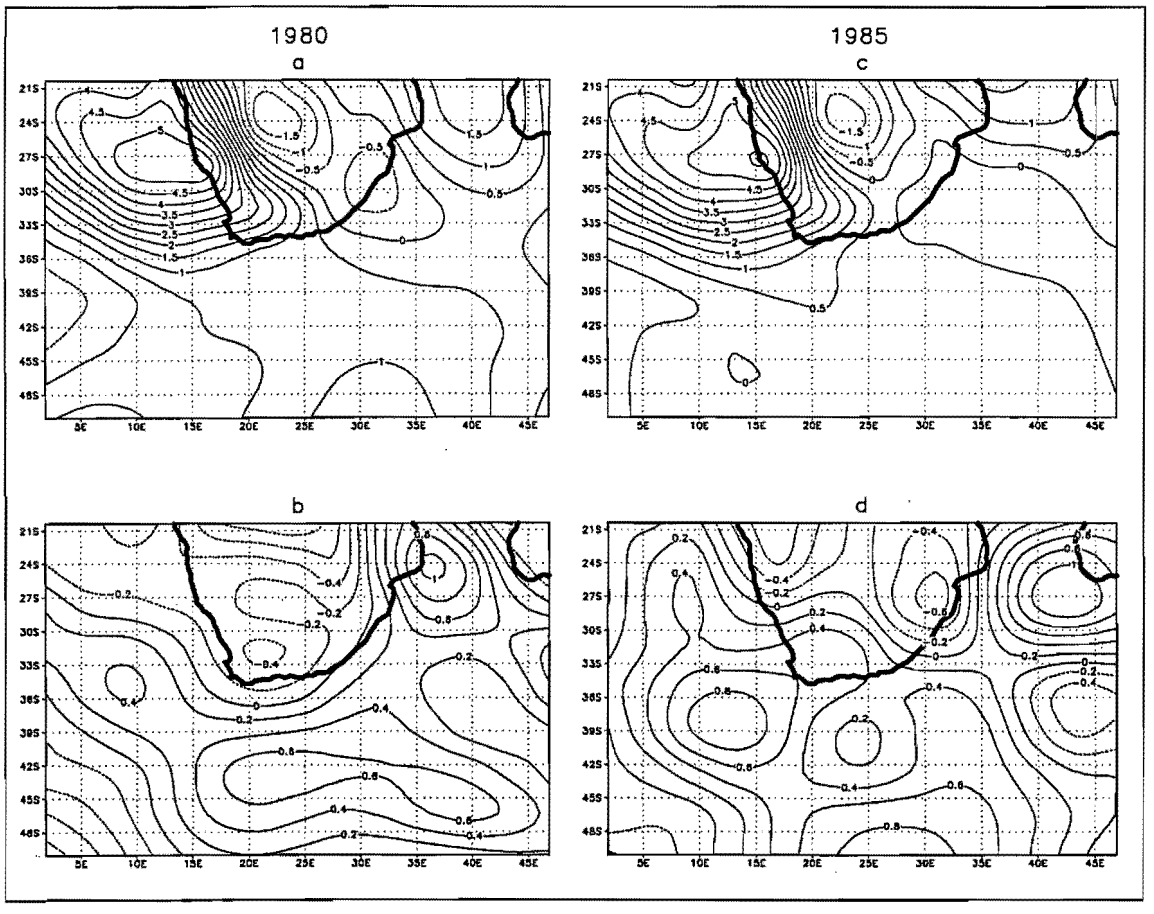

Figure 7.3 Meridional component (v-component) of the 900 hPa wind (m s^{-1}) for the controls of *a*) 1980 and *c*) 1985, and the perturbations minus the controls for *b*) 1980 and *d*) 1985.

Both years also exhibit an increase in equatorward flow over the Mozambique Channel and increased poleward flow to the west of this, over the land (Figure 7.3). These changes are related to the previously mentioned strengthening of the ridge associated with the tropical easterly wave, resulting in greater meridionality of the wave east of about 25°E. The increase

in southward flow over the eastern portion of the land is also related to the intensification of the South Indian Anticyclone, such that there is increased poleward flow on its western border. In both years, there is also a reduction in the equatorward flow on the west coast between about 21°S and 27°S (Figure 7.3). This region is associated with the tropical easterly wave, i.e. the western border of the trough, and may experience decreased flow due to the reduction in intensity of the trough (Figure 7.1).

It is desirable to investigate the influence which these near-surface wind and pressure changes have on the convergence and divergence patterns. In the controls, there is surface divergence over the south-western Indian Ocean related to subsidence and anticyclonic conditions (Figure 7.4*a* and *d*). In addition, divergence associated with the South Atlantic Anticyclone is evident over the west coast, the southern portion of the subcontinent and the south-eastern Atlantic Ocean (Figure 7.4*a* and *d*). The magnitude of divergence over the west coast is fairly high (Figure 7.4*a* and *d*), as a result of subsidence and anticyclonic conditions. The easterly wave over the land, evident in the sea level pressure field (Figure 7.1), is associated with low-level convergence to the east of the trough, while ahead of and west of the trough there is surface divergence (Figure 7.4*a* and *d*). These convergence and divergence fields are caused by the effect of changing the radius of curvature and the conservation of absolute vorticity. Changes to the divergence field as a consequence of the perturbation could result from a number of factors, for example kinematic (speed) changes, ageostrophic/agradient versus geostrophic/gradient flow, and changes in confluence or diffluence. Sometimes one or more of these effects will be operating and a combination of their relative strengths will determine the net result, therefore it is not always easy to identify a single factor that is causing a change in the divergence field.

In the perturbations of the current study, there is an increase in divergence over the south-eastern Atlantic Ocean in both years (Figure 7.4), presumably associated with an increase in intensity of the South Atlantic Anticyclone (Figure 7.1). A divergence anomaly is also located over the southern portion of the subcontinent (Figure 7.4*c* and *f*), which is likely to be related to increased ridging of the South Atlantic Anticyclone (Figure 7.1). The centre of this anomaly is positioned further east in 1980 compared to 1985 (Figure 7.4*c* and *f*), due to greater eastward ridging in 1980 (Figure 7.1). In both years, there is a convergence anomaly south of the subcontinent, which may be associated with decreases in wind speed. This anomaly (west of 25°E) in 1980 is located north of the anomaly in 1985 (Figure 7.4*c* and *f*), in

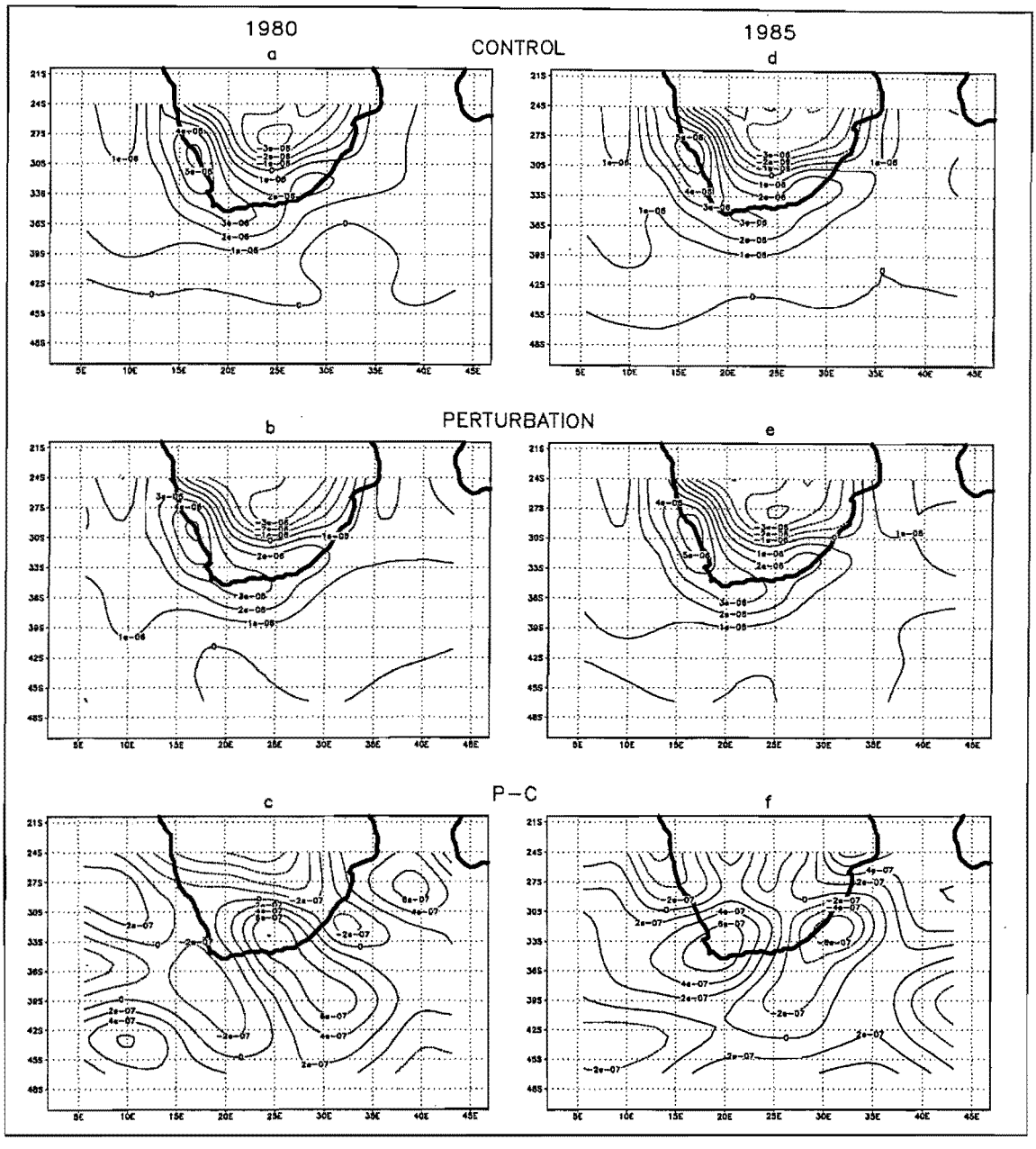

Figure 7.4 Horizontal divergence (s^{-1}) at the 900 hPa level for the controls of *a*) 1980 and *d*) 1985, and the perturbations of *b*) 1980 and *e*) 1985. Maps *c*) and *f*) show the perturbations minus the controls in 1980 and 1985 respectively.

relation to the respective positions of the wind speed decreases in each year (Figure 7.2*c* and *f*). There is also a convergence anomaly on the east coast, in the region of 32°S (Figure 7.4*c* and *f*), which may be due to a combination of reduced wind speeds (Figure 7.2) and increased poleward flow (Figure 7.3).

In both years, there is increased divergence over the south-western Indian Ocean north of 30°S (Figure 7.4*c* and *f*), associated with the increase in sea level pressure (Figure 7.1). This divergence anomaly extends westwards, over the adjacent land, diminishing the convergence that is present in the controls (Figure 7.4). West of the divergence anomaly is a region of increased convergence, near 25°E (Figure 7.4). These changes are associated with the

previously mentioned narrowing of the easterly wave trough (Figure 7.1). To the west of the easterly wave trough there is reduced divergence due to a decrease in the intensity of the trough (Figure 7.1) and a concomitant decrease in wind speeds (Figures 7.2 and 7.3).

Surface convergence is typically associated with the upward motion of air and unstable conditions, whereas the converse is true for surface divergence. Therefore, in summary, over South Africa the changes to the near-surface convergence and divergence fields in response to the perturbation suggest that there is reduced potential for uplift and precipitation over the southern and south-western portion of the country, south of about 30°S, and over the north-eastern regions of the country. Conversely, it appears that there may be an increased potential for uplift and rainfall over the east coast (near 32°S) and over the central interior between about 24°S and 28°S. The surface convergence and divergence patterns may, however, not produce the rainfall result expected if the conditions in the mid/upper troposphere are not suitable. Precipitation usually occurs when surface convergence is coupled with upper atmosphere divergence, whereas clear conditions are associated with surface divergence and upper atmosphere convergence. In addition to changes in convergence and divergence, precipitation changes may be affected by changes in humidity and moisture fluxes. As such, in the following paragraphs, anomalies at the 500 hPa level will be investigated, as well as changes to the moisture and temperature fields in response to the perturbation.

At the 500 hPa level, there is an increase in the geopotential height field over much of the analysis window in both years, especially in the region south-west of the subcontinent (Figure 7.5*b* and *d*). This increase corresponds to the sea level pressure increase associated with the southward extension and intensification of the South Atlantic Anticyclone (Figure 7.1), and as for sea level pressure anomalies, the height changes for 1980 are situated equatorward and slightly east of the 1985 changes. There is, however, a small decrease in the 500 hPa heights over the south-western Indian Ocean (Figure 7.5), which was not evident in the sea level pressure anomalies (Figure 7.1). These changes in the height field result in a decrease in the speed of the 500 hPa wind between about 27°S and 45°S and a slight increase in the wind speed north of this in both years (Figure 7.6*c* and *f*). The decrease in wind speed south of the continent was also found in the 900 hPa wind speed changes, although the upper air decrease extends further north over the land than do the decreases at 900 hPa, which are largely restricted to south of the subcontinent (Figures 7.2 and 7.6). There is also an increase in meridionality south of the subcontinent (Figure 7.6*a*, *b*, *d* and *e*) which is manifest by increased equatorward flow in the v-component of the 500 hPa wind (Figure 7.7). This

change is due to a larger increase in pressures over the south-western portion of the analysis window compared to the south-eastern portion (Figure 7.5).

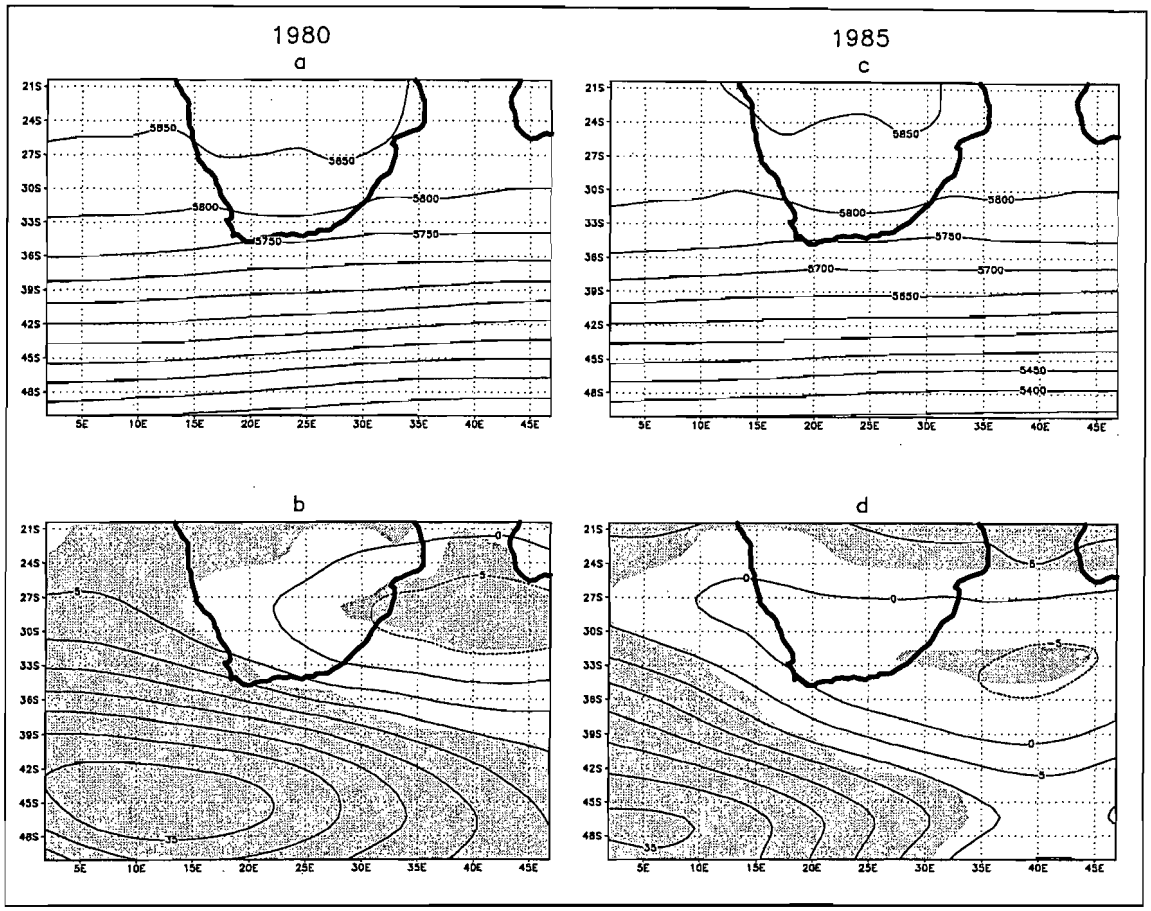

Figure 7.5 500 hPa heights (m) for the controls of *a*) 1980 and *c*) 1985, and the perturbations minus the controls of *b*) 1980 and *d*) 1985. Statistically significant differences at the 95% confidence level have been shaded.

It is clear from the geopotential height and wind fields that the flow at 500 hPa is relatively zonal over the analysis window and as such there are weaker convergence and divergence fields (Figure 7.8) compared to those set up near the surface (Figure 7.4) in both the controls and perturbations. The upper air divergence and convergence patterns differ between the two years in terms of the controls and the anomalies (perturbation minus control), but the perturbations exhibit similar regions of convergence and divergence (Figure 7.8). For example, in 1980 over the south-eastern Atlantic Ocean there is a relatively large convergence anomaly, which causes the divergence field in the control to be replaced by a convergence field in the perturbations (Figure 7.8). Unlike 1980, the control of 1985 already possesses a convergence field over the south-eastern Atlantic, but in the perturbations this field weakens, although there is an increase in convergence near to the west coast of South Africa (Figure 7.8). These changes in both years cause the perturbations to exhibit similar strength convergence fields over the south-eastern Atlantic Ocean (Figure 7.8*b* and *e*), which, coupled with surface divergence (Figure 7.4*b* and *e*), should promote subsiding air and stable

conditions over the Atlantic Ocean in the perturbations. It is interesting to note that if one compares the upper and near-surface fields for the perturbations over the south-western Indian Ocean, then it appears that there is divergence at both levels (Figures 7.4 and 7.8). This suggests that there is weaker subsidence, associated with the high pressure over the south-western Indian Ocean compared to the south-eastern Atlantic Ocean in the perturbations. Over the west coast, north of about 30°S, there is an upper air divergence anomaly in both years (Figure 7.8*c* and *f*), which, coupled with the surface convergence anomaly in this region (Figure 7.4*c* and *f*), may promote increased uplift and possibly more

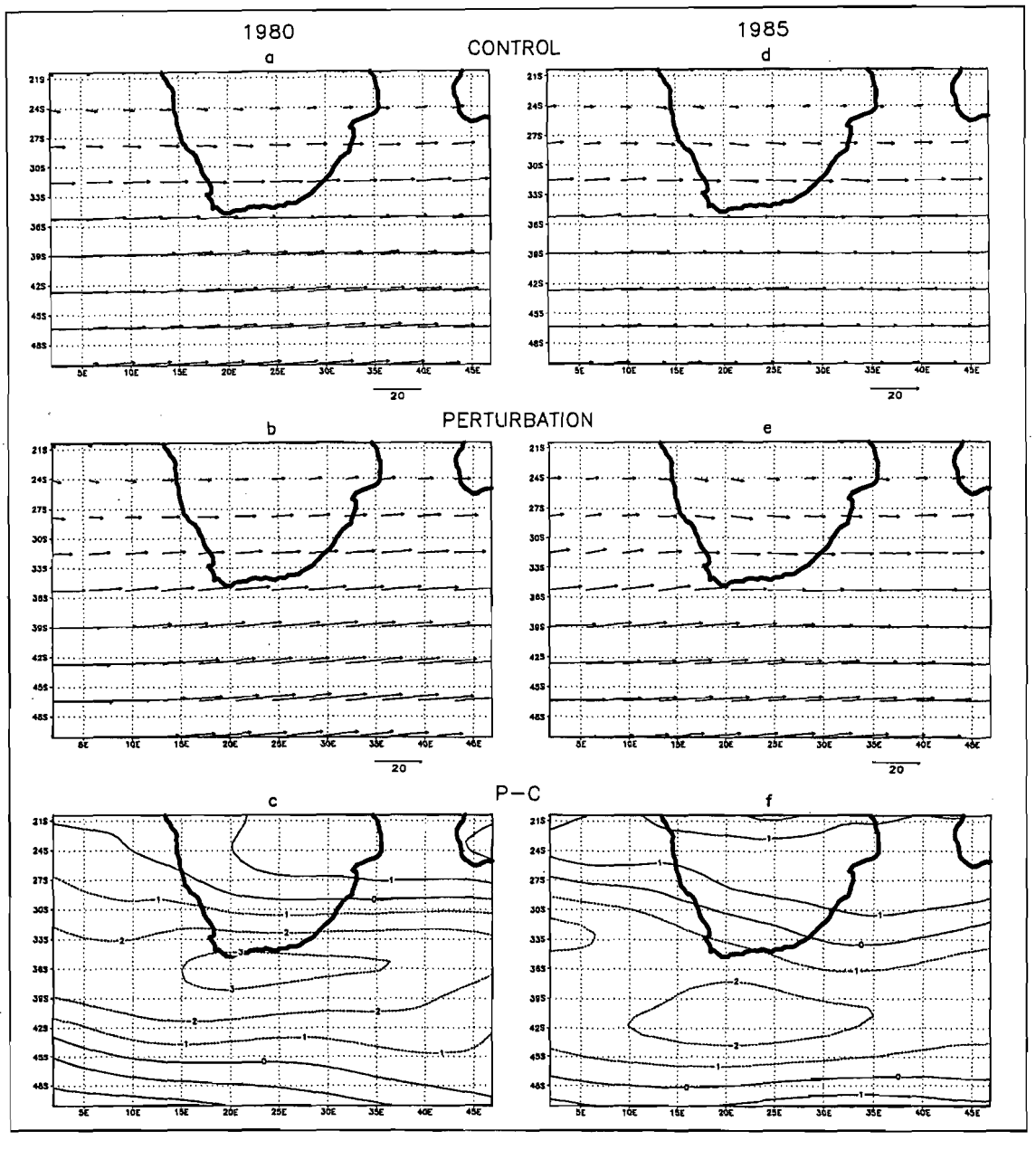

Figure 7.6 500 hPa wind direction and speed (m s^{-1}) for the controls of *a*) 1980 and *d*) 1985, and the perturbations of *b*) 1980 and *e*) 1985. Maps *c*) and *f*) show the change in wind speed between the perturbations and the controls in 1980 and 1985 respectively.

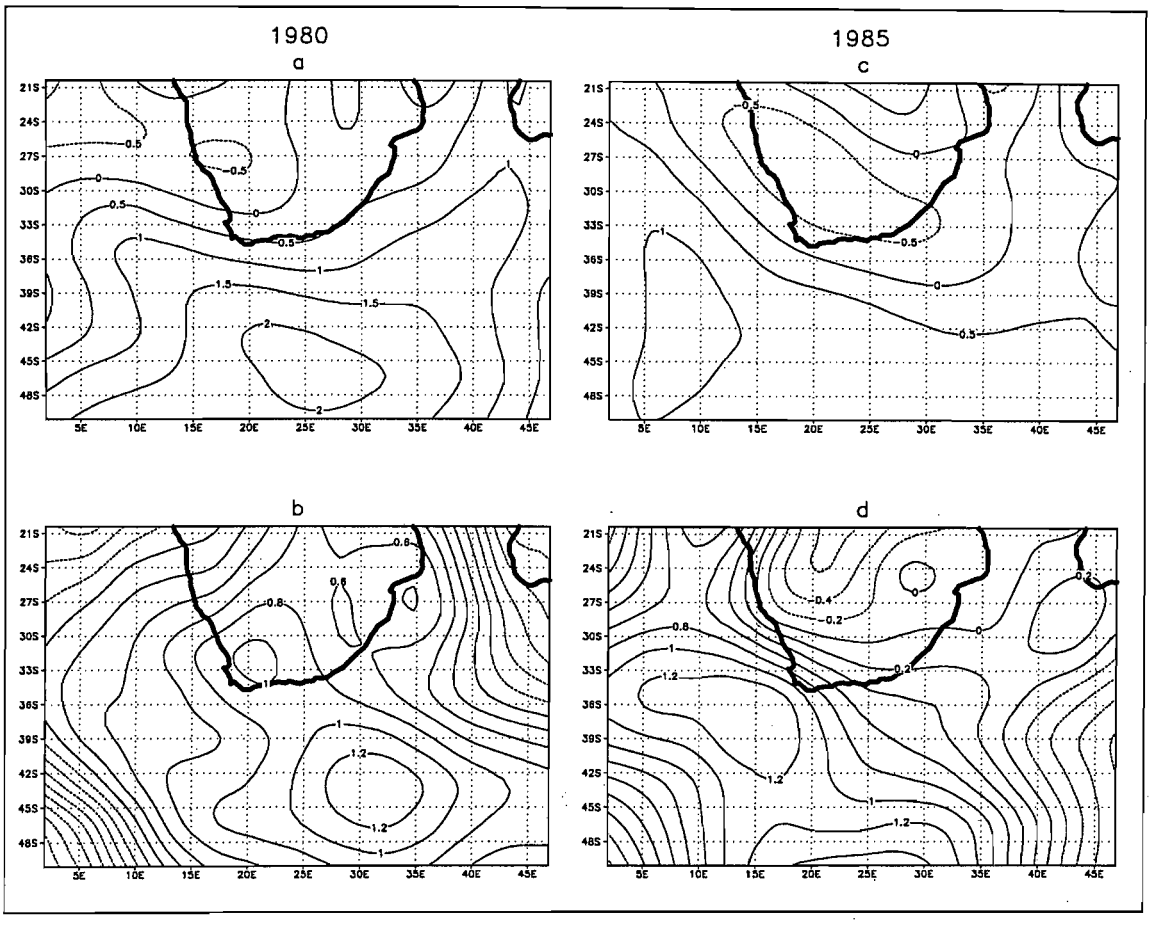

Figure 7.7 Meridional component (v-component) of the 500 hPa wind (m s^{-1}) for the controls of *a*) 1980 and *c*) 1985, and the perturbations minus the controls for *b*) 1980 and *d*) 1985.

rainfall. There is also a divergence anomaly north of 30°S over the eastern half of the land (Figure 7.8*c* and *f*) which overlaps with a surface convergence anomaly between about 25°E and 30°E (Figure 7.4*c* and *f*) and may result in increased precipitation in this region in response to the perturbation. Most of the other anomaly patterns of upper air convergence and divergence are contrasting between the two years. Since the magnitude of the control and perturbation 500 hPa level convergence and divergence is small relative to near the surface, these mid-tropospheric fields probably exert a smaller controlling effect on resulting mean precipitation. On a daily time scale, however, the position of the convergence and divergence patterns at the 500 hPa level may be more variable than the surface patterns, which could contribute to the small seasonal average for the mid-troposphere. Thus, the results do not negate the important influence which upper atmosphere convergence and divergence may play over shorter time scales.

Surface temperature changes in response to the perturbation are small, but there does seem to be an indication of slightly warmer temperatures over the west coast and cooler temperatures

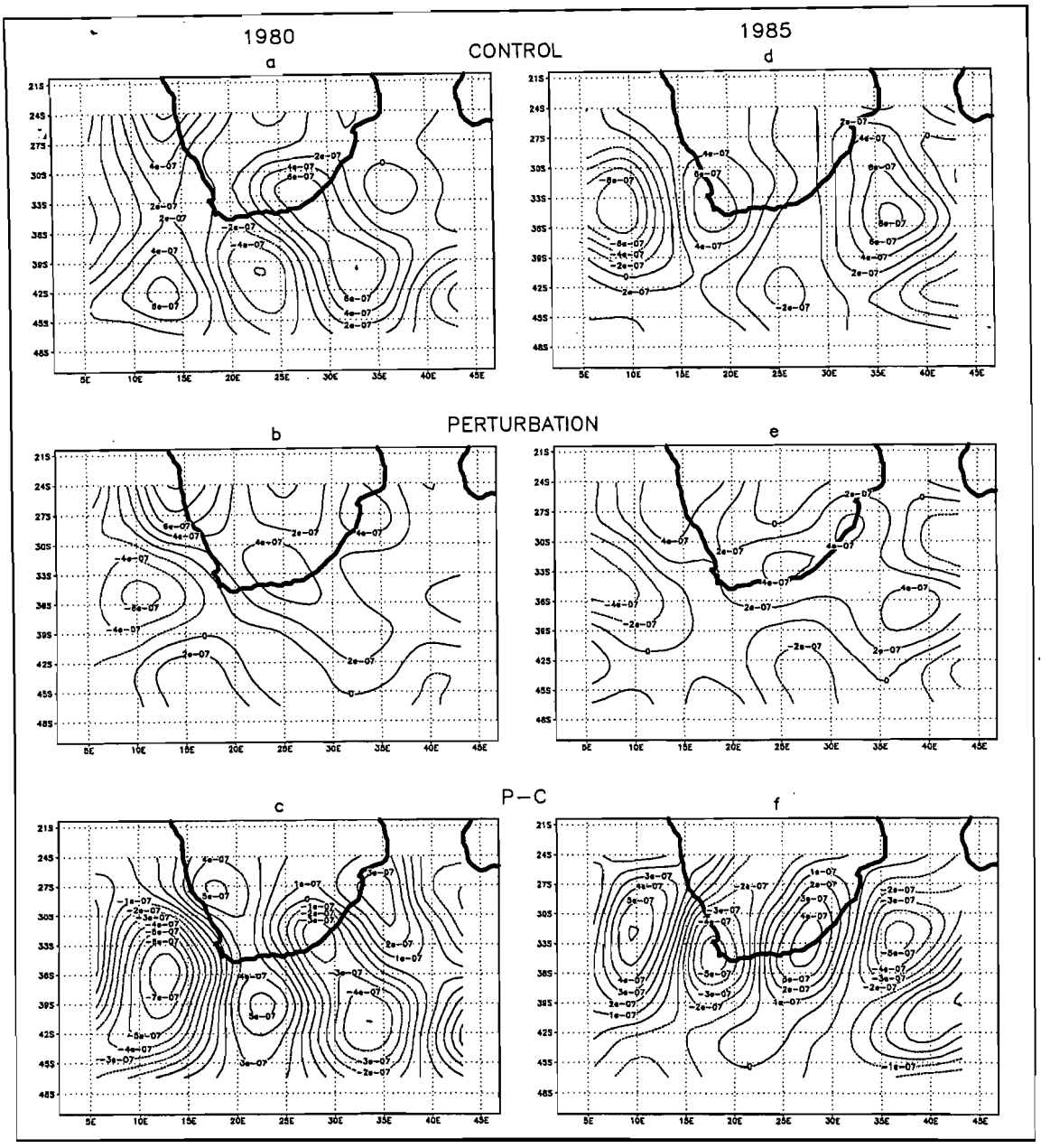

Figure 7.8 Horizontal divergence (s^{-1}) at the 500 hPa level for the controls of *a*) 1980 and *d*) 1985, and the perturbations of *b*) 1980 and *e*) 1985. Maps *c*) and *f*) show the perturbations minus the controls in 1980 and 1985 respectively.

over the east coast in the perturbations (Figure 7.9). There is also a general increase in temperatures south of 42°S in both years (Figure 7.9), which may be due to increased adiabatic warming caused by the increase in pressures in this region (Figures 7.1 and 7.5). There are also differences in the temperature response between the two years, for example in 1980 there are temperature increases over the western interior, whereas there are decreases in 1985. The 500 hPa temperature changes (Figure 7.10) largely correspond to the geopotential height changes (Figure 7.5), such that there is an increase in temperatures over the south-western half of the analysis window and a decrease over the south-western Indian Ocean and adjacent land. These anomalies may suggest an increase in subsidence and adiabatic warming south and south-west of the subcontinent, and an increase in uplift over regions of the Indian

Ocean and subcontinent, although there is not a corresponding decrease in sea level pressure in the latter regions. In addition, the 500 hPa temperature decreases may be associated with an increase in the equatorward movement of the air, evident over much of the analysis window (Figure 7.7), thus causing cooler air to be advected over the southern portion of the land. Although the southern section of the analysis window is also associated with increased equatorward flow, the effects of adiabatic changes, which would cause a temperature increase, probably override the marginally increased influx of cooler air.

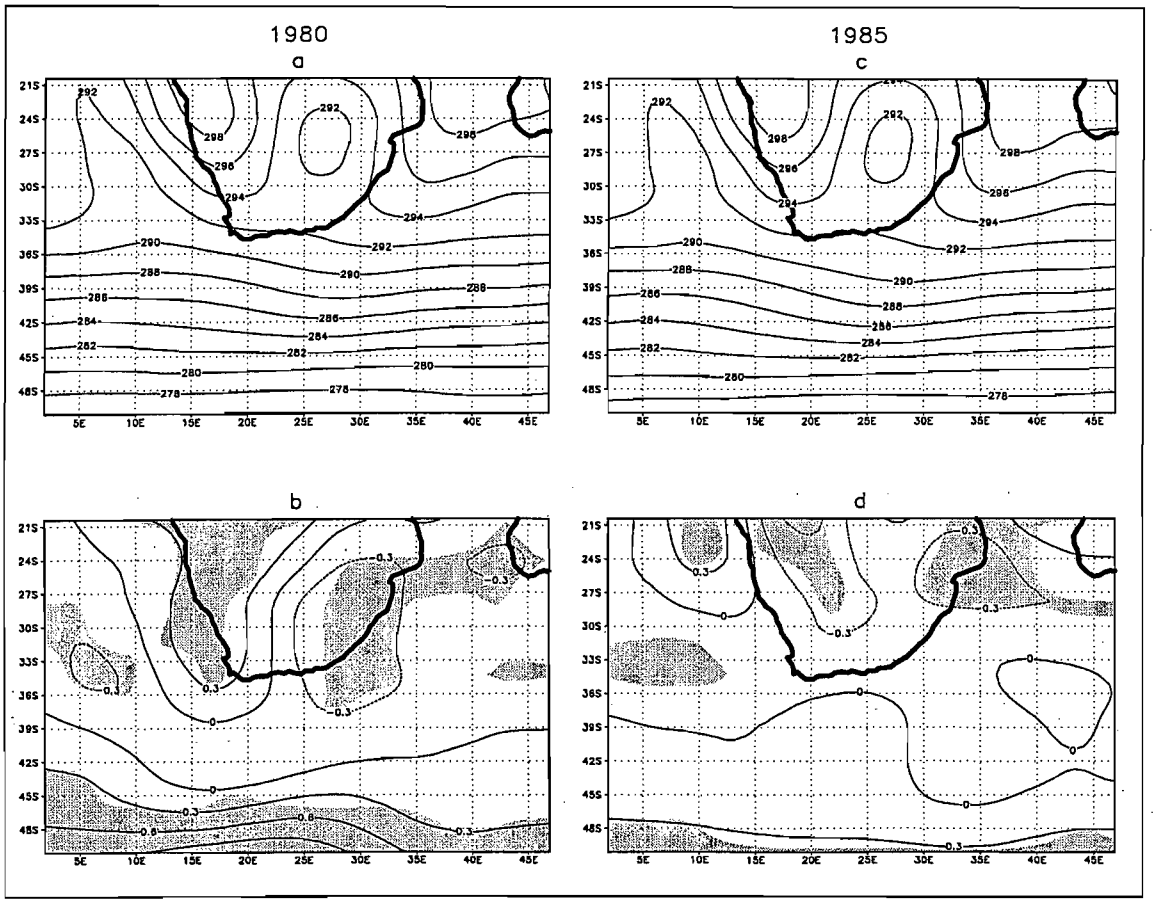

Figure 7.9 Surface temperature (K) for the controls of *a*) 1980 and *c*) 1985, and the perturbations minus the controls of *b*) 1980 and *d*) 1985. Statistically significant differences at the 95% confidence level have been shaded.

Specific humidity changes in response to the perturbation are small, both at the surface (Figure 7.11) and 500 hPa level (Figure 7.12) and although there are inconsistencies between the two years, there are some similarities. At the surface, there are small humidity increases over the tropical Atlantic Ocean and decreases over the south-western Indian Ocean in both years (Figure 7.11). Over the land there are some contrasting patterns of change, but both years show a slight decrease in humidities over the north-eastern portion of the subcontinent. At the 500 hPa level there is a general decrease in specific humidity over South Africa south of about 25°S, as well as decreases over the adjacent oceans extending down to about 40°S (Figure 7.12). In both years there are increases in humidity south of 40°S and in certain

regions of the tropics e.g. the southern Mozambique Channel (Figure 7.12). It is not clear whether these changes in specific humidity at both levels are climatically significant.

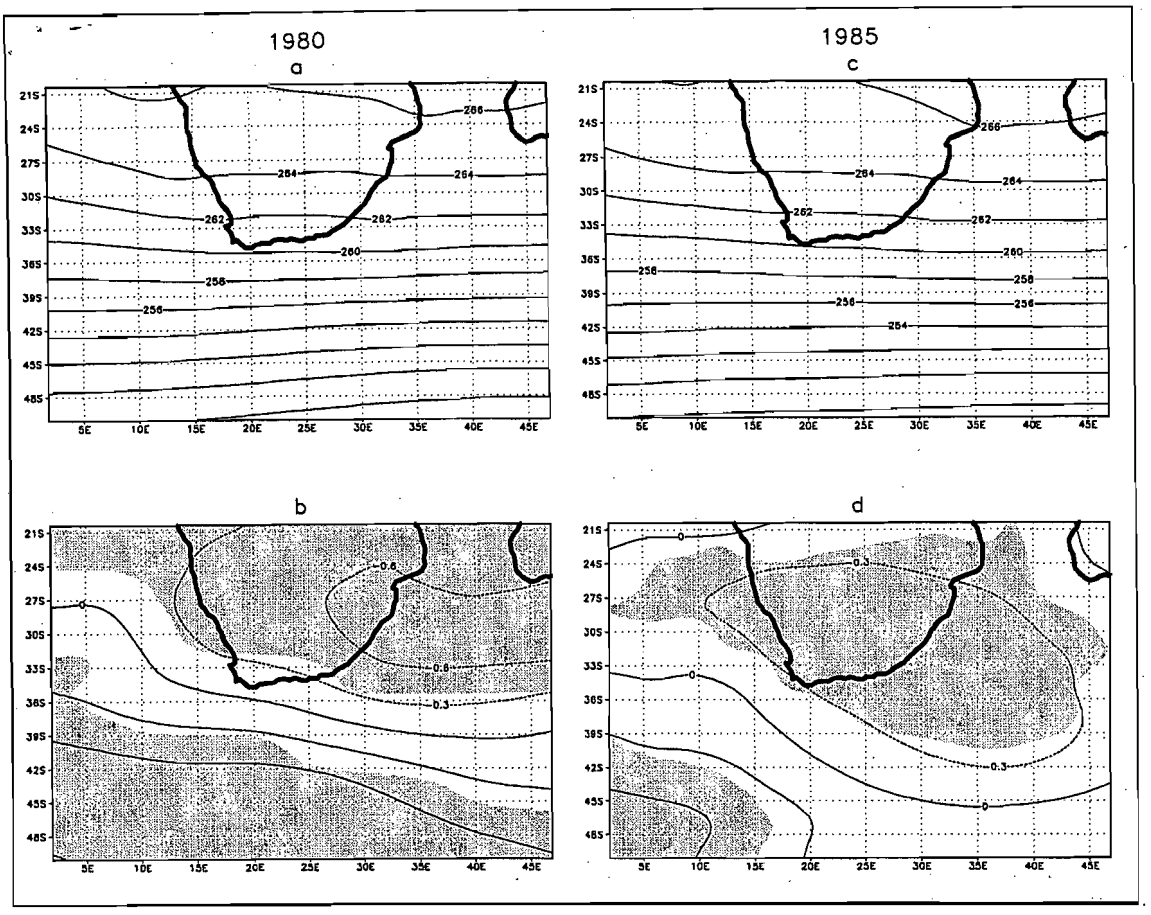

Figure 7.10 500 hPa level temperature (K) for the controls of *a*) 1980 and *c*) 1985, and the perturbations minus the controls of *b*) 1980 and *d*) 1985. Statistically significant differences at the 95% confidence level have been shaded.

Lastly, the moisture flux at the 700 hPa level has been examined and is shown in Figure 7.13 for the controls and perturbations. The moisture flux essentially reflects the circulation, since the calculation of the flux involves the wind field being weighted by specific humidity values. As such, changes in the magnitude of the flux in response to the perturbation (Figure 7.13*c* and *f*) largely mirrors changes in the speed of the 700 hPa wind (not shown). A westerly moisture flux in the midlatitudes is partially associated with the polar borders of the subtropical anticyclones (Peixoto and Oort, 1992). Therefore, with the southward extension of the South Atlantic Anticyclone in the present study (Figure 7.1), one might expect a decrease in the moisture flux in the region where the southern border of the anticyclone is located in the controls, and an increase in the flux further south. Along with the wind speed changes, this may account for some of the flux anomalies south of the subcontinent. In both years, there is an increase in the moisture flux over South Africa, between about 24°S and 30°S, and a decrease south of this in 1980 (Figure 7.13*c* and *f*). In 1985 the decrease is largely restricted to the southern and western portion of the country (Figure 7.13*c* and *f*). The

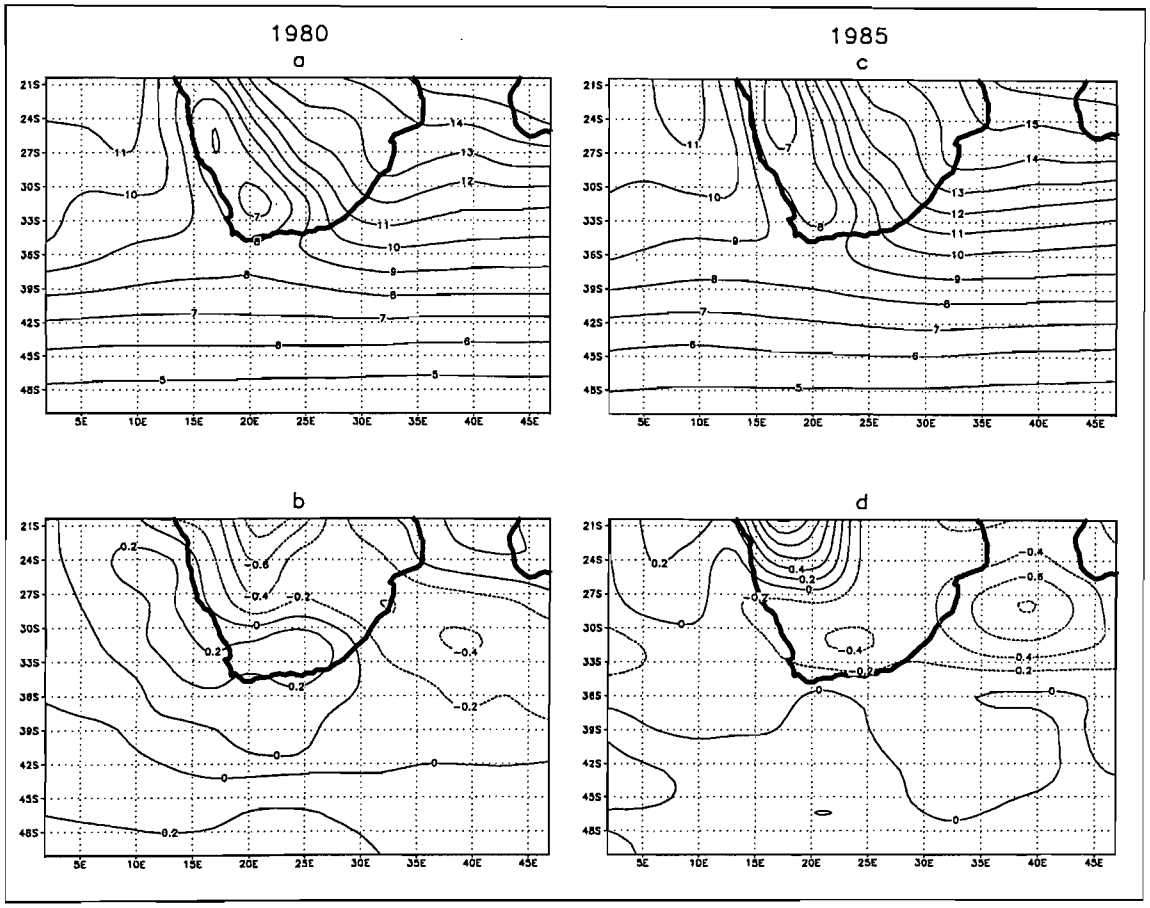

Figure 7.11 Surface specific humidity (g kg^{-1}) for the controls of *a*) 1980 and *c*) 1985, and the perturbations minus the controls of *b*) 1980 and *d*) 1985.

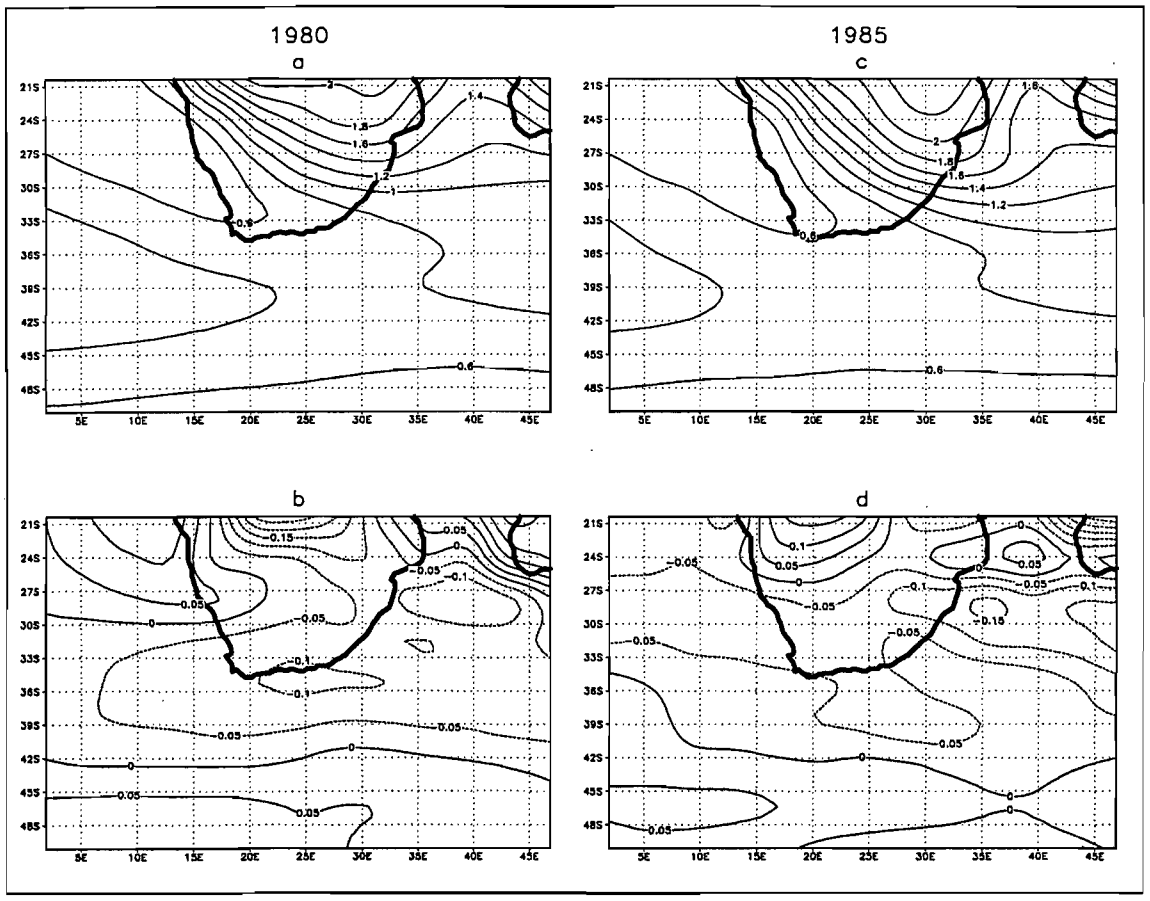

Figure 7.12 500 hPa level specific humidity (g kg^{-1}) for the controls of *a*) 1980 and *c*) 1985, and the perturbations minus the controls of *b*) 1980 and *d*) 1985.

difference in the positioning of the anomalies between the two years has the effect of producing very similar moisture fluxes in the perturbations (Figure 7.13*b* and *e*), since the moisture fluxes in the controls are quite different (Figure 7.13*a* and *d*). In the controls, 1980 is associated with larger moisture fluxes over the southern portion of the subcontinent compared to 1985 (south of about 27°S), but weaker fluxes north of this latitude (Figure 7.13*a* and *d*). These results suggest that the sea-ice and SST perturbation has forced the moisture flux circulation over southern Africa to a more similar state in the perturbation simulations between the two years than exists between the control simulations of the two years.

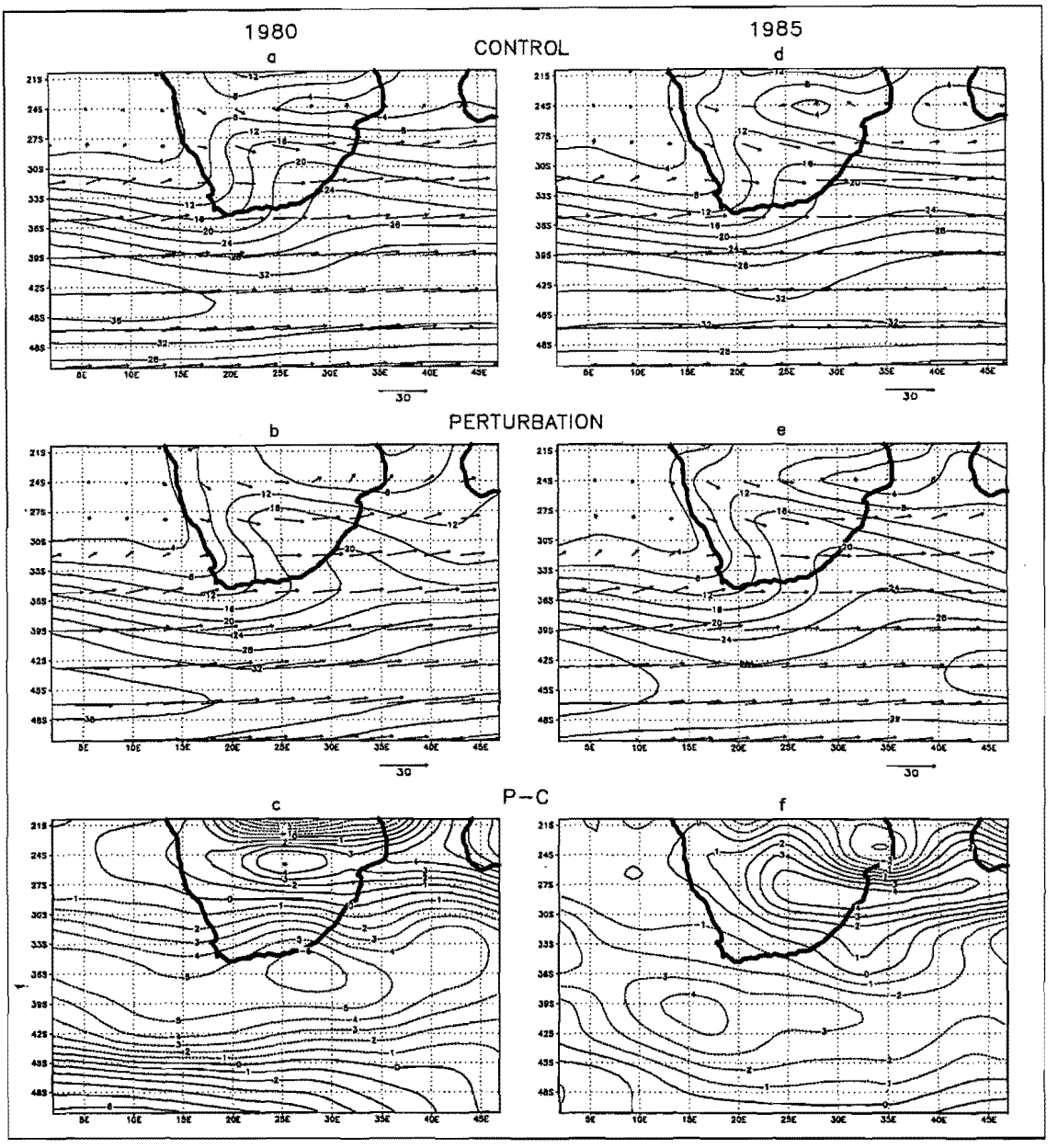

Figure 7.13 The direction and magnitude of the moisture flux (g kg^{-1} m s^{-1}) at the 700 hPa level for the controls of *a*) 1980 and *d*) 1985, and the perturbations of *b*) 1980 and *e*) 1985. Maps *c*) and *f*) show the change in the magnitude of the moisture flux between the perturbations and the controls in 1980 and 1985 respectively.

It appears that, in general, the moisture flux anomalies at the 700 hPa level complement the suggested potential changes in precipitation based on the convergence and divergence anomalies at 900 hPa. As previously mentioned, there is a general increase in near-surface divergence over the southern and south-western portion of the country, south of about 30°S (Figure 7.4), which is coupled to a general decrease in the 700 hPa moisture flux (Figure 7.13), suggesting a reduced potential for precipitation over this region. On the other hand, there is a general increase in near-surface convergence between about 24°S and 28°S (Figure 7.4), which is coupled to an increase in the 700 hPa moisture flux (Figure 7.13), suggesting an increased potential for precipitation over this region. These implied changes to precipitation over southern Africa, in response to the imposed SST and sea-ice perturbation, will be tested later in the chapter.

7.3 Twice-Daily Circulation at Sea Level

A Self-Organising Map, described in Chapter 3, is used to classify the twice-daily sea level pressure data over the southern African window into circulation types, in order to examine whether there is a difference in the frequency of types simulated by the control and perturbation experiments. This SOM technique allows a more detailed analysis of the circulation changes in response to the perturbation than is permitted from the examination of seasonal mean changes. Non-standardised twice-daily sea level pressure data corresponding to the 6 summer controls of 1980 and 1985 (total t=1080) were used to train the SOM. The SOM comprises 15 nodes (3 in the x-direction and 5 in the y-direction) in a rectangular topology and the weights of the nodes were initialised using linear initialisation. Training was run for a total of 30000 iterations and the initial learning rate and training radius were set to 0.05 and three respectively. The weights associated with each node of the trained SOM are presented on the meta-map in Figure 7.14.

The trained SOM was then separately presented with twice-daily data associated with the controls of 1980, the controls of 1985, the perturbations of 1980 and the perturbations of 1985. The percentage of time steps which mapped to each node are shown in Figure 7.15 for the controls and perturbations of each year. The nodes will be referred to by their numbers as shown on the meta-map (Figure 7.14) and the reader is reminded that the grids portrayed on Figure 7.15 correspond to the meta-map of nodes, e.g. the top right-hand grid block represents node number 1.

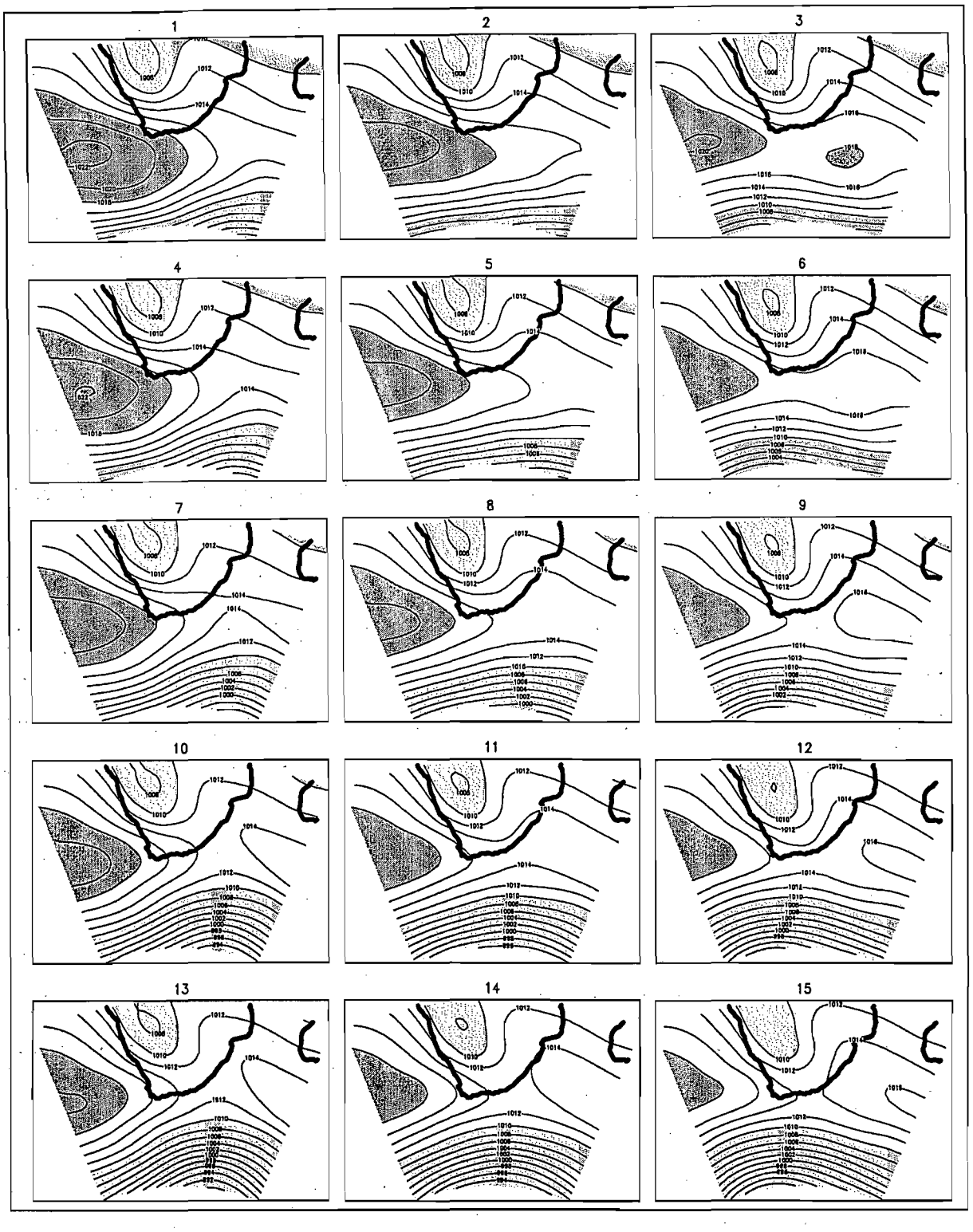

Figure 7.14 The meta-map for the SOM showing the 15 nodes (3×5) with their contoured weights. The weights represent sea level pressure, and values greater than 1018 hPa and less than 1010 hPa have been shaded.

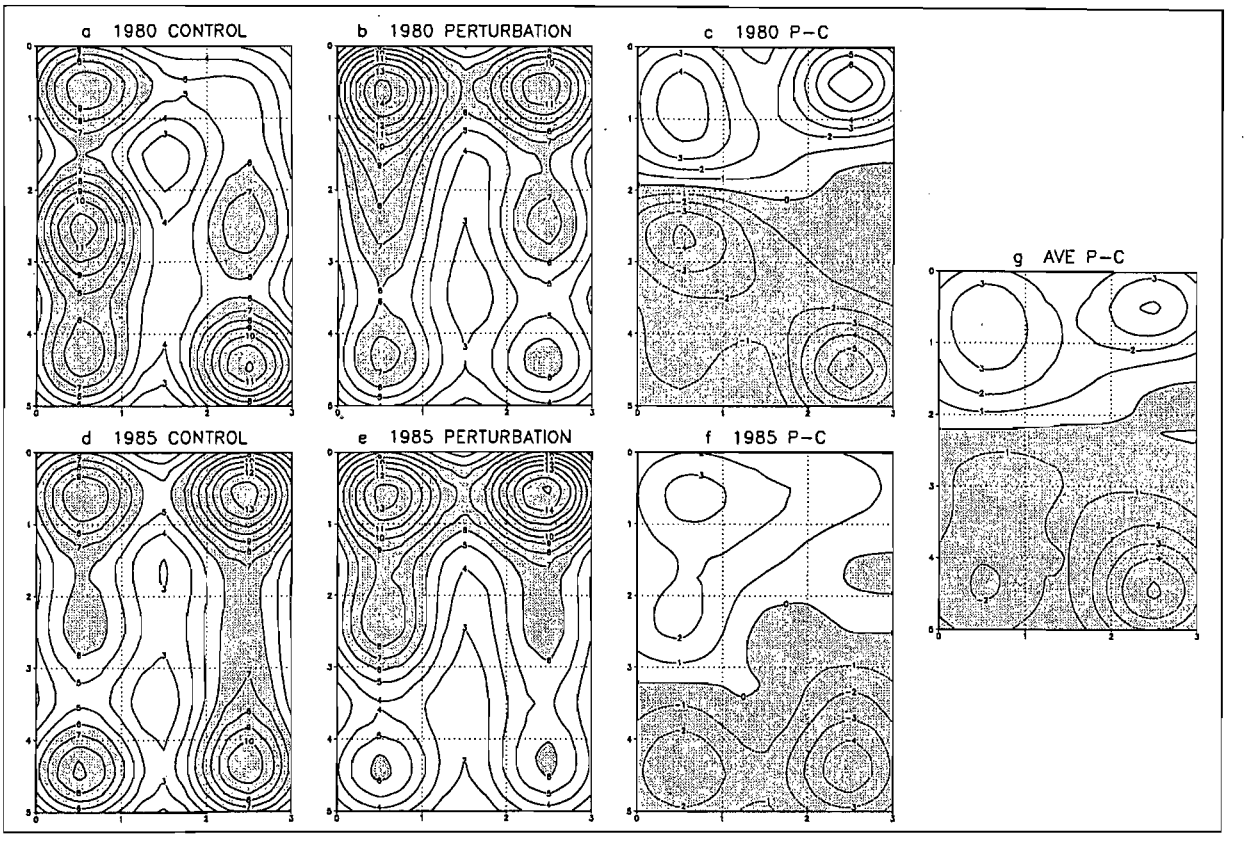

Figure 7.15 The percentage of days mapping to each node of the meta-map (Figure 7.14) for the controls of *a*) 1980 and *d*) 1985 and the perturbations of *b*) 1980 and *e*) 1985. Plots *c*) and *f*) show the difference between the controls and perturbations (perturbation minus control) in terms of the percentage of days mapping to each node in 1980 and 1985 respectively. Plot *g*) represents the average between the plots on *c*) and *f*), i.e. showing the average response between 1980 and 1985.

An examination of the change in the frequency of mappings to each node in response to the perturbation, suggest that in both years there is a decrease in the representation of the nodes falling in the lower half of the meta-map and an increase in the representation of the nodes near the top of the meta-map (Figure 7.15*c*, *f* and *g*). The distribution of mappings in the perturbation simulations clearly show a leaning towards node numbers 1 and 3, at the top of the meta-map, in comparison to the other nodes (Figure 7.15*b* and *e*). 1980 and 1985 exhibit a common increase in the representation of node number 1 and a common decrease in the representation of node number 15 in response to the imposed perturbation (Figure 7.15*c* and *f*). These two nodes represent extremes of the synoptic types portrayed. It is evident that as one moves from the top to the bottom of the meta-map there are a number of changes in the circulation characteristics of the types, which can be summarised as follows:

Moving from the top to the bottom of the meta-map

- the South Atlantic Anticyclone weakens and extends less into the midlatitudes.
- eastward ridging of the South Atlantic Anticyclone decreases.
- the midlatitude westerly wave intensifies and extends further north.
- the tropical easterly wave trough weakens.

- over the Indian Ocean, circulation associated with the South Indian Anticyclone becomes more apparent, while circulation associated with the tropical easterly wave becomes less apparent.

Related to the last point, the high pressures over the south-western Indian Ocean for the nodes at the top of the meta-map, appear to be associated with the eastward extension and ridging of the South Atlantic Anticyclone into the Indian Ocean region, rather than being associated with the South Indian Anticyclone. The above list essentially describes the characteristics of those types which experience a reduction in representation in response to the perturbation, since there is a decrease in representation of the types at the bottom of the meta-map (Figure 7.15*g*). The perturbation therefore favours those circulation types (e.g. nodes 1, 2 and 3) which exhibit a strong and dominant South Atlantic Anticyclone which extends fairly far south and displaces the midlatitude westerly wave (Figure 7.14). The high pressure shows a strong tendency to ridge eastward and to the south of the continent, with extended ridging into the Indian Ocean. A ridging anticyclone is usually associated with clear and hot weather over the South Western Cape region, often with strong south easterly winds, therefore an increase in ridging could cause an increase in aridity over this region. In contrast, it can also cause uplift and possible rainfall over the eastern and plateau regions of South Africa, due to a combination of weakening inland pressure gradients, changing curvature of the flow and mesoscale orographic forcing (Preston-Whyte and Tyson, 1988).

The circulation types which are favoured also exhibit sea level circulation patterns over the south-western Indian Ocean which are more characteristic of the tropical easterly wave than the closed cell of a predominant South Indian Anticyclone, suggesting that the centre of South Indian Anticyclone may be located further east in the synoptic types that are favoured. In terms of the easterly wave circulation, the synoptic types near the top of the meta-map possess lower pressures in the northern-most tropical zone of the analysis window, in comparison to the nodes closer to the bottom of the meta-map. This, together with the westerly wave and anticyclone changes, suggest that the circulation patterns are shifted southwards in the types that experience increased representation compared to those that experience decreased representation. The frequency changes also suggest that circulation types with deeper easterly wave troughs may be favoured over those with weaker troughs (Figures 7.14 and 7.15). This has implications for rainfall, since easterly waves are a major source of summer precipitation over the interior and eastern regions of South Africa. It has also been recognised that it is largely the occurrence of these rains that distinguish abnormally

wet years from dry years (Preston-Whyte and Tyson, 1988). The potential decrease in pressures over the northern section of the analysis window in response to the perturbation, including the deepening of the easterly wave trough, is not evident in the seasonal mean change (Figure 7.1), which instead suggests a small pressure increase over the region.

The change in the frequency of synoptic types simulated in the perturbations compared to the control simulations will be used to interpret the precipitation anomalies that are determined in the following section.

7.4 Precipitation Changes

In the downscaling procedure, described in Chapter 3, an artificial neural network (ANN) is used to obtain a relationship between a set of atmospheric predictors and local-scale precipitation. The atmospheric predictors comprise geopotential heights, temperature and specific humidity at the 500 and 700 hPa levels, as well as surface specific humidity. A lag (36 hours) and a lead (12 hours) of these variables are also included, together with the synoptic state indices derived from the SOM procedure (refer to Chapter 3).

During the training procedure, the ANN derives a relationship between the input NCEP/NCAR assimilation atmospheric predictors (interpolated to the GENESIS GCM T31 grid) and the target CCWR area averaged precipitation station data (presented on a 0.5° grid). The training has been performed using twice-daily data from the summer months (DJF) in the period extending from January 1980 to December 1988. Training has been executed separately for each target grid cell, but has only been performed for those grid cells for which there is sufficient target precipitation data from the CCWR data set. It was decided that if a grid point had less than 365 days of precipitation data in the extracted summer months, then there was too much missing data for a meaningful training process and the grid point was discarded from the analysis. For this reason, the precipitation results extend over a much smaller region of the subcontinent, essentially only portions of South Africa, compared to the results from the other atmospheric variables shown in this chapter.

The maps on Figure 7.16 are an indication of the validity of the downscaling procedure and show the difference between the downscaled precipitation derived from the NCEP/NCAR reanalysis atmospheric predictors and the actual recorded precipitation from the CCWR area averaged station data set. It is clear that the downscaled precipitation is an accurate representation of the observed pattern of precipitation, although the downscaling procedure

does show a tendency to derive too much precipitation, especially over the north-east coast of South Africa (south of Swaziland). In most regions there is less than a 0.6 mm day^{-1} difference between the downscaled and actual precipitation. Thus, in terms of the seasonal mean, the ANN downscaling functions are capable of adequately reproducing observed precipitation and may be deemed valid for use with the GCM data.

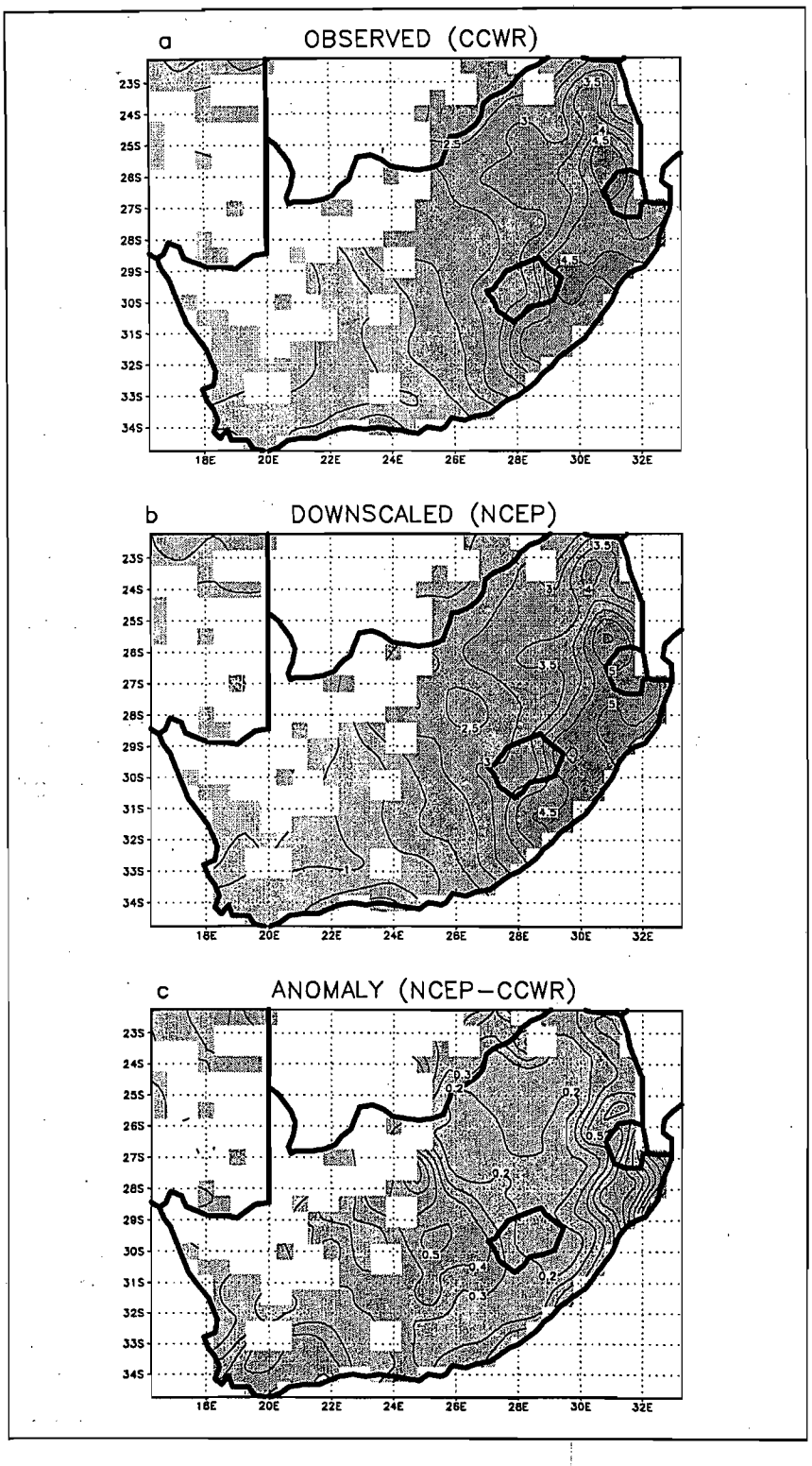

Figure 7.16 The *a*) observed CCWR area averaged precipitation station data, the *b*) precipitation data downscaled from the NCEP/NCAR reanalysis atmospheric predictor variables, and the *c*) downscaled precipitation minus the observed precipitation (*b* minus *c*), for DJF and averaged over the period 1980 to 1988. Precipitation is given in mm day^{-1}.

The same atmospheric predictor variables, mentioned above, have been extracted from the 1980 and 1985 control and perturbation simulation data from the GENESIS GCM and applied to the trained ANN in order to derive precipitation. The twice-daily data from the three replicates associated with each time period have been concatenated together for the control and perturbation of 1980 and 1985 respectively to produce the input data for the ANN. Figure 7.17 shows the summer (DJF) seasonal average (calculated for the period of 1980 to 1988) of CCWR observed precipitation (also shown in Figure 7.16*a*) and the 1980

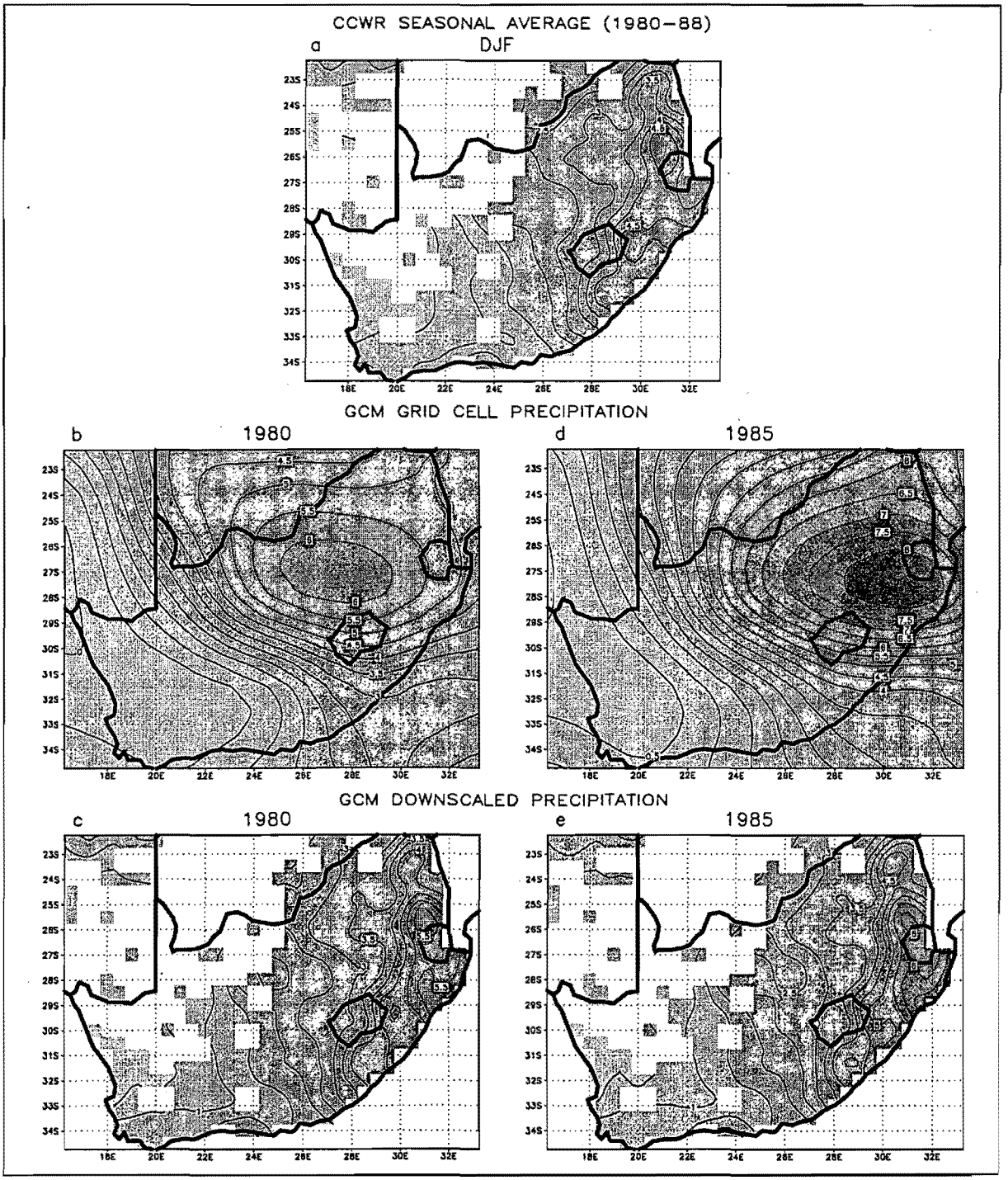

Figure 7.17 The *a*) seasonally averaged observed CCWR precipitation (identical to Figure 7.16*a*), the GCM control simulation *grid cell* precipitation output by the model in the summers of *b*) 1980 and *d*) 1985 respectively, and the GCM control simulation *downscaled* precipitation for the summers of *c*) 1980 and *e*) 1985 respectively. Precipitation is given in mm day^{-1}.

and 1985 control simulation summer grid cell precipitation output by the model, as well as the downscaled precipitation derived from the GCM atmospheric predictor variables. It is clear that the pattern and magnitude of the GCM downscaled precipitation (Figure 7.17*c* and *e*) is very similar to what is observed (Figure 7.17*a*) and is a vast improvement over the GCM grid cell precipitation (Figure 7.17*b* and *d*). The GCM grid cell precipitation does not capture the detailed spatial patterns and steep gradients observed over South Africa and the magnitude of precipitation is too large in the model (Figure 7.17*a*, *b* and *d*). In contrast, the downscaled precipitation derived from the atmospheric predictor variables from the model is much more realistic (Figure 7.17*a*, *c* and *e*). It does appear, however, that the magnitude of GCM downscaled precipitation is generally slightly larger than the CCWR observed precipitation (Figure 7.17*a*). Although an artifact of the downscaling procedure is to produce slightly wetter conditions than observed (refer to the above paragraph), the magnitude of GCM downscaled precipitation also appears to be slightly larger than the downscaled NCEP/NCAR reanalysis precipitation over the eastern half of the country (Figure 7.16*b*), suggesting that the GCM circulation (as defined by the atmospheric predictors) may be biased so as to produce conditions which are marginally too wet over this region. This precipitation bias is, however, significantly less than that of the GCM grid cell precipitation (Figure 7.17*b* and *d*). These results highlight the potential use of downscaling as a viable technique to overcome the inadequacies of GCM precipitation output at the regional scale. For a more complete discussion on the differences between GENESIS GCM grid cell precipitation and downscaled precipitation the reader is referred to Hewitson (1998).

Figure 7.18 shows the downscaled precipitation fields for the perturbation simulations, as well as the difference between the control and perturbation fields. In 1980 and 1985 it is evident that there is a common decrease in precipitation over the north-east coast of South Africa, between about 26°S and 29°S, and an increase in precipitation in the same general latitude band but over the central region of the country (north-west of Lesotho) (Figure 7.18*b* and *d*). In both cases the precipitation anomalies are small, but one would not have expected large changes to result from the spatially remote sea-ice and SST perturbation. It is not so much the magnitude of change which is important, since this will vary based on the size of the imposed perturbation, but rather the pattern and cohesiveness of the response and whether there is a plausible physical explanation for the precipitation changes.

The examination of the near-surface atmospheric fields earlier in this chapter did indeed suggest that there may be a reduced potential for uplift and rainfall over the north-eastern

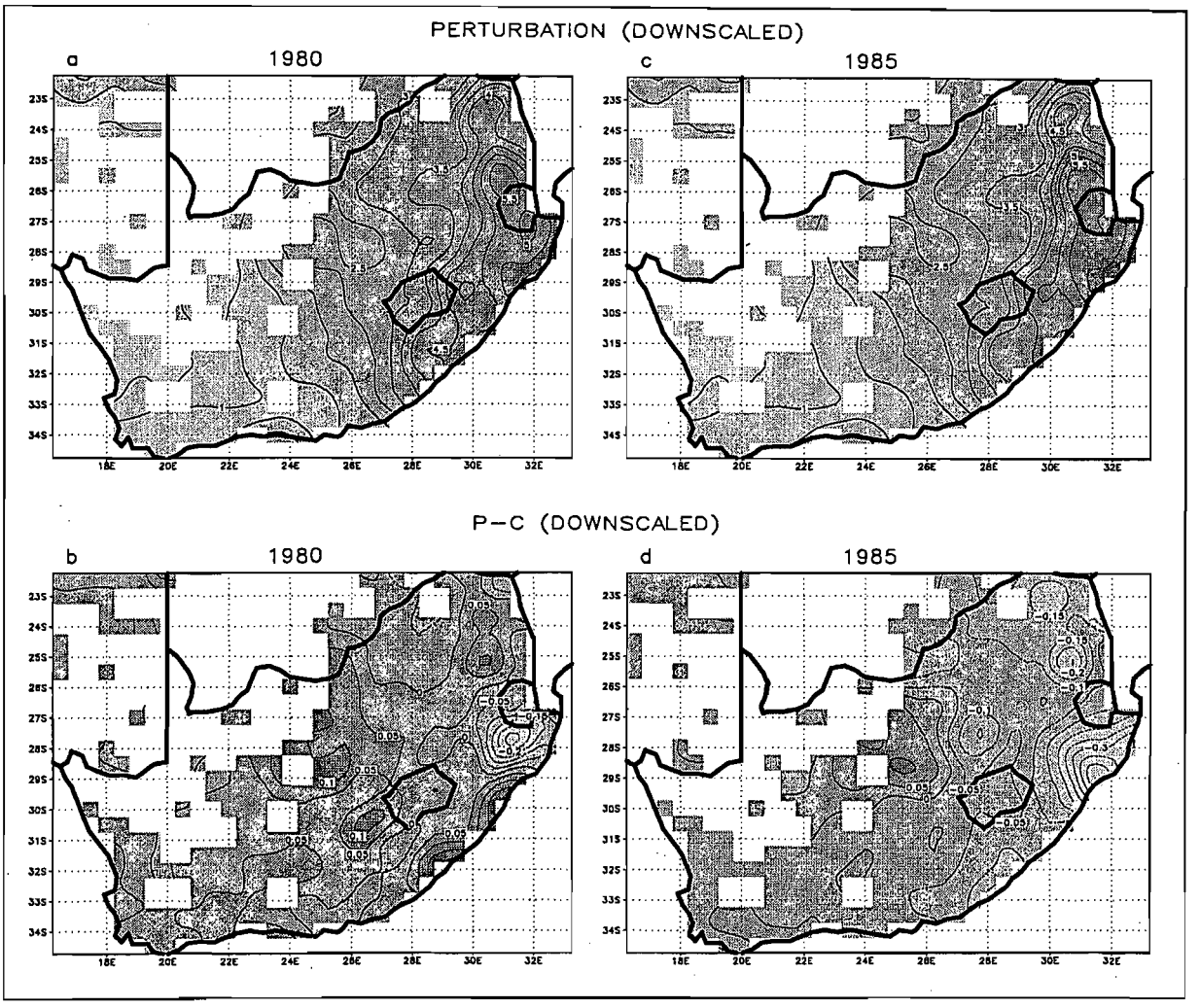

Figure 7.18 The GCM perturbation simulation *downscaled* precipitation for the summers of *a*) 1980 and *c*) 1985 respectively, and the perturbation simulation *downscaled* precipitation minus the control simulation *downscaled* precipitation (see Figure 7.17*c* and *e*) for the summers of *b*) 1980 and *d*) 1985 respectively. Precipitation is given in mm day^{-1}.

regions of the country and an increased potential for uplift and rainfall over the central interior between about 24°S and 28°S. The changes to the sea level pressure field (Figure 7.1) in response to the perturbation showed an increase in pressure over the north-east coast of South Africa, manifest by a strengthening of the ridge of the easterly wave. This pressure change also resulted in a narrowing (from the east) of the easterly wave trough, causing greater meridionality of the tropical wave over the interior of South Africa in the vicinity of 25°E, thus coinciding with the recorded precipitation increase in both years (Figure 7.18*b* and *d*). Associated with the narrowing of the easterly wave trough, there was an increase in the northerly component of the wind (Figure 7.3) and increased low level convergence over the central interior (Figure 7.4). In an easterly wave, rainfall occurs to the east of the trough line where surface convergence is strongest and there are winds of a northerly component. Accompanying upper level divergence is, however, also important for producing sustained and strong vertical uplift of air. At the 500 hPa level there was increased divergence north of

30°S over the eastern half of the land in the perturbations (Figure 7.8), which overlaps with the recorded surface convergence anomaly, thus corresponding to the increase in precipitation over the central interior (Figure 7.18*b* and *d*).

The precipitation decrease over the north-east coast of South Africa is associated with an increase in pressure over the south-western Indian Ocean and adjacent land (Figure 7.1). This pressure change resulted in an increase in near surface divergence over the ocean north of about 30°S, which extended westwards over the land, diminishing the convergence present in the controls (Figure 7.4). This divergence anomaly extended further inland in 1985 compared to 1980 (Figure 7.4), which may account for the more extensive decrease in precipitation over the eastern regions of South Africa north of 30°S in 1985 (Figure 7.18).

This preliminary study suggests that an Antarctic sea-ice and SST anomaly has the potential to alter circulation patterns and precipitation over the South African region. The precipitation changes obtained in the present study are small, but the similar and physically plausible nature of the response in 1980 and 1985 lends credence to the results, which imply that a reduction in Antarctic sea-ice extent could cause an increase in summer rainfall over the central interior, and a decrease in rainfall over the north-east coast of South Africa. A larger perturbation than that imposed in the present study may elicit a larger precipitation response over South Africa than is seen in these results.

7.5 Summary

This chapter has considered the atmospheric response to the sea-ice and SST perturbation over the South African region. The mean response of a number of variables has been considered, as well as possible changes in the frequency of circulation types simulated over the region. In order to investigate precipitation changes, the technique of downscaling has been used. This is an empirical process which derives regional precipitation fields (on a 0.5° grid) from the GCM circulation data over South Africa. The pattern and magnitude of the GCM downscaled precipitation is very similar to what is observed and is a vast improvement over the GCM grid cell precipitation output by the model. The results support the use of downscaled precipitation fields rather than GCM grid cell precipitation.

The major findings which are common to both 1980 and 1985 are summarised as follows:

In response to the Antarctic sea-ice reduction and warming of the ice-free waters there is

- a southward extension and intensification of the South Atlantic and South Indian Anticyclones.

- an increase in the representation of days with a strong and dominant South Atlantic Anticyclone which extends fairly far south and displaces the midlatitude westerly wave. As such, there are fewer days with a deep midlatitude westerly wave over the analysis window.

- a narrowing of the easterly wave trough over the interior of the country, producing greater meridionality of the flow in the region around 25°E.

- an increase in near surface divergence over the south-eastern Atlantic Ocean, southern portion of the country (generally south of 30°S) and Indian Ocean north of 30°S. The divergence anomaly over the Indian Ocean extends westwards over the land, diminishing the surface convergence present in the controls over the north-east coast of South Africa.

- an increase in near surface convergence over the central interior of the country (around 25°E) north of 30°S.

- an increase in the 700 hPa moisture flux between 24°S and 30°S and a decrease in the flux over the southern and western portion of South Africa. The perturbation appears to have forced the moisture flux circulation over southern Africa to a more similar state in the perturbation simulations between 1980 and 1985 than exists between the control simulations of the two years.

- an increase in summer rainfall over the central interior of South Africa (around 25°E and between about 26°S and 29°S), which appears to be associated with the narrowing of the easterly wave trough and increase in near surface convergence.

- a decrease in summer rainfall over the north-east coast of South Africa (between about 26°S and 29°S), which may be associated with the increase in pressure and near surface divergence over the south-western Indian Ocean region and adjacent land.

CHAPTER 8

The Winter Response over the Southern Hemisphere

8.1 Introduction

The previous two chapters have dealt with the impact of the sea-ice and SST perturbations in the summer months. The current and following chapters will consider the response during the winter months and will assume a similar structure to the previous chapters. Comparisons will be made with the summer season results and hypotheses based on observed data, as well as with other modelling studies. As has been mentioned in the introduction chapter, there are a number of differences between previous modelling studies and the current study, including the magnitude and positioning of the imposed sea-ice anomalies, the physics, parameterisations and resolution of the GCMs used, and the nature of the simulations performed. Nonetheless, comparisons are useful for identifying potentially robust responses to sea-ice reductions.

Chapter 5 described the control and perturbation sea-ice and SST data sets that have been used for the 1980 and 1985 winter perturbations. It is clear that the control sea-ice for 1985 is less extensive than 1980, thus the perturbations that have been imposed are situated slightly closer to the pole in 1985 (Figures 5.13 and 5.14). In both years, the largest sea-ice perturbation is found in the Weddell Sea sector, extending from about 60°W to 30°E (Figures 5.13 and 5.14). There is also a fairly large sea-ice perturbation in the Ross Sea sector in May 1985 (Figure 5.13). The perturbations are found between 60°S and 70°S, although they extend slightly north of 60°S in the Weddell Sea sector towards the end of winter (Figure 5.13). The largest SST perturbations are found in the Weddell Sea, western Indian and Ross Sea sectors (Figure 5.16). The SST perturbations in the Ross Sea sector in 1980 are positioned north and north-east of the Ross Sea, whereas in 1985 the perturbations include a more significant perturbation west of the Ross Sea than is seen for 1980. In the Weddell and western Indian sectors, the SST perturbations extend as far north as 45°S, while in most of the other sectors the anomalies lie between 50°S and 65°S (Figure 5.16). The difference between the two years in the positioning of these imposed sea-ice extent and SST anomalies is important in the ensuing discussion of the atmospheric response.

This chapter will demonstrate that there are quite frequently contrasting patterns of change between the winters of 1980 and 1985 in response to the imposed perturbations. This is especially true of the zonal mean plots, and it will be shown that to a large degree the longitude specific nature of the response causes the misleading averages. There are, however, also differences between the two years in terms of the two-dimensional field patterns of change. These differences will be shown to be related to differences in the magnitude and positioning of the sea-ice and SST perturbations, as well as differences in the positions of circulatory features in the control simulations of the two years. In terms of the latter point, there is often a common response between the two years where upon first examination there does not seem to be, since the anomalies are positioned relative to the location of the specific features in the control simulation of each year. Many of the contrasting results between 1980 and 1985 may also be a result of the inherently high variability of the atmosphere in middle to high latitudes during winter. The response to the sea-ice and SST perturbation is stronger in the winter season compared to the summer season in terms of the surface temperature, and latent and sensible heat flux increases in the regions of the sea-ice perturbation. However, in general, the overall atmospheric response in winter is less zonally uniform, and is not as consistent between the two years compared to summer.

It will be shown that the sea-ice and SST perturbation causes an increase in pressure between 30°S and 55°S over the Australian and New Zealand sector, and a southward shift of the pressure systems in this region. In contrast, in this zone over the Atlantic Ocean there is a decrease in pressure and a northward shift of the pressure systems. Many of the induced pressure changes will be shown to be related to changes in the 500 hPa planetary long waves. In response to the perturbation, wave number 1 decreases in amplitude, whereas wave number 3 increases in amplitude. The phase of wave number 3 shifts in the perturbations in both years such that one of the troughs becomes positioned over the western Atlantic (near the Weddell Sea), coincident with the sector of the largest sea-ice anomalies. It will be suggested that the phase change of wave number 3 is responsible for increased blocking in the region of Australia and New Zealand. In addition, the perturbation appears to cause a general increase in cyclone densities near 60°S and a decrease north of this, around 50°S, but there is a fair degree of longitudinal variation. In the following sections, the results will be presented and discussed in terms of the vertical cross sections and zonal averages, as well as the two-dimensional field response and the changes to the 500 hPa planetary waves and twice-daily circulation. The chapter also includes a brief comparison of the results between the summer and winter seasons.

8.2 Cross Sections

8.2.1 Temperature

Below 700 hPa, the zonally averaged temperature response is fairly similar between the two years. In both years there is a temperature increase near 65°S (Figure 8.1), which is likely to be the result of a modification of heat fluxes from the ice and SST manipulations. The response at this latitude for 1985 is stronger than 1980, with zonally averaged temperature increases ranging from 1 K near the surface to about 0.6 K at 700 hPa in 1985, in contrast with increases ranging from 0.8 K near the surface to virtually no change at 700 hPa in 1980 (Figure 8.1). Therefore, at high latitudes the temperature increase for 1980 is constrained

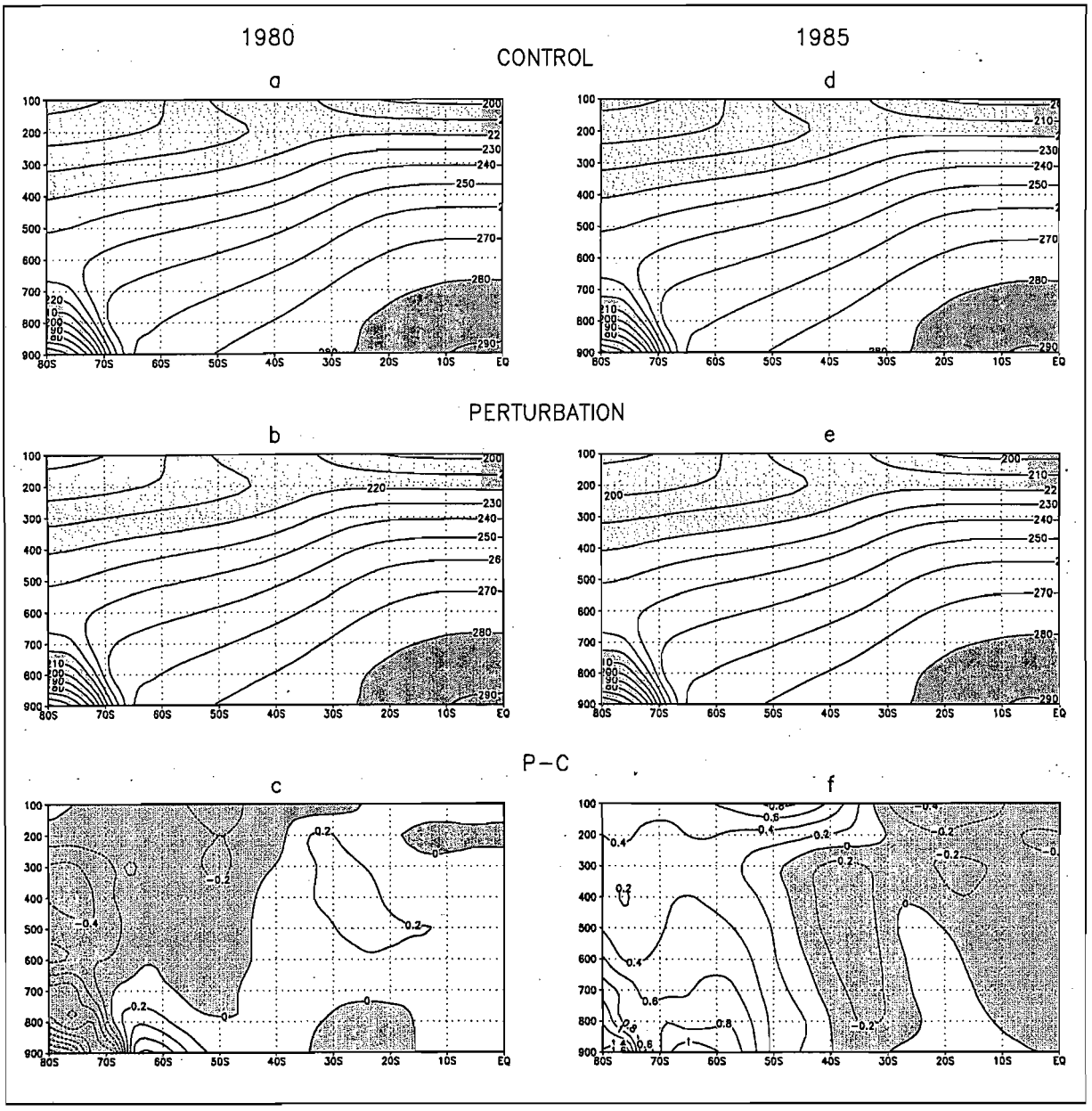

Figure 8.1 Vertical cross sections (y-axis denotes the pressure level in hPa) of the zonally averaged temperature (K) for the *a*) control and *b*) perturbation of 1980, and the *d*) control and *e*) perturbation of 1985. Temperatures in *a*, *b*, *d* and *e* which are greater than 280 K and less than 220 K have been shaded. Maps *c*) and *f*) show the plots of the perturbation field minus the control field for 1980 and 1985 respectively. Decreases in temperature have been shaded.

to below 700 hPa, whereas in 1985 the increase extends into the mid-troposphere. There are also larger surface temperature increases between 40°S and 50°S in 1985 compared to 1980, and there is a large temperature increase between 70°S and 80°S in 1985.

The near-surface winter temperature increase in response to the perturbation is larger than the change obtained for summer (Figure 6.1). In contrast to summer, the important mechanism causing the increase in winter is the modification of heat fluxes, rather than the ice-albedo feedback. The low intensity and oblique angle of insolation diminishes the influence of the surface albedo changes during winter (Raymo *et al.*, 1990).

8.2.2 Vertical Velocity

The largest vertical velocity anomalies are the regions of increased ascent found between 57°S and 68°S in 1980 and between 68°S and 80°S in 1985 (Figure 8.2). These regions correspond to the regions of largest surface temperature increase (Figure 8.1). The case for 1985 is confusing, since we would also expect increased ascent between 60°S and 70°S, coincident with the surface temperature increase. However, the region of increased ascent between 68°S and 80°S, associated with the largest surface temperature increase, may have overridden this effect, causing increased subsidence at neighbouring latitudes. There is also increased ascent between 55°S and 62°S, associated with surface temperature increases, which may also contribute to increased descent between 60°S and 70°S (Figure 8.1 and 8.2). Differences in the pattern of the surface temperature response between the two years (Figure 8.1) have contributed to differing patterns of vertical velocity anomalies. On average though, the region between 40°S and 65°S, coinciding with the rising limb of the Ferrel Cell, appears to be dominated by increased uplift in both years. In contrast, if one examines the descending limb of the Hadley Cell, between the equator and about 37°S, then in both years there is decreased subsidence between about 0°S and 15°S and, in general, increased subsidence in the southern portion of the cell. The zonally averaged vertical velocity anomalies are of the same order of magnitude as those obtained for summer.

8.2.3 Zonal Wind

As expected for winter, the jet stream is strongest at the 200 hPa level near 35°S (Figure 8.3*a* and *d*), in contrast to summer where it was strongest near 45°S (Figure 6.3*a* and *d*). In response to the perturbation there are opposing patterns of change in the zonal wind speed for the two years (Figure 8.3). South of 35°S, 1980 shows wind speed increases, whereas 1985

shows wind speed decreases. However, 1985 does simulate a wind speed increase below the 600 hPa level between 50°S and 60°S, which corresponds to the result for 1980 (Figure 8.3). Increases in wind speed at the 200 hPa level occur near 42°S in 1980 and near 32°S in 1985.

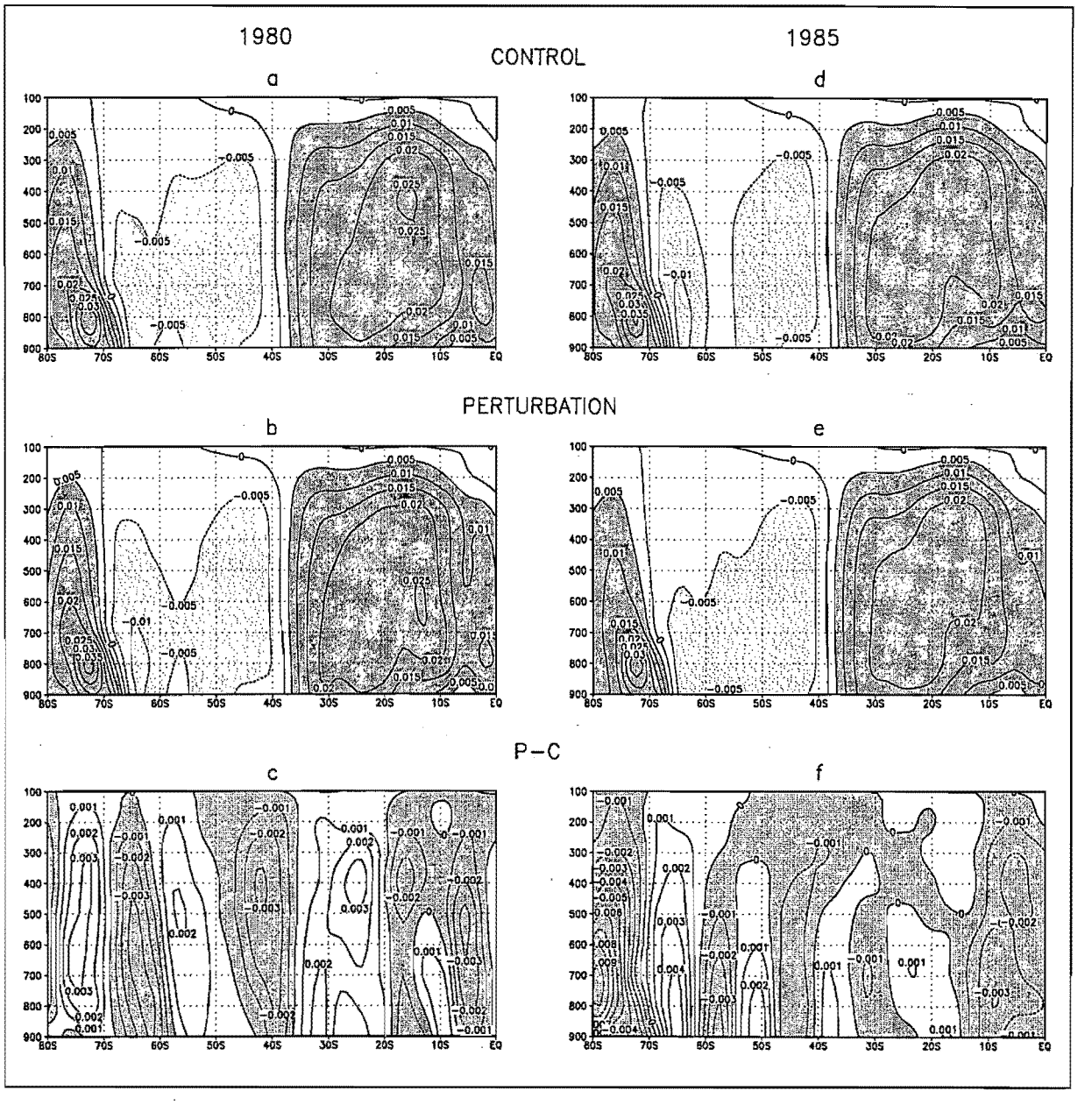

Figure 8.2 Vertical cross sections (y-axis denotes the pressure level in hPa) of the zonally averaged vertical velocities (Pa s^{-1}) for the *a*) control and *b*) perturbation of 1980, and the *d*) control and *e*) perturbation of 1985. Vertical velocities in *a*, *b*, *d* and *e* which are greater than 0.005 Pa s^{-1} and less than -0.005 Pa s^{-1} have been shaded. Maps *c*) and *f*) show the plots of the perturbation field minus the control field for 1980 and 1985 respectively. Decreases in vertical velocity have been shaded.

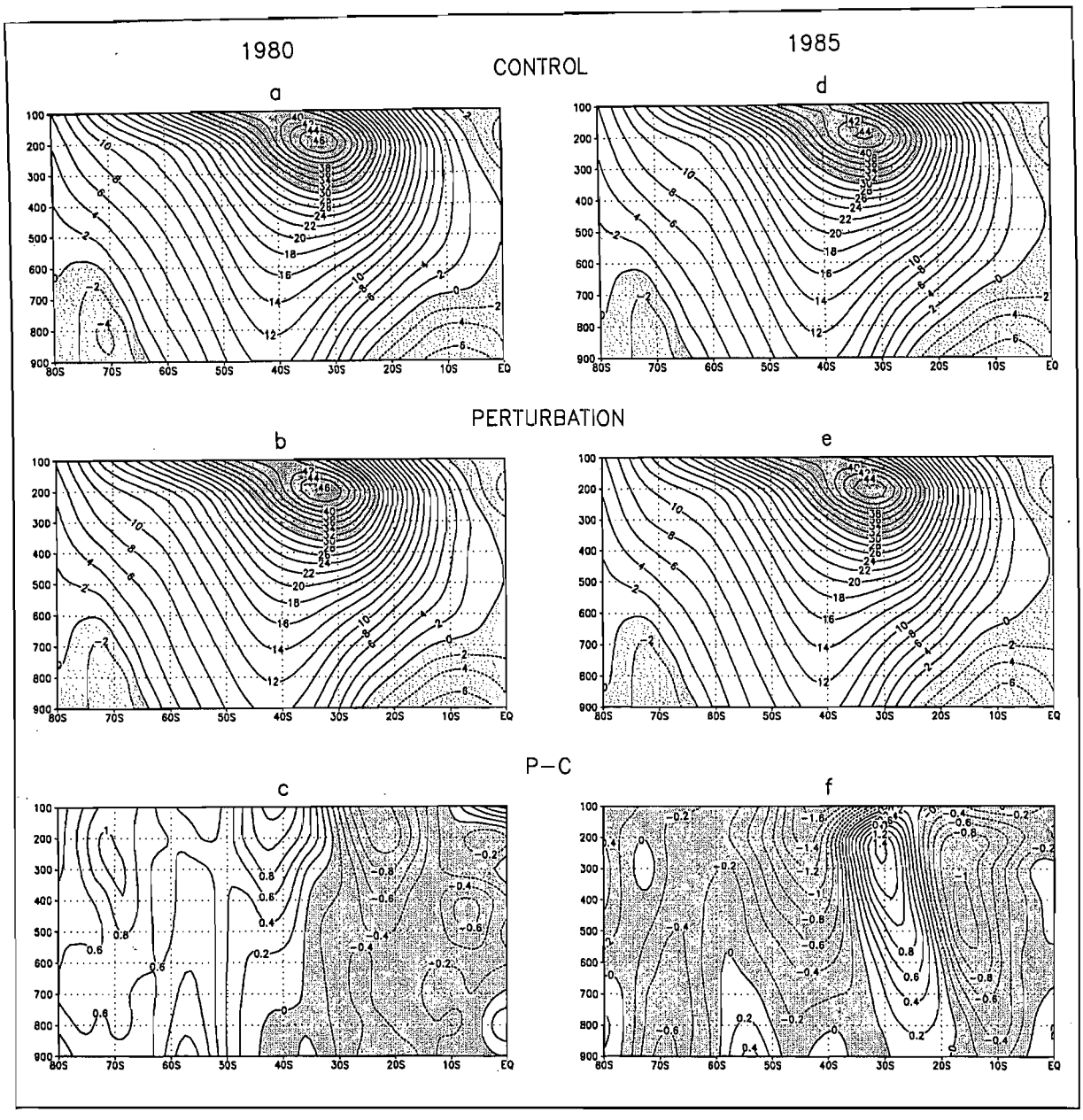

Figure 8.3 Vertical cross sections (y-axis denotes the pressure level in hPa) of the zonally averaged u-component of the wind speed (m s^{-1}) for the *a*) control and *b*) perturbation of 1980, and the *d*) control and *e*) perturbation of 1985. Wind speeds in *a*, *b*, *d* and *e* which are greater than 30 m s^{-1} and less than 0 m s^{-1} (i.e. easterlies) have been shaded. Maps *c*) and *f*) show the plots of the perturbation field minus the control field for 1980 and 1985 respectively. Decreases in wind speed have been shaded.

8.2.4 Specific Humidity

Both years display an increase in specific humidity between 40°S and 70°S in the lower troposphere (Figure 8.4). The increase is larger for 1985 and extends beyond the 700 hPa level. This increase is partly a response to the exposure of oceanic regions in the perturbation simulations, which were covered in ice in the controls, thus providing an additional moisture source. There is a general decrease in specific humidity between 20°S and 40°S and an increase further north in both years (Figure 8.4). Most of the changes in specific humidity are restricted to below the 500 hPa level.

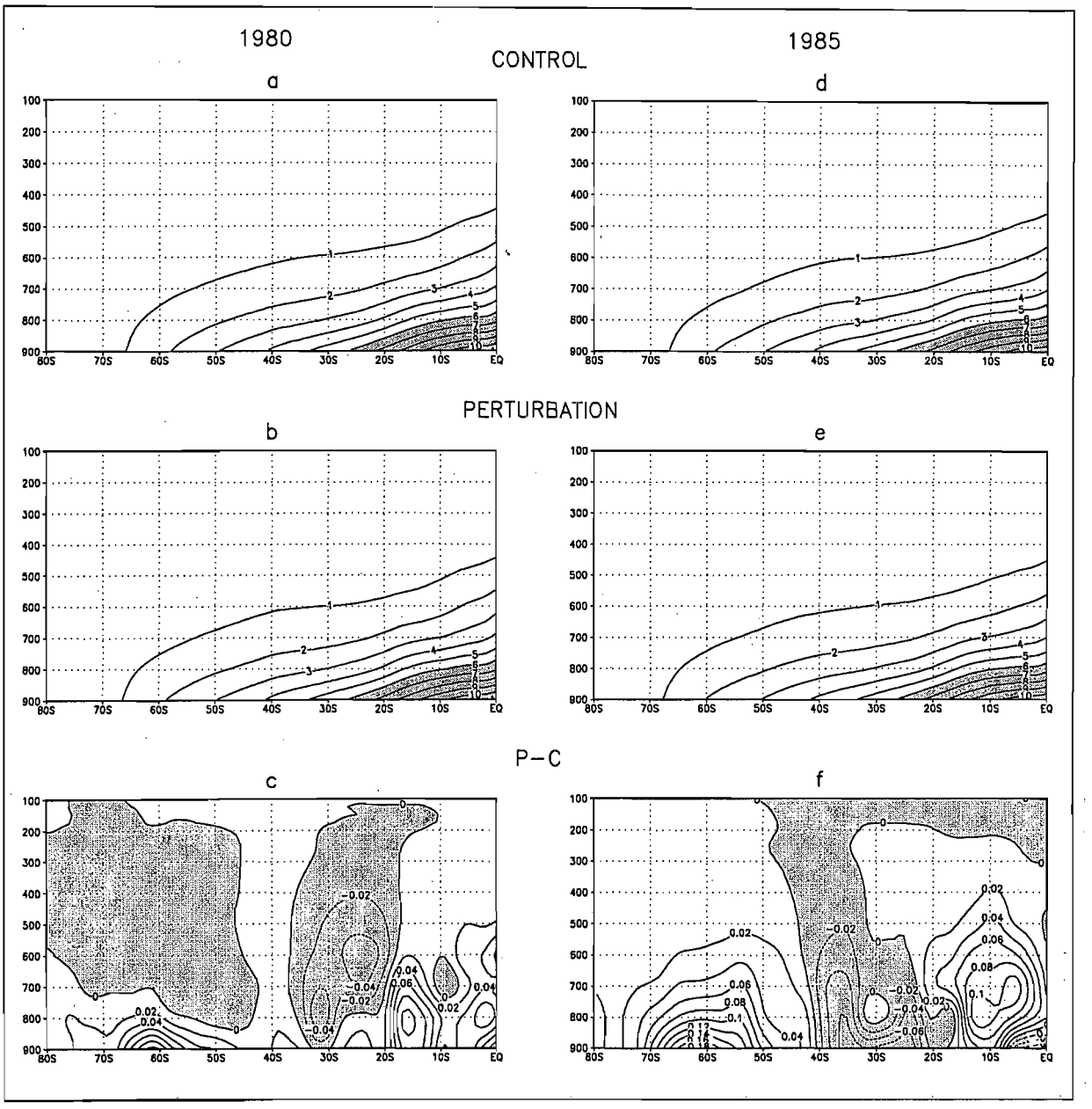

Figure 8.4 Vertical cross sections (y-axis denotes the pressure level in hPa) of the zonally averaged specific humidity (g kg^{-1}) for the *a*) control and *b*) perturbation of 1980, and the *d*) control and *e*) perturbation of 1985. Humidities in *a*, *b*, *d* and *e* which are greater than 6 g kg^{-1} have been shaded. Maps *c*) and *f*) show the plots of the perturbation field minus the control field for 1980 and 1985 respectively. Decreases in specific humidity have been shaded.

It is clear from the discussion of the four variables in the above sub-sections, that there are quite frequently conflicting patterns of change between the two years. Based on the results obtained for the summer season, it may be that the azonal nature of response is producing a misleading representation of the change in terms of zonal averages. In other words, there may be both increases and decreases in a certain variable around a latitude circle, which would produce an ambiguous zonal average. Clearly, the results need to be investigated further in terms of the spatial patterns, in order to identify changes that may be longitude specific. The

following section considers the zonally averaged response of certain variables, averaged over the sectors outlined in Chapter 6 and shown in Figure 6.5.

8.3 Zonal Averages

8.3.1 Surface Air Temperature

In response to the perturbation, surface air temperature, averaged over all longitudes (Figures 8.5*g* and 8.6*g*), increases in both years, especially at 62°S in 1980 and at 65°S in 1985. For 1980, the temperature increase is about 1.6 K, whereas it is slightly larger in 1985, being near 2 K (although with a larger standard deviation than 1980) (Figures 8.5*g* and 8.6*g*). The corresponding increases for the summer season (Figures 6.6*g* and 6.7*g*) were about 0.5 K, thus indicating a smaller response than in winter. The largest temperature increase (~2.5°) in both years is found in the western Indian sector (0° to 90°E), since this corresponds to the region of the largest sea-ice perturbation, especially near the Greenwich Meridian (Figure 5.14). This increase peaks near 62°S in both years, but there are larger temperature increases south of this (65°S - 70°S) in 1985 compared to 1980 (Figures 8.5*b* and 8.6*b*). This may be because the imposed sea-ice anomalies in 1985 extend closer to the pole (Figure 5.14). Large sea-ice anomalies have also been imposed in the Weddell Sea sector (60°W to 0°) in both years, and as such there are large surface temperature increases centred around 62°S in this region (Figures 8.5*f* and 8.6*f*). The standard deviations of the increase in this sector are, however, larger than those obtained for the western Indian sector.

There are clear differences between 1980 and 1985 in terms of the temperature response in the Ross Sea sector (160°E to 130°W) (Figures 8.5*d* and 8.6*d*). In 1980, there is a small temperature increase recorded near 60°S, but this drops off rapidly to the north and south and is associated with large standard deviations (Figure 8.5*d*). In contrast, in 1985 there is a definitive temperature increase, of up to about 2.5 K near 65°S (Figure 8.6*d*). This disparity is related to differences in the sea-ice perturbations between the two years, since there is a larger ice anomaly in the Ross Sea sector in 1985 compared to 1980, especially in the area just west and east of the sea (Figure 5.14). The sea-ice perturbation to the west of the Ross Sea lies close to the boundary of Antarctica, and therefore accounts for the large temperature increases that are recorded near 70°S (Figure 8.6*d*).

The surface temperature changes obtained are much smaller than those from other modelling studies investigating the effects of reduced winter Antarctic sea-ice extent, which reported

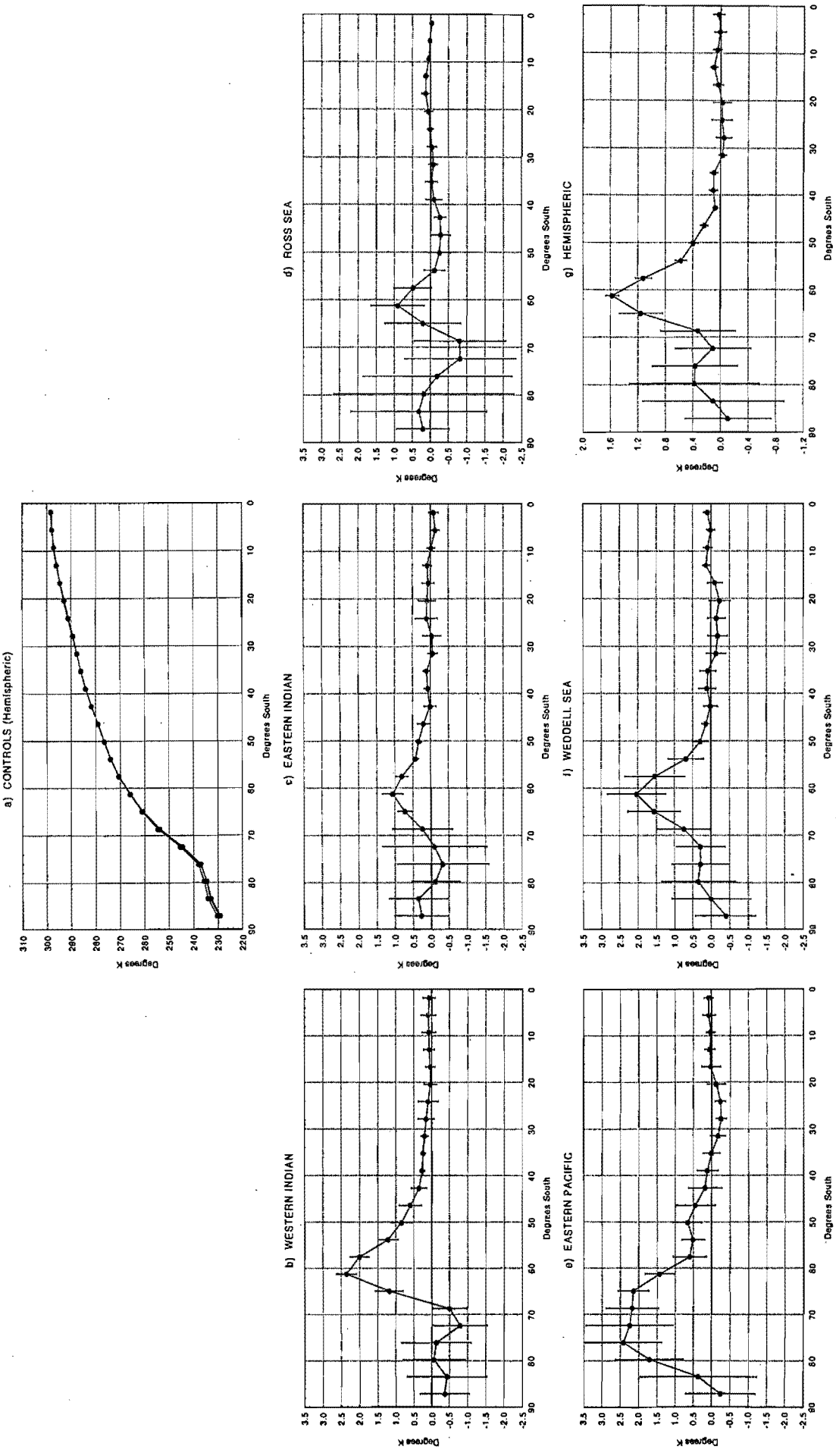

Figure 8.5 Zonal averages of surface air temperature (K) for 1980. *a)* shows the three controls averaged over all longitudes, while *b), c), d), e), f)* and *g)* show the means (circles) and standard deviations (bars) of the perturbation simulations minus the control simulations for zonal averages performed over the longitudinal sectors shown in Figure 6.5. For graph *g)* the zonal averaging is performed across all longitudes of the hemisphere.

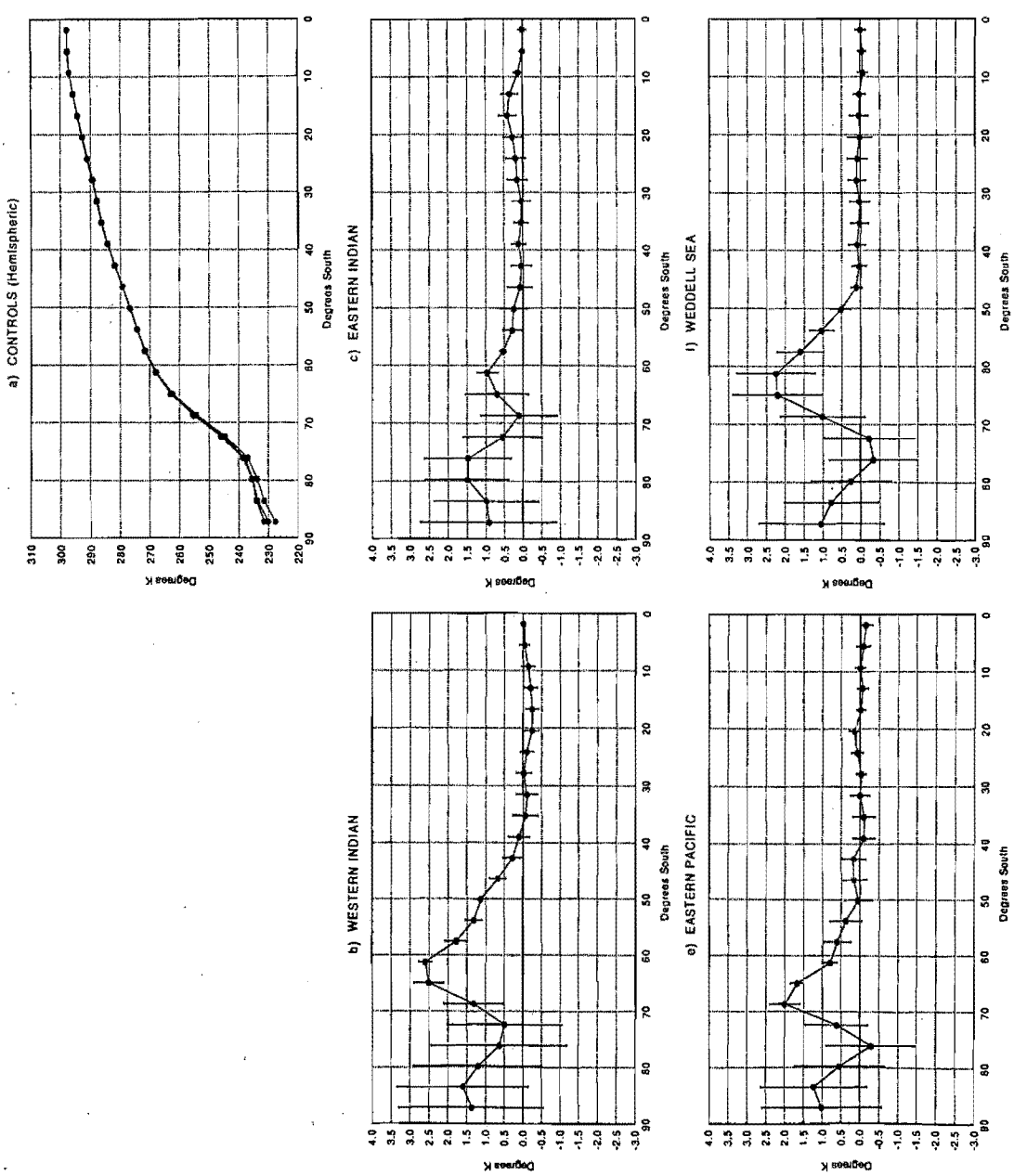

Figure 8.6 Zonal averages of surface air temperature (K) for 1985. *a)* shows the three controls averaged over all longitudes, while *b), c), d), e), f)* and *g)* show the means (circles) and standard deviations (bars) of the perturbation simulations minus the control simulations for zonal averages performed over the longitudinal sectors shown in Figure 6.5. For graph *g)* the zonal averaging is performed across all longitudes of the hemisphere.

temperature increases in the vicinity of the ice removal of about 10° to 20°C (Mitchell and Hills, 1986; Simmonds and Dix, 1987; Mitchell and Senior, 1989). This is not surprising, since the experiments of Mitchell and Hills (1986), Simmonds and Dix (1987) and Mitchell and Senior (1989) made use of considerably larger sea-ice perturbations than the present study, either removing all winter sea-ice (Simmonds and Dix, 1987) or removing all sea-ice equatorward of 66°S (Mitchell and Hills, 1986) or 67.5°S (Mitchell and Senior, 1989). In addition, the temperature increases in the present study are more widespread than in the other studies, in that the increase extends slightly further northward. This is due to the manipulation, and hence increase of SSTs in and around the sea-ice zone in the present study (refer to Chapter 5). In the other modelling studies, where the sea-ice was removed it was replaced with water at 0°C (Mitchell and Hills, 1986; Simmonds and Dix, 1987) or -1.8°C (Mitchell and Senior, 1989).

8.3.2 Sensible Heat Flux

In the controls, the winter sensible heat flux reaches a maximum of about 25 W m^{-2} near 58°S in both years (Figures 8.7*a* and 8.8*a*). The general effect of reducing sea-ice limits is to increase the surface sensible heat flux in the region of the ice removal in both years (Figures 8.7*g* and 8.8*g*), thus shifting the control peak of sensible heat flux slightly southwards. As for surface air temperature, the sensible heat flux increases are centred around 62°S in 1980 and 65°S in 1985 (Figures 8.7*g* and 8.8*g*). The hemispheric average increase for both years is between 4 and 5 W m^{-2}, which is much larger and more conclusive than the change recorded for the summer season (Figures 6.8 and 6.9). Unlike the surface air temperature increases, which extend north of 60°S (Figures 8.5 and 8.6), the increases in sensible heat flux are largely restricted to between 60°S and 70°S and in some sectors, for example the western Indian sector, there is actually a reduction in the flux north of 60°S (~40°S - 60°S) (Figures 8.7 and 8.8). This may be explained by anomalous warm air from the sea-ice reduction between 60°S and 70°S being advected northwards, and being warmer than the SSTs over which it flows, thus causing an anomalous downward flux of heat. In addition, zones of sensible heat flux decrease may be associated with surface air temperature increases in response to adiabatic changes.

The sensible heat flux increase associated with the sea-ice removal can be seen in all the sectors except for the eastern Indian sector in 1980 and the Ross Sea sector in 1985 (Figures 8.7 and 8.8). In both of these regions, there must be processes operating which result in

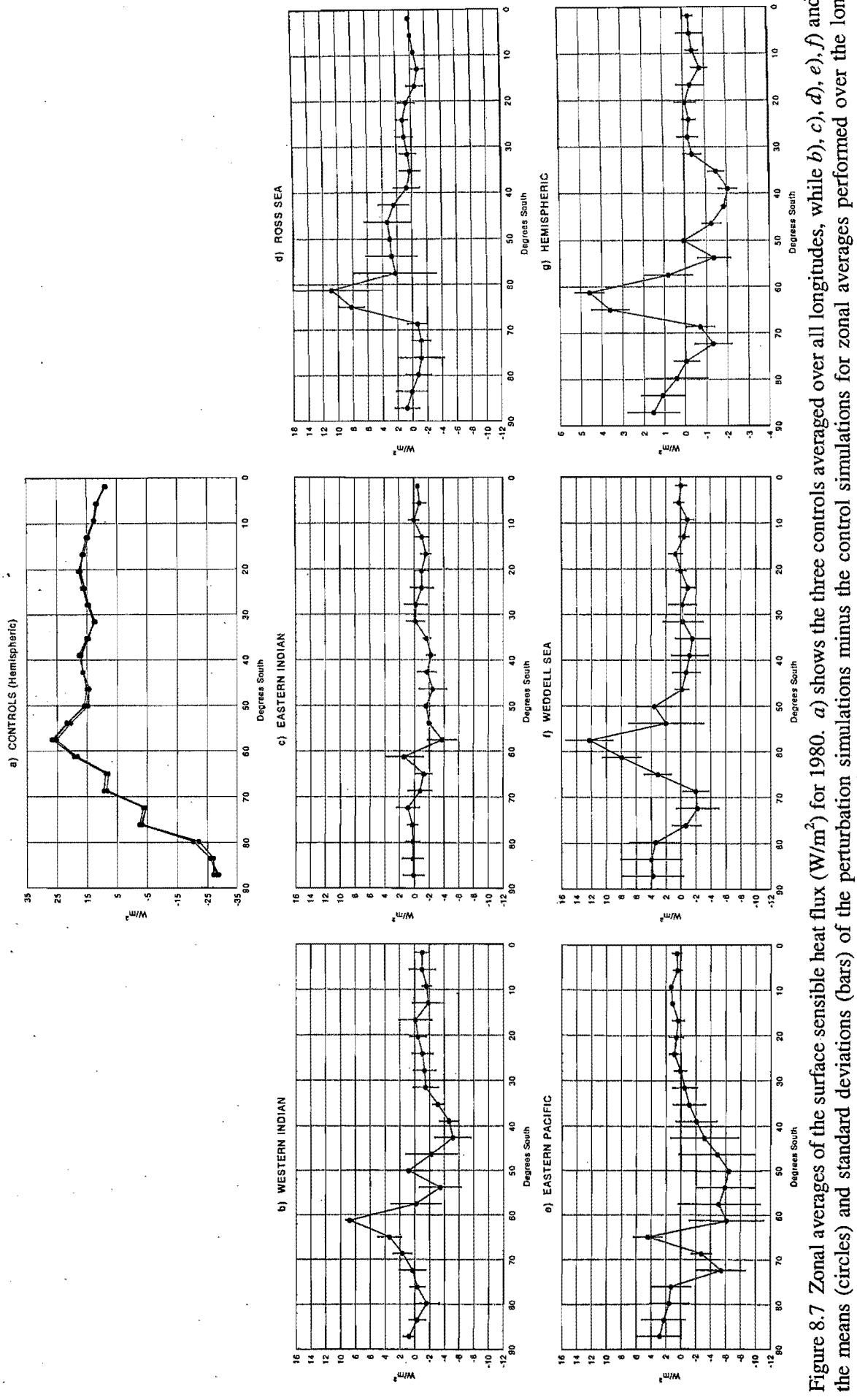

Figure 8.7 Zonal averages of the surface sensible heat flux (W/m^2) for 1980. *a)* shows the three controls averaged over all longitudes, while *b), c), d), e), f)* and *g)* show the means (circles) and standard deviations (bars) of the perturbation simulations minus the control simulations for zonal averages performed over the longitudinal sectors shown in Figure 6.5. For graph *g)* the zonal averaging is performed across all longitudes of the hemisphere.

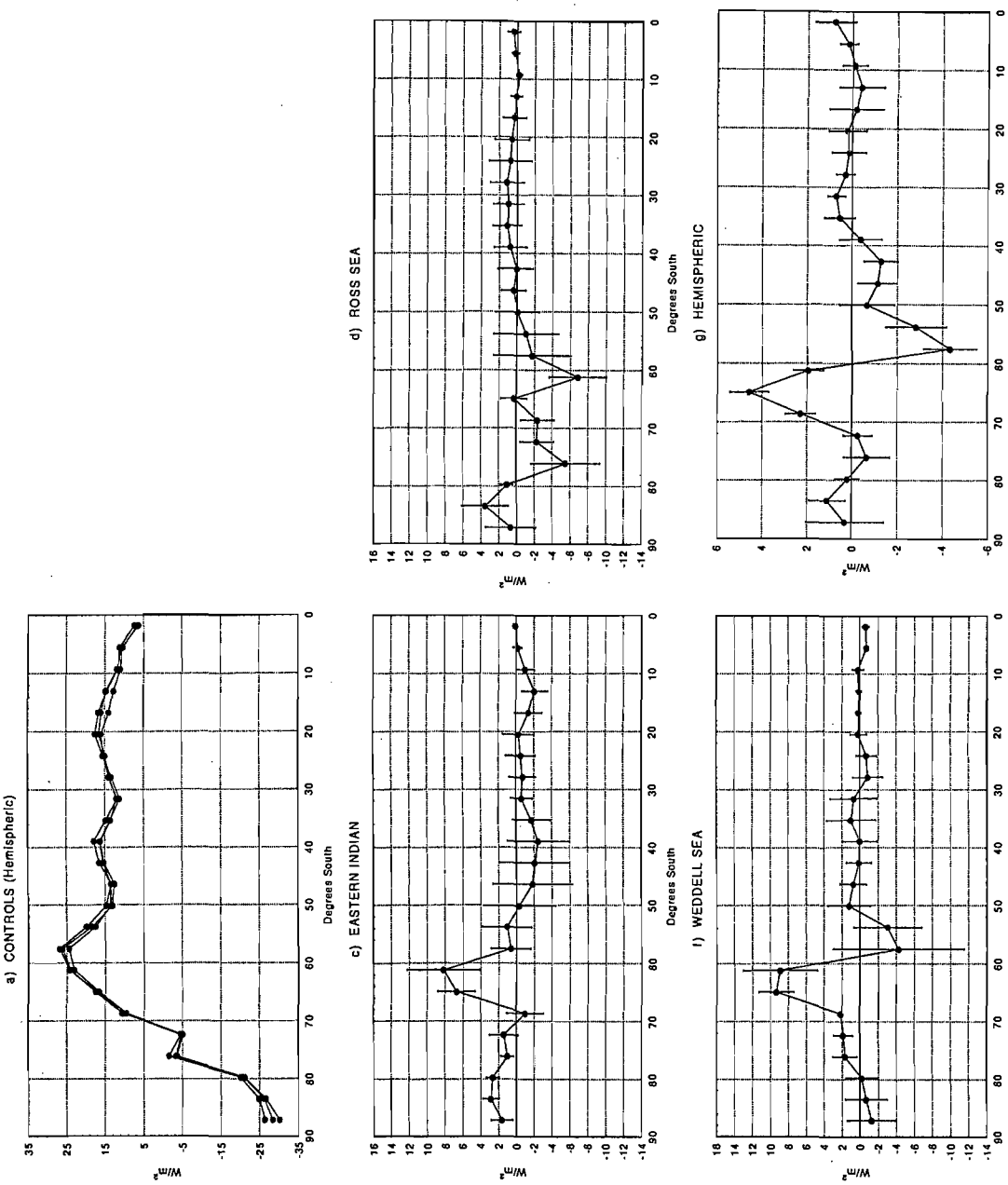

Figure 8.8 Zonal averages of the surface sensible heat flux (W/m^2) for 1985. *a)* shows the three controls averaged over all longitudes, while *b), c), d), e), f)* and *g)* show the means (circles) and standard deviations (bars) of the perturbation simulations minus the control simulations for zonal averages performed over the longitudinal sectors shown in Figure 6.5. For graph *g)* the zonal averaging is performed across all longitudes of the hemisphere.

warmer air temperatures compared to surface temperatures, thus promoting zero or negative sensible heat flux anomalies. Examples of such processes include adiabatic changes and advection of heat.

Mitchell and Hills (1986) and Mitchell and Senior (1989) also examined the change in sensible heat flux in response to reductions of winter sea-ice extent. They too obtained an increase in the sensible heat flux in the zone from which sea-ice was removed, as well as finding the flux decrease in adjacent latitudes to the north (~40°S to 60°S). However, the changes they obtained are orders of magnitude larger than those obtained for the present study. Mitchell and Hills (1986) found an increase of about 150 W m^{-2} and Mitchell and Senior (1989) found an increase of about 50 W m^{-2}. This difference may be due to a combination of the larger surface temperature increases obtained in their studies, as well as to improvements in the resolution and formulation of boundary layer processes in the model used in the present study compared to the other two studies. The GCM which Mitchell and Hills (1986) used only had 5 vertical levels in total, and the control sensible heat flux was overestimated (peak value of about 80 W m^{-2}). Mitchell and Senior (1989) used an 11 layer GCM and obtained both smaller control flux values (peaking at about 35 W m^{-2}) and perturbation anomalies than did Mitchell and Hills (1986). This suggests that increased resolution, and perhaps improved model physics, may produce a more realistic and smaller sensible heat flux anomaly than was obtained in the above two studies.

8.3.3 Latent Heat Flux

Latent heat fluxes peak at about 150 W m^{-2} near 13°S, and decrease towards the pole, with a flux of about 35 W m^{-2} at 60°S in both years (Figures 8.9*a* and 8.10*a*). In response to the sea-ice perturbation in 1980 and 1985, there is an average increase in the latent heat flux of about 6 to 8 W m^{-2} near 60°S (Figures 8.9 and 8.10). This increase is most prominent in the western Indian, eastern Pacific and Weddell Sea sectors in both the years, and can be attributed to the removal of sea-ice providing an additional moisture source for evaporation, and to the increase in SSTs, which raises the saturation vapour pressure at the surface and increases the potential for evaporation. The changes in the latent heat flux north of 60°S are largely ambiguous, do not always correspond between the two years and are associated with large standard deviations (Figures 8.9 and 8.10). In comparison to winter, the summer latent heat flux increases were much smaller, generally not exceeding 4 W m^{-2} (Figures 6.10 and 6.11).

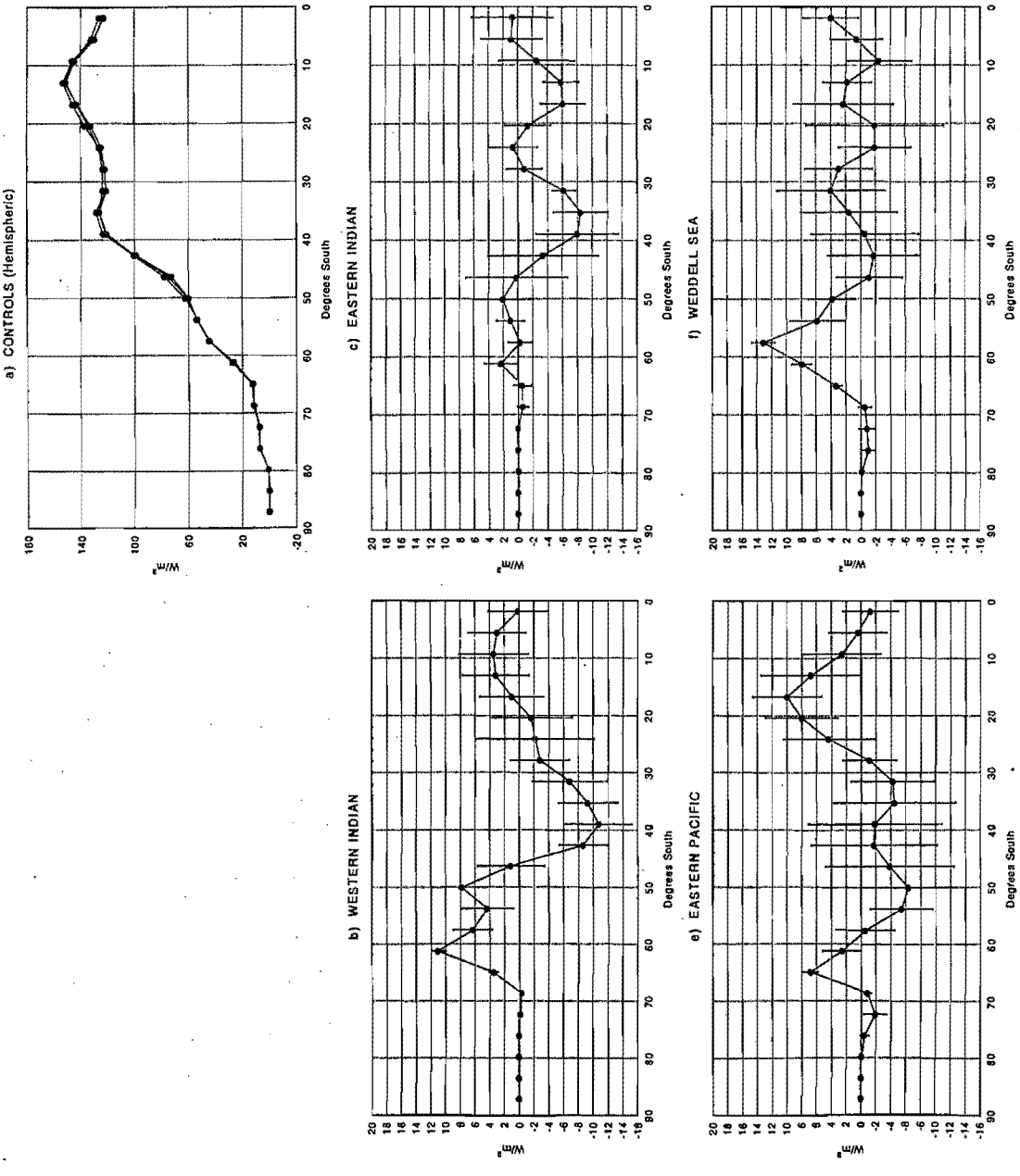

Figure 8.9 Zonal averages of the surface latent heat flux (W/m^2) for 1980. *a)* shows the three controls averaged over all longitudes, while *b), c), d), e), f)* and *g)* show the means (circles) and standard deviations (bars) of the perturbation simulations minus the control simulations for zonal averages performed over the longitudinal sectors shown in Figure 6.5. For graph *g)* the zonal averaging is performed across all longitudes of the hemisphere.

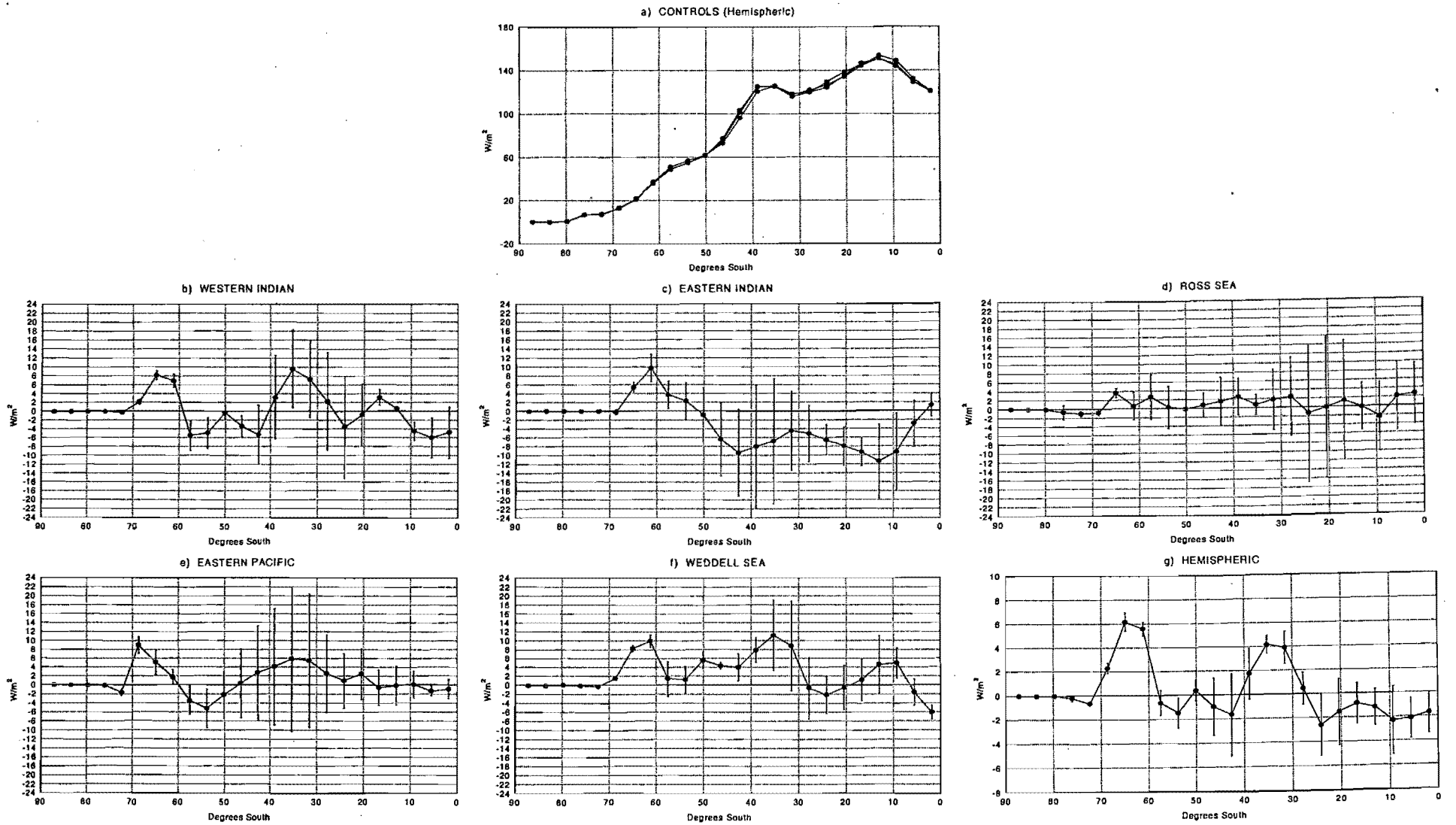

Figure 8.10 Zonal averages of the surface latent heat flux (W/m^2) for 1985. *a)* shows the three controls averaged over all longitudes, while *b), c), d), e), f)* and *g)* show the means (circles) and standard deviations (bars) of the perturbation simulations minus the control simulations for zonal averages performed over the longitudinal sectors shown in Figure 6.5. For graph *g)* the zonal averaging is performed across all longitudes of the hemisphere.

Once again, the flux changes obtained by Mitchell and Hills (1986) and Mitchell and Senior (1989), which were approximately 35 W m^{-2}, are larger than the present study. It is reasonable that this is because the rise in surface temperature was larger in their experiments.

8.3.4 Sea Level Pressure

Figures 8.11 and 8.12 show the sea level pressure changes in response to the perturbation in 1980 and 1985 respectively. It is clear that there are large standard deviations associated with the anomalies in all the sectors for both years and the results are largely inconclusive. This suggests that either there is no clear response in sea level pressure to the perturbation and the changes that are seen in the zonal plots merely represent natural variability, or, the sea level pressure response is longitudinally specific, and there may be changes of opposite sign within a given sector along a latitude circle. Slight variations in the positioning of sea level pressure anomalies between the two years can also exaggerate the differences between the years in terms of the zonally averaged plots, especially if the anomalies straddle sector boundaries. Thus, no conclusions can be made regarding the sea level pressure changes until the two-dimensional spatial pattern of anomalies has been examined.

8.3.5 500 hPa Wind

The same problem that was observed for sea level pressure, is found for the 500 hPa wind. The changes are generally associated with large standard deviations, and the contrasting patterns of change between sectors highlight the longitudinally specific nature of the response (Figures 8.13 and 8.14). For example, in the eastern Indian sector in both years there appears to be an increase in wind speeds near 50°S and 60°S, and a decrease in wind speeds further north (Figures 8.13 and 8.14). In contrast, in the eastern Pacific sector there is a decrease in wind speeds near 60°S and an increase near 40°S in both years (Figures 8.13 and 8.14). Incidentally, in both of these sectors, the 1985 response is situated slightly south of the 1980 response, and this may be related to the less extensive sea-ice in 1985 compared to 1980.

It is clear that as for sea level pressure, the nature of the wind speed changes will have to be examined in enhanced spatial detail. The following section examines the geographical distribution of these and other anomalies, as was done for the summer season results. There are four primary sub-sections which consider the response of the atmosphere in terms of *a*) temperature and pressure, *b*) the 500 hPa wind, *c*) midlatitude cyclones and storm tracks, and *d*) moisture.

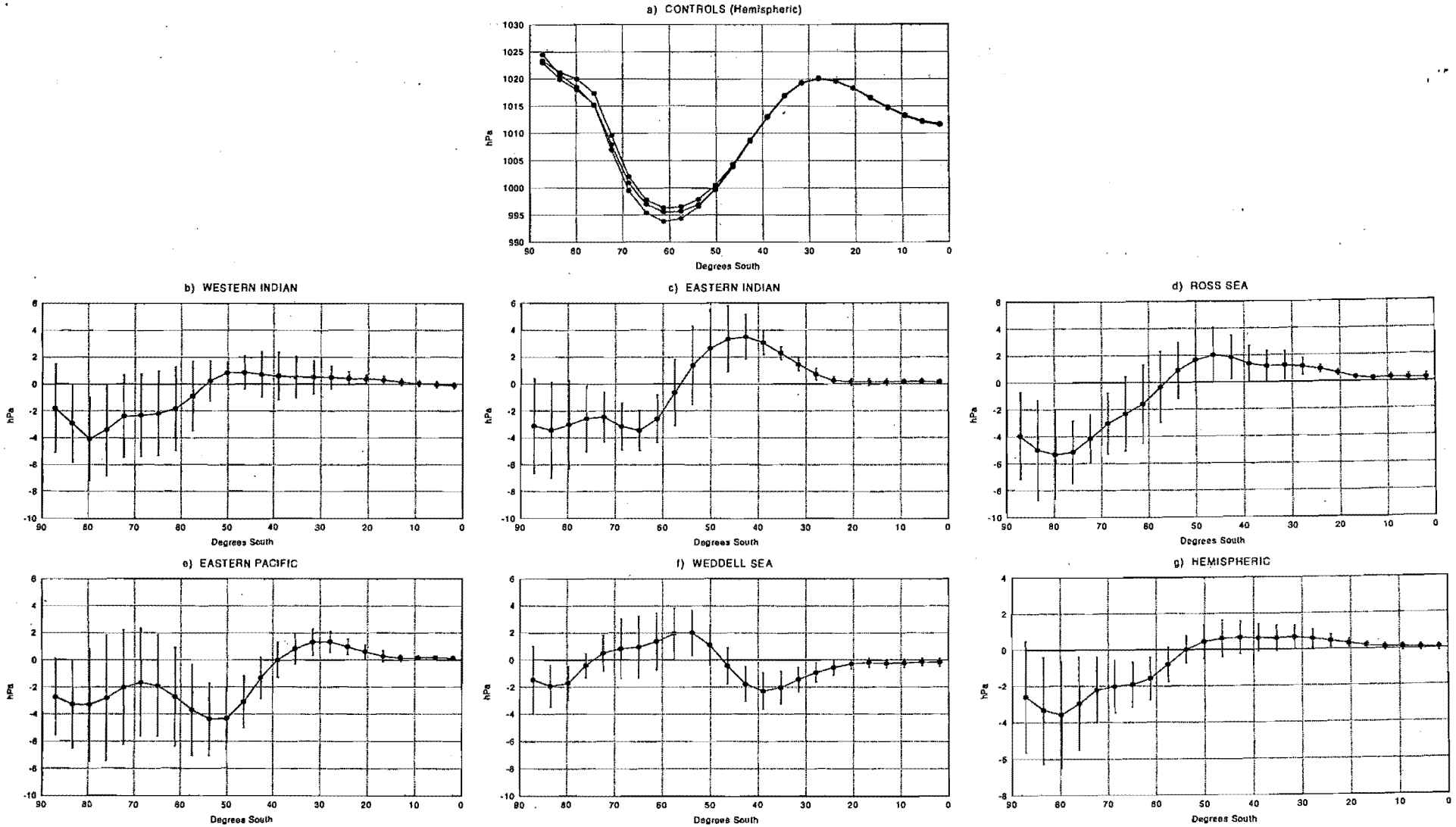

Figure 8.11 Zonal averages of sea level pressure (hPa) for 1980. *a*) shows the three controls averaged over all longitudes, while *b*), *c*), *d*), *e*), *f*) and *g*) show the means (circles) and standard deviations (bars) of the perturbation simulations minus the control simulations for zonal averages performed over the longitudinal sectors shown in Figure 6.5. For graph *g*) the zonal averaging is performed across all longitudes of the hemisphere.

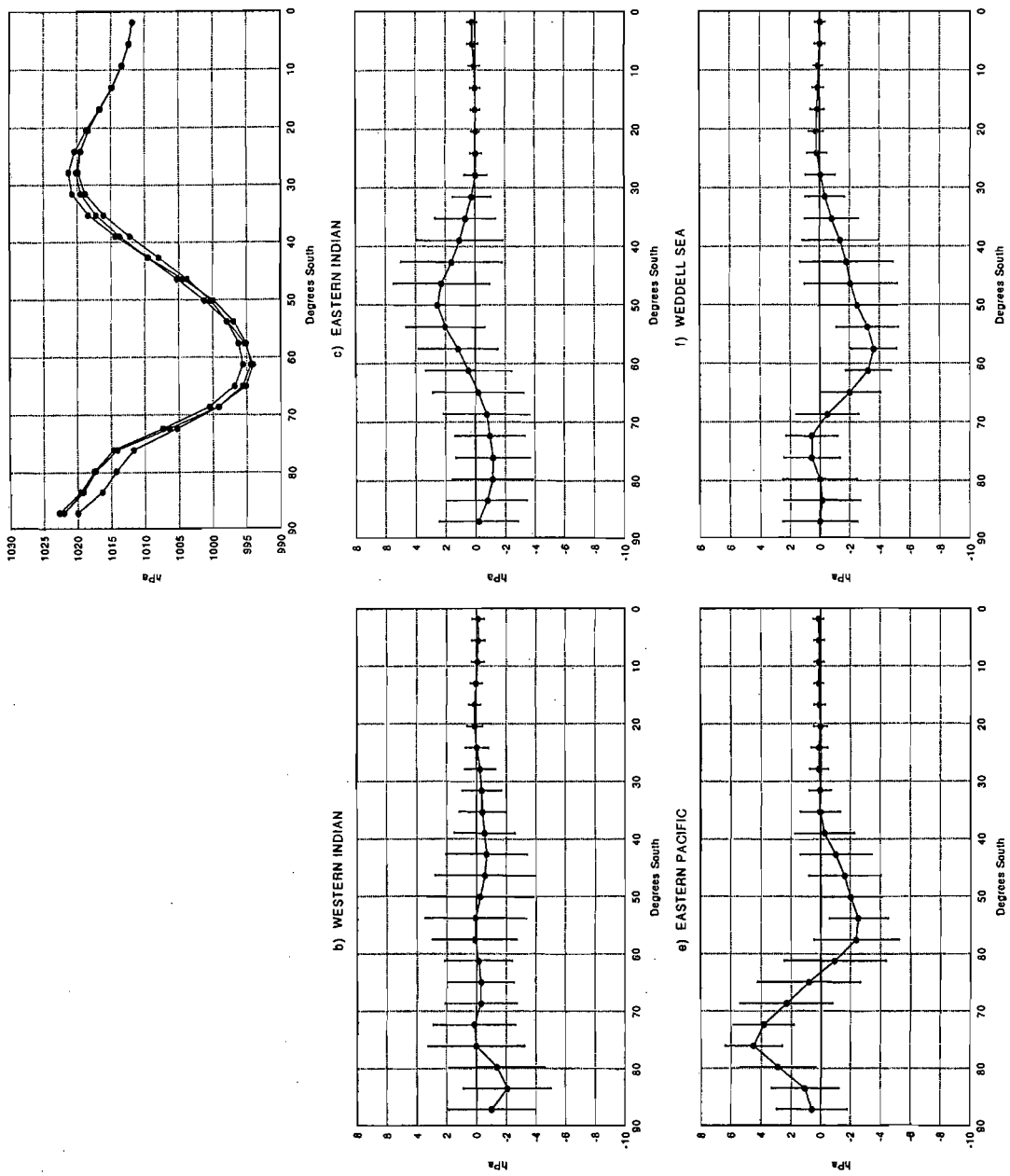

Figure 8.12 Zonal averages of sea level pressure (hPa) for 1985. *a)* shows the three controls averaged over all longitudes, while *b), c), d), e), f)* and *g)* show the means (circles) and standard deviations (bars) of the perturbation simulations minus the control simulations for zonal averages performed over the longitudinal sectors shown in Figure 6.5. For graph *g)* the zonal averaging is performed across all longitudes of the hemisphere.

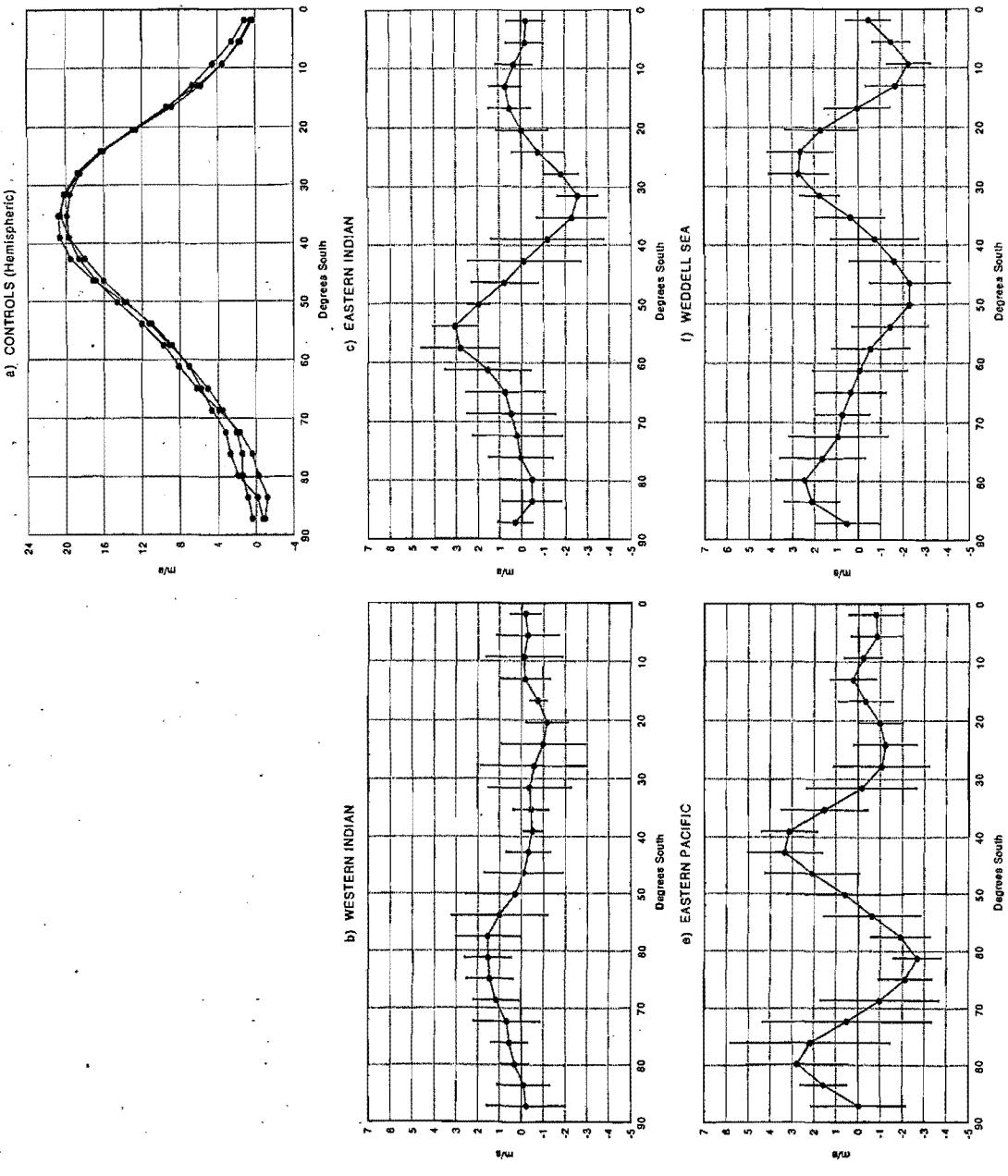

Figure 8.13 Zonal averages of the u-component of the 500 hPa wind speed (m/s) for 1980. *a)* shows the three controls averaged over all longitudes, while *b)*, *c)*, *d)*, *e)*, *f)* and *g)* show the means (circles) and standard deviations (bars) of the perturbation simulations minus the control simulations for zonal averages performed over the longitudinal sectors shown in Figure 6.5. For graph *g)* the zonal averaging is performed across all longitudes of the hemisphere.

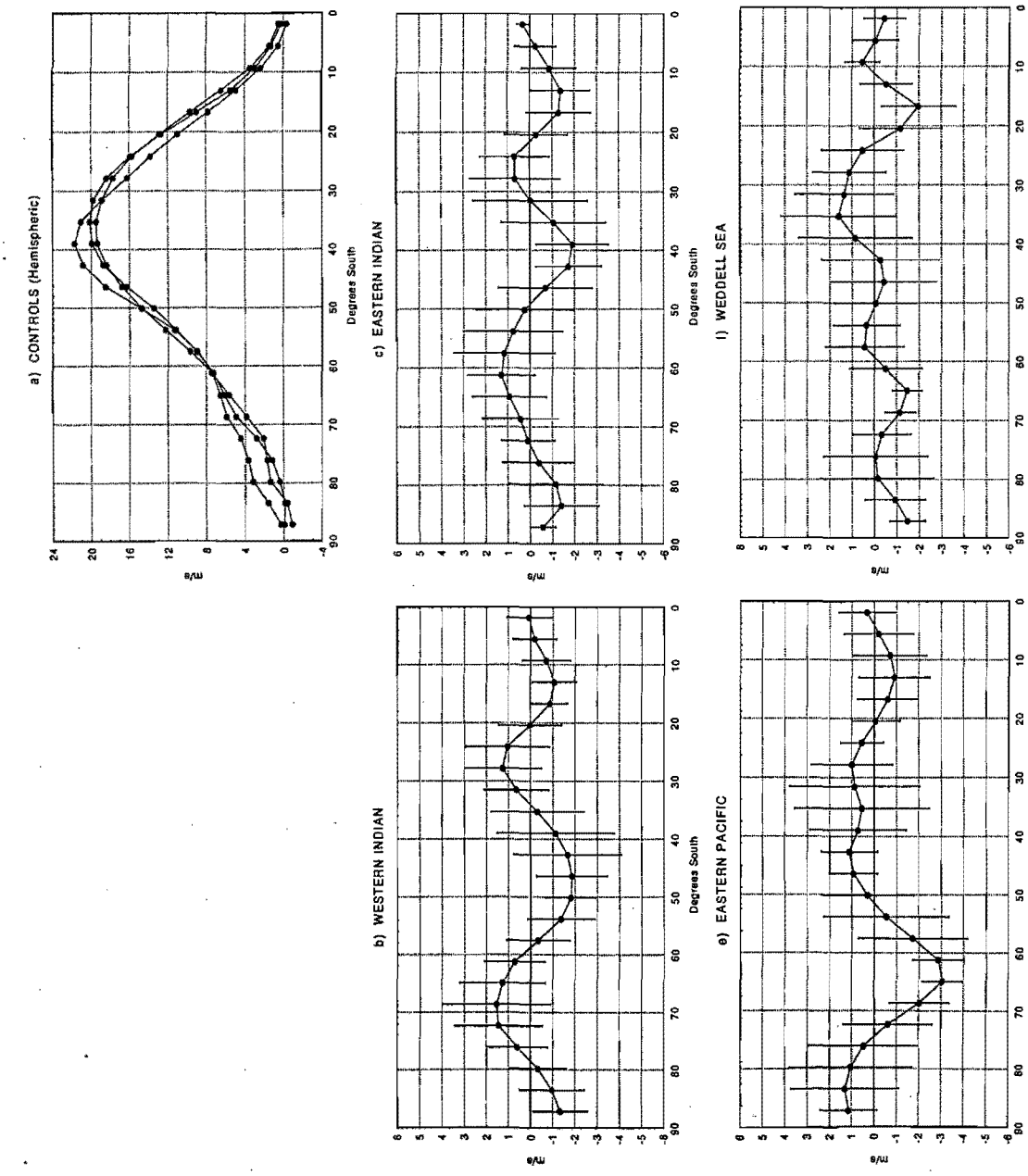

Figure 8.14 Zonal averages of the u-component of the 500 hPa wind speed (m/s) for 1985. *a)* shows the three controls averaged over all longitudes, while *b)*, *c)*, *d)*, *e)*, *f)* and *g)* show the means (circles) and standard deviations (bars) of the perturbation simulations minus the control simulations for zonal averages performed over the longitudinal sectors shown in Figure 6.5. For graph g) the zonal averaging is performed across all longitudes of the hemisphere.

8.4 Two-Dimensional Field Response

For many of the variables examined in this section, there are a number of positive and negative anomalies in response to the perturbation, for which causes could be speculated. It is beyond the scope of this thesis to address all of these detailed changes, therefore only what are perceived to be the major and interesting changes are considered.

8.4.1 Temperature and Pressure

8.4.1.1 Results

The effect of reducing sea-ice limits and increasing SSTs around Antarctica is to increase surface air temperatures in the general region between 50°S and 70°S (Figure 8.15). Associated with the asymmetry of sea-ice and SSTs about the pole, the increase extends further north over the Atlantic and western Indian portion of the hemisphere compared to the western Pacific region. This can also be seen in the previously shown zonal plots of surface air temperature change (Figures 8.5 and 8.6), where the temperature increase extends beyond 50°S in the Weddell Sea and western Indian sectors, but only just beyond 60°S in the Ross Sea sector. The temperature increases between 60°S and 70°S are largely due to the imposed sea-ice anomalies, whereas the increases between 50°S and 60°S may be related to the SST increases. The largest and most consistent increase in surface temperature between the two years is found in the south Atlantic region (Figure 8.15). This sector experiences the largest sea-ice and SST perturbation in both years (Figures 5.14 and 5.16). The increases between 60°S and 70°S in 1985 over this region are positioned slightly south of those in 1980 (Figure 8.15), which is related to the southward positioning of the sea-ice anomalies in 1985 compared to 1980 (Figure 5.14). In the Ross Sea sector, the temperature increase is larger in 1985 compared to 1980 (Figure 8.15), which may be due to the larger sea-ice anomalies in this region in 1985, especially just upstream and downstream of the sea (Figure 5.14*b*).

The zonally averaged results showed that the effect of reducing sea-ice limits and increasing surface temperatures between 60°S and 70°S, was to increase the surface sensible heat flux. One might expect that an increase in the turbulent fluxes of sensible heat should produce local reductions in sea level pressure associated with increased ascent. As such, in both years there are regions of significant sea level pressure decrease between 60°S and 70°S (Figure 8.16). The exact positions of the decreases do not exactly coincide between the two years, but this is to be expected since the years are characterised by different sea-ice extents and

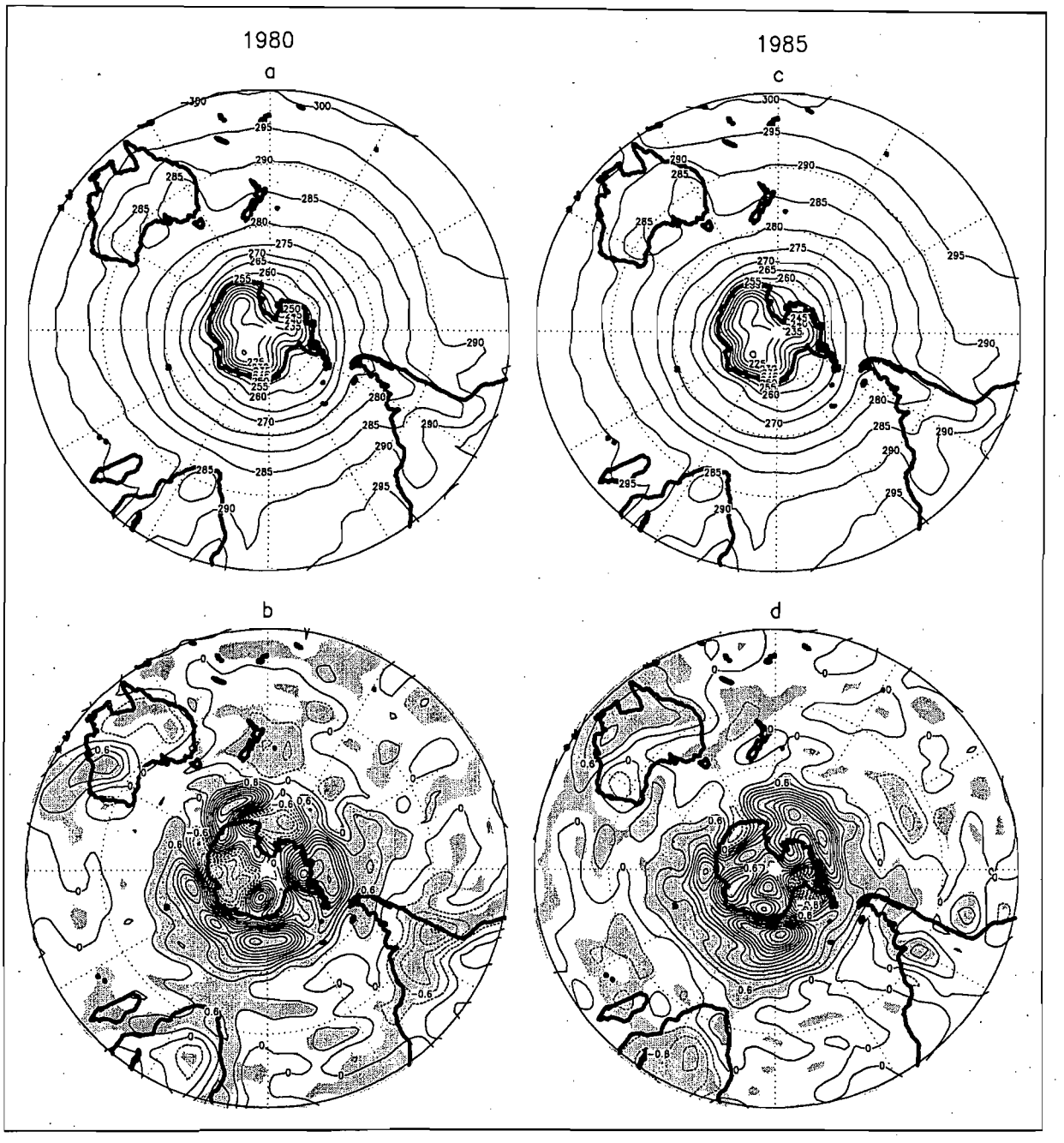

Figure 8.15 Surface temperature (K) for the controls of *a*) 1980 and *c*) 1985, and the perturbations minus the controls for *b*) 1980 and *d*) 1985. Statistically significant differences at the 95% confidence level have been shaded. Negative anomalies in *b*) and *d*) are depicted as dotted contours.

control sea level pressure patterns (Figure 8.16*a* and *c*), hence the dynamics are slightly different. Nonetheless, south of 50°S, both years show decreases in pressure over portions of the south Atlantic, south (1985) and south-west (1980) of New Zealand and over the south-eastern Pacific (Figure 8.16). These decreases in pressure extend to the 500 hPa level, but are positioned slightly west of the sea level pressure decreases (Figure 8.17). This indicates increased uplift in these regions, and as such there are corresponding patterns of 500 hPa temperature decrease due to adiabatic expansion (Figure 8.18).

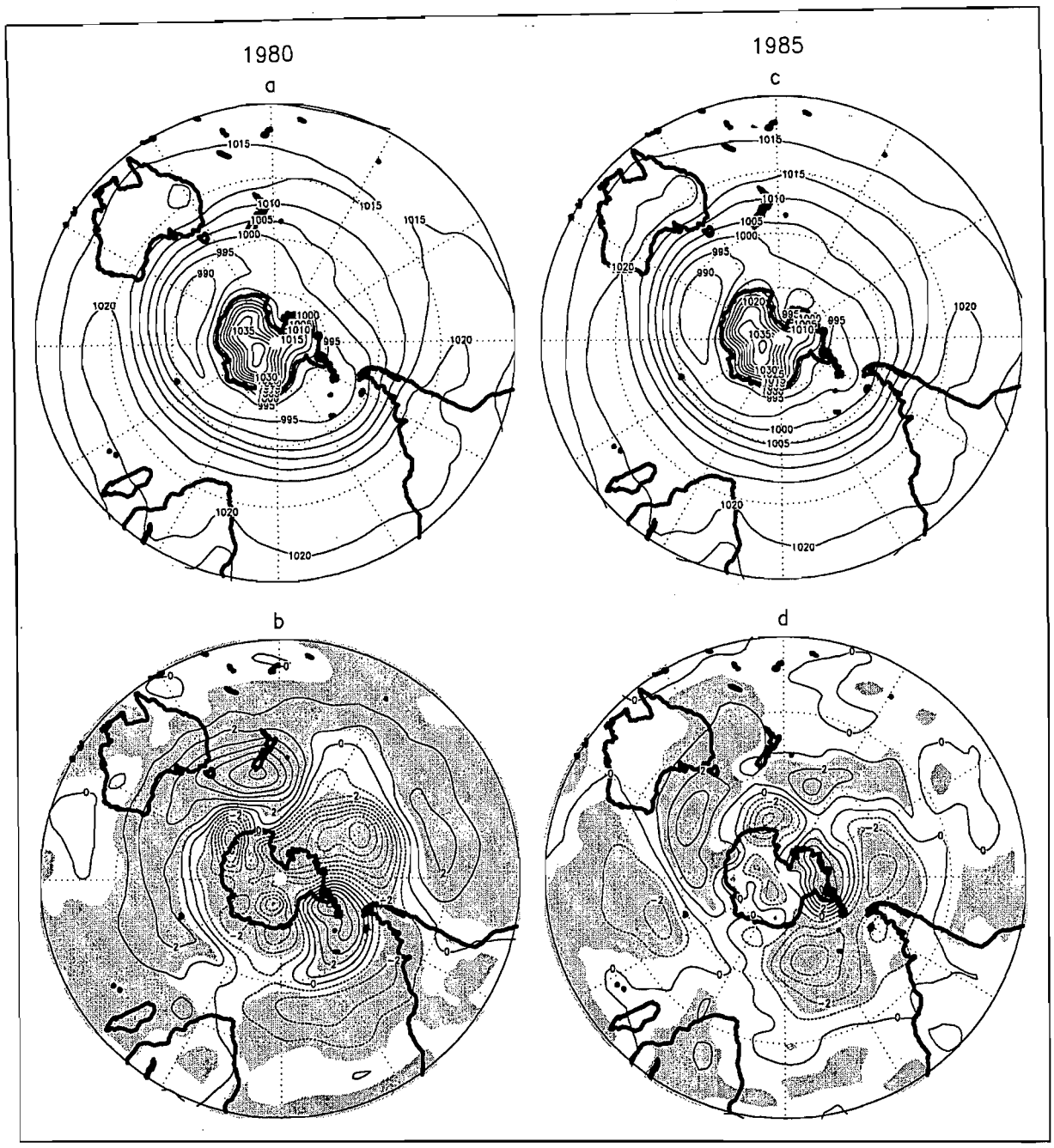

Figure 8.16 Sea level pressure (hPa) for the controls of *a*) 1980 and *c*) 1985, and the perturbations minus the controls for *b*) 1980 and *d*) 1985. Statistically significant differences at the 95% confidence level have been shaded. Negative anomalies in *b*) and *d*) are depicted as dotted contours.

The sea level pressure reductions over the south Atlantic and south-east Pacific are zonally more expansive than the other high latitude reductions and extend northwards of 50°S in both years (Figure 8.16). These pressure patterns may be responsible for producing the surface air temperature increases that are seen in the South African and South American sectors north of 50°S (Figure 8.15), such that there is northward advection of anomalously warm high latitude air on the western side of the anomalous low pressure troughs. The temperature increase in the South African sector may also be associated with increased subsidence, since portions of the anomaly are located in regions of sea level pressure (Figure 8.16) and 500 hPa height

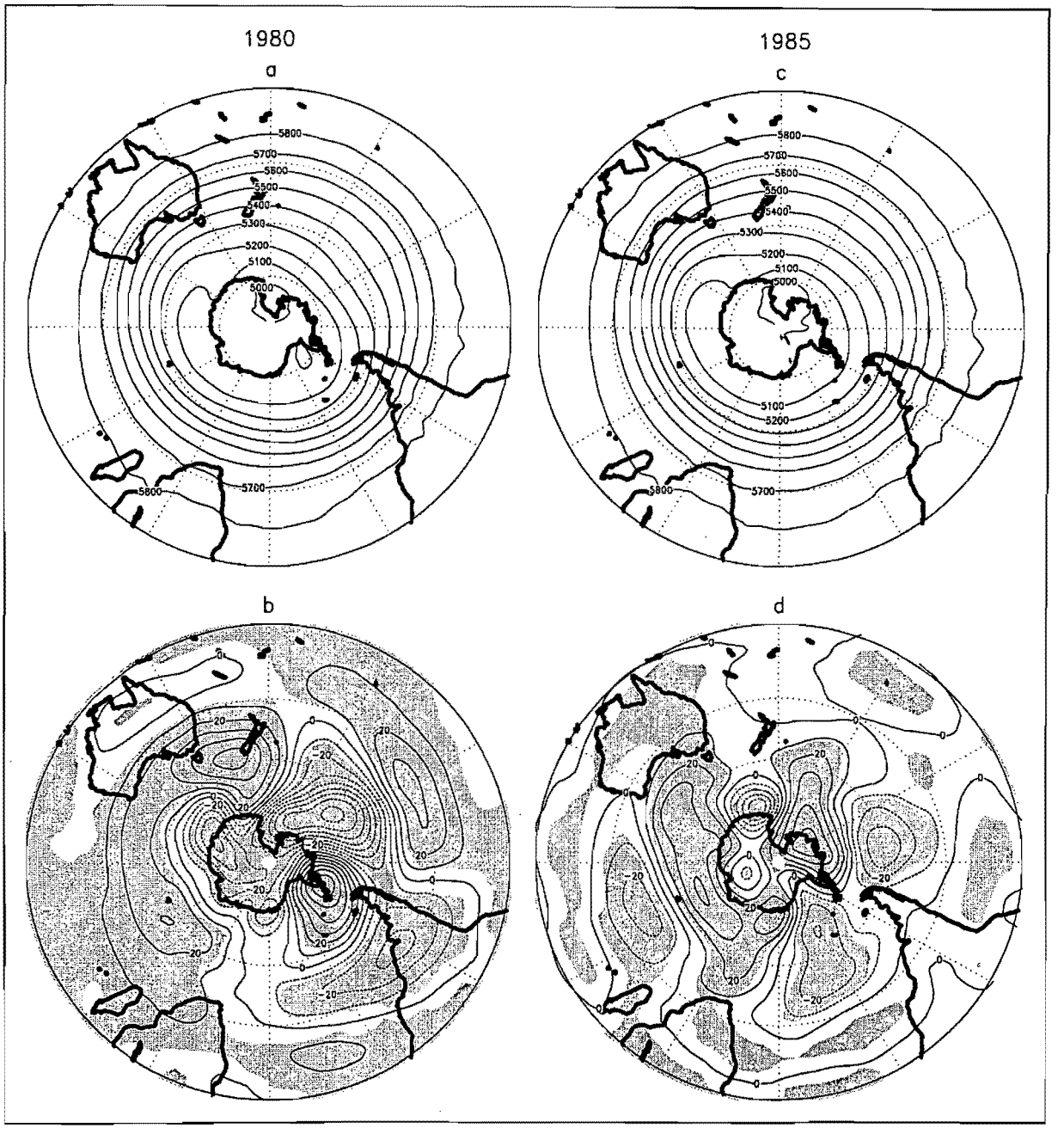

Figure 8.17 500 hPa geopotential heights (m) for the controls of *a*) 1980 and *c*) 1985, and the perturbations minus the controls for *b*) 1980 and *d*) 1985. Statistically significant differences at the 95% confidence level have been shaded. Negative anomalies in *b*) and *d*) are depicted as dotted contours.

increases (Figure 8.17). These explanations of the surface air temperature increases in portions of the western Indian and the eastern Pacific sectors substantiate the results found for the sensible heat fluxes (Figures 8.7 and 8.8). In both years in these two sectors the sensible heat flux north of 60°S is reduced (Figure 8.7 and 8.8), which indicates that processes such as advection or adiabatic warming are causing the air temperature to be higher than the surface temperature.

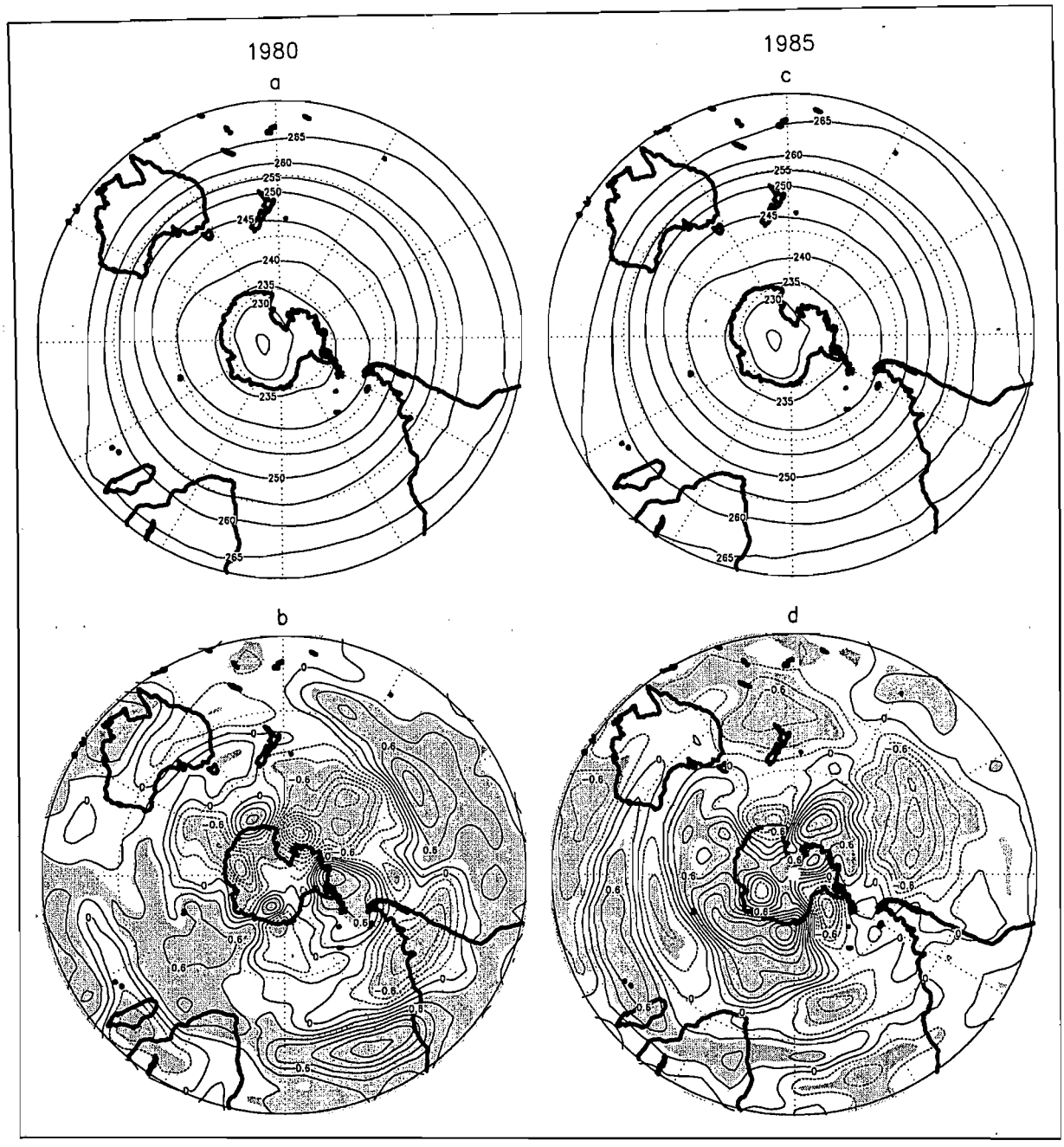

Figure 8.18 500 hPa level temperature (K) for the controls of *a*) 1980 and *c*) 1985, and the perturbations minus the controls for *b*) 1980 and *d*) 1985. Statistically significant differences at the 95% confidence level have been shaded. Negative anomalies in *b*) and *d*) are depicted as dotted contours.

There are also significant high latitude increases in pressure over the Antarctic Peninsula and near the dateline (~180°E in 1980 and ~160°W in 1985) in both years (Figure 8.16). These are associated with corresponding 500 hPa height (Figure 8.17) and temperature (Figure 8.18) increases, indicating increased subsidence in these regions. It is also important to note that these pressure increases may be responsible for the surface temperature increases in these regions due to increased adiabatic warming (Figure 8.15). The increases in pressure may be compensating for increased uplift at neighbouring longitudes. The pressure increases are also located where the imposed changes in sea-ice extent were small (Figure 5.14). These results

indicate that not all the surface air temperature increases around Antarctica may be caused directly from the sea-ice reduction.

There are a number of other similarities between the two years in terms of the pressure response, both at sea level (Figure 8.16) and the 500 hPa level (Figure 8.17). There is an increase in pressure in the Australian/New Zealand sector between 30°S and 55°S in both years (Figure 8.16 and 8.17), which may be related to increased blocking. This assertion will be further examined in the section concerning midlatitude cyclones. There is also a common decrease in pressure over the eastern Pacific (70°W to 150°W) in both 1980 and 1985 between about 40°S and 60°S, as well as a compensating increase in pressure north of this region (Figures 8.16 and 8.17). East of South America, over the Atlantic, there is a decrease in pressure between 30°S and 50°S, although the primary decrease in sea level pressure in 1980 is located north of the major decrease in 1985 (Figure 8.16 and 8.17). This may be because the increased subsidence over the Antarctic Peninsula extends further north in 1980 compared to 1985 (Figure 8.16). The pressure response over the Atlantic may be positioned further north in 1980 compared to 1985 due to more expansive sea-ice in 1980 (Figure 5.14). In addition, in the seasonally averaged *control* sea level pressure field (Figure 8.16*a* and *c*), the pressures in the circumpolar trough near the Weddell Sea extend further north in 1980 compared to 1985. For example, near 30°W the 995 hPa isobar extends to about 52°S in 1980, but only to about 62°S in 1985.

An interesting trans-hemispheric pattern which is prominent in both years between 30°S and 50°S is the negative pressure anomaly over the Atlantic Ocean and the positive pressure anomaly over the region encompassing Australia and New Zealand (Figures 8.16 and 8.17). These contrasting patterns may be linked to opposing shifts of the pressure systems in the two regions. A comparison of the respective control and perturbation sea level pressure plots for the two years (not shown) indicates a northward shift of the pressure systems over the western Atlantic and a southward shift of the pressure systems over the Australia/New Zealand region. This difference accounts for the confusing plots of zonally averaged vertical velocities (Figure 8.2), since it is clear that opposing results would be obtained for different longitudinal sectors. Therefore, over the Atlantic sector it is hypothesised that there is a northward expansion of the Ferrel Cell, because of the large sea-ice and SST perturbations in this region. In contrast, for the region by Australia and New Zealand, although there is a circumpolar reduction in surface pressure due to the sea-ice and SST perturbations, this pressure reduction

is less extensive compared to the Atlantic region. It is hypothesised that in the Australian/New Zealand region, there is a southward extension of the Hadley Cell. Many of the changes in the seasonally averaged sea level pressure and 500 hPa height fields mentioned above are related to changes in the phase and amplitude of the 500 hPa planetary waves, which will be considered in the following section.

8.4.1.2 Comparison with Previous Studies

A comparison of the temperature and sea level pressure responses can be made with earlier modelling studies investigating the impact of a reduction in Antarctic sea-ice. In the modelling experiment performed by Simmonds and Budd (1991) where all winter Antarctic sea-ice was removed, there were increases in surface temperature around Antarctica, with the largest anomalies positioned over the Weddell and Ross Seas. In the present study the temperature increases in the latter two regions are generally positioned north of the seas rather than over the seas, but this is because the sea-ice cover over the seas is not perturbed, whereas it is in the study of Simmonds and Budd (1991). In addition, their temperature increases only extend as far north as 60°S (Simmonds and Budd, 1991), whereas in the present study increases extend to about 50°S. This is because Simmonds and Budd (1991) did not alter SSTs outside the sea-ice zone, while in the present study SSTs are manipulated and hence increased in and around the sea-ice zone so as to extend the SST gradient to the new sea-ice boundary. The Antarctic sea-ice perturbation studies performed by Mitchell and Hills (1986), Simmonds and Dix (1987) and Mitchell and Senior (1989) did not consider the spatial response of surface air temperature, only zonally averaged anomalies, therefore direct comparisons are not possible.

In terms of sea level pressure, Mitchell and Hills (1986) also obtained decreases in pressure over much of the Atlantic Ocean south of 30°S and over middle to high latitudes of the central Pacific. South of 60°S, surrounding the Antarctic continent, they recorded a more uniform decrease in pressure than in the present study (Mitchell and Hills, 1986). In the present study, the decreases are punctuated by regions of increased pressure especially for 1985. This may be related to the larger sea-ice perturbation imposed in the former study, especially over the Indian and Pacific Oceans, since they removed all the sea-ice north of 66°S (Mitchell and Hills, 1986). There was an indication of increased pressures over the Drake passage and Antarctic Peninsula in their study (Mitchell and Hills, 1986), as is seen in the present study.

In the experiment performed by Simmonds and Dix (1987) where they removed all winter sea-ice in a perpetual July simulation, there were larger areas of sea level pressure increase around the Antarctic continent than found by Mitchell and Hills (1986). However, they did record high latitude decreases over the Weddell Sea, central Indian Ocean and near 180°E and these decreases generally coincided with the regions of largest sea-ice reduction (Simmonds and Dix, 1987). In contrast with the present study, Simmonds and Dix (1987) found sea level pressure decreases over New Zealand, although they did obtain pressure increases south of Australia, as in the present study. They also recorded significant sea level pressure increases north of 60°S over the south-east Atlantic, which is in opposition with the results obtained in the present study and the study of Mitchell and Hills (1986).

In a commentary on the studies done by Mitchell and Hills (1986) and Simmonds and Dix (1987), Mitchell and Hills (1987) note that the discrepancies in the results are largely confined to the boundary layer and may be partially caused by different model formulations of processes in this layer. In addition, contrasting results may be related to differences in the size and positioning of the anomalies, and the different control sea level pressure distributions. Incidentally, in both studies the pressures in the circumpolar trough are too high compared to both observed data and the present study. The changes in pressure recorded by Simmonds and Dix (1987) are of a similar magnitude to the changes recorded in the present study, despite the larger sea-ice perturbation in the former study. Mitchell and Hills (1987) suggest that it may not be so much the size of the temperature or sea-ice anomaly itself which is important in determining the atmospheric response, but rather the magnitude of the anomalous heating and its position relative to both the unperturbed flow, i.e. the major troughs and ridges, and the underlying pattern of surface temperature.

Mitchell and Senior (1989) repeated the experiments of Mitchell and Hills (1986) using an 11-layer GCM instead of a 5-layer GCM in order to produce a more realistic control simulation and found results similar to the previous study in that the largest decreases in pressure were found near the largest changes in sea-ice extent. As in the present study, they also found pressure decreases over the eastern Pacific and eastern Atlantic south of 30°S. However, in contrast with the results of the present study, they recorded sea level pressure decreases south of Australia, between 30°S and 50°S (Mitchell and Senior, 1989).

The sea level pressure anomalies in the present study are fairly similar to the results obtained from the most recent Antarctic sea-ice perturbation experiments which were performed by

Simmonds and Budd (1991). They executed four simulations with varying sea-ice concentration, such that the fraction of open water in the ice-pack was set to 0.05, 0.50, 0.80, and 1.00 respectively, where the last experiment was akin to the removal of all the sea-ice. In the experiment where all sea-ice was removed, there was a general decrease in pressure around the Antarctic continent, particularly over the Weddell Sea, over the south Indian Ocean near 80°E, and near the Ross Sea. In the present study, the pressure decreases in the Weddell Sea sector are positioned north of those found by Simmonds and Budd (1991), which may be related to the fact that their sea-ice anomalies extended further south than in the present study, i.e. sea-ice over the Weddell Sea itself was perturbed in their study, but was largely unperturbed in the present study. In addition, the temperature increases that they (Simmonds and Budd, 1991) recorded only extended as far north as 60°S, whereas in the present study increases extend to about 50°S due to the SST manipulation. Simmonds and Budd (1991) found an increase in pressure near 60°S over the Drake Passage and eastern Pacific Ocean, which may be comparable to the pressure increase that is recorded in the present study near the Antarctic Peninsula. They also recorded decreases in pressure, similar to the present study, over much of the Atlantic south of 30°S and increases in pressure south of Australia (Simmonds and Budd, 1991). In addition, the results that they obtained over the eastern Indian Ocean resemble those found for 1985 in the present study, i.e. a narrow region of pressure decrease around the continent, with an increase in pressure between about 50°S and 60°S and a decrease in pressure north of this.

Simmonds and Budd (1991) found that the proportion of significant sea level pressure anomalies between the 4 experiments increased as the concentration of sea-ice was decreased, such that the most significant changes were found for the case of the complete removal of the sea-ice. This was especially the case for the complementary increases in pressure which they generally found north of the high latitude decreases. Compared to the present study, the response that Simmonds and Budd (1991) obtained from removing all the sea-ice tends to be more spatially organized and zonally symmetrical, rather like the results obtained in the present study for summer. This may be due to larger sea-ice perturbations imposed over the Indian and Pacific Oceans relative to the Atlantic Ocean in their study compared to the present study, producing a more even distribution of sea-ice anomalies around the hemisphere.

It is clear that while there are a number of similarities in the sea level pressure response to the various sea-ice perturbations that have been performed, including that of the present study, there are also a number of differences. As has been mentioned previously, these differences may be ascribed to GCM differences in resolution, parameterisations and physics; differences in experimental design and in the size and positioning of the imposed anomalies; differences in the unperturbed flow of the control simulations as well as to the high variability of the climate at high and middle latitudes during winter. In addition, Simmonds and Budd (1991) comment that the response of sea level pressure is complicated by many factors including ocean temperatures, topography and changes in heat fluxes and baroclinicity. The modelling studies mentioned in this section have also been performed with earlier generation models of lower horizontal and vertical resolution than used in the present study, thus one might expect differences in the response in the present study. It is also important to reiterate that the sea-ice extent anomalies that have been imposed in the present study are significantly smaller than those used in the above mentioned studies.

Despite the differences between the models and the experiments performed there are similarities, and based on the cumulative results from these previous modelling studies it is suggested that the most robust sea level pressure changes in the present study include: a general decrease in sea level pressure between 60°S and 70°S around Antarctica, perhaps with the exception of the region near the Antarctic Peninsula and Drake Passage; a decrease in sea level pressure in the south Atlantic corresponding to the region of the largest sea-ice perturbation; a decrease in pressure over much of the Atlantic south of 30°S and an increase in pressure over the Australian region between 30°S and 55°S.

Although the above-mentioned pressure anomalies are given with respect to their geographical positioning, this section has shown that in terms of the details of the response it is rather the positioning of the anomalies relative to the major circulation features that is important. It has become clear that the results from 1980 and 1985 do not always converge in terms of the geographical positioning of the anomalies, but when one uses the major circulation features as a reference point and thus take the control circulation patterns into account, then many of the discrepancies in the results between the two years fall away. This observation applies to many of the variables that are examined in the subsequent sections.

8.4.2 500 hPa Wind

The changes in sea level pressure and 500 hPa heights have an impact on wind speed over the hemisphere. As expected, where the change in gradient of the 500 hPa heights is greatest (Figure 8.19), there are increases in the 500 hPa wind speed (Figure 8.20). In response to sea-ice reduction experiments, Mitchell and Hills (1986) found weaker mid-tropospheric westerly winds around the Antarctica, Simmonds and Dix (1987) reported weaker westerlies between 45°S and 70°S and positive anomalies north of this, Mitchell and Senior (1989) found reduced wind speeds north of 65°S and increased wind speeds to the south, and Simmonds

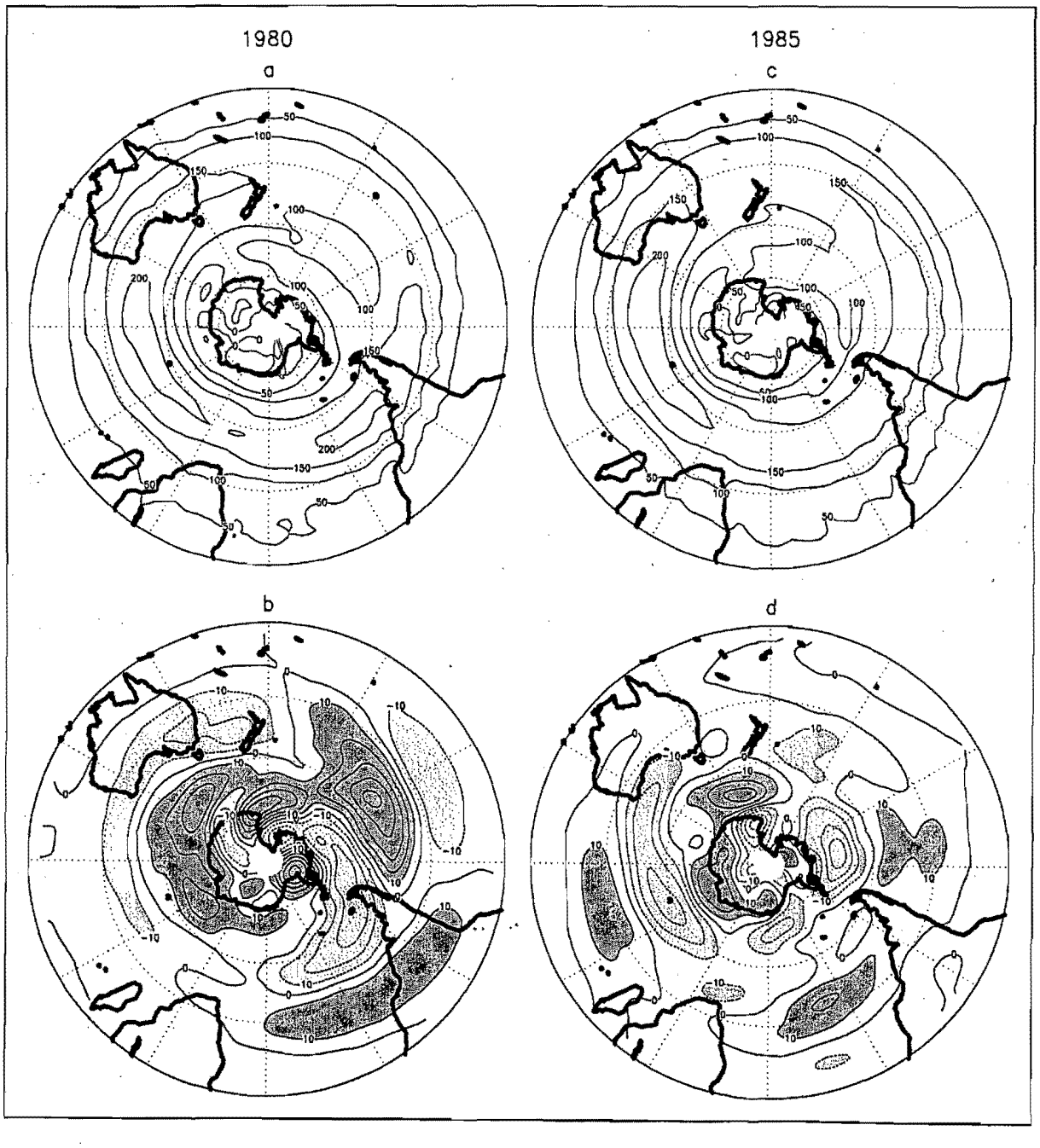

Figure 8.19 The 500 hPa geopotential height gradients (m per 3.7° latitude) (calculated for the north-south direction) for the controls of *a*) 1980 and *c*) 1985, and the perturbations minus the controls for *b*) 1980 and *d*) 1985. Anomalies greater than 10 m per 3.7° latitude and less than -10 m per 3.7° latitude have been shaded in *b*) and *d*).

and Budd (1991) found a weakening of the westerlies between about 40°S and 60°S and a strengthening of the westerlies further south. These studies suggested that in agreement with the thermal wind relationship, if there is a warm anomaly near 65°S, due to a sea-ice reduction, then one would expect easterly wind anomalies to the north, in the midlatitudes, and westerly wind anomalies to the south. However, all of the above studies examined wind speed changes exclusively from a zonally averaged perspective and results from the present study show that the geographic changes are not so simple or uniform. In both years there are regions between 30°S and 50°S where the 500 hPa wind speed increases in response to the perturbation (Figure 8.20), in contrast with the hypotheses formulated by the previous studies. This seems to be especially true over the central and eastern Pacific. In most of the other sectors between 30°S and 50°S, there are indeed reduced wind speeds (Figure 8.20). Similarly, in both years, apart from the eastern Pacific region, there appears to be a general increase in wind speeds between 50°S and 70°S i.e. over the zone where the sea-ice and SST anomalies are located (Figure 8.20), thus in agreement with the thermal wind effect. Both years also show a clear reduction in the speed of the wind between 10°S and 20°S over the Atlantic Ocean and Africa (Figure 8.20). The patterns of wind speed change in 1985 appear to be positioned slightly south of those in 1980, especially over the Atlantic and Indian Oceans, which again may be related to the northward positioning of anomalies in 1980 compared to 1985. The general difference in the wind anomaly pattern over the eastern Pacific compared to the rest of the hemisphere, may be due to the prominent increase in subsidence over the Antarctic Peninsula and Bellingshausen Sea in both years (Figure 8.17). This increase in pressure between 60°S and 70°S, and decrease in pressure to the north of this (Figure 8.17), serves to decrease the meridional pressure gradient between 50°S and 70°S (Figure 8.19) thereby causing a reduction in wind speeds south of 50°S (Figure 8.20).

A comparison of the wind speed changes in each year (Figure 8.20*c* and *f*) with respect to the location of the jet streams (given by wind speeds greater than 20 m s^{-1}) in the controls and perturbations (Figure 8.20*a*, *b*, *d* and *e*) shows that there is a general weakening of the jet stream, except over the eastern Pacific Ocean. It is also apparent that over the Atlantic Ocean, there is a slight northward shift of the jet stream (Figure 8.20). This shift is consistent with the previously hypothesised northward shift of the pressure systems in this region.

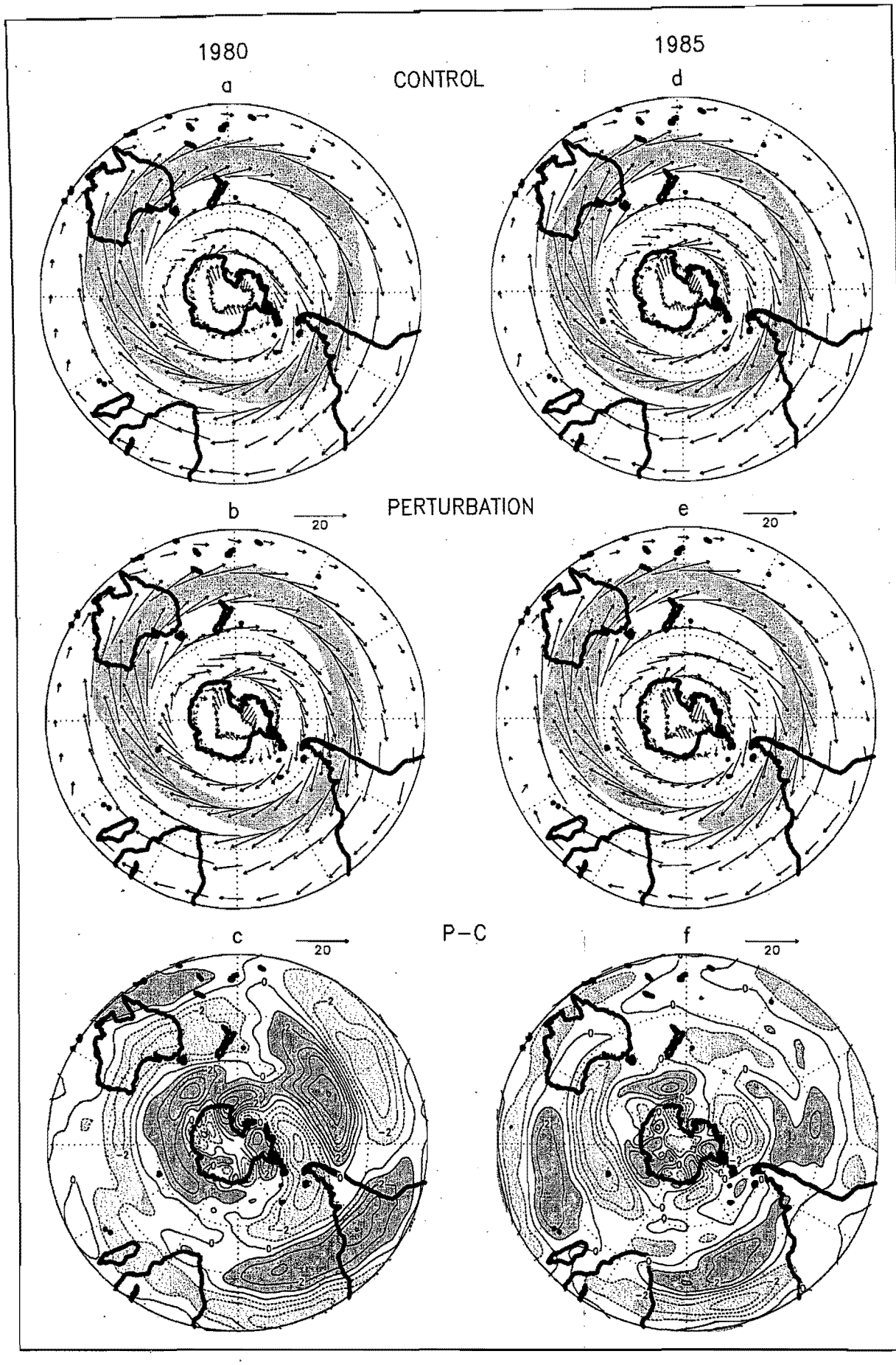

Figure 8.20 500 hPa wind direction and speed (m s^{-1}) for the controls of *a*) 1980 and *d*) 1985, and the perturbations of *b*) 1980 and *e*) 1985. Wind speeds greater than 20 m s^{-1} have been shaded. Maps *c*) and *f*) show the change in wind speed between the perturbations and the controls in 1980 and 1985 respectively. Anomalies greater than 1 m s^{-1} and less than -1 m s^{-1} have been shaded in *c*) and *f*).

8.4.3 Midlatitude Cyclones and Storm Tracks

Many of the changes in midlatitude cyclone density are related to changes in sea level pressure, such that there is a close association between decreases in pressure (Figure 8.16) and increases in cyclone density (Figure 8.21) and *vice versa.* For example, the decrease in pressure over the eastern Pacific (70°W to 150°W) in both 1980 and 1985 between about 40°S and 60°S (Figure 8.16 and 8.17), is associated with an increase in midlatitude cyclone

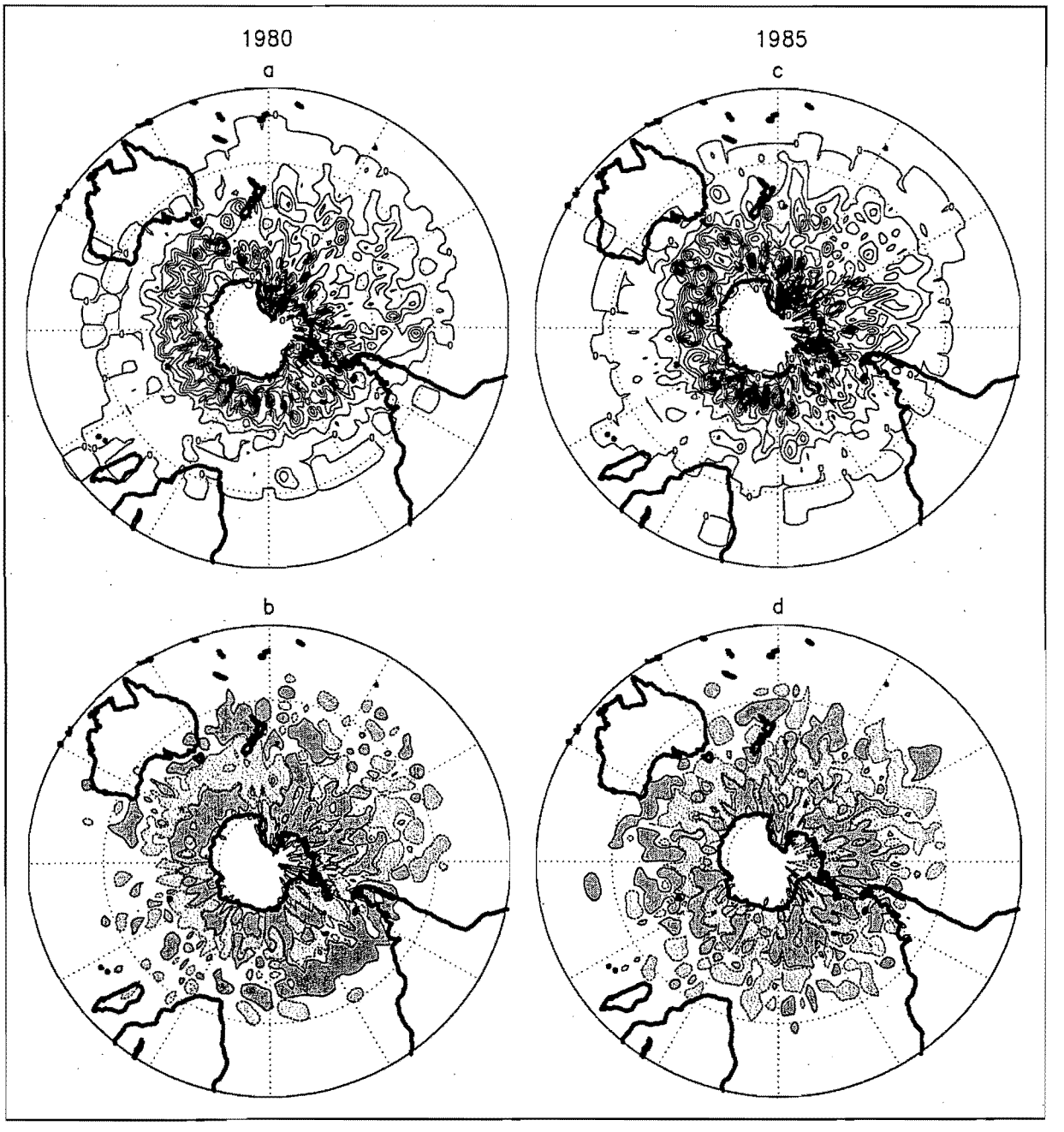

Figure 8.21 Midlatitude cyclone densities ($\times 10^{-3}$ cyclones (degrees latitude)$^{-2}$) for the controls of *a*) 1980 and *c*) 1985, where the contour interval is 0.5×10^{-3} cyclones (degrees latitude)$^{-2}$. Densities for the perturbations minus the controls are shown in *b*) and *d*) for 1980 and 1985 respectively. For clarity in *b*) and *d*), only anomalies greater than 0.2×10^{-3} cyclones (degrees latitude)$^{-2}$ and less than -0.2×10^{-3} cyclones (degrees latitude)$^{-2}$ are presented, and only the aforementioned contour lines are plotted.

densities (Figure 8.21), while north of this region there is a compensating increase in pressure (Figures 8.16 and 8.17) and reduction in midlatitude cyclone densities (Figure 8.21).

It was previously mentioned that the increase in pressure in the Australian/New Zealand sector between 30°S and 55°S in both years (Figure 8.16 and 8.17), may be related to increased blocking. Trenberth (1980) notes that in winter the formation of blocking highs in the New Zealand sector south of 45°S is coupled to the formation of cut-off lows between 20°S and 35°S in the Tasman Sea. The change in midlatitude cyclone density in the present study appears to show this blocking signature, with a general reduction in midlatitude cyclone densities between 40°S and 50°S in this region in both years and an increase in densities to the north of this, over the Tasman Sea (Figure 8.21).

As for the summer season, the changes in cyclone density may be directly related to the changes in sea-ice extent or indirectly via changes in baroclinicity or the positioning of oceanic fronts. Figure 8.22 shows the change in the meridional gradient of SSTs that was imposed in the experiments. With an increase in the SST gradient between 55°S and 70°S in both years (Figure 8.22), one might expect an increase in baroclinic activity and an increase in cyclone density and cyclogenesis. There does appear to be a general increase in cyclone densities, centred around 60°S (Figure 8.21*b* and *d*). The increases are most zonally expansive (extending between about 55°S and 70°S) in the region east of the Ross Sea, north and east of the Weddell Sea and south of Australia (Figure 8.21), thus associated with the major sea-ice perturbations, especially in the former two regions, and corresponding to major falls in sea level pressure (Figure 8.16).

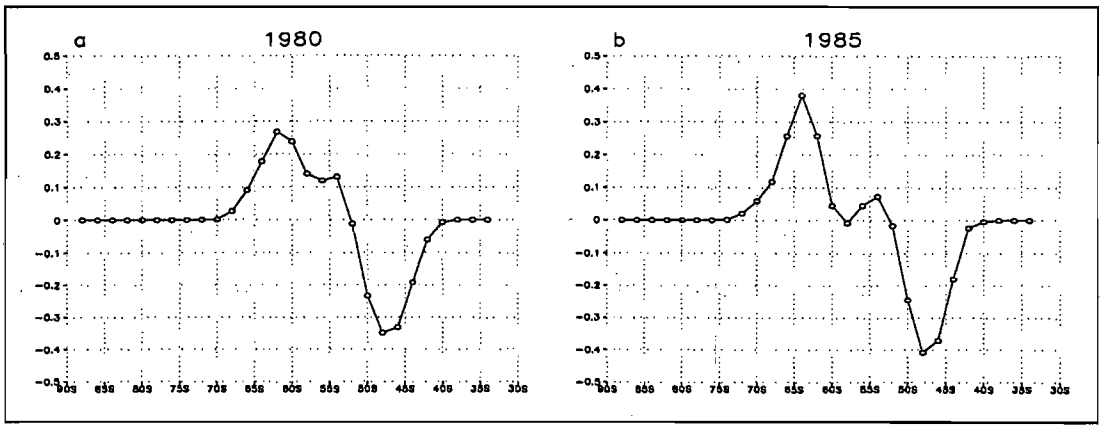

Figure 8.22 Change in the SST gradient (K per 3.7° latitude) (calculated for the north-south direction), in terms of the perturbation minus the control for *a*) 1980 and *b*) 1985.

Apart from perhaps being related to the increase in SST gradient, these cyclone density increases may be linked with the exposure of open water through the removal of sea-ice, thus causing a change in surface fluxes (increased sensible and latent heat fluxes) such that they enhance cyclogenesis. If one compares the average pattern of imposed sea-ice anomalies (Figure 5.14) to the pattern of cyclone density changes (Figure 8.21), then in both years there appear to be general increases in cyclone density in those regions from which sea-ice was removed at some stage during the winter simulation. The cyclone increases may also be related to increases in mesocyclogenesis associated with strong temperature gradients in the region of the perturbed sea-ice boundary.

Figure 8.22 shows that there are reduced SST gradients near 50°S in both years, which may result in decreased baroclinic activity and thus less cyclonic activity. There are reductions in cyclone density north of the higher latitude increases, and the decreases are generally positioned near 50°S, but there is a large degree of longitudinal variation (Figure 8.21).

In a modelling experiment where sea-ice concentration was reduced, Simmonds and Wu (1993) found a tendency for more cyclones to be found in the latitude band of 10°-15° latitude width centred on the Antarctic coastline and fewer to the north of this, reflecting a southward shift of the zone of maximum cyclone density. While this general trend of high latitude increase and decrease in adjacent northern latitudes is broadly consistent with the present study, there are a number of differences between the results. In the study by Simmonds and Wu (1993) the cyclone density increases generally did not extend beyond 60°S, in contrast to results of the present study. Furthermore, in both years of the present study, there are also regions of cyclone density decrease around Antarctica, whereas the results from Simmonds and Wu's (1993) paper suggest only increases. A comparison of the control, perturbation (not shown) and anomaly cyclone density maps for the present study shows a southward shift of the zone of maximum densities near the circumpolar trough in the region south of Australia in both years, but this result does not appear to hold true, or is not as clear, for the rest of the hemisphere (Figure 8.21). The southward shift in densities south of Australia may be linked to the previously mentioned shift of the pressure systems in this region.

In summary, in the present study the cyclone density increases seem to be centred around 60°S, whereas the increases from Simmonds and Wu's (1993) study were centred on the Antarctic coastline, near 70°S. Apart from the experiment where all the sea-ice was removed,

Simmonds and Wu (1993) were concerned with changes in sea-ice concentration and such changes may produce a slightly different response in terms of cyclone density than sea-ice changes that are imposed at the sea-ice edge, i.e. changes in extent, as in the present study. For example, Simmonds and Wu (1993) found an increase in cyclones over most of the Weddell Sea, where the present study records decreases over the sea (near 70°S). The sea-ice perturbations imposed in the present study do not extend over the southern portion of the Weddell Sea (Figure 5.14), whereas the perturbations in Simmonds and Wu's (1993) study would have affected the sea-ice in this region. The authors (Simmonds and Wu, 1993) did not examine cyclone changes north of about 45°S, therefore comparisons north of this latitude are not possible. As an aside, it is interesting to note that while it appears that changes in Antarctic sea-ice concentration or extent have a clear impact on cyclone densities in the Southern Hemisphere (as shown by the work of Simmonds and Wu (1993) and the present study) it seems, from a modelling study done by Murray and Simmonds (1995), that overall cyclone numbers in the Arctic are largely insensitive to sea-ice concentration changes, with an unexpected absence of cyclone density increases at high latitudes in response to sea-ice reductions.

As was mentioned in Chapter 6, concerning the results for the summer season, Godfred-Spenning and Simmonds (1996) found that the link between cyclone density and sea-ice extent is not particularly strong if examining correlations with observed data. They made this general conclusion for all the seasons, but did find that a greater proportion of significant correlations were found if time lags were introduced into the data and if they looked at 'upstream' and 'downstream' associations between the two variables. They also noted that the strongest relationships were most often found 5°-10° north and south of the sea-ice boundary and suggested that this indicates the predominance of oceanic fronts or baroclinic zones. Godfred-Spenning and Simmonds (1996) found that less extensive winter sea-ice in the western Ross Sea seemed to be related to a decrease in cyclone density and cyclogenesis between 5° and 15° north of the sea-ice edge in this region. This result is consistent with the cyclone density change found for 1980, but not for 1985 (Figure 8.21). They also found that a decrease in cyclogenesis on either side of the Antarctic Peninsula is associated with less extensive winter sea-ice. The present study does not consider changes in cyclogenesis, but does show reductions in cyclone density on either side of the peninsula south of 60°S in both years. In general, Godfred-Spenning and Simmonds (1996) observed that a reduced sea-ice extent is linked with fewer cyclones around 5° south of the sea-ice edge. This result is not clearly evident in the cyclone density changes from the present study. Their results also

suggest that stronger relationships are found when sea-ice extent changes are made to lag cyclone density changes and concluded that there is a greater tendency for the atmosphere to control sea-ice extent, rather than the reverse. Nonetheless, this does not mean that the latter is not important and that sea-ice changes could not produce significant feedbacks on the atmosphere.

Related to the cyclone density changes are changes in the storm tracks (Figure 8.23). Storm tracks have been identified in the present study by calculating the standard deviation of bandpass filtered (1.5 - 8.5 days) sea level pressure data and thus give some indication of pressure variability due to the passage of cyclones and anticyclones. Therefore, any changes to the storm tracks may reflect changes in cyclone density, cyclone mobility or shifts of the regions of maximum overlap between cyclone and anticyclone densities. In both years in the controls (Figure 8.23*a* and *c*) the regions of maximum sea level pressure variability (greater than 8 hPa) occur between about 45°S and 55°S over the eastern Pacific, western Atlantic and central Indian Oceans. These regions of sea level pressure variability which exceed 8 hPa will be referred to as the control storm tracks.

As has been previously noted, a direct comparison of the anomalies between the two years may yield opposing results because the positioning of the major features differ in the controls. What is more meaningful in terms of the dynamics involved, is the positioning of the anomalies relative to the positioning of the features in the controls. In 1980, there are clear decreases in the sea level pressure variability in the three regions of the storm track where there is maximum variability (greater than 9 hPa), i.e. near 100°W, 10°W and 90°E (Figure 8.23*b*). In 1985, there are also decreases in the sea level pressure variability associated with these three regions, but the positioning varies slightly in association with the positioning of the control storm tracks. For example, in 1980 the control region of maximum variability over the Indian Ocean is positioned near 50°S and 90°E and so is the anomalous decrease. In contrast, in 1985 the control region of maximum variability is positioned west and south of that in 1980, and so is the anomalous decrease. The magnitude of the reductions is greater in 1980 compared to 1985 and this may be related to the larger variabilities in these regions in the control of 1980 (Figure 8.23). Thus, in response to the perturbation, the cores of the major storm tracks, as they are represented in the controls, are reduced in 1980 and 1985.

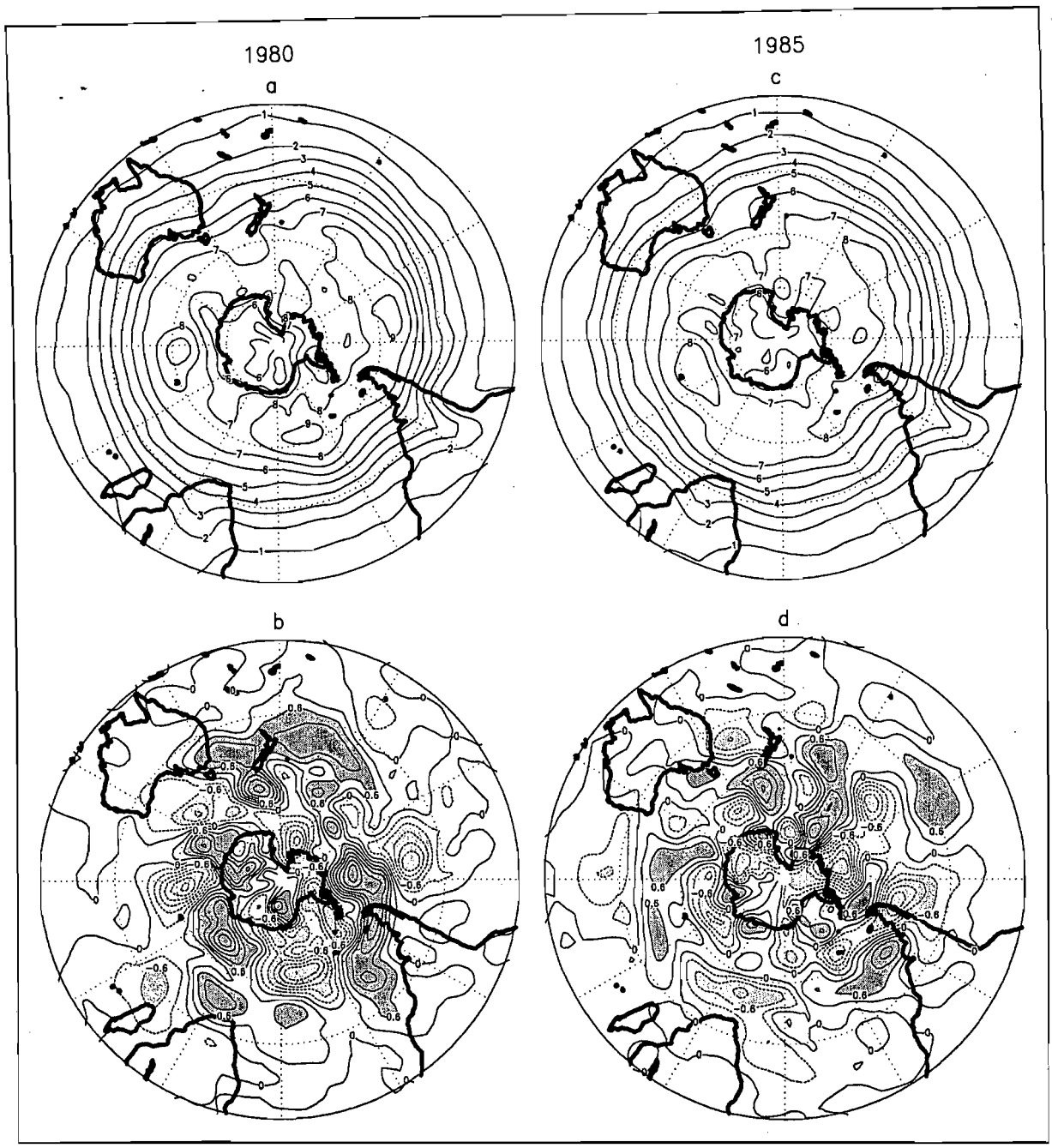

Figure 8.23 The standard deviation (hPa) of the bandpass (1.5-8.5 day) filtered sea level pressure data for the controls of *a*) 1980 and *c*) 1985, and the perturbations minus the controls for *b*) 1980 and *d*) 1985. Anomalies greater than 0.6 hPa and less than -0.6 hPa have been shaded in *b*) and *d*).

There are, however, also regions of enhanced sea level pressure variability within the major storm track zone (~45°S - 55°S), especially between the Atlantic and Indian storm track cores, as represented in the respective controls of the two years, and over the western Pacific Ocean (Figure 8.23). In addition, there are northward extensions and contractions of the storm tracks in response to the perturbation. Of particular note, there is a northward extension of the storm track between 30°S and 50°S over the western Atlantic Ocean and New Zealand region in both years (Figure 8.23*b* and *d*). Over the western Atlantic, the increase in sea level pressure variability is associated with a reduction in sea level pressure in

both years (Figure 8.16) and a clear increase in cyclone densities in 1980 (Figure 8.21*b*). In 1985, there are both increases and decreases in cyclone densities over this region (Figure 8.21*d*). These results suggest that the increase in sea level pressure variability is associated with an increase in the passage of cyclones, although this is less clear for 1985. South of New Zealand and Tasmania, the increase in sea level pressure variability may be a consequence of a higher frequency of blocking in this region and an increase in the degree of overlap of cyclone and anticyclone densities.

8.4.4 Atmospheric Moisture

As a result of the sea-ice and SST perturbation, one might expect an increase in surface specific humidities at high latitudes. The removal of sea-ice would provide an additional moisture source and an increase in surface air temperature would increase the saturation vapour pressure at the surface and increase the potential for evaporation into the lower layers of the atmosphere. Figure 8.24(*b* and *d*) shows that there is indeed a general increase in surface specific humidities south of 50°S, especially in the region east of the Weddell Sea in both years. This high latitude increase in specific humidity is not as clear at the 500 hPa level (Figure 8.25), but the precipitation increases south of 50°S (Figure 8.26*b* and *d*), although small, provides a good match with the surface humidity increases (Figure 8.24*b* and *d*). Apart from this high latitude change, the largest humidity anomalies are found between 10°S and 30°S, where the specific humidities are largest in the controls (Figure 8.24 and 8.25). The changes are generally small and there are also regions of opposing anomalies between the two years, thus it is unclear whether they represent a true response or natural variability. There are, however, some consistent responses between the two years. In both years there is an increase in surface specific humidity associated with the convergence zone, between 10°S and 20°S over the western Pacific (Figure 8.24). In 1980, this increase extends eastwards from the east coast of Australia to about 140°W, whereas it only extends to about 180°W in 1985. This difference may be related to differences in the controls, since the region experiencing humidities greater than 16 g kg^{-1} extends further east in 1980 compared to 1985 (Figure 8.24*a* and *c*). Corresponding increases in 500 hPa specific humidity (Figure 8.25) and precipitation (Figure 8.26) can also be seen in this region. An examination of the control and perturbation (not shown) plots for precipitation suggest that there is a slight southward shift of the region of maximum precipitation in this area in response to the perturbation. This may be related to the changes in pressure, which, as previously mentioned, suggest a southward shift in the

pressure belts in the Australasian region, thus causing the ITCZ and associated high rainfall to move slightly southwards.

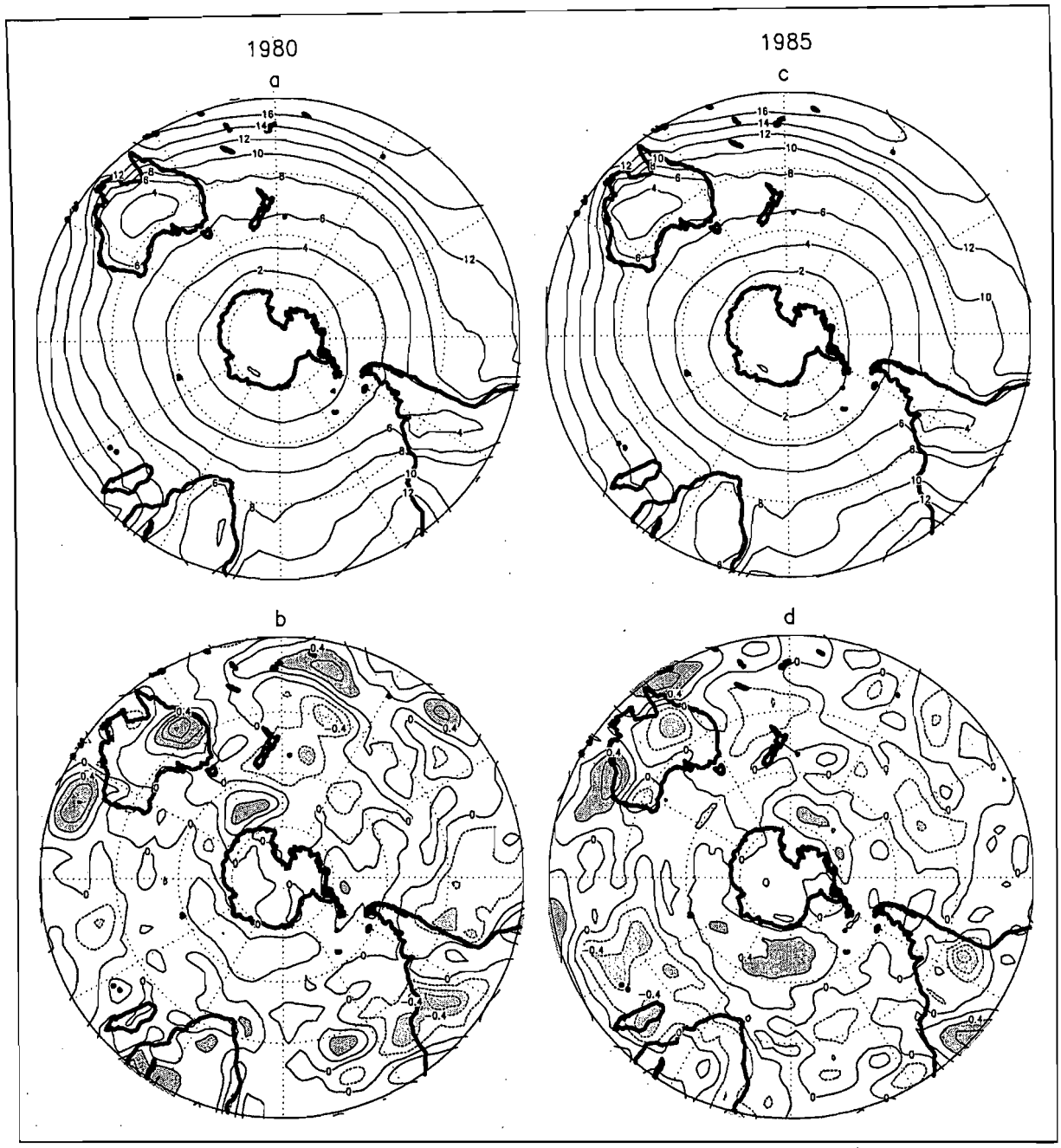

Figure 8.24 Surface specific humidity (g kg^{-1}) for the controls of *a*) 1980 and *c*) 1985, and the perturbations minus the controls for *b*) 1980 and *d*) 1985. Anomalies greater than 0.4 g kg^{-1} and less than -0.4 g kg^{-1} have been shaded in *b*) and *d*).

Over the Pacific region of high precipitation, near 30°S (Figure 8.26*a* and *c*), there is a general pattern of precipitation decrease between about 150°W and 120°W, a small region of increase near 120°W and a decrease between 120°W and 70°W (Figure 8.26*b* and *d*). This change is broadly consistent with the changes in surface specific humidities (Figures 8.24). The precipitation increase near 120°W is stronger in 1985 compared to 1980, whereas the

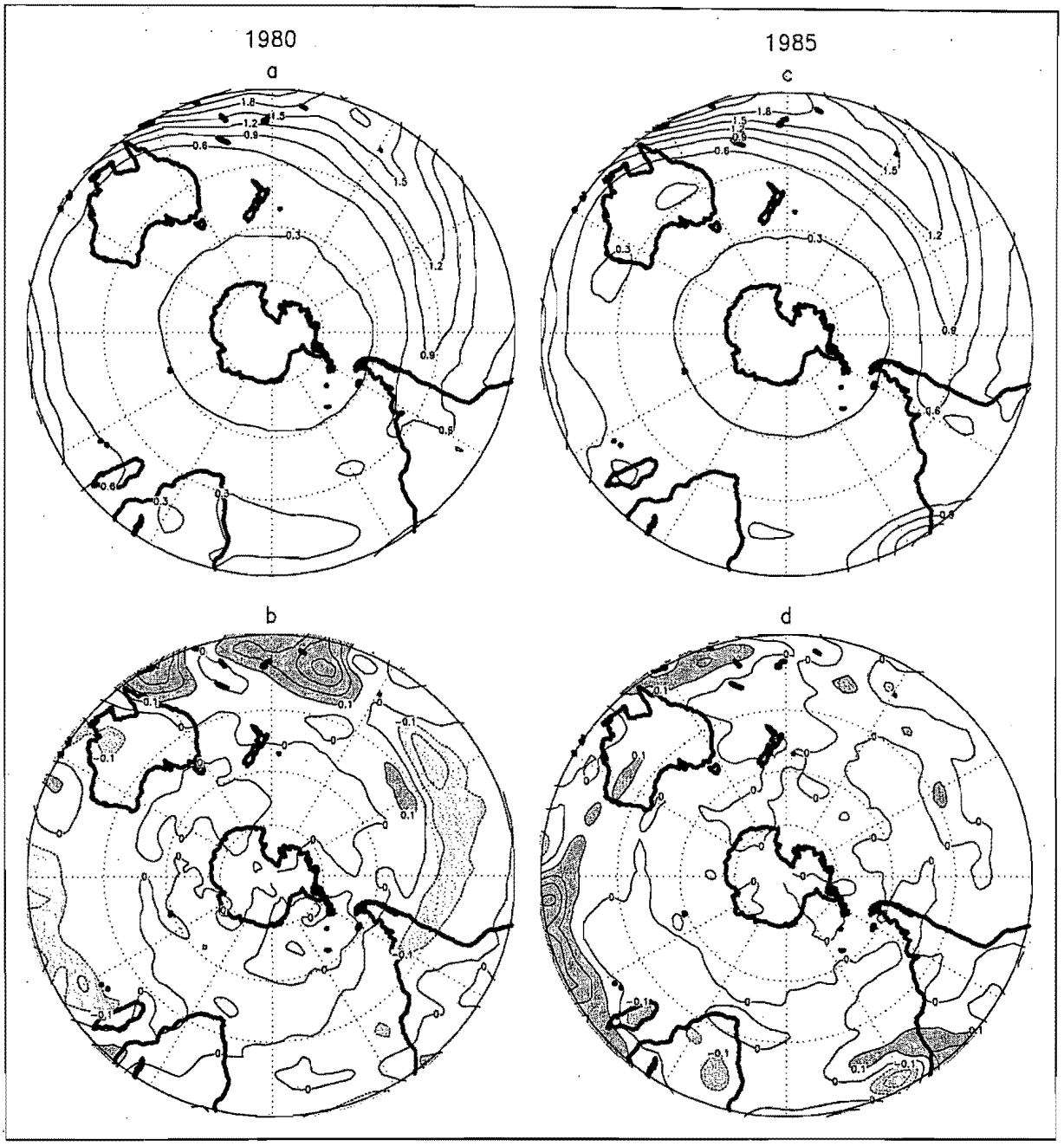

Figure 8.25 500 hPa level specific humidity (g kg^{-1}) for the controls of *a*) 1980 and *c*) 1985, and the perturbations minus the controls for *b*) 1980 and *d*) 1985. Anomalies greater than 0.1 g kg^{-1} and less than -0.1 g kg^{-1} have been shaded in *b*) and *d*).

reverse is true for the decrease between 120°W and 70°W. These precipitation changes correspond to the midlatitude cyclone density anomalies, such that there is an increase in cyclone densities near 120°W and a decrease in cyclone densities between 120°W and 70°W at this latitude in both years (Figure 8.21). This general decrease in the south Pacific convergence zone precipitation may be related to the predominance of positive sea level pressure anomalies in this region (Figure 8.16*b* and *d*). The sea level pressure increases in this region (near 30°S) are greater in 1980 compared to 1985 (Figure 8.16*b* and *d*), as are the precipitation decreases (Figure 8.26).

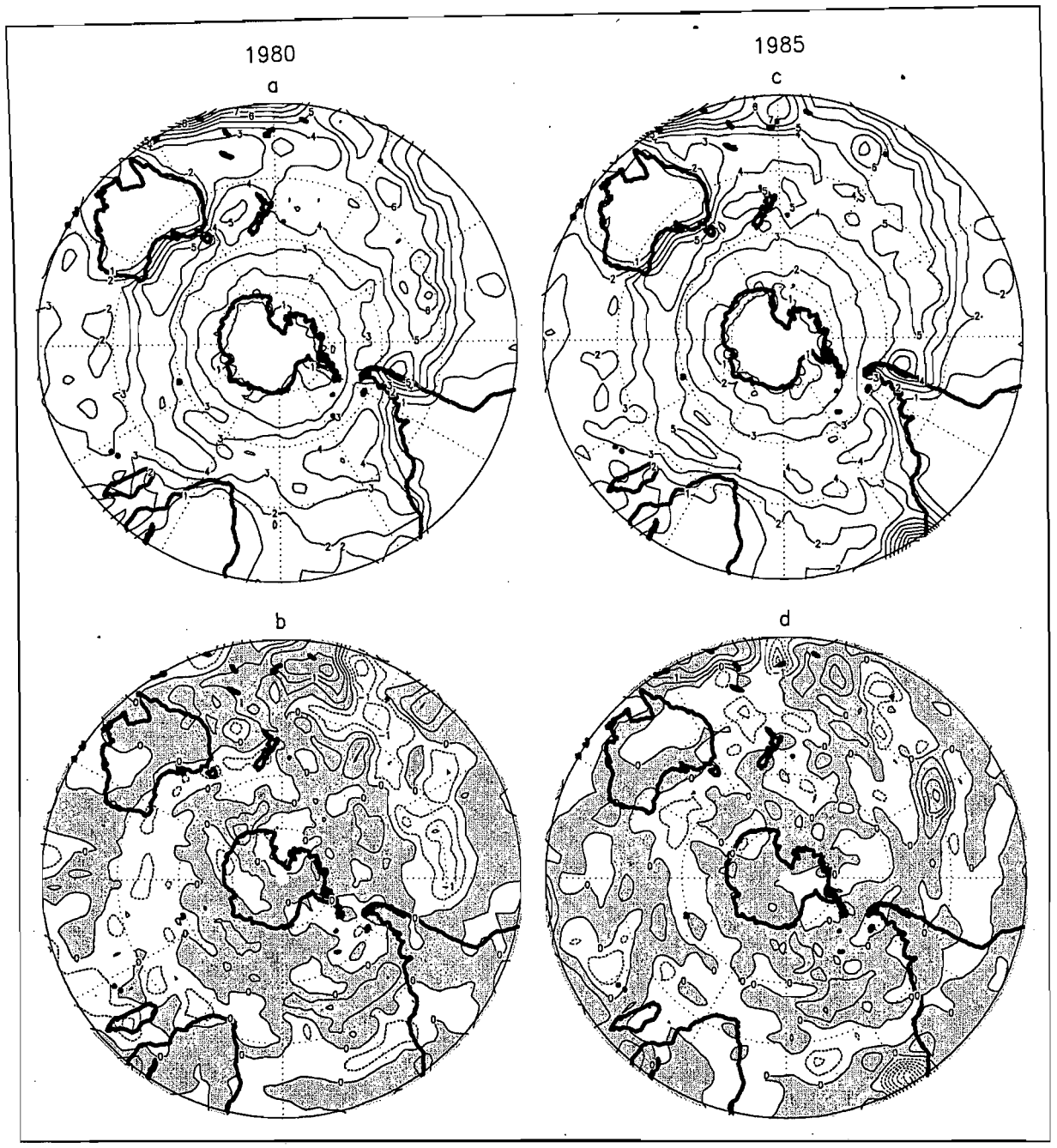

Figure 8.26 Precipitation (mm day^{-1}) for the controls of *a*) 1980 and *c*) 1985, and the perturbations minus the controls for *b*) 1980 and *d*) 1985. Positive anomalies have been shaded in *b*) and *d*).

It is clear from the control surface and 500 hPa specific humidities, as well as the control precipitation, that over the western Atlantic Ocean between 10°S and 20°S there are higher humidities and precipitation in 1985 compared to 1980 (Figures 8.24, 8.25 and 8.26). From examining the area north of this (not shown), it is apparent that these differences are a result of the northward positioning of the features in 1980 compared to 1985. As a result, the anomalies in 1980 are positioned north of those in 1985. For example, in 1985 there are clear reductions in surface specific humidity, 500 hPa specific humidity and precipitation near 10°S and 30°W (Figures 8.24, 8.25 and 8.26). Very similar reductions are evident for 1980 in the

area just north of 10°S (not shown). This again is indicative of the influence of more extensive sea-ice cover in 1980 compared to 1985.

A comparison of the control and perturbation plots for both years (not shown) show that apart from the general increase in precipitation near 35°S, there also appears to be a slight northward shift of the precipitation patterns over the western Atlantic. This may be related to the previously surmised northward shift of the pressure systems over this region.

The precipitation decreases over the Indian Ocean (Figure 8.26) are related to sea level pressure increases (Figure 8.16). The differences in the positioning of the precipitation decreases between the two years is related to the difference in the positioning of the sea level pressure anomalies. In both years, there is an increase in surface specific humidities over eastern southern Africa (Figure 8.24) and an associated increase in precipitation (Figure 8.26).

8.5 500 hPa Planetary Waves

8.5.1 Phase Changes

As for the summer season, the phases of planetary wave numbers 1, 2 and 3 have been examined for the control and perturbation simulations. There are no major changes in the phase of wave number 1 in response to the perturbation, except for the region south of 70°S (Figure 8.27). The phase changes of wave number 2 are either small or inconsistent between the two years (Figure 8.27). However, there appears to be a significant response to the perturbation in terms of the phase of wave number 3. Wave number 3 has been found to play an important role in determining the location of blocking during winter in the Southern Hemisphere (Trenberth and Mo, 1985; Preston-Whyte and Tyson, 1988; Sinclair *et al.*, 1997), and also seems to contribute significantly to interannual variability (Trenberth, 1980; Rogers and van Loon, 1982; Mo and White, 1985). In fact, it has been shown to contribute slightly more to interannual variability at 55°S than either wave numbers 1 or 2 (Trenberth, 1980).

The control phases of wave number 3 are quite different between the two years, especially south of 45°S, but the perturbation phases are more similar (Figure 8.27). In both years there is an eastward phase shift between 45°S and 62°S, and a westward phase shift between 30°S and 45°S (Figure 8.27). This positions the first ridge of the wave in the perturbations near 45°E in 1980 and 55°E in 1985 in the zone between 45°S and 62°S, and near 40°E in 1980

and 48°E in 1985 in the zone between 30°S and 45°S (Figure 8.27). The significance of these phase changes becomes evident upon examination of the position of the troughs of wave number 3 in the perturbations. In both years between 45°S and 62°S, the troughs in the perturbation simulations are positioned near the Weddell Sea (15°W in 1980 and 5°W in 1985), over the eastern Indian Ocean (105°E in 1980 and 115°E in 1985) and east of the Ross Sea (135°W in 1980 and 125°W in 1985). The same is true for the subtropical expression of the wave (~30°S - 45°S), although it is positioned slightly west (~5°) of the higher latitude portion of the wave. In 1980 these phase changes are apparent in the seasonally averaged pressure field, such that there are significant decreases in pressure at the longitudes mentioned above, except over the eastern Indian, where the subtropical trough (~30°S to 45°S) is supposed to be near 100°E (Figures 8.16 and 8.17). In 1985, the pressure changes corresponding to the phase shift of wave number 3 are less clear, especially south of 50°S (Figures 8.16 and 8.17), but there is a significant reduction in pressure near the Weddell Sea associated with both the midlatitude and subtropical phase shifts, and there are clear reductions in pressure near 108°E and 132°W associated with the subtropical phase shift.

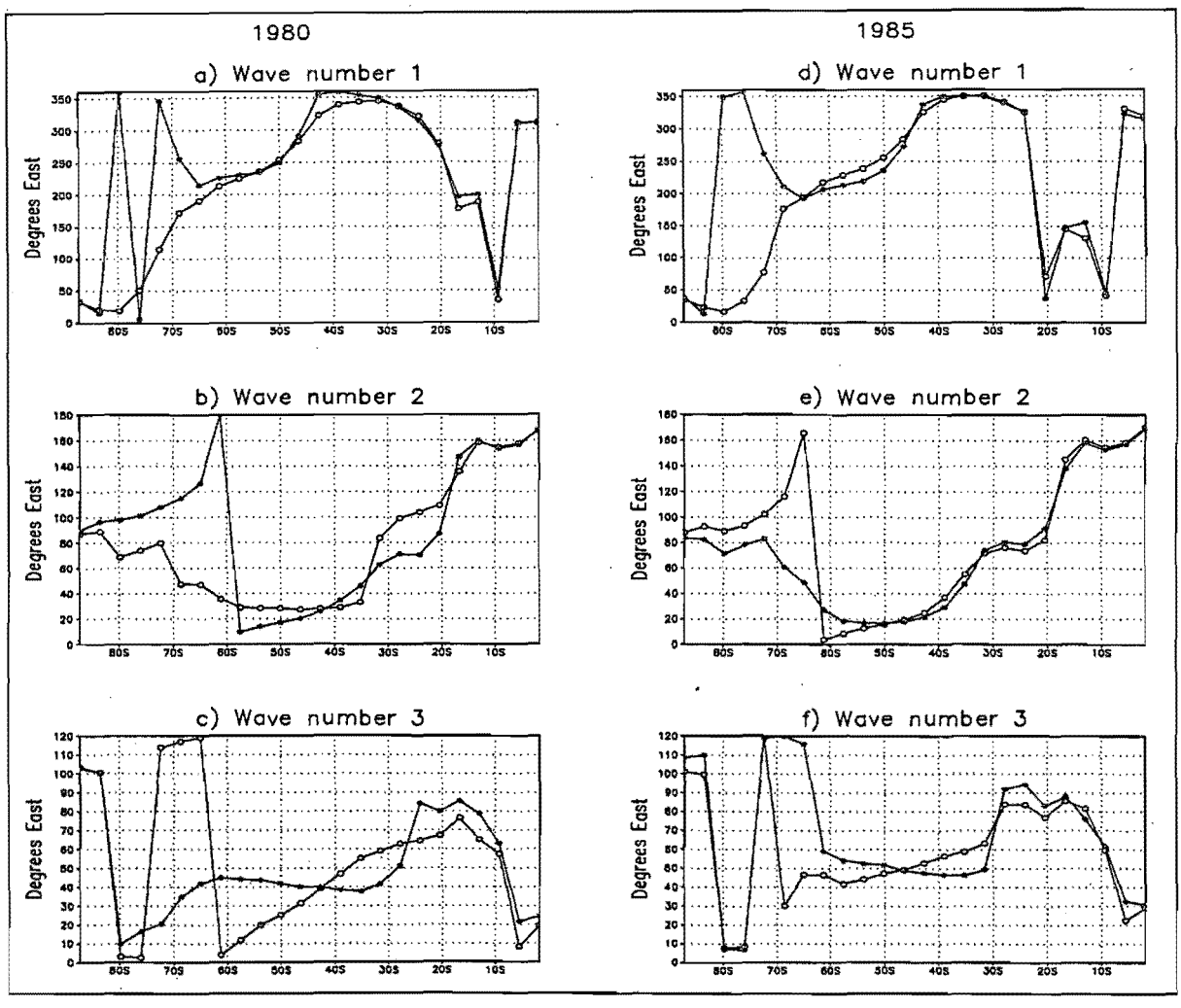

Figure 8.27 The phase (position of the first ridge) of seasonal wave numbers 1 to 3 for 1980 (*a-c*) and 1985 (*d-f*) for the control (open circles) and perturbation (closed circles) data.

The change in phase of wave number 3 is also responsible for increased blocking that is seen in the region of New Zealand and increased subsidence over the Antarctic Peninsula in both years (Figures 8.16 and 8.17). This is because the ridges of the wave in the perturbations between 30°S and 45°S are located near 160°E and 168°E in 1980 and 1985 respectively, and for the portion of the wave south of 45°S, there is a ridge near 75°W and 65°W in 1980 and 1985 respectively. In addition, between 30°S and 45°S in the perturbations, the harmonic analysis shows that there is a ridge located south-east of South Africa, near 40°E in 1980 and 48°E in 1985 (Figure 8.27). The 500 hPa height anomalies reflect this with a positive pressure anomaly in this region. It appears that the pressure changes near 60°S (Figures 8.16 and 8.17) in response to the phase changes are less clear in 1985 compared to 1980. This is not surprising, since in 1980 there is a 40° phase shift of wave number 3 at 60°S, whereas at the same latitude in 1985 there is only a 10° phase shift (Figure 8.27). In other words, in 1980 wave number 3 is almost completely out of phase between the control and perturbation, and one would therefore expect larger pressure anomalies associated with the shift of the wave in 1980 compared to 1985.

If one examines the imposed sea-ice perturbations in the two years (Figure 5.14), then there appears to be a 3-wave pattern in terms of the regions of largest sea-ice reduction, and these regions are located near the positions of the troughs of wave number 3 in the perturbation simulations i.e. near the Weddell Sea, the south-east/central Indian Ocean and the Ross Sea. This suggests that the perturbation has caused wave number 3 to become aligned (in terms of the troughs) with the regions of the major sea-ice reductions. It is suggested, however, that the trigger for the phase change of wave number 3 is the sea-ice perturbation in the Weddell Sea sector, primarily because the sea-ice reductions in this sector are the largest (Figure 5.14). There are also significant and consistent reductions in both sea level pressure (Figure 8.16) and 500 hPa heights (Figure 8.17) between 30°S and 70°S in this sector in both years. It is evident in the perturbation simulations that the phase of wave number 3 in 1980 is positioned slightly west of that in 1985 (Figure 8.27), such that the trough near the Weddell Sea is at 15°W in 1980 and 5°W in 1985. This may be related to the sea-ice perturbations, since in 1985 there is a maximum perturbation near the Greenwich Meridian, whereas in 1980 there is a more even spread of perturbations over the Weddell Sea sector, with a larger perturbation north of the sea, between 15°W and 30°W, compared to 1985 (Figure 5.14).

It was previously suggested that the position of the anomalous heating relative to the unperturbed flow may play a vital role in determining the atmospheric response to a sea-ice perturbation (Mitchell and Hills, 1987). This suggestion is supported by the results in this section. The unperturbed flow of 1980 and 1985 is quite different in terms of the major troughs and ridges associated with wave number 3, therefore a different anomaly is produced relative to the control. Upon closer examination, however, it is clear that the perturbation simulations are forced by the sea-ice reduction towards a more similar flow pattern between the two years, than existed between the control simulations.

8.5.2 Amplitude Changes

The amplitude of wave number 1 is found to decrease in response to the perturbation in 1980 and 1985, in terms of both the sub-polar and subtropical expression of the wave (Figure 8.28). Wave number 1 accounts for between 70 and 90% of the variance of the mean pattern in middle to high latitudes of the Southern Hemisphere, thus dominating the climatological mean flow at the 500 hPa level (Trenberth, 1980; Quintanar and Mechoso, 1995a). However, waves 1, 2 and 3 contribute virtually equally to the variability on monthly and interannual time scales, which reaches a maximum near 55°S (Trenberth, 1980).

As was suggested in the chapter on the summer season, the amplitude changes of wave number 1 may be related to changes in the symmetry of SSTs around Antarctica. Figure 8.29 shows the SST distribution at 54°S in both years. At this latitude, the phase of wave number 1 is such that the ridge is positioned near 130°W and the trough near 50°E (Figure 8.27), therefore the wave has a similar asymmetric distribution about the pole as the SST distribution. The SSTs near 54°S show slightly reduced asymmetry in the perturbations compared to the controls (Figure 8.29), which may be partially responsible for the reduction in amplitude of wave number 1 near this latitude. There are, however, no SST differences between the controls and perturbations near 35°S (not shown), but the thermal effects of the changes further south may extend to this region through the atmosphere.

The reduction in amplitude of wave number 1 is manifest in the 500 hPa height changes (Figure 8.17). As mentioned previously, near 56°S in both the controls and perturbations, the ridge of the wave is positioned east of the Ross Sea, near 130°W, and the trough is positioned over the south-west Indian Ocean, near 50°E (Figure 8.27). In both years, there is a decrease in the 500 hPa heights near 130°W and an increase in the heights over the south-west Indian

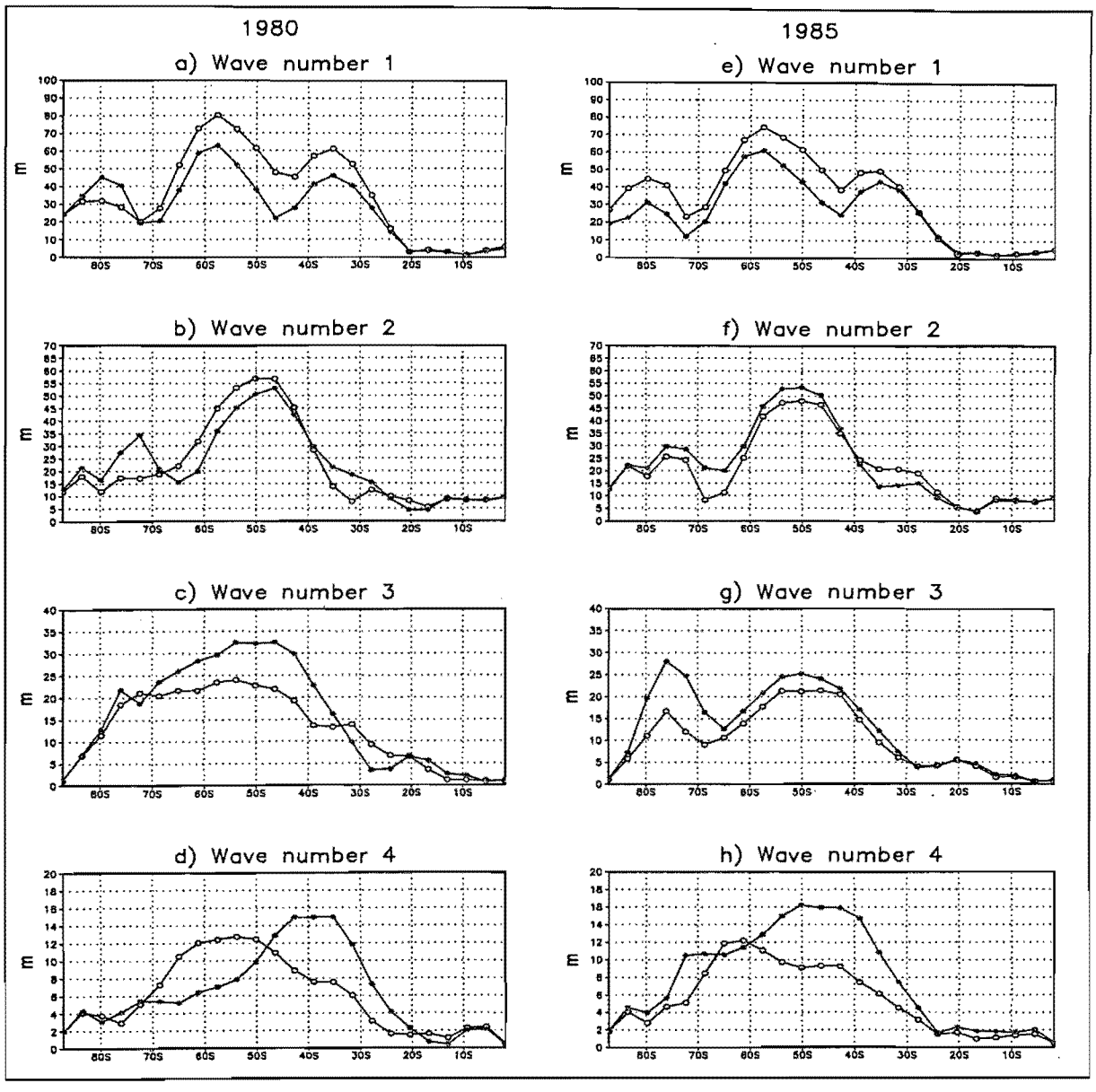

Figure 8.28 The amplitude (m) of seasonal wave numbers 1 to 4 for 1980 (*a-d*) and 1985 (*e-h*) for the control (open circles) and perturbation (closed circles) data.

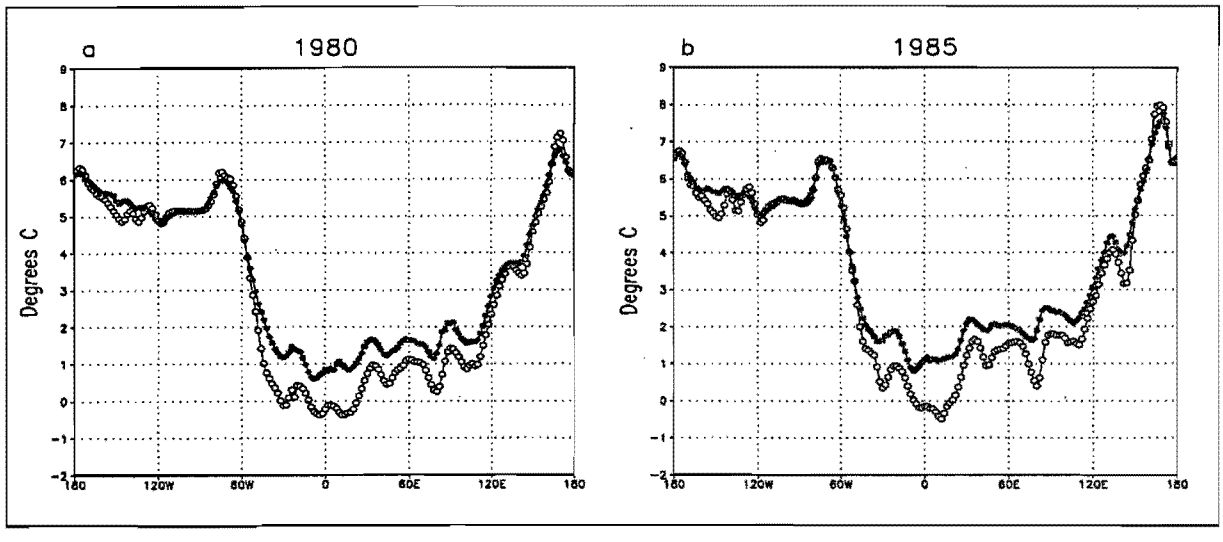

Figure 8.29 The SST (°C) distribution for the control (open circles) and perturbation (closed circles) data at 54°S in *a*) 1980 and *b*) 1985.

Ocean (Figure 8.17), which thus correspond to a decrease in the amplitude of wave number 1 at 56°S. Similarly, near 35°S in both the controls and perturbations, the ridge of the wave is positioned north of the Weddell Sea (~10°W) and the trough is positioned near New Zealand (~170°E). An examination of the 500 hPa heights (Figure 8.17) show a previously mentioned trans-hemispheric pattern of negative pressure anomalies over the Atlantic Ocean and the positive pressure anomalies over the western Pacific, near New Zealand, which would thus be associated with a reduction in the amplitude of wave number 1. The increase in pressure near New Zealand at 35°S is stronger in 1980 compared to 1985 (Figure 8.17), which relates to the larger amplitude decrease of wave number 1 in the subtropics in 1980 (Figure 8.28).

1980 and 1985 show conflicting amplitude changes for seasonal wave number 2 (Figure 8.29), thus the results are inconclusive and may suggest that there is not a cohesive response from this wave to the perturbation. This is in contrast to the results obtained in a modelling study by Quintanar and Mechoso (1995b), which suggested that at polar latitudes the phase and amplitude of wave number 2 at the 300 hPa level is related to wave number 2 asymmetries in SST and sea-ice.

Near 45°S, where the amplitude of wave number 1 is small due to the phase difference between the subpolar and subtropical peaks, the other long waves become of greater importance. It appears that the amplitudes of both wave numbers 3 and 4 increase in this region (Figure 8.29). Seasonal wave number 3 increases in amplitude in both 1980 and 1985 in the midlatitudes, but more so for 1980 (Figure 8.29). It has already been mentioned that the imposed sea-ice changes exhibit a 3-wave pattern, and this may be responsible for increasing the intensity of the atmospheric wave. The response of wave number 4 is slightly different between the two years, since in 1980 there is an increase in amplitude between 20°S and 47°S and a decrease between 50°S and 70°S, and in 1985 there is an increase in amplitude between 30°S and 60°S (Figure 8.29). The signature of wave number 4 in 1985 can be seen in the midlatitudes of the 500 hPa height anomaly field (Figure 8.17*d*). There is, however, a consistent response of wave number 4 in both years, in that the peak amplitude has shifted northwards, from 55°S to 40°S in 1980, and from 60°S to 45°S in 1985. Once again, the positioning of the wave for 1980, in both the controls and perturbations, is equatorward of that in 1985, thus perhaps being related to the differences in sea-ice extent between the years.

As for the summer season, the twice-daily amplitudes of wave numbers 1 and 2 have been averaged together in order to represent the long waves, and the amplitudes of wave numbers 5, 6 and 7 have been averaged to represent the medium wavelength waves. The medium wavelength waves exhibit larger amplitudes and contribute to a larger proportion of the 500 hPa height variability on a daily time scale compared to the seasonal time scale (van Loon and Jenne, 1972). As for the summer season, most of the poleward sensible heat flux in the Southern Hemisphere is accomplished by eastward moving waves of medium wavelengths (Kao *et al.*, 1971). Figure 8.30 shows that there is an overall decrease in the twice-daily amplitudes of the long waves in both years, but that there is virtually no change in the amplitudes of the medium waves in response to the perturbation. As has been mentioned previously, the reduction in amplitude of the long waves may be due to the thermal effects of reduced SST and sea-ice asymmetries about the pole.

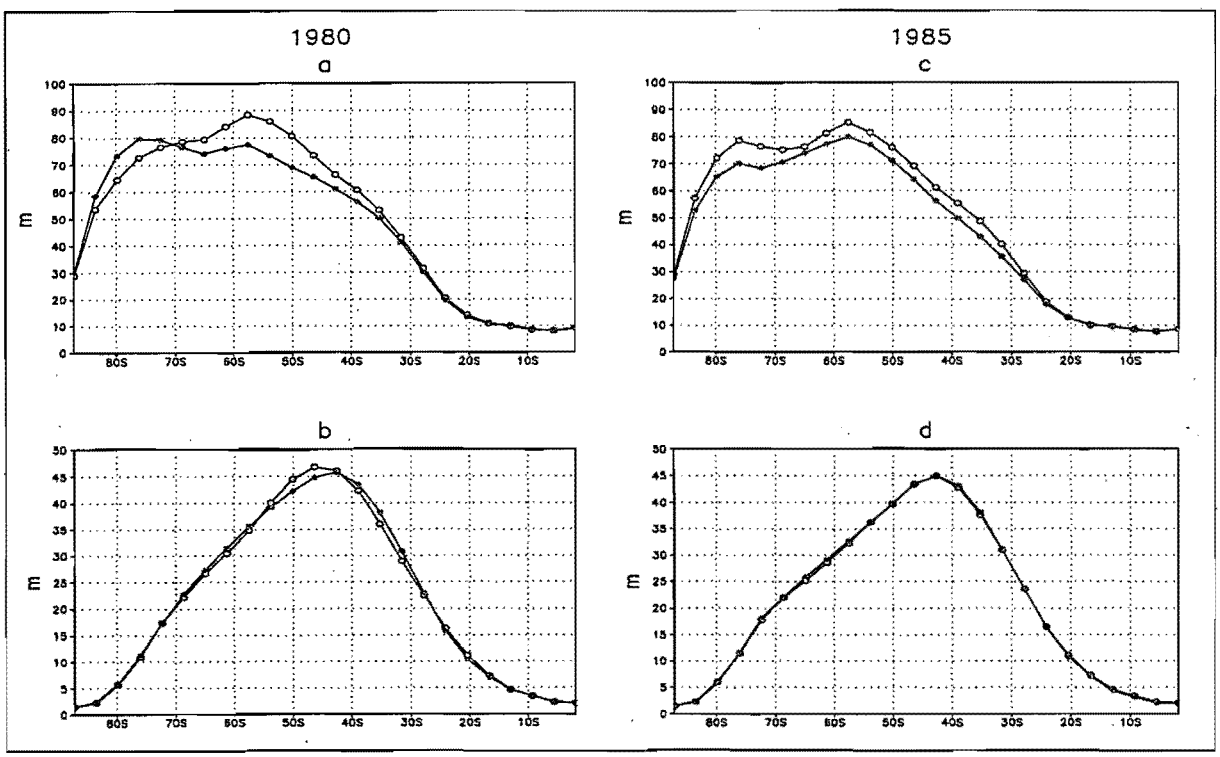

Figure 8.30 The amplitude (m) of the twice-daily long waves grouped together (wave numbers 1 and 2) for the controls (open circles) and perturbations (closed circles) of *a*) 1980 and *c*) 1985; and the twice-daily medium length waves grouped together (wave numbers 5, 6 and 7) for the controls (open circles) and perturbations (closed circles) of *b*) 1980 and *d*) 1985.

8.6 Change in Twice-Daily Circulation at Sea Level and the 500 hPa Level

As in Chapter 6, a Self-Organising Map is used here to classify the twice-daily sea level pressure and 500 hPa height data over the Southern Hemisphere (30°S to 60°S) into related categories, in order to examine whether the perturbation has caused a change in the frequency of circulation types simulated over the season. The same data preparation and analysis procedure that was used for the summer season has been used for winter. In summary for both the sea level pressure and 500 hPa height data, a SOM was trained with non-standardised twice-daily data corresponding to the combined controls of 1980 and 1985 (total t=1104). A network of 48 nodes (6 in the x-direction and 8 in the y-direction) was selected for the SOM and the weights of the nodes were initialised using linear initialisation. A rectangular topology was used for the array of nodes, and the initial learning rate was set to 0.05, with an initial training radius of 4. Training was run for a total of 30 000 iterations. After the SOM had been trained with the control data from both years, the weights of each node could be decomposed and the array of nodes displayed on a meta-map. The trained SOM was then separately presented with twice-daily data associated with the controls of 1980, the controls of 1985, the perturbations of 1980 and the perturbations of 1985. In each case, every time step is mapped to the node whose circulation it most closely resembles.

8.6.1 Sea Level Pressure

The meta-map for sea level pressure is shown in Figure 8.31, and the percentage of time steps which map to each node are shown in Figure 8.32 for the controls and perturbations of 1980 and 1985. In the text, the nodes will be referred to by their numbers as shown on the meta-map (Figure 8.31). A comparison of the distributions of the percentage of time steps which are associated with each node in the control and perturbation of each year, shows that there is a reduction in the representation of the nodes in the first column (left-hand side) of the meta-map (Figure 8.32). The positioning of the decreases in the two years (Figure 8.32*c* and *f*) is associated with the control distributions (Figure 8.32*a* and *d*). In other words, in the controls for 1980 and 1985, node numbers 31 and 43 receive a large proportion of mappings in this column, and in both years these nodes experience a reduction in representation in the perturbations compared to the controls. In the control of 1980, node number 13 in this column is also favoured, and also experiences reduced representation in the perturbation. In 1980, there is an increase in the representation of the circulation types described by the nodes near the top of the right-hand column of the meta-map, whereas in 1985 the increase is focused on the first row of the meta-map (Figure 8.32). Figure 8.32*g* shows the average response for the two years. From these results, it appears that the perturbation is favouring

sea level pressure circulation types between 30°S and 60°S (Figure 8.32) which are characterised by:

- a "bipolar" low feature at high latitudes, with the lows positioned near South America and Australia.
- a trough over the Atlantic, but whose expression at high latitudes is not as deep as the lows mentioned above.
- a ridge over, or to the east of New Zealand.
- fairly zonal flow near 40°S.

The difference between the circulation types favoured by 1980 and 1985 generally relates to the positioning of features. The primary circulation types which increased in the perturbation compared to the control are associated with node numbers 6 and 18 in 1980, and node number 3 in 1985 (Figure 8.32). By comparing these nodes, it can be seen that the "bipolar" lows, mentioned above, are positioned south-west of the continents in 1980 and south of the continents in 1985. These lows are also slightly less expansive in 1985 compared to 1980. There is also slightly stronger ridging in the central Pacific in 1985 (Figure 8.31).

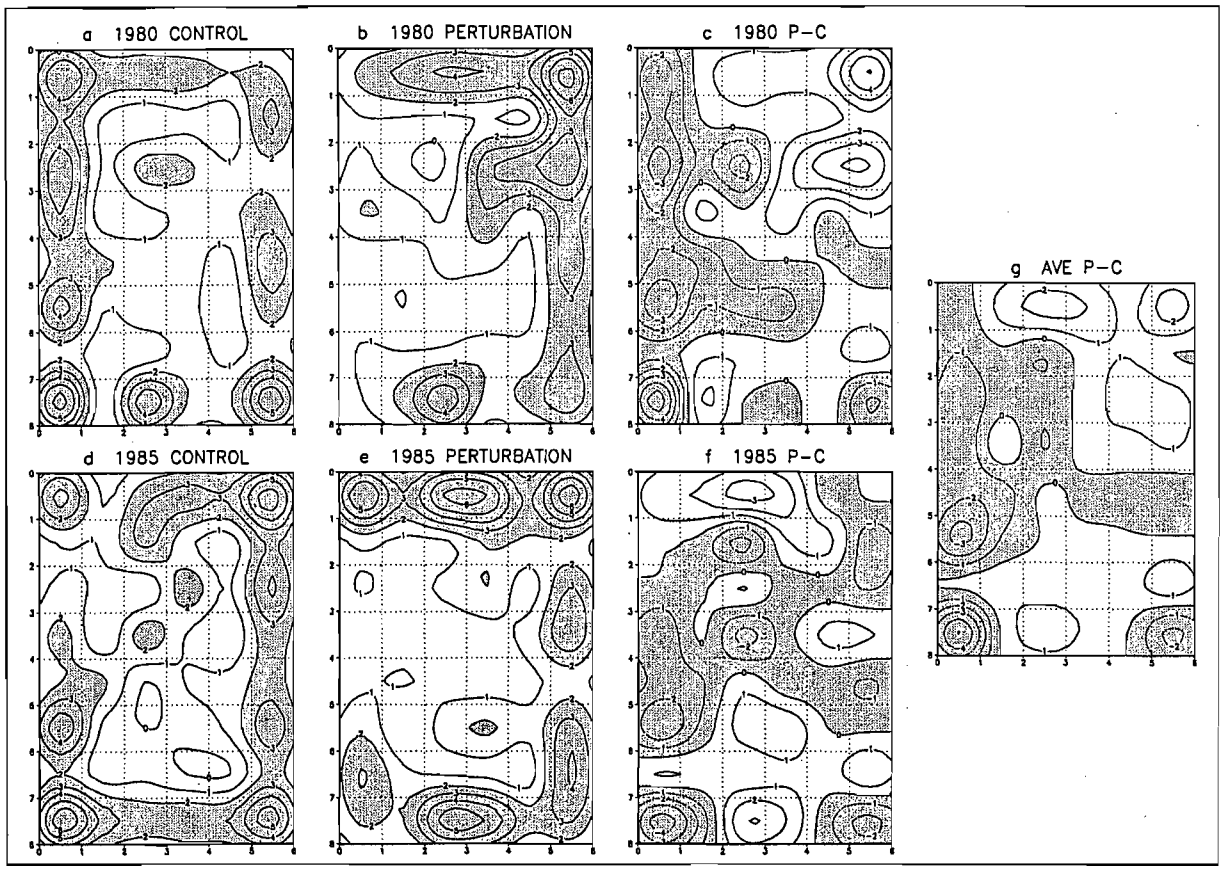

Figure 8.32 The percentage of days mapping to each node of the meta-map (Figure 8.31) for the controls of *a*) 1980 and *d*) 1985 and the perturbations of *b*) 1980 and *e*) 1985. Plots *c*) and *f*) show the difference between the controls and perturbations (perturbation minus control) in terms of the percentage of days mapping to each node in 1980 and 1985 respectively. Plot *g*) represents the average between the plots on *c*) and *f*), i.e. showing the average response between 1980 and 1985.

The nodes that experience the largest reduction in representation in response to the perturbation (node numbers 31 and 43) are associated with a large trough over Australian/New Zealand sector (Figure 8.31). This trough is more extensive, both zonally (especially towards New Zealand) and meridionally, compared to the trough that is simulated in the favoured circulation types mentioned in the paragraph above. In other words, the circulation types that are favoured by the SOM in response to the perturbation (primarily centred around node numbers 3, 6 and 18) exhibit higher pressures over the Australian/New Zealand sector, manifest by a more constrained low pressure trough, compared to those types that experience a reduction in representation. This is in agreement with the seasonal mean sea level pressure response which shows positive sea level pressure anomalies in this region (Figure 8.16) and a southward shift of the pressure systems in response to the perturbation. In addition, the circulation types that experience an increase in representation in each year (primarily centred around node numbers 3, 6 and 18) are associated with lower pressures over the Atlantic Ocean compared to those circulation types that are reduced in response to the perturbation (node numbers 31 and 43) (Figure 8.31). This also agrees with the average sea level pressure response which shows negative pressure anomalies between 30°S and 60°S over the Atlantic in both years and a northward shift of the pressure systems in response to the perturbation (Figure 8.16).

Both years also experience a reduction in the representation of the circulation type given by node number 48 (bottom right-hand corner) (Figures 8.32). This circulation pattern is associated with a strong ridge over the eastern Pacific Ocean, near 45°S (Figure 8.32). The circulation patterns of the nodes that are favoured in each year (primarily centred around node numbers 3, 6 and 18) tend to have troughs near this region, and furthermore, the mean sea level pressure response to the perturbation shows negative sea level pressure anomalies in this area (Figure 8.32). It was mentioned previously, that in 1980 node number 13, which has a fairly high representation in the control, shows a decrease in representation in response to the perturbation (Figure 8.31). This node also possesses a circulation pattern that has a strong ridge west of South America and an extensive trough in the Australian/New Zealand region (Figure 8.32), which may account for the decrease in representation.

8.6.2 500 hPa Heights

The meta-map for the 500 hPa heights is shown on Figure 8.33, and the percentage of time steps which map to each node are shown in Figure 8.34 for the controls and perturbations of 1980 and 1985 respectively. It appears that the distribution of circulation types simulated has

changed in response to the perturbation such that the nodes in the top half of the first column and the far right-hand column are favoured in the perturbations (Figure 8.34). In fact, the distribution of circulation types favoured are more similar between the perturbations of 1980 and 1985 than between the controls of the two years (Figure 8.34). This suggests that although the two years may have had different "starting points", the perturbation has forced similar "end-points". The same can actually be seen for the sea level pressure SOM results (Figure 8.31). The differences between the controls of the two years largely accounts for the differences between the positioning of the anomalies. The average anomaly response between the two years (Figure 8.34*g*) essentially reflects the distribution of favoured circulation types in the perturbations (Figure 8.34*b* and *e*), such that nodes in the far right-hand column and top left-hand corner are of increased importance in the perturbations and the nodes in the bottom left-hand portion of the meta-map are less frequently mapped to in the perturbations compared to the controls.

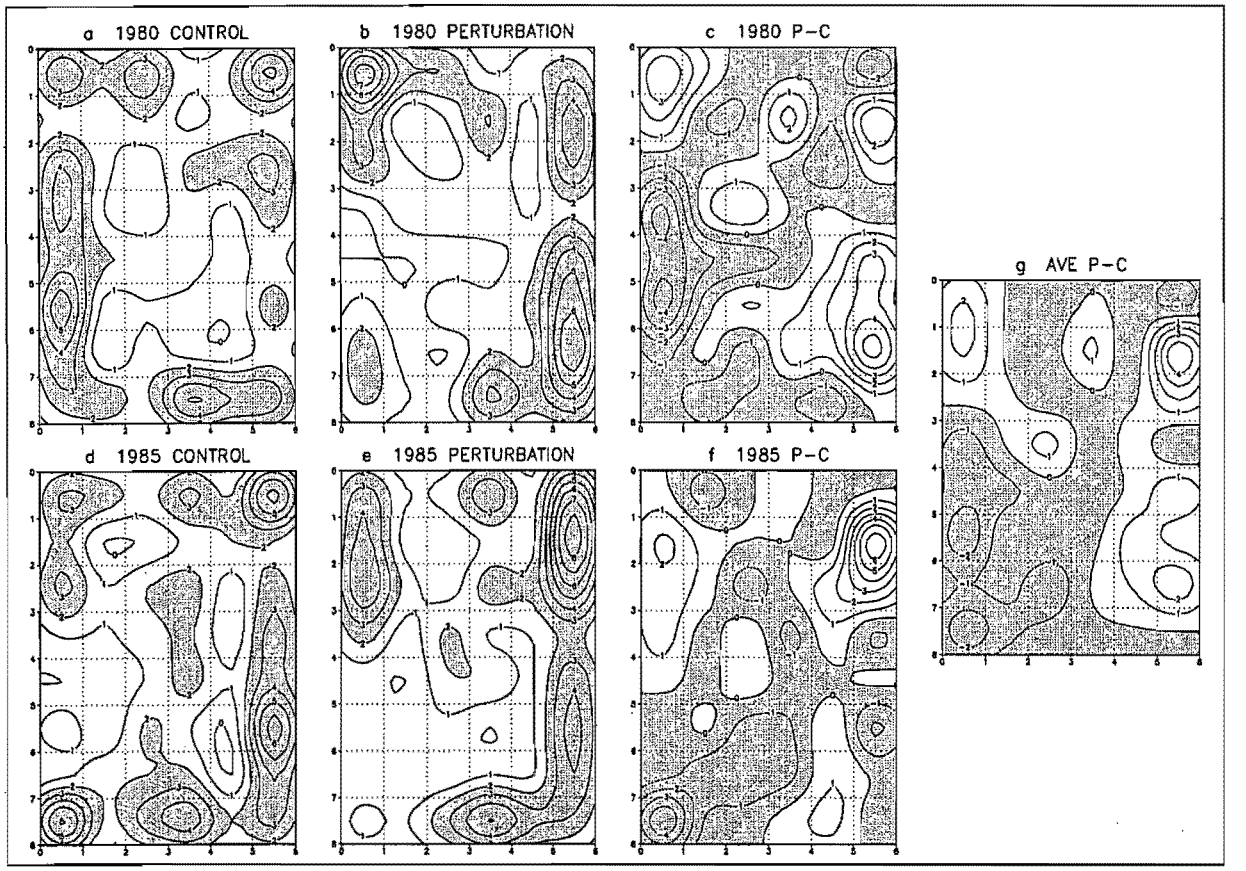

Figure 8.34 The percentage of days mapping to each node of the meta-map (Figure 8.33) for the controls of *a*) 1980 and *d*) 1985 and the perturbations of *b*) 1980 and *e*) 1985. Plots *c*) and *f*) show the difference between the controls and perturbations (perturbation minus control) in terms of the percentage of days mapping to each node in 1980 and 1985 respectively. Plot *g*) represents the average between the plots on *c*) and *f*), i.e. showing the average response between 1980 and 1985.

A comparison of the circulation patterns of the nodes that are favoured (centred around nodes 1, 12, and 42) and those that become less important (centred around nodes 31 and 43) yields

similar conclusions to those made for sea level pressure. The nodes that show a decrease in representation are associated with a circulation pattern which exhibits a strong ridge over the central to eastern Pacific, whereas this ridge is weaker and in some cases replaced with a trough in the nodes that are favoured (Figure 8.33). This corresponds to the seasonally averaged 500 hPa height result, which shows negative pressure anomalies over much of this region in response to the perturbation in both years (Figure 8.17). There are also higher pressures south-east of South Africa, near about 40°E, in the circulation patterns of the nodes that are favoured compared to the patterns of the nodes that exhibit reduced representation (Figure 8.33). Again, this corresponds to the seasonally averaged 500 hPa height result, which shows positive pressure anomalies in this region. These differences mentioned for the above two regions, i.e. over the central Pacific and eastern Indian Oceans, also agree with the result of a reduced amplitude of wave number 1 in the perturbations compared to the controls (Figure 8.28). The phase of wave number 1 near 55°S is such that the ridge is positioned over the Pacific, near 130°W, and the trough is positioned south-east of South Africa, near 50°E (Figure 8.27). Thus, the nodes which show increased representation in response to the perturbation have a smaller amplitude wave number 1 and therefore more symmetrical flow around the pole compared to those nodes that experience reduced representation. In addition, in the perturbations, the ridge of wave number 3 is positioned south-east of South Africa, near 45°S (Figure 8.27), thus contributing to the increased pressures that are seen in this region in the circulation types that are favoured.

As for the sea level pressure results, the nodes that are favoured (centred around nodes 1, 12, and 42) have higher pressures in the Australian/New Zealand region compared to those that experience reduced representation (centred around nodes 31 and 43) (Figure 8.33). The positioning of one of the ridges of wave number 3 in this region in the perturbations, as well as the amplitude reduction of the subtropical expression of wave number 1 in response to the perturbation (Figures 8.27 and 8.28), contribute to the increased pressures that are seen in this region in the circulation types that are favoured. In addition, for the nodes that experience increased representation in the perturbation simulations, there are clear wave-3 and wave-4 patterns, especially for the nodes positioned on the right-hand side of the meta-map (Figure 8.33). These may relate to the increase in amplitude of these waves that was found from the Fourier analysis (Figure 8.28). In response to the perturbation, the maximum expression of wave number 4 increased and moved northwards, to near 43°S in both years (Figure 8.28). An examination of node number 12, which displays an increase in representation in both years, shows a clear wave number 4 pattern near this latitude (Figure 8.33).

8.7 Comparison with Summer

There are both similarities and differences between the Southern Hemisphere summer and winter season responses to the sea-ice and SST perturbation. As has been mentioned previously, in response to the sea-ice removal and SST increases there are larger surface temperature increases around Antarctica in winter compared to summer. Similarly, there are much larger and more conclusive increases in surface sensible and latent heat fluxes around Antarctica in winter. The larger heat flux anomalies in winter are to be expected, since the flux response is a function of both the surface temperature change and the surface-atmosphere temperature differential. The weaker temperature response in summer may be because high latitude inversions are generally weaker during summer compared to winter, and therefore in summer there is a greater potential for the dispersion of low level temperature anomalies through convection. The seasonally averaged temperature increase in summer does not generally exceed 1.5 K (Figure 6.16), whereas in winter there are temperature anomalies exceeding 3 K in certain regions south of 50°S (Figure 8.15). In addition, in winter there are larger surface air temperature increases, as well as a greater proportion of statistically significant increases, between 60°S and 70°S, i.e. over the sea-ice zone, compared to summer (Figures 6.16 and 8.15). The results seem to suggest that the summer surface temperature increases are largely due to the SST increases rather than directly to the sea-ice reductions.

It is clear from the sea level pressure and 500 hPa height anomalies in the two seasons (Figures 6.17, 6.19, 8.16 and 8.17), that the summer response is more zonally uniform than the winter response. For summer, there are pressure decreases south of 50°S and increases between 30°S and 50°S, and there is a general southward shift of the Hadley cell. In contrast, in winter although there is a southward shift of the Hadley cell over the Australian/New Zealand region, there is a northward shift of the pressure systems over the Atlantic. In both seasons between 30°S and 50°S there is a tendency for increased ridging near Australia and New Zealand in response to the perturbation. The pressure anomalies over the Southern Hemisphere for 1980 appear to be positioned slightly north of those in 1985 in both seasons, associated with the more extensive sea-ice cover in 1980. In general, midlatitude cyclone densities increase over the regions from which sea-ice was removed and decrease to the north of this (around 50°S) in both seasons (Figures 6.23 and 8.21), although there is more variation in this response in winter. In addition, in winter there are regions where there are increases in cyclone density north of the region of decrease, and there are also larger anomalies between 30°S and 50°S in winter compared to virtually no change over this zone in summer.

The changes in the 500 hPa wind speed are a response to the pressure anomalies and therefore show greater longitudinal variation in winter compared to summer (Figures 6.21 and 8.20). In particular, for winter the wind speed changes over the eastern Pacific generally show contrasting patterns of change compared to the rest of the hemisphere. Excluding the eastern Pacific in winter, in both seasons there are similar wind anomalies, in that there tends to be an increase in wind speeds at high to middle latitudes (~50°S - 65°S) and a reduction in wind speeds to the north of this (~30°S - 40°S). These changes are in broad agreement with what is expected from the thermal wind relationship i.e. a warm anomaly between 50°S and 70°S, due to the sea-ice reductions and SST increases, results in westerly wind anomalies over the region of the temperature increase and easterly wind anomalies to the north.

Both seasons show a reduction in the amplitude of wave number 1, which, as mentioned previously, may be related to reduced asymmetry of the SST distribution around the pole due to the perturbation. The trough of the subpolar/midlatitude expression of wave number 1 is found over the western Indian and the ridge over the central Pacific, thus having the same asymmetric distribution as the SSTs. In addition, the results from the SOM investigation of twice-daily sea level pressure and 500 hPa height data in both seasons shows a tendency to favour those circulation types in the perturbation simulations that exhibit fairly zonal and symmetrical flow between 30°S and 50°S, and in particular those types with a reduced ridge over the central Pacific compared to the controls.

The more zonally consistent response in summer compared to winter, which is clearly seen in variables such as sea level pressure, 500 hPa heights and 500 hPa wind speed, may have occurred for a number of reasons. Firstly, the summer months in the experiment are associated with less overall sea-ice than the winter months, therefore there is reduced asymmetry around the pole with respect to the sea-ice distribution and the sea-ice anomalies in summer. Secondly, the sea-ice perturbations imposed in the summer season are more evenly distributed around the hemisphere, in particular, there is a sea-ice reduction over the Ross Sea which is comparable to the reduction near the Weddell Sea (Figure 5.11). In contrast, the sea-ice perturbation in the winter season is found primarily over the Atlantic and western Indian Oceans i.e. near the Weddell Sea sector (Figure 5.14). Lastly, the sea level pressure maps for both years in each season show that there is a more zonally symmetric organisation of the control pressure systems in summer (Figure 6.17) compared to winter (Figure 8.16). This is clearly seen around 50°S, where there is stronger ridging over the central Pacific in relation to other longitudes in winter compared to summer (Figures 6.17 and

8.16). This may also relate to the larger control amplitude of wave number 1 in winter (Figures 8.28). In summer the peak amplitude of the wave in middle to high latitudes is about 55 m (Figure 6.30), whereas in winter it is about 75 m (Figure 8.28).

Crowley *et al.* (1994) performed model perturbation experiments to examine the effect of altered Arctic sea-ice and Greenland ice sheet cover on the climate. They commented that the seasonal differences obtained in their study at high latitudes seemed to indicate that the response in summer was a close reflection of the thermal perturbation, whereas the winter response of the atmosphere to the altered temperature field was embedded in the high-latitude flow pattern. This may also be the case for the present study and may account for some of the differences in the positioning of pressure anomalies in the winter season between 1980 and 1985, as well as differences between other similar modelling studies, since the high-latitude flow patterns may differ. Winter is also characterised by more energetic circulation compared to summer, owing to the enhanced equator-pole temperature gradient, and this may result in a stronger, yet more variable, response during this season.

8.8 Summary

This chapter describes the atmospheric response of the Southern Hemisphere to the sea-ice and SST perturbation in the winter season. The perturbation appears to have produced a similar response between the two years in general, although there are a number of differences. These differences may be related to differences in the positioning and magnitude of the sea-ice and SST perturbations in the two years, differences in the circulation patterns and positioning of features in the controls of the two years, or a particular difference may represent natural variability and indicate that there is not a clear response to the perturbation. The major findings which are consistent between the two years are summarised below:

- The sea-ice perturbation is found primarily over the Atlantic and western Indian Oceans.

- In general, the atmospheric response for 1985 appears to be located poleward of the 1980 response. This may be related to the differences in sea-ice extent between the two years, since the sea-ice in 1980 is more expansive than in 1985.

- There is an increase in the surface sensible heat flux in the region from which sea-ice was removed (~60°S - 70°S).

- There is a general increase in the latent heat flux near 60°S, especially in the western Indian, eastern Pacific and Weddell Sea sectors.

- There is a high latitude increase in surface specific humidity, especially in the region just east of the Weddell Sea near 60°S.

- There is an increase in surface air temperatures between about 50°S and 70°S in response to the perturbation. The largest and most consistent increase between 1980 and 1985 is found over the South Atlantic, near the Greenwich Meridian, associated with the largest sea-ice and SST perturbation.

- At high latitudes, between about 50°S and 70°S, there are reductions in sea level pressure over the south Atlantic, south (1985) and south-west (1980) of New Zealand and over the south-east Pacific Ocean. These pressure decreases extend to the 500 hPa level and are also associated with 500 hPa temperature decreases, indicating increased uplift and adiabatic cooling.

- There are also increases in sea level pressure at high latitudes. Both years exhibit pressure increases over the Antarctic Peninsula and near 180°E. These pressure increases are associated with 500 hPa height and temperature increases indicating increased subsidence and adiabatic warming. These regions of increased subsidence may be responsible for some of the surface air temperature increases around Antarctica.

- Over middle/subtropical latitudes, between about 30°S and 55°S, there is an increase in pressure over the Australian/New Zealand sector and a decrease in pressure over the Atlantic Ocean. These anomalies are related to a southward shift of the pressure systems over the Australian/New Zealand region and a northward shift over the western Atlantic.

- The above-mentioned changes in pressure can be related to changes in the phase and amplitude of the 500 hPa planetary waves. In particular, in both years the phase of wave number 3 shifts eastward in response to the perturbation such that the troughs of the midlatitude/subpolar (~45°S - 62°S) expression of the wave are positioned near the Weddell Sea (~10°W), over the eastern Indian Ocean (~110°E) and east of the Ross Sea (~130°W) in the perturbations. The subtropical (~30°S - 45°S) expression of the wave

shifts westward in both years, which positions the troughs slightly westward (~5°) of the higher latitude portion of the wave in the perturbations. It is suggested that the trigger for the phase change of wave number 3 is the large sea-ice perturbation over the Atlantic Ocean (Weddell Sea sector). These phase changes also account for the increase in subsidence over the Antarctic Peninsula and in the region of New Zealand. In addition, wave number 3's amplitude increases in response to the perturbation.

- The amplitude of wave number 1 decreases in response to the perturbation, perhaps associated with the reduced asymmetry of the SST distribution. The amplitude change of the subpolar expression of the wave is manifest in the 500 hPa heights by a decrease in pressure east of the Ross Sea (near 130°W) and an increase in pressure over the south-west Indian Ocean (near 50°E). The amplitude change of the subtropical expression of the wave (~35°S) is manifest by an increase in pressure near New Zealand (~170°E) and a decrease in pressure over the Atlantic (~10°W). It is clear that the pressure changes caused by the phase shifts of wave number 3, mentioned in the previous paragraph, are in sympathy with the pressure changes expected as a result of a reduction in the amplitude of wave number 1.

- The pattern of 500 hPa wind speed anomalies over the eastern Pacific are generally in opposition with the pattern over the rest of the hemisphere. Apart from this region, there is a general increase in wind speeds between 50°S and 70°S and a decrease in speeds between 30°S and 50°S, in general agreement with a positive thermal anomaly at high latitudes and the thermal wind relationship. Apart from the eastern Pacific region, these changes result in a general weakening of the jet stream and a slight northward shift of the jet over the Atlantic.

- There is a general increase in midlatitude cyclone densities near 60°S, which may be associated with a change in surface fluxes due to the exposure of the ocean surface in the perturbations and an increase in the SST gradient between 55°S and 70°S, perhaps causing an increase in baroclinicity. There is a general decrease in cyclone densities north of the high latitude increases, which may be associated with reduced SST gradients near 50°S and thus a potential reduction in baroclinicity. In certain regions there are also density increases north of these decreases, around 30°S and 40°S.

CHAPTER 9

Implications of the Winter Sea-Ice Perturbation for Southern Africa

9.1 Introduction

This chapter focuses on southern Africa in order to investigate whether the winter sea-ice perturbation has the capacity to significantly influence the climate of the subcontinent. The previous chapter, which considered the broad Southern Hemisphere response, showed contrasting positions of many of the anomalies in the two years, largely due to differences between the climate state in 1980 and 1985, as well as differences between the imposed sea-ice and SST distributions. It remains to be seen in the present chapter, whether the atmospheric response to the perturbation elicits a consistent response over the southern African window (20°S to 50°S; 2°E to 47°E), especially in terms of precipitation.

Southern Africa, as depicted in the analysis window, is largely dry during winter, apart from the south-western Cape and south coast of South Africa which receive rainfall associated with westerly waves and their attendant cold fronts. In comparison to summer, the subtropical anticyclones intensify and move northwards during winter and there is an equatorward expansion of the westerlies south of the country. The mean near-surface circulation over the interior plateau is anticyclonic during winter, and subsidence prevails over much of the region. The effect of this subsidence is to produce an elevated inversion layer which suppresses convection and also intersects with the height of the escarpment, preventing the influx of moisture over the escarpment and into the interior from the Indian Ocean. In contrast, during summer the upper air inversion weakens and the height of the base of the inversion is somewhat more elevated than in winter, permitting the influx of moist air from the Indian Ocean. The reader is referred to Preston-Whyte and Tyson (1988) for a good summary and discussion of the weather of southern Africa.

This chapter follows the same format as was used for the summer season (Chapter 7). Firstly, the mean climatic response is investigated in terms of a number of variables, and then the twice-daily sea level pressure is considered using a Self-Organising Map. Lastly, changes to precipitation over the subcontinent will be examined using the technique of downscaling.

9.2 Mean Seasonal Response

Figure 9.1 shows the sea level pressure fields of the controls and perturbations in both years. A continental high pressure is evident over the eastern portion of the land and there is a weak trough over the north-western region of the subcontinent (Figure 9.1*a* and *d*). The influence of the midlatitude westerly circulation is visible over the southern half of the analysis window (Figure 9.1*a* and *d*). In response to the imposed perturbations there is an increase in the spatial extent of the continental high pressure in both years, as well as a significant increase in pressure over regions of the Indian Ocean (Figure 9.1*c* and *f*). As a consequence of the increase in extent of the continental high pressure, there is a narrowing of the eastern half of the trough located over the west coast (Figure 9.1*a*, *b*, *d* and *e*). In 1980 there is a significant

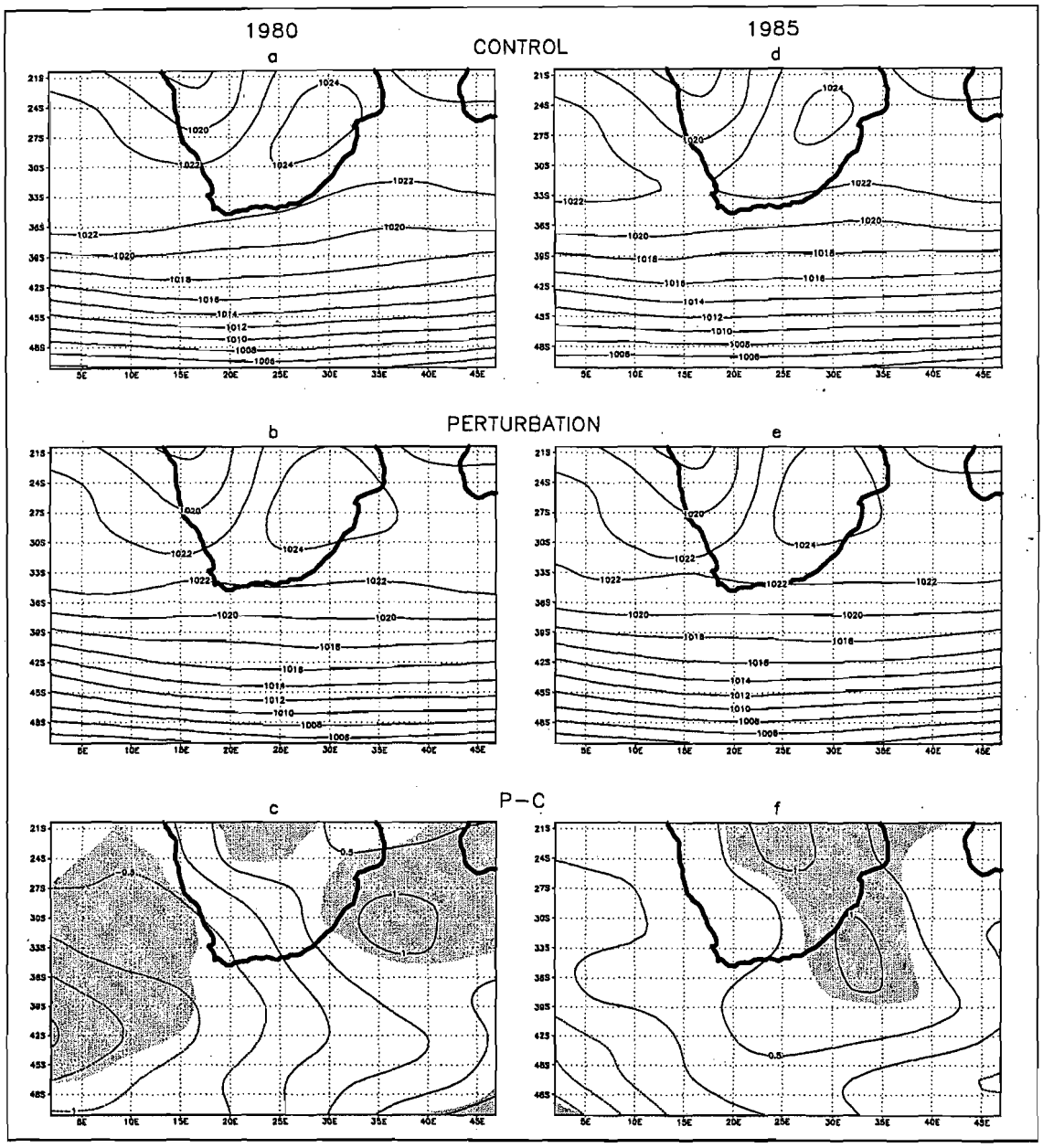

Figure 9.1 Sea level pressure (hPa) for the controls of *a*) 1980 and *d*) 1985, and the perturbations of *b*) 1980 and *e*) 1985. Maps *c*) and *f*) show the perturbations minus the controls for 1980 and 1985 respectively. Statistically significant differences at the 95% confidence level have been shaded.

reduction in pressure over the Atlantic Ocean (Figure 9.1*c* and *f*), whereas in 1985 this decrease occurs further west, as was seen in the plots of the hemisphere in the previous chapter (Figure 8.16). As such, over the analysis window there is a northward extension of lower, midlatitude pressures over the Atlantic sector and a weakening of the South Atlantic Anticyclone, but less so in 1985 than 1980 (Figure 9.1). In addition, a comparison of the controls and perturbations in both years shows that the changes in pressure over the southern Indian and Atlantic Oceans cause the flow near 34°S to be more zonal in the perturbations than in the controls (Figure 9.1*a*, *b*, *d* and *e*). It is interesting to note that the circulation associated with the perturbations of the two years resemble each other more closely than do the two controls, suggesting that the imposed sea-ice and SST anomalies may have forced the circulation to converge to a more similar state between the two years.

The anticyclonic circulation over the subcontinent and adjacent oceans is evident in the 900 hPa wind field of the controls and perturbations (Figure 9.2). In both years there is an increase in the speed of the wind over most of the subcontinent, particularly over the western half and north-eastern corner (Figure 9.2*c* and *f*). This is a response to the strengthening and increase in extent of the continental high pressure (Figure 9.1), the effect of which can also be seen in the meridional component of the wind (Figure 9.3*b* and *d*). There is an increase in the southward flow associated with the continental high pressure over much of the subcontinent, while there is increased equatorward flow over the north-eastern portion of the land and Indian Ocean (Figure 9.3*b* and *d*). The slight westward shift of the trough over the west coast (Figure 9.1) may also account for some of the increases in southward flow over the coastal region (Figure 9.3*b* and *d*). South of 35°S there are conflicting patterns of wind speed change between the two years (Figure 9.2*c* and *f*). In this region, the changes in the v-component of the wind seem to suggest that there is increased southward flow west of about 20°E, but there are contrasting anomalies east of this longitude (Figure 9.3*b* and *d*).

These near-surface wind and pressure anomalies have the potential to modify the fields of convergence and divergence that are shown in the controls of 1980 and 1985 for the 900 hPa level (Figure 9.4). Related to the anticyclonic conditions, divergence fields dominate over the land and Atlantic and Indian Oceans in the controls (Figure 9.4*a* and *d*). There is a small convergence field over the north-western region of the land in 1985 (Figure 9.4*d*), which may be related to the weak trough over the west coast (Figure 9.1*d*). As was found with the sea level pressure fields, the perturbations of the two years resemble each other more closely than do the controls, in terms of both the magnitude and patterns of convergence and divergence

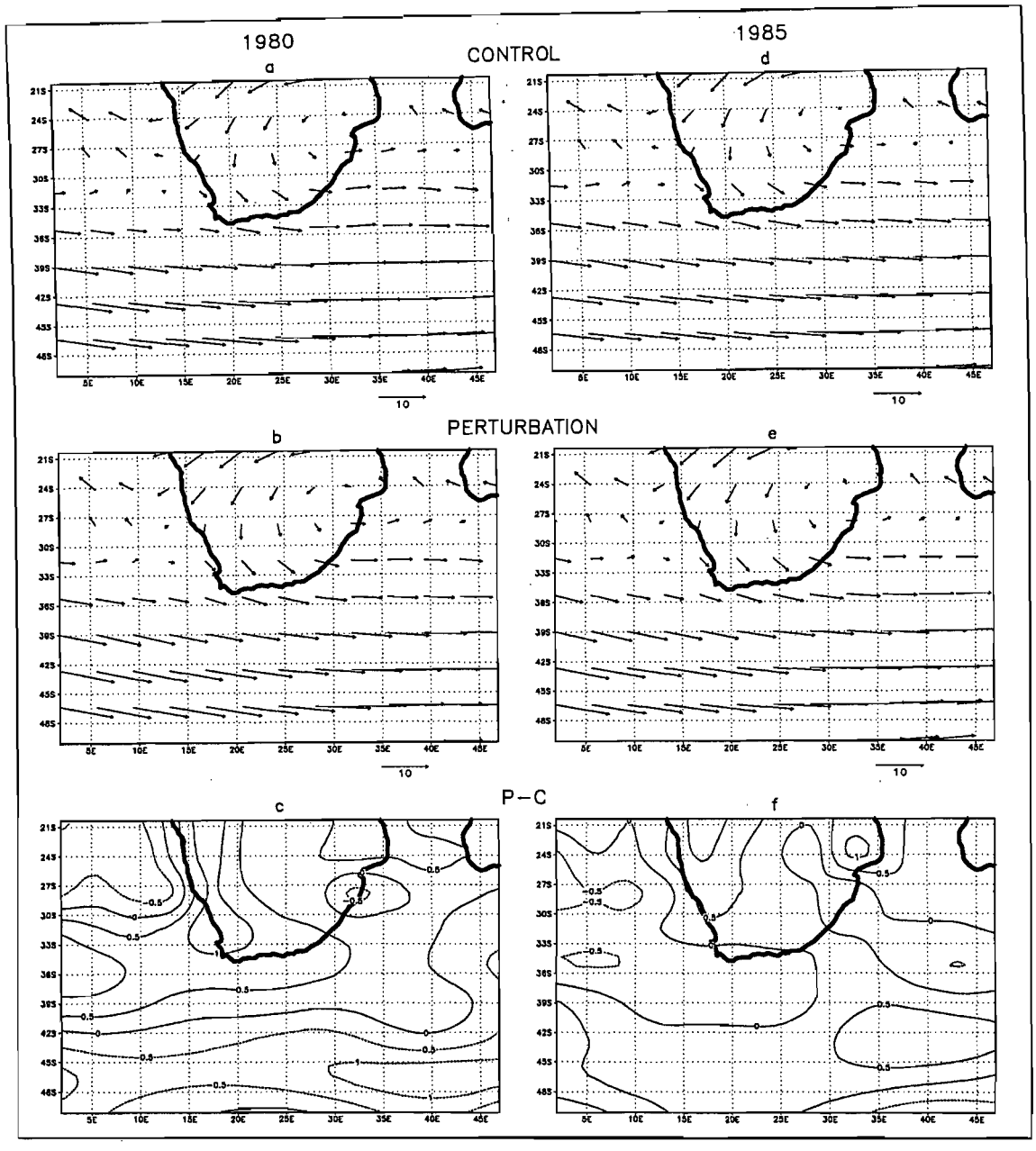

Figure 9.2 900 hPa wind direction and speed (m s^{-1}) for the controls of *a*) 1980 and *d*) 1985, and the perturbations of *b*) 1980 and *e*) 1985. Maps *c*) and *f*) show the change in wind speed between the perturbations and the controls in 1980 and 1985 respectively.

(Figure 9.4). There are, however, similar anomaly patterns over the land in both years (Figure 9.4*c* and *f*). As a result of the increase in intensity and spatial extent of the continental high pressure in the perturbations (Figure 9.1), there is an increase in 900 hPa divergence over much of the eastern half of South Africa and adjacent Indian Ocean (Figure 9.4*c* and *f*). There is also a convergence anomaly over the western and southern portion of the land in response to the perturbation (Figure 9.4*c* and *f*), which may be related to the increased southward flow associated with the western border of the continental high pressure, as well as convergence associated with the eastern half of the trough over the west coast (Figure 9.3*b* and *d*). There is diminished divergence over the eastern Atlantic Ocean, probably due to the combination of weaker winds (Figure 9.2), reduced northward flow (Figure 9.3) and the slight

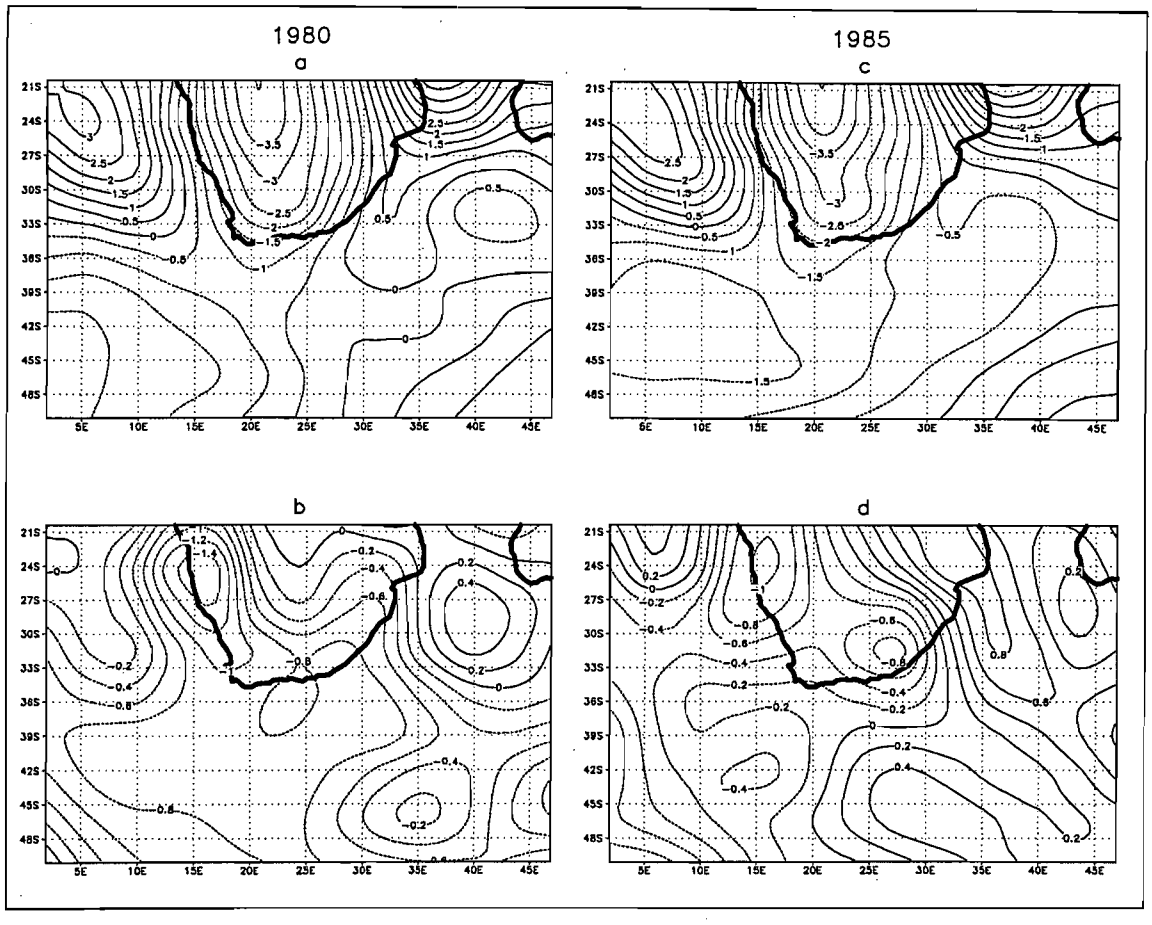

Figure 9.3 Meridional component (v-component) of the 900 hPa wind (m s^{-1}) for the controls of *a*) 1980 and *c*) 1985, and the perturbations minus the controls for *b*) 1980 and *d*) 1985.

weakening of the South Atlantic Anticyclone (Figure 9.1). The near-surface changes in convergence and divergence over the land suggest that there may be the potential for increased uplift and rainfall over the west coast, the south-western Cape and south coast, and a strengthening of the subsidence over the eastern half of the land in the perturbations. However, as mentioned in Chapter 7, it is also essential to investigate the potential humidity and 500 hPa level anomalies.

There is an increase in the 500 hPa height field over much of the analysis window in response to the perturbation, with the largest increases occurring south-east and south of Africa in 1980 and 1985 respectively (Figure 9.5*b* and *d*). These pressure increases may be related to the phase and amplitude changes of wave number 3 that were mentioned in the previous chapter. In the controls at about 35°S, the first ridge of wave number 3 is positioned near 60°E, whereas in the perturbations the ridge is positioned west of this, near 40°E in 1980 and 48°E in 1985 (Figure 8.27). This, together with the increase in amplitude of wave number 3 (without regard to phase) (Figure 8.28), may partially account for the increase in 500 hPa heights over the analysis window. In response to the pressure changes, there is a decrease in

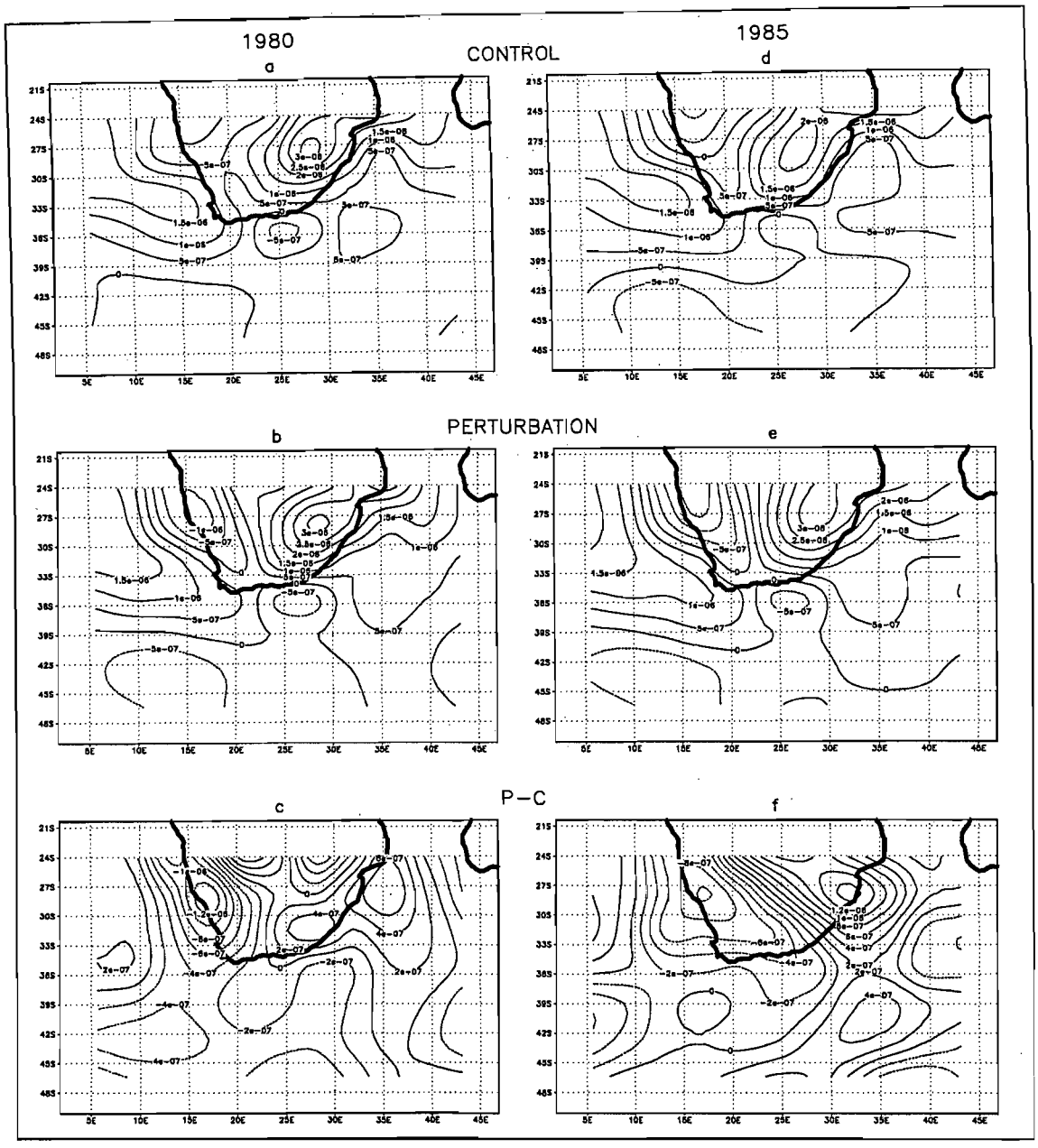

Figure 9.4 Horizontal divergence (s^{-1}) at the 900 hPa level for the controls of *a*) 1980 and *d*) 1985, and the perturbations of *b*) 1980 and *e*) 1985. Maps *c*) and *f*) show the perturbations minus the controls in 1980 and 1985 respectively.

the speed of the 500 hPa wind over most of the land, especially the northern and eastern sections (Figure 9.6*c* and *f*). There is also predominantly a decrease in wind speeds over the Indian Ocean sector in both years (Figure 9.6*c* and *f*). Over the Atlantic Ocean, however, there is an increase in wind speeds between about 24°S and 33°S, but south of this there are contrasting anomalies in the two years. Owing to the positioning of the 500 hPa height anomaly in the centre of the analysis window in 1985 (Figure 9.5*d*), there is an increase in southward flow over the western half of the window and an increase in northward flow over the eastern half of the window (Figure 9.7*d*). In contrast, in 1980 the height anomaly is positioned further east than in 1985 (Figure 9.5*b*) and there is an increase in southward flow

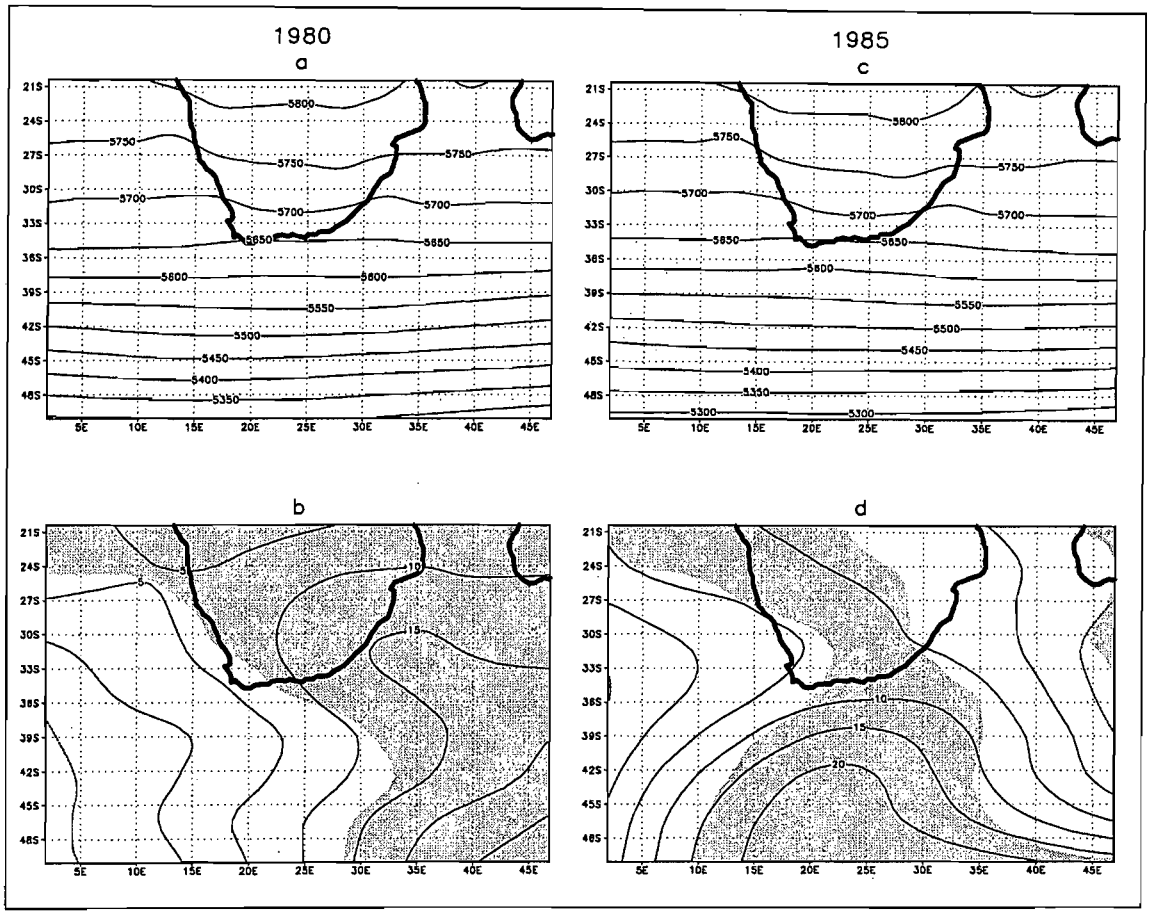

Figure 9.5 500 hPa heights (m) for the controls of *a*) 1980 and *c*) 1985, and the perturbations minus the controls of *b*) 1980 and *d*) 1985. Statistically significant differences at the 95% confidence level have been shaded.

over most of the analysis window, except portions of the Indian Ocean (Figure 9.7*b*). These broad differences in the v-component of the 500 hPa wind between the two years are manifest as contrasting patterns of change over the African subcontinent, except over the south-western and north-western regions where there is increased southward and northward flow respectively in both years (Figure 9.7*b* and *d*). The anomalies in both years suggest that the midlatitudes to the west of southern Africa are dominated by the eastern half of a westerly wave trough, more so in the perturbations than in the controls (Figure 9.7). This trough may be related to the drop in pressure over the Atlantic Ocean in response to the perturbation that was observed in the plots of the hemisphere from the previous chapter (Figure 8.17).

At the 500 hPa level there are similar convergence and divergence anomalies over southern Africa in the two years (Figure 9.8*c* and *f*). The divergence field over the north-west coast strengthens and extends southwards in the perturbations, and there is also a divergence anomaly over the south coast, west of about 25°E, in both years (Figure 9.8). These divergence anomalies overlie the 900 hPa convergence anomalies (Figure 9.4), suggesting that there is an increased potential for uplift and rainfall over the west and south coasts in the

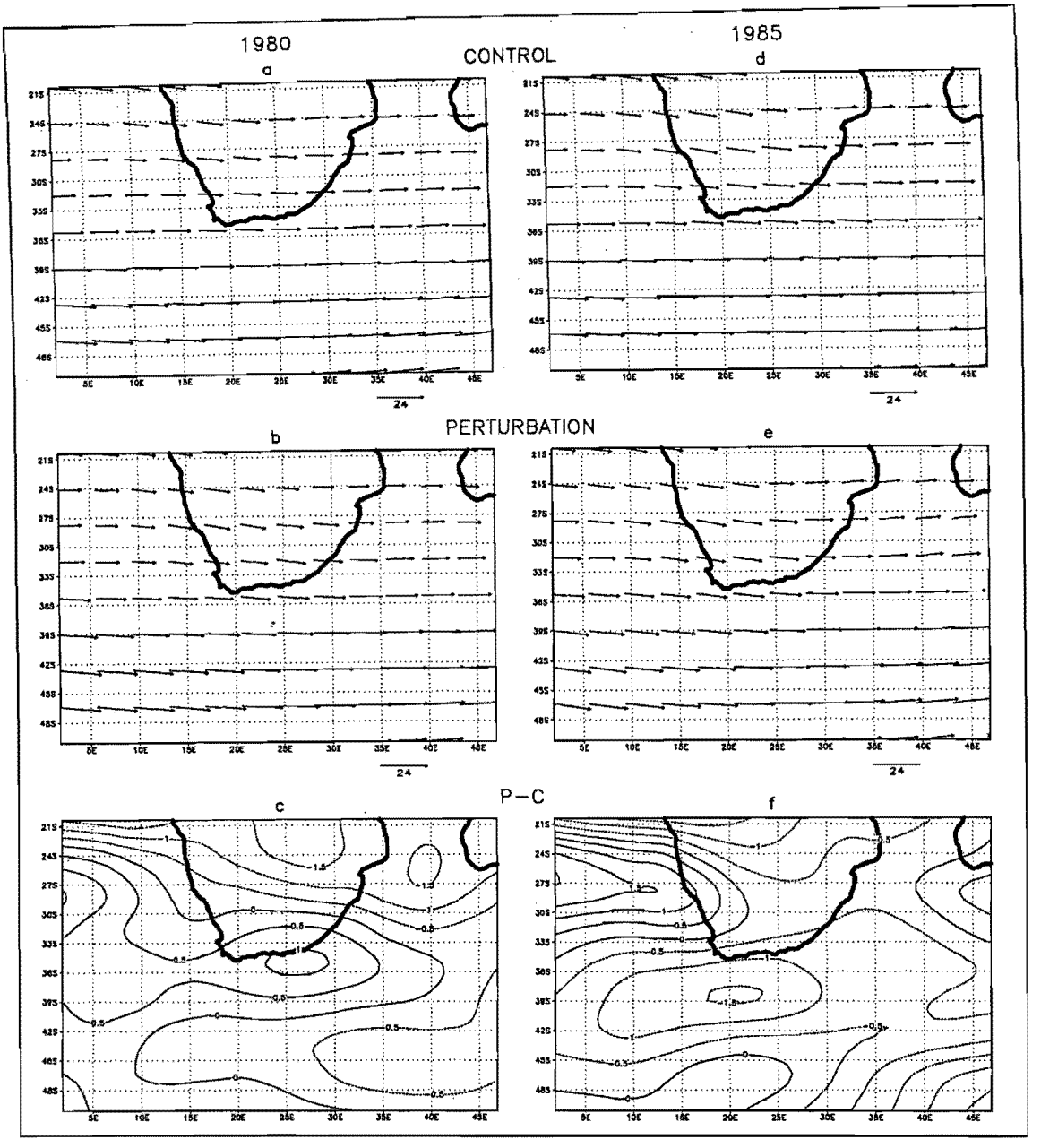

Figure 9.6 500 hPa wind direction and speed (m s^{-1}) for the controls of *a*) 1980 and *d*) 1985, and the perturbations of *b*) 1980 and *e*) 1985. Maps *c*) and *f*) show the change in wind speed between the perturbations and the controls in 1980 and 1985 respectively.

perturbations. Over most of the rest of southern Africa, namely the interior and east coast, there is a convergence anomaly in both years (Figure 9.8*c* and *f*). This upper air convergence anomaly generally overlies the 900 hPa divergence anomaly (Figure 9.4), suggesting that owing to the strengthening of the continental high pressure, there is increased subsidence and a reduced potential for uplift and rainfall over the central interior and east coast in the perturbations compared to the controls.

There are surface temperature increases in the midlatitudes, as well as over the western and southern portion of the subcontinent in response to the perturbation (Figure 9.9*b* and *d*). These temperature anomalies largely correspond to increases in the southward flow of air at

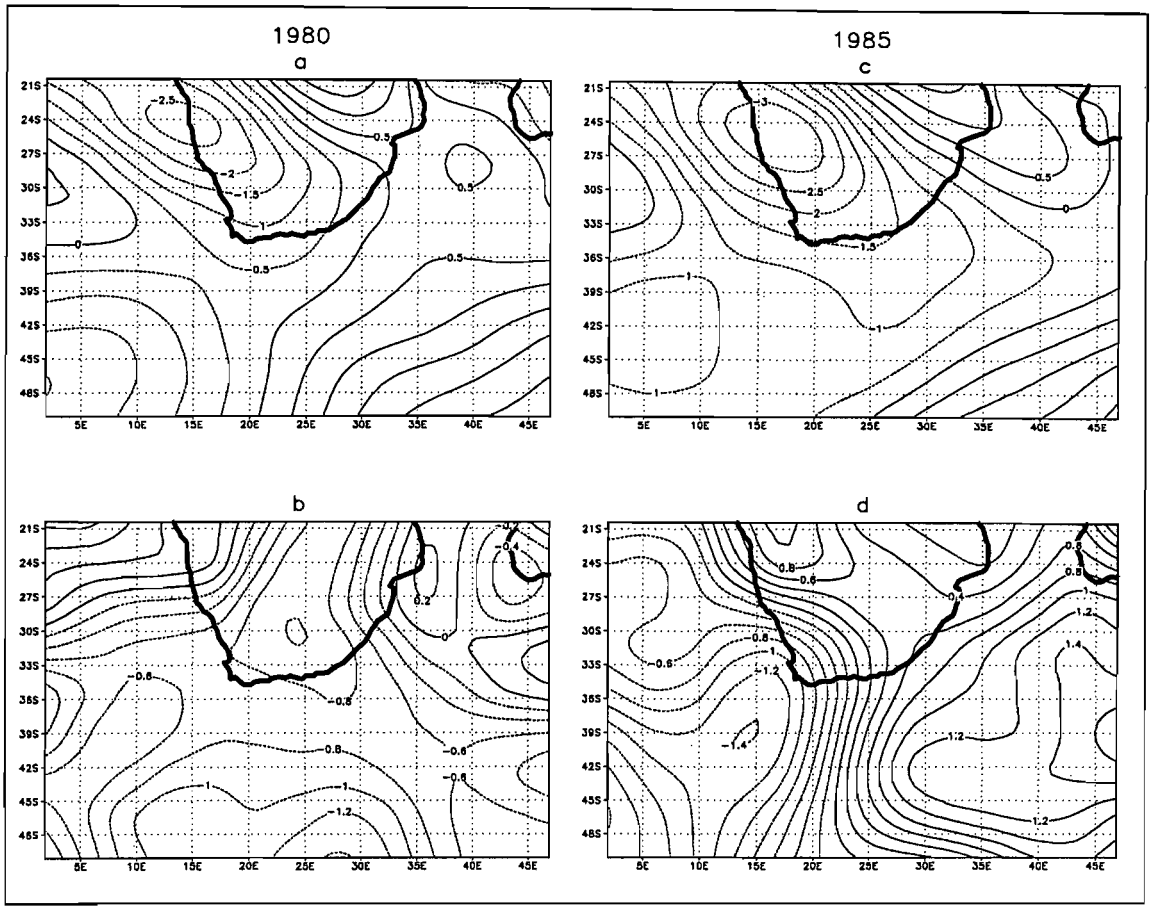

Figure 9.7 Meridional component (v-component) of the 500 hPa wind (m s^{-1}) for the controls of *a*) 1980 and *c*) 1985, and the perturbations minus the controls for *b*) 1980 and *d*) 1985.

the 900 hPa level (Figure 9.3*b* and *d*), which suggests that the temperature changes may be a response to increased advection of warmer air from lower latitudes. There are also increases in the 500 hPa temperature field (Figure 9.10), and the patterns of change largely mirror the 500 hPa geopotential height increases (Figure 9.5). East of 25°E and south of about 35°S the geopotential height and temperature increases at the 500 hPa level (Figures 9.5 and 9.10) overlap with the surface temperature and sea level pressure increases (Figures 9.1 and 9.9) in both years, indicating that the temperature anomalies in this region may be a response to increased subsidence and adiabatic warming. A similar result might be expected over the eastern half of southern Africa and the adjacent Indian Ocean, what with the increase in the extent of the continental high pressure (Figure 9.1) and the convergence and divergence anomalies favouring increased subsidence (Figures 9.4 and 9.8). However, although there is an increase in the 500 hPa temperatures over this region (Figure 9.10), there is a decrease in surface temperatures in 1985 (Figure 9.9*d*). This region in 1985 is subjected to an increase in magnitude of equatorward flow at the 900 hPa level, more so than 1980 (Figure 9.3). Therefore, an increase in the advection of colder air from high latitudes may have overcome the potential increase in surface temperatures from adiabatic warming.

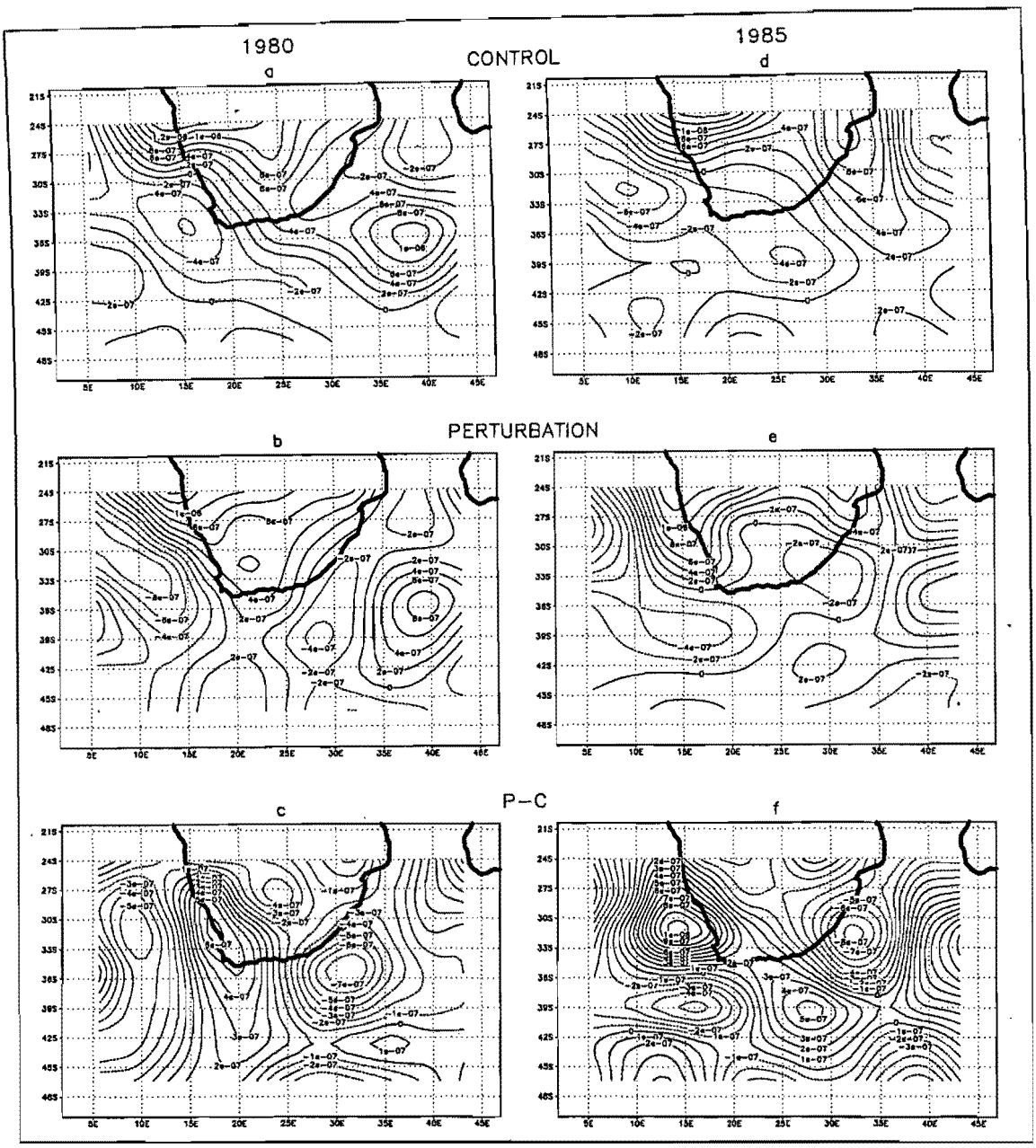

Figure 9.8 Horizontal divergence (s^{-1}) at the 500 hPa level for the controls of *a*) 1980 and *d*) 1985, and the perturbations of *b*) 1980 and *e*) 1985. Maps *c*) and *f*) show the perturbations minus the controls in 1980 and 1985 respectively.

The changes in the surface and 500 hPa specific humidity fields are small in response to the perturbation and there are contrasting patterns of change over southern Africa at both levels between the two years, although at the 500 hPa level both years suggest that there may be a small increase in humidity over the land south of about 30°S (Figures 9.11 and 9.12). The surface changes indicate an increase in humidity south of the NW-SE diagonal of the analysis window (Figure 9.11) and the 500 hPa level changes show a decrease in humidity over the Indian Ocean (Figure 9.12), which may be a response to the increase in subsidence over the region.

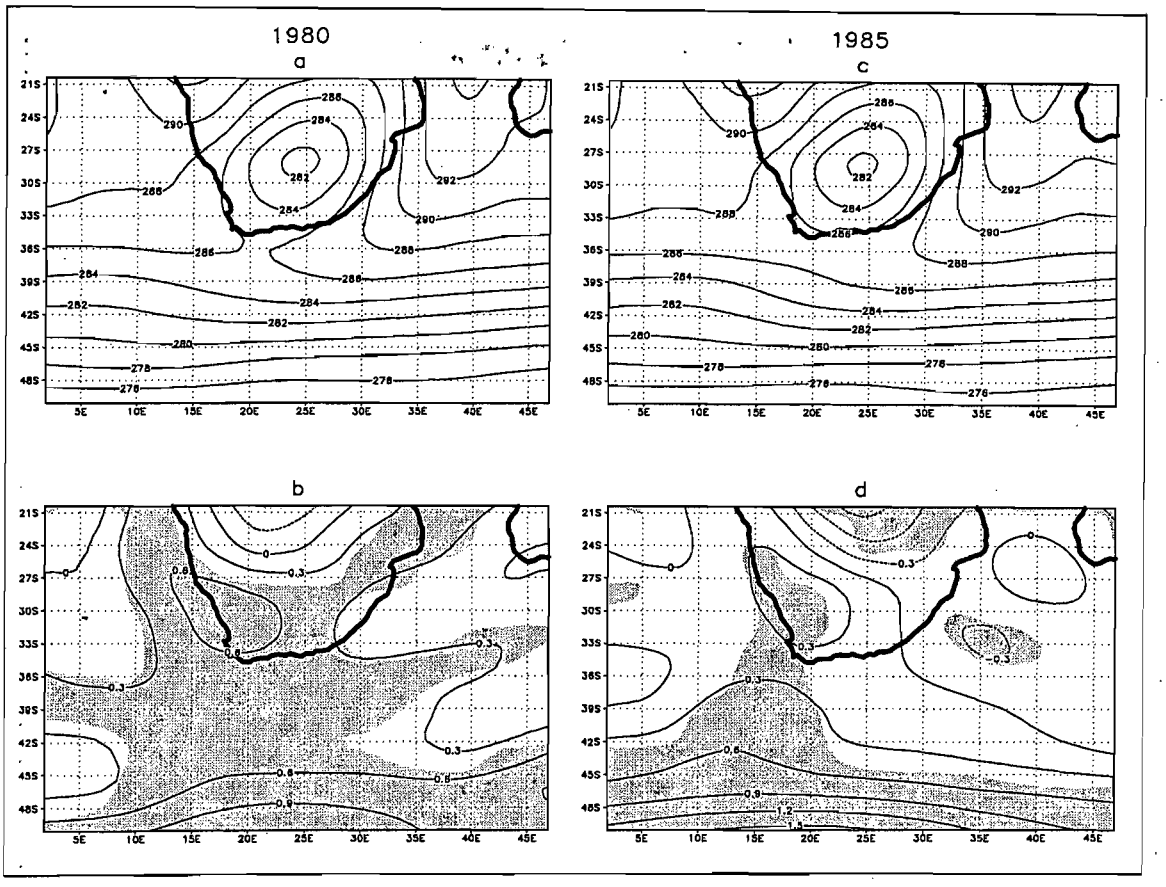

Figure 9.9 Surface temperature (K) for the controls of *a*) 1980 and *c*) 1985, and the perturbations minus the controls of *b*) 1980 and *d*) 1985. Statistically significant differences at the 95% confidence level have been shaded.

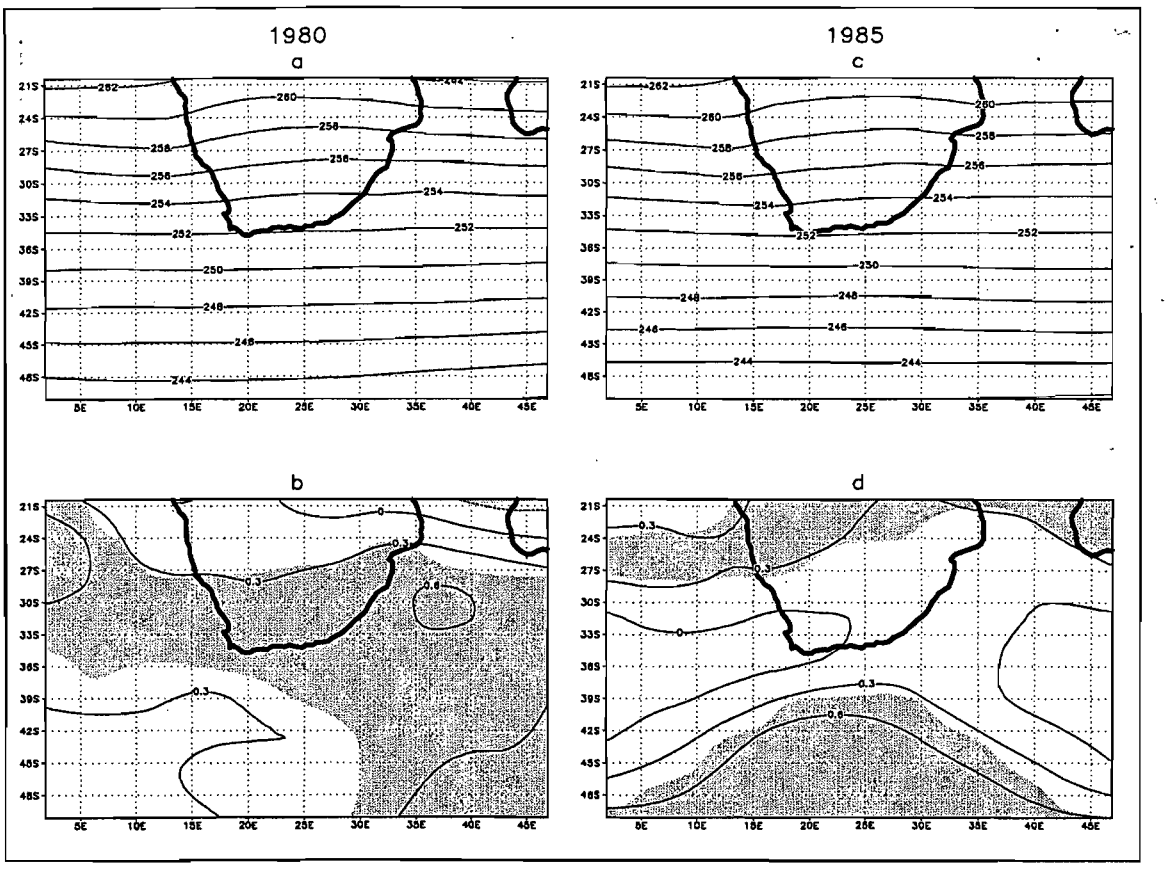

Figure 9.10 500 hPa level temperature (K) for the controls of *a*) 1980 and *c*) 1985, and the perturbations minus the controls of *b*) 1980 and *d*) 1985. Statistically significant differences at the 95% confidence level have been shaded.

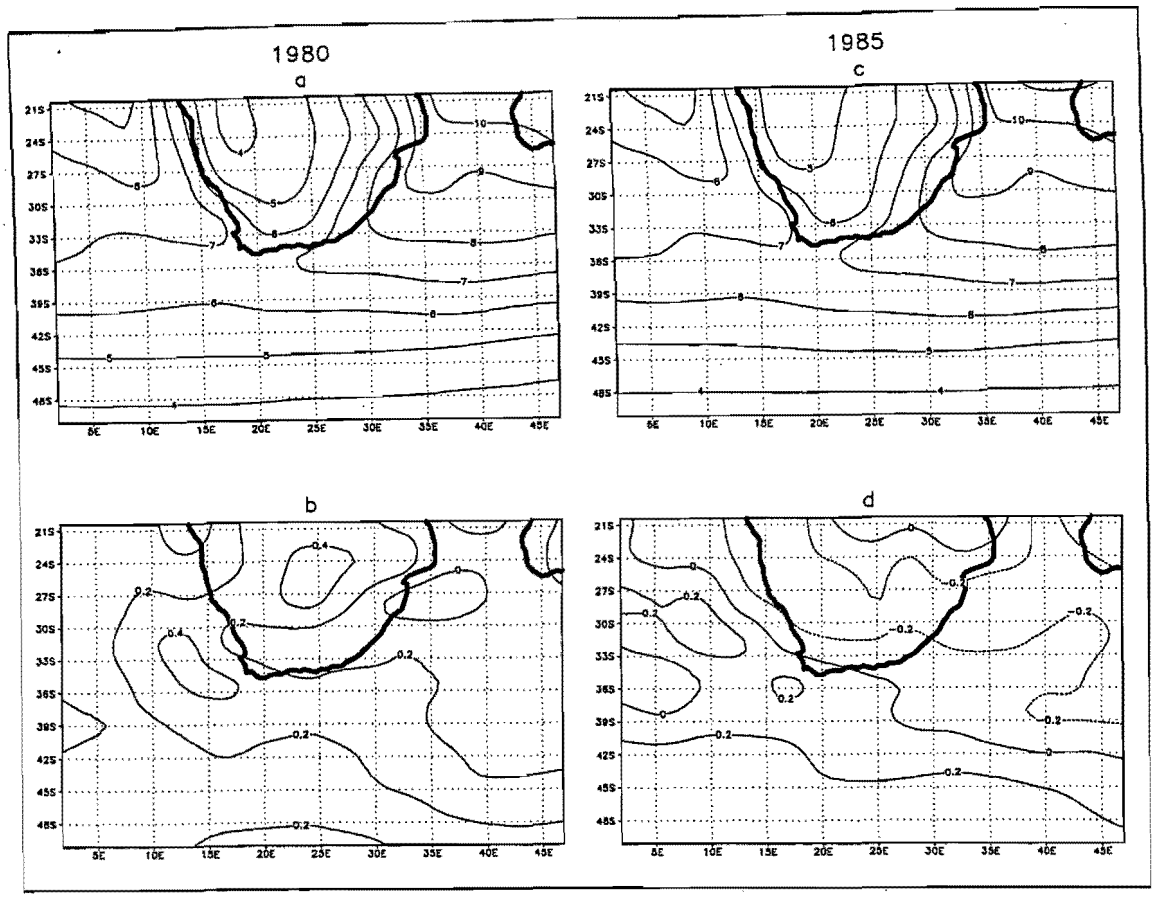

Figure 9.11 Surface specific humidity (g kg^{-1}) for the controls of *a*) 1980 and *c*) 1985, and the perturbations minus the controls of *b*) 1980 and *d*) 1985.

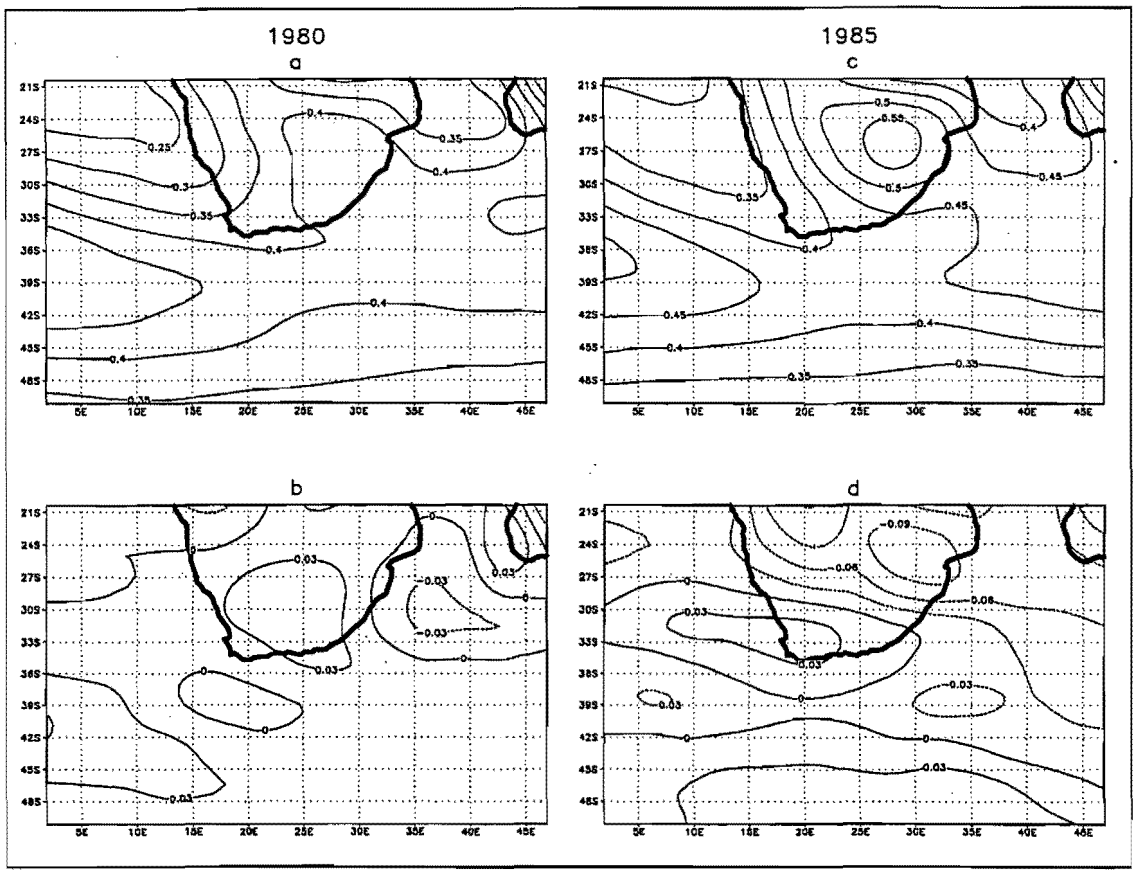

Figure 9.12 500 hPa level specific humidity (g kg^{-1}) for the controls of *a*) 1980 and *c*) 1985, and the perturbations minus the controls of *b*) 1980 and *d*) 1985.

Lastly, the change in the moisture flux at the 700 hPa level has been investigated and is shown in Figure 9.13. As has been mentioned with other variables, the moisture flux magnitudes over southern Africa are more similar between the perturbations of the two years than between the controls (Figure 9.13), again lending credence to the idea that the imposed perturbation has forced the circulation of the two years towards a more similar state. There is a decrease in the moisture flux over most of the interior and north-eastern southern Africa as well as over the adjacent Indian Ocean (Figure 9.13*c* and *f*). Both years indicate an increase in the flux over the Atlantic Ocean, which extends over the western and southern regions of southern Africa, especially in 1980 (Figure 9.13*c* and *f*). These moisture flux anomalies support the previously made suggestions that there may be an increased potential for rainfall

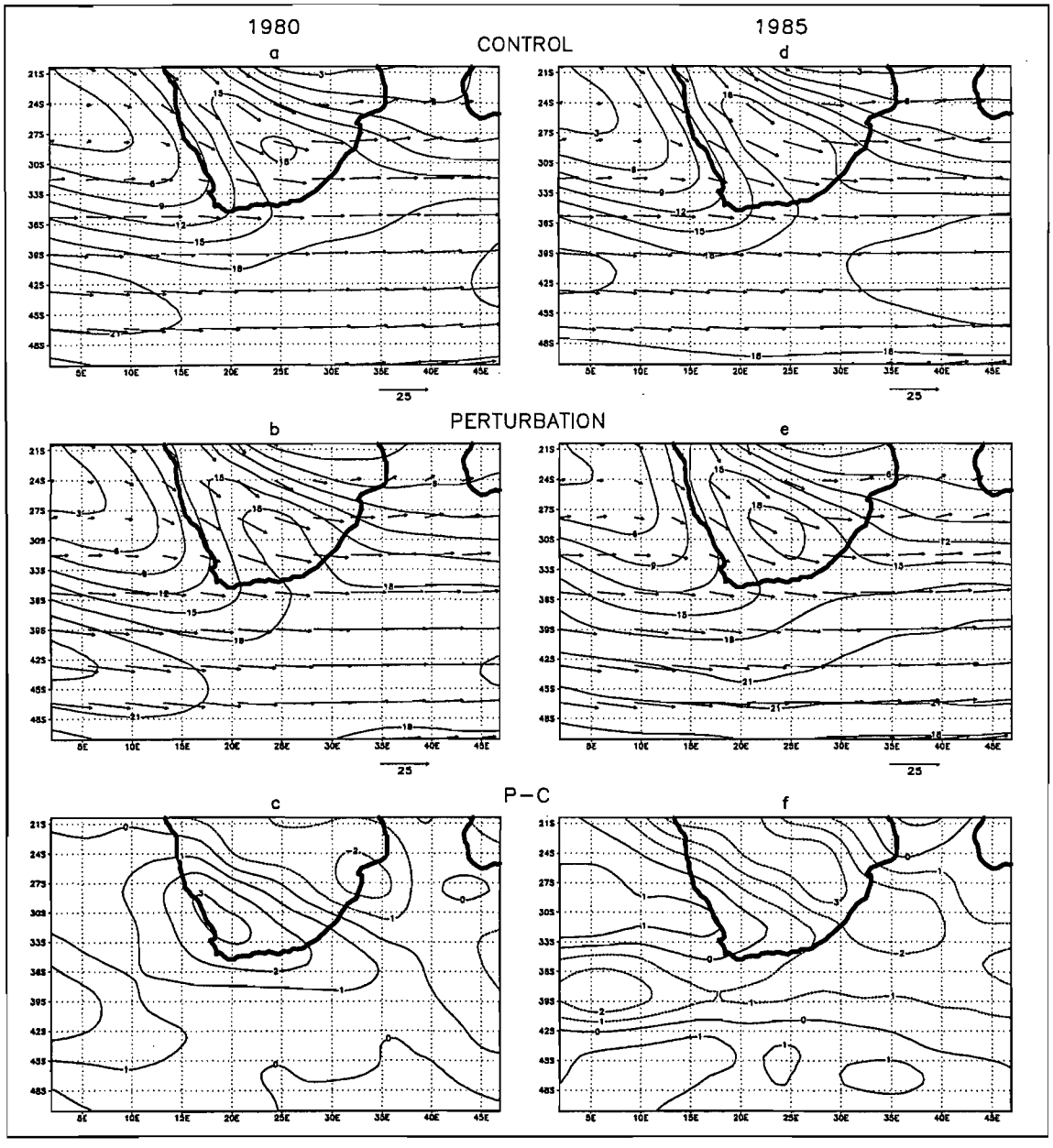

Figure 9.13 The direction and magnitude of the moisture flux (g kg^{-1} m s^{-1}) at the 700 hPa level for the controls of *a*) 1980 and *d*) 1985, and the perturbations of *b*) 1980 and *e*) 1985. Maps *c*) and *f*) show the change in the magnitude of the moisture flux between the perturbations and the controls in 1980 and 1985 respectively.

over the west and south coasts and a reduced potential for rainfall over the central interior and east coasts of southern Africa in the perturbations compared to the controls. It remains to be seen, later in the chapter, whether these inferred precipitation changes actually occurred.

9.3 Twice-Daily Circulation at Sea Level

The twice-daily sea level pressure data over the southern African window are classified into circulation types using a SOM. As for the summer season, non-standardised twice-daily sea level pressure data corresponding to the 6 winter controls of 1980 and 1985 (total t=1104) were used to train a SOM comprising 15 nodes (3 in the x-direction and 5 in the y-direction) in a rectangular topology. The nodes were initialised using linear initialisation and training was run for a total of 30000 iterations, with the initial learning rate and training radius set to 0.05 and three respectively. The weights associated with each node of the trained SOM are shown on the meta-map in Figure 9.14. The trained SOM was then presented with twice-daily data associated with the controls and perturbations of 1980 and 1985 respectively and the percentage of time steps which mapped to each node are given in Figure 9.15. As has been mentioned previously, the nodes are referred to by the numbers shown on the meta-map (Figure 9.14), and the grids displayed on Figure 9.15 correspond to the arrangement of nodes on the meta-map.

Both years show a common decrease in representation of node numbers 4, 5, 7, 8 and 10 (around the left-hand side and centre of the meta-map) and an increase in representation of node numbers 2 and 3 (at the top of the meta-map) and 12 and 14 (in the bottom right-hand corner of the meta-map) (Figure 9.15). Those circulation types which experienced reduced representation are, in general, characterised by a strong South Atlantic Anticyclone in comparison to the South Indian Anticyclone, and related to this, the westerly wave in the midlatitudes is positioned such that there is anticyclonic circulation south of the Atlantic Ocean and cyclonic circulation south of the Indian Ocean (Figure 9.14). In contrast, the nodes that are favoured in response to the perturbation, generally have higher pressures over the Indian Ocean compared to the Atlantic Ocean and for node numbers 2, 3 and 12 the westerly wave trough axis is positioned south or south-west of southern Africa such that there is anticyclonic circulation south of the Indian Ocean. Node number 14 is associated with a centrally situated westerly wave ridge and high pressures over most of the analysis window (Figure 9.14). In the distribution of types simulated in the perturbations, it appears that both years tend to favour the nodes which fall on the right-hand side of the meta-map in contrast to the left-hand side (Figure 9.15*b* and *e*), which was not the case in the controls of the two years

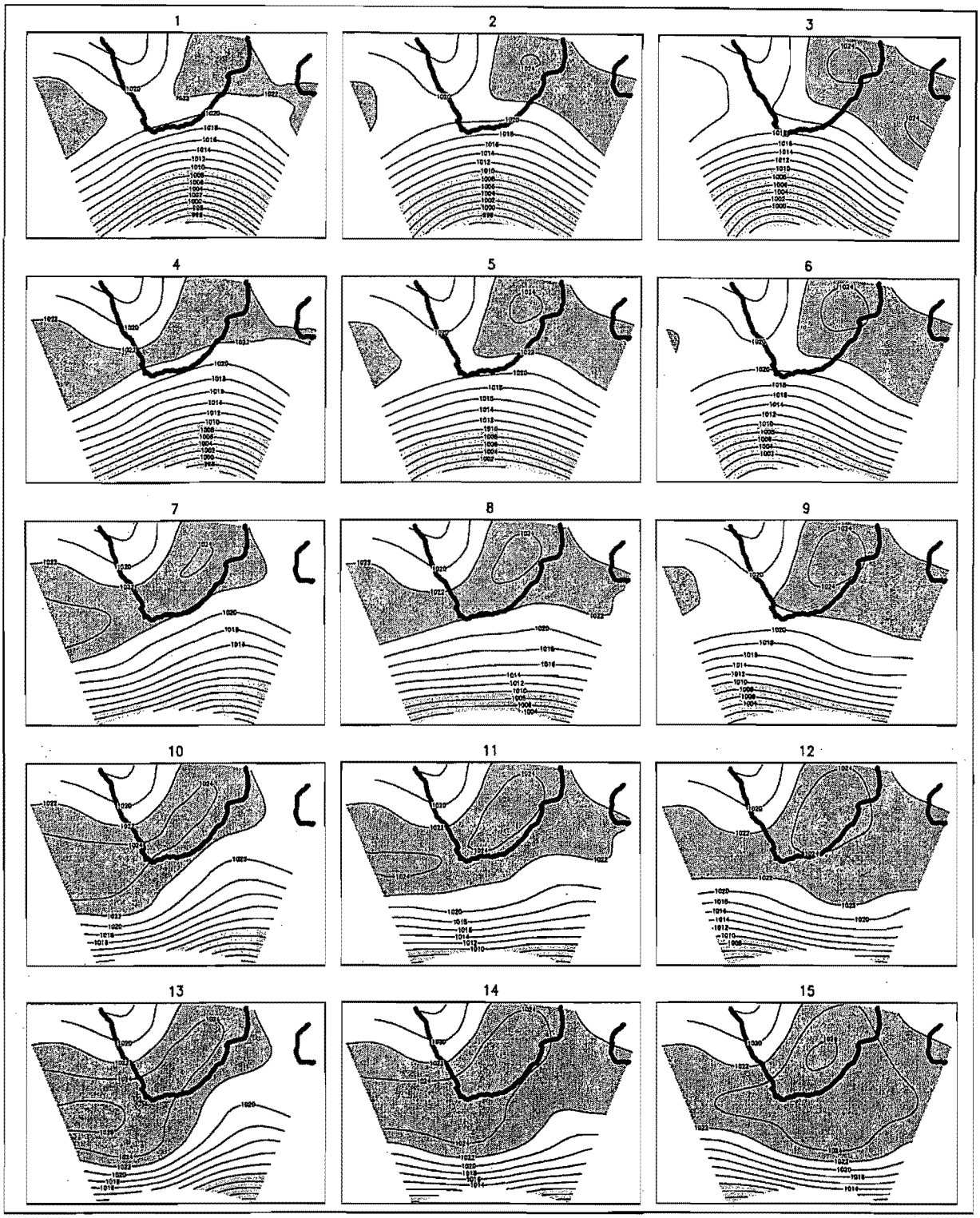

Figure 9.14 The meta-map for the SOM showing the 15 nodes (3×5) with their contoured weights. The weights represent sea level pressure, and values greater than 1022 hPa and less than 1010 hPa have been shaded.

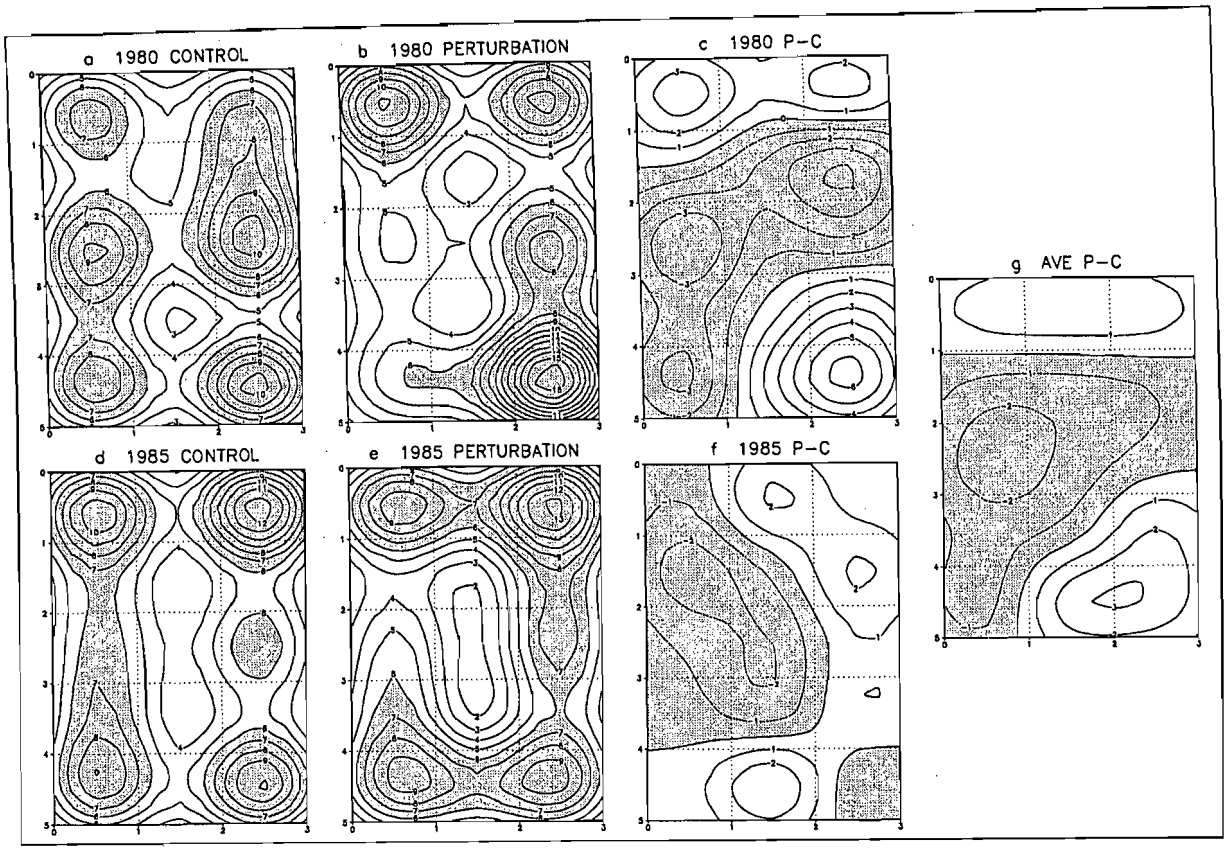

Figure 9.15 The percentage of days mapping to each node of the meta-map (Figure 9.14) for the controls of *a*) 1980 and *d*) 1985 and the perturbations of *b*) 1980 and *e*) 1985. Plots *c*) and *f*) show the difference between the controls and perturbations (perturbation minus control) in terms of the percentage of days mapping to each node in 1980 and 1985 respectively. Plot *g*) represents the average between the plots on *c*) and *f*), i.e. showing the average response between 1980 and 1985.

(Figure 9.15*a* and *d*). If one moves from left to right across the meta-map, there is a reduction in the strength of the South Atlantic Anticyclone and an increase in the strength of the South Indian and continental anticyclones (Figure 9.14). All these features are therefore favoured in the perturbations more than in the controls.

The top of the meta-map represents synoptic types that possess deeper westerly waves that extend further northwards compared to the bottom of the meta-map (Figure 9.14). In the perturbations (Figure 9.15*b* and *e*), as in the controls (Figure 9.15*a* and *d*), there does not seem to be a particular bias towards either more or less extensive westerly waves over the analysis window. Although, 1980 does seem to especially favour node number 15 in the perturbations (Figure 9.14*b* and *c*), which shows high pressures over much of the analysis window and anticyclonic circulation associated with a westerly wave which is situated quite far south (Figure 9.15). 1985 favours this node less that 1980 in the perturbations (Figure 9.15), largely because of the positioning of the westerly wave. The seasonal mean anomaly maps of meridional flow at the 900 hPa level in the midlatitudes suggest that in 1980 there is increased southward flow over most of the window, whereas in 1985 there is increased

southward flow over the western half of the window and increased northward flow over the eastern half of the window (Figure 9.3), thus imposing a centrally located ridge in the westerlies in 1985 and a ridge which is located off-centre (east of the analysis window) in 1980. Node number 15 is predominately associated with southward flow in the midlatitudes, thus more closely resembling the seasonal change for 1980 compared to 1985.

In summary, the SOM results imply that the imposed sea-ice and SST perturbation has caused a shift towards synoptic types that are characterised by a strong continental anticyclone, high pressures over the Indian Ocean (generally higher than those over the Atlantic) and a westerly wave trough which is positioned south or south-west of the subcontinent, such that there is cyclonic circulation south of the Atlantic Ocean and anticyclonic circulation south of the Indian Ocean.

9.4 Precipitation Changes

The same downscaling procedure that was described in Chapter 7 for the summer season has been used here for the winter season. An artificial neural network (ANN) has been trained to derive a relationship between the input NCEP/NCAR assimilation atmospheric predictors (interpolated to the GENESIS GCM T31 grid) and the target CCWR observed precipitation data (presented on a 0.5° grid). As mentioned in Chapter 7, the atmospheric predictor variables comprise surface specific humidity, 700 hPa and 500 hPa geopotential heights, 700 hPa and 500 hPa temperatures and 700 hPa and 500 hPa specific humidities, as well as a lag (36 hours) and a lead (12 hours) of these variables and the synoptic state indices derived from the SOM procedure (refer to Chapter 3). The training has been performed using twice-daily data from the winter months (JJA) in the period extending from June 1980 to August 1988. As for the summer season, training has only been performed for those grid cells for which there are more than 365 days of observed precipitation data in the extracted winter months.

Figure 9.16 shows the seasonal average for the observed CCWR precipitation data and the downscaled precipitation derived from the NCEP/NCAR reanalysis atmospheric predictors. The downscaled precipitation is a good representation of the observed pattern of precipitation, although, as for the summer season, the downscaling procedure does show a tendency to derive too much precipitation. The largest difference between the downscaled and actual precipitation over the grid cells that have been analysed is about 0.5 mm day^{-1} (Figure 9.16*c*). Thus, in terms of the seasonal mean, the ANN downscaling functions are capable of

adequately reproducing observed winter precipitation over South Africa and may be deemed valid for use with the GCM data.

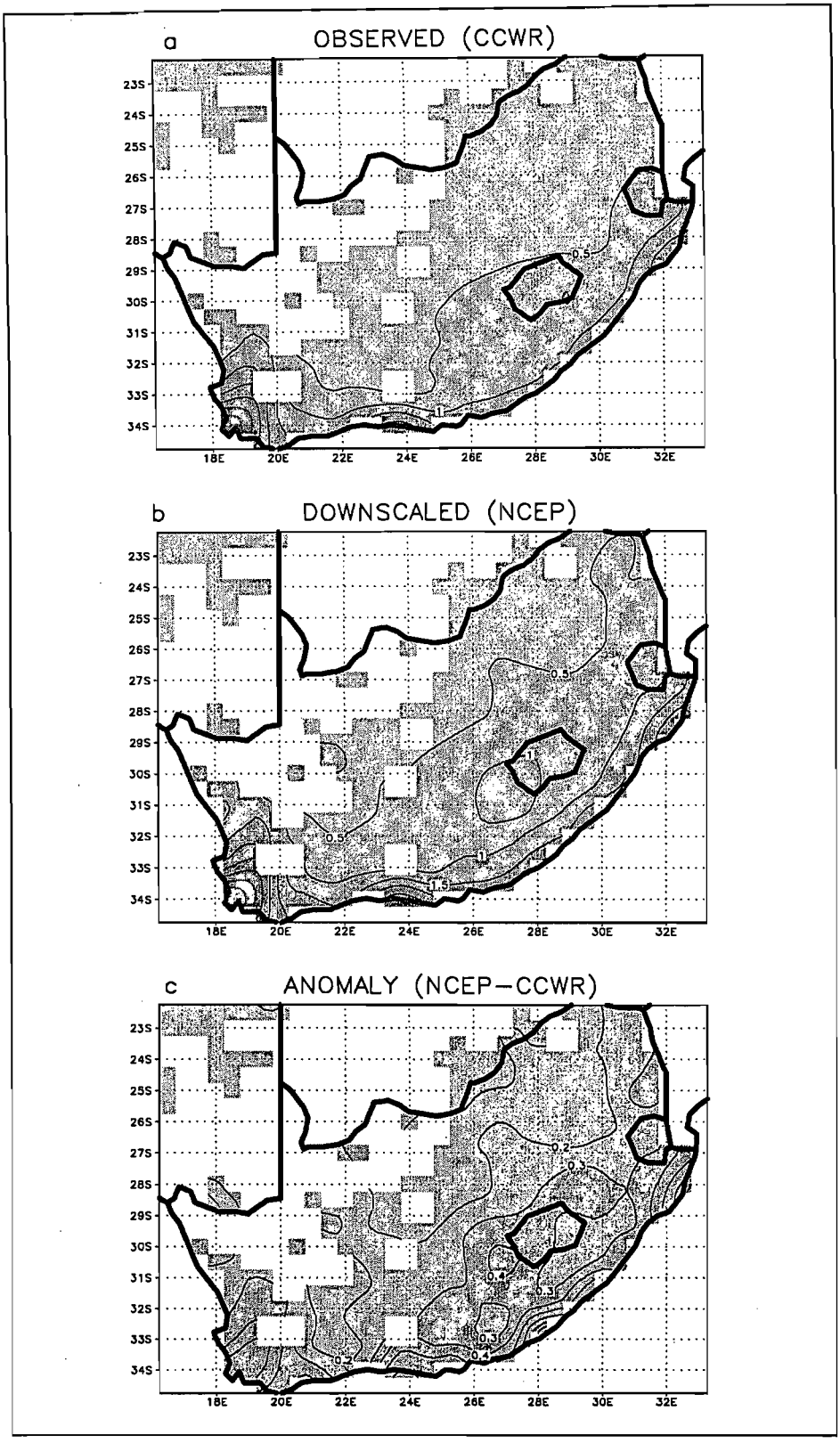

Figure 9.16 The *a*) observed CCWR area averaged precipitation station data, the *b*) precipitation data downscaled from the NCEP/NCAR reanalysis atmospheric predictor variables, and the *c*) downscaled precipitation minus the observed precipitation (*b* minus *c*), for JJA and averaged over the period 1980 to 1988. Precipitation is given in mm day^{-1}.

Data from the atmospheric predictor variables of the 1980 and 1985 winter control and perturbation simulations have been applied to the trained ANN downscaling functions in order to derive precipitation. As for the summer season, the twice-daily data from the three replicates associated with the controls and the perturbations respectively have been concatenated together for both 1980 and 1985 in order to produce the input data for the ANN. Figure 9.17 shows the winter (JJA) seasonal average of CCWR observed precipitation (also shown in Figure 9.16*a*), as well as the 1980 and 1985 control simulation winter grid cell precipitation output by the model and the downscaled precipitation derived from the GCM atmospheric predictor variables. The pattern and magnitude of the GCM downscaled precipitation (Figure 9.17*c* and *e*) is very similar to what is observed (Figure 9.17*a*), although the magnitude of GCM downscaled precipitation is generally slightly larger than observed. This bias appears to be a result of the downscaling procedure, which, as mentioned in the above paragraph, produces slightly wetter conditions than observed. The magnitude of the GCM downscaled precipitation (Figure 9.17*c* and *e*) is very similar to the NCEP/NCAR reanalysis downscaled precipitation (Figure 9.16), suggesting that the model circulation (as defined by the atmospheric predictor variables) over the South African region must be fairly realistic.

The GCM downscaled precipitation (Figure 9.17*c* and *e*) is a vast improvement over the GCM grid cell precipitation (Figure 9.17*b* and *d*). The GCM grid cell precipitation is generally larger than observed, more so than the downscaled precipitation, and does not capture the steep gradients and localised patterns of rainfall observed over South Africa (Figure 9.17). These results show that it is desirable to use the downscaled, derived fields of GCM precipitation rather than the grid cell precipitation output by the model.

The control simulation and observed precipitation fields (Figure 9.17) show that only a small proportion of South Africa receives rainfall during winter, with the rainfall being concentrated in the south-western Cape and along the south-west and south coasts. The majority of this rainfall is frontal in origin and thus affected by changes in the midlatitudes. Figure 9.18 shows the downscaled precipitation fields for the perturbation simulations, as well as the difference between the control and perturbation fields. It is evident that the precipitation changes are very small, and that the only change that may be of any significance is the increase in precipitation over the west coast and south-western Cape in both years (Figure 9.18*b* and *d*).

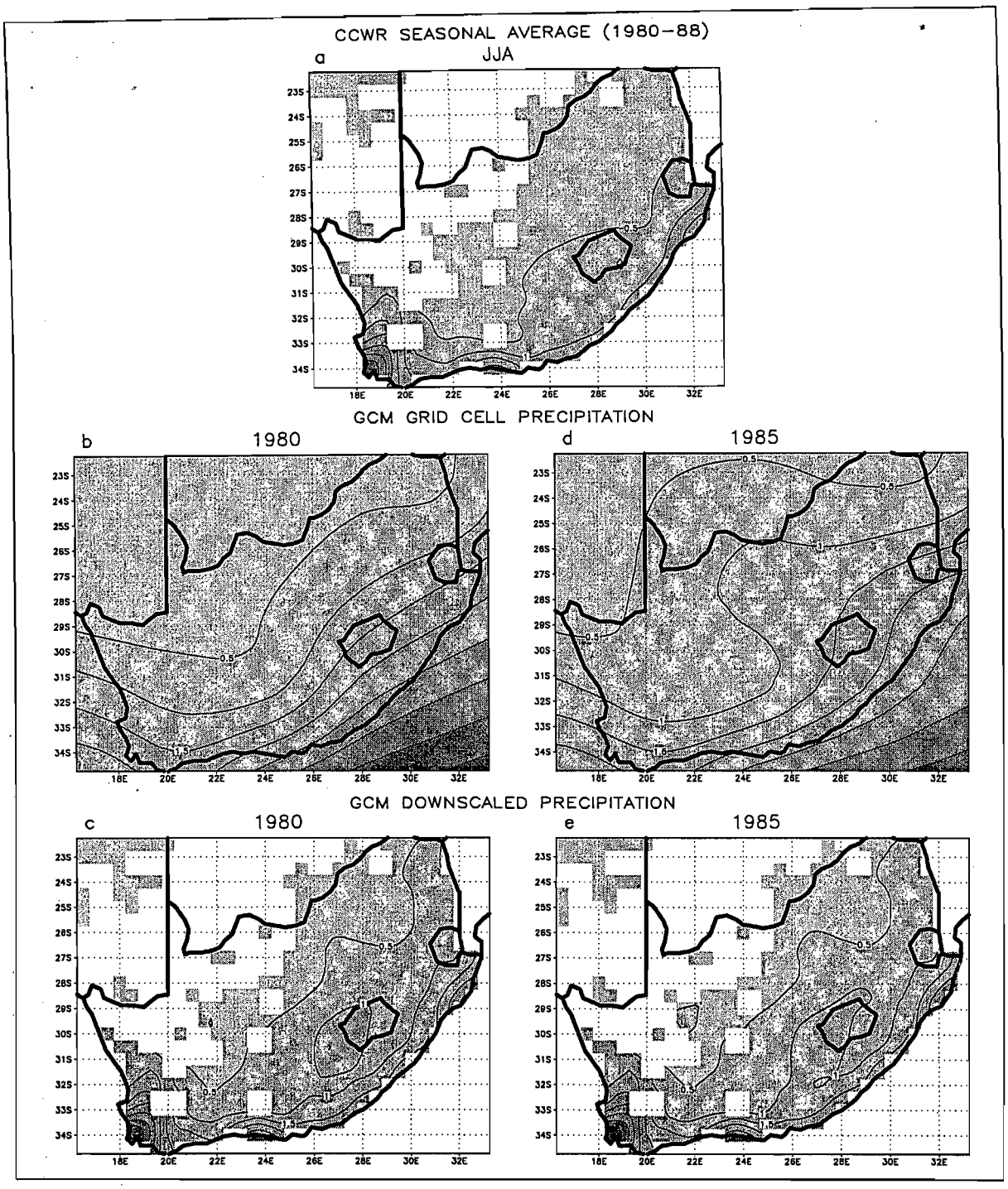

Figure 9.17 The *a*) seasonally averaged observed CCWR precipitation (identical to Figure 9.16*a*), the GCM control simulation *grid cell* precipitation output by the model in the winters of *b*) 1980 and *d*) 1985 respectively, and the GCM control simulation *downscaled* precipitation for the winters of *c*) 1980 and *e*) 1985 respectively. Precipitation is given in mm day^{-1}.

The major conclusion drawn from the preceding analyses in this chapter of the mean response of certain atmospheric variables was that there may be the potential for increased uplift and rainfall over the west coast and south-western Cape, and a reduced potential for rainfall over the eastern half of the country. Although very small, there does seem to be a general indication of reduced rainfall over the eastern half of the country, especially in 1985 (Figure 9.18). The basis for suggesting that there may be a decrease in the already small amount of

rainfall over this region, is because there is an increase in the spatial extent of the continental high pressure in the perturbations, producing increased surface divergence and increased upper level convergence (Figures 9.1, 9.4 and 9.8). These anomalies are stronger in 1985 compared to 1980, therefore accounting for the more widespread decrease in precipitation in 1985 (Figure 9.18).

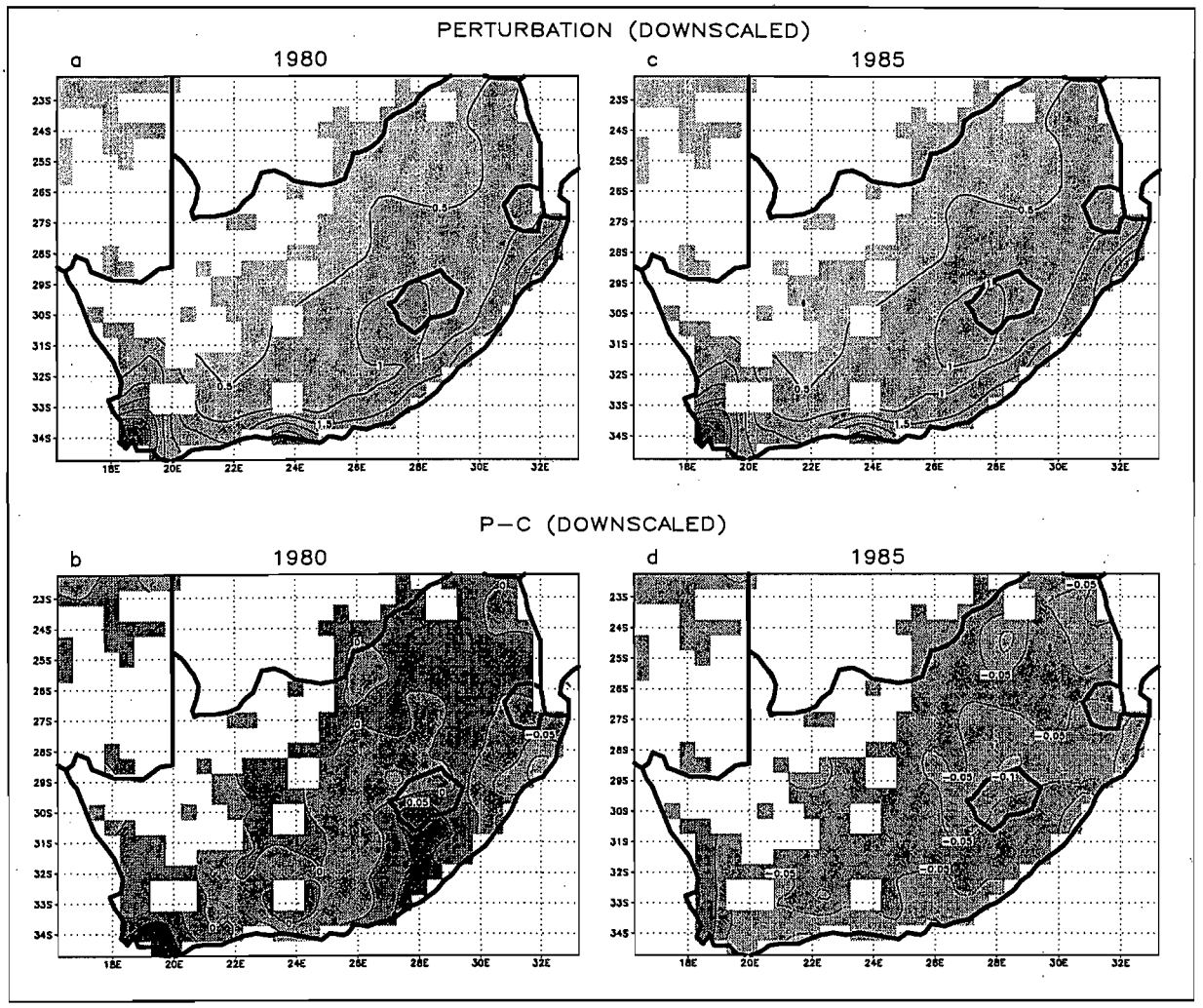

Figure 9.18 The GCM perturbation simulation *downscaled* precipitation for the winters of *a*) 1980 and *c*) 1985 respectively, and the perturbation simulation *downscaled* precipitation minus the control simulation *downscaled* precipitation (see Figure 9.17*c* and *e*) for the winters of *b*) 1980 and *d*) 1985 respectively. Precipitation is given in mm day^{-1}.

As mentioned above, the increase in precipitation over the west coast and south-western Cape can be explained by the results obtained from the other atmospheric variables which have been examined. There is a decrease in midlatitude/sub-tropical sea level pressure west of South Africa in both years (Figure 9.1). This decrease is positioned closer to South Africa in 1980 (extending westwards from about 24°E) compared to 1985 (extending westwards from about 15°E) (Figure 9.1), which may contribute to the more spatially extensive increase in precipitation over the south-western Cape in 1980 compared to 1985 (Figure 9.18). The manifestation of this decrease in pressure is that there is a northward extension of lower,

midlatitude pressures over the Atlantic sector and a weakening of the South Atlantic Anticyclone, but more so in 1980 compared to 1985 (Figure 9.1). The seasonal mean changes also show that there is a southward extension of the trough that is positioned over the west coast. Changes to the wind field at the 900 hPa level display an increase in the northerly component of the wind over the west coast and south-western Cape (Figure 9.3). Over this region, winds originating from the north-west are the important rain-bearing winds. There is also a 900 hPa convergence anomaly (Figure 9.4) and an upper-level divergence anomaly over the west coast and south-western Cape in response to the perturbation, which indicates increasingly favourable conditions for uplift and rainfall. Furthermore, there is an increase in the 700 hPa moisture flux over the western portion of the country in the perturbations of both years (Figure 9.13).

The change in the frequency of synoptic types simulated in the perturbations compared to the controls indicates an increased preference for days which have higher pressures over the Indian Ocean compared to the Atlantic Ocean, and where the axis of the westerly wave trough is positioned south or south-west of South Africa, rather than east of the country. It is suggested that the extensive decrease in pressure over the Atlantic Ocean, that was shown in the previous chapter, may have resulted in an increased frequency or intensity of cold fronts approaching South Africa and affecting the west coast and south-western Cape, but that these fronts may then be preferentially steered southwards, away from the country, as a result of relatively stronger high pressures south and east of South Africa in the perturbations. The largest increases in the 500 hPa geopotential height and sea level pressure field over the South African region are found south, south-east and east of the country (Figure 9.1 and 9.5). It has been suggested that this pressure increase may be related to the phase and amplitude changes of the subtropical expression of wave number 3.

In conclusion, although the precipitation changes caused by the sea-ice perturbation are very small, the common increase in rainfall over the west coast and south-western Cape in 1980 and 1985 is physically plausible. It is thought that the sea-ice perturbation in the Weddell Sea sector is responsible for the drop in pressures over much of the Atlantic Ocean (refer to Figure 8.16) and that this has a direct effect on the cold fronts affecting the western portion of South Africa. Owing to the small magnitude of the precipitation changes, it can probably be said that sea-ice perturbations of a similar size to that imposed in the present study would not have a very important controlling effect on winter rainfall over the country. Nevertheless, in

light of the cohesiveness of the response obtained in the present study, it is possible that a larger perturbation may cause a larger precipitation change over the region.

9.5 Summary

This chapter has considered the regional atmospheric response to the sea-ice and SST perturbation over southern Africa during the winter season. The mean seasonal response of the climate has been considered, as well as possible changes in the frequency of circulation types simulated over the region. Precipitation changes have been investigated by means of downscaling, and, as was found for the summer season, the pattern and magnitude of the GCM downscaled precipitation is very similar to what is observed and is a large improvement over the GCM grid cell precipitation output by the model. It has become evident from examining a number of variables, in particular sea level pressure, 900 hPa convergence and divergence fields and the 700 hPa moisture flux, that the perturbation appears to have forced the circulation over southern Africa to a more similar state in the perturbation simulations between 1980 and 1985 than exists between the control simulations of the two years.

The major findings which are common to both 1980 and 1985 are summarised as follows:

In response to the Antarctic sea-ice reduction and warming of the ice-free waters there is

- an increase in the spatial extent of the continental high pressure and an increase in pressure over much of the Indian Ocean.

- a southward extension of the west coast trough.

- a northward extension of lower, midlatitude pressures over the Atlantic Ocean and a weakening of the South Atlantic Anticyclone.

- an increase in 900 hPa divergence over much of the eastern half of South Africa and adjacent Indian Ocean and an increase in convergence over the western and southern portion of the country.

- an increase in 500 hPa convergence over the interior and east coast of South Africa and an increase in upper-level divergence over the west and south coasts of the country.

- a decrease in the 700 hPa moisture flux over most of the interior and eastern regions of South Africa, and an increase in the moisture flux over the western and southern portions of the country.

- an increase in the frequency of days which have higher pressures over the Indian Ocean compared to the Atlantic Ocean, and where the axis of the westerly wave trough is positioned south or south-west of South Africa, rather than east of the country.

- not much change to the precipitation field, although there does seem to be a physically plausible and consistent increase in precipitation over the west coast and south-western Cape in both 1980 and 1985.

SECTION IV

Synthesis

CHAPTER 10

Conclusion

10.1 Overview and Summary

10.1.1 Introduction

The present study has considered the response of an atmospheric general circulation model to a reduction in Antarctic sea-ice extent during summer and winter. The response has been investigated over the entire Southern Hemisphere, although specific emphasis has been placed on southern Africa. The research has aimed to increase our understanding of sea-ice atmosphere interactions, as well as to provide an indication of the influence that negative sea-ice anomalies may have on the climate, in the context of interannual differences in sea-ice extent, as well as the reduction in sea-ice that may occur in the future as a consequence of anthropogenically induced global warming.

There have been previous modelling studies which have addressed this issue of the atmospheric effect of a reduced Antarctic sea-ice extent (*viz.*, Simmonds, 1981; Mitchell and Hills, 1986; Simmonds and Dix, 1987; Mitchell and Senior, 1989), but these studies used extreme sea-ice anomalies, not seen in the present climate regime. The current study has made use of smaller anomalies, closer to the magnitude of observed interannual variability. There are also a number of other important differences between this sea-ice sensitivity study and past studies. For example, the present study uses a finer resolution and more current GCM than used previously; examines the summer season, while past studies only addressed winter months; and is more extensive than former studies, in terms of the number of simulations performed and the number of variables considered (cf. Simmonds, 1981; Mitchell and Hills, 1986; Simmonds and Dix, 1987; Mitchell and Senior, 1989). A particular objective of this thesis has been to establish whether Antarctic sea-ice anomalies have the capacity to affect the climate over South Africa, especially in terms of precipitation. This has not been considered in the past.

In the sea-ice sensitivity simulations, sea-ice and SSTs were prescribed in the GCM, such that the sea-ice perturbation could be isolated and not complicated by feedbacks between the ocean, ice and atmosphere. The control simulations were forced by observed present-day SSTs and sea-ice extents, while in the perturbation simulations SST and sea-ice anomalies

were introduced. A sea-ice algorithm, based on observed patterns of ice growth and decay, was devised in the present study to obtain the anomalous sea-ice and SST fields for the perturbations. Where sea-ice was removed it was replaced by an interpolated gradient of SSTs extending to the new sea-ice boundary, thus including the effect of warming the ice-free waters. For the sensitivity experiment, the control and perturbation simulations were restarts of the AMIP configured simulation from the GENESIS GCM, and the summers of 1979/80 and 1984/85 and winters of 1980 and 1985 were selected for the study. Three replicates were performed for each of the four periods for both the control and perturbation conditions.

10.1.2 Validation of the GENESIS GCM

Before using the GENESIS (ver. 2.0.a) GCM for the sea-ice sensitivity experiments, the model was subjected to an evaluation procedure, more rigorous than has been previously performed for this GCM over the Southern Hemisphere. This was necessary, since the reliability of the results from the sensitivity experiments are related to the ability of the model to simulate present-day conditions. GENESIS has been found to capture the large-scale features of the observed climate reasonably well, and many of the discrepancies between the observed and GCM data can be ascribed to inadequate spatial resolution. The model simulates the pattern of sea level pressures fairly realistically, especially the seasonal strength and position of the subtropical high pressure belt, although the south-east Pacific and Indian high pressures are slightly too weak during summer. The midlatitude pressure gradient is too weak in the GCM due to pressures in the circumpolar trough being higher than observed. This trough is also positioned slightly equatorward of the trough in the observed data, which influences the zonal averages of wind speed and midlatitude cyclone densities. The region over the Antarctic continent is particularly problematic in terms of surface air temperature and sea level pressure, and a storm track analysis indicated that there is slightly too much variability in the sea level pressure field in the model compared to observed, especially over the eastern Pacific in the midlatitudes.

A source of uncertainty in all GCMs stems from the use of parameterisations to represent sub-grid scale processes and this has a particularly large impact on variables related to the hydrological cycle, such as humidity and precipitation. Surface and 500 hPa specific humidities are generally too low in the model in summer and winter, and precipitation is overestimated, especially in the region of the South Pacific Convergence Zone.

An examination of the 500 hPa planetary waves showed that the model captures the phase of seasonal wave number 1, the latitudinal position of the subpolar and subtropical amplitude peaks and the relative seasonal changes in amplitude, but the amplitude of the subpolar peak is smaller than observed. The model fields, in general, are found to be more zonal than observed, which may be a consequence of the resolution of the model, such that it cannot capture all the high frequency forcings that contribute to the amplitude of the large-scale waves.

Despite the model biases that have been mentioned above, it appears that the GENESIS (ver. 2.0.a) GCM is able to capture the circulation dynamics of the present-day climate. Since the changes that occur as a result of varying sea-ice extent in the model will be a function of the dynamics, the model was judged adequate for use in the sensitivity simulations.

10.1.3 Response over the Southern Hemisphere

The sensitivity simulations showed that the atmospheric response over the Southern Hemisphere is to some degree sensitive to the positioning and magnitude of the introduced SST and sea-ice anomalies in both seasons. For example, the summer and winter control sea-ice is less expansive in 1985 compared to 1980, and similarly for the perturbation ice data sets. This difference results in the ensuing pressure anomalies in 1985 being positioned southward of those in 1980. The study has also shown that viewing the results from a zonally averaged perspective can be misleading, especially when the imposed sea-ice and SST anomalies are azonal. This is particularly the case for the winter season, where there is considerable longitudinal variation in the response for many of the variables.

In general, the response in the summer season is more zonally uniform than during winter, especially in terms of the wind and pressure data. This was ascribed to the more even distribution of sea-ice anomalies in summer, the reduced asymmetry of the sea-ice distribution around the pole in summer, and the more zonally symmetric organisation of the control pressure systems in summer compared to winter. The results for the summer season are also more consistent between the two study periods, *viz.* 1980 and 1985, compared to those for winter. Many of the inconsistencies in winter are related to differences between the two years in the magnitude and positioning of the sea-ice anomalies, differences in the positions of circulation features in the control simulations, as well as the high variability of the atmosphere during winter in middle to high latitudes. When the former two differences are taken into account, it is often found that the years respond in a similar fashion to the

perturbation. For example, the unperturbed flow is quite different in 1980 and 1985 in terms of the position of the troughs and ridges associated with wave number 3, especially south of 45°S. Therefore, in response to the perturbation, different pressure anomalies are produced relative to the controls of the two years. Upon closer examination, however, it is clear that the phases of wave number 3 in the perturbations is comparable between the two years and that the sea-ice perturbation forced the circulation towards a more similar flow pattern than existed between the control simulations.

As expected, the removal of sea-ice and the warming of the ice-free waters produces an increase in surface temperatures, and sensible and latent heat fluxes over the anomalies in both seasons. These increases are, however, much smaller in summer compared to winter. In both seasons the sea-ice perturbation causes a general lowering of sea level pressure between 50°S and 70°S, although there are high latitude regions of sea level pressure increase, especially during winter.

For summer, there is increased subsidence between 30°S and 50°S, associated with a strengthening and southward extension of the descending limb of the Hadley Cell. In contrast, in winter although there is a southward shift of the Hadley Cell over the Australian/New Zealand region, there is a northward shift of the pressure systems over the Atlantic. In both seasons, there is a tendency for increased ridging near Australia and New Zealand between 30°S and 50°S. The wind speed changes in summer and winter are in broad agreement with what would be expected from the thermal wind relationship, i.e. where there is a warm anomaly between 50°S and 70°S due to the sea-ice and SST perturbation, one would expect westerly wind anomalies over the perturbation and easterly wind anomalies to the north. As such, there tends to be an increase in 500 hPa wind speeds in middle to high latitudes (~50°S - 65°S) and a reduction in wind speeds to the north of this (~30°S - 40°S). However, for the winter season this change is less uniform and in general over the eastern Pacific there are contrasting patterns of wind speed change compared to the rest of the hemisphere.

The general pressure decrease around Antarctica is related to the response found for midlatitude cyclone densities, such that there is an increase in cyclone densities around 60°S in both seasons. North of this high latitude increase, there is a decrease in midlatitude cyclone densities. In winter, the increase in pressure in the New Zealand region between 30°S and 55°S, appears to be related to increased blocking in the perturbation simulations.

The sea-ice and SST perturbation produces a reduction in the amplitude of wave number 1 in summer and winter. It is hypothesised that this is related to the reduced asymmetry of the SST distribution around the pole in the perturbations compared to the controls. The results from the SOM investigation of the twice-daily circulation data support this finding, showing that the perturbation favours circulation types exhibiting fairly zonal and symmetrical flow between 30°S and 50°S, and especially those types that have a less prominent ridge over the central Pacific compared to the controls.

The 500 hPa height anomalies in winter are clearly related to changes in the phase and amplitude of the 500 hPa planetary waves. In particular, in both years the phase of wave number 3 shifts eastward in response to the perturbation such that the troughs of the midlatitude/subpolar (~45°S - 62°S) expression of the wave are positioned near the Weddell Sea, over the eastern Indian Ocean and east of the Ross Sea in the perturbations. The subtropical (~30°S - 45°S) expression of the wave undergoes a westward phase shift in both years, positioning the troughs slightly westward (~5°) of the higher latitude portion of the wave in the perturbations. It is suggested that the trigger for the phase change of wave number 3 is the large sea-ice perturbation over the Atlantic Ocean. These phase changes account for the increase in subsidence that is found over the Antarctic Peninsula and in the region of New Zealand.

10.1.4 Response over Southern Africa

One of the aims of the present study has been to examine the potential influence that Antarctic sea-ice extent has on the climate of southern Africa. As such, the results of both the summer and winter sea-ice and SST perturbations have been examined in more detail over this region. The variable of primary concern for the area is precipitation, but it has been shown that the GCM grid cell precipitation output by the model is unable to capture the detailed spatial patterns and steep gradients observed over South Africa and the magnitude of precipitation is too large in the model in both summer and winter. In order to circumvent this problem, the technique of downscaling has been used to derive regional scale precipitation, on a 0.5° grid, from a set of atmospheric predictors. This is an empirical approach to downscaling which initially determines a relationship between data from a set of observed atmospheric predictor variables and observed regional scale precipitation. Then, once this function has been validated, it is applied to the data from the GCM set of atmospheric variables in order to derive precipitation. It is important to note that while most of the analysis included the southern African region and adjacent oceans, the investigation of

precipitation changes considered only South Africa. The reason for this is that in many regions of southern Africa there was insufficient data for a meaningful downscaling procedure.

The downscaling procedure has shown that the pattern and magnitude of the GCM downscaled precipitation is very similar to what is observed in both seasons and is a vast improvement over the GCM grid cell precipitation. It was clearly desirable to use the downscaled fields of GCM precipitation rather than the grid cell precipitation output by the model. The results have highlighted the potential use of downscaling as a viable technique to overcome the inadequacies of GCM precipitation output at the regional scale.

For the summer season the sea-ice perturbation results in a southward extension and intensification of the South Atlantic and South Indian Anticyclones. There is an increase in the representation of days with a strong and dominant South Atlantic Anticyclone and fewer days with a deep midlatitude westerly wave over the analysis window. The increase in pressures over the Indian Ocean results in a near-surface divergence anomaly which extends westwards over the land, diminishing the surface convergence present in the controls over the north-east coast of South Africa. This is associated with a decrease in summer rainfall over the north-east coast of South Africa (between about 26°S and 29°S). There is also a narrowing of the easterly wave trough over the interior of the country, producing greater meridional flow in the region around 25°E. This causes an increase in near surface convergence north of 30°S and over the central interior of the country, and is associated with an increase in summer rainfall (around 25°E and between about 26°S and 29°S).

In the winter season, in response to the sea-ice perturbation, there is an increase in the spatial extent of the continental high pressure and an increase in pressure over much of the Indian Ocean. This results in an increase in 900 hPa divergence and 500 hPa convergence over much of the eastern half of South Africa and adjacent Indian Ocean, and appears to be associated with a decrease in the 700 hPa moisture flux. In contrast, as a result of the large sea-ice perturbation in the Weddell Sea sector causing a drop in pressures over much of the Atlantic Ocean, there is a weakening of the South Atlantic Anticyclone and a southward extension of the west coast trough. This is associated with an increase in 900 hPa convergence and 500 hPa divergence, and an increase in the 700 hPa moisture flux over the west and south coasts of the country. These results appear to cause a small increase in winter precipitation over the west coast and south-western Cape in both 1980 and 1985.

In both seasons, the precipitation response to the sea-ice perturbation is small, but the results are cohesive, physically plausible and there is a similar response in 1980 and 1985. Thus, it seems likely that a larger perturbation than that imposed in the present study would elicit a larger precipitation response over South Africa than is seen in these results. It is also important to remember that the South African response to a sea-ice perturbation may be modulated by other factors which have not been considered, for example the phase of ENSO or the QBO. Nonetheless, this preliminary study has suggested that an Antarctic sea-ice and SST anomaly has the potential to affect circulation patterns and precipitation over the South African region.

10.2 Constraints and Caveats

There are a number of limitations associated with the present study which must be taken into account when assessing the results. Perhaps the most obvious constraint is that this study has not considered the feedback from the atmosphere to the ocean and ice. "The sea-ice / atmosphere relationship is mutual and reciprocal" (Hanna, 1996, p382) and there are complex interactions involved. The present study has used prescribed sea-ice and SSTs so that the impact of the sea-ice anomalies on the climate could be studied in a controlled manner. It is important to recognise, however, that this is a simplification and that the presence of full sea-ice and ocean models could modify the results. The ocean and sea-ice may play important roles in the evolution of atmospheric anomalies, producing smaller or larger effects than are seen in the present study. For example, one of the findings of the present study was that there was an increase in the density of midlatitude cyclones at high latitudes, near 60°S, in response to the sea-ice reduction. Jacobs and Comiso (1993) suggest that there is a positive feedback between cyclone density and sea-ice extent. With greater storminess, warmer air is imported from the north-west and the winds generate local convergence and divergence in the sea-ice, such that greater shear and ridging in regions of convergence reduces the sea-ice cover (Jacobs and Comiso, 1993). The divergence of sea-ice produces larger areas of open water, increasing sensible and latent heat fluxes from the ocean, thus intensifying cyclonic activity (Jacobs and Comiso, 1993). In general, this implies that the cyclone density increase in the present study may be underestimated in a real-world situation, since, if permitted, the density increase could have caused an additional decrease in sea-ice cover, which would subsequently have caused a further increase in cyclone numbers. Thus, it is important to emphasize that the present study is not a forecast of the real climatic changes that would occur if sea-ice cover was less than normal, but is rather an initial attempt to identify key processes and the sensitivity (as opposed to a forecast) of the atmosphere to sea-ice changes. In addition, this

research has not considered the impact of changes in sea-ice concentration or thickness on the atmosphere, only changes in extent.

There are a number of caveats associated with the study in terms of the GCM used. It was clear from the validation section that, like most GCMs, the GENESIS model was unable to accurately capture all the observed dynamics and thermodynamics of the atmosphere. This is always going to be a problem with modelling studies, since by definition, a model is a simplification of reality. The question is, however, whether or not the dynamics of the model are acceptable such that the response to the perturbation simulations is representative of what could occur in reality. This topic has been discussed in Chapter 4, and although the model was deemed adequate for use in the sensitivity study, there is always the likelihood that improved model physics and parameterisations could modify the results.

In addition, the resolution of the model should be taken into account, in terms of the scale of analysis, since the reliability of model output decreases as one approaches the scale of the GCM grid cell. A limited resolution also means that a certain amount of information is lost in the model, and sub-grid scale information is not captured. A comment by Mitchell and Hills (1986) which is pertinent to the present study, is that in places the model may not have sufficient horizontal resolution to respond to the small-scale forcing from the anomaly. GCMs are also obviously restricted by the present state of knowledge of the physics of the atmosphere and interactions within the climate system, but despite their limitations, they are the most appropriate tools available to use to investigate the kinds of questions posed in the current thesis.

Finally, it has become apparent through this research that although there are a number of similarities between the results from this study and others investigating the impact of reduced Antarctic sea-ice, there are also a number of differences. These differences may be related to different sea-ice anomalies (the present study imposed less extreme sea-ice anomalies compared to previous studies) and experimental designs used, but they may also be a result of differences between the various GCMs. It is not possible at this stage to conclusively identify which of the simulated results are sensitive to the contrasting treatment of processes in GCMs, and are thus model specific. Only by increasing the number of studies performed, with different GCMs, will it be possible to determine which models are producing the most realistic response.

10.3 Recommendations

This study has examined the atmospheric response to a sea-ice perturbation embedded in the non-El Niño years of 1980 and 1985 of an AMIP configured simulation. It would be an interesting complementary study to perform similar experiments in El Niño years in order to determine whether there is a different response. Furthermore, longer simulations with reduced sea-ice, perhaps 10 years in duration, would facilitate the research of lower frequency and longer term responses to the perturbation, for example, as to whether a reduced Antarctic sea-ice extent could affect the El Niño Southern Oscillation, or the Semi-Annual Oscillation. Performing the simulations in different years would also help to resolve the variability of the atmospheric response. Similarly, it would be advantageous in future studies to use much larger ensembles of GCM simulations in order to help detect a definitive sea-ice-atmosphere signal above the noise. It would also be valuable to perform similar experiments to the present study, but varying sea-ice concentration and/or thickness. Although there have been modelling studies which have modified sea-ice concentration, the topic should be re-examined using contemporary GCMs, and should investigate a range of time-scales and variables, with an additional focus on the atmospheric response in non-polar regions.

Finally, the present study has highlighted that the atmosphere is sensitive to fairly small changes in sea-ice extent, and this reinforces the need for better sea-ice models in fully-coupled ocean-atmosphere GCMs. The IPCC (1996) notes that a common problem with coarse resolution coupled GCMs is that the sea-ice edge in the Antarctic is too far poleward. Results from the present research suggest that errors in sea-ice extent, as simulated by sea-ice models, may distort atmospheric circulation.

Antarctic sea-ice occupies a fairly remote part of the world, from an anthropogenic perspective, but, as demonstrated by the present study, it plays a crucial role in climate dynamics and variability and has the potential to affect lower latitudes. A better understanding of the contribution that the Antarctic region makes to the climate of the Southern Hemisphere is essential for improved seasonal and short term forecasting, and will aid predictions of the climatic implications of possible global warming.

REFERENCES

Ackley, S.F., 1981. A review of sea-ice weather relationships in the Southern Hemisphere. In: *Sea Level, Ice, and Climatic Change* (Proceedings of the Canberra Symposium, Dec, 1979). I. Allison, Ed. IAHS Publication No. 131, p127-159.

Ackley, S.F. and Keliher, T.E., 1976. Antarctic sea-ice dynamics and its possible climatic effects. *AIDJEX Bulletin*, **33**, 53-76.

Anderssen, E.C., 1965. A study of atmospheric long waves in the Southern Hemisphere. *Notos*, **14**, 57-65.

Barron E.J., Fawcett P.J., Peterson W.W., Pollard D., and Thompson S.L., 1995. A "simulation" of mid-Cretaceous climate. *Paleoceanography,* **10**, 953-962.

Barron E.J., Peterson W.W., Pollard D. and Thompson S.L., 1993. Past climate and the role of ocean heat transport: model simulations for the Cretaceous. *Paleoceanography,* **8**, 785-798.

Bergengren, J.C., and Thompson, S.L., 1998. Modeling the effects of global climate change on natural vegetation, Part I. The equilibrium vegetation ecology model. Submitted to Climatic Change.

Blackmon, M.L., 1976. A climatological spectral study of the 500 mb geopotential height of the Northern Hemisphere. *Journal of the Atmospheric Sciences*, **33**, 1607-1623.

Boer, G.J., McFarlane, N.A., and Lazare, M., 1992. Greenhouse gas-induced climate change simulated with the CCC second-generation general circulation model. *Journal of Climate*, **5**, 1045-1077.

Bromwich, D.H., Chen, B., and Pan, X., 1995. Intercomparison of simulated polar climates by global climate models. *Sixth Symposium on Global Climate Change*, American Meteorological Society, Dallas, Texas, January 15-20, 1995. Preprints volume (J9) p14-19.

Brundrit, G.B. and Shannon, L.V., 1989. Cape storms and the Agulhas Current: a glimpse of the future? *South African Journal of Science*, **85**, 619-620.

Budd, W.F., 1982. The role of Antarctica in southern hemisphere weather and climate. *Australian Meteorological Magazine*, **30**, 265-272.

Budd, W.F., 1991. Antarctica and global change. *Climatic Change*, **18**, 271-299.

Carleton, A.M., 1979. A synoptic climatology of satellite-observed extratropical cyclone activity for the southern hemisphere winter. *Archives for Meteorology, Geophysics and Bioclimatology, Series B.*, **27**, 265-279.

Carleton, A.M., 1981. Ice-ocean-atmosphere interactions at high southern latitudes in winter from satellite observation. *Australian Meteorological Magazine*, **29**, 183-195.

Carleton, A.M., 1988. Sea ice-atmosphere signal of the Southern Oscillation in the Weddell Sea, Antarctica. *Journal of Climate*, **1**, 379-388.

Carleton, A.M., 1989. Antarctic sea-ice relationships with indices of the atmospheric circulation of the Southern Hemisphere. *Climate Dynamics*, **3**, 207-220.

Carleton, A.M., 1992. Synoptic interactions between Antarctica and lower latitudes. *Australian Meteorological Magazine*, **40**, 129-147.

Carleton, A.M., 1995. On the interpretation and classification of mesoscale cyclones from satellite infrared imagery. *International Journal of Remote Sensing*, **16(13)**, 2457-2485.

Carleton, A.M. and Carpenter, D.A., 1990. Satellite climatology of 'polar lows' and broadscale climatic associations for the southern hemisphere. *International Journal of Climatology*, **10**, 219-246.

Cavalieri, D.J. and Parkinson, C.L., 1981. Large-scale variations in observed Antarctic sea ice extent and associated atmospheric circulation. *Monthly Weather Review*, **109**, 2323-2336.

Changnon, D., Noel, J.J. and Maze, L.H., 1995. Determining cyclone frequencies using equal-area circles. *Monthly Weather Review*, **123**, 2285-2294.

Chiu, L.S., 1983. Variation of Antarctic sea ice: an update. *Monthly Weather Review*, **111**, 578-580.

Crane, R.G. and Hewitson, B.C., 1998. Doubled CO_2 precipitation changes for the Susquehanna Basin: Downscaling from the GENESIS general circulation model. *International Journal of Climatology*, **18**, 65-76.

Crowley T.J. and Baum S.K., 1994. General circulation model study of late Carboniferous interglacial climates. *Palaeoclimates*, **1**, 3-21.

Crowley T.J., Baum S.K. and Kim K.Y., 1993. General circulation model experiments with pole-centered supercontinents. *Journal of Geophysical Research*, **98**, 8793-8800.

Crowley T.J., Yip K-J.J. and Baum S.K., 1994. Effect of altered Arctic sea ice and Greenland ice sheet cover on the climate of the GENESIS general circulation model. *Global and Planetary Change*, **9**, 275-288.

Crowley T.J., Yip K-J.J., Baum S.K. and Moore S.B., 1996. Modelling Carboniferous coal formation. *Paleoclimates* **2**, 159-177.

de la Mare, W.K., 1997. Abrupt mid-twentieth-century decline in Antarctic sea-ice extent from whaling records. *Nature*, **389**, 57-60.

Dümenil, L. and Schröder, S., 1989. The impact of an ice-free Arctic Ocean on the general circulation in winter. In: *Research Activities in Atmospheric and Oceanic Modelling*, 13, WMO/TD 332, 7.42-43, World Meteorological Organisation, Geneva.

Fletcher, J.O., Mintz, Y., Arakwa, A. and Fox, T., 1973. Numerical simulation of the influence of Arctic sea ice on climate. In: *Proceedings of the IAMAP/IAPSO/SCAR/WMO Symposium on Energy Fluxes over Polar Surfaces* (Moscow, August 1971), p181-218. WMO Tech. Note no. 129.

Foley J.A., 1994. The sensitivity of the terrestrial biosphere to climatic change: a simulation of the middle Holocene. *Global Biogeochemical Cycles,* **8**, 505-525.

Gates, W.L., 1992. AMIP: The Atmospheric Model Intercomparison Project. *Bulletin of the American Meteorological Society,* **73(12),** 1962-1970.

Gillooly, J.F. and Walker, N.D., 1984. Spatial and temporal behaviour of sea-surface temperatures in the South Atlantic. *South African Journal of Science*, **80**, 97-100.

Gloersen, P. and Campbell, W.J., 1991. Recent variations in Arctic and Antarctic sea-ice covers. *Nature*, **352**, 33-36.

Gloersen, P., Campbell, W.J., Cavalieri, D.J., Comiso, J.C., Parkinson, C.L. and Zwally, H.J., 1993. Satellite passive microwave observations and analysis of Arctic and Antarctic sea ice, 1978-1987. *Annals of Glaciology*, **17**, 149-154.

Godfred-Spenning, C.R. and Simmonds, I., 1996. An analysis of Antarctic sea-ice and extratropical cyclone associations. *International Journal of Climatology*, **16**, 1315-1332.

Gordon, A.L., 1981. Seasonality of Southern Ocean sea ice. *Journal of Geophysical Research*, **86**, 4193-4197.

Grose, W.L. and Hoskins, B.J., 1979. On the influence of orography on the large-scale atmospheric flow. *Journal of the Atmospheric Sciences*, **36**, 223-234.

Hanna, E., 1996. The role of Antarctic sea ice in global climate change. *Progress in Physical Geography*, **20**(4), 371-401.

Harrison, M.S.J., 1986. A synoptic climatology of South African rainfall variations. Unpublished Ph.D thesis, University of Witwatersrand, Johannesburg, South Africa, 341 pp.

Hartmann, D.L., 1977. Stationary planetary waves in the southern hemisphere, *Journal of Geophysical Research*, **82**, 4930-4934.

Herman, G.F. and Johnson, W.T., 1978. The sensitivity of the general circulation to Arctic sea ice boundaries: a numerical experiment. *Monthly Weather Review*, **106**, 1649-1664.

Hewitson, B.C., 1997. *A methodology for developing regional climate change scenarios from general circulation models.* Water Research Commission, Report 594/1/97, Pretoria, South Africa, 35 pp.

Hewitson, B.C., 1998. *Deriving regional climate change scenarios from general circulation models.* Water Research Commission, Report K5/806, Pretoria, South Africa, in press.

Hewitson, B.C. and Crane, R.G. (eds.), 1994. *Neural nets: Applications in geography.* Kluwer Academic Publishers, Dordrecht, The Netherlands, 194 pp.

Hewitson, B.C. and Crane, R.G., 1996. Climate downscaling: Techniques and application. *Climate Research*, **7(2)**, 85-95.

Higgins, R.W., Yao, Y-P., Chelliah, M., Ebisuzaki, W., Janowiak, J.E., Ropelewski, C.F. and Kistler, R.E., 1996. Intercomparison of the NCEP/NCAR and the NASA/DAO Reanalyses (1985-1993). U.S. Department of Commerce, National Oceanic and Atmospheric Administration, National Weather Service, NCEP/Climate Prediction Center ATLAS No. 2.

Howarth, D.A., 1983. An analysis of the variability of cyclones around Antarctica and their relationship to sea-ice extent. *Annals of the Association of American Geographers*, **73(4)**, 519-537.

Hudson, D.A., 1997. Southern African climate change simulated by the GENESIS GCM. *South African Journal of Science*, **93**(9), 389-403.

Hudson D.A. and Hewitson B.C., 1997. Midlatitude cyclones south of Africa in the GENESIS GCM. *International Journal of Climatology*, **17**, 459-473.

Hunt, B.G., Gordon, H.B., and Davies, H.L., 1995. Impact of the greenhouse effect on sea-ice characteristics and snow accumulation in the polar regions. *International Journal of Climatology*, **15**, 3-23.

Intergovernmental Panel on Climate Change (IPCC), 1990. *Climate Change, The IPCC Scientific Assessment.* J.T. Houghton, G.J. Jenkins and J.J. Ephraums, (Eds.), Cambridge University Press, Cambridge, 365 pp.

Intergovernmental Panel on Climate Change (IPCC), 1992. *Climate Change 1992, The Supplementary Report to the IPCC Scientific Assessment.* J.T. Houghton, B.A. Callander and S.K. Varney, (Eds.), Cambridge University Press, Cambridge, 200 pp.

Intergovernmental Panel on Climate Change (IPCC), 1996. *Climate Change 1995 - The Science of Climate Change: Contribution of Working Group 1 to the Second Assessment Report of the Intergovernmental Panel on Climate Change.* J.T. Houghton, L.G. Meira Filho, B.A. Callander, N. Harris, A. Kattenberg and K. Maskell, (Eds.), Cambridge University Press, Cambridge. 572 pp.

Jacobs, S.S. and Comiso, J.C., 1993. A recent sea-ice retreat west of the Antarctic peninsula. *Geophysical Research Letters,* **20(12)**, 1171-1174.

James, I.N., 1988. On the forcing of planetary-scale Rossby waves by Antarctica. *Quarterly Journal of the Royal Meteorological Society,* **114**, 619-637.

Jenkins, G., 1995. Early earth's climate: cloud feedback from reduced land fractions and ozone concentrations. *Geophysical Research Letters,* **22**, 1513-1516.

Johannessen, O.M., Miles, M., and Bjorgo. E., 1995. The Arctic's shrinking sea ice. *Nature*, **376**, 126-127.

Jones, D.A. and Simmonds, I., 1993. Time and space spectral analyses of Southern Hemisphere sea level pressure variability. *Monthly Weather Review,* **121**, 661-672.

Joubert, A.M. and Tyson, P.D., 1996. Equilibrium and coupled GCM simulations of future southern African climates. *South African Journal of Science*, **92**, 471-484.

Jury, M.R. and Pathack, B., 1991. A study of climate and weather variability over the tropical southwest Indian Ocean. *Meteorology and Atmospheric Physics*, **47**, 37-48.

Jury, M.R.; Pathack, B.; Campbell, G.; Wang, B. and Landman, W., 1991. Transient convective waves in the tropical southwest Indian Ocean. *Meteorology and Atmospheric Physics*, **47**, 27-36.

Kalnay, E., Kanamitsu, M., Kistler, R., Collins, W., Deaven, D., Gandin, L., Iredell, M., Saha, S., White, G., Woollen, J., Zhu, Y., Chelliah, M., Ebisuzaki, W., Higgins, W., Janowiak, J., Mo, K.C., Ropelewski, C., Wang, J., Leetmaa, A., Reynolds, R., Jenne, R. and Joseph, D. 1996. The NCEP/NCAR 40-year reanalysis project. *Bulletin of the American Meteorological Society*, **77(3)**, 437-471.

Kao, S.-K., Jenne, R.L. and Sagendorf, J.F., 1970. The kinetic energy of large-scale atmospheric motion in wavenumber-frequency space: 2. Mid-troposphere of the Southern Hemisphere. *Journal of the Atmospheric Sciences*, **27**, 1008-1020.

Kao, S.-K., Jenne, R.L. and Sagendorf, J.F., 1971. Wavenumber frequency spectra of the meridional transport of sensible heat in the mid-troposphere of the Southern Hemisphere. *Pure and Applied Geophysics*, **86**, 159-170.

Karoly, D.J., 1985. An atmospheric climatology of the southern hemisphere based on ten years of daily numerical analyses (1972-82): II Standing wave climatology. *Australian Meteorological Magazine*, **33**, 105-116.

Kiehl, J.T. and Williamson, D.L., 1991. Dependence of cloud amount on horizontal resolution in the National Centre for Atmospheric Research community climate model. *Journal of Geophysical Research*, **96**, 10955-10980.

King, J.C., 1994. Recent climatic variability in the vicinity of the Antarctic Peninsula. *International Journal of Climatology*, **14**, 357-369.

Kohonen, T., 1989. *Self-organization and associative memory*. Springer-Verlag, Berlin (3rd Edition).

Kohonen, T., 1990. The self-organizing map. *Proceedings of the IEEE*, **78(9)**, 1464-1480.

Kohonen, T., Hynninen, J., Kangas, J. and Laaksonen, J., 1996. SOM_PAK: The self-organizing map program package. Technical Report A31, Helsinki University of Technology, Laboratory of Computer and Information Science, Finland.

König, W., Sausen, R. and Sielmann, F., 1993. Objective identification of cyclones in GCM simulations. *Journal of Climate*, **6**, 2217-2231.

Lambert, S.J., 1988. A cyclone climatology of the Canadian Climate Center general circulation model. *Journal of Climate*, **1**, 109-115.

Ledley, T.S., 1988. For a lead-temperature feedback in climatic variation. *Geophysical Research Letters*, **15(1)**, 36-39.

Le Marshall, J.F. and Kelly, G.A.M., 1981. A January and July climatology of the Southern Hemisphere based on daily numerical analyses 1973-77. *Australian Meteorological Magazine,* **29,** 115-123.

Le Treut, H. and Kalnay, E., 1990. Comparison of observed and simulated cyclone frequency distribution as determined by an objective method. *Atmosphera.,* **3,** 57-71.

Liang, X-Z., Wang, W-C., Samel, A.N., Pollard, D. and Thompson, S.L., 1995. Systematic biases of SUNYA/NCAR AMIP simulations. Proceedings of the First International AMIP Scientific Conference, World Climate Programme Research, WCRP-92, WMO/TD-No. 732, p181-186.

Lindesay, J.A., 1988a. Southern African rainfall, the Southern Oscillation and a Southern Hemisphere semi-annual cycle. *Journal of Climatology*, **8**, 17-30.

Lindesay, J.A., 1988b. The Southern Oscillation and atmospheric circulation changes over southern Africa. Unpublished Ph.D thesis, University of Witwatersrand, Johannesburg, South Africa, 284 pp.

Lucas, M.I. and Lindesay, J.A., 1991. Global climate change: Environmental and climatic links between Antarctica and South Africa. *South African Journal of Antarctic Research*, **21(2)**, 193-219.

Main, J.P.L., 1997. Seasonality of Circulation in Southern Africa using the Kohonen Self-Organising Map. Unpublished M.Sc. Thesis, University of Cape Town, Cape Town, South Africa, 84 pp

Mason, S.J., 1990. Temporal variability of sea surface temperatures around Southern Africa: a possible forcing mechanism for the 18-year rainfall oscillation? *South African Journal of Science*, **86**, 243-252.

Mason, S.J., 1992. Sea surface temperatures and South African rainfall variability. Unpublished Ph.D. thesis, University of the Witwatersrand, Johannesburg, South Africa, 235 pp.

Mason, S.J. and Lindesay, J.A., 1993. A note on the modulation of Southern Oscillation-southern African rainfall associations with the Quasi-Biennial Oscillation. *Journal of Geophysical Research*, **98**, 8847-8850.

Mayes, P.R., 1985. Secular variations in cyclone frequencies near the Drake Passage, Southwest Atlantic. *Journal of Geophysical Research*, **90**, 5829-5939.

McFarlane, N.A., 1987. The effect of orographically excited gravity-wave drag on the circulation of the lower stratosphere and troposphere. *Journal of the Atmospheric Sciences*, **44**, 1775-1800.

Meehl, G.A., Hurrell, J.W. and van Loon, H., 1997. A Modulation of the Mechanism of the Semiannual Oscillation in the Southern Hemisphere. Studies in Climate II, NCAR Technical Note 433, p122-137.

Meehl, G.A., and Washington, W.M., 1990. CO_2 climate sensitivity and snow-sea-ice albedo parameterization in an atmospheric GCM coupled to a mixed-layer ocean model. *Climatic Change*, **16**, 283-306.

Mey, R.D., Walker, N.D. and Jury, M.R., 1990. Surface heat fluxes and marine boundary layer modification in the Agulhas Retroflection region. *Journal of Geophysical Research*, **95**, 15997-16015.

Mitchell, J.F.B. and Hills, T.S., 1986. Sea-ice and the antarctic winter circulation: A numerical experiment. *Quarterly Journal of the Royal Meteorological Society,* **112**, 953-969.

Mitchell, J.F.B. and Hills, T.S., 1987. Reply to comment by Simmonds and Dix on 'Sea-ice and the antarctic winter simulation; a numerical experiment' by J.F.B. Mitchell and T.S. Hills. *Quarterly Journal of the Royal Meteorological Society,* **113**, 1401-1403.

Mitchell, J.F.B. and Senior, C.A., 1989. The antarctic winter; simulations with climatological and reduced sea-ice extents. *Quarterly Journal of the Royal Meteorological Society,* **115**, 225-246.

Mo, K.C. and White, G.H., 1985. Teleconnections in the Southern Hemisphere. *Monthly Weather Review*, **113**, 22-37.

Murray, R.J. and Simmonds, I., 1991. A numerical scheme for tracking cyclone centres from digital data. Part 1: development of the scheme. *Australian Meteorological Magazine,* **39,** 155-166.

Murray, R.J. and Simmonds, I., 1995. Responses of climate and cyclones to reductions in Arctic winter sea ice. *Journal of Geophysical Research*, **100**, 4791-4806.

Newson, R.L., 1973. Response of a general circulation model of the atmosphere to removal of the arctic ice-cap. *Nature*, **241**, 39-40.

Openshaw, S., 1994. Neuroclassification of spatial data. In: *Neural Nets: Applications in Geography*. Hewitson, B.C. and Crane, R.G. (Eds.)., Kluwer, Dordrecht, p53-70.

Otto-Bliesner B.L., 1993. Tropical mountains and coal formation: a climate model study of the Westphalian (306 Ma). *Geophysical Research Letters,* **20**, 1947-1950.

Peixoto, J.P., and Oort, A.H., 1992. *Physics of Climate.* American Institute of Physics, New York. 520 pp.

Pollard, D., and Thompson, S.L., 1994. Sea-ice dynamics and CO_2 sensitivity in a global climate model. *Atmosphere-Ocean,* **32(2)**,449-467.

Pollard, D. and Thompson, S.L., 1995a. Users' guide to the GENESIS Global Climate Model Version 2.0. Interdisciplinary Climate Systems Section, Climate and Global Dynamics Division, National Center for Atmospheric Research, Boulder, Colorado, 93 pp.

Pollard, D. and Thompson, S.L., 1995b. Use of a land-surface-transfer scheme (LSX) in a global climate model: the response to doubling stomatal resistance. *Global and Planetary Change,* **10,** 129-161.

Preston-Whyte, R.A. and Tyson, P.D., 1988. *The atmosphere and weather of Southern Africa*. Oxford University press, Cape Town, 374 pp.

Quintanar, A.I. and Mechoso, C.R., 1995a. Quasi-stationary waves in the Southern Hemisphere. Part I: Observational Data . *Journal of Climate*, **8**, 2659-2672.

Quintanar, A.I. and Mechoso, C.R., 1995b. Quasi-stationary waves in the Southern Hemisphere. Part II: Generation Mechanisms. *Journal of Climate*, **8**, 2673-2690.

Randel, W.J., 1988. The seasonal evolution of planetary waves in the southern hemisphere stratosphere and troposphere. *Quarterly Journal of the Royal Meteorological Society,* **114**, 1385-1409.

Raymo, M.E., Rind, D. and Ruddiman, W.F., 1990. Climatic effects of reduced Arctic sea ice limits in the GISS II general circulation model. *Paleoceanography*, **5(3)**, 367-382.

Reynolds, R.W., 1988. A real-time global sea surface temperature analysis. *Journal of Climate*, **1**, 75-86.

Reynolds, R.W. and Roberts, L., 1987. A global sea surface temperature climatology from in situ, satellite and ice data. *Tropical Ocean-Atmosphere Newsletter*, **37**, 15-17. [Available from Rosentiel School of Marine and Atmospheric Science, 4600 Rickenbacker Causeway, Miami, FL 33149.]

Rogers, J.C. and van Loon, H., 1982. Spatial variability of sea level pressure and 500 mb height anomalies over the Southern Hemisphere., *Monthly Weather Review*, **110**, 1375-1392.

Royer, J.F., Planton, S. and Déqué, M., 1990. A sensitivity experiment for the removal of Arctic sea ice with the French spectral general circulation model. *Climate Dynamics*, **5**, 1-17.

Schlesinger, M.E. and Mitchell, J.F.B., 1987. Climate model simulations of the equilibrium climatic response to increased carbon dioxide. *Reviews of Geophysics*, **25**, 760-798.

Senior, C.A. and Mitchell, J.F.B., 1993. Carbon dioxide and climate: the impact of cloud parameterization. *Journal of Climate*, **6,** 393-418.

Serafini, Y.V. and Le Treut, H., 1988. Modélisation des climats extrêmes: impact sur le climat d'une fonte des glaces Arctiques. Note Interne LMD no 144, Laboratoire de Météorologie Dynamique, Paris.

Serreze, M.C., Box, J.E., Barry, R.G. and Walsh, J.E., 1993. Characteristics of Arctic synoptic activity, 1952-1989. *Meteorology and Atmospheric Physics,* **51,** 147-164.

Simmonds, I., 1981. The effect of sea-ice on a general circulation model of the Southern Hemisphere. In: *Sea Level, Ice, and Climatic Change* (Proceedings of the Canberra Symposium, Dec, 1979). I. Allison, Ed. IAHS Publication No. 131, p193-206.

Simmonds, I. and Budd, W.F., 1990. A simple parameterization of ice leads in a General Circulation Model, and the sensitivity of climate to change in Antarctic ice concentration. *Annals of Glaciology*, **14**, 266-269.

Simmonds, I. and Budd, W.F., 1991. Sensitivity of southern hemisphere circulation to leads in the Antarctic pack ice. *Quarterly Journal of the Royal Meteorological Society,* **117**, 1003-1024.

Simmonds, I. and Dix, M., 1987. Comments on paper 'Sea-ice and the Antarctic winter circulation: A numerical experiment' by J.F.B. Mitchell and T.S. Hills, 1986. *Quarterly Journal of the Royal Meteorological Society,* **113**, 1396-1401.

Simmonds, I., Dix, M., Rayner, P. and Trigg, G., 1989. Local and remote response to zonally uniform sea-surface temperature in a July general circulation model. *International Journal of Climatology*, **9**, 111-131.

Simmonds, I. and Jacka, T.H., 1995. Relationships between the interannual variability of Antarctic sea ice and the southern oscillation. *Journal of Climate*, **8**, 637-647.

Simmonds, I. and Wu, X., 1993. Cyclone behaviour response to changes in winter southern hemisphere sea-ice concentration. *Quarterly Journal of the Royal Meteorological Society*, **119**, 1121-1148.

Sinclair, M.R., 1994. An objective cyclone climatology for the southern hemisphere. *Monthly Weather Review,* **122,** 2239-2256.

Sinclair, M.R., 1995. A climatology of cyclogenesis for the southern hemisphere. *Monthly Weather Review,* **123,** 1601-1619.

Sinclair, M.R., Renwick, J.A. and Kidson, J.W., 1997. Low-frequency variability of Southern Hemisphere sea level pressure and weather system activity. *Monthly Weather Review*, **125**, 2531-2543.

Smith, R.N.B., 1990. A scheme for predicting layer clouds and their water content in a general circulation model. *Quarterly Journal of the Royal Meteorological Society*, **116,** 435-460.

Squire, V.A., 1994. Atmosphere-ice-ocean: do we really understand what is going on? In: *Antarctic science. Global concerns.* G. Hempel, Ed., Springer-Verlag, p82-89.

Stouffer, R.J., Mantle, S. and Bryan, K., 1989. Interhemispheric asymmetry in climate response to a gradual increase of atmospheric CO_2. *Nature*, **342**, 660-662.

Streten, N.A., 1983. Antarctic sea ice and related atmospheric circulation during FGGE. *Archives for Meteorology, Geophysics and Bioclimatology, Series A*, **32**, 231-246.

Streten, N.A. and Troup, A.J., 1973. A synoptic climatology of satellite observed cloud vortices over the southern hemisphere. *Quarterly Journal of the Royal Meteorological Society*, **99,** 56-72.

Taljaard, J.J., 1967. Development, distribution, and movement of cyclones and anticyclones in the southern hemisphere during the IGY. *Journal of Applied Meteorology,* **6,** 973-987.

Thompson, S.L. and Pollard, D., 1995. A global climate model (GENESIS) with a land-surface-transfer scheme (LSX). Part 1: Present-day climate. *Journal of Climate,* **8**, 732-761.

Thompson, S.L. and Pollard, D., 1997. Greenland and Antarctic mass balances for present and doubled atmospheric CO_2 from the GENESIS Version-2 Global Climate Model. *Journal of Climate,* **10**(5), 871-900.

Trenberth, K.E., 1979. Interannual variability of the 500 mb zonal mean flow in the Southern Hemisphere. *Monthly Weather Review*, **107**, 1515-1524.

Trenberth, K.E., 1980. Planetary waves at 500 mb in the Southern Hemisphere. *Monthly Weather Review*, **108**, 1378-1389.

Trenberth, K.E., 1981. Observed Southern Hemisphere eddy statistics at 500 mb: Frequency and spatial dependence. *Journal of the Atmospheric Sciences,* **38**, 2585-2605.

Trenberth, K.E., 1991. Storm tracks in the Southern Hemisphere. *Journal of the Atmospheric Sciences,* **48,** 2159-2178.

Trenberth, K.E., 1996. Coupled Climate System Modelling. In: *Climate Change. Developing Southern Hemisphere Perspectives*. Giambelluca, T.W. and Henderson-Sellers, A. (Eds.). John Wiley and Sons, Chichester. 475 pp.

Trenberth, K.E. and Mo, K.C., 1985. Blocking in the Southern Hemisphere. *Monthly Weather Review*, **113**, 3-21.

Tyson, P.D., 1984. The atmospheric modulation of extended wet and dry spells over South Africa, 1958-1978. *Journal of Climatology*, **4**, 621-635.

Van Bebber, W.J., 1882. Typische Witterungsercheinungen. *Archiv der Dt. Seewarte Hamburg*, **5**(3), 45.

Van Heerden, J., Terblanche, D.E and Schulze, G.C., 1988. The Southern Oscillation and South African summer rainfall. *Journal of Climatology*, **8**, 577-597.

Van Loon, H., 1965. A climatological study of the atmospheric circulation in the Southern Hemisphere during the IGY, Part 1: 1 July 1957 - 31 March 1958. *Journal of Applied Meteorology,* **4,** 479-491.

Van Loon, H., 1967. The half-yearly oscillations in middle and high southern latitudes and the coreless winter. *Journal of the Atmospheric Sciences*, **24**, 472-486.

Van Loon, H. and Jenne, R.L., 1972. The zonal harmonic standing waves in the Southern Hemisphere. *Journal of Geophysical Research*, **77**, 992-1003.

Von Storch, H., Zorita, E. and Cubasch, U., 1993. Downscaling of global climate Change estimates to regional scales: An application to Iberian rainfall in wintertime. *Journal of Climate*, **6**, 1161-1171.

Wadhams, P., 1994. The Antarctic sea ice cover. In: *Antarctic science. Global concerns*. G. Hempel, Ed., Springer-Verlag, p45-59.

Walker, N.D., 1990. Links between South African summer rainfall and temperature variability of the Agulhas and Benguela current systems. *Journal of Geophysical Research*, **95**, 3297-3319.

Walker, N.D. and Lindesay, J.A., 1989. Preliminary observations of oceanic influences on the February-March 1988 floods in central South Africa. *South African Journal of Science*, **85**, 164-169.

Wallace, J.M., Lim, G.-H. and Blackmon, M.L., 1988. Relationship between cyclone tracks, anticyclone tracks, and baroclinic waveguides. *Journal of the Atmospheric Sciences,* **45,** 439-462.

Warshaw, M. and Rapp, R.P., 1973. An experiment on the sensitivity of a global circulation model. *Journal of Applied Meteorology*, **12**, 43-49.

Watkins, A.B. and Simmonds, I., 1995. Sensitivity of numerical prognoses to Antarctic sea ice distribution. *Journal of Geophysical Research*, **100**, 22681-22696.

Watterson, I.G., Dix, M.R., Gordon, H.B. and McGregor, J.L., 1995. The CSIRO nine-level atmospheric general circulation model and its equilibrium present and doubled CO_2 climates. *Australian Meteorological Magazine*, **44**, 111-125.

Weatherly, J.W., Walsh, J.E. and Zwally, H.J., 1991. Antarctic sea ice variations and seasonal air temperature relationships. *Journal of Geophysical Research*, **96**, 15119-15130.

Wilks, D.S., 1995. *Statistical methods in atmospheric science*. Academic Press, San Diego, 467pp.

Willmott, C.J., Clinton, M.R. and Philpot, W.D., 1985a. Small-scale climate maps: A sensitivity analysis of some common assumptions associated with grid-point interpolation and contouring. *The American Cartographer*, **12(1),** 5-16.

Willmott, C.J., Ackleson, S.G., Davis, R.E., Feddema, J.J., Klink, K.M., Legates, D.R., O'Donnell, J. and Rowe, C.M., 1985b. Statistics for the evaluation and comparison of models. *Journal of Geophysical Research*, **90,** 8995-9005.

Willmott, C.J., Webber, S.R. and Power, H., 1996. Better statistics for the evaluation of model performance. The Association of American Geographers 92nd Annual Meeting, North Carolina, book of abstracts, p316.

Wilson, C.A. and Mitchell, J.F.B., 1987. A doubled CO_2 climate sensitivity experiment with a global climate model including a simple ocean. *Journal of Geophysical Research*, **92**, 13315-13343.

Xie, P. and Arkin, P.A., 1996. Analyses of global monthly precipitation using gauge observations, satellite estimates and numerical model predictions. *Journal of Climate*, **9**, 840-858.

Xie, P. and Arkin, P.A., 1998. Global monthly precipitation estimates from satellite-observed outgoing longwave radiation. *Journal of Climate*, **11**, 137-146.

Xie, S., Bao, C., Xue, Z, Zhang, L. and Hao, C., 1994. Interaction between Antarctic sea ice and ENSO events. *Proceedings of the NIPR Symposium on Polar Meteorology and Glaciology*, **8**, 95-110.

Young, R.E. and Houben, H., 1989. Dynamics of planetary-scale baroclinic waves during Southern Hemisphere winter. *Journal of the Atmospheric Sciences*, **46**(10), 1365-1383.

Zwally, H.J., Comiso, J.C., Parkinson, C.L., Campbell, W.J., Carsey, F.D. and Gloersen, P., 1983. Antarctic sea ice, 1973-1976: Satellite passive microwave observations. NASA Spec. Publ., SP-459.

APPENDIX A

Acronyms

AGCM	Atmospheric General Circulation Model
AMIP	Atmospheric Model Intercomparison Project
ANN	Artificial Neural Network
CAC	Climate Analysis Center (USA)
CCWR	Computer Center for Water Research (South Africa)
CDC	Climate Diagnostics Center (NOAA, USA)
COADS	Comprehensive Ocean Atmosphere Data Set
COLA	Center for Ocean, Land and Atmosphere (USA)
CPC	Climate Prediction Center (NCEP, USA)
EMC	Environmental Modeling Center (NCEP, USA)
ENSO	El Niño Southern Oscillation
EOF	Empirical Orthogonal Function
GCM	General Circulation Model
GENESIS	Global Environmental and Ecological Simulation of Interactive Systems
IPCC	Intergovernmental Panel on Climate Change
ITCZ	Intertropical Convergence Zone
LSX	Land-Surface-Transfer Scheme
MAE	Mean Absolute Error
NASA	National Aeronautics and Space Administration, USA
NCAR	National Center for Atmospheric Research, USA
NCEP	National Centers for Environmental Prediction, USA
NOAA	National Oceanic and Atmospheric Administration, USA
QBO	Quasi-Biennial Oscillation
RMSE	Root-Mean Square Error
SAHP	South Atlantic High Pressure (subtropical)
SIHP	South Indian High Pressure (subtropical)
SOI	Southern Oscillation Index
SOM	Self-Organising Map
SST	Sea Surface Temperature

APPENDIX B

Spherical Interpolation Equations

The distance ($d_{j,k}$) between two points, j and k, on a sphere is calculated using

$$\cos d_{j,k} = \sin \phi_j \sin \phi_k + \cos \phi_j \cos \phi_k \cos(\lambda_j - \lambda_k),$$

where ϕ refers to degrees latitude, and λ refers to degrees longitude.

The data points are weighted according to their distance from the grid point to be interpolated to. The weight (S_k) of data point k, for example, is obtained using the following conditional equations:

If	$d_{j,k} \le r_j/3$	then	$S_k = d_{j,k}^{-1}$
If	$r_j/3 < d_{j,k} \le r_j$	then	$S_k = \frac{27}{4r_j}\left(\frac{d_{j,k}}{r_j} - 1\right)^2$
If	$d_{j,k} > r_j$	then	$S_k = 0$

where r_j is the search radius from grid point j (point of the interpolated value), and $d_{j,k}$ is the spherical distance from grid point j to data point k.

The "directional isolation" of each data point relative to all nearby data points within the search radius and with respect to grid point j, is calculated according to the following equation:

$$T_k = \sum_{l=1}^{n_j} S_l[1 - \cos \theta_j(k,l)], \qquad l \neq k$$

where n_j represents the number of data points within the search radius, r_j , and $\theta_j(k,l)$ is the angle between nearby data points k and l, with grid point j at the apex of the angle. The angle, $\theta_j(k,l)$, is calculated from

$$\cos\theta_j(k,l) = \frac{\cos d_{k,l} - \cos d_{j,k}\cos d_{j,l}}{\sin d_{j,k}\sin d_{j,l}} \qquad l \neq k\,.$$

The final modified weights are then determined by

$$W_k = S_k{}^2\left(1 + T_k \Big/ \sum_{l=1}^{nj} S_l\right), \qquad l \neq k$$

where W_k is the weight for data point k with respect to grid point j. The data values (z_k) within the search radius are then linearly summed to obtain the interpolated value (z_j), according to the following equations:

$$\text{If} \quad d_{j,l} > \varepsilon \quad \text{then} \quad z_j = \sum_{k=1}^{nj}(W_k \times z_k) \Big/ \sum_{k=1}^{nj} W_k$$

$$\text{If} \quad d_{j,l} \leq \varepsilon \quad \text{then} \quad z_j = m^{-1}\sum_{k=1}^{m} z_k$$

where m is the number of data points within ε of grid point j. When the data points are sufficiently close to the grid point to be interpolated to (i.e. within ε of j), then the interpolated value will assume their average value. The distance ε is calculated from

$$\text{If} \quad (\max\phi_j)\,(\min\phi_j) \geq 0 \quad \text{then}$$

$$\varepsilon = 0.01\max\ \{\ (0.5\times\Delta\lambda)\ \times\ [\cos(\max\phi_j) + \cos(\min\phi_j)],\ \Delta\phi\ \}$$

$$\text{If} \quad (\max\phi_j)\,(\min\phi_j) < 0 \quad \text{then}$$

$$\varepsilon = 0.01\max\ \{\ (0.5\times\Delta\lambda)\ \times\ [\cos(\max|\phi_j|) + 1],\ \Delta\phi\ \}\,,$$

where $\max\phi_j$ and $\min\phi_j$ are the largest and smallest latitudes found among the grid points.